Bauhaus-Universität Weimar

Research Training Group 1462

Evaluation of Coupled Partial Models for the Assessment of Restraint Effects in Concrete Structures

Bewertung von gekoppelten Partialmodellen für die Beurteilung von Zwangbeanspruchungen in Betonstrukturen

DISSERTATION
zur Erlangung des akademischen Grades
Doktor-Ingenieur (Dr.-Ing.)
an der Fakultät Bauingenieurwesen
der Bauhaus-Universität Weimar

vorgelegt von
Bastian Jung
geboren am 06.08.1985
in Erfurt, Thüringen

Gutachter: Prof. Dr. Guido Morgenthal
Prof. Ph.D. Dong Xu
Prof. Dr. rer. nat. Tom Lahmer

Tag der Disputation: 01.06.2015

BAUHAUS
UNIVERSITÄTSVERLAG

Vorwort und Danksagung

Die vorliegende Arbeit entstand an der Bauhaus-Universität Weimar in den Jahren 2010 bis 2014 am Graduiertenkolleg 1462 „Bewertung gekoppelter numerischer und experimenteller Partialmodelle im Konstruktiven Ingenieurbau”. Während dieser Zeit wurde die Arbeit auch in einem dreimonatigen Aufenthalt an der Tongji University in Shanghai weiterentwickelt. Der Deutschen Forschungsgemeinschaft DFG danke ich an dieser Stelle ausdrücklich für die finanzielle Unterstützung.

Herrn Prof. Dr. Guido Morgenthal gilt mein besonderer Dank für das entgegengebrachte Vertrauen, eine solche Forschungsarbeit im Rahmen des Graduiertenkollegs zu beginnen und mit dieser vorliegenden Dissertation abzuschließen. Weiterhin bedanke ich mich bei Ihm für die Förderung, die sehr gute wissenschaftliche Betreuung der Thematik, die fachliche Diskussion der Ansätze und der Ergebnisse sowie dem weiteren Vorgehen. Insgesamt bedanke ich mich für die optimale und zielgerichtete Zusammenarbeit.

Herrn Prof. Dong Xu danke ich sehr, dass ich die Möglichkeit hatte die Tongji University in Shanghai für die wissenschaftliche Kooperation besuchen zu können. Besonders danke ich Ihm, dass ich die Dissertation dem Lehrstuhl ”Bridge Engineering” vorstellen konnte und zahlreiche fachliche Korrespondenz bekam. Weiterhin bedanke ich mich für den exzellent organisierten Forschungsaufenthalt in Shanghai.

Herrn. Prof. Dr. rer. nat. Tom Lahmer danke ich für die Übernahme des Koreferats meiner Disseration und für die vielfältigen methodischen Ansätzen zur stochastischen Analyse und die Frage der Modellqualität. Dies ermöglichte mir, die Zielstellung der Arbeit mit Ergebnissen auf Basis von quantitativen Methoden zu erarbeiten.

Den PostDocs des Graduiertenkollegs danke ich für die hilfreichen Diskussionen und Seminare, die während der Promotionszeit durchgeführt wurden. Besonderen Dank spreche ich ausdrücklich Herrn Dr.-Ing. Holger Keitel aus. Sein fachliches Wissen und die Implementierung eines universal einsatzfähigen FEM Modells haben diese Arbeit sehr hilfreich unterstützt.

Ohne die freundschaftliche Hilfe vieler Kollegen am Graduiertenkolleg sowie der Professur „Modellierung und Simulation - Konstruktion“ wäre es nicht möglich gewesen die vorliegende Arbeit zu bearbeiten. Mein besonderer Dank gilt Dr.-Ing. Hendrik Schröter, Henning Stutz, Hem Bahadur Motra und Samira Marzban.

Meinen Eltern sowie meinem Bruder Heiko und meinen Großeltern danke ich für die Unterstützung und das Ermöglichen einen solchen Weg gehen zu können. Meiner Freundin Anja danke ich herzlichst, dass sie mir immer den Rücken freigehalten hat und mich immer wieder motiviert hat die Arbeit abzuschließen.

Meinem jetzigen Vorgesetzten, Herrn Hans Hartmann (SGHG Bautechnik mbH), danke ich für die Unterstützung während der Endphase der Dissertation.

BAUHAUS
UNIVERSITÄTSVERLAG

BAUHAUS
UNIVERSITÄTSVERLAG

Contents

List of Abbreviations and Symbols **IX**

List of Figures **XIX**

List of Tables **XXIII**

1 Introduction **1**

2 Statistics, model evaluation, and reliability **5**
- 2.1 Uncertainty Analysis . . . 5
  - 2.1.1 Fundamentals of uncertainty analysis . . . 5
  - 2.1.2 Aleatoric parameter uncertainty . . . 8
  - 2.1.3 Epistemic model uncertainty . . . 9
  - 2.1.4 Total uncertainty and partial model quality . . . 15
- 2.2 Sensitivity Analysis . . . 17
- 2.3 Probabilistic material properties . . . 18
  - 2.3.1 Probability distribution . . . 18
  - 2.3.2 Probabilistic concrete material properties . . . 22
  - 2.3.3 Probabilistic reinforcing steel material properties . . . 26
- 2.4 Probabilistic loading conditions . . . 27
- 2.5 Global and partial model quality evaluation . . . 28
  - 2.5.1 Evaluation of coupled partial models . . . 28
    - 2.5.1.1 Sensitivity according to model class . . . 28
    - 2.5.1.2 Sensitivity according to model choice . . . 30
    - 2.5.1.3 Global model quality of coupled partial models . . . 30
  - 2.5.2 Partial model assessment . . . 31
  - 2.5.3 Coupling quality assessment . . . 33
- 2.6 Reliability methods . . . 35
  - 2.6.1 Full-probabilistic reliability method . . . 35
  - 2.6.2 Second-moment reliability method . . . 36
  - 2.6.3 Semi-probabilistic safety concept of Eurocode . . . 40
  - 2.6.4 Non-linear safety concept for concrete structures . . . 43

BAUHAUS
UNIVERSITÄTSVERLAG

3 Modelling aspects of restraint sensitive concrete structures 45
3.1 Material models . . . 45
3.1.1 Concrete material properties . . . 45
3.1.1.1 Classification . . . 45
3.1.1.2 Compressive strength . . . 46
3.1.1.3 Tensile strength . . . 47
3.1.1.4 Modulus of elasticity . . . 50
3.1.2 Concrete in compression . . . 52
3.1.2.1 Fracture process . . . 52
3.1.2.2 Compressive material models . . . 55
3.1.3 Concrete in tension . . . 58
3.1.4 Reinforced concrete in tension - tension stiffening . . . 62
3.1.4.1 Characteristic strains for cracking stages . . . 67
3.1.4.2 Modified steel strains . . . 70
3.1.4.3 Multi-linear material model . . . 72
3.1.4.4 Exponential function . . . 73
3.1.4.5 Effective concrete area in tension . . . 74
3.1.5 Reinforcing steel . . . 78
3.1.6 Prestressing steel . . . 80
3.2 Creep of Concrete . . . 80
3.2.1 Phenomenon and models . . . 80
3.2.2 Comparison and evaluation of creep models . . . 84
3.3 Shrinkage of Concrete . . . 86
3.3.1 Phenomenon and models . . . 86
3.3.2 Comparison and evaluation of shrinkage models . . . 87
3.4 Thermal action on concrete structures . . . 89
3.4.1 Prediction of temperature . . . 89
3.4.2 Prediction of stress levels . . . 94
3.4.3 Design recommendations . . . 95
3.4.4 Monitoring temperature in concrete structures . . . 100
3.5 Restraint effects . . . 103
3.5.1 Theory and experimental studies . . . 103
3.5.2 Cross sectional analysis . . . 107
3.5.3 Structural analysis . . . 109
3.5.4 Restraint sensitive structures . . . 114
3.5.4.1 Buildings . . . 114
3.5.4.2 Integral and semi-integral bridges . . . 115
3.6 Pile foundation . . . 123
3.6.1 Vertically loaded piles . . . 123
3.6.1.1 Single pile . . . 124
3.6.1.2 Pile group . . . 131

3.6.2 Lateral loading . . . 148
3.6.2.1 Deformation and failure mechanism . . . 148
3.6.2.2 Models for pile groups under lateral loading . . . 149

4 Simulation methods 157
4.1 Energy Method with Integral Description of the Material Behaviour . . . 157
4.2 Finite Element Method . . . 159

5 Partial model quality evaluation 161
5.1 Material modelling of reinforced concrete . . . 161
5.1.1 Cross section and material models . . . 162
5.1.2 Deterministic load-deformation behaviour . . . 164
5.1.3 Probabilistic load-deformation behaviour . . . 166
5.1.3.1 Input parameters . . . 166
5.1.3.2 Stress-strain relationship . . . 168
5.1.3.3 Load-deformation behaviour . . . 171
5.1.4 Uncertainty analysis . . . 174
5.1.4.1 Parameter uncertainty . . . 174
5.1.4.2 Model uncertainty . . . 177
5.1.4.3 Total uncertainty and model quality evaluation . . . 178
5.1.4.4 Influence of reinforcement ratio . . . 180
5.1.5 Assessment of uncertainty hypothesis . . . 183
5.2 Pile foundation models . . . 187
5.2.1 Uncertainty analysis of pile foundation models . . . 188
5.2.1.1 Stochastic input parameters . . . 188
5.2.1.2 Model uncertainty by deterministic simulation . . . 189
5.2.1.3 Parameter uncertainty by probabilistic simulation . . . 195
5.2.1.4 Total uncertainty . . . 197

6 Integrative assessment method 201
6.1 Integrative sensitivity analysis . . . 201
6.2 Integrative global model quality evaluation . . . 204
6.3 Application to semi-integral concrete bridges . . . 209
6.3.1 Geometry and Material Properties . . . 209
6.3.2 Limit states and material modelling . . . 211
6.3.3 Model classes and structural response values . . . 212
6.3.4 Results of integrative assessment method . . . 214
6.3.4.1 Sensitivity indices and local response significance factor . . . 214
6.3.4.2 Integrative sensitivity analysis . . . 222
6.3.4.3 Integrative global model quality evaluation . . . 225
6.3.4.4 Design recommendations . . . 226
6.4 Semi-integral concrete bridges neglecting foundation flexibility . . . 227
6.5 Girder bridge on bearings . . . 230

7 Conclusions **233**

8 Outlook **237**

9 Bibliography **239**

Solemn Declaration **263**

Publications of the Author **265**

Curriculum Vitae **267**

A Appendix - modelling aspects **269**
- A.1 Restraint effects . . . 269
- A.2 Pile foundation . . . 270

B Appendix - partial model quality evaluation **275**
- B.1 Evaluation of concrete material models . . . 275
  - B.1.1 Comparative study of model uncertainty . . . 275
  - B.1.2 Samples in equilibrium condition for all loading levels . . . 275
  - B.1.3 High reinforcement ratio . . . 277
  - B.1.4 Medium reinforcement ratio . . . 277
  - B.1.5 Low reinforcement ratio . . . 279
- B.2 Pile foundation . . . 280

C Appendix - integrative sensitivity analysis **285**
- C.1 Semi-integral concrete bridges . . . 285
- C.2 Semi-integral concrete bridges neglecting foundation stiffness . . . 293
- C.3 Concrete girder bridge . . . 295

BAUHAUS
UNIVERSITÄTSVERLAG

List of Abbreviations and Symbols

General abbreviations

AEMM	Age-Adjusted Effective Modulus Method
AIC	Akaike Information Criterion
BEM	Boundary Element Method
BIC	Bayesian Information Criterion
B 3	Bažant and Bajewa model
CC	plain concrete under compression
CDF	cumulative distribution function
CLM	characteristic load method
CT	plain concrete under tension
DAfStb	german: Deutscher Ausschuss für Stahlbeton, German Board for Reinforced Concrete
DIN	german: Deutsches Institut für Normung, German Institute for Standardisation
EC 2	Eurocode 2
EIM	Energy Method with Integral Description of the Material Behaviour
EMM	Effective Modulus Method
FEM	Finite Element Method
FORM	first-order reliability method
GL 2000	Gradner and Lockman model
GM	global model
HPC	high performance concrete
HSC	high strength concrete
LHS	Latin Hypercube Sampling
LN	log-normal distribution
MC 90	Model Code 1990
MC 90-99	Updated knowledge of the Model Code 1990
MC 10	Model Code 2010
MLE	maximum likelihood estimator
MSF	Model Selection Factor
N	normal distribution
NC	normal-consolidated soil
NSC	normal strength concrete
OC	over-consolidated soil
RCT	reinforced concrete under tension
PM	partial model
PMC	Probabilistic Model Code
PDF	probability density function
RP	reference period
SLS	serviceability limit state
TS	tension stiffening
ULS	ultimate limit state
bar	tensile bar
beam	flexural member
br-func	broken rational function
e-func	exponential function
lin-el	linear-elastic
mod-steel	modified steel strains
multi-lin	multi-linear function

General indices

I	uncracked stage
II	cracked stage
$_{\mathrm{accep}}$	acceptable
$_{\mathrm{sup}}$	superior
$_{\mathrm{min}}$	minimum
$_{\mathrm{max}}$	maximum
$_{\mathrm{eff}}$	effective
$_{m}$	mean value of variable
$_{v}$	vertical direction
$_{u}$	horizontal direction
$_{\mathrm{rel}}$	relative determination
$_{\mathrm{perm}}$	permissible determination

Symbols for model assessment

M	model class
MC	model choice
cov	covariance
$CV(\ldots)$	coefficient of variation
$CV_{\mathrm{mod}}^{\mathcal{M}_i}$	model uncertainty
$CV_{\mathrm{par}}^{\mathcal{M}_i}$	parameter uncertainty
$CV_{\mathrm{tot}}^{\mathcal{M}_i}$	total uncertainty
$V(\ldots)$	variance
$\mathcal{M}_i$	one specific model
$\mathcal{M}_{ref}$	reference model
$\mu^{\mathcal{M}_i}$	mean value of model response
MQ_{GM}	global model quality
$\overline{MQ}_{\mathrm{GM}}$	integrative global model quality

BAUHAUS
UNIVERSITÄTSVERLAG

MQ_{PM}	partial model quality
Prob	probability
S_i	first-order sensitivity index
S_{Ti}	total-effect sensitivity index
$\overline{S}_{Ti}^{\mathrm{M/MC}}$	integrative total-effects sensitivity index
$\mathcal{S}_Y$	local response significance factor
X	model input
Y	model output
$\epsilon_{\Delta}^{\mathcal{M}_i}$	model error with respect to reference model
$\epsilon^{\mathcal{M}_{ref}}$	error of reference model
$\sigma^{\mathcal{M}_i}$	standard deviation of model response
b	one-sided quantile value
n	position in structure
N	total number of all positions
n_{comb}	model combinations
n_{M}	random variables
$n_{\mathrm{M,red}}$	number of non-negligible random variables
Y	model response
$\overline{Y}$	mean model response

Symbols for reliability analysis

CV	coefficient of variation
CV_G	coefficient of variation for permenant action
P_d	design point
E	effect of action
$E(...)$	expected value
E_d	design value of effect of action
E_k	characteristic value of effect of action
F	action
F_d	design value of action
F_k	characteristic value of action
G	safe region
G^*	failure region
R	resistance
R_d	design value of resistance
R_k	characteristic value of resistance
X	random variable
Z	safety margin, failure criterion
b	fractile distance
$g(\mathbf{X})$	limit state function
α_E	global weighting factor of effect of loading
$\alpha_{E,i}$	inner weighting factor of effect of loading
α_R	global weighting factor of resistance
$\alpha_{R,i}$	inner weighting factor of resistance
β	reliability index
β_{min}	reliability index for fixed design point
$f_X(x)$	probability density function of random variable X
γ_F	partial safety factor for action
γ_F^G	partial safety factor for permanent action
γ_M	partial safety factor for resistance
γ_c	partial safety factor for concrete
γ_s	partial safety factor for reinforcing and prestressing steel
μ	mean value
μ_E	mean value of effect of loading
$\mu_{E,i}$	mean value of i-th effect of loading
μ_G	average value of permanent action
σ	standard deviation
σ_E	standard deviation of effect of loading
$\sigma_{E,i}$	standard deviation of i-th of effect of loading
σ_R	standard deviation of resistance
$\sigma_{R,i}$	standard deviation of i-th of resistance
p_f	probability of failure
Φ	cumulative standardised normal distribution

Symbols for concrete models

E_{c0}	tangent modulus of elasticity
E_{cm}	secant modulus of elasticity
C_c	creep compliance
J_c	total compliance
F_{ct}	concrete tension force
F_b	bond force
$F_{b,m}$	mean bond force
α_{aggre}	influence coefficient of concrete aggregates
$\alpha_{E_{cm}}$	coefficient between E_{c0} and E_{cm}
α_{fl}	coefficient for computation of concrete flexural strength
α_{sp}	coefficient for computation of concrete splitting tensile strength
α_T	thermal expansion coefficient
ϵ_{c1}	strain at mean concrete compressive strength
$\epsilon_{c,\mathrm{lim}}$	limit concrete compressive strain
$\epsilon_{c,sh}$	concrete shrinkage strain
$\epsilon_{c,\mathrm{tot}}$	total concrete strain
$\epsilon_{c,cr}$	creep strain
ϵct	concrete strain at tensile stress
φ_c	dimensionless linear creep coefficient
σ_{ct}	concrete tensile stress
τ_{bm}	mean value of bond strength
f_c	concrete compressive strength
f_{ck}	characteristic concrete compressive strength
$f_{ck,\mathrm{cyl}}$	characteristic concrete compressive strength of a cylinder
$f_{ck,\mathrm{cube}}$	characteristic concrete compressive strength of a cube

f_{ct}	axial tensile strength
f_{ctm}	average axial tensile strength
$f_{ctk,0.05}$	5% quantile of characteristic tensile strength
$f_{ctk,0.95}$	95% quantile of characteristic tensile strength
$f_{ct,\text{sp}}$	tensile splitting strength
$f_{ct,\text{fl}}$	flexural strength
f_{cm}	mean concrete compressive strength
l_s	transmission length
$l_{s,m}$	mean transmission length
$l_{s,\text{max}}$	maximum transmission length
s_r	distance between the cracks
$s_{r,m}$	mean spacing between the cracks
t	time
t_0	time of beginning of loading

Symbols for reinforcing steel models

$\varnothing_s$	bar diameter
$\epsilon_{s,m}$	mean steel strain
ϵ_s^I	reinforcement strain in uncracked concrete
ϵ_{s2}^{II}	reinforcement strain in the crack
ϵ_{sr}^I	steel strain at the point of zero slip under cracking forces reaching f_{ctm}
ϵ_{sr}^{II}	reinforcement strain at the crack under cracking forces reaching f_{ctm}
$\Delta\epsilon_{sr}$	increase of steel strain in the cracking state
$\Delta\epsilon_{s,m}$	mean increase of steel strain in the cracking state
ϵ_{sy}	reinforcement strain at yield strength
σ_s	reinforcing steel stress
σ_{sr}^I	steel stress in the crack, when first crack has formed
σ_{srn}	steel stress in the crack, when stabilised crack pattern has formed (last crack)
f_{yk}	characteristic reinforcing yielding strength
f_{tk}	characteristic reinforcing tensile strength
$\beta_{t,m}$	integration factor for the steel strain along the transmission length
β_t	integration factor for the steel strain along the mean transmission length
A_s	area of reinforcement
E_s	reinforcement modulus of elasticity
α_s	modular ratio
ρ_s	geometrical reinforcement ratio
$\rho_{s,\text{eff}}$	effective geometrical reinforcement ratio
δ	ductility factor taking into account ratio f_t/f_y

Symbols for cross section properties

A_c	area of concrete
$A_{c,\text{eff}}$	effective concrete area in tension
A_i	ideal cross-section area
A_s	area of reinforcement
A_{s1}	area of tensile reinforcement
EI	bending stiffness
I_i	ideal moment of inertia
N_r	crack normal force
$\alpha_{h_{c,\text{eff}}}$	factor determining effective depth of concrete area in tension
b	width
c	concrete cover
d	effective depth
d_1	distance cross-section edge to centroid of reinforcement
$h_{c,\text{eff}}$	effective concrete area in tension depth
ρ_s	geometrical reinforcement ratio
$\rho_{s,\text{eff}}$	effective geometrical reinforcement ratio
ω_{s1}	mechanical reinforcement ratio
x^I,x^{II}	depth of compressive zone in uncracked and cracked stage

Symbols for analysis methods

$\Pi_{\text{total}}^{\text{C}}$	total potential energy in cross-section
$\Pi_{\text{i}}^{\text{C}}$	strain energy in cross-section
$\Pi_{\text{e}}^{\text{C}}$	potential energy of external forces in cross-section
$\Pi_{\text{i}}^{\text{E}}$	strain energy in element
$\Pi_{\text{e}}^{\text{E}}$	potential energy of external forces in element
$K_{v,\text{lin}}$	linear vertical foundation stiffness
N	normal force
M_y	bending moment about y axis
M_z	bending moment about z axis
$\epsilon_x(y,z)$	axial strain in cross-section
κ_y	curvature in y direction
κ_z	curvature in z direction
$\epsilon_{c,\sigma}(t)$	stress dependent strain
$\epsilon_{c,n}(t)$	stress independent strain
$\epsilon_{c,el}(t)$	elastic strain
$\epsilon_{c,pl}(t)$	plastic strain
$\epsilon_{c,da}(t)$	damage strain
$\epsilon_{c,cr}(t)$	creep strain
$\epsilon_{c,sh}(t)$	shrinkage strain
$\epsilon_{c,el}(t)$	temperature strain
λ	slenderness ratio
λ_{col}	column slenderness ratio
l_0	effective column length
i	radius of gyration of uncracked cross-section
t	time

BAUHAUS
UNIVERSITÄTSVERLAG

u	displacement in horizontal direction
v	displacement in transverse element direction
w	displacement in vertical direction

Symbols for pile models

α_v	interaction factor
l_P	pile length
d_P	pile diameter
r_0	pile radius
h_b	soil layer depth from pile base to bedrock
n_P	number of piles in the group
n_s	elements along pile shaft
E_P	pile modulus of elasticity
A_P	pile cross-section area
E	soil modulus of elasticity
E_s	soil oedometric modulus
$F(\underline{\sigma})$	yield criterion depending on stress state
G_s	soil shear modulus
ν_s	soil *Poisson*'s ratio
φ	friction angle
φ'	effective friction angle
c	cohesion
c_u	undrained shear strength
K_0	earth pressure at rest coefficient
τ	shear stress
τ_0	shear stress at pile shaft
τ_f	cohesive strength
σ_z	vertical total stress
γ	shear strain
ρ_{dsh}	degree of soil homogeneity
$r_{m,\mathrm{s}}$	radius at which shear stress becomes negligible for single pile
$r_{m,\mathrm{g}}$	radius at which shear stress becomes negligible for pile group
r_g	influence factor of pile group behaviour for shear stress distribution
s	pile spacing
r_{ij}	pile radii between each neighbouring piles
P_t	pile cap vertical load
P_b	pile base load
P_s	pile shaft load
$U_s\left(r_{ij}, z\right)$	soil settlement field around pile
w_t	pile cap settlement
w_b	pile base settlement
w_s	pile shaft settlement
α_t	total interaction factor
α_b	base-to-base interaction factor
α_s	shaft-to-shaft interaction factor
f_{s,i,j,n_s}	shaft interaction factor
$f_{b,i,j}$	base interaction factor
α_{uf}	deflection interaction factor of fixed-headed piles
$\psi_s\left(r_{ij}, z\right)$	attenuation function for free-field soil settlement
$\psi_b\left(r_{ij}\right)$	attenuation function for soil settlement around pile base

BAUHAUS
UNIVERSITÄTSVERLAG

List of Figures

1.1 Mean deflections analysed with different models at the Palau bridge in normal and logarithmic scales [37] . . . 3

2.1 Hypothesis of relationship between model complexity and model uncertainty, based on [399] 6
2.2 Interval of equal probability for the Latin Hypercube Sampling method . . . 8
2.3 Determination of model uncertainty statistics assessed for a number of mathematical or physical experiments, based on [105] and Eq. 2.9 . . . 10
2.4 Comparison of ultimate load observed in experimental study P_{exp} with calculated load P_{calc} for over-reinforced beams in four-point bending [279], low friction (LF) and high friction (HF) condition considered for constitutive compressive concrete model, normal strength concrete (NSC), high strength concrete (HSC), fibre-reinforced high strength concrete (FRHSC), small for beam length $L = 3.60\,\text{m}$, large for beam length $L = 7.20\,\text{m}$ . . . 12
2.5 Comparisons between several prediction models and experimental test results for load-deformation behaviour of concrete slabs according to JAEGER and MARTI [192, 193], hor. axis: displacement w [mm], vert. axis: bending moment M_y [kNm] . . . 13
2.6 Left: normal distribution with different mean and variance, right: log normal distribution with zero mean and different variance, based on [285] . . . 20
2.7 Standard deviation σ_{f_c} as a function of the compressive strength f_c, assessed for 173 construction projects by TUE et al. [397] . . . 22
2.8 Coefficient of variation for material testing $CV_{f_{c,mt}}$ and for structural measurements $CV_{f_{c,str}}$ as a function of the compression strength f_c, assessed for 173 construction projects [397] . 24
2.9 Probability density function of effect of action part E and resistance part R for failure criterion $R - E < 0$, based on [299] . . . 37

3.1 Probabilistic distribution of concrete compressive strength according to EC 2 recommended for concrete grade C 25/30 . . . 46
3.2 Influence of concrete compressive strength f_{cm} on axial concrete tensile strength f_{ctm} according to MC 90 [74], REMMEL [340], *fib* Bulletin 42 [186], MC 10 [187], measurement data [186] . . . 48
3.3 Experimental data and empirical relationships between splitting, flexural and axial concrete tensile strength . . . 50
3.4 Concrete moduli of elasticity E_c as a function of compressive strength f_{cm} according to WEE et al. [404], MC 90 [74], MC 10 [187], and EC 2 [101] . . . 52
3.5 Non-linear behaviour of plain concrete measured in uniaxial compressive experiments . . . 53

3.6 Effect of specimen slenderness on concrete compressive strength for different frictional test conditions, Round-Robin testing programme RILEM TC 148-SSC [343], ACBM...Center for Advanced Cement-based Materials, DUT...Delft University of Technology, ENEL...Centro di Ricerca Idraulica e Strutturale (ENEL-Cris) Laboratories, EUT...Eindhoven University of Technology, THD...Technische Hochschule Darmstadt 55
3.7 Non-linear material models (MC 90, MC 90-99, MC 10, EC 2) of plain concrete in uniaxial compression for various concrete grades 58
3.8 Load-deformation behaviour of concrete bar under uniaxial tension, based on [179] 59
3.9 Differentiation of concrete in tension into stress-strain and stress-crack opening relation according to fictitious crack model, based on [179] 59
3.10 Several models for stress-strain and stress-crack opening relationship for concrete in tension 61
3.11 Transmission from steel to concrete for single crack, based on [185] 63
3.12 Idealised behaviour of a reinforced concrete member, based on [74] 65
3.13 Strain distribution in single crack and stabilised crack stage, based on [74] 66
3.14 Modelling of tension stiffening effect by modification of reinforcement (left side) or concrete stress-strain relationship (right side), based on [220] 67
3.15 Stress-strain tension stiffening model for modified steel strains, based on [74] 69
3.16 Behaviour of a reinforced concrete bar subjected to imposed deformation in the crack formation stage 70
3.17 Relationship between reinforcement stress σ_s (vert. axis) and strain ϵ_s (hor. axis) observed in reinforced concrete bars due to increasing axial force for various diameters and concrete strengths [162] 70
3.18 Modified stress-strain diagram of reinforcement bars considering tension stiffening, according to [126, 127, 187] 72
3.19 Stress-strain diagram of concrete under tension considering tension stiffening, models according to “e-func” [313], “multi-lin” [74, 187] 73
3.20 Reinforced concrete element subjected to combined loading of bending and normal forces, based on [220] 75
3.21 Finite Element and mechanical model between two cracks of a structural element subjected to bending and normal force, based on [220] 75
3.22 Tensile tie representing concrete contribution between cracks for flexural members, based on [185] 76
3.23 Height of the effective concrete area $h_{c,\text{eff}}$ (grey areas), based on [101, 187] 76
3.24 Accumulative crack propagation in thick structural components with concentrated reinforcement bars at the surfaces, based on [220, 268] 78
3.25 Load-deformation behaviour of thick concrete wall due to external tensile force and uniform temperature component [352], hor. axis: average reinforcing steel strain $\epsilon_{s,m}$, vert. axis: relative reinforcing steel stress σ_s 78
3.26 Effective depth $h_{c,\text{eff}}$ depending on load condition and element thickness, based on DAfStb 466 [227] 79
3.27 Stress-strain relationship of reinforcing steel, based on [187] 79
3.28 Stress-strain relationship of prestressing steel, based on [187] 80

3.29 Influence factors affecting thermal response, based on [324, 385], vertical lines 1-1, 2-2, 3-3 necessary for one-dimensional analysis 90
3.30 Validation of numerical model by FOUAD for simulation of temperature distributions, [114] 93
3.31 Vertical distribution of longitudinal thermal strain, based on [324] 94
3.32 Temperature profile according to EC 1-1-5 [104] 95
3.33 Temperature differences for concrete bridge decks according to EC 1-1-5 [104] 98
3.34 Load cases for combined loading of external load and temperature in a frame bridge, based on [11] 99
3.35 Temperature distribution of bridge deck during a hot summer day [159] 101
3.36 Temperature measurements and computed gradients of long-term monitoring of prestressed concrete girder bridge assessed by MAURER et al. [269] 103
3.37 Distinction of action on structures into direct and indirect action 104
3.38 System for analysis of restraint effects based on several design procedures, based on [389] 106
3.39 Geometry of rectangular and box-girder cross section for cross sectional analysis 108
3.40 Influence of reinforcement ratio on load-bearing behaviour of rectangular cross section with dimensions 100/50/95 in [cm] 109
3.41 Influence of reinforcement ratio on load-bearing behaviour of box girder with dimensions 220/500/210/250/20/25 in [cm] 110
3.42 Concrete slab in office building due to external load and temperature restraint, based on [85, 267] 110
3.43 Load-deformation behaviour of concrete slab due to external load q, results: DJOUAHRA [85], compared to own simulations by multi-lin model according to Sec. 3.1.4.3 111
3.44 Load-deformation behaviour of concrete slab for combined loading of external load q and temperature constant $\Delta T_{N,\text{cont}}$, results: DJOUAHRA [85], compared to own simulations by multi-lin model according to Sec. 3.1.4.3 112
3.45 Geometry and loading conditions for continuous reinforced concrete beam subjected to combined mechanical and temperature gradient loading, $\omega_{s1} = 0.10$ 112
3.46 Load-bearing behaviour of continuous reinforced concrete beam subjected to combined mechanical and temperature gradient loading, $\omega_{s1} = 0.10$ 113
3.47 Influence of reinforcement ratio ω_{s1} on degradation of restraint forces caused by temperature gradient $T_{M,\text{cool}} = -10\,\text{K}$ 113
3.48 Sensitive restraints on concrete wall/foundation and slab system 115
3.49 Different types of semi-integral bridges, bearing at the abutments, except the semi-integral bridge with a fixed point at one abutment, based on [264] 116
3.50 Semi-integral "*Viaduct Scherkondetal*" 118
3.51 Comparison of longitudinal sections for conventional superstructure with bearings and semi-integral bridge, based on [264, 366] 119
3.52 Time-dependent horizontal bridge deck displacement u due to creep, shrinkage, and thermal variations for integral bridges 120
3.53 Analysis of integral abutment bridges 121
3.54 Integral bridge "*Taxiway Bridge East 1*" at Frankfurt Airport [386] 123
3.55 Decoupling between effects due to pile shaft and pile base, based on [332] 124
3.56 Deformation mode and hypothetical pile influence variation, based on [332] 124

BAUHAUS
UNIVERSITÄTSVERLAG

3.57 Load-settlement ratio for several pile slenderness ratios based on [332] in comparison with Boundary Element Method (BEM) [17] 128
3.58 Sign convention for pile foundation with multi-layered soil stratification, based on [291] . . 128
3.59 Comparison of settlement prediction for incompressible pile in two-layer soil, $\chi_1 = 2.5$, $\chi_2 = 1.0$, Mylonakis and Gazetas [291], Poulos and Davis [320], and Valliappan et al. [400] 131
3.60 Spacing definition of similarly loaded piles, based on [334] 132
3.61 Load-settlement ratio for piles in a 3x3 rigid group, incompressible soil $\nu_s = 0.5$, $s_x = s_y = 5r_0$, $r_g = 6r_0$, model Randolph et al. [334] 135
3.62 Schematic illustration for analysis of the influence of a head-loaded source pile on an adjacent (unloaded) receiver pile in a layered soil, based on [291] 136
3.63 Sign convention for pile foundation model by Mylonakis and Gazetas [291] for vertically loaded pile groups 137
3.64 Interaction factors for piles embedded in single-layer soil for several dimensionless base stiffness Ω, based on [291] 139
3.65 Interaction factors α_s for piles in two-layer soil according to Mylonakis et al. [291] for various soil stiffness ratios E_1/E_2 and pile embedment ratios h_1/l_P, compared with Kaynia [205] and Valliappan et al. [400], $E_P/E_1 = 1000$, $\nu_s = 0.40$, $\chi_1 = 2.50$, $\chi_2 = 1.00$ for $E_1/E_2 = 1$ and $E_1/E_2 = 1/2$, $\chi_2 = 0.75$ for $E_1/E_2 = 1/4$ 140
3.66 Increase in principal stresses σ'_I, σ'_{III}, due to incremental vertical loading up to *Mohr-Coulomb* failure criterion, based on [353] 142
3.67 Imaginary plane below the pile base with corresponding subareas, based on [353] 143
3.68 Pile layout for 5x5 group with corresponding effective influence areas determined by "magical" radius r_m for corner, edge, central, and interior pile 144
3.69 Comparison between mathematical model and numerical simulation based on Rudolf [353] for 5x5 pile group, $r_{m,\mathrm{g}} = l_p$, cohesive soil, normally-consolidated, $E = 6.5\,\mathrm{MN/m^2}$, $l_P = 9.0\,\mathrm{m}$, $d_P = 0.9\,\mathrm{m}$, $s_x = s_y = 6d_P$, $K_{v,\mathrm{lin}} = 594\,\mathrm{MN/m}$ 145
3.70 Comparison between prediction models and full-scale test of a 3x3 pile group investigated by Koizumi et al. [217], models: Randolph et al. [334], Mylonakis et al. [291], Rudolf [353] 147
3.71 Pile failure mechanism of single piles and pile groups under lateral load, based on [113] . . 148
3.72 Pile failure mechanism of pile groups due to lateral translation and rotation, based on [113] 149
3.73 Definition of degree of homogeneity ρ_{dsh}, modified shear modulus G^*, and departure angle ψ, based on [331] 150

4.1 Integral formulation of stress-strain material models for Energy Method with Integral Description of the Material Behaviour (EIM), concrete material description as an example . . 157

5.1 Rectangular cross section 163
5.2 Deterministic load-deformation behaviour of rectangular cross section 165
5.3 Joint probability distribution for correlated parameters of concrete and reinforcing steel for 1000 samples 168
5.4 Joint probability distribution for uncorrelated parameters of reinforcing steel for 1000 samples169
5.5 Probabilistic σ-ϵ relationship for plain concrete under compression and tension 169

5.6 Probabilistic σ-ϵ relationship for reinforced concrete in tension, concrete models 170
5.7 Probabilistic σ-ϵ relationship for reinforced concrete in tension, modified steel strain model 170
5.8 Probabilistic load-deformation behaviour of rectangular cross section simulated by linear-elastic model "lin-el", 1000 samples 171
5.9 Probabilistic load-deformation behaviour of rectangular cross section simulated by broken rational function model "br-func", 1000 samples 172
5.10 Probabilistic load-deformation behaviour of rectangular cross section simulated by exponential function model "e-func", 1000 samples 172
5.11 Probabilistic load-deformation behaviour of rectangular cross section simulated by multi-linear model "multi-lin", 1000 samples 173
5.12 Probabilistic load-deformation behaviour of rectangular cross section simulated by modified steel strain model "mod-steel", 1000 samples 173
5.13 Load level dependency of parameter uncertainty of material models 174
5.14 Load level dependency of random input parameter sensitivity on response of "mod-steel" material model 176
5.15 Load level dependency of model uncertainty of material models 178
5.16 Load level dependency of total uncertainty and model quality of material models 179
5.17 Reinforcement ratio dependency of model quality for medium and low reinforcement ratio 181
5.18 Assessment of uncertainty hypothesis for material models of reinforced concrete, hor. axis: complexity with $I_{c,\text{lin-el}} = 4$, $I_{c,\text{br-func}} = 31$, $I_{c,\text{e-func}} = 96$, $I_{c,\text{multi-lin}} = 112$, $I_{c,\text{mod-steel}} = 114$, ver. axis: uncertainty 186
5.19 Geometry and soil conditions for pile group arrangements 187
5.20 Correlated samples between friction angle φ and soil modulus of elasticity E, and uncorrelated samples between soil *Poisson*'s ratio ν_s and soil modulus of elasticity E for pile foundation assessment, 10000 samples 189
5.21 Pile foundation stiffness prediction for linear and non-linear loading condition, RANDOLPH [334], MYLONAKIS [291], RUDOLF [353] 190
5.22 Load-bearing behaviour of pile group for different pile arrangement (2x2, 4x1) and pile spacing ($s/d = 2$, $2/d = 10$), non-linear model RUDOLF [353] 191
5.23 Dependency of stiffness or settlement response quantity for model uncertainty assessment, example: RANDOLPH et al. [334] in relation to reference model RUDOLF [353], group 2x2 (II) with $s/d_P = 2$ 192
5.24 Model uncertainty $CV_{\text{mod}}^{\mathcal{M}_i}$ for pile foundation assembly 4x1 (I) and 2x2 (II), RANDOLPH et al. [334], MYLONAKIS et al. [291], reference model RUDOLF [353] 194
5.25 Probabilistic simulation of vertical pile foundation stiffness for either elastic or non-linear models, group 4x1 (I) with $s/d_P = 2$, 10000 samples 195
5.26 Parameter uncertainty $CV_{\text{par}}^{\mathcal{M}_i}$ for pile foundation arrangement 4x1 (I) and 2x2 (II), RANDOLPH et al. [334], MYLONAKIS et al. [291], RUDOLF [353] 196
5.27 Total uncertainty $CV_{\text{tot}}^{\mathcal{M}_i}$ for pile foundation arrangement 4x1 (I) and 2x2 (II), RANDOLPH et al. [334], MYLONAKIS et al. [291], RUDOLF [353] 198
5.28 Model quality $MQ_{\text{PM}}^{\mathcal{M}_i}$ for pile foundation arrangement 4x1 (I) with pile space ratio $s/d_P = 2$, RANDOLPH et al. [334], MYLONAKIS et al. [291], RUDOLF [353] 199

6.1 Sensitivity of partial models for simply supported beam in cracked stage with constant partial model quality and local response significance . . . 203
6.2 Variable partial model quality of simply supported beam in cracked stage with partial model's sensitivity and local response significance . . . 205
6.3 Longitudinal geometry of semi-integral concrete bridges and tendon eccentricity with respect to box girder centre line (left side); isometric view of semi-integral concrete bridge and cross section geometry of the box girder and the piers (right side) . . . 210
6.4 Timeline of inner and outer loading conditions for the limit states . . . 211
6.5 Response values of semi-integral concrete bridges for assessment of load-bearing behaviour based on integrative sensitivity analysis . . . 214
6.6 Relative scatter of model predictions for each model combination, ultimate limit state, semi-integral concrete bridge with pier height $H^1 = 5\,\mathrm{m}$ . . . 214
6.7 Total-effects sensitivity index $S^{\mathrm{M},\sigma_{c2}}_{Ti,X_i}$ for concrete stresses σ_{c2} at box girder's bottom level with respect to position at superstructure (left side), and for piers's inner side at bridge axis B (right side); semi-integral concrete bridge with pier height $H^1 = 5\,\mathrm{m}$ . . . 216
6.8 Total-effects sensitivity index $S^{\mathrm{M},w}_{Ti,X_i}$ for vertical displacements w with respect to position at superstructure (left side), and bridge axis B (right side); semi-integral concrete bridge with pier height $H^1 = 5\,\mathrm{m}$ . . . 217
6.9 Local response significance factors $\mathcal{S}_Y$ for serviceability limit state and pier height $H^1 = 5\,\mathrm{m}$; concrete stress at top and bottom level: relative definition $\mathcal{S}_{\sigma_{c1,2},\mathrm{rel}}$, permissible definition $\mathcal{S}_{\sigma_{c1,2},\mathrm{perm}}$, horizontal displacements $\mathcal{S}_{u,\mathrm{rel}}$, vertical displacements $\mathcal{S}_{w,\mathrm{rel}}$ . . . 219
6.10 Local response significance factors $\mathcal{S}_Y$ for the ultimate limit state and the pier height $H^1 = 5\,\mathrm{m}$; concrete stress at top and bottom level: relative definition $\mathcal{S}_{\sigma_{c1,2},\mathrm{rel}}$, permissible definition $\mathcal{S}_{\sigma_{c1,2},\mathrm{perm}}$, horizontal displacements $\mathcal{S}_{u,\mathrm{rel}}$, vertical displacements $\mathcal{S}_{w,\mathrm{rel}}$ . . . 221
6.11 Integrative sensitivity indices $\overline{S}^{\mathrm{M},Y}_{Ti,X_i}$ for semi-integral concrete bridges with different pier heights (H^1, H^2) in serviceability limit state (SLS), 7 model classes considered, foundation flexibility additionally modelled . . . 223
6.12 Integrative sensitivity indices $\overline{S}^{\mathrm{M},Y}_{Ti,X_i}$ for semi-integral concrete bridges with different pier heights (H^1, H^2) in ultimate limit state (ULS), 7 model classes considered, foundation flexibility additionally modelled . . . 224
6.13 Sensitivity indices and local response significance factors for vertical w and horizontal u displacements with respect to positions at superstructure (left side), and bridge axis B (right side); semi-integral concrete bridge with pier height $H^1 = 5\,\mathrm{m}$ and fixed support conditions in serviceability limit state . . . 228
6.14 Integrative sensitivity indices $\overline{S}^{\mathrm{M},Y}_{Ti,X_i}$ for semi-integral concrete bridges with different pier heights (H^1, H^2) in serviceability limit state (SLS) and ultimate limit state (ULS), 6 model classes considered, foundation flexibility neglected . . . 229
6.15 Integrative sensitivity indices $\overline{S}^{\mathrm{M},Y}_{Ti,X_i}$ for concrete girder bridge in serviceability limit state (SLS) and ultimate limit state (ULS), 5 model classes . . . 230

A.1 *Mindlin* solution [280] for vertical load at a certain depth in elastic half-space, based on [315]271
A.2 Comparison between mathematical model and numerical simulation of resistance-settlement relation for single pile with various soil conditions, based on the study by RUDOLF [353, 353]272

BAUHAUS
UNIVERSITÄTSVERLAG

A.3 Comparison between mathematical model and numerical simulation based on RUDOLF [353] for 5x5 pile group, $r_{m,\text{g}} = l_p$, cohesive soil, over-consolidated, $E = 11.0\,\text{MN/m}^2$, $l_P = 18.0\,\text{m}$, $d_P = 0.9\,\text{m}$, $s_x = s_y = 6d_P$, $K_{v,\text{lin}} = 1017\,\text{MN/m}$ 273

B.1 Load level dependency of model uncertainty of material models 275
B.2 Number of samples without material failure 276
B.3 Probabilistic σ-ϵ relation for reinforced concrete in tension, concrete models until crack formation stage 277
B.4 Probabilistic σ-ϵ relation for bi-linear model of reinforcing steel 277
B.5 Deterministic load-bearing behaviour of rectangular cross-section for medium reinforcement ratio 278
B.6 Load level dependency of model and parameter uncertainty of material models for medium reinforcement ratio 278
B.7 Load level dependency of total uncertainty of material models for medium reinforcement ratio 278
B.8 Deterministic load-bearing behaviour of rectangular cross-section for low reinforcement ratio 279
B.9 Load level dependency of model and parameter uncertainty of material models for low reinforcement ratio 279
B.10 Load level dependency of total uncertainty of material models for low reinforcement ratio . 280
B.11 Model uncertainty $CV_{\text{mod}}^{\mathcal{M}_i}$ for pile foundation assembly 4x1 (I) and 2x2 (II), RANDOLPH et al. [334], MYLONAKIS et al. [291], reference model RUDOLF [353] 282
B.12 Parameter uncertainty $CV_{\text{par}}^{\mathcal{M}_i}$ for pile foundation arrangement 4x1 (I) and 2x2 (II), RANDOLPH et al. [334], MYLONAKIS et al. [291], RUDOLF [353] 283
B.13 Total uncertainty $CV_{\text{tot}}^{\mathcal{M}_i}$ for pile foundation arrangement 4x1 (I) and 2x2 (II), RANDOLPH et al. [334], MYLONAKIS et al. [291], RUDOLF [353] 284

C.1 Total-effects sensitivity index $S_{Ti,X_i}^{\text{M},\sigma_{c1}}$ for concrete stress at top level of the box girder σ_{c1} with respect to position x at superstructure (left side), and bridge pier outside at axis B (ride side) 286
C.2 Total-effects sensitivity index $S_{Ti,X_i}^{\text{M},\sigma_{c2}}$ for concrete stress at bottom level of the box girder σ_{c2} with respect to position x at superstructure (left side), and bridge pier inner side at axis B (ride side) 287
C.3 Total-effects sensitivity index $S_{Ti,X_i}^{\text{M},\sigma_{s1}}$ for reinforcement stress at top level of the box girder σ_{s1} with respect to position x at superstructure (left side), and bridge pier outside at axis B (ride side) 288
C.4 Total-effects sensitivity index $S_{Ti,X_i}^{\text{M},\sigma_{s2}}$ for reinforcement stress at bottom level of the box girder σ_{s2} with respect to position x at superstructure (left side), and bridge pier inner side at axis B (ride side) 289
C.5 Total-effects sensitivity index $S_{Ti,X_i}^{\text{M},u}$ for horizontal displacement u with respect to position x at superstructure (left side), and bridge pier at axis B (ride side) 290
C.6 Total-effects sensitivity index $S_{Ti,X_i}^{\text{M},w}$ for vertical displacement w with respect to position x at superstructure (left side), and bridge pier at axis B (ride side) 291

BAUHAUS
UNIVERSITÄTSVERLAG

List of Tables

2.2 Literature review for model/modelling uncertainty θ_{mod}, Probabilistic Model Code (PMC), Normal Strength Concrete (NSC), High Strength Concrete (HSC), normal distribution (N), log normal distribution (LN), not mentioned (n.m.), reinforcement (reinf) 16
2.3 Stochastic material properties for concrete assessed by various researches, Normal Strength Concrete (NSC), normal distribution (N), log normal distribution (LN), not mentioned (n.m.) 24
2.4 Correlation between concrete material properties 26
2.5 Stochastic material properties of reinforcing steel assessed by various research studies, normal distribution (N), log normal distribution (LN), Weibull distribution (W) 27
2.6 Correlation between reinforcement material properties 27
2.7 Stochastic characteristic of loading conditions 28
2.8 Relationship between reliability index β and probability of failure p_f, 1 year reference period, linear problem with theory of first order, [299] 38
2.9 Determination of reliability index β according to Eurocode [53, 136], ultimate limit state (ULS), serviceability limit state (SLS, irreversible), reference period (RP) 41

3.2 Effect of aggregate type on concrete modulus of elasticity 52
3.5 Values for $\beta_{t,m}$ and τ_{bm} for deformed reinforcing bars according to MC 90 [74] and MC 10 [187] 67
3.6 Determination of effective depth of concrete in tension $h_{c,\text{eff}}$ 77
3.7 Coefficients of variation [-] of prediction errors of various creep models 85
3.8 Coefficients of variation [-] of prediction errors of various shrinkage prediction models . . . 88
3.9 Thermal material properties 91
3.10 Coefficients of thermal expansion for water-cured concrete with several aggregate types [260, 322] 92
3.11 Characteristic values of temperature components according to DIN EN 1991-1-5/NA:2010-12 [139], linear gradients for asphalt surface thickness of 5 cm 97
3.12 Characteristic values of temperature components and combination factors according to LICHTE [248] (reference temperature $T_0 = 10\,^\circ\text{C}$) in comparison to DIN EN 1991-1-5/NA:2010-12 [139], 100 % equal to DIN EN 1991-1-5, linear gradients for asphalt surface thickness of 5 cm 99
3.13 Characteristic values of thermal action assessed by SOUKHOV [383] using measurement and meteorological data, $T_0 = 10\,^\circ\text{C}$ 102
3.14 Extreme temperature values of monitoring of HPC prestressed girder bridge in Germany between 05/2001-05/2004 [269] 103
3.15 Influence of restraint effect caused by support settlement depending on design procedure, based on [389] 106

3.18 Parameter study of RUDOLF [353, 354] for determining nomograms for settlement analysis of pile groups . . . 141
3.19 Pile model characteristics for vertical loading condition . . . 146
3.20 Parameters for load-deflection and moment-deflection equations [51] . . . 154

5.1 Material models considered for evaluation of prognosis model quality, abbreviations of the models are defined in first column . . . 164
5.2 Material input parameters for deterministic and probabilistic analysis, LN. . . log normal distribution, N. . . normal distribution . . . 167
5.3 Influence of reinforcement ratio on concrete material models's evaluation, load level M_y (μ) for 90 % of samples without material failure, minimum and maximum coefficients of variation shown for entire load-deformation simulation analysis . . . 182
5.4 Complexity of material models for reinforced concrete, CC...concrete in compression, CT...concrete in tension, RCT...reinforced concrete in tension SC...steel in compression, ST...steel in tension 184
5.5 Stochastic input parameters of pile and soil properties, variation information based on [68, 183, 311, 312, 310] . . . 188
5.6 Deterministic elastic prediction of vertical pile foundation stiffness for pile groups 4x1, 2x2 with pile diameter $d_P = 1.0$ m, pile length $l_P = 20$ m, and various pile space/pile diameter ratios s/d_p in comparison to single pile stiffness . . . 190

6.1 Influence of structural local position on sensitivity of partial models and global model quality analysed by integrative sensitivity analysis for a simply supported, cracked, concrete beam 207
6.2 Material properties of concrete, reinforcing steel, and prestressing steel for superstructure and piers of semi-integral concrete bridges . . . 211
6.3 Loading conditions . . . 212
6.4 Global Model Quality Evaluation based on Partial Model Quality Scenario in the Serviceability Limit State . . . 225

A.1 Material properties for sectional analysis of restraint effects . . . 269
A.2 Reinforcement area for restraint effect analysis depending on reinforcement ratio . . . 269
A.3 Soil properties considered in the study by RUDOLF [353], NC...normal-consolidated, OC...overconsolidated . . . 272
A.4 Pile spaces r_{ij} in pile group 5x5 with pile diameter $d_P = 0.9$ m for various pile space-pile diameter ratios $s/d_P = 6$ . . . 274

B.1 Pile spaces r_{ij} in pile group 4x1 with pile diameter $d_P = 1.0$ m for various pile space-pile diameter ratios s/d_P . . . 280
B.2 Pile spaces r_{ij} in pile group 2x2 with pile diameter $d_P = 1.0$ m for various pile space-pile diameter ratios s/d_P . . . 281

C.1 Integrative sensitivity indices $\overline{S}^{M,Y}_{Ti,X_i}$ for semi-integral concrete bridge with pier height $H_1 =$ 5 m in serviceability limit state (SLS) and ultimate limit state (ULS), 7 model classes considered, foundation stiffness additionally modelled . . . 292

C.2 Integrative sensitivity indices $\overline{S}_{Ti,X_i}^{M,Y}$ for semi-integral concrete bridge with pier height $H_2 =$ 10 m in serviceability limit state (SLS) and ultimate limit state (ULS), 7 model classes considered, foundation stiffness additionally modelled . . . 293

C.3 Integrative sensitivity indices $\overline{S}_{Ti,X_i}^{M,Y}$ for semi-integral concrete bridge with pier height $H_1 =$ 5 m in serviceability limit state (SLS) and ultimate limit state (ULS), 6 model classes considered, foundation stiffness neglected . . . 294

C.4 Integrative sensitivity indices $\overline{S}_{Ti,X_i}^{M,Y}$ for semi-integral concrete bridge with pier height $H_2 =$ 10 m in serviceability limit state (SLS) and ultimate limit state (ULS), 6 model classes considered, foundation stiffness neglected . . . 294

C.5 Integrative sensitivity indices $\overline{S}_{Ti,X_i}^{M,Y}$ for concrete girder bridge in serviceability limit state (SLS) and ultimate limit state (ULS) . . . 295

BAUHAUS
UNIVERSITÄTSVERLAG

1 Introduction

Numerical simulations in the field of civil engineering are common for the design process of structures and the assessment of existing buildings. Particularly, such approximation models of the “real” physical behaviour of structures are regularly applied in the case of complex systems with a high number of unknowns, geometrical and/or material non-linear behaviour, sophisticated models for the underlying phenomena, an irregular geometry of the structure, or a large number of load cases and load combinations. The behaviour of these structures is analytically difficult to determine and is approximated with numerical simulation methods especially the Finite Element Method (FEM).

By using FEM, the real structure is transferred into a numerical global model (GM, e.g. concrete bridge). In the process of designing engineering structures, several physical phenomena (e.g. material modelling, concrete shrinkage, soil models, pile foundation, interaction models) are represented by partial models (PM). These partial models are coupled together to predict the behaviour of the observed structure (GM) under different load cases and ambient conditions, such as geometric conditions, material properties, environmental, and loading conditions.

Engineers have to decide which phenomena should be considered in the global structural model. Subsequently, the engineer determines which models are suitable for computing the physical processes in order to determine the structural behaviour realistically and efficiently. This decision-making process is often made by engineering judgement based on knowledge and experience. The selection of different models is thus often qualitative. In general, a large set of other models exists, whereby the complexity and accuracy varies considerably between the models for representing different phenomena.

In most cases, the model includes some amount of inaccuracy and incompleteness. For an improved and more efficient model application, a lack of theoretical knowledge or a deliberate simplification is often introduced in the model description, which may cause some errors in the model output. In most cases, model uncertainty, also known as modelling error, gets involved in the model prognosis, which may be considered by the commonly known partial safety factors in guidelines and design textbooks. Nevertheless, consideration must be given to the fact that the partial safety factors in the design codes according to the model uncertainty consider “small” computational errors, exclusively. As an assumption for the definition of the model uncertainty's partial safety factors, the structural model is generally able to, on average, analyse the load-bearing behaviour [349]. Not considered in these safety factors are the errors due to the selection of generally inappropriate models and detailed information about the uncertainty. Furthermore, no specific information is given to model adequateness and hence such model selection is again solely based on engineering judgement.

Many global structural models are already available for different types of engineering structures. In general, the coupling between various partial models is found to be extra important for structures that cannot be decoupled into the structural components for analysis purposes. Some researchers investigate the importance and consequence of model selection in different structural engineering fields, such as:

•2012	Bažant et al. [29, 28]	analysed measured structural bridge deflections such as appeared at the Palau bridge [37, 38]; emphasised the importance of creep model choice on the structural behaviour, see Fig. 1.1,
•2011	Guo et al. [154]	discussed the importance of the consideration of certain phenomena (creep, shrinkage, cracking of concrete and corrosion) in order to determine a more accurate time-dependent reliability analysis method,
•2011	Pan et al. [307]	applied uncertainty analysis with respect to the model prediction of the long-term behaviour of long-span, prestressed, concrete, continuous, rigid-frame bridges; the main goal of this study is the computation of the difference between several numerical models in comparison to measurement data,
•2010	Barr et al. [19]	concluded that changes in prestress due to shrinkage, creep, relaxation, and elastic shortening are reasons for complicated accurate prognosis of long-term deformations of prestressed concrete bridges; comparisons between long-term measurements over three years and the modelled deformations illustrate the significance of model selection with respect to these phenomena,
•2008	Baker [15]	estimated structural damages due to extreme loadings under an earthquake event by uncertainty propagation method; this study declared the uncertainty due to the model selection process to be a significant and important component in the analysis,
•2007	Yang [414]	investigated uncertainty and sensitivity analysis of time-dependent effects due to creep and shrinkage, time-dependent axial shortening and time-dependent prestress forces in an actual concrete girder bridge,
•2001	Sanayei et al. [362]	determined the importance of the model selection using structural health monitoring data; this study concluded that model selection is a process which is affected by the interdependency between modelling error and parameter estimation.

These studies exemplify the importance of the model selection on the simulation results and corresponding conclusions. For example, the study of Bažant et al. [37, 38] emphasises the importance of the creep model choice on the model responses in comparison to the measurement on the structure, see Fig. 1.1. Consequently, the main conclusion is that the engineering decision about the consideration or negligence of different phenomena (partial models) is crucially important for the establishment of global structural models. Nevertheless, the consideration or the negligence of a certain partial model and the coupling to the other phenomena in the global model are often based on experts' opinion. The quantification of each partial model's influence on the overall structural behaviour is almost never considered in studies, such as those mentioned above. Subsequent investigations as for example reliability analysis, risk analysis, or the simulation of the load-bearing behaviour of structures, are commonly analysed for only one global model scenario of the object with underlying pre-selected partial models and model descriptions. Subsequently,

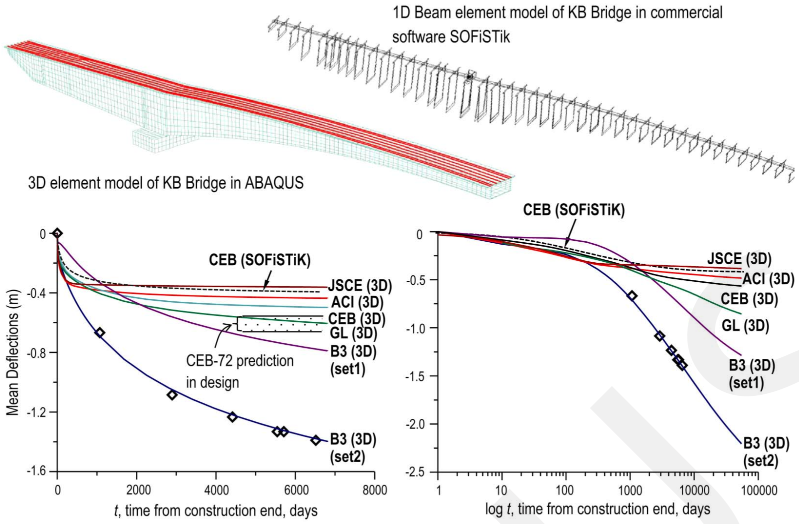

Figure 1.1: Mean deflections analysed with different models at the Palau bridge in normal and logarithmic scales [37]

some questions arise:

- For which of the several existing phenomena should the engineer take into account for a more complex and accurate model to represent the global structural model?
- When can the engineer choose simplified models or even neglect certain phenomena?
- What is the influence of a certain phenomenon in comparison with other phenomena with respect to the structural load-bearing behaviour?
- How can the uncertainty in the model prediction be reduced?
- How can the reliability of the structural design be increased?.

The qualitative model selection is not capable of recommending detailed answers to such questions. In contrast, the quantitative model evaluation developed by KEITEL et al. [210, 211], with the contribution of this thesis' author, assists the model selection process with numerical simulations in order to reduce the modelling uncertainty. The analysis of the phenomena's influence on the structural load-bearing behaviour explains the engineering selection of more accurate or simplified models based on a quantitative approach. This analysis can significantly reduce the uncertainty in the model prediction if the engineer selects partial models with high prediction quality for the more sensitive phenomena. Hence, a clear insight into the structural behaviour and the subsequent quantitative model selection can provide a more reliable approach to the structural design.

However, this quantitative evaluation method of coupled partial models only provides information on local positions of the structure. Based on the evaluation method by KEITEL et al., changing the importance of the partial models and varying corresponding partial model qualities along the structural positions results in a varying global model quality. In practical engineering problems, there is no requirement to establish various global models with the corresponding best prediction quality at a local position in the structure for the design purposes. For example, it would not be feasible for practical engineering projects to choose a certain global model with a high quality to predict a response quantity at the side span of a bridge structure and subsequently select an also high-quality but different global model to evaluate the same response quantity at the mid span. The structural engineer needs to have a global model with an acceptable overall prediction quality. But

- What are the partial models' influences with respect to the entire structure?
- What is the global structural prediction quality for the entire structure?
- Is the global model quality the lowest or highest quality of all positions?
- Is the global model quality the average of both?
- Is the global model quality the numerical integration of all qualities at each position along the structure?
- What is the significance of each position with respect to the entire structure?
- Is it possible to quantify a prediction quality with accordance to certain engineering design criteria?

These questions cannot be answered by the local position's quality assessment. Moreover, the assessment at local positions is not reasonable for non-linear physical simulations in which the global safety check is necessary, in structures that a false position identification may appear, due to complicated and interactive conditions, or for dynamic analysis of structures.

Therefore, the integrative assessment method is established here to quantitatively compute the answers for these questions. The assessment at local positions is enhanced to the integrative assessment method of the entire structural load-bearing behaviour. The integrative assessment method is applied to semi-integral concrete bridges in order to emphasise the applicability of the method for structures with interactive and complex structural components. The study about the influencing phenomena for such types of restraint sensitive structures shows that there is a lack of material models' assessment for reinforced concrete and pile foundation models. Hence, both phenomena are evaluated according to the uncertainty in the model prediction. Parametric studies under varying assumptions in the uncertainty analysis quantify significant conclusions. These partial model qualities can be subsequently considered in the assessment of the entire structure by applying the proposed integrative assessment method.

Finally, the integrative assessment method for the entire structure can automatically consider any design requirement, such as stress limitations, displacement limits, reinforcement design and others. Hence, the global model qualities quantified by this method allow for the selection of an adequate model to meet design criteria with high reliability in the model predictions. A quantitative comparison between several global structural models is then clearly feasible on the entire structural level. The integrative assessment method assists the structural engineer in the decision making process in various project's design phases. The engineer can then choose a structural model with an adequate prediction quality for the entire structure in order to obtain more reliable simulation results and finally a safer design.

This analysis illustrates where the global structural model has to use more accurate partial models and where more simplified partial models can suffice. Therefore, the integrative assessment method is a powerful methodology, which can significantly reduce the uncertainty in model predictions. The design of engineering structures in accordance with the recommendations of codes and guidelines should be performed based on the results of a global structural model with a high prediction quality in order to obtain a more reliable and safer design. Therefore, the probability of occurrence of structural damages during lifetime, which generally leads to high maintenance, repair, and refurbishment costs, can be clearly reduced. Finally, the quantitative comparison of a few global structural models can increase the confidence in the computed results and also in the entire structural design.

BAUHAUS
UNIVERSITÄTSVERLAG

2 Statistics, model evaluation, and reliability

2.1 Uncertainty Analysis

2.1.1 Fundamentals of uncertainty analysis

A computational model is a description of a phenomenon either based on physical, theoretical, or empirical investigation. Inside these models, relevant variables X_i are used as the model input variables, which are in most cases random and not deterministic variables. Therefore, the model output Y can be interpreted as:

$$Y = f\left(X_1, X_2, \ldots, X_i\right) , \tag{2.1}$$

in which $f(\ldots)$ is the model function. As a first guess, it may be obvious to assume that the model is complete and exact in the determination of the phenomenon. In the case that all variables X_i are known in a particular system of interest (e.g. determined by specific experiments), the model output is predicted without any error. This is a very optimistic and maybe naive assumption, because in most cases the model underlies some amount of inaccuracy and incompleteness mainly due to assumptions in the model abstraction process. For an improved and efficient model application, a theoretical lack of knowledge or a deliberate simplification is often introduced in the model description, which may cause some errors in the model output. Therefore, model uncertainty (modelling error) is in most cases involved in the model prognosis.

In order to evaluate how closely a model approximates the real system of interest, it is not simply a matter of comparing model results and empirical data [399]. The identification and the assessment of the uncertainties underlying a model is a necessary and helpful methodology for the development and application of engineering models. In order to design structures, the underlying uncertainties have to be considered in the simulation and design [160]. Being taken into account the model uncertainty, a more reliable model output $Y^{'}$ can be determined according to the measurement/model reference data by [105]:

$$Y^{'} = f^{'}\left(X_1, X_2, \ldots, X_i; \theta_{\mathrm{mod},1}, \theta_{\mathrm{mod},2}, \ldots, \theta_{\mathrm{mod},j}\right) , \tag{2.2}$$

in which $f'(\ldots)$ is the model function including the model uncertainties $\theta_{\mathrm{mod},j}$. These quantities are parameters representing the model uncertainties that can be treated as random variables.

In general, the uncertainty in a model output is caused by aleatoric (parameter randomness $X_1 \ldots X_i$) and epistemic (model errors $\theta_{\mathrm{mod},1} \ldots \theta_{\mathrm{mod},j}$) uncertainties, see Fig. 2.1. Increase in the complexity in the model description can reduce model uncertainty, because the accuracy is increased in describing the "real" phenomenon (e.g. material behaviour). However, if more model input parameters are needed for the analysis of sophisticated model with high model complexity, greater parameter uncertainty will arise due to imprecision and randomness in the input parameters.

The most adequate model is the model with acceptable model uncertainty and suitable parameter uncertainty. For the evaluation of the model output, both uncertainty sources can be investigated by combining both into the total uncertainty of the model prognosis, see Fig. 2.1. Finally, the assessment of model, parameter, and total uncertainty results in the quantification of model quality of the prediction and subsequently assists model selection based on a quantitative approach. Hence, the most adequate model should be used for structural analysis, design, reliability assessment, and any other purposes. In various research studies, several terminologies are used for the uncertainty description which are listed as follows:

- **epistemic uncertainty** afterwards referred to as **model uncertainty** and
  also referred to as:
    - reducible uncertainty
    - subjective uncertainty
    - intrinsic uncertainty
    - state-of-knowledge uncertainty
    - systematic error
- **aleatoric uncertainty** afterwards referred to as **parameter uncertainty**.
  also referred to as:
    - variability
    - irreducible uncertainty
    - inherent uncertainty
    - stochastic uncertainty

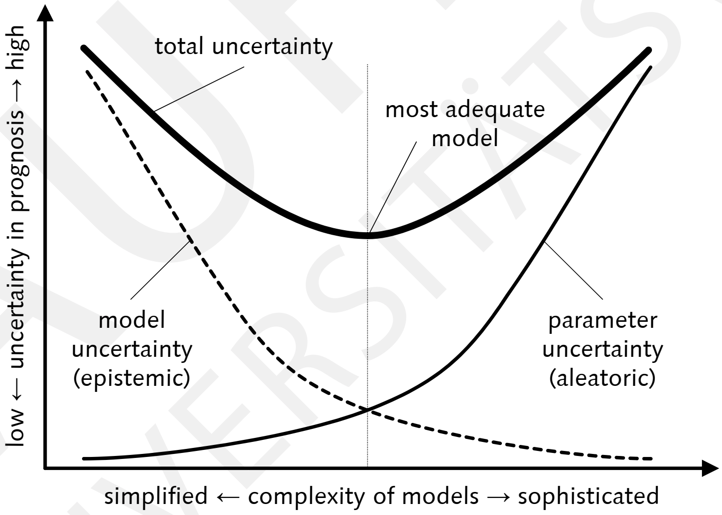

Figure 2.1: Hypothesis of relationship between model complexity and model uncertainty, based on [399]

The parameter uncertainty is caused by the inherent uncertainty of model input parameters, such as material properties, geometric dimensions, or empirically determined parameters. The comparison between the deterministic model output and the "reality" is commonly determined by experimental measurements. Such experimental studies can be similarly seen as a model description, called physical model, with underlying measurement uncertainties. Nevertheless, experimental data are generally used for the comparison between mathematical and physical models, which usually leads to a discrepancy between results from both modelling techniques.

This source of uncertainty in the mathematical model description is assessed in the model uncertainty, which is quantified in the conceptual error of the model caused by simplification or even by lack of knowledge about the "real" physical phenomenon. The validation of a model is the study of whether a model representing a physical phenomenon predicts the actual physical phenomenon with sufficient accuracy [12]. The use of experimental measurements is a regularly used method for analysing the discrepancy between model predictions and experimental studies.

There are a lot of engineering fields and applications where researchers and engineers state the substantial and crucial importance of uncertainty assessment of numerical simulations. For example, the uncertainty analysis is applied to hydrological, hydraulic and environmental models [406], groundwater models [121], reliability and risk analyses [88, 109, 293], road safety assessment [168] and large-scale physics-based simulations [309]. The results may affect the decision-making in these various engineering issues.

In a study by Riley [345], an overview of existing uncertainty quantification methods is presented. The *Bayes*'ian model averaging approach [241], the adjustment factor approach [423], and the modified adjustment factor approach [346] are all commonly used methods. The limited availability of experimental data points for approaches, such as the *Bayes*'ian model averaging, is clearly recognisable in the preliminary design phase of engineering structures. Therefore, the adjustment factor approach is reasonable to use for uncertainty analysis without specific experimental data. This method introduces in the response of a certain model $Y^{\mathcal{M}_i}$ a sort of additive E_a^* "adjustment" directly on the prediction of a reference model $Y^{\mathcal{M}_{\text{ref}}}$ in order to account for the uncertainty associated with it [423]:

$$Y^{\mathcal{M}_i} = Y^{\mathcal{M}_{\text{ref}}} + E_a^* \,. \tag{2.3}$$

Only one source of uncertainty, which is the model uncertainty, is included in this approach. Using the concept of additive model framework uncertainty, Most [286] enhanced this approach by additionally taking into account the parameter uncertainty. Assuming an additive total uncertainty, the output of a single model is approximated by:

$$Y^{\mathcal{M}_i^*} \approx Y^{\mathcal{M}_i} + \epsilon_{\Delta}^{\mathcal{M}_i} + \epsilon^{\mathcal{M}_{\text{ref}}}, \tag{2.4}$$

where $\epsilon_{\Delta}^{\mathcal{M}_i}$ is the model uncertainty with respect to the reference model. The error of the reference model itself is defined as $\epsilon^{\mathcal{M}_{\text{ref}}}$ and is assumed to be a constant additive term for each model [286]. Therefore, the knowledge about the exact value of the reference model error is not necessary.

If the differentiation between the complexity of the models cannot be evaluated in a clear theoretical argumentation (e.g. which model considers which physical phenomena in which complexity), the evidence theory initiated by Dempster [80] and developed by Shafer [376] can be used for the uncertainty assessment with the extension by Park and Grandhi [309].

The most adequate model with the highest prediction quality is the model with the lowest total uncertainty. This model should be subsequently used in structural engineering studies in order to achieve a greater confidence in the simulation results and finally to ensure a reliable structural design. The quantification of the model quality using the uncertainty analysis with the adjustment factor approach [286], presented in this section, is suitable for the assessment in the range of the mean values of the input parameters. Furthermore, theoretical studies, as published by Kiureghian [216], have to be conducted for a reliability analysis. Because of the significant influence of the distribution type and the bias of the total uncertainty due to the failure probability, the assumptions with respect to the model uncertainty should be redefined

BAUHAUS
UNIVERSITÄTSVERLAG

in order to quantify model quality in the failure regions.

2.1.2 Aleatoric parameter uncertainty

A mathematical closed-form solution for the analysis of the probabilistic characteristics of a system of interest is rarely feasible and therefore computational algorithms are necessary. This method relies on a repeated random sampling of the input variables in order to simulate the results of the models (input - output relationship for each sample). The Monte Carlo method is still a commonly applied strategy in order to obtain random input parameters and associated simulation results. Nevertheless, extensive computational effort is necessary for the computation of the randomness for large structures, many input parameters, time-dependent analysis, reliability analysis of structures and for non-linear responses in the models.
In order to improve sampling precision and decrease the required sample size in a probabilistic simulation, the Latin Hypercube Sampling (LHS) is investigated by MacKay [254]. This algorithm is an effective sampling method that enables a reliable approximation of the stochastic properties even for a small number of samples and high dimensional random variables. Further development of this method by Iman [184] improves the accurate consideration of correlation between input parameters. As a first step, each input variable is subdivided into K non-overlapping intervals on the basis of equal probability. Therefore, the probability in each interval is $1/K$ and the algorithm provides that only one sample x_i^k (k actual sample of sample size K) is considered in the analysis of the model output, see Fig. 2.2. The centroid in each interval can be assumed to be a representative value of the sample in the case that the number of intervals K is greater than the number of variables N.

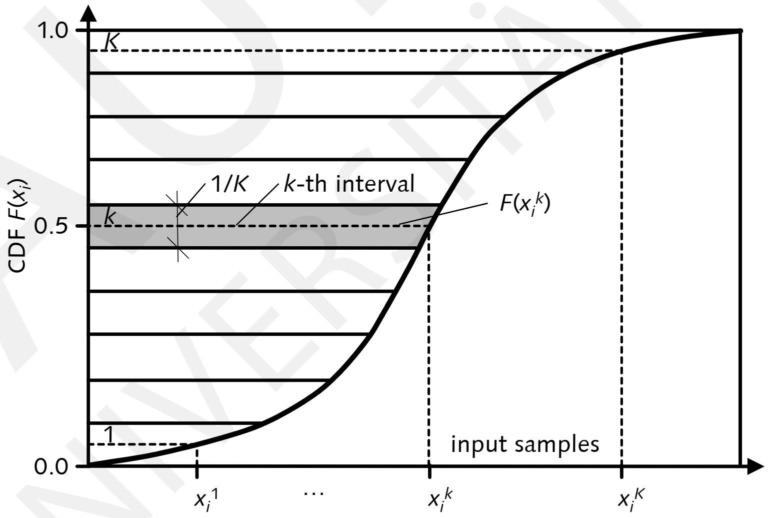

Figure 2.2: Interval of equal probability for the Latin Hypercube Sampling method

In order to consider the adequate probabilistic characteristics of the underlying distribution functions, it is necessary to couple the input variables x_i^k with tables of random permutations of rank number. Therefore, a matrix of K rows and N columns is computed for the random input parameters. Moreover, the efficiency and accuracy of the LHS sampling methodology is independent of the dimensions of the random vectors, which have to be considered in the analysis of the model. In conclusion, the main advantage of this computational algorithm is to significantly reduce the number of required simulations in probabilistic analyses with the same accuracy compared to Monte Carlo simulation.

In general, the parameter uncertainty is quantified by the variance in the model output of each model caused by its underlying probabilistic input parameters. The aleatoric parameter uncertainty of each model $\mathcal{M}_i$ is computed by the quotient of the standard deviation $\sigma^{\mathcal{M}_i}_{\text{par},Y}$ and the mean value $\mu^{\mathcal{M}_i}$, which leads to the dimensionless coefficient of variation $CV^{\mathcal{M}_i}_{\text{par},Y}$. Therefore, the mean value of the model output Y for K number of samples is defined as:

$$\overline{Y} = \frac{1}{K}\sum_{k=1}^{K} Y^k \,, \tag{2.5}$$

the standard deviation of the model output:

$$\sigma^{\mathcal{M}_i}_{\text{par},Y} = \frac{1}{K-1}\sum_{k=1}^{K}\left(Y^k - \overline{Y}\right)^2 \,, \tag{2.6}$$

and the coefficient of variation:

$$CV^{\mathcal{M}_i}_{\text{par},Y} = \frac{\sigma^{\mathcal{M}_i}_{\text{par},Y}}{\mu^{\mathcal{M}_i}} \,. \tag{2.7}$$

The standard deviation of a model output is often used as a scatter indicator to compare different models. This strategy penalises models that computes, for the same coefficient of variation, a higher mean model output, because the standard deviation is automatically raised. High differences in the mean model output occurs for example in the comparison between linear and non-linear models. Thus, for the model evaluation, the coefficient of variation is applied in this thesis in order to evaluate the models in a dimensionless strategy.

2.1.3 Epistemic model uncertainty

Experimental and monitoring data as reference

A common approach for the assessment of model uncertainty is concerned with the comparison between the prognosis of the mathematical (computational) model with either physical (experimental) data or some more sophisticated model, which is supposed to be a more accurate representation of the phenomenon. In comparative studies between model predictions and the reference (experiment, sophisticated model), probabilistic characteristics can be assessed for the model uncertainties, see Fig. 2.3. Quantifying the difference between mathematical and physical models in such a way that the computational model predicts accurately, on average, the test results, determines the mean value of the model uncertainty. Therefore, the model uncertainty random variable $\theta_{\text{mod},\mathcal{M}_i}$ for each model $\mathcal{M}_i$ can be determined by [63, 105]:

$$\theta_{\text{mod},\mathcal{M}_i} = \frac{Y_{\text{meas/ref}}}{Y_{\mathcal{M}_i}} \quad \text{or} \quad \theta_{\text{mod}} = \frac{Y_{\text{meas/ref}}}{\left[\sum_{i=1}^{n_{\mathcal{M}_i}} Y_{\mathcal{M}_i}\right]/n_{\mathcal{M}_i}} \,, \tag{2.8}$$

in which $Y_{\text{meas/ref}}$ in the output of the measurement or the reference model and $Y_{\mathcal{M}_i}$ is the response of the actual considered model. These uncertainties account for random effects that are neglected in the models due to simplifications in the mathematical description.

A very large set of representative laboratory and monitoring data on real structures where all input parameters X_i, describing the load effects, environmental conditions, and the material's resistances, are measured or controlled is the ideal situation for quantifying the model uncertainties. In such a case that all parameters and conditions are known, then the model uncertainty has the nature of an intrinsic uncertainty [105]. In

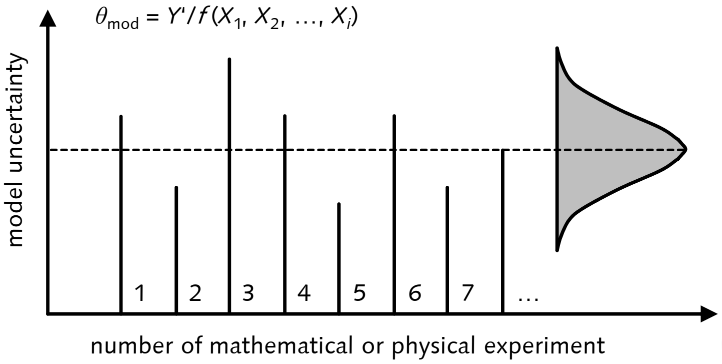
$\theta_{\text{mod}} = Y'/f(X_1, X_2, \ldots, X_i)$
model uncertainty
1
2
3
4
5
6
7
...
number of mathematical or physical experiment

Figure 2.3: Determination of model uncertainty statistics assessed for a number of mathematical or physical experiments, based on [105] and Eq. 2.9

contrast, a limited number of available measurements for a specific system of interest can cause a large statistical uncertainty. Moreover, in the measurements itself, an additional source of uncertainty is included which affects both the input parameters and the output variables.

Therefore, an adequate set of measurements is often absent and a purely statistical evaluation of model uncertainties is limited. In probabilistic analysis, such as reliability assessment, the properties of the model uncertainties are commonly based on engineering judgement. In the Probabilistic Model Code (PMC) [105], the comparison of several model predictions is stated to be reasonable in order to assist the decision making process under model uncertainties. A frequently applied method for considering this uncertainty into the computational model, see Fig. 2.3, is:

$$Y' = \theta_{\text{mod}} f\left(X_1, X_2, \ldots, X_i\right) . \tag{2.9}$$

For models defined in design guidelines such as Eurocode 2 (EC 2) or Model Code 2010 (MC 10), the mean value of model uncertainty can be larger than unity, due to the inherent conservative description of such models. In the case that measurement data are used, applications of measured properties rather than nominal or characteristic values are preferred in calculating the model prognosis. Nevertheless, computational models such as the Finite Element models implicate advantages in comparison to physical experiments, since the former allows a well-controlled input definition [105]. In general, the modelling uncertainties may be subdivided into:

• load models	variability in a structural component, between several structural components of the same structure, between various structures,
• load effect simulation models	linear-elastic, non-linear analysis of strains, stresses, section forces in elements, considerations of connections, imperfections, etc.,
• local stiffness and resistance models	description of element behaviour, material modelling, hardening and softening, thermal properties.

A summary of assumptions with respect to the consideration of model uncertainties, which depend on the types of structural members or the physical phenomenon, is listed in Tab. 2.2. A normal distribution is extensively applied for the description of randomness of model uncertainty. In most cases, these determinations are usually based on engineering judgement and can only be seen as estimations if no further information is available. For example, the output of Finite Element models are the basis for the judgement based on the

Probabilistic Model Code (PMC). But what does a Finite Element model mean? No further information is available to clarify the underlying model characteristics, such as material description, long-term behaviour, load conditions, loading level, constraint conditions, and so on.

Model uncertainty studies on concrete elements

Based on the Round-Robin test project on strain-softening behaviour of concrete in uniaxial compression, see Sec. 3.1.2, a second Round-Robin test programme of highly reinforced concrete beams (over-reinforced) is investigated under four-point bending. The failure of the concrete elements is caused by the failure in compression. The rectangular beams are tested at Aalborg University in Denmark in 1996 including 4 different types of beams [279]:

• normal strength concrete (NSC)	$f_{cm} \approx 23\,\mathrm{MN/m^2}$	$L = 3.60\,\mathrm{m},\ h = 0.20\,\mathrm{m},\ b = 0.1\,\mathrm{m}$ $L = 7.20\,\mathrm{m},\ h = 0.40\,\mathrm{m},\ b = 0.2\,\mathrm{m}$
• high strength concrete (HSC)	$f_{cm} \approx 118\,\mathrm{MN/m^2}$	$L = 3.60\,\mathrm{m},\ h = 0.20\,\mathrm{m},\ b = 0.1\,\mathrm{m}$
• fibre-reinforced HSC (FRHSC)	$f_{cm} \approx 114\,\mathrm{MN/m^2}$	$L = 3.60\,\mathrm{m},\ h = 0.20\,\mathrm{m},\ b = 0.1\,\mathrm{m}$

where each type is tested three times. Each beam is highly reinforced with the same reinforcement ratio of about $\omega_{s1} = 7.3\,\%$. The compressive zone is unreinforced in the midsection between external loads in order to force and localise compressive failure. Based on the test results including the material properteris and experimental conditions, researchers are intially invited to this research project to investigate numerical models. Finally, seven research institutions contributed to this study. The outcome of this study is presented by van Mier and Ulfkjær [279] with comparisons between the numerical predictions and the experimental results obtained from maximum external load, ductility, and size effect. The models used to compare the experimental results are all based on numerical methods and are shortly introduced:

• König et al.	[223]	different constitutive models over certain parts of compressive zone, identification for ranges of constitutive models necessary
• Légeron et al.	[243]	curvature integration method (CIM, computation of depth of neural axis for a certain curvature from equilibrium considerations) or simplified Finite Element Method (SFEM, multilayer beam elements, plane sections are assumed to remain plane)
• Bascoul et al.	[21]	Finite Element Method with multilayered short elements, strain in reinforcement as same as surrounding concrete, successive equilibrium states
• Kang et al.	[201]	fibre beam elements, half of beam is modelled using four elements only
• Ožbolt et al.	[306]	3D- Finite Element Model, 8-node solid elements, microplane model as constitutive law, only one fourth is modelled, and
• Kotsovos	[231]	3D- Finite Element Model, 27-node brick elements, steel is modelled by means of line elements without transversal stiffness.

The comparison between the ultimate load observed in the experimental study P_{exp} with the calculated load P_{calc} based on the previously introduced models is shown in Fig. 2.4. All analyses, except results of Kotsovos (maximum concrete compressive strain is limited), are within 15 % of the measured maximum load. In studies by Bascoul et al. [21] and König et al. [223], low and high friction concrete properties (from uniaxial compressive tests) are analysed. In general, low friction prognoses always underestimate the experimental maximum load by up to 15 %. In contrast, high friction material properties lead to overestimation of up to 16 %. Perhaps the truth lies somewhere in between as van Mier et al. suggest [279]. This extensive experimental and numerical research project is used in the assessment of model uncertainty by Schlune et al. [370], see Tab. 2.2.

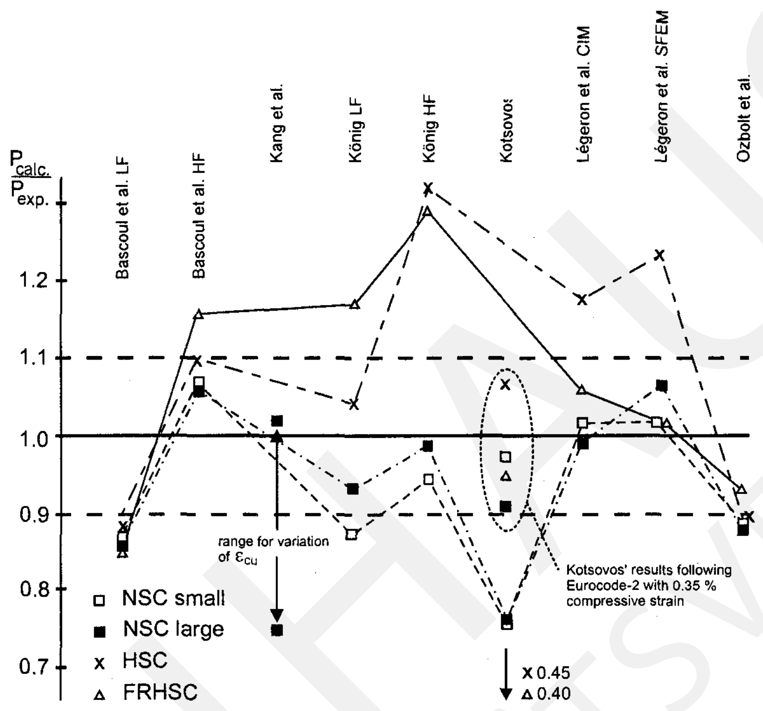

Figure 2.4: Comparison of ultimate load observed in experimental study P_{exp} with calculated load P_{calc} for over-reinforced beams in four-point bending [279], low friction (LF) and high friction (HF) condition considered for constitutive compressive concrete model, normal strength concrete (NSC), high strength concrete (HSC), fibre-reinforced high strength concrete (FRHSC), small for beam length $L = 3.60\,\mathrm{m}$, large for beam length $L = 7.20\,\mathrm{m}$

In the project "Sustainable Bridges - Assessment for Future Traffic Demands and Longer Lives" [63], various research studies are assessed and summarised in order to accurately account for the modelling error in the simulation of bridges in particular. The modelling errors for bridge members in bending and shear are listed in Tab. 2.2.

For the prediction of shear capacity of reinforced concrete beams, Somo and Hong [382] quantify the model uncertainty of commonly applied models. In total, the database contains 1146 test beams subjected to point loads and uniformly distributed loads in which detailed information for the shear capacity prognosis is available. Models according to the American Concrete Institute, the Canadian Standard Association, modified compression field theory, and shear friction methods are used for the statistical evaluation of model uncertainty, see Tab. 2.2. The ratio computation between the experimental test results and the predictions evaluates the model uncertainty.

For beams without stirrups, the recommendations of the design codes significantly underestimate the shear capacity and therefore the mean value is about $\mu_{\theta_{\mathrm{mod}}} \approx 1.6$ and $CV_{\theta_{\mathrm{mod}}} \approx 0.6$. The prognosis of shear capacity for RC beams with stirrups is more reliable and leads to $\mu_{\theta_{\mathrm{mod}}} \approx 1.2$ and $CV_{\theta_{\mathrm{mod}}} \approx 0.3$. This model uncertainty is assessed for all shear span-to-depth ratios (a/d) which are tested in the database. For ratios

BAUHAUS
UNIVERSITÄTSVERLAG

$a/d > 2$, a reduced uncertainty is analysed and the accuracy of the prognosis models is increased.

Large-scale shear/bending tests on reinforced concrete slabs are performed in 2002 and 2003 at the Institute of Structural Engineering at the Swiss Federal Institute of Technology in Zurich [193]. Afterwards, an international study for the prediction of the expected load-deformation response of the test specimens is motivated by JAEGER and MARTI, which leads finally to contributions by BELLETTI at al. (University of Parma), BENTZ and COLLINS (University of Toronto), BUTSCHER and VILL (Vienna University of Technology), CERVENKA and PRYL (Cervenka Consulting, Praha), CHE and VECCHIO (Dalian University of Technology and University of Toronto), FOSTER (University of New South Wales, Sydney), KOLLEGER (Vienna University of Technology), and SUSETYO and VECCHIO (University of Toronto) [192].

The evaluation of the experimental results and the computational models pronounced once again the modelling challenge of the non-linear behaviour of reinforced concrete, which still poses significant problems even for experienced researchers using both simplified (moment-curvature relationship) or complex models (Finite Element analysis), see Fig. 2.5. The application of relatively simple hand calculations can still be highly justified in the case that they are judiciously used, which may provide predictions that are comparable to those obtained from more complex numerical simulations. For some tests, a failure due to flexural fracture mechanism with plastic strains in the reinforcement is observed and for slabs without shear reinforcement, a shear fracture process occurs.

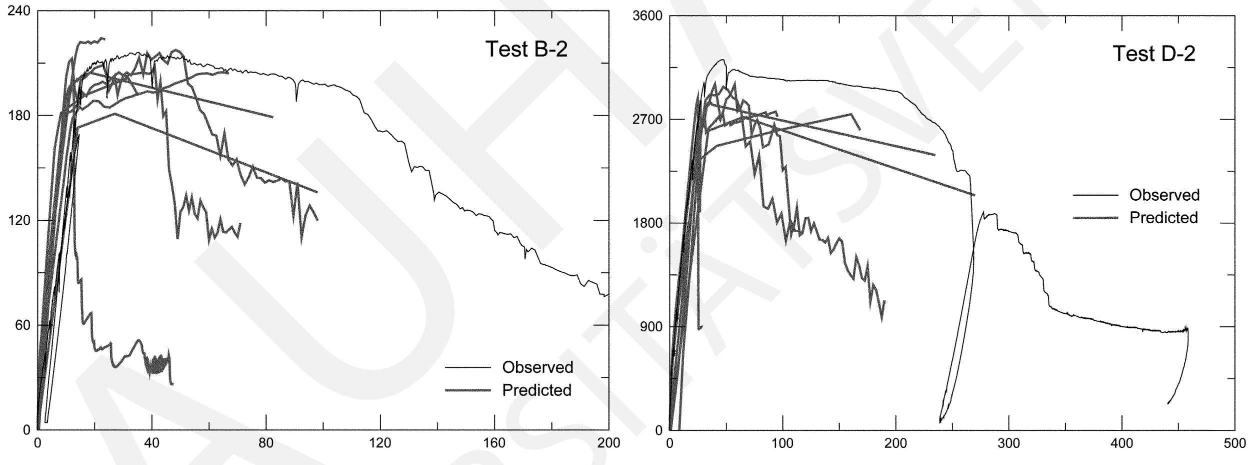

(a) $h = 20$ cm, 0°, with shear reinforcement

(b) $h = 50$ cm, 0°, with shear reinforcement

Figure 2.5: Comparisons between several prediction models and experimental test results for load-deformation behaviour of concrete slabs according to JAEGER and MARTI [192, 193], hor. axis: displacement w [mm], vert. axis: bending moment M_y [kNm]

In the modelling uncertainty study by SCHLUNE et al. [370], the discrepancy between the model predictions for slabs with shear failure is much higher $0.24 \leq CV_{\theta_{\text{mod}}} \leq 0.34$ in comparison to slabs with bending failure $0.03 \leq CV_{\theta_{\text{mod}}} \leq 0.11$, see Tab. 2.2. Moreover, the behaviour of slender slabs ($h = 20$ cm) can be modelled more accurately in comparison to compact slabs ($h = 50$ cm). In the case that the bending reinforcement is not aligned with the principal bending moment direction, the models overestimate the maximum failure load observed in the experiment. Nevertheless, this model uncertainty assessment is based exclusively on the maximum admissible external load. The load-deformation curve in the post-peak and pre-peak range is not considered, which may be significant.

All information about the research studies according to the assessment of model/modelling uncertainty is listed in Tab. 2.2. For beams in bending, a variation of the model uncertainty is quantified in the range of

BAUHAUS
UNIVERSITÄTSVERLAG

$0.06 \leq CV_{\theta_{\text{mod}}} \leq 0.25$. In the case that plastic strains occur in the reinforcement (ductile failure mechanism design), the model uncertainty is low. Compressive failure in beams (over-reinforced beams) leads to a higher model uncertainty and intermediate values are reasonable. Moreover, high strength concrete beams with a high amount of reinforcement lead to the highest model uncertainty in the above mentioned range. Shifting the angle of reinforcement away from the direction of principal moments in concrete slabs leads to an average discrepancy between the models considered in comparison to the experimental results. This can be taken into account in the average value of the model uncertainty by a quantity of about $0.9 \leq \mu_{\theta_{\text{mod}}} \leq 1.1$.
The prediction of shear capacity for concrete beams and slabs is subjected to higher model uncertainties in the range of $0.10 \leq CV_{\theta_{\text{mod}}} \leq 0.35$. Structures with plastic strains in the failure condition lead to a better agreement and a model uncertainty in the lower range could be applied for the simulation. Failure due to concrete crushing in small structures without combined loading conditions leads to an uncertainty in the middle of the above mentioned range. Combined compressive and shear loadings for large structures cause the highest model uncertainties. Shear capacity analysis may considerably overestimate the measured test results, which lead to a mean model uncertainty of about $0.7 \leq \mu_{\theta_{\text{mod}}} \leq 1.0$.
Despite the studies presented here, the data to quantify model uncertainty of non-linear analysis are scarce and might be neither representative nor conclusive. The model uncertainty generally depends on the chosen model description approach and solution technique. Therefore, these model uncertainties vary in a wide range. Until more research is assessed that allows the model uncertainty to be quantified more accurately, the choice of the model uncertainty is often dependent on engineering judgement and can be subjective. However, it might be better to choose a conscious and reasonable model uncertainty than assuming a coefficient of variation of $CV_{\theta_{\text{mod}}} = 2.5 \dots 5.0$ for all kinds of non-linear models independent of shear or bending failure mechanism, as is considered in design codes such as the Eurocode 2.

Most complex model as reference

According to the estimation of model uncertainty in a specific system of interest, a certain model can be used as the reference model $\mathcal{M}_{\text{ref}}$ in order to evaluate the differences in the several predictions. Different models' output is caused by the lack of knowledge of the simplified models in relation to the most complex model considered in the evaluation. Experimental data could be used for this purpose as previously discussed, but usually in the design process of engineering structures, no specific measurement data exist. Therefore, the most complex model can be set as a benchmark. By using the model with the highest complexity, it is safe to assume that the accuracy of the description of the physical phenomena should also be the highest. The model uncertainty of the other more simplified models $\mathcal{M}_i$ is defined as [286]:

$$V\left(\epsilon_{\Delta}^{\mathcal{M}_i}\right) \approx b^2 \left(\overline{Y}^{\mathcal{M}_i} - \overline{Y}^{\mathcal{M}_{\text{ref}}}\right)^2 , \tag{2.10a}$$

$$CV\left(\epsilon_{\Delta}^{\mathcal{M}_i}\right) = CV_{\text{mod},Y}^{\mathcal{M}_i} \approx \frac{b \cdot \left(\overline{Y}^{\mathcal{M}_i} - \overline{Y}^{\mathcal{M}_{\text{ref}}}\right)}{\overline{Y}^{\mathcal{M}_{\text{ref}}}} . \tag{2.10b}$$

This model uncertainty is computed using the mean responses of the models $\overline{Y}$. The absolute differences between the reference model and the more simplified models are the basis for determining the model uncertainty [286]. The variance of the model uncertainty is unknown and therefore it is necessary to make an assumption about the form of the underlying distribution in order to obtain a valid confidence level. In engineering applications, a reasonable assumption is that the underlying distribution is normal, because many simulation results encountered in practice can be well approximated by this distribution type [285].

A moderate divergence from normality will have little effect on the validity of this assumption. Based on this assumption, the factor b in Eq. 2.10a can be chosen in correspondence to a certain one-sided quantile value (confidence boundaries defined by percentage points $t_{\alpha,\nu}$):

$$97.5\% \rightarrow \qquad b = 1/t_{0.025,\infty} = 1/1.960 \qquad = 0.510\,, \tag{2.11a}$$
$$95.0\% \rightarrow \qquad b = 1/t_{0.050,\infty} = 1/1.645 \qquad = 0.608\,, \tag{2.11b}$$
$$90.0\% \rightarrow \qquad b = 1/t_{0.100,\infty} = 1/1.282 \qquad = 0.780\,. \tag{2.11c}$$

2.1.4 Total uncertainty and partial model quality

The total variance of a certain model considering the variance of the model output, the model uncertainty, and the variance of the error of the reference model itself is approximately [286]:

$$\underbrace{V(Y^{\mathcal{M}_i^*})}_{CV^{\mathcal{M}_i}_{\text{tot},Y}} \approx \underbrace{V(Y^{\mathcal{M}_i})}_{CV^{\mathcal{M}_i}_{\text{par},Y}} + \underbrace{b^2(\overline{Y}^{\mathcal{M}_i} - \overline{Y}^{\mathcal{M}_{ref}})^2}_{CV^{\mathcal{M}_i}_{\text{mod}}} + \underbrace{V(\epsilon^{\mathcal{M}_{ref}})}_{\text{not considered}} \;. \tag{2.12}$$

The variance of the most complex model itself is additive to each individual model. Therefore, the exact value is not crucially important for the assessment of several models and is consequently not further addressed in this thesis. The total uncertainty, defined as the variance (dimensional criteria) mentioned above, is redefined to the dimensionless coefficient of variation by:

$$CV^{\mathcal{M}_i}_{\text{tot},Y} = \sqrt{{CV^{\mathcal{M}_i}_{\text{par},Y}}^2 + {CV^{\mathcal{M}_i}_{\text{mod},Y}}^2}\,. \tag{2.13}$$

This restatement from the dimensional expression of the uncertainty to the dimensionless indication enables a more precise quantification with respect to the relative model responses. Otherwise, the dimensional uncertainty is related to the magnitude of the model output. The most adequate model of all the models considered is the one with the smallest sum of the model and parameter uncertainty. This leads to the following definition of the model quality based on the corresponding total uncertainty:

$$MQ^{\mathcal{M}_i}_{\text{PM},Y} = 1 - CV^{\mathcal{M}_i}_{\text{tot},Y}\,. \tag{2.14}$$

For high total uncertainties $CV^{\mathcal{M}_i}_{\text{tot}} > 1.0$, the model quality for each partial model can also be related to the minimum total uncertainty of all models considered based on the study by Keitel [206] by:

$$MQ^{\mathcal{M}_i}_{\text{PM},Y} = \frac{\text{MIN}\left[CV^{\mathcal{M}}_{\text{tot},Y}\right]}{CV^{\mathcal{M}_i}_{\text{tot},Y}}\,. \tag{2.15}$$

Consequently, the application of this relative definition of the prediction quality $MQ^{\mathcal{M}_i}_{\text{PM},Y}$ is no longer a clear statistical expression of the uncertainty. Therefore, Eq. 2.14 is applied in this thesis for the evaluation of the partial model quality based on the total uncertainty, see Sec. 5.1 for the evaluation of material models for reinforced concrete and Sec. 5.2 for the assessment of pile foundation models.

BAUHAUS
UNIVERSITÄTSVERLAG

Table 2.2: Literature review for model/modelling uncertainty θ_{mod}, Probabilistic Model Code (PMC), Normal Strength Concrete (NSC), High Strength Concrete (HSC), normal distribution (N), log normal distribution (LN), not mentioned (n.m.), reinforcement (reinf)

Literature		Member/ Phenomenon	$f_X(x)$	$\mu_{\theta_{\text{mod}}}$ [-]	$CV_{\theta_{\text{mod}}}$ [-]
PMC, load effect simulation	[105]	moments in frames	LN	1.00	0.10
		axial forces in frames	LN	1.00	0.05
		shear forces in frames	LN	1.00	0.10
		moments in plates	LN	1.00	0.20
		forces in plates	LN	1.00	0.10
Caspeele et al.	[64]	load effect uncertainties	LN	1.0	0.10
PMC, local stiffness and resistance	[105]	bending moment capacity	LN	1.20	0.15
		shear capacity	LN	1.40	0.25
		connection capacity	LN	1.00	0.10
Casas et al.	[63]	reinforced/prestressed concrete, bending	N	1.02	0.06
		reinforced/prestressed concrete, shear with reinf.	N	1.07	0.10
		reinforced/prestressed concrete, shear without reinf.	N	1.20	0.10
EC 2-1-1	[101]	steel	N	1.0	0.025
		concrete	N	1.0	0.050
Schlune et al. van Mier et al.	[370] [279]	small beam, compressive failure, NSC,	n.m.	0.93	0.10
		large beam, compressive failure, NSC,	n.m.	0.94	0.11
		beam with compressive failure, HSC	n.m.	1.02	0.25
Schlune et al.	[370]	flexural member	LN	1.0	0.05
Allaix et al.	[5]	continuous RC beam	LN	1.1	0.07
		slender column, combined loading	LN	1.2	0.15
Caspeele et al.	[64]	beam in bending	LN	1.2	0.15
		column in compression	LN	1.0	0.10
Somo et al.	[382]	RC beams, shear failure, with stirrups	LN	1.24	0.32
		RC beams, shear failure, without stirrups	LN	1.63	0.58
Schlune et al. Jaeger et al.	[370] [192] [193]	slab, $h = 20$ cm, 45°, no shear reinf.	n.m.	0.79	0.27
		slab, $h = 20$ cm, 45°, with shear reinf.	n.m.	0.89	0.09
		slab, $h = 20$ cm, 0°, no shear reinf.	n.m.	1.00	0.24
		slab, $h = 20$ cm, 0°, with shear reinf., Fig. 2.5(a)	n.m.	1.04	0.05
		slab, $h = 50$ cm, 45°, no shear reinf.	n.m.	0.72	0.34
		slab, $h = 50$ cm, 45° , with shear reinf.	n.m.	0.89	0.11
		slab, $h = 50$ cm, 0°, no shear reinf.	n.m.	0.97	0.29
		slab, $h = 50$ cm, 0°, with shear reinf., Fig. 2.5(b)	n.m.	1.12	0.03

BAUHAUS
UNIVERSITÄTSVERLAG

2.2 Sensitivity Analysis

The uncertainty analysis quantifies the variance in the model prediction caused by the scatter in the model input parameters and the discrepancy between the models assessed in comparison to experimental data or the most complex model of the considered ones. In contrast, the sensitivity analysis investigates how the uncertainty (variance) in the model response can be related to the model input parameters [360]. Therefore, the sensitivity analysis allows the quantification of the influence of each probabilistic model input parameter with respect to the model output. This analysis quantifies which parameters are influential or can be seen as deterministic values, because their variance does not affect the model output variance.

Several methods are available in order to compute the sensitivity indices, such as partial derivatives, scatter-plots, Elementary Effects Method, Variance-based Methods, or Factor Mapping and Metamodelling. These methods can be distinguished by several criteria such as how these methods can consider non-linearity in the model output or interactions between the input parameters, and what is the number of possible input parameters or the number of simulation runs.

The Elementary Effects Method can analyse computationally demanding models and still compute sensitivity values with a relatively small number of accurately distributed sample points and a small number of model runs [360]. This method is effective at identifying the few important parameters in a model that contains several parameters, especially in the case when the number of input parameters is too large to apply computationally demanding variance-based methods.

Variance-based methods compute the sensitivity indices by decomposing the model output's variance. These methods are independent of the model characteristics (linear, non-linear), and able to handle full range of input factor variation; they can compute interaction effects between the input parameters among the pure sensitivity values of each individual parameter. The main disadvantage of the variance-based measures is their computational effort. Further information about variance based sensitivity indices, such as first-order, total-effects, and higher-order indices, is discussed in Sec. 2.5.

Consequent to the computational effort of variance-based sensitivity analysis, researchers aim to develop efficient numerical algorithms such as Factor Mapping and Metamodelling. Such methods transfer the computational model, such as a finite element model of a structure, into a mathematical description of different functions or arbitrary shaped areas or even volumes. Therefore, a relatively small number of simulations in the original computational model is performed in order to obtain the necessary data points for developing the mathematical model. Subsequently, the sensitivity analysis is computed based on the mathematical model, which is much faster and more efficient than the computational effort of the original model. Attention should be paid to the approximation error introduced by this transformation between both models.

In accordance with SALTELLI et al. [360, 361], the selection of an adequate sensitivity analysis depends on:

- the computational effort of computing the model,
- the number of input parameters,
- the model characteristics (e.g. non-linearity),
- the consideration of interactions between the model input parameters, and
- the motivation for the analysis and its target.

In the computation of a sensitivity analysis, the input parameters are mostly assumed to be independent. Experiments on model input parameters such as material characteristics, see Sec 2.3, show in many cases a certain correlation between the input parameters. Hence, some methods are limited to uncorrelated parameters. In the study by Xu and Gertner [413], the variance in the model output is subdivided into correlated and uncorrelated parameter contributions. This subdivision is analysed using regression-based methodology. Therefore, the total uncertainty in the model output can be quantitatively decomposed into partial variances consisting of correlated variations and uncorrelated variations. A high reliability of this method is assessed for the case where the relationship between input parameters and model output is approximately linear. Nevertheless, this method may also be applicable for non-linear models depending on the degree of non-linearity. This method is applied to the evaluation of material models for reinforced concrete, see Sec. 5.1.

2.3 Probabilistic material properties

2.3.1 Probability distribution

A random experiment is a procedure in which the outcome differs even though it is repeated in the same manner every time. The possible outcome of the random experiment is the sample space. A random variable, denoted by an uppercase letter X, is a function that assigns a real number to each outcome in the sample space of a random experiment. Obtaining the results of an experiment, the measured value of the random variable is denoted by a lowercase letter x. A discrete random variable (or discrete sample space) is a random variable with a finite (or countably infinite) range [285]. In contrast, a continuous random variable (or continuous sample space) is a random variable with an interval (either finite or infinite) of real numbers for its range. The probability distribution assigns a probability to each measurable subset of the possible outcomes of a random experiment. Experiments whose sample space are encoded by discrete random variables can be specified by a probability mass function. Continuous random variables can be specified by a probability density function. For a discrete random variable X with possible values x_1, x_2, ... x_N a probability mass function is a function such that [285]:

$$f\left(x_i\right) \geq 0\,, \tag{2.16a}$$

$$\sum_{i=1}^{N} f\left(x_i\right) = 1\,, \tag{2.16b}$$

$$f\left(x_i\right) = P\left(X = x_i\right). \tag{2.16c}$$

The cumulative distribution function (CDF) of a discrete random variable X, denoted as $F(x)$ is

$$F\left(x\right) = P\left(X \leq= x\right) = \sum_{x_i \leq x} f\left(x_i\right)\,, \tag{2.17a}$$

$$0 \leq F\left(x\right) \leq 1\,. \tag{2.17b}$$

An alternative method to describe the distribution of a discrete random variable can also be used for continuous random variables. Because the number of possible values of X is uncountably infinite for a continuous random variable, X has a distinctly different distribution from the discrete random variables mentioned above. But, as in the discrete case, many physical systems can be modelled by the same or similar continuous random variables [285]. Density functions are commonly used in engineering in order to describe physical systems. A probability density function (PDF) $f(x)$ can be used to describe the probability distribution of a continuous random variable X. For a continuous random variable X, a probability density function is a function such that:

$$f(x) \geq 0 \tag{2.18a}$$

$$\int_{-\infty}^{+\infty} f(x)\,\mathrm{d}x = 1\,. \tag{2.18b}$$

A histogram is an approximation of a probability density function. For each interval of the histogram, the area of the bar equals the relative frequency (proportion) of the measurements in the interval. The cumulative distribution function of a continuous random variable X is:

$$F(x) = P\,(X \leq x) = \int_{-\infty}^{x} f(x)\,\mathrm{d}x\,. \tag{2.19}$$

The quantity $\mu = E[X]$ of the random variable X is defined in such a way that the operator E determines the average or expected value of X. Based on this determination, standard deviation σ of the random variable can be computed by:

continuous random variable:

$$\sigma = \sqrt{E\left[(X-\mu)^2\right]}\,, \tag{2.20}$$

discrete random variable:

$$\sigma = \sqrt{\frac{1}{N}\left[(x_1-\mu)^2 + (x_2-\mu)^2 + \ldots + (x_N-\mu)^2\right]}\,, \tag{2.21}$$

in which the mean value can be determined by:

$$\mu = \frac{1}{N}\left(x_1 + x_2 + \ldots + x_N\right)\,. \tag{2.22}$$

A moment of a probability distribution (quantitative measure of shape of a set of data points) about the mean value of the random variable is the central moment. This quantity is the expected value of the deviation of the random variable from the mean. Stochastic properties of a random variable can be described by the several moments which can be subsequently considered in the probability distribution of the random variable. In general, the important central moments are up to the order of four, which is adequate for the description of the probabilistic characteristic of a random variable:

First central moment: mean value

$$\mu_1 = \mu \qquad = E\left((X-\mu)\right)\,, \tag{2.23}$$

Second central moment: variance

$$\mu_2 = V(X) = \sigma^2 = E\left((X-\mu)^2\right)\,, \tag{2.24}$$

Standardised third moment: skewness

$$\mu_3 = \gamma_1 \qquad = \frac{E\left((X-\mu)^3\right)}{\sigma^3}\,, \tag{2.25}$$

Standardised fourth moment: kurtosis

$$\mu_4 = \beta_2 \qquad = \frac{E\left((X-\mu)^4\right)}{\sigma^4}\,. \tag{2.26}$$

The coefficient of variation CV is a normalised quantity to determine the spread of a probability distribution expressed as a percentage. The relationship between mean value μ, standard deviation σ and CV is defined as:

$$CV = \frac{\sigma}{\mu} \,. \tag{2.27}$$

The most widely applied distribution model of a random variable is a normal distribution. Whenever a random experiment is replicated, the random variable that equals the average result over the replicates shifts to a normal distribution as the number of replicates becomes large (known as central limit theorem, De Moivre in 1733) [285]. This work was lost in the past, and Gauss independently developed a normal distribution nearly 100 years later. Although De Moivre was later credited with the discovery, a normal distribution is also referred to as a *Gauss*'ian distribution. In Eq. 2.29, the probability density function (PDF) of the normal distribution is defined in which $E(X) = \mu$ determines the centre and $V(X) = \sigma^2$ is the width of the curve. For different mean and variance, Fig. 2.6 shows the corresponding normal probability density functions.

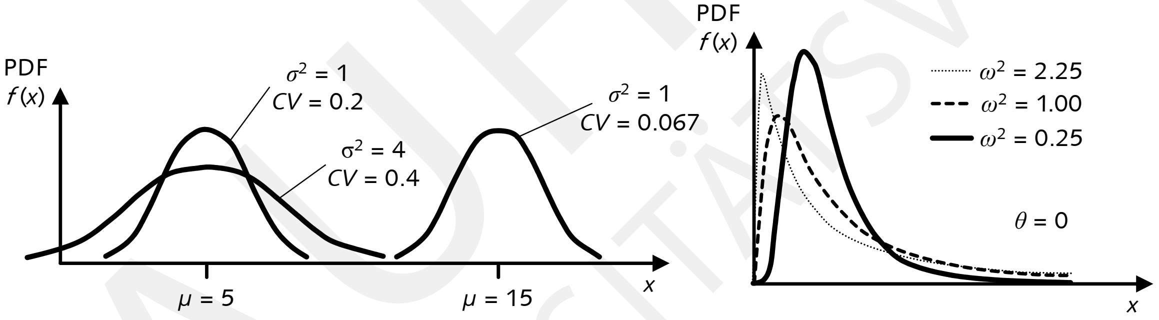

Figure 2.6: Left: normal distribution with different mean and variance, right: log normal distribution with zero mean and different variance, based on [285]

Random variables may follow an exponential relationship as $x = \mathrm{e}^m$. In the case that the exponent is a random variable M, then $X = \mathrm{e}^M$ is a random variable with a distribution of interest. A special case is when M underlies a normal distribution. Therefore, the distribution of X is called a log normal distribution. The name follows from the transformation $\ln X = M$, which means that the natural logarithm of X is normally distributed [285]. The CDF determined in Eq. 2.30 is based on the mean θ and the variance ω^2. For different variance and mean value, Fig. 2.6 shows the corresponding log normal probability density functions (PDF). The weibull distribution is often used to model time-dependent problems, such as failure assessment. The parameters in the distribution enable high flexibility to model phenomena in which the number of failures increases, decreases, or remains constant with time. In Eq. 2.33, the CDF, expected value, and variance are defined based on the scale parameter $\delta > 0$ and the shape parameter $\beta > 0$ [285].

distribution	domain	$f(x)$	$E(X)$	$V(X)$	
uniform	$a \leq x \leq b$	$1/(b-a)$	$\frac{(a+b)}{2}$	$\frac{(b-a)^2}{12}$	(2.28)
normal	$-\infty \leq x \leq \infty$	$\frac{1}{\sqrt{2\pi}\sigma} \mathrm{e}^{\frac{-(x-\mu)^2}{2\sigma^2}}$	μ	σ	(2.29)
log normal	$0 < x < \infty$	$\frac{1}{x\omega\sqrt{2\pi\sigma}} \mathrm{e}^{-\frac{(\ln x-\theta)^2}{2\omega^2}}$	$\mathrm{e}^{\theta+\omega^2/2}$	$\mathrm{e}^{2\theta+\omega^2}\left(\mathrm{e}^{\omega^2}-1\right)$	(2.30)
exponential	$0 \leq x \leq \infty$	$\lambda \mathrm{e}^{-\lambda x}$	$\frac{1}{\lambda}$	$\frac{1}{\lambda^2}$	(2.31)
gamma	$x > 0$	$\frac{\lambda^r x^{r-1} \mathrm{e}^{-\lambda x}}{\Gamma(r)}$	$\frac{r}{\lambda}$	$\frac{r}{\lambda^2}$	(2.32)
weibull	$x > 0$	$\frac{\beta}{\delta}\left(\frac{x}{\delta}\right)^{\beta-1} \mathrm{e}^{-\left(\frac{x}{\delta}\right)^{\beta}}$	$\delta\Gamma\left(1+\frac{1}{\beta}\right)$	$\delta^2\Gamma\left(1+\frac{2}{\beta}\right) -\delta^2\left[\Gamma\left(1+\frac{1}{\beta}\right)\right]^2$	(2.33)

In the case that more than one random variable should be considered in the system of interest (in the probability space), it is generally appropriate to determine a measure for the relationship between the variables in order to describe the influence the variables have on each other and how they vary together. Therefore, the covariance *cov* is a reasonable linear estimator for the combined interaction in parameter randomness and can be determined between two variables X_1 and X_2 according to (continuous and discrete random variables):

$$cov(X_1, X_2) = \sigma_{X_1X_2} = E\left[(X_1 - \mu_{X_1})(X_2 - \mu_{X_2})\right] = E\left(X_1X_2\right) - \mu_{X_1}\mu_{X_2}\,. \tag{2.34}$$

Moreover, the correlation ρ_{X_1,X_2} is another measure of the linear relationship between two random variables. This estimator relates the covariance to the product of the standard deviation of each variable. Hence, the correlation is a dimensionless variable that may be applied to compare the linear relationships between pairs of variables in different units. Two random variables are termed correlated when a non-zero correlation exists between both. In contrast, in the relationship between independent random variables, no interaction in their joint probability distribution is expected and both parameters can be termed uncorrelated $\rho_{X_1X_2} = 0$. The correlation quantity is defined as:

$$\rho_{X_1X_2} = \frac{cov(X_1, X_2)}{\sqrt{V\left(X_1\right)V\left(X_2\right)}} = \frac{\sigma_{X_1X_2}}{\sigma_{X_1}\sigma_{X_2}}\,. \tag{2.35}$$

In the case that the covariance between X_1 and X_2 is positive, negative, or zero, the correlation between X_1 and X_2 is positive, negative, or zero, because $\sigma_{X_1} > 0$ and $\sigma_{X_2} > 0$. Therefore, the range of correlation between two random variables is $-1 \leq \rho_{X_1X_2} \leq +1$.

2.3.2 Probabilistic concrete material properties

In a fundamental experimental study by Rüsch [357] in 1969, various concrete specimens of several construction sites are assessed up to the compressive strength of $f_c \approx 50\,\mathrm{MN/m^2}$. This study concluded that the probabilistic characteristics of the compressive strength can be described by normal distribution with sufficient accuracy. The standard deviation of the specimens is analysed to be on average $\overline{\sigma}_{f_c} = 4.7\,\mathrm{MN/m^2}$ for the considered concrete grades.

Tue et al. analysed the probabilistic property of the concrete compressive strength by evaluating 173 construction projects within a total of 5027 test specimens and published the results of the tests in 2005 [397]. This study investigated a linear function of standard deviation of the concrete compressive strength in dependence on the concrete grade as determined by a mathematical regression. Therefore, the standard deviation σ_{f_c} slightly increases with higher concrete compressive strength f_c, see Fig. 2.7, which is determined by:

$$\sigma_{f_c} = \frac{f_c}{48.44} + 2.80\frac{\mathrm{MN}}{\mathrm{m}^2}\,. \tag{2.36}$$

The mean standard deviation of the concrete compressive strength decreased over the last decades in the comparison between the study by Rüsch in 1969 and the study by Tue et al. in 2005. The recent investigation by Tue et al. determines a decrease in the average of the standard deviation by 20% to $\overline{\sigma}_{f_c} = 3.6\,\mathrm{MN/m^2}$ [397] compared to Rüsch.

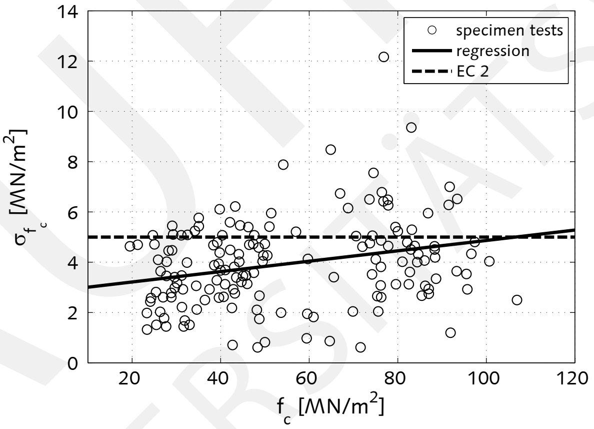

Figure 2.7: Standard deviation σ_{f_c} as a function of the compressive strength f_c, assessed for 173 construction projects by Tue et al. [397]

Tue et al. [397] performed additional laboratory experiments of concrete compressive strength with cylindrical or cubic test specimens to evaluate the stochastic characteristics. Therefore, the coefficient of variation of concrete compressive strength is determined as follows:

$$CV_{f_{c,mt}} = \frac{2.80\frac{\mathrm{MN}}{\mathrm{m}^2}}{f_c} + \frac{1}{48.44}\,, \tag{2.37}$$

in dependence of the concrete grade f_c. The index *mt* in Eq. 2.37 is the abbreviation for material testing, which means that the experimental data are measured in laboratory tests and not at the construction sites. In general, a difference between the compressive strengths appears between measurements in laboratory experiments and specimens taken from the structures. Uncertain material properties in building concrete structures occur from [397]:

- scatter in the base material for concrete,
- imprecise production,
- scatter quality of placing the concrete,
- different effects of the concrete curing and,
- scatter quality of concrete in the case of supplier consortium.

Construction supervision with quality control (material testing) can determine the first two items of uncertainty mentioned above. König et al. [226] and Macgregor et al. [252] analysed concrete cores taken from structures in order to determine the rest of the uncertainty sources in structural concrete placed in buildings.

For the whole range of concrete grades up to $f_c \approx 50\,\mathrm{MN/m^2}$, the characteristic structural strength is approximately 85% of the characteristic cylinder compressive strength [226, 252]. Therefore, the uncertainty in the structural compressive strength $CV_{f_{c,str}}$ increases in comparison to the uncertainty in the laboratory material testing $CV_{f_{c,mt}}$. Based on these assumptions, the relationship between the $CV_{f_{c,mt}}$ and $CV_{f_{c,str}}$ is [397]:

$$CV_{f_{c,str}} = 0.091 + 0.85 \cdot CV_{f_{c,mt}} \,. \tag{2.38}$$

The index *str* in Eq. 2.38 is the abbreviation for structure. Using Eq. 2.38 and Eq. 2.37, the coefficient of variation for the structural strength in dependence of the compressive strength is:

$$CV_{f_{c,str}} = 0.10855 + \frac{2.38\,\frac{\mathrm{MN}}{\mathrm{m^2}}}{f_c} \,. \tag{2.39}$$

The variation of the concrete compressive strength for material testing and measurements in structures is shown in Fig. 2.8. The coefficient of variation CV_{f_c} of normal strength concrete is clearly higher in the range of $20\,\mathrm{MN/m^2} \leq f_c \leq 55\,\mathrm{MN/m^2}$ in comparison to high strength concrete. Therefore, the relationship between CV_{f_c} and f_c decreases with increasing compressive strength [379]. In many design codes, such as the Eurocode 2 (EC 2), the standard deviation for normal strength concrete is assumed to be $\sigma_{f_c} = 5\,\mathrm{MN/m^2}$, which similarly describes the relationship between strength and uncertainty, see Fig. 2.8. Nevertheless, the determination by Tue et al. [397] describes this relationship more accurately and is applied in this thesis.

Moreover, the compressive strength, the modulus of elasticity E_c and the tensile strength f_{ct} significantly affect the stiffness, strength, and load-deformation behaviour of a concrete structural component. These material characteristics are similarly uncertain and cannot be classified as deterministic values. Many different studies addressing the determination of uncertainty description of the concrete material characteristics are summarised in Tab. 2.3. The rows are ordered according to the material property and subsequently according to the year of publications.

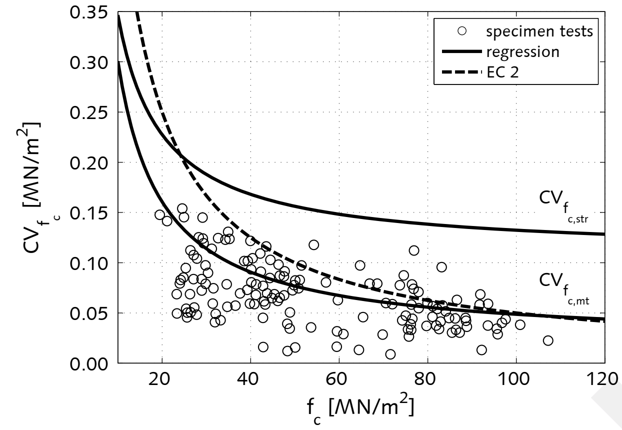

Figure 2.8: Coefficient of variation for material testing $CV_{f_{c,mt}}$ and for structural measurements $CV_{f_{c,str}}$ as a function of the compression strength f_c, assessed for 173 construction projects [397]

Table 2.3: Stochastic material properties for concrete assessed by various researches, Normal Strength Concrete (NSC), normal distribution (N), log normal distribution (LN), not mentioned (n.m.)

Material Property	$f_X(x)$	Condition	μ [MN/m²]	σ [MN/m²]	CV [−]	Literature Year	Ref.
concrete compressive strength f_c	N	for all NSC	≤ 50	4.7	0.081 ... 0.235	1969	[357]
	N				0.05 ... 0.25	1974	[289]
	N LN Weibull				0.10 ... 0.20	1981	[373]
	n.m.		36.4	3.7	0.10	1986	[22]
	N	precasting works	≤ 20		0.125 ... 0.200	1992	[384]
		big construc. site			0.200 ... 0.275		
		small construc. site			0.275 ... 0.350		
		precasting works	≥ 20	2.5 ... 4.0			
		big construc. site		4.0 ... 5.5			
		small construc. site		5.5 ... 7.0			
	LN				0.06	2001	[105]
	LN		21.20	2.12	0.10	2002	[149]
	N		23.16	2.58	0.11	2004	[388]
	N LN Weibull	material testing structural strength			$\frac{2.80}{f_c} + \frac{1}{48.44}$ $0.10855 + \frac{2.38}{f_c}$	2005	[397]
	N				0.05 ... 0.15	2007	[63]
	n.m.		24.6	2.63	0.107	2007	[379]
			49.9	4.04	0.081		
			90.8	5.18	0.057		
	N		28.0	2.24	0.08	2007	[387]

continued on next page

Stochastic material properties for concrete (continued)

Material	$f_X(x)$	Condition	μ	σ	CV	Literature	
Property			[MN/m^2]	[MN/m^2]	[$-$]	Year	Ref.
	N	for all NSC	≤ 50	5.0	0.086 … 0.250	2011	[101]
	LN	C 20	23.8	5.1	0.21	2012	[370]
	LN	C 40	40.8	8.8	0.21		
	LN	C 60	57.8	5.6	0.10		
	LN	C 60	74.8	6.3	0.08		
	LN	C 25	33.7	5.7	0.17	2013	[5]
	LN	C 35	40.6	5.4	0.13		
	n.m.	C 20/25	39.84	2.13	0.054	2013	[421]
	n.m.	C 25/30 B3	47.03	2.28	0.049		
	n.m.	C 25/30 XC1	53.42	2.62	0.049		
	n.m.	C 30/37 H	58.56	3.24	0.055		
	LN		40	6	0.15	2014	[64]
concrete tensile strength f_{ct}	N				$\geq CV_{f_c}$	1992	[384]
	LN				0.30	2001	[105]
	LN		2.72	0.57	0.211	2002	[149]
	N		2.27	0.24	0.10	2004	[388]
	N		2.2	0.26	0.12	2007	[387]
	n.m.	C 20/25	3.10	0.48	0.155	2013	[421]
	n.m.	C 25/30 B3	4.13	0.69	0.168		
	n.m.	C 25/30 XC1	4.17	0.51	0.124		
	n.m.	C 30/37 H	5.01	0.72	0.143		
concrete modulus of elasticity E_c	LN				0.18	1995	[401]
	LN				0.08	1997	[47]
	LN				0.15	2001	[105]
	LN		30,450	3,197	0.105	2002	[149]
	N		30,522	3,662	0.12	2004	[388]
	N				0.08	2007	[63]
	N		28,800	1,440	0.05	2007	[387]
	n.m.	C 20/25	31,150	1,131	0.042	2013	[421]
	n.m.	C 25/30 B3	30,822	2,654	0.086		
	n.m.	C 25/30 XC1	35,456	1,982	0.056		
	n.m.	C 30/37 H	35,522	2,643	0.074		

In comparison to the compressive strength of concrete, a higher variance in the tensile concrete strength is observable, which is similarly assessed by [74]. Similarly, the modulus of elasticity also shows a greater uncertainty as compared to the compressive strength, as presented in Tab. 2.3.

In addition to the information about the distribution type, the mean value, and the coefficient of variation, the relationship/interaction of a certain material property with the other properties is important for the adequate description of probability distributions. Therefore, the determination of the correlation is significant for the assessment of models. The correlation between concrete compressive strength f_c, concrete tensile strength f_{ct}, and concrete modulus of elasticity E_c is shown in Tab. 2.4.

The correlation between the compressive and tensile strengths is between 0.7 and 0.9, which is similar to the correlation between the compressive strength and the modulus of elasticity. In contrast, the correlation between the tensile strength and the modulus of elasticity is lower and is between 0.6 and 0.7.

Table 2.4: Correlation between concrete material properties

Material Property X		Y	Correlation $\rho_{XY}[-]$	Lit.
f_c	$\Longleftrightarrow$	f_{ct}	0.9	[388]
			0.8	[387]
			0.7	[149]
f_c	$\Longleftrightarrow$	E_c	0.73	[388]
			0.9	[387]
			0.9	[149]
f_{ct}	$\Longleftrightarrow$	E_c	0.6	[388]
			0.7	[387]
			0.6	[149]

2.3.3 Probabilistic reinforcing steel material properties

The yield strength is a significant material property of reinforcing steels for the simulation and design of reinforced concrete structures. Based on the determination of the strength parameter, the transition between elastic and plastic curvatures in a reinforced concrete cross-section is defined. Moreover, the proof of allowable steel stress also significantly depends on the yield strength. The randomness of this material quantity is mainly dependent on the specific production batch and other production influences. However, only general statistical data that satisfactorily describe the entire group of reinforcing steels is adequate for the description of this property for probabilistic analysis [401].

In Tab. 2.5, the probabilistic characteristics of reinforcing steel are listed according to the yield strength f_y, ultimate strength f_u, and the modulus of elasticity E_s and according to the year of publications. The modulus of elasticity of reinforcing steel is very low and in many studies a deterministic mean value is applied in the analysis. Nevertheless, a certain amount of variance occurs even in this material property, which can be considered by $CV_{E_s} \leq 0.03$.

The variance in the yielding strength is found to be higher than one in the modulus of elasticity. In several studies, the coefficient of variation for this material property is assessed to be $CV_{f_y} = 0.05$. The uncertainty in the ultimate strength can be of a similar or even higher magnitude compared to the yielding strength.

The correlation between the reinforcing steel parameters is rarely assessed or is very often not considered in the analysis. According to the probabilistic model code [105], the correlation is listed in Tab. 2.6, which determines a correlation between the yielding and ultimate strengths of 0.85 and no dependence between the other relationships of the reinforcing steel properties.

Table 2.5: Stochastic material properties of reinforcing steel assessed by various research studies, normal distribution (N), log normal distribution (LN), Weibull distribution (W)

Material	$f_X(x)$	Condition		μ	σ	CV	Literature	
Property		Profile	Manuf.	[MN/m^2]	[MN/m^2]	[$-$]	Year	Ref.
reinforcing steel yielding strength f_y	N LN					0.08 ... 0.10	1974	[289]
	N W					0.06	1981	[373]
	n.m.			470	33	0.07	1986	[22]
	N	same	different			0.01 ... 0.04	1992	[384]
	LN	different	same			0.04 ... 0.07		
	LN	same	different			0.05 ... 0.08		
	N	different	different			0.06 ... 0.12		
	n.m.			557.0	25.9	0.05	2000	[3]
	N	different manuf.		560	30	0.05	2001	[105]
	LN			510		0.05 ... 0.15	2007	[63]
	N			582	29.1	0.05	2007	[387]
	N			550	30	0.05	2012	[370]
	LN			560	30	0.05	2013	[5]
	LN			560	30.24	0.054	2014	[64]
reinforcing steel tensile strength f_u	n.m.			620	82	0.13	1986	[22]
	N					$\geq CV_{f_y}$	1992	[384]
	n.m.			659.9	16.6	0.03	2000	[3]
	N	different manuf.		644	40	0.06	2001	[105]
	LN			550		0.05 ... 0.15	2007	[63]
	LN			644	40	0.06	2013	[5]
reinforcing steel modulus of elasticity E_s	constant			2.05 e^5			2001	[105]
	LN			2.10 e^5	4,200	0.02	2007	[63]
	N			2.10 e^5	6,300	0.03	2007	[387]

Table 2.6: Correlation between reinforcement material properties

Material Property X		Y	Correlation $\rho_{XY}[-]$	Lit.
f_y	$\Longleftrightarrow$	f_u	0.85	[105]
f_y	$\Longleftrightarrow$	E_s	0	[105]
f_u	$\Longleftrightarrow$	E_s	0	[105]

2.4 Probabilistic loading conditions

In addition to the influence of material properties on the load-deformation behaviour and resistance of a structural element, the loading condition on real structures is also affected by uncertainties. Most of the loading conditions are not fixed deterministic values, because even the dead load of a concrete element underlies some variance in the loading condition, see Tab. 2.7. In general, variable loads such as live loads in residential or commercial buildings, or snow loads are much more uncertain compared to dead loads.

The focus of this thesis is the assessment of the phenomena which determine the physical load-deformation behaviour of concrete structures (resistance side). Therefore, the loading conditions are not considered with any uncertainty quantity in order to evaluate concrete structures exclusively for the resistance side.

Table 2.7: Stochastic characteristic of loading conditions

Loading condition	CV [-]	Lit.	Characteristic value	Lit.
permanent load				
dead load normal weight concrete, 300 mm	0.05	[72]	average value	[136]
variable load				
live load for house building	0.54	[384]	average value	[136]
live load for warehouse	0.81	[384]	98%-fractile or nominal value	[136]
snow	0.45	[130]	98%-fractile	[138]

2.5 Global and partial model quality evaluation

2.5.1 Evaluation of coupled partial models

On the geometric level, the numerical simulation of structures subdivides the entire structure into structural components. On a conceptual level, however, these parts are then modelled by suitable partial models (PM), which mathematically describe different phenomena such as the time-dependent behaviour of concrete or the stress-strain relationship of the surrounding soil. The coupling between the PM integrates the phenomena of the structural components into the global model (GM) of the entire structure.

Global models for numerical simulation approaches utilize different model classes (M) with subordinate partial models. Interactions and couplings of these PM are necessary to determine an appropriate structural behaviour. The reliability of the model prediction can be assessed by an evaluation method quantifying the prediction quality of coupled partial models according to the method by KEITEL et al. [211]. Therefore, the comparison between different global structural models can be evaluated quantitatively which increases the reliability of a calculation model in a reasonable manner by selecting an adequate model with acceptable prediction quality. Hence, this method is able to detect optimal as well as efficient model combinations for reliable predictions.

In order to quantify the global model prediction quality, the first evaluation step is to quantify whether a phenomenon has an influence on a certain structural response value or the phenomenon can be neglected in the numerical simulation or modelled with simplified partial models. The importance of these PM with respect to the global response of the structure can be quantified using variance based sensitivity analysis, see Sec. 2.5.1.1 and 2.5.1.2. In the case that a PM influences the structural behaviour, it is necessary to quantify the prediction quality of the partial model MQ_{PM} and then subsequently combine both sets of information into the global model quality MQ_{GM}^{Y} for the entire structure. Therefore, the following evaluation method developed by KEITEL et al. [211] enables the assessment of global model quality MQ_{GM}^{Y}.

2.5.1.1 Sensitivity according to model class

The first step is to quantify whether the model class (phenomenon) has an influence on a certain target value at a certain position in the structure. Therefore, variance based global sensitivity estimators [176, 360, 381] allows the quantitative assessment of the phenomenon's importance in relation to the structural response

quantities Y (e.g. displacements, stresses). In general, sensitivity analysis is the study of how the output of a model Y is related to the model input X. In the evaluation of the global model quality, the sensitivity indices are used for the quantification of the phenomenon‘s importance. By using discrete random variables for selecting (activating or deactivating a certain PM) the model class, the sensitivity study in this case is not an estimation of uncertainty, but a quantified value of the influence of the model class (X_i).
Each of the classes of partial models i, e.g. shrinkage of concrete, is represented by a discrete random parameter with the two discrete values:

$$X_i \in \{0,1\}\,, \text{ with } i = 1, \ldots, n_M\,, \tag{2.40}$$

wherein n_M represents the number of considered partial models. A value of $X_i = 0$ denotes the deactivated partial model class i, for example, when shrinkage is not considered, and $X_i = 1$ denotes the activated partial model class i, e.g. when shrinkage is considered. The global model Y is calculated for all possible combinations of X_i with $i = 1 \ldots n_M$. A finite number of possible model class (partial models) combinations $n_{\text{comb}} = 2^{n_\text{M}}$ is necessary for the assessment of the sensitivity indices, whereby the partial models representing the same physical phenomenon are related to the equivalent model class:

$$n_{\text{comb}} = 2^{n_\text{M}} \tag{2.41}$$

with n_M random variables (model classes in global model). Due to the discrete random parameters, the sensitivity indices can be computed based on the results of model Y for the n_{comb} model combinations without the usual need for specific sensitivity estimators, which require high computational effort.
The first-order sensitivity index S_i established by SOBOL [381] can be used to compute the exclusive influence of a certain model input X_i (such as PM) on the structural response of the global model:

$$S_i = \frac{V\left(E\left(Y|X_i\right)\right)}{V\left(Y\right)}\,, \tag{2.42}$$

where $V\left(E\left(Y|X_i\right)\right)$ is the variance of the expected value of Y when conditioning with respect to X_i and $V(Y)$ is the unconditional variance of Y. Due to interactions in complex engineering problems, higher order sensitivity indices are needed. The total-effects sensitivity index S_{Ti} investigated by HOMMA and SALTELLI [176] calculates the overall influence of a specific partial model while also considering the interaction with the other PM in the global model:

$$S_{Ti} = 1 - \frac{V\left(E\left(Y|X_{\sim i}\right)\right)}{V\left(Y\right)}\,, \tag{2.43}$$

where $V\left(E\left(Y|X_{\sim i}\right)\right)$ is the variance of the expected value of Y when conditioning with respect to all parameters except for X_i. In general, the total-effects sensitivity index S_{Ti} should be used for the quantitative evaluation of the importance of various phenomena in engineering structures.
A measure of the interaction between X_i and other model classes is the difference between S_i and S_{Ti}. For each model class, a partial model with an adequate complexity and accuracy has to be used for the sensitivity evaluation in the first step. High values of the sensitivity indices show a significant influence of the model class on the global model response at a certain position in the structure. Model classes with sensitivity indices smaller than a given threshold (e.g. $S_{Ti}^{\text{M}} < 0.03$) shall be neglected for the next evaluation method step [211]. In other words, no further investigations about their partial model quality are necessary.

The unimportant model classes are excluded for the subsequent evaluation steps of the global model quality assessment.

2.5.1.2 Sensitivity according to model choice

The second step is to quantify the model choice influence of certain partial models for the same phenomenon in relation to the other phenomena. The model choice (MC) assessment is similarly computed using the variance based sensitivity analysis by computing S_{Ti}^{MC}. It is also based on sensitivity studies [211, 360]. In comparison to the first step, the phenomena are not constrained to be activated or deactivated; they are analysed with respect to certain models in the second evaluation step. For example, in the case that the shrinkage of the concrete is an important phenomenon (in the first step: $S_{Ti,\mathrm{shrinkage}} \geq 0.03$), the second step quantifies the influence of the selection of a certain shrinkage model. This is in relation to the model choices of all the other sensitive phenomena (e.g. creep, material models, pile foundation stiffness).
The choice of each PM within a model class (MC) is controlled by X_i. The total-effect sensitivity index indicates how this choice leads to a variation of the global model response according to a certain output value. The total-effects sensitivity index quantifies the effect that the model choice has on the global model's response at a particular position in the structure. On one hand, low values express that the choice of different partial models representing the same phenomenon predicts a similar partial model output. On the other hand, the choice of a PM in this model class does not significantly affect the structural load-bearing behaviour. These effects are quantified by the sensitivity indices which transfer the partial model quality for a certain phenomenon into a global model quality of the structural model. Finally, these sensitivity indices can be seen as weighting factors for the partial model quality MQ_{PM} in the assessment of the numerical global model $MQ_{\mathrm{GM},Y}$.

2.5.1.3 Global model quality of coupled partial models

The global model quality $MQ_{\mathrm{GM},Y}$ of coupled partial models is quantified by a path on a graph (graph theory see [69, 84, 203, 204]) in which the vertex is the quality of the partial model $MQ_{\mathrm{PM},Y}^{\mathcal{M}_i}$ and the edges are the coupling quantities. A number between 0 and 1 expresses this quality. 0 signifies a poor and 1 a high $MQ_{\mathrm{PM},Y}^{\mathcal{M}_i}$. These quantitative values come from the evaluation of the PM itself, using uncertainty, complexity, or robustness criteria [32, 49, 207, 209, 234, 286], see Sec. Sec. 2.1 and 2.5.2. Assuming a perfect data coupling between each of the model classes, the model quality of a global structural model is defined as [211]:

$$MQ_{\mathrm{GM},Y} = \sum_{i=1}^{n_{\mathrm{M,red}}} \frac{S_{Ti,X_i}^{\mathrm{MC}} \cdot MQ_{\mathrm{PM},Y}^{\mathcal{M}_i}}{\sum\limits_{i=1}^{n_{\mathrm{M,red}}} S_{Ti,X_i}^{\mathrm{MC}}} , \tag{2.44}$$

where $MQ_{\mathrm{PM},Y}^{\mathcal{M}_i}$ is the partial model quality of a certain partial model i in the model class M. The variable $n_{\mathrm{M,red}}$, determined by the first evaluation step, is the number of considerable model classes influencing the global response quantity and S_{Ti,X_i}^{MC} is the total-effects sensitivity index for the model choice assessment. It is obvious, that the sensitivity indices strongly influence the structural model quality. However, the focus in this evaluation method is the development of the evaluation methodology and the application to local structural response values.
Due to the interaction between the structural components, the sensitivity indices are strongly variable

BAUHAUS
UNIVERSITÄTSVERLAG

with respect to the position in the structure, see Sec. 6.1. Consequently, the global model quality for the same partial model combination also changes from position to position. Therefore, the existing sensitivity analysis at local positions in the structure is upgraded to the integrative sensitivity analysis, see Sec. 6. This improvement allows the overall assessment of phenomena importance in relation to the entire structural load-bearing behaviour by taking into account the response significance at each position in the structure. Finally, for each partial model combination, a global prediction quality can be assessed for the entire structure. Therefore, the quality assessment is no longer depending on the position to be evaluated, because all positions can be considered simultaneously in the integrative sensitivity analysis.

2.5.2 Partial model assessment

In general, numerous analytical and numerical models for each of the partial models are applied in construction projects and research studies. In addition, new models are going to be developed with additional knowledge better able to describe "real" phenomena. Therefore, selecting models is not a simple and trivial task. When analysing the uncertainty in the numerical simulation, the quantitative model evaluation poses the question of which partial model should be chosen in comparison to the other considered models.

In the case that experimental data are available for a certain object of interest (e.g. certain concrete mixture), the **stochastic model selection** (*Bayes*ian model selection) proposed e.g. by MacKay [253], and Beck et al. [39] can be applied for the assessment of the prediction of different models representing the same phenomenon. For particular experimental data, this method computes the probability that a model has in comparison to the measurement points *MP* using the *likelihood* function [90]. The likelihood is a function of the parameters of a statistical model, which may be determined in order to analyse the relationship between the model input parameters and the corresponding given model output (predictions and experimental data).

In addition to that, it is appropriate according to [253] to consider a penalty for over-parameterisation in the models represented by the *Ockham* factor, which is proposed by Gull [153].

Hence, simplified models are always preferred in comparison to more sophisticated ones assuming that both models have the same *likelihood*. This is a more reasonable approach than the *Akaike Information Criterion* (AIC) [1] and the *Bayesian Information Criterion* (BIC) [374]. AIC and BIC judge exclusively on the models depend on the pure number of parameters, defined by:

$$\mathrm{AIC} = 2k - 2\ln\left(\hat{\mathcal{L}}\right) \qquad \text{Akaike} \quad [1]\,, \tag{2.45}$$

$$\mathrm{BIC} = k\ln(MP) - 2\ln\left(\hat{\mathcal{L}}\right) \qquad \text{Schwarz} \quad [374]\,, \tag{2.46}$$

in which k is the number of free parameters in each model to be estimated, $\hat{\mathcal{L}}$ is the maximised value of the *likelihood* function of the model $\mathcal{M}_i$, and MP is the number of observations or measurement points. In contrast, the *Model Selection Factor* (MSF) takes into account the probabilities of the prior and posterior model parameters and should be used for the model assessment in comparison to AIC and BIC criterions [209]. Based on the *Bayes*'theorem, the MSF can be interpreted as the probability of model $\mathcal{M}_i$ to be most adequate (higher MSF expresses a higher model accuracy) and is defined as:

$$P\left(\mathcal{M}_i|X_m, M\right) = \frac{p\left(X_m|\mathcal{M}_i, M\right) P\left(\mathcal{M}_i|M\right)}{p\left(X_m|M\right)}\,, \tag{2.47}$$

in which:

$$p\left(X_m|M\right)=\sum_{i=1}^{N_m}p\left(X_m|\mathcal{M}_i,M\right)P\left(\mathcal{M}_i|M\right)\ , \tag{2.48}$$

is based on the theorem of total probability where M is a model class representing the same phenomenon by partial models and N_m is the number of PM with the group M. The prior engineering judgement of the model's plausibility/accuracy is expressed by $P\left(\mathcal{M}_i|M\right)$ and the sum is equal to unity:

$$\sum_{i=1}^{N_m}P\left(\mathcal{M}_i|M\right)=1\,. \tag{2.49}$$

The evidence of the model $\mathcal{M}_i$ in comparison to the experimental data X_m is expressed by the theorem of total probability:

$$p\left(X_m|\mathcal{M}_i,M\right)=\int_{\theta_i}p\left(X_m|\theta_i,\mathcal{M}_i,M\right)p\left(\theta_i|\mathcal{M}_i\right)\mathrm{d}\theta_i\,, \tag{2.50}$$

in which θ_i is the parameter vector of model $\mathcal{M}_i$, $p\left(X_m|\theta_i,\mathcal{M}_i,M\right)$ is the *likelihood* and $p\left(\theta_i|\mathcal{M}_i\right)$ is the prior probability density function of θ_i defined by the engineer. The posterior PDF of the parameter vector in a globally identifiable case may be approximated by a *Gauss*ian distribution [39]. Hence, the evidence for model $\mathcal{M}_i$ based on the optimal parameter vector $\hat{\theta}_i$ is defined as:

$$p\left(X_m|\mathcal{M}_i,M\right)=\frac{p\left(X_m|\hat{\theta}_i,\mathcal{M}_i\right)p\left(\hat{\theta}_i|\mathcal{M}_i\right)}{p\left(\hat{\theta}_i|X_m,\mathcal{M}_i\right)}\,, \tag{2.51}$$

in which the *Ockham* factor is considered by the ratio $p\left(\hat{\theta}_i|\mathcal{M}_i\right)/p\left(\hat{\theta}_i|X_m,\mathcal{M}_i\right)$. The probability of each partial model in the model class computed by Eq. 2.47 determines the prognosis quality of the PM. According to [206], the highest probability of a certain model amongst all considered models MAX $\left[P\left(\mathcal{M}|X_m,M\right)\right]$ corresponds to the highest prediction quality. Based on the normalised model selection factor MSF^N, the quality of each $\mathcal{M}_i$ is defined as:

$$\mathrm{MSF}^N=\frac{P\left(\mathcal{M}_i|X_m,M\right)}{\mathrm{MAX}\left[P\left(\mathcal{M}|X_m,M\right)\right]}\,. \tag{2.52}$$

The assessment of models based on experimental data can also be analysed based on **uncertainty analysis** considering parameter and model uncertainty. Due to the randomness of the model input parameters, a variation in the model predictions is caused. Model uncertainty represents the inconsistency between the experimental data and the model prognosis. This uncertainty can be taken into account by the model uncertainty factor ψ_{mod} [209]. The expected value of the model uncertainty is $E_{\psi_{\text{mod}}}=1$ and a mean coefficient of variation $\overline{CV}_{\text{mod}}$ can be determined by [25]:

$$\overline{CV}_{\text{mod}}=\frac{1}{\overline{Y}_{\text{meas}}}\cdot\left[\frac{1}{MP-1}\sum_{i=1}^{MP}\left(Y^i_{\text{meas}}-Y^i_{\text{sim}}\right)^2\right]^{\frac{1}{2}}\,, \tag{2.53}$$

in which $\overline{Y}_{\text{meas}}$ is the mean value of all measurements, MP is the number of measurements, "meas" is the abbreviation for measurement, and "sim" for simulation. This model uncertainty factor can be multiplied by the simulation results which leads to a measure for the agreement between the mean model prediction and the mean of the experimental measurements [209]. The probabilistic simulation computes a variation in the model prediction and the uncertainty of the model prediction is used as an indicator for the model evaluation, see Sec. 2.1.

In the modelling uncertainty strategy of Snowling and Kramer [380], similar to total uncertainty, a *Model Utility Factor* U_i considers the model response to changes in the model input (in this study called sensitivity, synonymous to parameter uncertainty) and the closeness of model to measurements (in this study called model error, synonymous to model uncertainty)

$$U_i = 1 - \sqrt{\frac{K_s S_i^2 + K_e E_i^2}{K_s + K_e}} \, , \tag{2.54}$$

in which S_i is the sensitivity value for model i (relative to maximum sensitivity) with k_s are the weighting constants for sensitivity, E_i is the error value (relative to maximum error) with k_e are the weighting constants for error. This *Model Utility Factor* is in the range of 0 and 1, where a larger value of U represents a greater model utility. If the model uncertainty, sensitivity, and the model error are valued equally, then $k_s = k_e = 1.0$. Moreover, in order to prove the general hypothesis that more complex models compute more accurate results with higher parameter uncertainty and less model uncertainty (see Fig. 2.1), a mathematical determination of the model complexity I_c is proposed [380]:

$$I_c = \sum_{j=1}^{n_j} \sum_{i=1}^{N_i} X_i r_i \, , \tag{2.55}$$

in which N_i is the number of state variables, n_j is the number of processes flowing to or from state variable i, X_i is the number of parameters used to describe the process j, and r_i is the number of mathematical operations used to describe the process j. The complexity of the mathematical description as well as the number of degrees of freedom for each individual model are considered in the model complexity factor.

In the case that **no measurement data** are available, the uncertainty analysis is similarly capable of considering the uncertainties due to the non-deterministic model input parameters as well as uncertainties due to the model prediction error [286]. With the help of this probabilistic model evaluation, the model selection is provided decisively in a quantitative manner. Hence, the question of the considered models is the most adequate can be answered by the use of uncertainty analysis, see Sec. 2.1.

For the evaluation of the creep phenomenon, recommendations can be found in Sec. 3.2.2 and for the shrinkage of concrete in Sec. 3.3.2. The non-linear material modelling of reinforced concrete is evaluated in this thesis and is presented in Sec. 5.1. Moreover, the assessment of pile foundation models for predicting the stiffness of pile groups is discussed in Sec. 5.2.

A **multicriteria** evaluation method considers several criteria instead of focusing on a certain model characteristic. In the study by Reuter et al. [341, 342], uncertainty, sensitivity, robustness, and reliability are considered in the evaluation methodology. Therefore, the selection of an adequate model for the structural analysis can be assisted in a quantitative manner.

2.5.3 Coupling quality assessment

In structural engineering, an evaluation method for the assessment of coupled partial models is published by Keitel et al. [211]. This method is applied on a conventional prestressed concrete box girder bridge without any consideration of the coupling quality. In a cooperative study by Keitel et al. [210] with contribution of the author of this thesis, the evaluation method is enhanced in order to assess the coupling

quality between the partial models and the coupling importance on the global model prediction quality.
In addition to first-order S_i and total-effects S_{Ti} sensitivity indices, the higher-order indices S_{ij} are computed, which are directly proportional to the interaction effects to specific parameters/classes i and j of partial models. For S_{ij}, the following definition holds [360]:

$$S_{ij} = \frac{V\left(E\left(Y|X_i, X_j\right)\right) - V_i - V_j}{V\left(Y\right)} = \frac{V\left(E\left(Y|X_i, X_j\right)\right)}{V\left(Y\right)} - S_i - S_j \,. \tag{2.56}$$

Common types of coupling in engineering are uni- and bidirectional coupling methods [119]. The first one denotes the data transfer from PM k to PM l, but not in the opposite direction. Conversely, the bidirectional coupling allows the additional data transfer from PM l back to PM k. The method to determine the coupling quality is not addressed in detail here, because this method is discussed in [210]. Let α be a model quantity appearing in both partial models k and l at the same structural node, for example the supporting force of a bridge pier, which is present in the pier itself and also at the top of the pile foundation. A perfect data coupling ensures consistent data in both models, $\alpha^k = \alpha^l$, which refers to data coupling quality of $cq_{\alpha,k-l} = 1$. As the differences in transferred data increase, which mean that $\alpha^k \neq \alpha^l$, the quality of the coupling decreases down to a quality of zero when no data is transferred, $\alpha^k \neq 0$ and $\alpha^l = 0$.
In the case that the coupling quality is assessed for coupled partial models that are ordered before the investigated response value, for example the influence of the bridge pier material model on the support moment of the pier, which is used to calculate the settlements of the foundation, the backward coupling might influence the coupled quantities to some extent, but it is not obligatory. In this case, the quality is defined with respect to the influence of the partial models before and after the coupling [210]:

$$CQ^{B}_{k-l} = \frac{\frac{1}{N_f}\sum\limits_{\alpha=1}^{N_f}\left(cq_{\alpha,k-l}\sum\limits_{i\leq k} S_{i,\alpha}\right) + \overline{cq}_{l-k}\frac{1}{N_f}\sum\limits_{\alpha=1}^{N_f}\left(\sum\limits_{i=1}^{N_p} S_{Ti,\alpha} - \sum\limits_{i\leq k} S_{i,\alpha}\right)}{\frac{1}{N_f}\sum\limits_{\alpha=1}^{N_f}\sum\limits_{i} S_{i,\alpha}} \,, \tag{2.57}$$

with N_f is the number of different forward coupling quantities, cq is the data coupling quality, $\overline{cq}$ is the mean data coupling quality, CQ is the quality of partial model coupling, and α is the model quantity.
The forward data coupling quality $cq^f_{\alpha,k-l}$ is directly linked to the sensitivity indices of α. For backward data coupling quality, this is not possible, because it cannot be determined which of the backward coupling quantities has an influence on α. Furthermore, the number of forward and backward coupling quantities might differ. Hence, the mean value of the sensitivity indices of α is multiplied with the mean of the backward data coupling quality $\overline{cq}^b_{l-k}$. The prediction quality of the global model for an output quantity γ depends on the quality of the partial models, their influence on the quantity of interest, and the coupling quality. The quality of the partial model i, MQ_i, is determined in separate studies, for example using uncertainty analysis [286] or other strategies [234]. The quality MQ_i is weighted by the influence of the partial model i on quantity γ, quantified by the total-effects sensitivity index S^{γ}_{Ti} calculated according to Sec. 2.5.1.1.
As the sum of all S^{γ}_{Ti} might be larger than one, a normalisation with respect to $\sum_{j=1}^{M} S^{\gamma}_{Tj}$ is required. In addition, the quality contribution of each partial model is multiplied by the coupling quality CQ_c of each

of the $N_{c,i,\gamma}$ couplings that are necessary to transfer the data from PM_i to the quantity of interest γ. The resulting model quality of the global model GM for quantity γ becomes:

$$MQ^{\gamma}_{GM} = \sum_{i=1}^{M} \left[\frac{S^{\gamma}_{Ti}}{\sum_{j=1}^{M} S^{\gamma}_{Tj}} MQ_i \prod_{c=1}^{N_{c,i,\gamma}} CQ_c \right] . \tag{2.58}$$

The coupling quality CQ_c of the partial models a and b being coupled is once more distinguished into two cases depending on the position of the output quantity γ:

$$CQ_c = \begin{cases} CQ^{A}_{a-b} & \text{if } \gamma \text{ is after coupling } c \\ CQ^{B}_{a-b} & \text{if } \gamma \text{ is before coupling } c \end{cases} \tag{2.59}$$

Using this algorithm, different combinations of couplings and partial models can be compared quantitatively and the best possible model combinations can be detected while the loss of quality using worse model combinations can be found.

In the cooperative study in [210], it is finally assessed that partial models with an average prediction quality in combination with a high coupling quality should be preferred more than high partial model qualities in combination with a low coupling quality.

2.6 Reliability methods

2.6.1 Full-probabilistic reliability method

The general problem in the design and the assessment of engineering structures is the non-deterministic effect of the action E and the non-deterministic resistance of the structure R [106, 164, 299, 384]. The single probability of the load part or the resistance part is not separately important for the safety assessment of structures. It is more important to asses the joint probability of the combinations of both parts.

The computation of structural failure, such as undesired or unsafe conditions, is defined according to the limit state function $g(\mathbf{X})$ by the set $\mathcal{F} = \{\mathbf{X} : g(\mathbf{X}) \leq 0\}$ [55]. The limit state function is regularly referred to as the safety margin $Z = g(\mathbf{X})$. The probability of failure p_f is defined as the probability of the occurrence of $\mathcal{F}$. Therefore, p_f is a unique quantity, i.e. not depending on the particular choice of the limit state function, and is defined as:

$$p_f = \textbf{Prob}\left[\{\mathbf{X} : g\left(\mathbf{X}\right) \leq 0\}\right] . \tag{2.60}$$

Due to the multiple basic variables X_i, which are present in the analysis of engineering structures, the computation of the failure probability can be written as [55]:

$$p_f = \textbf{Prob}\left[g\left(X_1, X_2, \ldots X_i\right) \leq 0\right] = \int_{g(\mathbf{X}) \leq 0} \overset{\ldots}{} \int f_{\mathbf{X}}(\mathbf{x}) \mathrm{d}\mathbf{x} \tag{2.61}$$

The computation of the integral of the failure probability, defined in Eq. (2.61), is mathematically challenging due to the necessary solution of the limit state function $g(\mathbf{x})$. In particular, a non-linear load-bearing behaviour of the structure requires an iterative numerical approach. The sole purpose of the limit state function, in this context, is to provide and define the bounds of the integration. The point on the limit state function with the associated highest probability for the basic vaiables $\mathbf{X}$ is termed as the design Point P_d. A very narrow region around P_d contributes to the quantity of the integral $\mathbf{Prob}[\mathcal{F}]$.
The probability of failure p_f is the volume under the probability density $f_{E,R}$ for the combinations $e > r$. This quantity defines the probability of the structure to exceed a certain criterion defined by the limit state function. For each of the different criterion, such as stress limitations or deformation control, or ultimate design, it is important to define/recommend an acceptable probability of failure $p_{f,\text{accep}}$. Therefore, the probability of failure of the structure can be compared to the acceptable probability of failure by:

$$p_f < p_{f,\text{accep}} \,. \tag{2.62}$$

In the case that $p_f > p_{f,\text{accep}}$, the actual design/layout of the structure cannot meet the design criteria. Therefore, some items and conditions in the structure should be changed in order to allow an acceptable safety level of the structure.

2.6.2 Second-moment reliability method

The mathematical definition of the probability of failure is defined in Eq. (2.61). The analytical solution of this integral is limited to very special restrictions [73]. The first-order reliability method (FORM) is published by Hasofer and Lind [164], is a commonly used approximation method for the assessment of the safety of a structure. The basic limitations and assumptions are:

- first and second central moments of basic variables are exclusively considered,
- correlated basic variables are transformed into uncorrelated ones,
- basic variables are transformed into standard normal distributed ones,
- probability density is normally distributed and
- limit state function is linear

In the case of the above-mentioned requirements, the exact analytical solution of the integral of the failure region in the probability density function is defined as:

$$p_f = \Phi\left(-\beta\right) \tag{2.63}$$

with β is the reliability index and Φ is the cumulative standardised normal distribution. A non-linear limit state function will lead to an inaccuracy in Eq. (2.63) due to the linearisation of the limit state function. Therefore, the relationship between the failure probability and the reliability index is approximated as:

$$p_f \approx \Phi\left(-\beta\right) \tag{2.64}$$

The error in the assessment of the failure probability using the FORM depends mainly on the characteristics of the failure function. This approximation error cannot be analytically computed [73]. In the case of basic variables with a non-normal underlying distribution, a transformation from the so-called physical space x

into the standard normal space u is necessary. For uncorrelated basic variables, the transformation is defined as:

$$Y_i = \Phi^{-1}\left[F_{X_i}(X_i)\right]; \quad i = 1 \ldots n \tag{2.65}$$

$$U_i = \Phi^{-1}\left(F_i(X_i)\right) \tag{2.66}$$

with U_i are the standardised normal parameters. The inverse transformation is consequently defined as:

$$X_i = F_i^{-1}\left(\Phi(U_i)\right) . \tag{2.67}$$

The second-moment reliability methods, the so-called level II reliability methods, are only approximations of the level III precisely simulated probability of failure. The concept was originally developed because of the lack of information on the tail of the distributions of the loading and the resistance parts. For the computation of the reliability index using the second-moment reliability methods, the exclusively influencing stochastic parameters are the mean values and the standard deviations of the basic variables [164]. Therefore, only the first and second central moments (see Sec. 2.3.1) of the probabilistic input variables are taken into account and therefore the approximation methods are the so-called second-moment reliability methods.

The probability of these variables is expected to be concentrated within a few standard deviations from the mean values. Therefore, the criterion of the level III simulations methods ($\mathbf{Prob}\left[g(\mathbf{X}) \leq 0\right] < p_{f,\text{accep}}$) is replaced by a criterion involving the mean value and the standard deviation of the basic variables.

The probability density $f_{E,R}$ is the volume for specific combinations of the effect of the action part and the resistance part (e, r). The point with the highest probability is visible in the case of the mean values μ_E and μ_R (top of the probability density). The failure criterion $R - E < 0$ is often considered in structural engineering and the following definitions are related to this criterion, see Fig 2.9. The safety margin Z (failure criterion) is also referred to as the limit state function $g(\mathbf{X})$ is defined as:

$$Z = g(\mathbf{X}) = R - E . \tag{2.68}$$

Therefore, the limit state of a structure appears in the case of the condition that the effect of the actions is co-occurring with an identical resistance of the structure ($e = r$). For the failure criterion $Z = R - E$, the limit state function is a 45° rotated e, r-plane measured from the point of origin.

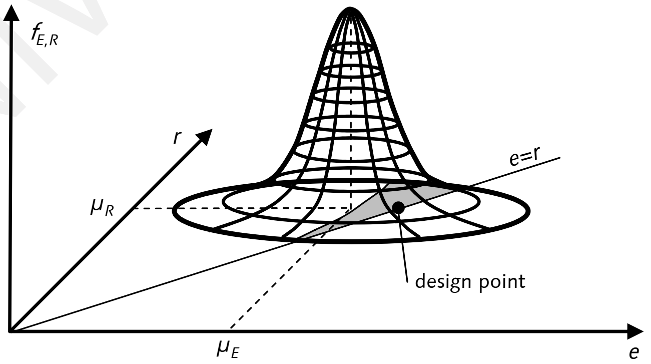

Figure 2.9: Probability density function of effect of action part E and resistance part R for failure criterion $R - E < 0$, based on [299]

The exceedance of the resistance of the structure occurs for the combinations of e, r in which $e > r$. Therefore, the structure is subjected to the failure condition, which is in the so-called failure region $G^*(E, R)$ with $Z(E, R) < 0$ [164]. In contrast, the safety of the structure occurs for all combinations of e, r ahead of the limit state function in which $e < r$. Therefore, the structure is deemed to be in the safe condition, which is in the so-called safe region $G(E, R)$ with $Z(E, R) > 0$.
The shift of the point of origin of the probability density $f_{E,R}$ to the centre of the plan area as well as the normalisation of the effect of action and the resistance according to the corresponding standard deviations σ_E and σ_R allows the computation of the design point P_d. The normalised coordinates of the transformed coordinate system are defined as:

$$\hat{e} = \frac{e - \mu_E}{\sigma_E} \tag{2.69}$$

$$\hat{r} = \frac{r - \mu_R}{\sigma_R} \tag{2.70}$$

The contour lines of the probability density are transferred into circles due to the normalisation. The limit state function according to the normalised coordinates is defined as:

$$\hat{r} \cdot \sigma_R + \mu_R - \hat{e} \cdot \sigma_E - \mu_E = 0\,. \tag{2.71}$$

The division of the normalised limit state function by $\sqrt{\sigma_R^2 + \sigma_E^2}$ leads to the form of the *Hesse*´ian normal form of a straight line [329].

$$\hat{r} \cdot \frac{\sigma_R}{\sqrt{\sigma_R^2 + \sigma_E^2}} - \hat{e} \cdot \frac{\sigma_E}{\sqrt{\sigma_R^2 + \sigma_E^2}} + \frac{\mu_R - \mu_E}{\sqrt{\sigma_R^2 + \sigma_E^2}} = 0 \tag{2.72}$$

Therefore, each term is comprehensible and interpretable. The last term of Eq. (2.72) defines the length as the perpendicular distance from the point of origin to the limit state function. The cut of the probability density at this point in the direction of the perpendicular line with the corresponding length/distance between the point of origin and the limit state function defines the reliability index β. This relation is feasible in the case of the normalisation of the coordinates. The reliability index according to Eq. (2.72) is:

$$\beta = \frac{\mu_R - \mu_E}{\sqrt{\sigma_R^2 + \sigma_E^2}}\,. \tag{2.73}$$

The reliability index is interpretable as the fractile-distance in the case of the assumed underlying normal distribution of the probability density $f_{E,R}$. Hence, the relationship between the reliability index β and the probability of failure p_f for a linear limit state function is described by a standardised normal distribution.

Table 2.8: Relationship between reliability index β and probability of failure p_f, 1 year reference period, linear problem with theory of first order, [299]

β	5.2	4.7	4.2	3.7	3.0	2.5	2.0
p_f	10^{-7}	10^{-6}	10^{-5}	10^{-4}	10^{-3}	$5 \cdot 10^{-3}$	10^{-2}

The coefficients of the first two terms in Eq. (2.72) are denoted as the weighting factors. They are geometrically interpreted as the cosine direction of the limit state function.

$$-\cos(\varphi_r) = \frac{\sigma_R}{\sqrt{\sigma_R^2 + \sigma_E^2}} \cong \alpha_R \tag{2.74}$$

$$-\cos(\varphi_e) = \frac{-\sigma_E}{\sqrt{\sigma_R^2 + \sigma_E^2}} \cong \alpha_E \tag{2.75}$$

$$\sqrt{\alpha_R^2 + \alpha_E^2} = 1 \tag{2.76}$$

The potential changes of the reliability index β are mainly caused by the variations in e and r. The coefficients α_R and α_E express the sensitivity of β according to the uncertain effect of action and resistance. Hence, these coefficients are the so-called weighting factors. For example, the reliability index β can be more sensitive due to the variations of the resistance part r than on the effect of action part e with the same magnitude ($\Delta r = \Delta e$). In summary, the position of the design point is defined to be:

$$\widehat{e}_d = -\alpha_E \cdot \beta \tag{2.77}$$

$$\widehat{r}_d = -\alpha_R \cdot \beta \tag{2.78}$$

The position of the design point P_d for a given reliability index β is exclusively dependent on the standard deviations σ_E, σ_R, which are closely linked to the weighting factors α_R, α_E. The ratio between the standard deviations σ_E/σ_R controls the position of the design point.

A simplification of the probabilistic load-resistance problem is helpful for engineering practice and the design of structures. Therefore, the weighting factors α_E, α_R are chosen as constant factors and the design point P_d is consequently fixed. Consequently, it has to be taken into account that some certain inaccuracy is introduced. This inexactness depends on the actual σ_E/σ_R ratio.

The reliability index is defined as the shortest distance between the point of origin of the probability density and the limit state function. The greater the perpendicular distance from the limit state function to the point of origin is, the greater the actual safety of the considered design situation will be. In order to resist the uncertainty caused by the assumption of the fixed design point, the weighting factors are ordinarily defined as $\sigma_E = -0.7$ and $\sigma_R = 0.8$ [299]. Hence, the design point P_d lies outside with respect to the circumscribed circle for the required reliability index β. The magnitude of the difference is 6% according to [222, 349].

$$\sqrt{\alpha_R^2 + \alpha_E^2} = \sqrt{(-0.7)^2 + 0.8^2} = 1.06\,. \tag{2.79}$$

For the initial coordinate system (e, r), the coordinates of the design point are:

$$E_d = \mu_E + \widehat{e} \cdot \sigma_E = \mu_E - \alpha_E \cdot \beta \cdot \sigma_E \tag{2.80}$$

$$R_d = \mu_R + \widehat{r} \cdot \sigma_R = \mu_R - \alpha_R \cdot \beta \cdot \sigma_R \tag{2.81}$$

The quantity E_d is the design value of the effect of action and the quantity R_d is the design value of the resistance. The design proof with these quantities is appropriate for the constant weighting factors $\alpha_E = -0.7$ and $\alpha_R = -0.8$.

BAUHAUS
UNIVERSITÄTSVERLAG

In "reality", there exist more than two probabilistic quantities for the assessment of the reliability of structures. The graphical interpretation of the safety index β is therefore difficult to capture in a 2D-representation. The probability density function for two probabilistic parts is graphically interpretable as a hill. This complexity of density function increases for more than two uncertain reliability parts. The probability density function with the corresponding safety index β is a sphere in the case of three stochastic input parts. The graphical representation of the probability density function of the reliability assessment is not presentable for more than three influence factors. The definition of the weighting factors α_E, α_R is applied in analogy to the reliability analysis with two probabilistic parts. In contrast, each weighting factor is considered as the product of a global weighting factor and an inner weighting factor. The global weighting factors are defined as $\alpha_E = -0.7$ for the effect of action part and $\alpha_R = 0.8$ for the resistance part.
In addition, the inner weighting factors $\alpha_{S,i}$, $\alpha_{R,i}$ are defined for the special stochastic effect of action quantities E_1, E_2, ..., E_i and the special stochastic resistance quantities R_1, R_2, ..., R_i. The German Institute for Standardisation (german: Deutsches Institut für Normung, abbreviation DIN) investigates the magnitudes of the inner weighting factors to be [128]:

- $\alpha_{R,1} = \alpha_{E,1} = 1.0$ for the quantity with the highest influence on the scatter and
- $\alpha_{R,i} = \alpha_{E,i} = 0.4$ for the quantities remaining.

The design values for the effect of action part E_d is extended for the design situations with a multitude of effect of action conditions E_i. This extension of the design value is based on Eq. (2.80) and is defined as:

$$E_{i,d} = \mu_{E,i} - \alpha_E \cdot \alpha_{E,i} \cdot \beta \cdot \sigma_{E,i} \tag{2.82}$$

$\mu_{E,i}$	...	mean value of the i-th effect of action component
$\sigma_{E,i}$	...	standard deviation of the i-th effect of action component
α_E	...	global weighting factor of the effect of action part ($\alpha_E = -0.7$)
$\alpha_{E,i}$	...	inner weighting factor of the effect of action part ($\alpha_{E,1} = 1.0$ for the predominant effect of action condition, $\alpha_{E,i} = 0.4$ for the remaining ones)

In analogy, the design value of the resistance part is based on Eq. (2.81) and is defined as:

$$R_{i,d} = \mu_{R,i} - \alpha_R \cdot \alpha_{R,i} \cdot \beta \cdot \sigma_{R,i} \tag{2.83}$$

$\mu_{R,i}$	...	mean value of the i-th resistance component
$\sigma_{R,i}$	...	standard deviation of the i-th resistance component
α_R	...	global weighting factor of the resistance part ($\alpha_R = 0.8$)
$\alpha_{R,i}$	...	inner weighting factor of the resistance part ($\alpha_{R,1} = 1.0$ for the predominant resistance condition, $\alpha_{R,i} = 0.4$ for the remaining ones)

2.6.3 Semi-probabilistic safety concept of Eurocode

The practical and daily designs of engineering structures using the Eurocode are generally based on the semi-probabilistic design concept of Eurocode 0 [136]. Therefore, different limit states are defined including the characteristic value, the partial safety factors, and the design rules.
The semi-probabilistic concept is commonly used in the design of engineering structures. The check of the necessary safety does not take into account the full scope of the distribution functions of the loading and

the resistance quantities. Various design criteria are investigated with deterministic values. The uncertainty of one single parameter is considered by the individual partial safety factors. Therefore, the common design concept of the Eurocode is the semi-probabilistic design concept, which is in general a simplified approach compared to the probabilistic design concept, see Sec. 2.6.1.

The determinations of the partial safety factors assists and simplifies the design practice. The computation of the design variables excluding the partial safety factors is previously defined according to Eq. (2.80) for the effect of actions E_d and according to Eq. (2.81) for the resistance R_d. The application of this definition is exclusively appropriate in the case of the exact knowledge of the mean values and the variances of all considered input quantities of the single effects of loading and the single resistances (probabilistic design concept). In general, this knowledge is extremely limited and consequently unsuitable for the daily design practice. Therefore, the variances of the input values for the design of engineering structures are considered by the partial safety factors in the semi-probabilistic design concept.

For the determination of the **partial safety factors**, it is necessary to establish a socially acceptable safety level expressed by the safety index β. The predefinition of the safety index quantity is, among other things, dependent on the consequences of failure of the structure, and the so-called consequence classes, which are linked to the reliability classes, see Tab. 2.9.

Table 2.9: Determination of reliability index β according to Eurocode [53, 136], ultimate limit state (ULS), serviceability limit state (SLS, irreversible), reference period (RP)

Consequence class	Reliability class	Description	Target values for β 1 year RP	50 years RP
CC 3	RC 3	high consequence for loss of human life, or economic, social or environmental consequences very great	5.2	4.3
CC 2	RC 2	medium consequence for loss of human life, economic, social or environmental consequences considerable	4.7 (ULS) 2.9 (SLS)	3.8 (ULS) 1.5 (SLS)
CC 1	RC 1	low consequence for loss of human life, and economic, social or environmental consequences small or negligible	4.2	3.3

The partial safety factors applied in the practical design of structures are defined for the reliability class RC 2 with the useful life of 50 years. In the case of structures such as power plants, bridges or dams, a different consequence and reliability classes are predefined. Consequently, the target value of the reliability index increases (lower probability of failure) for the structures with a pronounced importance for the society. In addition to the partial safety factors, the **characteristic values** are a strongly influential aspect of the safety concept of the Eurocodes. The quantity of the partial safety factors is always connected with the definition of the corresponding characteristic values. The characteristic values are established as reference values, which are representative quantities of the loading condition and the resistance. Hence, the question of the definition of the representative values arises. For example, the characteristic value of the wind loading can be referred to as the mean value of a certain reference period or can even be defined as the maximum magnitude of a certain reference period. The definition of the fractile quantities is usually applied for the material properties. For example, the 5%-fractile can be defined for the concrete compressive strength. Consequently , the characteristic values of the loading condition and the resistance are linked to a certain probability of occurrence. It can be assumed that the characteristic values are exceeded or undershot in the reference period with the corresponding probability of occurrence.

The definition of the characteristic values for the loading is dependent on the **loading condition**, see Tab. 2.7. The loads related to the permanent loading have less variation of their load magnitude over the service life of the structure. The variation in the range of the mean value is generally minor for the permanent loading condition. Hence, the coefficient of variation CV of the permanent loads is $CV \leq 0.10$ [299] and the mean value is representative for the permanent load magnitude. The characteristic value of the dead load loading condition is defined according to the mean material density quantities [137].

The variability of the load magnitude as well as the probability of occurrence of the variable loads lead to a higher variance $CV > 0.10$ [299] in comparison to the permanent loads. The representative value of the variable loads cannot be exclusively expressed by the mean value of the load magnitude. The consideration of the stochastic properties of the probability density function is not possible for the application of the mean value as the characteristic value for the variable loads. For example, the average wind load magnitude over a certain time period cannot be stated as a representative quantity. The information about the maximum and minimum peak values is not considered in the mean value.

The representative load magnitudes of the variable loads are defined in relation to a certain confidence bound of the probability density function. Therefore, the fractile values are applied in the determination of the characteristic values for the variable loads. In general, the load magnitude of a variable load is stated to be representative, if the quantity will be exceeded only once in the service life. In the case of a 50-year design life, the exceedance probability of the characteristic value is $1/50 = 0.02$. This representative value of the variable load magnitude is also called the 98%-fractile, see Tab. 2.7. The nominal values are tradionally applied, but are not related to a statistical distribution characteristic.

The mean values of the probability density functions are not representative quantities for the various material properties. The variation of the material properties is in general $CV > 0.1$. Therefore, the characteristic values for the material properties are also related to fractile confidence bounds, see Sec. 3.1.

The **partial safety factors** consider the different variances of the special effects of the actions and the resistance conditions by the individual partial safety factors. This concept with the partial safety quantities allows for a uniform design safety level for a wide range of different structures. In contrast, the past design concept with the global safety factors (e.g. [131, 132, 133]) did not consider the independence of the variable effects of the action parts and the resistance parts. Consequently, a uniform safety level cannot be achieved by the global safety factor concept.

The computation of the effect of actions E is associated with various uncertainties. The stochastic characteristics of the loading F, the divergence of the geometric parameters in the structure to their nominal values of the building drawing, and errors due to the computational model are the main sources of uncertainty which are considered in the partial safety factors.

The partial safety factors for the loading part consider the following sources of uncertainty:

- variances in the loading conditions,
  such as adverse deviation according to the characteristic values
- variances in the geometric parameters constructed,
  such as differences between the nominal geometric parameters of the building drawings and the constructed geometry
- model uncertainty.
  such as uncertainty due to the computational model for the analysis of the effect of actions

Uncertainties on the resistance part occur similarly, which are caused by the transfer from the material properties to the structural resistances. The partial safety factors for the resistance part consider the following uncertainties [299]:

- variances in the material properties,
  such as adverse deviation according to the characteristic values
- variances in the geometric parameters constructed,
  such as differences between the nominal geometric parameters of the building drawings and the constructed geometry
- model uncertainty.
  such as uncertainty due to the computational model for the analysis of the resistance of the structure

However, consideration must be given to the fact that the partial safety factors according to the model uncertainty exclusively consider "small" computational errors. On average, the structural model is able to simulate the load-bearing behaviour adequately with the assumed partial uncertainty safety factors [349]. The errors due to the selection of generally inappropriate models are not considered in these safety factors.
The **design rules** define the combination regulations between the partial safety factors and the characteristic values in dependence of limit states. For the structural engineering design practice, the serviceability limit state (SLS) and the ultimate limit state (ULS) are the most influential components of the analysis and the design of structures. The other components of the limit states in the design and the life cycle assessment of structures are the durability, the robustness, the redundancy, the economy, the environmental compatibility, the sustainability, and the forming [299].
The design concept of the Eurocode is based on the limit state design in the SLS and ULS. In addition, different design situations have to be considered in the limit states. The general design requirement is independent of the limit state and the design situation and is defined by:

$$E_d \leq R_d \quad \text{resp.} \quad \frac{E_d}{R_d} \leq 1\,. \tag{2.84}$$

2.6.4 Non-linear safety concept for concrete structures

A non-linear simulation of an entire structure requires a safety level, which is comparable with the conventional cross section design methods using the linear-elastic determination of the section forces and the subsequent non-linear design of critical cross sections. In the conventional design procedure, a strict decomposition between the section force analysis and the load capacity of the cross sections is used which is generally independent of the types of structures. No coupling between the cross section design and the force analysis is considered in this design procedure. Therefore, this design procedure is a simplified methodology, while still ensuring a minimum safety margin [224]. The "real" distribution of the loading and resistance in the entire structure and the interaction between both cannot be considered in this design approach. The reduced quantile material properties including the material safety factors are used for the design of structures with the linear-elastic computation of the section-forces and the subsequent design of the critical cross sections.
Design procedures for non-linear structural analyses have been investigated in recent decades. The simulation with non-linear material models more adequately predicts the stiffness and force distribution in the

structure. Therefore, the actual load-deformation behaviour can only be represented by considering the average material properties, because the results obtained using design values are not able to predict the "real" behaviour. Hence, a discrepancy between the commonly used design of critical cross sections applying the design values and the non-linear structural simulation is obvious. Nowadays, a non-linear safety concept is proposed in the EC 2 [141] and MC 10 [187]. Therefore, a safety factor γ_R for the resistance part is introduced representing a safety margin on a structural level. This safety factor also considers the required level of safety which ensures that no failure in the structure occurs in the case that the material properties at any position in structure fall below the lower fractile-values. It is necessary to consider the influence of the uncertainty in the material properties on the cross section bearing capacity as well as on the load-deformation behaviour of the structure [224].

More information about the non-linear safety concept of EC 2 and MC 10 for concrete structures with various comparative case studies can be found in ALLAIX et al. [5], CERVENKA [65, 66], JACKSON [191], SCHLUNE et al. [369, 370], and WOLIŃSKI [411]. The main limit state equation for the non-linear simulation of structures, according to the non-linear safety concept of EC 2, with respect to the German National Annex [141], is defined as:

$$E_d \leq \frac{R}{\gamma_R} \Rightarrow R\left(f_{cR};\, f_{yR};\, f_{tR};\, f_{p0.1R};\, f_{pR}\right) . \tag{2.85a}$$

Therein, the safety concept of the EC 2 defines the "calculation" material properties (expressed by index "R") for the physical non-linear simulations as follows:

$$f_{cR} = 0.85 \cdot \alpha \cdot f_{ck} \,, \tag{2.85b}$$

$$f_{yR} = 1.10 \cdot f_{yk} \,, \tag{2.85c}$$

$$f_{tR} = 1.08 \cdot f_{yR} \quad \text{B 500B} \,, \tag{2.85d}$$

$$f_{tR} = 1.05 \cdot f_{yR} \quad \text{B 500A} \,, \tag{2.85e}$$

$$f_{p0.1R} = 1.10 \cdot f_{p0.1k} \,, \tag{2.85f}$$

$$f_{pR} = 1.10 \cdot f_{pk} \,, \tag{2.85g}$$

$$\gamma_R = \begin{cases} 1.3 & \text{permanent and transient design condition} \\ 1.1 & \text{accidental design condition} \end{cases} . \tag{2.85h}$$

These computational average values ensure the independence of structural safety checks, with respect to the failure model (ductile or brittle), by considering a consistent global safety factor for the structural bearing capacity. In the ultimate limit state with the permanent design condition, the consistent global safety factor is visible for the ratio f_{cR}/f_{cd} and f_{yR}/f_{yd}:

$$\frac{f_{cR}}{f_{cd}} = \frac{0.85 \cdot \alpha \cdot f_{ck}}{\alpha \cdot f_{ck}/\gamma_c} = 1.275 \approx 1.3 \,, \tag{2.86}$$

$$\frac{f_{yR}}{f_{yd}} = \frac{1.1 \cdot f_{yk}}{f_{yk}/\gamma_s} = 1.265 \approx 1.3 \,. \tag{2.87}$$

The failure of the system is controlled by the check of the material limit strains for the steel and the concrete. In the case of geometric non-linearities in the entire structure or in structural components, the failure is reached at the indifferent equilibrium [11].

3 Modelling aspects of restraint sensitive concrete structures

3.1 Material models

3.1.1 Concrete material properties

3.1.1.1 Classification

In general, concrete can be classified into several categories such as density and strength. The classification with respect to the oven-dry density of hardened concrete is defined as [187, 420]:

- lightweight aggregate concrete $800 \leq \rho \leq 2000\,\mathrm{kg/m^3}$
- normal weight concrete $2000 < \rho \leq 2600\,\mathrm{kg/m^3}$
- heavy weight concrete $\rho > 2600\,\mathrm{kg/m^3}$

Engineering structures for ordinary buildings and bridges are mainly constructed with normal weight concrete. Therefore, the theory about the concrete material models in this thesis is based on normal weight concrete.

The strength classification is related to the compressive strength which categorises concrete grades. The design guidelines Model Code 90 (MC 90) [74] and Model Code 10 (MC 10) [187] classify concrete according to the compressive strength of cylindrical specimens. In contrast, the Eurocode 2 (EC 2) [101] classifies the strength grades in an dual designation considering the compressive strength of cylinders (first number) and cubes (second number). The guideline EN 206 [103] specifies characteristics of cylinder strengths from $12\,\mathrm{MN/m^2}$ (normal strength) to $100\,\mathrm{MN/m^2}$ (high strength), which are covered by the design codes and guidelines MC 10 and EC 2 [101] in the following grades:

- Model Code 90 and Model Code 10 C 12, C 16, C 20, C 25, C 30, C 35, C 40, C 45, C 50, C 55, C 60, C 70, C 80, C 90, C 100, C 110, C 120
- Eurocode 2 C 12/15, C 16/20, C 20/25, C 25/30, C 30/37, C 35/45, C 40/50, C 45/55, C 50/60, C 55/67, C 60/75, C 70/85, C 80/95, C 90/105

For a characteristic compressive strength of $f_{ck} \leq 50\,\mathrm{MN/m^2}$, the concrete grades are classified to normal strength concrete (NSC). Concrete grades with $f_{ck} > 50\,\mathrm{MN/m^2}$ are classified as high strength concrete (HSC) [187].

BAUHAUS
UNIVERSITÄTSVERLAG

3.1.1.2 Compressive strength

In laboratory experiments, concrete compressive strength can be measured in a uniaxial compression test. For example, the strength according to the Model Code 90 [74] should be tested for cylinders $f_{ck,\mathrm{cyl}}$, 150 mm in diameter and 300 mm in depth, which are stored in water at $20 \pm 2°\mathrm{C}$ and tested at the age of 28 days. The international European standard EN 206 [103] specifies that the laboratory test be performed according to the recommendations of EN 12390 [102]. Therefore, the characteristic compressive strength should be tested with cylinders 150 mm in diameter and 300 mm in depth and with cubes of 150 mm edge length $f_{ck,\mathrm{cube}}$. In addition, the international standard code ISO 1920 [188] recommends the same cylindrical geometry for the compressive test.

In general, the concrete compressive strength depends on the size and shape of specimen, water/cement ratio, degree of hydration and moisture state, concrete age and curing, type and strength class of cement, type and amount of additions and in some cases on the type of admixtures [185]. The aggregate strength and stiffness significantly affect the concrete compressive strength for high strength concrete ($f_{ck,\mathrm{cyl}} \geq 55\,\mathrm{MN/m^2}$). Thus, the strength of HPC depends primarily on concrete composition and conditions during concrete hardening. Conversion factors may be used in order to consider different test specimen sizes, curing effects, and environmental conditions [10, 292].

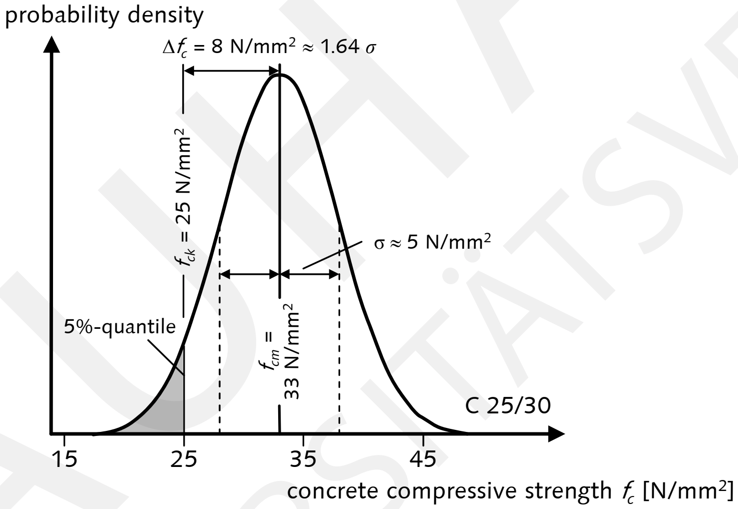

Figure 3.1: Probabilistic distribution of concrete compressive strength according to EC 2 recommended for concrete grade C 25/30

For each concrete grade, the test results of the compressive strength vary around an average value. Hence, it is also important to determine lower and upper bound values representing quantiles and fractiles, respectively. Material properties related to a certain quantile are referred to as characteristic values. The characteristic compressive strength f_{ck} is defined as the strength below 5% of all test specimens may be expected to fall. For the purpose of verification in design and estimation of other concrete properties, it is necessary to refer to a mean value of compressive strength f_{cm} which is generally defined as:

$$f_{cm} = f_{ck} + \Delta f \,. \tag{3.1}$$

The MC 90 recommends a value of $\Delta f = 8\,\mathrm{MN/m^2}$ independent of the concrete grade. In the updated textbook of Model Code 1990 (MC 90-99) [185], the scatter in the concrete compressive stress is defined as $\Delta f = 1.64 \cdot \sigma_{f_c}$. This determination is related to the 5% quantile of the normal distribution. Thus, the standard deviation can be assessed separately for each concrete class. In the current version of EC 2 [101] and MC 10, [187], the randomness in the compressive strength is assumed to be normally distributed and the variance is determined to be $\sigma_{f_c} = 5\,\mathrm{MN/m^2}$, independent of the concrete grade. For the concrete grade C 25/30, Fig. 3.1 shows the assumed normal distribution with the average value $f_{cm} = 33\,\mathrm{MN/m^2}$ and the characteristic strength $f_{ck} = 25\,\mathrm{MN/m^2}$. This determination is commonly applied to the design of structures for the cases where no specific experimental data about the uncertainty (randomness) in this strength property is available. However, measurements on actual concrete specimens are much more reliable than those general approximations in design guidelines in order to analyse the probabilistic material characteristics. The results of such experimental investigations on actual concrete are mentioned in Sec. 2.3.2.

3.1.1.3 Tensile strength

Concrete tensile strength depends primarily on the parameters which also influence the compressive strength such as the type and strength class of cement or water/cement ratio. The correlation between tensile and compressive strength is not proportional, particularly for higher strength concrete (HSC). An increase in compressive strength, such as for HSC, cause only to a small increase in tensile strength [221]. The increasing brittleness of the cement paste with increasing compressive strength is one of the reasons for this phenomenon. The increase in brittleness is due to the crack propagation in the cement paste being less hindered by voids, due to a finer and denser pore structure [340].

The tensile strength is influenced by shape, size, surface condition, and mineralogical character of the aggregates [161]. Another main influencing factor on the tensile strength is the test method (uniaxial tensile, tensile splitting, and flexural testing). In this context, the tensile strength is generally more size and shape dependent than the compressive strength [185]. However, the size effect becomes less pronounced as the concrete compressive strength increases [351]. In addition to the size dependence and different test methods, internal stresses such as drying shrinkage can significantly influence concrete tensile strength [186]. Hence, this material property should be taken into account with caution in the design of structures.

In general, tensile strength basically refers to the axial tensile strength f_{ct} determined in laboratory uniaxial tensile tests. Due to experimental difficulties in performing such experiments, the axial strength is almost exclusively determined in research [185]. However, uniaxial tensile testing is the most appropriate method in order to determine the concrete tensile strength, because of its specimen size independence [187].

Therefore, uniaxial tension tests on unnotched specimens provide reliable measurement data establishing relationships between compressive and tensile concrete strength [186]. Without specific experimental data for a particular concrete, the concrete axial tensile strength on average f_{ctm} (in $[\mathrm{MN/m^2}]$) may be computed relative to the compressive strength as follows:

$$f_{ctm} = 1.40 \cdot \left(\frac{f_{ck}}{10\,\mathrm{MN/m^2}}\right)^{2/3} \qquad \text{MC 90 [74]}\,, \tag{3.2a}$$

$$f_{ctm} = 2.12 \cdot \ln\left(1 + \frac{f_{cm}}{10\,\mathrm{MN/m^2}}\right) \qquad \text{Remmel [340]}\,, \tag{3.2b}$$

$$f_{ctm} = 2.64 \cdot \left(\ln\left(\frac{f_{cm}}{10\,\mathrm{MN/m^2}}\right) - 0.1\right) \qquad \textit{fib}\text{ Bulletin 42 [186]}\,, \tag{3.2c}$$

$$f_{ctm} = 0.30 \cdot (f_{ck})^{2/3} \qquad \leq \text{C}\,50/60 \quad \text{MC}\,10\ [187],\ \text{EC}\,2\ [101]\,, \tag{3.2d}$$

$$f_{ctm} = 2.12 \cdot \ln\left(1 + \frac{f_{cm}}{10\,\text{MN/m}^2}\right) > \text{C}\,50/60 \quad \text{MC}\,10\ [187],\ \text{EC}\,2\ [101]\,. \tag{3.2e}$$

More recent measurement data including tests on high performance concretes are used in REMMEL's study [340], see Eq. 3.2b. These measurements are mainly observed on notched specimens. The results of this study are considered for high strength concrete in the Mode Code 10 and the Eurocode 2 for concrete grades >C 50/60. In the textbook *fib* Bulletin 42 [186], the empirical relationship between concrete compressive strength and axial tensile strength, see Eq. 3.2c, is investigated for unnotched specimens. This leads to higher determination of the tensile strength compared to Eq. 3.2b. A comparison of the empirical relationship assessed by several research studies between concrete compressive and tensile strength considering measurement data (*fib* Bulletin 42) is shown in Fig. 3.2.

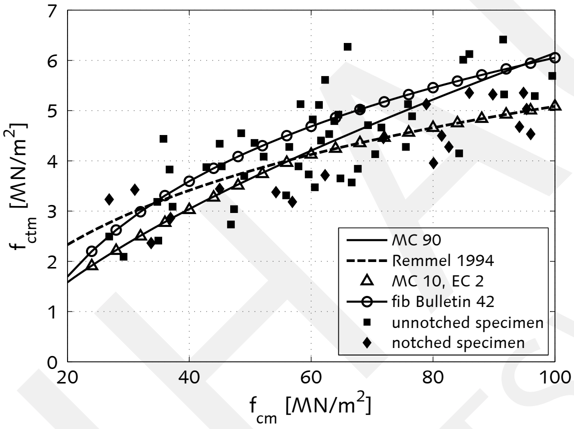

Figure 3.2: Influence of concrete compressive strength f_{cm} on axial concrete tensile strength f_{ctm} according to MC 90 [74], REMMEL [340], *fib* Bulletin 42 [186], MC 10 [187], measurement data [186]

For some design requirements, such as minimum reinforcement or deflection control, it might be necessary to determine tensile strength to its quantiles. In the Model Code 1990 [74], it is proposed:

• for deflections	mean or lower quantile value	$f_{ctk,0.05}$, f_{ctm},
• for minimum reinforcement	upper quantile value	$f_{ctk,0.95}$,
• for stability verifications	mean value	f_{ctm},
• for crack width calculation	mean value	f_{ctm},

in which $f_{ctk,0.05}$ is the lower 5% quantile and $f_{ctk,0.95}$ is the upper bound 95% quantile. These probabilistic properties of the axial tensile strength may be computed by (f_{ctk} in [MN/m^2]):

$$f_{ctk,0.05} = 0.95 \cdot \left(\frac{f_{ck}}{10\,\text{MN/m}^2}\right)^{2/3} \qquad \text{MC}\,90\ [74]\,, \tag{3.3a}$$

$$f_{ctk,0.95} = 1.85 \cdot \left(\frac{f_{ck}}{10\,\text{MN/m}^2}\right)^{2/3} \qquad \text{MC}\,90\ [74]\,, \tag{3.3b}$$

$$f_{ctk,0.05} = 0.7 \cdot f_{ctm} \qquad \text{MC}\,10\ [187],\ \text{EC}\,2\ [101]\,, \tag{3.3c}$$

$$f_{ctk,0.95} = 1.3 \cdot f_{ctm} \qquad \text{MC}\,10\ [187],\ \text{EC}\,2\ [101]\,. \tag{3.3d}$$

In MC 90, the ratio between the average strength and the quantiles is similarly defined as $0.95/1.40 \approx 0.7$, and $1.85/1.40 \approx 1.3$. Upper and lower quantiles of concrete tensile strength are similarly recommended by MC 90, MC 10 and EC 2.

As a consequence of the experimental difficulties in uniaxial tensile testing, in many instances, concrete tensile strength is assessed in splitting (tensile splitting strength $f_{ct,\mathrm{sp}}$) or flexural tests (flexural strength $f_{ct,\mathrm{fl}}$), according to EN 12390 [102] or ISO 1920 [188], respectively. A comparison of the strength magnitudes shows that flexural strength is higher than axial strength and the tensile splitting strength is closer to axial strength [292]. Similar to the size effect in compressive strength, tensile splitting and flexural strength are dependent on various conditions in the test setup. In contrast, axial tensile strength is much less sensitive to several testing conditions. Hence, the uniaxial tensile test is the most appropriate method to determine the concrete fracture properties in tension. Nevertheless, in many instances, the tensile splitting strength is determined due to a more practical testing technique. This strength depends mainly on specimen shape [161, 347], specimen size [30, 200], and width of bearing strips [348]. In the case narrow bearing strips are used, the effect of specimen shape or size is not significant within the usual range of test specimen sizes [348]. The critical stresses act at some distance from the concrete surface and therefore the tensile splitting strength is much less sensitive to curing conditions [171]. Therefore, tensile splitting strength data shows less variance (measurement uncertainty) compared to data obtained from flexural tests.

In the case that tensile strength properties are not determined by means of direct tests, empirical conversion factors can be used to determine the axial tensile strength. The transition between axial and tensile splitting strength may be computed by:

$$f_{ctm} = 0.9 \cdot f_{ct,\mathrm{sp}} \qquad \text{MC 90 [74]}\,, \tag{3.4a}$$

$$f_{ctm} = 0.95 \cdot f_{ct,\mathrm{sp}} \qquad \text{DAfStb 444, R}{\small\text{EMMEL}}\text{ [340]}\,, \tag{3.4b}$$

$$f_{ctm} = \frac{2.635 \cdot \ln(f_{cm}) - 6.322}{2.329 \cdot \ln(f_{cm}) - 4.71} \cdot f_{ct,\mathrm{sp}} \qquad \textit{fib}\text{ Bulletin 42 [186]}\,, \tag{3.4c}$$

$$f_{ctm} = 1.0 \cdot f_{ct,\mathrm{sp}} \qquad \text{MC 10 [187]}\,. \tag{3.4d}$$

In MC 90, the conversion factor between axial tensile and splitting strength is defined as $\alpha_{\mathrm{sp}} = 0.9$. This determination is based on the study of HEILMANN [166], in which this relationship is experimentally investigated between compressive strength and axial strength and compressive strength and splitting strength, respectively. . Therefore, the ratio between axial and splitting strength is defined as [166]:

$$\alpha_{\mathrm{sp}} = \frac{f_{ctm}}{f_{ct,\mathrm{sp}}} = \frac{0.24 \cdot f_{c,\mathrm{cube}}^{2/3}}{0.27 \cdot f_{c,\mathrm{cube}}^{2/3}} = 0.89\,. \tag{3.5}$$

In the textbook *fib* Bulletin 42 [186], α_{sp} is defined according to Eq. 3.4c and is in the range between $\alpha_{\mathrm{sp}}(f_{cm} = 20\,\mathrm{MN/m^2}) = 0.69$ and $\alpha_{\mathrm{sp}}(f_{cm} = 160\,\mathrm{MN/m^2}) = 0.99$, see Fig. 3.3(a). The study by REMMEL (DAfStb 444, [340]) recommends a conversion factor of 0.95. New comprehensive experimental and numerical investigations by MALÁRICS and MÜLLER [255, 256, 257] determined, that conversion should be performed in relation to various specimen geometries and concrete types. This study proposes conversion factors for several geometries and concrete types, which are in general $\alpha_{\mathrm{sp}} > 1.0$, see Fig. 3.3(a). As a compromise between the different effects in the splitting testing, MC 10 proposes $\alpha_{\mathrm{sp}} = 1.0$. Moreover, an extensive evaluation of the ratio between tensile splitting and compressive strength for several concrete grades can be found in [9, 415].

The flexural test is another method to determine the concrete strength in tension. The flexural strength strongly depends on the size of the testing beam [249, 336]. In particular, flexural strength is sensitive to the depth of the specimen beam [288]. Furthermore, the results of flexural tests are influenced by notches and notch size, test setup (three or four-point bend test [124]) and curing conditions [186].

The effect of the beam depth may be computed according to Eq. 3.6, which defines conversion between flexural strength and axial tensile strength α_{fl} as:

$$f_{ctm} = f_{ct,\mathrm{fl}} \cdot \frac{\alpha_{\mathrm{fl}} \left(\dfrac{h_b}{h_0}\right)^{0.7}}{1 + \alpha_{\mathrm{fl}} \left(\dfrac{h_b}{h_0}\right)^{0.7}} \qquad \text{MC 90 [74], MC 90-99 [185], MC 10 [187]} . \tag{3.6}$$

with h_b the depth of the beam and $h_0 = 100\,\mathrm{mm}$. The effect of maximum aggregate size on tensile strength is neglected in Eq. 3.6 and thus it is only valid for $h_b > 50\,\mathrm{mm}$. As the depth of the beam increases, flexural strength approaches axial tensile strength. In MC 90, the value of $\alpha_{\mathrm{fl}} = 1.5$ is proposed. This factor depends on the brittleness of the concrete with respect to the testing concrete beams. Experimental results show that the ratio $f_{ct,\mathrm{fl}}/f_{ctm}$ decreases with beam depth, due to higher brittleness [288]. Therefore, the factor should increase for higher beam depths, see Fig. 3.3(b).

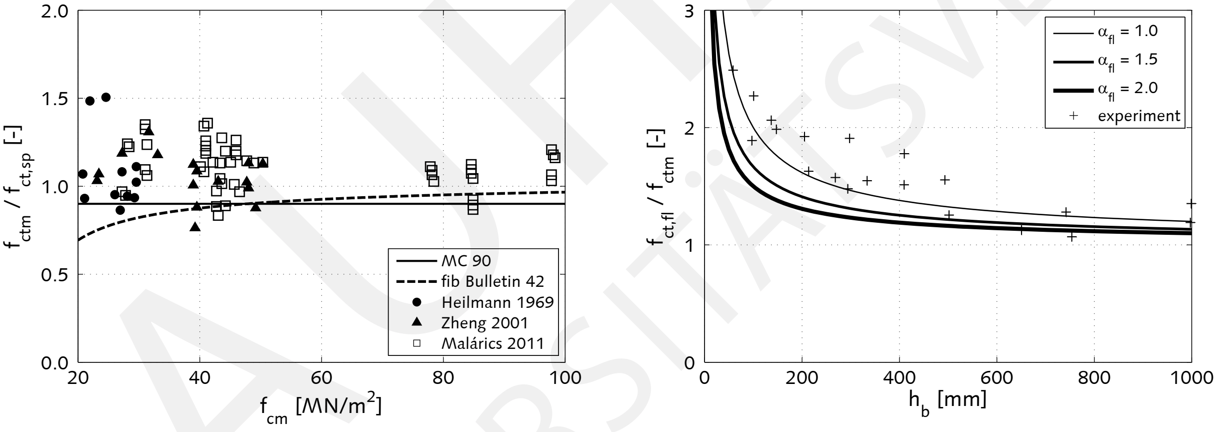

(a) Ratio between concrete axial and splitting tensile strength according to various experiments, HEILMANN [166], ZHENG [417], MALÁRICS [255], $\alpha_{\mathrm{sp}} = 0.9$ according to MC 90 [74], *fib* Bulletin 42 [186]

(b) Influence of beam depth on ratio between concrete flexural and axial tensile strength according to MC 90-99 [185]

Figure 3.3: Experimental data and empirical relationships between splitting, flexural and axial concrete tensile strength

3.1.1.4 Modulus of elasticity

The concrete modulus of elasticity is mainly influenced by hydrated cement paste and aggregate stiffness similar to the influence it has on compressive strength [185]. On one hand, concrete modulus of elasticity can be simulated on the basis of the composite materials theory in the case that the moduli of the components are known [163, 398]. On the other hand, a number of empirical formulas is proposed in design codes and guidelines. These determinations estimate the modulus of elasticity relative to the compressive strength. In these empirical relationships, the modulus of elasticity raises with an increase in concrete strength, which confirms the commonly observed trend in experiments [404].

The concrete modulus of elasticity is defined either as the tangent E_{c0} at the origin of the stress-strain relationship or as the secant E_{cm} between the origin and concrete compression strain at a stress level of $\sigma_c = -0.40 \cdot f_{cm}$. The tangent modulus of elasticity does not include initial plastic deformations and is approximately equal to the slope of the secant of the unloading branch (rapid unloading condition). In contrast, the secant modulus of elasticity includes some irreversible strains and therefore $E_{c0} > E_{cm}$ (normal strength concrete). The tangent modulus of elasticity at the age of 28 days may be determined by:

$$E_{c0} = \alpha_{\text{aggre}} \cdot 2.15 \cdot 10^4\,\text{MN/m}^2 \cdot \left(\frac{f_{cm}}{10\,\text{MN/m}^2}\right)^{1/3} \qquad \text{MC 90 [74], MC 10 [187],} \tag{3.7a}$$

$$E_{c0} = 1.02 \cdot 10^4\,\text{MN/m}^2 \cdot (f_{cm})^{1/3} \qquad \text{Wee et al. [404],} \tag{3.7b}$$

$$E_{c0} = 1.05 \cdot 2.20 \cdot 10^4\,\text{MN/m}^2 \cdot \left(\frac{f_{cm}}{10\,\text{MN/m}^2}\right)^{0.3} \qquad \text{EC 2 [101],} \tag{3.7c}$$

and the secant modulus of elasticity by:

$$E_{cm} = 0.85 \cdot E_{c0} \qquad \text{MC 90 [74],} \tag{3.8a}$$

$$E_{cm} = \alpha_{E_{cm}} \cdot E_{c0} \qquad \text{MC 10 [187],} \tag{3.8b}$$

$$\alpha_{E_{cm}} = 0.80 + 0.20 \cdot \frac{f_{cm}}{88\,\text{MN/m}^2} \leq 1.0\,.$$

$$E_{cm} = 1/1.05 \cdot E_{c0} \approx 0.95 \cdot E_{c0} \qquad \text{EC 2 [101].} \tag{3.8c}$$

Experimental measurements and regression analysis by Wee et al. [404] on 163 cylindrical specimens (see Eq. 3.7b) are used for comparison to the empirical models of MC 90, MC 10, and EC 2. A small improvement in accuracy is assessed for Wee in comparison to other models, as is expected. Nevertheless, the general shape is almost identical for all considered models, see Fig 3.4(a). Moreover, the determination of the tangent and secant modulus of elasticity are similarly defined in MC 90 and MC 90-99.

In MC 90 and EC 2, a strength independent ratio is proposed between the tangent and secant modulus of elasticity $\alpha_{E_{cm}} = E_{cm}/E_{c0}$. The ratio is determined as $\alpha_{E_{cm}} = 0.85$ in MC 90 and $\alpha_{E_{cm}} \approx 0.95$ in EC 2. In contrast, experimental results show that the difference between first loading up to $\sigma_c = -0.4 \cdot f_{cm}$ and the unloading branch decreases with an increase in compressive strength [187]. For example, the difference is smaller than 3 % for concrete grades higher than C 80/95. Therefore, MC 10 considers the strength dependence in the ratio between both moduli of elasticity, see Eq. 3.8b. The comparison between different empirical determinations of the secant modulus of elasticity E_{cm} as a function of the compressive strength is shown in Fig. 3.4(b).

For designing purposes, secant modulus of elasticity should be used for an elastic analysis of concrete structures in order to account for initial plastic strains [74, 110, 185]. In contrast, tangent modulus of elasticity may be used for non-linear compressive and tensile stress-strain relationships as well as for an estimate of concrete creep [187]. The effect of aggregate type on modulus of elasticity can be considered approximately by multiplying E_{c0} by the aggregates influence coefficients α_{aggre}, see Tab. 3.2. The values listed in Tab. 3.2 should be seen as indicative and crude approximations that are reasonable for general

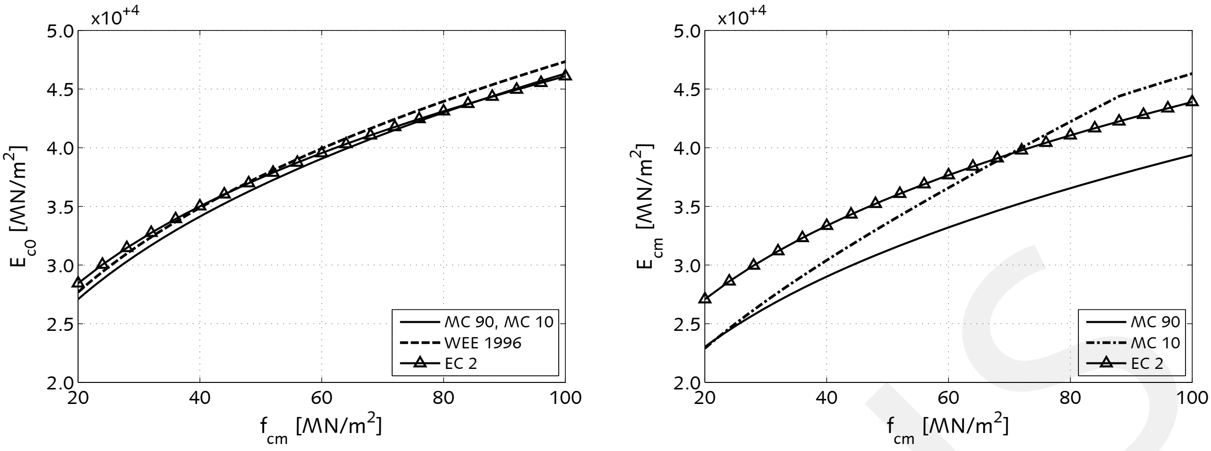

(a) Tangent modulus of elasticity E_{c0}

(b) Secant modulus of elasticity E_{cm}

Figure 3.4: Concrete moduli of elasticity E_c as a function of compressive strength f_{cm} according to Wee et al. [404], MC 90 [74], MC 10 [187], and EC 2 [101]

applications such as parametric studies. More accurate consideration of the influence of aggregate stiffness on concrete modulus of elasticity can be assessed by direct experimental measurements. If the structure is sensitive to variations in elastic stiffness, E_c should be experimentally determined, which may significantly reduce uncertainties in model predictions and allow for a more reliable design of the structure.

Table 3.2: Effect of aggregate type on concrete modulus of elasticity

Aggregate type	α_{aggre}		
	MC 90, MC 90-99, MC 10 [74, 185, 187]	EC 2 [101]	DAfStb 525 [126]
Basalt, dense limestone	1.20	1.20	1.05 - 1.45
Quartzitic	1.00	1.00	0.80 - 1.20
Limestone	0.90	0.90	0.70 - 1.10
Sandstone	0.70	0.70	0.55 - 0.85

3.1.2 Concrete in compression

3.1.2.1 Fracture process

The material behaviour of plain concrete in compression is characterised by a non-linear stress-strain relation. With increasing stress level, concrete tends to soften as a consequence of concrete microcracking. At a stress level of about 40% of compressive strength, bond cracks are already present in the aggregate-paste interface and start to grow in the case of further increase in load. These cracks propagate into the matrix at a stress level in the concrete of about 80% of compressive strength. The predominant direction of crack propagation is parallel to the external load. This system of microcracks causes the non-linear material behaviour of concrete in compression [74]. On one hand, the microcracking of lower and medium strength of concrete is concentrated in the hydrated cement paste and in the paste-aggregate interfaces. On the other hand, for high strength concrete, microcracks can also pass through aggregates. Thus, different crack patterns may be developed for NSC and HSC.

A further stress increase induces crack growth and shorter cracks join to form longer ones. The concrete compressive strength is reached in the case that under a constant stress, sudden, unstable fracture occurs. This can be observed if the length of one or more of several microcracks becomes critical [185]. For loading with a constant strain rate, the external force is reduced after the ultimate load is reached. Therefore, microcracks continue to grow in a stable fashion and a descending portion of the stress-strain relationship can be observed in experimental compressive tests [391].

The fracture region of the irreversible strains due to the microcrack formation is limited to a certain width in which the compressive strains are concentrated [185], particularly for strains $\epsilon_c > |\epsilon_{c1}|$, in which ϵ_{c1} refers to the strain at the compressive strength. Hence, compressive failure is a discrete phenomenon [278]. The descending relationship for concrete in compression is influenced by the specimen or member geometry, boundary conditions and possibilities for load distribution in the structure. Consequently, the post-peak range in the stress-strain relationship is size dependent and thus not only a property being influenced by the material characteristic itself [186].

Experimental studies by van Mier [276, 277] show that decreasing specimen depth leads to an increase in ductility due to the concentrated microcracking, see Fig. 3.5(a). For longer specimens, the strain concentrations become smeared and the descending branch is steeper. In contrast, the behaviour of plain concrete under compression in the pre-peak region is almost independent of the specimen size, due primarily to observed constant fracture energy, which is studied by Sangha and Dhir [363].

In addition to the specimen size effect, the study by Kotsovos [230] analyses the influence of different testing techniques on the concrete behaviour in compression. Varying degrees of frictional restraint across the loaded surfaces are a significant effect on the descending portion of concrete's stress-strain relationship. For both normal and high strength concrete, the compressive strength depends mainly on the loading platen and specimen slenderness used in the test. In the case of rigid steel loading plates, an increase in specimen strength is observable with decreasing slenderness. In contrast, the reduction of the friction (e.g. by inserting a sheet of teflon between steel loading platen and concrete specimen) allows for independence between slenderness ratio (h/d) and measured strength [343]. In comparison, the ascending portion is essentially independent of the compressive testing technique and slenderness when low-friction loading plates are used. The strain rate in experiments additionally determines the post-peak behaviour of concrete in compression, which is initially investigated by Rüsch [356].

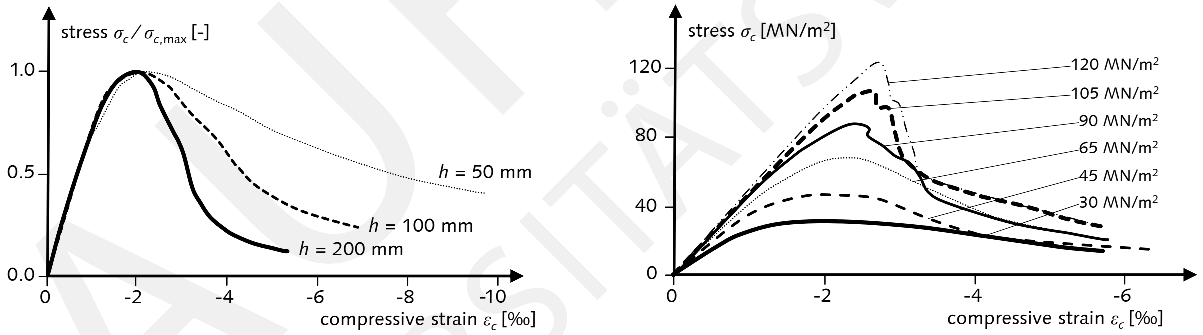

(a) Influence of specimen depth (200, 100, 50 mm) on uniaxial stress-strain curve for a constant cross-section 100 x 100 mm^2, based on [276, 277]

(b) Influence of concrete grade on uniaxial stress-strain curves, based on [404]

Figure 3.5: Non-linear behaviour of plain concrete measured in uniaxial compressive experiments

BAUHAUS
UNIVERSITÄTSVERLAG

In general, concrete compressive behaviour can be characterised as quasi-brittle with a sudden failure mechanism [8, 34]. For lower concrete strength, the post-peak behaviour of concrete in compression is rather ductile and becomes more and more brittle with increase in strength [185]. A very brittle behaviour of plain concrete is visible for high strength concrete. Such dependences between strength, stiffness, and failure mechanism is observed in experiments by WEE [404], see Fig. 3.5(b). Moreover, the behaviour in the softening range is shown to be more ductile if the specimen slenderness is decreased. In conclusion, the modelling of the descending branch is significantly influenced by the specimen size and testing boundary conditions and, thus, the post-peak stress-strain behaviour is a mixture of material and structural properties [343].

Finally, the modelling of the descending branch is subjected to higher experimental and modelling uncertainties compared to the pre-peak region. A comparison between various material models and experiments are investigated e.g. by LU, ZHAO [250] and WEE [404], which similarly illustrates that the difference between empirical models and measurements is much higher than the post-peak region.

Moreover, an extensive data bank is investigated for the "RILEM TC 148-SSC: Test Methods for the Strain-Softening Response of Concrete" project which is proposed by VAN MIER in 1993 [343]. This comprehensive Round-Robin test programme is performed in ten different laboratories around the world, such as Delft University of Technology, Technische Hochschule Darmstadt, University of Minnesota, and University of Sydney. The goal of this research project is to develop a reliable standard test method for measuring strain softening of concrete under uniaxial compression. Specimen slenderness and boundary restraint are the main variables that are analysed in the test programme, see Fig. 3.6. Specimen shape and size are additionally investigated. Both normal strength concrete with a strength of about 45 $\mathrm{MN/m^2}$ and high strength concrete with a strength of about 75 $\mathrm{MN/m^2}$ are analysed in several laboratories. Assessment of all tests concluded that reliable and reproducible strain-softening measurements can be made for specimens with a slenderness ratio $1.0 \leq h/d \leq 2.0$ with teflon platens between the steel plates and the concrete specimen. An axial platen-to-platen deformation technique can be applied for normal strength concrete, whereas a combination of axial and lateral deformation (or combination of axial deformation and axial load) should be used for high strength concrete. More information about the test method can be found in [344] which provides detailed recommendations for the specimen, instrumentation, test apparatus, test performance, and test results/report.

The effects in the post-peak stress-strain relationship mentioned above are difficult to capture in smeared material models and, thus, are not considered in empirical material models. In addition to the higher model uncertainties, the load-deformation behaviour of reinforced and prestressed concrete structures have to permit, in general, a certain amount of ductile deformations [40]. Therefore, the concrete compressive failure is not generally suitable for concrete structures. Hence, the descending branch for high compressive strains $|\epsilon_c| > |\epsilon_{c,\mathrm{lim}}|$ is not further addressed in this thesis. The compressive strain $|\epsilon_c| = |\epsilon_{c,\mathrm{lim}}|$ is identified with the failure condition in the compressive material models. The pre-peak behaviour of concrete is much less sensitive to size effects and boundary test conditions. Therefore, the models mentioned in Sec. 3.1.2.2 are accurate for the description of the non-linear concrete behaviour under compression especially in the pre-peak stress level range.

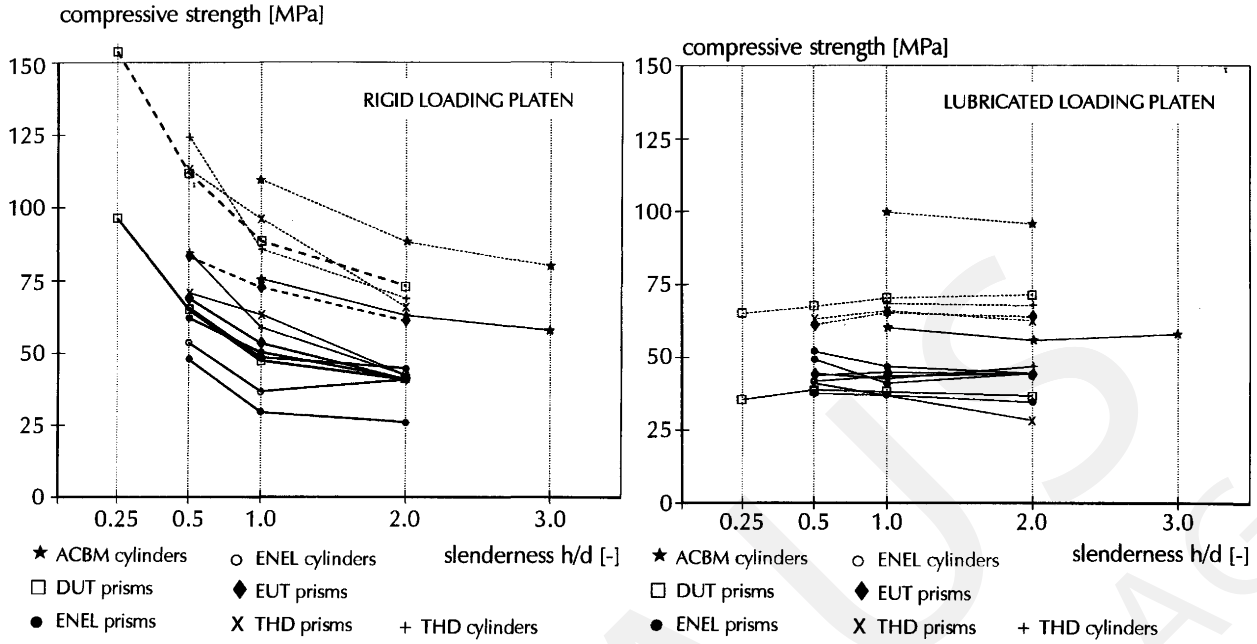

(a) rigid loading platen (b) lubricated loading platen

Figure 3.6: Effect of specimen slenderness on concrete compressive strength for different frictional test conditions, Round-Robin testing programme RILEM TC 148-SSC [343], ACBM...Center for Advanced Cement-based Materials, DUT...Delft University of Technology, ENEL...Centro di Ricerca Idraulica e Strutturale (ENEL-Cris) Laboratories, EUT...Eindhoven University of Technology, THD...Technische Hochschule Darmstadt

3.1.2.2 Compressive material models

A basic non-linear concrete compressive model is investigated by Hognestad [173]. This study defines the material behaviour by a second-degree parabola:

$$\sigma_c = -f_{cm} \cdot \left[2\left(\frac{\epsilon_c}{\epsilon_{c1}}\right) - \left(\frac{\epsilon_c}{\epsilon_{c1}}\right)^2 \right] . \tag{3.9}$$

The ratio between tangent modulus of elasticity at the origin and secant modulus at the peak stress is assumed to be constant and independent of compressive strength, which contradicts the experimental observations. A further development is found by Sargin [364]. This study establishes a broken-rational function in order to describe the material behaviour which is defined as:

$$\sigma_c = -f_{cm} \cdot \frac{A \cdot \left(\frac{\epsilon_c}{\epsilon_{c1}}\right) + B \cdot \left(\frac{\epsilon_c}{\epsilon_{c1}}\right)^2}{1 + C \cdot \left(\frac{\epsilon_c}{\epsilon_{c1}}\right) + D \cdot \left(\frac{\epsilon_c}{\epsilon_{c1}}\right)^2} . \tag{3.10}$$

The coefficients A, B, C, and D are computed according to all of the strain rates including ascending and descending branches. An extension of this model by Wang et al. [403] separately defines two sets of coefficients for both branches, whose predictions matching the experimentally determined descending branch more adequately. Furthermore, a material model is proposed by Carreira and Chu [61]. This model estimates the experimental measurements with a serpentine curve.

The material models considered in current editions of design codes and guidelines are based on the study by SARGIN [364], see Eq. 3.10. Model characteristics and a comparison between the different model predictions are presented in the following paragraphs.

Model Code 90

The Model Code 90 [74] defines the non-linear compressive stress-strain relationship for a smeared (more ductile in post-peak range) crack propagation which may be observable in experiments with a great specimen depth, see Fig. 3.5(a). This non-linear function approximates the measured σ_c-ϵ_c data points by the following definition:

$$|\epsilon_c| < |\epsilon_{c,\mathrm{lim}}| \qquad \sigma_c = -f_{cm} \cdot \frac{\dfrac{E_{c0}}{E_{c1}} \dfrac{\epsilon_c}{\epsilon_{c1}} - \left(\dfrac{\epsilon_c}{\epsilon_{c1}}\right)^2}{1 + \left(\dfrac{E_{c0}}{E_{c1}} - 2\right) \dfrac{\epsilon_c}{\epsilon_{c1}}} \tag{3.11}$$

with the tangent modulus E_{c0} according to Eq. 3.7a, the strain at the mean concrete compressive strength $\epsilon_{c1} = -2.2 \cdot 10^{-3}$ and the secant modulus of elasticity from the origin to the peak $E_{c1} = -f_{cm}/\epsilon_{c1}$. For higher compressive strains than ϵ_{c1}, the MC 90 concrete material model is valid up to $|\sigma_c| / f_{cm} \geq 0.5$. At the descending stress value $\sigma_{c,\mathrm{lim}} = -0.5 \cdot f_{cm}$, the limit strain $\epsilon_{c,\mathrm{lim}}$ is defined for restricting the applicability of the model. The limit strain can be computed by:

$$\frac{\epsilon_{c,\mathrm{lim}}}{\epsilon_{c1}} = \frac{1}{2} \left(\frac{1}{2} \frac{E_{c0}}{E_{c1}} + 1\right) + \left[\frac{1}{4} \left(\frac{1}{2} \frac{E_{c0}}{E_{c1}} + 1\right)^2 - \frac{1}{2}\right]^{1/2} . \tag{3.12}$$

Furthermore, MC 90 specifies the descending branch of the σ_c-ϵ_c for strains $|\epsilon_c| > |\epsilon_{c,\mathrm{lim}}|$ by either a non-linear or a linear function. Due to the reasons mentioned above, these high compressive strains are not further discussed or considered in the simulation results. The non-linear concrete compressive material model of MC 90 is shown in Fig 3.7(a) for various concrete strength grades.

Updated knowledge of Model Code 90

In MC 90, the strain at the maximum compressive stress $\epsilon_{c1} = -2.2 \cdot 10^{-3}$ is assumed to be constant and independent of concrete strength. The comparison of experimental results shows a correlation between strength and corresponding strain value, see Fig. 3.5(b). Therefore, the MC 90-99 extended the compressive concrete material model of MC 90 in order to take into account the increase of ϵ_{c1} with increasing strength grade. The non-linear function is basically the same as defined in Eq. 3.11, but the strain value at the strength ϵ_{c1} is determined by:

$$\epsilon_{c1} = -1.7 \cdot 10^{-3} - 1.0 \cdot 10^{-3} \cdot \left(\frac{f_{cm}}{70\,\mathrm{MN/m^2}}\right) . \tag{3.13}$$

The non-linear concrete compressive material model of MC 90-99 is shown in Fig 3.7(b) for various concrete strength grades.

Model Code 10

The broken rational function of Model Code 90, see Eq. 3.11, is similarly defined in the Model Code 10. Some quotients are redefined as $\eta = \epsilon_c / \epsilon_{c1}$ and $k = E_{c0}/E_{c1}$ and therefore:

$$|\epsilon_c| < |\epsilon_{c,\mathrm{lim}}| \qquad \sigma_c = -f_{cm} \cdot \frac{k \cdot \eta - \eta^2}{1 + (k-2)\,\eta} \,. \tag{3.14}$$

The determination of ϵ_{c1} is based on the studies by MEYER [275] and POPOVICS [314] and is defined by:

$$\epsilon_{c1} = -1.6 \cdot 10^{-3} \cdot \left(\frac{f_{cm}}{10\,\mathrm{MN/m^2}} \right)^{0.25} \,. \tag{3.15}$$

The values for $\epsilon_{c,\mathrm{lim}}$ recommended in MC 10 are in good agreement with experimental results of GRIMM [152] and MEYER [275]. The non-linear concrete compressive material model of MC 10 is shown in Fig 3.7(c) for various concrete strength grades.

Eurocode 2

The Eurocode 2 [101] approximates the non-linear concrete compressive behaviour by a broken rational function in the same way as defined in the Model Code 10, see Eq. 3.14. The strain at the peak stress is defined as (f_{cm} $\left[\mathrm{MN/m^2}\right]$):

$$\epsilon_{c1} = -7.0 \cdot 10^{-4} \cdot (f_{cm})^{0.31} \geq -2.8 \cdot 10^{-3} \,. \tag{3.16}$$

The ultimate permissible compressive strain is defined as $\epsilon_{c,\mathrm{lim}} = -3.5 \cdot 10^{-3}$ for concrete grades C 12/15 up to C 50/60. For high strength concrete, the ultimate limit strain can be computed by (f_{cm} $\left[\mathrm{MN/m^2}\right]$):

$$\epsilon_{c,\mathrm{lim}} = -2.8 \cdot 10^{-3} - 27 \cdot 10^{-3} \cdot \left[(98 - f_{cm})/100 \right]^4 \,. \tag{3.17}$$

The non-linear concrete compressive material model of EC 2 is shown in Fig 3.7(d) for various concrete strength grades.

Comparison of material models

The non-linear concrete compressive models are illustrated in Fig. 3.7 for the concrete classes C 20/25 ($f_{cm} = 28\,\mathrm{MN/m^2}$), C 40/50 ($f_{cm} = 48\,\mathrm{MN/m^2}$), C 60/75 ($f_{cm} = 68\,\mathrm{MN/m^2}$) and C 80/95 ($f_{cm} = 88\,\mathrm{MN/m^2}$). Therefore, normal strength concrete (C 20/25 and C 40/50) and high strength concrete (C 60/75 and C 80/95) are considered in the illustration of the material models. For the material model of MC 90 [74], each of the different concrete classes reaches their corresponding peak stress (f_{cm}) at the same strain value of magnitude $\epsilon_{c1} = -2.2 \cdot 10^{-3}$. More accurate consideration of the strength depending on this strain value is considered in MC 90-99 and even more precisely in MC 10 and EC 2. Comparison between the latter two models shows only small differences in the model predictions in the pre-peak range and in the determination of ϵ_{c1}. In contrast, the post-peak and especially the ultimate compressive strain are defined differently in both models.

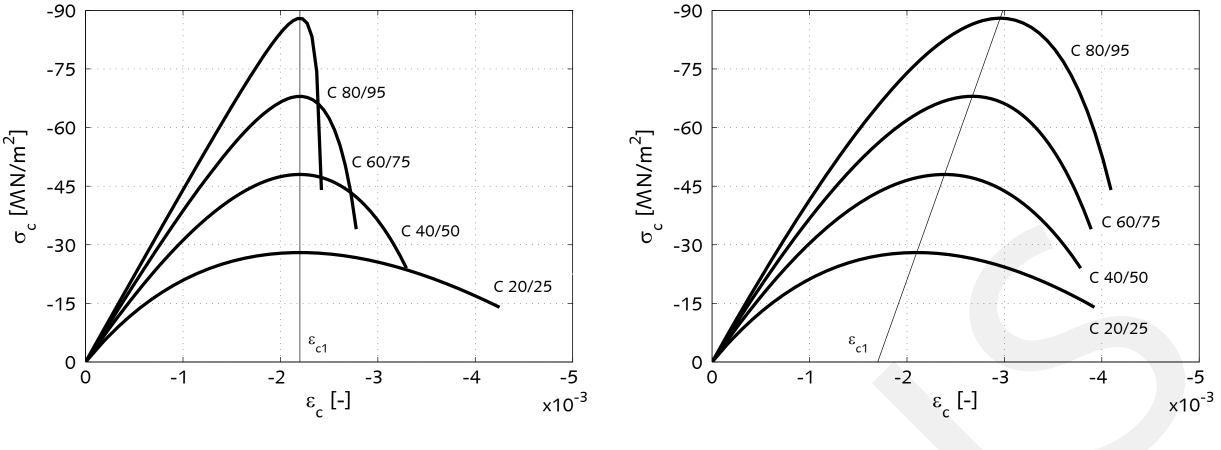

(a) MC 90 [74]

(b) MC 90-99 [185]

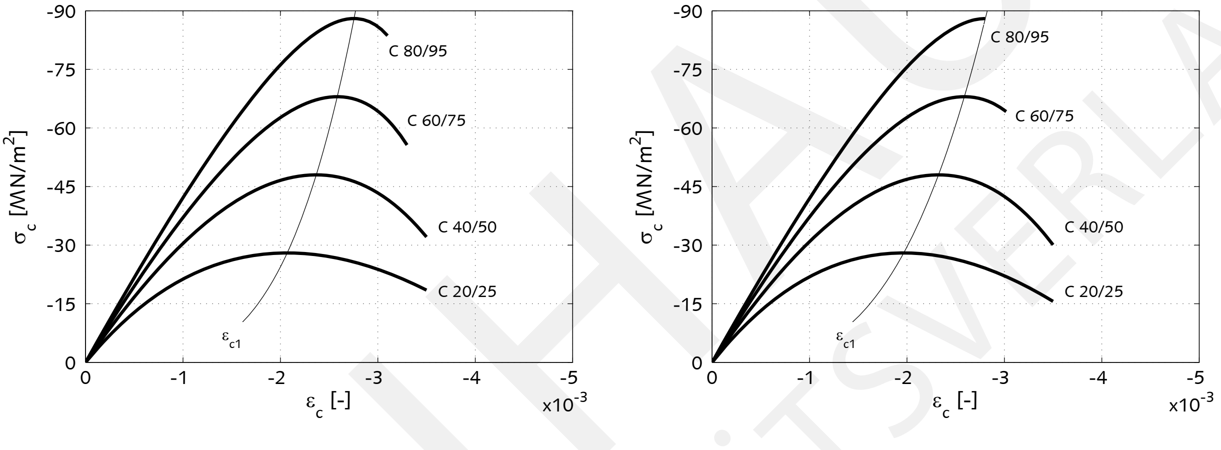

(c) MC 10 [187]

(d) EC 2 [101]

Figure 3.7: Non-linear material models (MC 90, MC 90-99, MC 10, EC 2) of plain concrete in uniaxial compression for various concrete grades

3.1.3 Concrete in tension

In concrete specimens subjected to uniaxial tension, the material initially behaves linear-elastic almost up to the peak load [179]. On a macro-level point of view, the stresses and strains are uniformly distributed over the tensile bar. Hence, the load-deformation behaviour can be directly represented by a material stress-strain relationship. The initiation of propagating microcracks is observable at a stress level of about 70 % − 80 % of the tensile strength [185, 225, 262], see Fig. 3.8. In experiments by HEILMANN et al. [167], a difference between the linear-elastic material behaviour and the measurements is visible at a stress level of about 60% of the tensile strength. However, the specimens are loaded under an eccentric normal force in these experiments which may cause this difference. The concrete fracture process in tension is an even more discrete phenomenon when compared to concrete in compression. For a load-controlled test, the fracture occurs when the maximum attainable load is reached which determines the concrete tensile strength. In a deformation-controlled test, the post-peak behaviour can be additionally observed as shown in Fig. 3.8.
For axially loaded tensile specimen, the corresponding limit strain ϵ_{ct}^{*} for $0.75 f_{ct}$ as an indicator for initiation of microcracking is investigated by several studies:

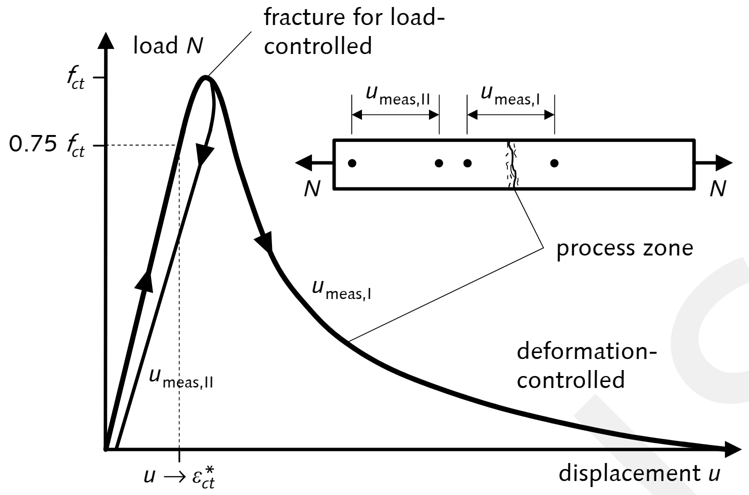
load N
fracture for load-controlled
f_{ct}
0.75 f_{ct}
$u_{\text{meas,II}}$
$u_{\text{meas,I}}$
N
N
process zone
$u_{\text{meas,I}}$
deformation-controlled
$u_{\text{meas,II}}$
$u \to \varepsilon_{ct}^*$
displacement u

Figure 3.8: Load-deformation behaviour of concrete bar under uniaxial tension, based on [179]

	ϵ_{ct}^* [‰]	author	reference
•	0.08-0.10	Hordijk	[179] ,
•	0.10	Mark et al.	[262] ,
•	0.08	Schlangen	[368] .

In the case of a stress level close to the maximum admissible stress, concrete strains start to localize within a narrow zone of micro-cracks. Crack propagation primarily occurs in a perpendicular direction with respect to the external stress. A system of more or less parallel but initially discontinuous microcracks propagates and develops into a continuous macro-crack which builds the so-called process zone (softening zone). Tensile stresses can still be transmitted in the process zone and thus is also referred to as a cohesive crack [185]. Due to the variability of concrete tensile strength along the tensile specimen, the process zone appears at the section with corresponding lowest strength. If the process zone develops within the measured length, this data determines the load-deformation behaviour with consideration for the softening branch, corresponding to displacement $u_{\text{meas,I}}$ shown in Fig. 3.8. The increase in deformation in the process zone causes a decrease in external load. Hence, the concrete outside this zone is unloaded due to load reduction, which is illustrated by the displacement $u_{\text{meas,II}}$ in Fig. 3.8. In the descending branch of the load-deformation behaviour, the displacement is built up by strains and crack opening. Therefore, the deformation process can not be exclusively described by concrete strain. In order to model the tensile behaviour of concrete, deformation is separated into a stress-strain behaviour in the uncracked branch and a stress-crack opening relation for the crack, see Fig. 3.9.

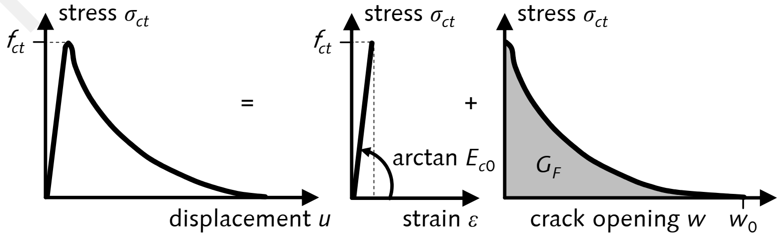
stress σ_{ct}
f_{ct}
=
displacement u
stress σ_{ct}
f_{ct}
arctan E_{c0}
strain ε
+
stress σ_{ct}
G_F
crack opening w
w_0

Figure 3.9: Differentiation of concrete in tension into stress-strain and stress-crack opening relation according to fictitious crack model, based on [179]

In the case that the cohesive crack reaches a critical size, an unstable fracture can only be avoided by a reduction of the external stress (deformation controlled). The descending branch of concrete in tension consequently occurs and a steady increase of deformation occurs due to gradual opening of the crack. In the case that the crack surfaces are completely separated, the maximum crack opening size w_0 can be determined. The experimental study of w_0 is very difficult due to the long tail of the descending branch. The material properties for the concrete tensile descending branch are investigated in several studies. In the case that no specific experimental data is available, the maximum crack opening w_0 may be determined by:

$$w_0 = 5.14 \cdot G_F/f_{ctm} \qquad \text{Hordijk} \quad [179]\,, \tag{3.18}$$

$$w_0 = G_F/f_{ctm} \cdot \begin{cases} 8 & \text{for aggregate size: 8 mm} \\ 7 & \text{for aggregate size: 16 mm} \\ 5 & \text{for aggregate size: 32 mm} \end{cases} \qquad \text{MC 90} \quad [74]\,, \tag{3.19}$$

$$w_0 = 5 \cdot G_F/f_{ctm} \qquad \text{MC 10} \quad [187]\,, \tag{3.20}$$

and the fracture energy G_F by:

$$G_F = \int_{w=0}^{w=w_0} \sigma_{ct}(w)\,\mathrm{d}w\,, \tag{3.21}$$

$$G_F = f_{cm}^{0.7} \cdot \begin{cases} 4 & \text{for aggregate size: 8 mm} \\ 6 & \text{for aggregate size: 16 mm} \\ 10 & \text{for aggregate size: 32 mm} \end{cases} \qquad \text{MC 90} \quad [74]\,, \tag{3.22}$$

$$G_F = 73 \cdot f_{cm}^{0.18} \qquad \text{MC 10} \quad [187]\,. \tag{3.23}$$

The fracture energy G_F is a material characteristic which describes the resistance of a material subjected to tensile stresses by defining the energy which is required to propagate a tensile crack of unit area (dimension $\mathrm{Nmm/mm^2}$ or N/mm) [185]. This property depends primarily on water/cement ratio, maximum aggregate size and concrete age [179]. Moreover, it depends on the sizes of the structural members which is not taken into account in the above mentioned empirical relationships (only aggregate size considered), which results in a discrepancy between these determinations compared to experimental data of up to ±30 % [74]. Due to the substantial increase in concrete brittleness with higher strength grades $f_{cm} > 80$, a fracture energy limit is proposed in MC 90-99 [185]. In general, it is very useful to determine G_F from uniaxial tensile tests. However, indirect tests (e.g. three-point bending tests on notched beams) are most frequently used, because these tests are easier to perform [187]. In a recent comprehensive study by Hoover and Bažant et al. [177, 178], an experimental test program is performed for one batch of concrete with a total of 164 concrete specimens within three hours, which results in a low uncertainty in the measurement data. This data bank may allow an adequate comparison of existing models as well as development of more accurate models.

The stress-strain relationship for uncracked concrete and the stress-crack opening relationship for cracked concrete in tension proposed in the design guidelines MC 90 [74], MC 10 [187], and by Hillerborg [169] are illustrated in Fig. 3.10(a).

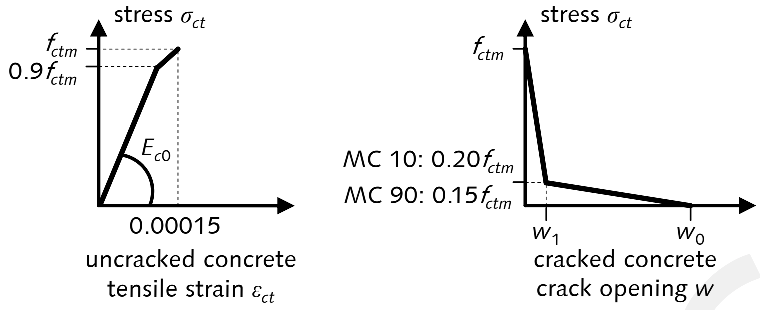
stress σ_{ct}
f_{ctm}
$0.9f_{ctm}$
E_{c0}
0.00015
uncracked concrete
tensile strain ε_{ct}
stress σ_{ct}
f_{ctm}
MC 10: $0.20f_{ctm}$
MC 90: $0.15f_{ctm}$
w_1
w_0
cracked concrete
crack opening w

(a) MC 90 [74] and MC 10 [187]

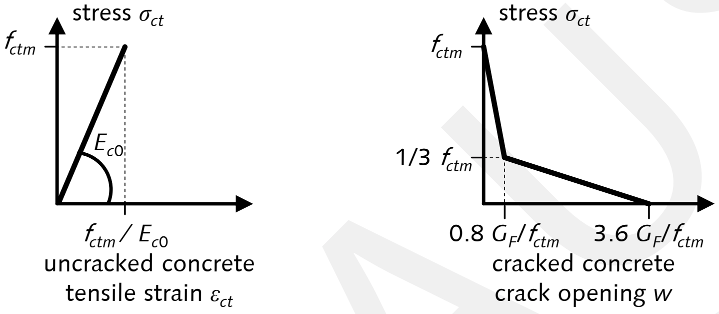
stress σ_{ct}
f_{ctm}
E_{c0}
f_{ctm} / E_{c0}
uncracked concrete
tensile strain ε_{ct}
stress σ_{ct}
f_{ctm}
1/3 f_{ctm}
$0.8\ G_F/f_{ctm}$
$3.6\ G_F/f_{ctm}$
cracked concrete
crack opening w

(b) Hillerborg [169]

Figure 3.10: Several models for stress-strain and stress-crack opening relationship for concrete in tension

The **fictitious crack model** by Hillerborg et al. [170] and the crack band model by Bažant and Oh [33] are two of the most important cohesive crack models which take into account the fracture and deformation processes. The fictitious crack model is capable of correctly modelling the existence of a discrete crack, but the path of such cracks should be estimated beforehand in such a way that a suitable finite element mesh can be chosen. An evident crack is interpreted as a crack that cannot transfer tensile stress. In contrast, crack-closing stresses appear in the fictitious crack (process zone). Axially loaded, notched specimens are analysed in the study by Hillerborg et al. [170] and a material model defined as a stress-crack opening function is developed based on the measured force-displacement relationship. For the numerical simulation, the observed concrete tensile stress-crack opening relationship is approximated by either linear or bi-linear functions.

For the **crack band model** proposed by Bažant and Oh [33], the crack is partially smeared and corresponds to the width of the finite element representing the crack band [185]. Therefore, the fracture process is limited to a certain band in which the cohesive crack develops, whereas in other regions the strain decrease as the tensile stress is reduced. Therefore, a distinction should be made carefully between regions in which fracture develops and those outside the fracture zone. Based on the original proposal, the optimum effective width of the crack band front is found to be about three-times the maximum aggregate size.

The discrete phenomenon of cracking and crushing can also be modelled by a smeared approach defining average stress-strain relationships. These smeared crack models are particularly suitable for applications where many cracks may occur in the entire structure [16, 151]. Therefore, the non-linear load-deformation behaviour of structures can be adequately analysed by applying the smeared compression, tension, and tension stiffening models [224]. For discrete simulations, the bond stress-slip relationship is more explicitly described in order to obtain adequate results. In this thesis, only smeared stress-strain relationships are applied for the modelling of the material behaviour.

3.1.4 Reinforced concrete in tension - tension stiffening

The fracture process of plain concrete is significantly different than that of reinforced concrete. Therefore, it is necessary to investigate the crack propagation separately for reinforced concrete. On one hand, all tension forces in a cracked section are exclusively balanced by reinforcing steel. On the other hand, some tension forces in between neighbouring cracks are transmitted from steel to surrounding concrete by bond stresses. Therefore, the pieces of concrete between the cracks contribute to the stiffness of the element [185]. Hence, this effect is denoted with the term "tension stiffening“. The tension stiffening effect for prestressing steel is not considered in this thesis. Recommendations and models can be found in [219]. For combined reinforcing and prestressing steel, their combined influence on the tension stiffening may be considered in a ratio between bond stiffness of both steel materials [396]. In general, the tension stiffening effect is mainly influenced by [162]:

- concrete strength,
- reinforcement ratio, and reinforcement layout,
- bond characteristics,
- loading level,
- concrete cover, and
- type of loading (instantaneous, long-term, or repeated).

The distribution of bond stresses along the process zone (discontinuity area) is non-linear as it is shown in Fig. 3.11(a). Due to the fact that the distance between several cracks varies, it is quite difficult to compute the contribution of concrete by an exact analytical determination. Furthermore, the bond behaviour between concrete and reinforcement is mainly influenced by the following aspects [220]:

- concrete behaviour due to 3-dim. high compressive stresses under ribbed reinforcing bars,
- internal cracks and longitudinal cracks,
- reinforcement surface characteristics,
- reinforcement strain,
- concrete mixture,
- residual stresses,
- external stresses, and
- concrete creep and shrinkage.

In addition, the bond description is sensitive to the distance of the steel layer to the surface or the neighbouring bars, and sensitive to the distance of the considered section point to the next crack. All of these factors influence the relationship between the slip (relative displacement between concrete and steel) and the bond stress. Therefore, a universal bond model for the bond-slip relationship is not easy to develop [220]. For practical applications it is quite useful to simplify the bond-stress relationship [294]. The average and constant bond stress τ_{bm} along the bar (dotted line in Fig. 3.11(a)) enables a simplified calculation of the tension stiffening effect. Therefore, the assumed bond-slip relationship is illustrated in Fig. 3.11(b).

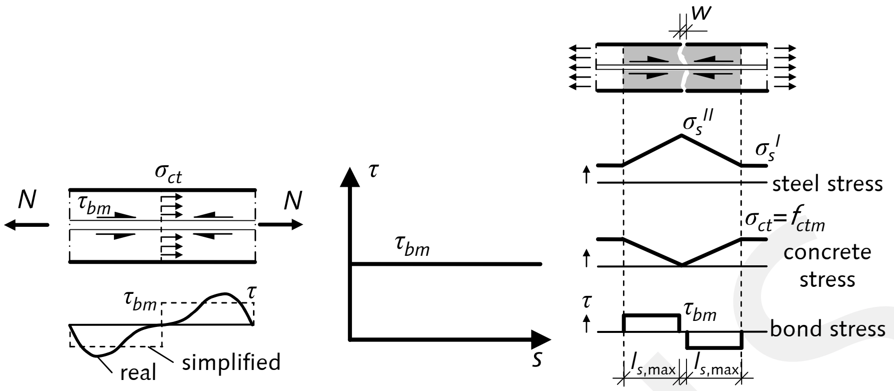

(a) Force transmission (b) Rigid-plastic bond stress-slip relation (c) Stress distribution over discontinuity area

Figure 3.11: Transmission from steel to concrete for single crack, based on [185]

The contribution of concrete in tension between adjacent cracks may be considered by increasing the stiffness of the tensile reinforcement. In the case that this effect is neglected in the analysis of concrete structures, the stiffness of a reinforced concrete bar or a flexural member is underestimated and inaccurate results are obtained [74].

In general, the analysis of deformation, material stress, and crack width are significantly sensitive to the cracking stage which might appear in sections of the structural members. Therefore, the consideration of the characteristics of each crack stage should be made from the first crack up to the yielding in reinforcement. The several cracking stages are defined as follows:

① uncracked stage,
② crack formation stage,
③ stabilised cracking stage,
④ steel yielding stage.

The strains in concrete and steel are equal ($\epsilon_c = \epsilon_s$) in the uncracked stage and the stiffness of the element is equal to the linear-elastic stiffness ($E_c A_i^I$, $E_c I_i^I$). At a certain loading level the concrete tensile stress reaches the tensile strength and somewhere the first crack occurs at a section with the lowest elastic stiffness. Hence, concrete tensile stresses at the location where the concrete is cracked are $\sigma_{ct} = 0$ and reinforcing steel is subjected to the full tensile force. The concrete is activated to carry a part of the tensile force at both sides of the crack due to the bond stress along the discontinuity area. The bond strength influences the distance which is necessary to redevelop the full tensile force in the concrete [185]. The assumption of a constant bond stress along the steel bars leads to a linear distribution of concrete and steel stress over the transmission region, see Fig. 3.11(c). New cracks are not able to appear within this region, because the concrete tensile strength cannot be reached here. At a certain distance $l_{s,\max}$ from the crack, the concrete tensile stress reaches the tensile strength again and another new crack can occur. Therefore, the force which causes a neighbouring crack over the length $l_{s,\max}$ must be:

$$F_{ct} = A_c \cdot f_{ctm} = E_s \cdot A_s \cdot \epsilon_s^I \, . \tag{3.24}$$

Along the length $l_{s,\max}$ a bond force F_b between steel and concrete is transmitted by virtue of the action of bond stresses. The bond force can be described by [185, 220]:

$$F_b = \varnothing_s \cdot \pi \cdot \tau_{bm} \cdot l_{s,\max} = E_s \cdot A_s \cdot \Delta\epsilon_{sr} \tag{3.25}$$

$\varnothing_s$ ... bar diameter
τ_{bm} ... mean value of bond strength, see Tab.3.5
A_s ... area of reinforcement
E_s ... reinforcement modulus of elasticity

Equalizing the forces F_{ct} from Eq. 3.24 and F_b from Eq. 3.25 results in:

$$l_{s,\max} = \frac{1}{4} \cdot \frac{f_{ctm}}{\tau_{bm}} \cdot \frac{\varnothing_s}{\rho_s} \tag{3.26}$$

where $\rho_s = A_s/A_c$ is the geometrical reinforcement ratio of a tensile bar. For a flexural member, the effective ratio $\rho_{s,\text{eff}} = A_s/A_{c,\text{eff}}$ should be applied with the determination of the effective concrete area in tension $A_{c,\text{eff}}$ as discussed in Sec. 3.1.4.5. Considering the effect of the concrete cover on the maximum transmission length, the Model Code 2010 defines the length as [187]:

$$l_{s,\max} = k \cdot c + \frac{1}{4} \cdot \frac{f_{ctm}}{\tau_{bm}} \cdot \frac{\varnothing_s}{\rho_s} \tag{3.27}$$

where k is an empirical parameter to take the influence of the concrete cover into account (assumed to be $k = 1.0$) and c is the concrete cover. This equation is valid for structures where the concrete cover is not more than 75 mm.

With increasing loading level, gradually more and more cracks are formed in the crack formation stage. Hence, the stiffness of the structural member decreases. In the case that a new crack appears just at the end of a discontinuity region, the smallest possible crack distance is found. The maximum crack distance occurs, where the next crack is formed at a distance smaller than $2 \cdot l_{s,\max}$. Hence, the crack distance s_r varies between $l_{s,\max} \leq s_r \leq 2 \cdot l_{s,\max}$. The final stage in the crack formation stage occurs when, finally, overlapping of the discontinuity regions is reached in the entire structural member.

A further increase in loading increases the force in the reinforcement bar which is characteristic of the stabilised cracking stage. The force in the concrete between the cracks cannot increase anymore since the bound stresses reach their maximum permissible value. Therefore, the concrete contribution to the stiffness between the cracks is constant and only crack widening is supposed to occur in the stabilised cracking stage [187]. Hence, the relationship between the tensile force and the elongation is parallel to the line of pure reinforcement steel, see Fig. 3.12.

Another increase in load leads finally to plastic deformations in the reinforcement steel, which is characterised for the steel yielding stage. The crack stages of a reinforced concrete member in comparison to pure reinforcement are qualitatively shown in Fig. 3.12.

Single crack

Whenever cracks appear, single cracks play an important role. In the case that the first crack occurs, the distribution of concrete and reinforcing steel strain is shown in Fig. 3.13(a). Slip between concrete and steel

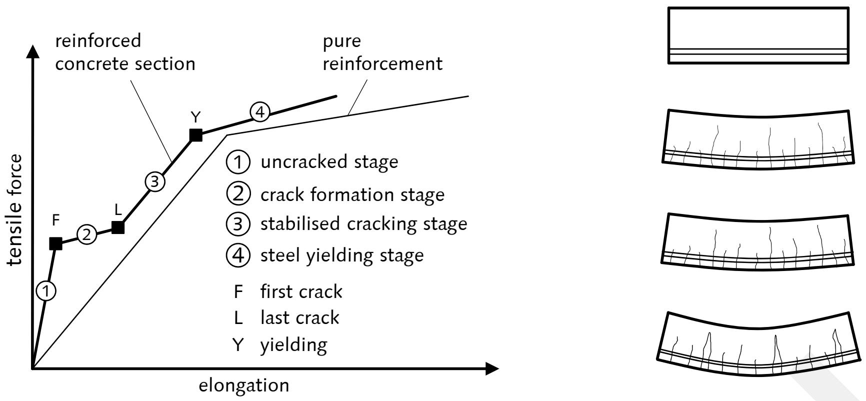
reinforced
concrete section
pure
reinforcement
tensile force
elongation
F
L
Y
①
②
③
④
① uncracked stage
② crack formation stage
③ stabilised cracking stage
④ steel yielding stage
F first crack
L last crack
Y yielding
uncracked stage
crack formation stage
stabilised cracking stage
steel yielding stage

(a) force-elongation relation (b) crack pattern

Figure 3.12: Idealised behaviour of a reinforced concrete member, based on [74]

occurs in the range of the transmission length. Therefore, concrete and steel strains are not equal ($\epsilon_c \neq \epsilon_s$). In contrast, some parts of the area between the cracks remains in the uncracked stage ($\epsilon_c = \epsilon_s$). The mean steel strain can be computed by [74, 220]:

$$\epsilon_{s,m} = \epsilon_s^{II} - \beta_{t,m} \cdot \Delta\epsilon_{sr} = \epsilon_s^{II} - \beta_{t,m} \left(\epsilon_{sr}^{II} - \epsilon_{sr}^{I}\right) \tag{3.28}$$

$\beta_{t,m}$	...	integration factor for steel strain along transmission length $\beta_{t,m} = 0.60$ for crack formation, see Tab.3.5
$\epsilon_{s,m}$	...	mean steel strain
ϵ_s^I	...	reinforcement strain in uncracked concrete
ϵ_{s2}^{II}	...	reinforcement strain in crack
ϵ_{sr}^I	...	steel strain at point of zero slip under cracking forces reaching f_{ctm}
ϵ_{sr}^{II}	...	reinforcement strain at crack under cracking forces reaching f_{ctm}
$\Delta\epsilon_{sr}$	...	increase of steel strain in cracking stage

Stabilised cracking

After the crack formation is finished, it is necessary to define mean spacing $s_{r,m}$ between the cracks in order to analyse the concrete contribution in the stabilised cracking stage, see Fig. 3.13(b).
The mean distance between the cracks can be taken as [74]:

$$s_{r,m} = \frac{2}{3} \cdot 2 \cdot l_{s,\max} = \frac{4}{3} \cdot l_{s,\max} \,. \tag{3.29}$$

Hence, the transmission length is reduced $l_{s,m} = \frac{2}{3} l_{s,\max}$ and the average bond force transferred remains:

$$F_{b,m} = \frac{2}{3} \cdot F_b = \frac{2}{3} \cdot A_s \cdot E_s \cdot \Delta\epsilon_{sr} \,. \tag{3.30}$$

As a result, the average steel strain from the crack to the section in the middle between the cracks is reduced to:

$$\Delta\epsilon_{s,m} = \frac{2}{3} \Delta\epsilon_{sr} \,. \tag{3.31}$$

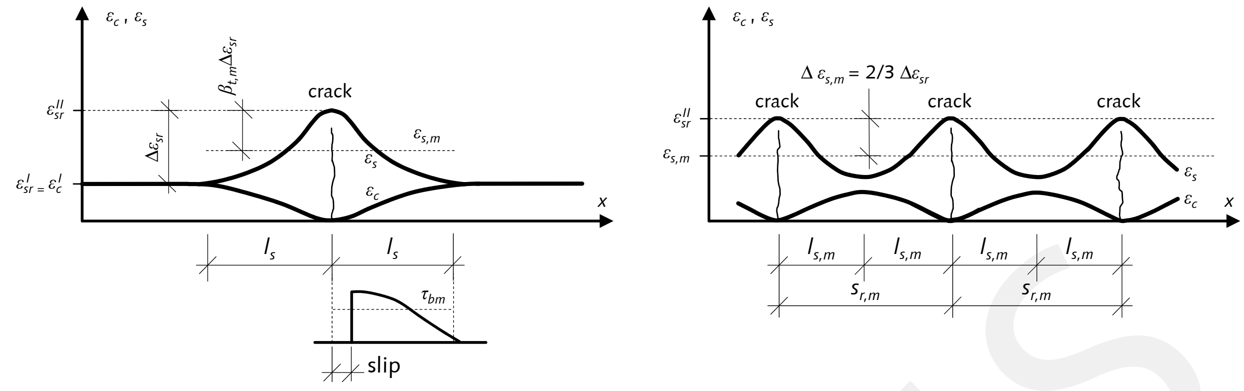
ε_c , ε_s
$\beta_{t,m}\Delta\varepsilon_{sr}$
crack
ε_{sr}^{II}
$\Delta\varepsilon_{sr}$
$\varepsilon_{s,m}$
ε_s
ε_c
$\varepsilon_{sr}^{I} = \varepsilon_c^{I}$
x
l_s
l_s
τ_{bm}
slip
ε_c , ε_s
$\Delta\,\varepsilon_{s,m} = 2/3\ \Delta\varepsilon_{sr}$
crack
crack
crack
ε_{sr}^{II}
$\varepsilon_{s,m}$
ε_s
ε_c
x
$l_{s,m}$
$l_{s,m}$
$l_{s,m}$
$l_{s,m}$
$s_{r,m}$
$s_{r,m}$

(a) single crack stage

(b) stabilised crack stage with $s_{r,m} = \frac{4}{3} l_{s,\max}$

Figure 3.13: Strain distribution in single crack and stabilised crack stage, based on [74]

The mean reinforcement strain $\epsilon_{s,m}$ over the entire discontinuity area can be taken as:

$$\epsilon_{s,m} = \epsilon_s^{II} - \beta_{t,m} \cdot \Delta\epsilon_{s,m} = \epsilon_s^{II} - \beta_{t,m} \cdot \frac{2}{3}\Delta\epsilon_{s,r} = \epsilon_s^{II} - \beta_t \cdot \Delta\epsilon_{s,r} \tag{3.32}$$

β_t ... $\beta_t = \frac{2}{3}\beta_{t,m}$,
$\beta_{t,m}$ according to Tab.3.5,
0.40 for instantaneous loading,
0.25 for long-term and repeated loading.

The coefficient $\beta_{t,m}$ is the shape factor accounting for the concrete stress distribution over crack spacing $s_{r,\max}$. The assumptions of constant bond stress and linear stress distribution in the crack discontinuity areas for all cracking stages results in $\beta_{t,m} = 0.6$, which is recommended by MC 90 [74] and MC 10 [187] in the case of deformed reinforcement bars and short-term (instantaneous) loading conditions. The analysis of the load-bearing behaviour of structures with potentially several cracks is generally focused on the average structural behaviour [420]. Instead of the maximum crack spacing $s_{r,\max}$, the average crack spacing $s_{r,m} \approx 2/3 \cdot s_{r,\max}$ is used for the description of concrete strain between the adjacent cracks. Therefore, the average smeared concrete strain between the cracks reaches $\epsilon_{ct,m} \approx 2/3 \cdot \epsilon_{ct}$ and consequently $\beta_t = 2/3 \cdot 0.6 = 0.4$ [126, 127, 187]. The values for the integration factor for the steel strain along the transmission length $\beta_{t,m}$ and bond stress τ_{bm} according to MC 90 [74] and MC 10 [187] are listed in Tab. 3.5.

In the experimental study by KÖNIG and FEHLING [220], the best accuracy between measured and computed crack widths is found for the rigid-plastic bond stress-slip relation (τ_{bm}). In the case of the short term loading condition, they determine $\tau_{bm} = 2.0 \cdot f_{ctm}(t)$ and $\beta_{t,m} = 0.6$. For the analysis of single cracks in the long term or repeated loading condition, accurate results are obtained, reducing the average bond stress to 70%. In contrast, in the analysis of the stabilised cracking stage (long term) the bond stress remain to be equal to the short term determination, but the contribution of the concrete is reduced to 70%. The comparison between the research of KÖNIG and FEHLING [220] and the recommendations in MC 90 [74], respectively MC 10 [187] result in very good agreement for the determination of τ_{bm} and $\beta_{t,m}$.

The bond characteristic between concrete and reinforcement may be weakened through the number of load cycles in the repeated loading condition. In general, the loss in the bond force for the single crack initiation can be summed to 30 % and thus the transmission length increases significantly [220]. A similar

Table 3.5: Values for $\beta_{t,m}$ and τ_{bm} for deformed reinforcing bars according to MC 90 [74] and MC 10 [187]

	Crack formation stage	Stabilised cracking stage
Short term, instantaneous loading	$\beta_{t,m} = 0.6$ $\tau_{bm} = 1.8 \cdot f_{ctm}(t)$	$\beta_{t,m} = 0.6$ $\tau_{bm} = 1.8 \cdot f_{ctm}(t)$
Long term, repeated loading	$\beta_{t,m} = 0.6$ $\tau_{bm} = 1.35 \cdot f_{ctm}(t)$	$\beta_{t,m} = 0.38\ (0.4)$ $\tau_{bm} = 1.8 \cdot f_{ctm}(t)$

phenomenon is observed for long-term loading conditions. The creep of bond reduces the force transmission between concrete and reinforcement. The long-term loading condition in the SLS leads to a time dependency of the shape factor due to the creep of the bond. Therefore β_t for ribbed reinforcement bars reduces over time from $\beta_t = 0.40\,(t = 0)$ to $\beta_t = 0.25\,(t \rightarrow \infty)$ [187].
The time-dependent concrete tensile strength $f_{ctm}(t)$ can be considered in the determination of the bond characteristic in order to predict the development of additional cracks more accurately. Nevertheless, the phenomenon of concrete hardening is not further addressed in this thesis and is neglected in the simulation results.

3.1.4.1 Characteristic strains for cracking stages

In the case of a cracked reinforced concrete section, it is necessary to take into account the tension stiffening effect in order to adequately compute the corresponding stiffness determined by the force in the reinforcement and, thus, the neutral axis in the section. Force and position of the neutral axis are both influenced by the stiffness of the embedded reinforcement bars, which can be described by the tension stiffening effect [220]. The modification of either the reinforcement or concrete stress-strain relationship may be applied for the computational analysis of reinforced concrete structures, see Fig. 3.14.

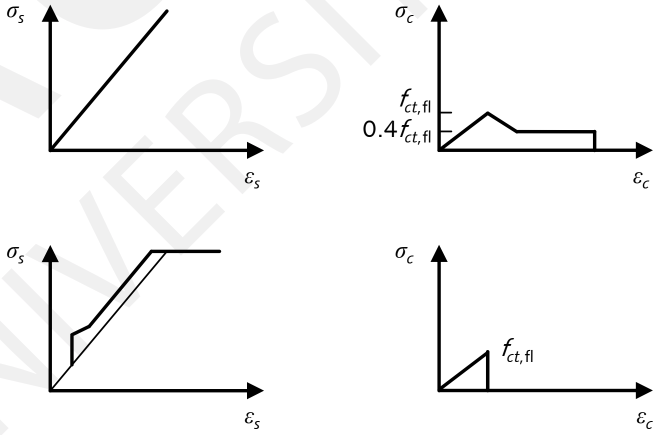

Figure 3.14: Modelling of tension stiffening effect by modification of reinforcement (left side) or concrete stress-strain relationship (right side), based on [220]

The characteristic stages of the reinforced concrete cross-sections are uncracked stage, crack formation stage, stabilised cracking stage, and steel yielding stage. For each stage, it is possible to compute strain values for the determination of transitions between the cracking stages of the cross-section. The characteristic strains (considered as average steel strain $\epsilon_{s,m}$) are defined for each cracking stage (see Fig. 3.15) to [74, 127]:

① uncracked stage

$$0 < \sigma_s \leq \sigma_{sr}^{II} \qquad \epsilon_{s,m} = \epsilon_s^{I} \tag{3.33}$$

② crack formation stage

$$\sigma_{sr}^{II} < \sigma_s \leq \sigma_{srn} \qquad \epsilon_{s,m} = \epsilon_s^{II} - \frac{\beta_t\left(\sigma_s - \sigma_{sr}^{II}\right) + \left(\sigma_{srn} - \sigma_s\right)}{\sigma_{srn} - \sigma_{sr}^{II}} \cdot \left(\epsilon_{sr}^{II} - \epsilon_{sr}^{I}\right) \tag{3.34}$$

③ stabilised cracking stage

$$\sigma_{srn} < \sigma_s \leq f_y \qquad \epsilon_{s,m} = \epsilon_s^{II} - \beta_t\left(\epsilon_{sr}^{II} - \epsilon_{sr}^{I}\right) \tag{3.35}$$

④ steel yielding stage

$$f_y < \sigma_s \leq f_t \qquad \epsilon_{s,m} = \epsilon_{sy} - \beta_t\left(\epsilon_{sr}^{II} - \epsilon_{sr}^{I}\right) + \delta\left(1 - \frac{\sigma_{sr}^{II}}{f_y}\right)\left(\epsilon_s^{II} - \epsilon_{sy}\right) \tag{3.36}$$

$\epsilon_{s,m}$ ... mean reinforcement strain
ϵ_{sy} ... reinforcement strain at yield strength
$\epsilon_{s,m}$ ... mean reinforcement strain
ϵ_s^{I} ... reinforcement strain in uncracked stage
ϵ_s^{II} ... reinforcement strain in cracked stage
σ_s ... steel stress in crack (pure steel)
σ_{sr}^{I} ... steel stress in uncracked stage, when internal forces cause $\sigma_c = f_{ctm}$
σ_{sr}^{II} ... steel stress in cracked stage for crack driving forces
σ_{srn} ... steel stress in crack, when stabilised crack pattern appears (last crack)
β_t ... shape factor of concrete contribution in discontinuity area
0.40 for short-term loading, 0.25 for long-term or cyclic loading
f_y, f_t ... yield and tensile strength of reinforcement
δ ... coefficient to take into account ratio f_t/f_y representing ductility characteristic
0.8 for high ductile steel (B 500B), 0.6 for normal ductile steel (B 500A)

In the case of a centrically reinforced tensile member, the crack normal force N_r for short-term loading can be determined by [185]:

$$N_r = A_c f_{ctm} \cdot \left(1 + \alpha_s \rho_{s,\text{eff}}\right) , \tag{3.37}$$

and the steel stress in the crack σ_{sr} for N_r can be computed by [187]:

$$\sigma_{sr} = \frac{N_r}{A_s} = \frac{f_{ctm}}{\rho_{s,\text{eff}}}\left(1 + \alpha_s \rho_{s,\text{eff}}\right) , \tag{3.38}$$

where $\alpha_s = E_s/E_c$ is the modular ratio. The steel stress at the last crack defining the initiation of the stabilised cracking stage (no undisturbed areas in the tensile bar) may be computed by [185]:

$$\sigma_{srn} = 1.3 \cdot \sigma_{sr} \tag{3.39}$$

with $\sigma_{sr} = \sigma_{sr}^{II}$ is the reinforcing stress in the single crack. Therefore, the computation of the mean steel strain in the crack formation stage according to Eq. 3.34 becomes [74, 127]:

$$\epsilon_{s,m} = \epsilon_s^{II} - \frac{\beta_t\left(\sigma_s - \sigma_{sr}^{II}\right) + \left(1.3 \cdot \sigma_{sr}^{II} - \sigma_s\right)}{0.3 \cdot \sigma_{sr}^{II}} \cdot \left(\epsilon_{sr}^{II} - \epsilon_{sr}^{I}\right) . \tag{3.40}$$

BAUHAUS
UNIVERSITÄTSVERLAG

The analysis of imposed deformations influences the crack formation stage. In the case of a continually increasing elongation, the force in the tensile bar will drop after the occurrence of the first crack. This is due to the fact, that on one side, the stiffness of the bar is reduced, and on the other side, the total strain of the bar should remain constant (principle of imposed deformation). The increase in external deformation leads to an increase in the tensile force, which cannot exceed the cracking force in the member, because the development of additional cracks prevents this. Hence, the crack formation stage caused by imposed deformations may be considered by the dotted line in Fig 3.15 [74, 185].

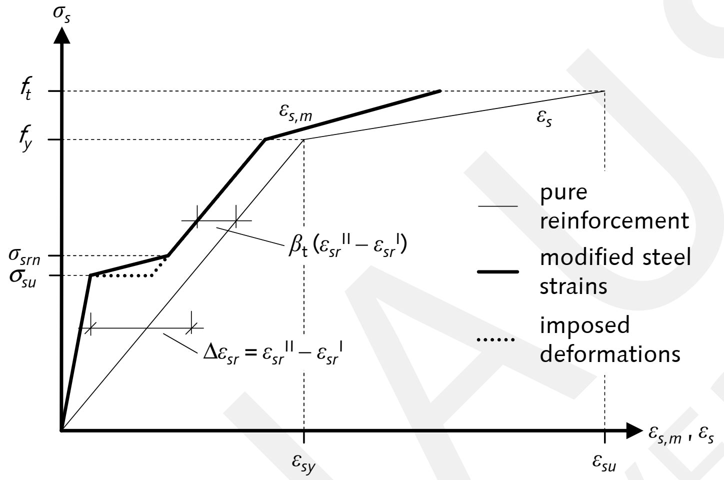

Figure 3.15: Stress-strain tension stiffening model for modified steel strains, based on [74]

The basic assumption for the horizontal determination of the crack formation stage (see Fig 3.15) is that the concrete tensile strength is constant over the tensile bar. Hence, the tensile cracking force is similarly constant $N_{r,1} = N_{r,2}$, see Fig. 3.16(a). A theoretical analysis by [93] applied this definition for a study on continuous beams subjected to a temperature gradient. Experimental studies [162, 212, 390] showed, that the horizontal line is not observable in the performed measurements. Due to the fact that the concrete tensile strength in the tensile bar varies approximately between $f_{ctk,0.05} < f_{ct} < f_{ctk,0.95}$, an increase in the tensile cracking force for the initiation of the second crack is visible $N_{r,1} \neq N_{r,2}$, see Fig. 3.16(b). The second crack occurs at the local position where slightly higher tensile strength is present compared to the tensile strength of the first crack.

Nevertheless, several uncertainties such as the accuracy of reinforcement placement, the real effective tensile strength, and the construction quality, strongly affect the crack formation stage. Hence, the horizontal simplified approach may be accurate enough for practical applications [187, 220].

The ratio between loading level for the start of the stabilised cracking stage $N_{r,\text{last}}$ and the start of the crack formation stage $N_{r,1}$ may be considered in the crack formation stage by the term $\sigma_{srn} = 1.3 \cdot \sigma_{sr}$, see Eq. 3.39. The experimental study by HARTL [162] analysed the concrete contribution to the element stiffness for 3 different concrete strength grades, 4 varying reinforcement steel diameters with 6 prismatic specimens for each condition (72 specimens total). The results of the uniaxial tensile tests illustrate that the reinforcement stress at the final stage in the crack formation stage in relation to the crack initiation $N_{r,\text{last}}/N_{r,1}$ is equal to 1.00 for ∅8 mm, 1.10 for ∅12 mm, 1.30 for ∅18 mm, and 1.60 for ∅24 mm, see Fig. 3.17. Furthermore, in the stabilised cracking stage the tension stiffening effect ΔN is found to be on average ≈ 40% of the cracking force ΔN_r, respectively $\Delta\sigma_s = 0.40 \cdot \sigma_{sr} = 0.4 \cdot N_r/A_s$. In conclusion, the above mentioned determination of the general approach ($\sigma_{srn} = 1.3 \cdot \sigma_{sr}$) is related to a variability

BAUHAUS
UNIVERSITÄTSVERLAG

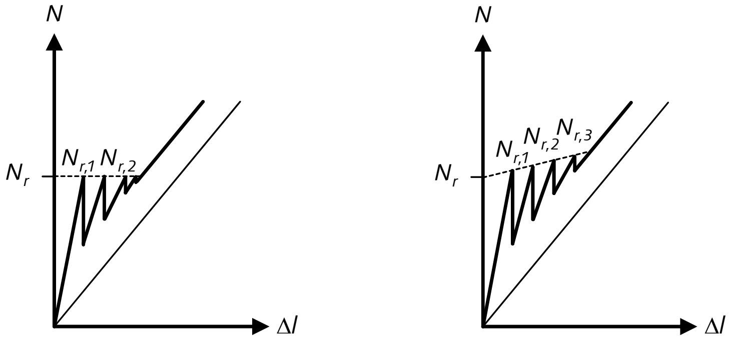

(a) Constant concrete tensile strength, based on [185]

(b) Concrete tensile strength approx. varies between $f_{ctk,0.05} < f_{ctm} < f_{ctk,0.95}$, based on [187]

Figure 3.16: Behaviour of a reinforced concrete bar subjected to imposed deformation in the crack formation stage

in the concrete tensile strength assessed by a normal distribution with an average coefficient of variation $CV_{f_{ctm}} = 0.10$ [162].

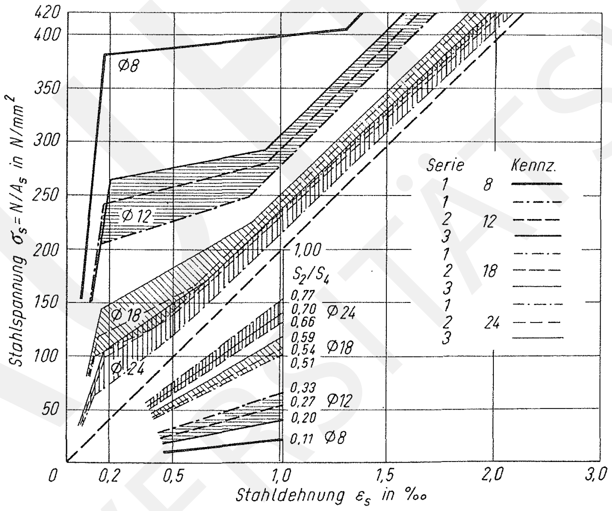

Figure 3.17: Relationship between reinforcement stress σ_s (vert. axis) and strain ϵ_s (hor. axis) observed in reinforced concrete bars due to increasing axial force for various diameters and concrete strengths [162]

3.1.4.2 Modified steel strains

The material model that determines the modified reinforcing steel strains ("mod-steel") [126, 127, 187] takes into account the tension stiffening effect by reducing the strains of pure reinforcement bars. The stress-strain relationship for the modified steel strains and the pure reinforcing steel is shown in Fig. 3.18. In order to establish the stress-strain relationship for the "mod-steel" material model, the strain values Eq. 3.41 to Eq. 3.49 and the corresponding stress values Eq. 3.50 to Eq. 3.53 are considered in this model.

The intersection between the stress-strain definitions allows a clear association of the simulation results with the characteristics of the cracking stages, which is of significant importance to the analysis of structures. Therefore, differentiation should be established between each cracking stage. For the consideration of the tension stiffening effect, a modified stress-strain relationship of the embedded reinforcement (σ_s-$\epsilon_{s,m}$) can be established according to [126, 127, 187]:

① uncracked stage

$$\epsilon_{s1} = \epsilon^{I}_{sr,\mathrm{bar}} \cdot \frac{d - x^{I}}{h - x^{I}} \tag{3.41}$$

② crack formation stage

$$\epsilon_{s2} = \frac{\sigma_{s2}}{E_s} - \beta_t \cdot \Delta\epsilon \tag{3.42}$$

③ stabilised cracking stage

$$\epsilon_{s3} = \frac{f_y}{E_s} - \beta_t \cdot \Delta\epsilon \tag{3.43}$$

④ steel yielding stage

$$\epsilon_{s4} = \frac{f_y}{E_s} - \beta_t \cdot \Delta\epsilon + \delta \cdot \left(1 - \frac{\sigma_{s1}}{f_y}\right) \cdot \left(\epsilon_{su} - \frac{f_y}{E_s}\right) \tag{3.44}$$

with:

$$\epsilon^{I}_{sr,\mathrm{bar}} = \frac{f_{ctm}}{E_{c0m}} \tag{3.45}$$

$$\epsilon^{II}_{sr,\mathrm{bar}} = \frac{f_{ctm} \cdot A_{c,eff}}{A_{s1} \cdot E_s} \tag{3.46}$$

$$\epsilon^{I}_{sr,\mathrm{beam}} = \epsilon^{I}_{sr,\mathrm{bar}} \tag{3.47}$$

$$\epsilon^{II}_{sr,\mathrm{beam}} = \frac{f_{ctm} \cdot I_i}{A_{s1} \cdot E_s \cdot z_{iu} \cdot (h - d_1 - x^{II}/3)} \tag{3.48}$$

$$\Delta\epsilon = \mathrm{MIN}\left(\epsilon^{II}_{sr,\mathrm{bar}} - \epsilon^{I}_{sr,\mathrm{bar}}\, ; \, \epsilon^{II}_{sr,\mathrm{beam}} - \epsilon^{I}_{sr,\mathrm{beam}}\right) \tag{3.49}$$

The properties of the cross-section are considered in the computation of the strain values by the amount of reinforcement A_{s1}, the moment of inertia I_i, the effective concrete area in tension $A_{c,eff}$ and the depth of the compressive zone in the uncracked stage x^{I} as well as in the cracked stage x^{II}. The ductility of the reinforcement is defined by the coefficient δ and for commonly used high ductility reinforcing steels $\delta = 0.8$. The indices "bar" and "beam" express the solution for the strains with respect to a tensile bar and flexural member, respectively.

① uncracked stage

$$\sigma_{s1} = \epsilon^{II}_{sr,\mathrm{beam}} \cdot E_s \tag{3.50}$$

② crack formation stage

$$\sigma_{s2} = \sigma_{s1} \cdot 1.3 \tag{3.51}$$

③ stabilised cracking stage

$$\sigma_{s3} = f_y \tag{3.52}$$

④ steel yielding stage

$$\sigma_{s4} = f_t \tag{3.53}$$

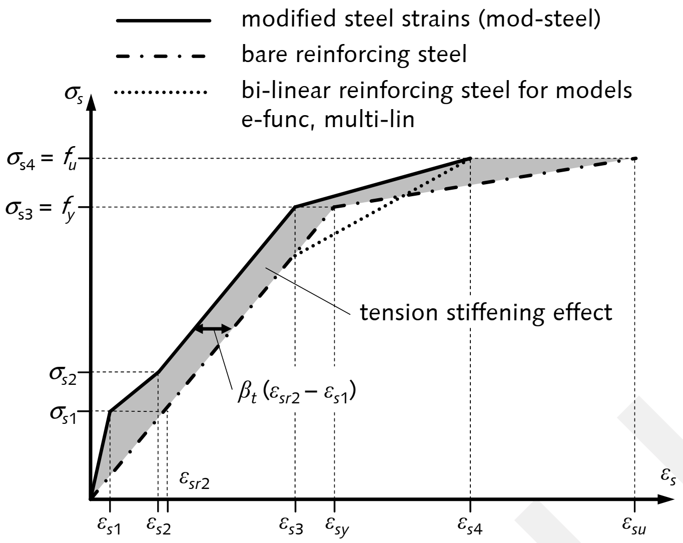

Figure 3.18: Modified stress-strain diagram of reinforcement bars considering tension stiffening, according to [126, 127, 187]

For combination of external load and centric restraint, the modification of the reinforcing steel stress-strain relationship may not be adequate [85]. A significant divergence in the initial stiffness based on this model in comparison to the analytical elastic in-plane stiffness EA_i^I and bending stiffness EI_i^I exists for the purely normal force ("bar") or bending force ("beam") oriented modification. On one side, the analytical solution of the in-plane stiffness can be analysed accurately by the normal force oriented stress-strain modification. In contrast, by applying the bending force oriented modification, the in-plane stiffness may be considerably underestimated. On the other side, the analytical solution of the bending stiffness can be determined by the bending force oriented description, whereas the normal force oriented definition overestimates these stiffness values. Finally, it is not possible to simultaneously describe the analytical in-plane and bending stiffness [267]. The modification of the concrete stress-strain relationship in the cracked tensile zone, see Sec. 3.1.4.3 ("multi-lin") and Sec. 3.1.4.4 ("e-func"), may be more adequate for the combined loading of external bending load and normal force.

As an alternative to the modification of the reinforcing steel strains, the tension stiffening effect can be considered by modifying the concrete stress-strain relationship in the effective tensile zone. In the initial uncracked stage, the assumption of linear-elastic stress-strain relationship allows the exact consideration of the in-plane and bending stiffness of the cross-section. Moreover, the analytical cracking section forces (N_{cr}, M_{cr}) can be simulated for any combination between normal force and bending moment. Various models are investigated and a discussion of several models can be found in [308]. Two models are considered in this thesis, the multi-linear material model (Sec. 3.1.4.3) and the exponential function model (Sec. 3.1.4.4).

3.1.4.3 Multi-linear material model

The characteristic cracking stage values are considered in the multi-linear tension stiffening model "multi-lin" [74, 187] for the stress-strain relationship of the concrete, see Fig. 3.19. The model can be applied for the subsection of the effective concrete area in tension (RCT), see Sec. 3.1.4.5. Therefore, the tension stiffening effect is not considered by reducing the strain values of the reinforcement bars, but it is taken into account in the concrete stress-strain relationship. The strain values are similarly computed according to Eq. 3.41 to Eq. 3.49 and the corresponding stress values are illustrated in Fig. 3.19. Therefore, the strain at the intersection between crack formation and the stabilised cracking stage can be computed by $\epsilon_{c2} = \epsilon_{s2}$ and at the intersection between stabilised cracking and steel yielding stage by $\epsilon_{c3} = \epsilon_{s3}$. The maximum admissible strain may be determined by $\epsilon_{c4} = \epsilon_{s4}$.

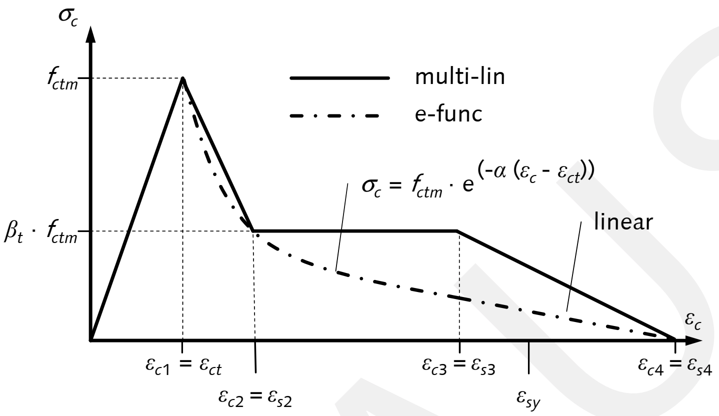

Figure 3.19: Stress-strain diagram of concrete under tension considering tension stiffening, models according to “e-func” [313], “multi-lin” [74, 187]

3.1.4.4 Exponential function

Another model is an exponential function (“e-func”) by Pölling [313], which was originally developed for the stress-strain relationship of plain concrete after reaching its tensile strength. In this function, the parameter α controls the slope of the descending branch, see Fig. 3.19. This value can be computed in such a way that an intersection appears between the models “multi-lin” and “e-func” at the strain magnitude ϵ_{c2}. This intersection point can be directly computed by:

$$\alpha = -1 \cdot \left(\frac{\ln \beta_t}{\epsilon_{c2} - \epsilon^{I}_{sr,\text{bar}}} \right) . \tag{3.54}$$

Therefore, this model for the cracked plain concrete is adopted for the description of the tension stiffening effect. However, a clear differentiation in the stress-strain relationship between the crack formation stage and the stabilised cracking stage is not possible. The model “e-func”’ may be applied in the “reinforced” concrete subsection (RCT), see Sec. 3.1.4.5. The stress in the reinforced tensile cross-section zone is computed in the crack formation and stabilised cracking stages by the following model based on the study of Pölling [313]:

$$\sigma(\epsilon_{ct} < \epsilon_c < \epsilon_{s3}) = f_{ctm} \cdot \mathrm{e}^{-\alpha(\epsilon_c - \epsilon_{ct})} . \tag{3.55}$$

After the final stage in the stabilised cracking stage is reached, the concrete is linearly modelled in the strain range of $\epsilon_{c3} < \epsilon_c < \epsilon_{c4}$. For plain concrete, the parameter α is calculated in such a way that the integral under the tensile range gives the fracture energy G_F. This energy must be assigned to an equivalent length of the finite element (l_{eq}), taking into account the tensile softening in a stress-strain relationship. Hence, the fracture energy is converted into a specific volume fracture energy g_t^* considering the type, integration

BAUHAUS
UNIVERSITÄTSVERLAG

rule (n_{int} ... number of integration points), size and shape of the element. An accurate determination can be found as follows [258, 313]:

$$g_t^* = \frac{G_F}{l_{\text{eq}}} \quad , \tag{3.56}$$

with the equivalent length l_{eq} coupled to the element size:

$$l_{\text{eq}} = l^{(e)}/n_{\text{int}} \qquad \text{1 D elements} \qquad \text{with } l^{(e)} \text{ element length}\,, \tag{3.57}$$

$$l_{\text{eq}} = \sqrt{A^{(e)}/n_{\text{int}}} \qquad \text{2 D elements} \qquad \text{with } A^{(e)} \text{ element area}\,, \tag{3.58}$$

$$l_{\text{eq}} = \sqrt[3]{V^{(e)}/n_{\text{int}}} \qquad \text{3 D elements} \qquad \text{with } V^{(e)} \text{ element volume}\,. \tag{3.59}$$

Very big elements may lead to inaccurate results and a critical length should be considered in the element size determination:

$$l_{\text{eq}} = \frac{2G_F E_c}{f_{ct}^2}\,. \tag{3.60}$$

For simulations of engineering structures, Bažant and Oh [33] recommend limiting the equivalent length to:

$$l_{\text{eq}} \leq \frac{G_F E_c}{f_{ct}^2}\,. \tag{3.61}$$

Finally, the parameter α can be estimated for plain concrete by [313]:

$$\frac{1}{\alpha} = \frac{g_t^*}{f_{ct}} - \frac{1}{2}\frac{f_{ct}}{E_c}\,. \tag{3.62}$$

3.1.4.5 Effective concrete area in tension

For the determination of the cracking process, it is necessary to analyse the amount of bond force transferred from steel to concrete which causes additional cracks. This force significantly influences the crack spacing and consequently the tension stiffening effect. In the case that the entire concrete tensile area contributes to the cracking process, then the cracking force can be computed on the entire concrete section area A_c. In contrast, only a certain amount of the cracking force based on full concrete tensile contribution is enough to cause an additional crack [227]. This phenomenon is considered to determine the model of the effective concrete area. In this conceptual model, the required force is computed by the product of the effective concrete area and the concrete tensile strength. Hence, the concrete in tension is modelled by a centric tensile bar with the cross-section $A_{c,\text{eff}}$.

Similarly, the tension stiffening mechanism is determined for centrically reinforced concrete tensile bars considering the concrete contribution between the cracks in the area $A_{c,\text{eff}}$. The bond force that causes a new crack can be determined $F_b = F_{ct} = f_{ctm}A_{c,\text{eff}}$. For structural elements subjected to both bending and normal forces (see Fig. 3.20), it is not clear which bond force causes an additional crack between two existing cracks with maximum crack spacing in between [220]. Therefore, it is necessary to determine the concrete compressive force, bond force, and also the interaction of both on the plate stress state between the two existing cracks.

On one side, the bond behaviour is non-linear between steel and concrete. On the other side the ultimate capacity of the tensile zone is dependent on the stress redistribution capacity when uneven stress distribution in the cross-section occurs. Therefore, non-linear plate analysis is necessary in order to determine the

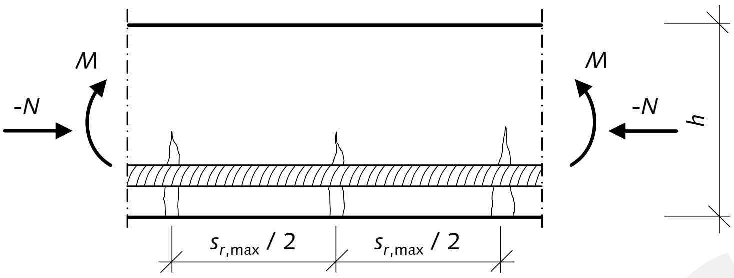

Figure 3.20: Reinforced concrete element subjected to combined loading of bending and normal forces, based on [220]

effective concrete area in tension [227]. Plain concrete in tension can still sustain tensile stress after crack initiation, see Sec. 3.1.3. These effects are considered in the load-deformation analysis by König and Fehling [220] with a parametric study including various assumed crack spaces s_r, concrete compressive forces F_c, and distances of reinforcement bars to surface d_1, see Fig. 3.21.

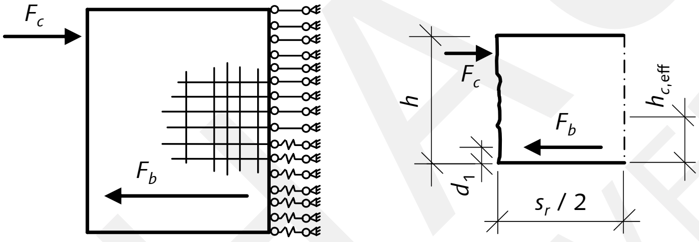

Figure 3.21: Finite Element and mechanical model between two cracks of a structural element subjected to bending and normal force, based on [220]

In this study, non-linear Finite Element simulations of plate stress states including several conditions allows an adequate computation of the bond force. One of the major findings is that the distribution of the bond stresses along the transmission length does not significantly influence the bond force. Hence, a constant bond stress distribution can be used for the determination of F_b, see Fig. 3.11(b). In the case of small crack spaces compared to the cross-section depth ($s_r/h \approx 0.20$), concrete tensile stresses exclusively appear close to the reinforcement layer. Therefore, the bond force is limited to [220]:

$$F_b = \underbrace{2 \ldots 3 \cdot (h-d)}_{h_{c,\text{eff}}} \cdot f_{ctm} \cdot b \tag{3.63}$$

were b is the cross-section width. For higher ratio s_r/h, the concrete compressive force significantly affects load-deformation behaviour. Very large crack spaces ($s_r/h \approx 0.90$) lead to a plain strain distribution in the centre of the two cracks. Hence, the greatest bond force can be computed for such crack spaces. A similar non-linear plate analysis is investigated by Fischer [111] which defines the effective depth as:

$$h_{c,\text{eff}} = (h-d) + s_r/2\,, \tag{3.64a}$$

with a lower limit value (less concrete contribution) determined by:

$$h_{c,\text{eff}} = 2.5 \cdot (h-d)\,. \tag{3.64b}$$

Based on these findings, it is possible to determine an effective concrete area in tension, which transfer the tensile zone of a structural element subjected to bending and normal forces into a fictitious axially loaded tensile bar [220]. Hence, the concrete in tension contributes to the stiffness of beams, slabs, and walls comparable to a tensile tie between cracks [74], see Fig. 3.22.

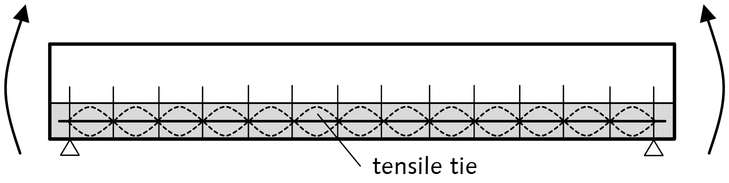

Figure 3.22: Tensile tie representing concrete contribution between cracks for flexural members, based on [185]

In order to compute the crack spaces adequately, the effective concrete area in tension $A_{c,\mathrm{eff}}$ is defined as:

$$A_{c,\mathrm{eff}} = h_{c,\mathrm{eff}} \cdot b\,, \tag{3.65a}$$

$$A_{c,\mathrm{eff}} \cdot f_{ctm} = F_b\,. \tag{3.65b}$$

This equilibrium condition would lead to an iterative analysis of the effective area depending on the crack space. In general, various research studies recommend the application of general determinations such as:

$$h_{c,\mathrm{eff}} = 7.5 \cdot \varnothing_s \qquad \text{thin element} \quad \text{Leonhardt} \quad [245,\ 246]\,, \tag{3.66}$$

$$h_{c,\mathrm{eff}} = d_1 + 8 \cdot \varnothing_s \leq h/2 \qquad \text{thick element} \quad \text{Leonhardt} \quad [244]\,, \tag{3.67}$$

$$h_{c,\mathrm{eff}} = \alpha_{h_{c,\mathrm{eff}}} \cdot (h - d) \qquad \text{König and Fehling} \quad [220]\,. \tag{3.68}$$

On one side, the determination by LEONHARDT according to Eq. 3.66 and Eq. 3.67 leads to higher inaccuracies in comparison to Eq. 3.68 and corresponding experimental measurements [367]. On the other side, the effective depth dependency on the reinforcement diameter results in an iterative procedure. Therefore, the determination according to Eq. 3.68 is adopted in guidelines MC 10 [187]) and codes EC 2 [101]. For different types of cross-section, the determination of the effective concrete depth $h_{c,\mathrm{eff}}$ is illustrated in Fig 3.23.

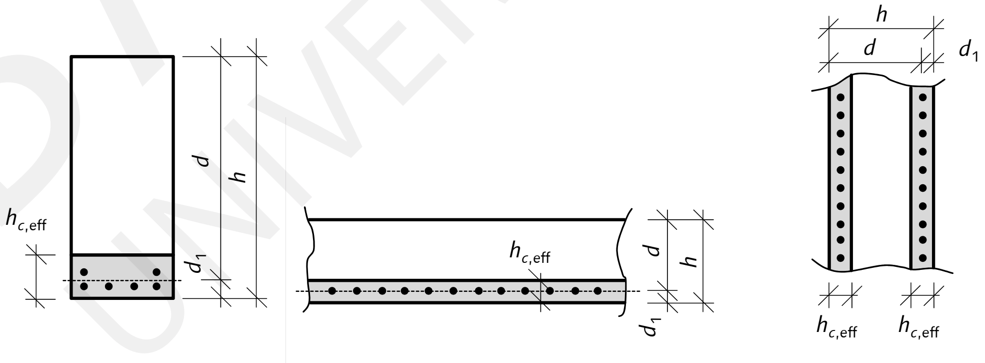

(a) beam (b) slab (c) wall in tension

Figure 3.23: Height of the effective concrete area $h_{c,\mathrm{eff}}$ (grey areas), based on [101, 187]

The several definitions of $h_{c,\mathrm{eff}}$ are listed in Tab. 3.6 and may be used in the absence of a more refined model. Simulations based on fracture mechanics approaches [8, 33, 172] could be applied for a more accurate analysis.

Table 3.6: Determination of effective depth of concrete in tension $h_{c,\text{eff}}$

Component	$h_{c,\text{eff}}$	Literature	
bending	$< (h - x^I)/3$	German concrete society	[78]
centric tensile force	$< h/3$	German concrete society	[78]
absolute	$3.0(h - d)$	König and Fehling	[220]
absolute	$(h - d) + s_r/2$	Fischer	[111]
not mentioned	$\text{MIN} \begin{cases} 2.5(h - d) \\ (h - x^I)/3 \\ h/2 \end{cases}$	EC 2	[101]
beam	$2.5(h - d) < (h - x^I)/3$	MC 90 and MC 10	[74, 187]
slab	$\text{MIN} \begin{cases} 2.5(h - d) \\ (h - x)/3 \end{cases}$		
wall in tension	$\text{MIN} \begin{cases} 2.5(h - d) \\ h/2 \end{cases}$		

The depth limitation for elements in bending $(h - x)/3$ [78] should not be applied to large cross-sections with a regular reinforcement layout over the web depth [220]. In the case of the limit according to the centric tensile force, the boundary $h/3$ [78] should be applied for cross-sections with $h > 30\,\text{cm}$. In the case that the maximum crack space is in the range of the cross-section depth and the top and bottom layers are reinforced, the effective depth for the centric normal force condition should be defined as $h/2$ for each layer [220]. Various experimental studies including, centric tensile force, bending loading condition, prestressed elements, and elements designed for resisting restraint effects within a total of 250 tests are analysed by König and Fehling [220]. The comparison between computed and measured crack widths illustrate the best accuracy applying the determination of $h_{c,\text{eff}} = 3.0(h - d)$. In the EC 2 with respect to the German National Annex [141], the determination of $2.5(h - d)$ is recommended for concentrated reinforcement layout and thin structural elements with the ratio $h/(h - d) \leq 10$ for flexure and $h/(h - d) \leq 5$ for centric tension, respectively. For more compact structural elements, the effective concrete area may increase up to $5.0(h - d)$, see Fig. 3.26. In the case that the reinforcement is not embedded in the range of $(h - x)/3$, this limit should be increased to $(h - x^I)/2$ where x^I is the compressive zone depth in the uncracked stage [141].

For thick structural components (e.g. thick walls, bridge abutments, bridge piers) under tension with reinforcement at the surface, the crack propagation is decisively different from that of thinner elements. Differentiation between the crack propagation of thin and thick elements is very important in order to ensure a more reliable and economical design. Otherwise, the reinforcement layout in thick elements may be overestimated [268]. Between separating cracks additional incipient cracks occur, which propagate initially from the surface of the thick element. Whereas in thinner tensile bars only separating cracks appear [352]. In the study of Leonhardt [244], this phenomenon is interpreted by a different effective tensile area in thick elements. In gerneral, the effective concrete area in tension is much smaller than the cross-section depth, see Fig. 3.24. Therefore, accumulative crack propagation may occur at the surfaces for concentrated reinforcement bars [220].

BAUHAUS
UNIVERSITÄTSVERLAG

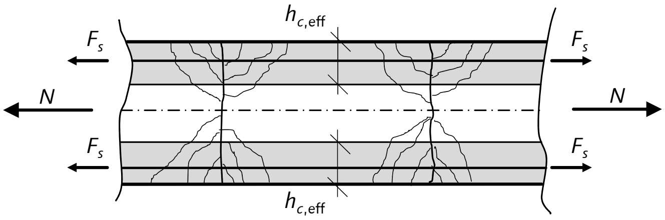

Figure 3.24: Accumulative crack propagation in thick structural components with concentrated reinforcement bars at the surfaces, based on [220, 268]

In order to determine the crack propagation in thick reinforced concrete walls, tensile tests on horizontal layers of walls with the dimensions $b/h/l$ equal to $100/16/600\,[\text{cm}]$ are tested by ROSTÁSY et al. [352] in deformation controlled tests. In addition to the external tensile load, the influence of residual stresses caused by restraint temperature load (uniform temperature component, $T_0 \approx +20\,°\text{C}$, $T_{N,\text{E1}} = +20\,°\text{C}$, $T_{N,\text{E2}} = +5\,°\text{C}$, $T_{N,\text{E3}} = -20\,°\text{C}$) on the load-deformation behaviour is studied, see Fig. 3.25. With increasing thermal load, the crack initiation occurs at a lower external load level due to a higher prestrain. Therefore, the tension stiffening of concrete is decreased with increasing restraint thermal condition. The degradation of in-plane stiffness is obvious in the loading ranges in which the stiffness after each crack initiation inclines more and more flatter.

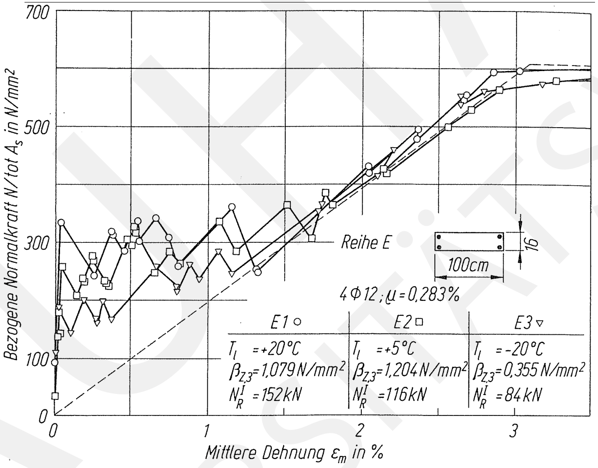

Figure 3.25: Load-deformation behaviour of thick concrete wall due to external tensile force and uniform temperature component [352], hor. axis: average reinforcing steel strain $\epsilon_{s,m}$, vert. axis: relative reinforcing steel stress σ_s

Based on the presented theoretical and experimental investigations, the depth of the effective concrete area in tension is recommended in the design guideline DAfStb 466 [227] for centric tension and flexural loading and varying ratio between h/d_1, see Fig. 3.26. This determination is recommended in the Eurocode 2 with respect to the German National annex [141].

3.1.5 Reinforcing steel

The material properties characterising the mechanical behaviour of reinforcing steel are the yield strength f_y, tensile strength f_t and the strain at maximum force ϵ_{su}. The characteristic yield strength f_{yk} corresponds to the 0.2 % offset in the stress-strain relationship. In the design of reinforced concrete structure,

BAUHAUS
UNIVERSITÄTSVERLAG

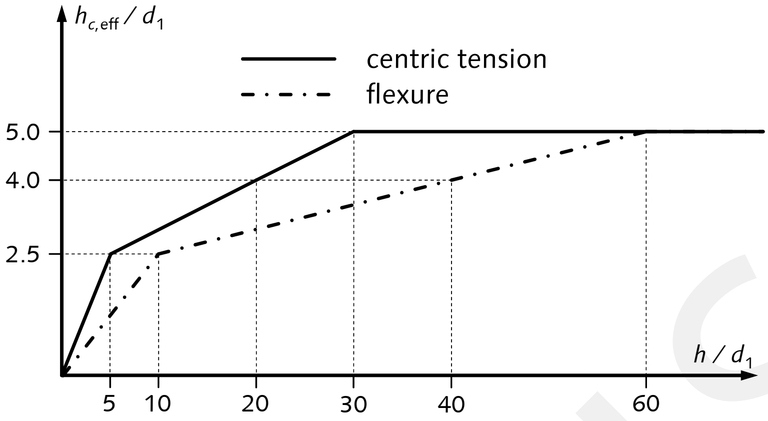

Figure 3.26: Effective depth $h_{c,\mathrm{eff}}$ depending on load condition and element thickness, based on DAfStb 466 [227]

the engineers generally expects reinforcement to yield in the ULS before failure of a member or structure occurs. Indeed, the yield strength can be appreciably stronger than assumed in design [187]. Therefore, a flexural member may not collapse in a ductile failure mechanism due to the fact that the concrete reaches the ultimate compressive strain before yielding occurs in the reinforcing steel. An overstrength on the order of 30 % may be observable in experiments as a general approximation [75]. Diversity and evolution in the manufacturing processes for bars and wires result in various stress-strain relationships, see Fig. 3.27.

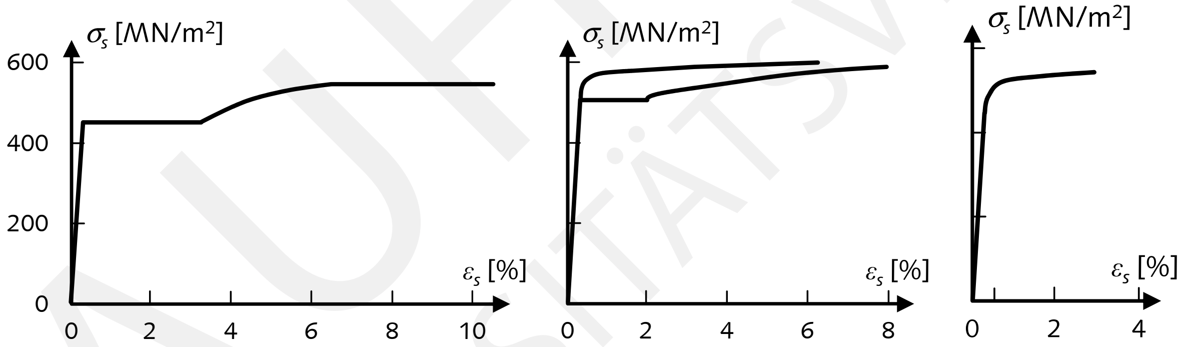

(a) hot-rolled bars, heat-trated bars, micro-alloyed bars (b) upper curve: cold-worked bars, lower curve: low carbon, heat-treated bars (c) cold-worked wires

Figure 3.27: Stress-strain relationship of reinforcing steel, based on [187]

In the case that moment redistribution is taken into account in design, adequate ductility is necessary and for design purposes four ductility classes are defined for steel grades with a characteristic yield strength of $f_{yk} \leq 600\,\mathrm{MN/m^2}$. These classes are related to the characteristic strength ratio f_{tk}/f_{yk} and ultimate strain value ϵ_{uk}. These classes are as follows [187]:

	f_{tk}/f_{yk}	ϵ_{uk}
• class A	≥ 1.05	$\geq 2.5\,\%$
• class B	≥ 1.08	$\geq 5.0\,\%$
• class C	≥ 1.15 and ≤ 1.35	$\geq 7.5\,\%$
• class D	≥ 1.25 and ≤ 1.45	$\geq 8.0\,\%$

In seismic regions, where high ductility of the structure is required, the classes C and D are commonly used. For structures in seismically inactive regions, class B reinforcement bars are used [135]. The actual material behaviour as shown in Fig 3.27 can be simplified in calculations by an idealised bi-linear relationship with the parameters $E_s = 200,000\,\mathrm{MN/m^2}$, f_y, f_t, and ϵ_u. A more complex model is investigated by MENEGOTTO and PINTO [273], which is generally adequate for describing the stress-strain relationship of reinforcing steel as well as stainless and prestressing steel and may also be applicable for cyclic loading and varying amplitudes [187]. In that case, the parameters describing the more complex stress-strain relationship should be adjusted to the relevant characteristic values.

3.1.6 Prestressing steel

For design purposes, the mechanical properties are the upper limit of the tensile strength f_{pt} (UTS), the 0.1 % proof stress $f_{p0.1}$ (yield stress), and the strain at maximum stress ϵ_{pu}. The grade of the prestressing steel is often denoted by the UTS value. Indicative stress-strain relationships for prestressing steel in tension is shown in Fig. 3.28. The nominal value of the modulus of elasticity of prestressing steel E_p can be approximated as $205,000\,\mathrm{MN/m^2}$ for wires, and $195{,}000\,\mathrm{MN/m^2}$ for strands [187]. In general, this mechanical property should be declared and certified by the manufacturer. The loss of stress by relaxation is an important phenomenon in the long-term behaviour of prestressed steel. However, this phenomenon is not addressed further in this thesis.

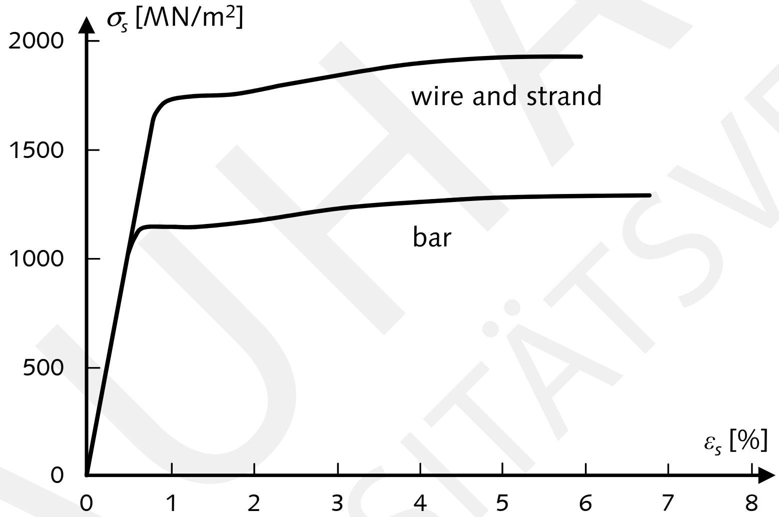

Figure 3.28: Stress-strain relationship of prestressing steel, based on [187]

The actual material behaviour as shown in Fig 3.28 can be simplified in simulations by an idealised bi-linear relationship with the parameters E_p, $f_{p0.1}$, f_{pt}, and ϵ_{pu}. The model by MENEGOTTO and PINTO [273] may also be used for prestressing steel [187].

3.2 Creep of Concrete

3.2.1 Phenomenon and models

The phenomenon of increasing concrete strain over time, caused by a constant sustained load, is termed creep of concrete. Creep depends both on internal factors, such as material properties of concrete and its composition, and on external parameters, such as ambient climate. In general, creep of concrete does not depend on its compressive strength or age at loading per se, but rather on its composition and degree of hydration. With decreasing water/cement-ratio, or cement content, or increasing degree of hydration, the creep of concrete decreases. Different types of cement result in different degrees of hydration and the creep depends more on the degree of hydration rather than on the age of concrete for a given time [74].

Experimental studies observed that creep of concrete is a non-linear phenomenon. This non-linearity with respect to creep-inducing stresses is measured in creep experiments with a constant stress, particularly when the stress exceeds $\sigma_c > 0.4 f_{cm}(t_0)$ [185]. Moreover, the non-linearity is observable even below this stress magnitude in experiments with a variable stress history. Microcracking due to shrinkage or high load levels and stress-induced ageing under load are the main reasons for the non-linear creep behaviour. The capacity of concrete in tension is less important than the capacity in compression and, thus, the tensile creep of concrete is not studied in detail. The behaviour for loading below the concrete tensile strength can be assumed to be approximately similar to the compressive creep behaviour [147, 187]. In a detailed study by KORDINA et al. [229], the tensile creep compliance is investigated to be similar to the compressive creep compliance and the assumption of equal creep factors for the compressive and tensile zones is proofed for flexural members. In the case of restrained drying shrinkage, the tensile creep may be a phenomenon that should be taken into account in the analysis [44].

In case of linear creep, the dimensionless linear creep coefficient φ_c is used to determine the ratio between the creep strain $\epsilon_{c,cr}$ and the elastic strain $\epsilon_{c,el}$. Therefore, the creep of concrete can be described as a multiple of the elastic concrete deformation:

$$\epsilon_{c,cr}\left(t, t_0\right) = \varphi_c\left(t, t_0\right) \epsilon_{c,el}\left(t_0\right) . \tag{3.69}$$

The time- and stress-dependent total strain of concrete is defined as (neglecting post-hardening of concrete):

$$\epsilon_{c,tot}\left(t, t_0\right) = \epsilon_{c,el}\left(t_0\right) + \epsilon_{c,cr}\left(t, t_0\right) = \sigma_c\left(t_0\right)\left[\frac{1+\varphi_c\left(t, t_0\right)}{E_{c,t_0}}\right] , \tag{3.70a}$$

$$= \sigma_c\left(t_0\right)\left[\frac{1}{E_{c,t_0}} + \frac{\varphi_c\left(t, t_0\right)}{E_{c,28}}\right] . \tag{3.70b}$$

Instead of utilizing the modulus of elasticity at the time of initial loading (E_{c,t_0}, Eq. 3.70a), some creep models, such as [123, 185], relate the creep coefficient to the 28-day value of concrete stiffness ($E_{c,28}$, Eq. 3.70b). Recommendations for the consideration of the post-hardening of concrete can be found in [206]. The total compliance of concrete $J_c(t, t_0)$ is introduced as following:

$$\epsilon_c\left(t, t_0\right) = \sigma_c\left(t_0\right) J_c\left(t, t_0\right) . \tag{3.71}$$

Due to the bond between concrete and steel, a permanent redistribution of stresses occurs in composite cross-sections and structural elements. Therefore, the constant stress or deformation state is not practically relevant and the creep analysis needs to be modified into integral or differential formulations in order to consider variable stresses or displacements [185]. The superposition principle of BOLTZMANN [48] for linear visco-elastic materials can be used for describing concrete linear creep at variable loading levels. Different starting points of loading or durations of loading, as defined in an explicit loading history, can be considered for the computation of creep strains based on the superposition principle [259]. Based on the assumption of linearity, the application of the principle of superposition is consistent. The non-linear behaviour of concrete causes certain unavoidable predicted uncertainty when linear superposition is applied to creep of concrete under variable stress, particularly for unloading or decreasing strains [74]. Nevertheless, this principle describes the behaviour of concrete under variable stresses reasonably well if the stresses are within the service stress range [185]. Therefore, the concrete strain at a certain time according to the BOLTZMANN principle is defined as:

$$\epsilon_c(t) = \sigma_c\left(t_0\right) J_c\left(t, t_0\right) + \Delta\sigma_c\left(t, t_1\right) J_c\left(t, t_1\right) + \ldots + \Delta\sigma_c\left(t, t_i\right) J_c\left(t, t_i\right) \ . \tag{3.72}$$

This sum can be converted into an integral description [74]:

$$\epsilon_c(t) = \sigma_c\left(t_0\right) J_c\left(t, t_0\right) + \int_{t_0}^{t} J_c\left(t, \tau\right) \frac{\partial\sigma_c(\tau)}{\partial\tau} \mathrm{d}\tau \, , \tag{3.73}$$

where τ are the time-steps in the time-integration of the load-history analysis. Several theories and approaches exist based on different descriptions of the total or creep compliance for the determination of the long-term behaviour of concrete. Theory of elastic creep with the Effective Modulus Method (EMM), the Age-Adjusted Effective Modulus Method (AEMM) [23, 394], and the solidification theory [35, 36] are mentioned here. Further discussion can be found in [147, 206]. The models for determining the creep compliance are only applicable in the case of linear creep, which takes place up to a stress level of approx. $\sigma_c < 0.4 f_{cm}(t_0)$.

Rheological models [46, 165, 270, 378] or an increase in the linear creep compliance applying a dimensionless, empirically determined stress-dependent factors [31, 35, 187, 83, 150] are approaches which allow the consideration of non-linear creep behaviour. Moreover, in the thesis by DIENER [83] the superposition principle is assessed to be inadequate in the case of non-linear creep. The stress history $\sigma_c(t)$ is converted into a differential formulation of time and stress, respectively. Therefore, the integral of the creep compliance is converted into a summation [83, 206].

The models described henceforth are commonly used for the description of linear creep theory by computing the linear creep coefficient. For the analysis of the creep coefficient, either the product or summation ansatz are applied in these models. Combining a notational creep coefficient, which depends on the concrete age at loading, and a time function, describing the development of creep with time, the product ansatz is defined as [206]:

$$\varphi_c\left(t, t_0\right) = \left[k_1\left(t_0\right) k_2\right] k_3\left(t - t_0\right) \ , \tag{3.74}$$

in which k_1, k_2, k_3 are functions or coefficients. This approach is considered in the Model Code 90 [74], the updated knowledge of the MC 90 [185] and in the design guideline of the American Concrete Institute [6]. The summation of visco-elastic and visco-plastic creep components leads to the summation ansatz [206]:

$$\varphi_c\left(t, t_0\right) = k_1\left(t, t_0\right) + k_2\left(t, t_0\right) \ . \tag{3.75}$$

This approach is considered in the Model Code 2010 [187]. In the majority of research and design practice, the following prediction models are applied for the time-dependent increase of the creep compliance:

American Concrete Institute	ACI 209	[6]
BAŽANT and BAJEWA	B 3	[24, 25, 26]
Model Code 90-99	MC 90-99	[185]
GARDNER and LOCKMAN	GL 2000	[123]

The model recommended by the American Concrete Institute **ACI 209** is based on the product ansatz, see Eq. 3.74, and considering a hyperbolic time function [274] and an ultimate creep coefficient $\varphi_{c,\infty}$. Therefore, the linear creep coefficient is defined as:

$$\varphi_c\left(t, t_0\right) = \varphi_{c,\infty}\left(t_0\right)\left[\frac{\left(t-t_0\right)^{\psi}}{d+\left(t-t_0\right)^{\psi}}\right] , \tag{3.76}$$

with the total compliance defined as:

$$J_c\left(t, t_0\right) = \frac{1}{E_{cm,t_0}} + C_c\left(t, t_0\right) = \frac{1}{E_{cm,t_0}} + \frac{\varphi_c\left(t, t_0\right)}{E_{cm,t_0}} . \tag{3.77}$$

The values of $\psi = 0.6$ and $d = 10\,\mathrm{d}$ are recommended and $\varphi_{c,\infty}\left(t_0\right)$ depends on concrete age at the beginning of loading t_0, relative humidity RH, concrete mixture, volume-surface ratio V/S, and fresh and hardened concrete properties.

The model by BAŽANT and BAJEWA **B 3** follows the summation ansatz, see Eq. 3.75. The creep compliance is subdivided into the instantaneous compliance q_1, the basic creep compliance $C_{c,0}$, and the drying creep compliance $C_{c,d}$. The total creep compliance is defined as:

$$J_c\left(t, t_0, t_d\right) = q_1 + C_{c,0}\left(t, t_0\right) + C_{c,d}\left(t, t_0, t_d\right) , \tag{3.78}$$

in which q_1 is the instantaneous compliance, $C_{c,0}$ the basic creep compliance, and $C_{d,0}$ the drying creep compliance. The basic creep compliance considers visco-elastic, nonaging visco-elastic, and visco-plastic components with a certain time function for each component. Moreover, the influence of temperature can be considered in this model. In contrast to the other models presented in this section, the time-independent compliance is computed by $1/E_0 = 0.6/E_{cm,28}$ instead of $1/E_{c,t_0}$. Therefore, the asymptotic instantaneous modulus E_0 is based on the $E_{cm,28}$ secant modulus of elasticity at 28th day. Hence, the short-term creep compliance, which is included in any experiment for the determination of the modulus of elasticity, is effectively separated. Therefore, this model is a description of the phenomenon with the most physical background information of the considered models and is based on the solidification theory [207].

Based on the recommendations of the International Federation for Structural Concrete (*fib*), the creep model defined in the **MC 90-99** is investigated considering the product ansatz. This model is generally similar to the model ACI 209 except the definition of the notional creep coefficient $\varphi_{c,0}$. The creep coefficient is related to the 28-day value of modulus of elasticity and is defined as:

$$\varphi_c\left(t, t_0\right) = \varphi_{c,0}\beta_c t, t_0 = \varphi_{c,0}\left[\frac{\left(t-t_0\right)}{\beta_H+\left(t-t_0\right)}\right]^{0.3} , \tag{3.79}$$

with the total creep compliance defined as:

$$J_c\left(t, t_0\right) = \frac{1}{E_{c,t_0}} + C_c\left(t, t_0\right) = \frac{1}{E_{c,t_0}} + \frac{\varphi_c\left(t, t_0\right)}{E_{c0,28}} . \tag{3.80}$$

In contrast to these models, the model by Gardner and Lockman **GL 2000** is a purely empirically developed regression model. The experimental creep data is used from the RILEM database (518 creep tests) [287]. The creep coefficient refers to the 28-day value of modulus of elasticity and can be determined by:

$$\varphi_c(t,t_0) = \Phi(t_c)\left[2\left(\frac{(t-t_0)^{0.3}}{(t-t_0)^{0.3}+14}\right)\right] + \left(\frac{7}{t_0}\right)^{0.5}\left(\frac{t-t_0}{t-t_0+7}\right)^{0.5} + \Phi(t_c)\left[2.5\left(1-1.8086\,RH^2\right)\left(\frac{t-t_0}{t-t_0+0.15\left(\frac{V}{S}\right)^2}\right)\right]. \tag{3.81}$$

The creep compliance can be analysed identically to Eq. 3.80. The creep coefficient is defined by relative humidity, cement type, and volume/surface ratio. No ultimate creep coefficient is assumed as it is determined in ACI 209 and MC 90-99. Even for a large load duration, a steady increase in the creep compliance is predicted by these models. The factor $\Phi(t_c)$ takes into account the drying before loading.

3.2.2 Comparison and evaluation of creep models

Randomness in material properties and environmental conditions, and the error in the models can cause a considerable predicted uncertainty in the structural analysis. In general, this predicted uncertainty is higher after short loading durations than after long loading durations [74]. In the design guideline MC 90-99, the variation in the prediction of the creep compliance is estimated with $CV_{\text{MC 90-99}} = 0.2$ [74]. Comparison of these creep models to experimental data (RILEM data bank [287]) is investigated by Gardner [122]. If all available input information is used, GL 2000 is the best predictor of the compliance, followed by B 3 and MC 90-99, see Tab. 3.7. For the case that only the concrete strength is used as input information, GL 2000 and B 3 show higher accuracy in comparison to ACI 209 and MC 90-99. In the study of Goel et al. [148], predicted values of creep are compared with the experimental results of [358] and the RILEM data bank [287]. Conclusions based on the comparison between the prediction of the creep compliance and the experimental measurements are: ACI 209 underestimates the experimental compliances, MC 90-99 is reasonable, B 3 agrees better, and GL 2000 performed best out of these models. In the statistical evaluation of creep models by Al-Manaseer et al. [2], model MC90 -99, B 3 and GL 2000 are considered the best models to predict the creep measurements based on the RILEM data bank. In general, these models tend to underestimate the creep phenomenon.

In the unbiased statistical comparison of creep prediction models by Bažant et al. [32], the variation of the prediction error is quantified in comparison to the experimental data, see Tab. 3.7. This method introduces a weighing data, which is capable of eliminating the bias due to improper data sampling in the database. The statistics of prediction errors are evaluated by the method of least squares with the maximum likelihood criterion. In the statistical comparison by Gardner [122], each time interval is equally weighted and the overall standard deviation of the data from the model predictions is not statistically justified. Instead of averaging the squared errors, the averaging in the model assessment by Gardner is linear in the standard deviation. This linear averaging dismisses the validity of the maximum likelihood criterion and central limit theorem of the theory of probability. Similarly, Al-Manaseer recommends a careful prove the selection and interpretation of the data and the evaluation/statistical methods. The conclusions regarding the accuracy of the model prediction are strongly dependent on the strategy chosen for both issues.

Concrete of different mixtures tested in experiments shows that the relative increase in time-dependent deformation differs much less than the total increase. Therefore, other influencing parameters are excluded in the statistical analysis and the relative compliance is defined by [32]:

$$\overline{J}_c\left(t,t'\right) = J_c\left(t,t'\right)/J_0\,, \tag{3.82}$$

in which J_0 is the initial creep compliance for three-day sustained load. In the results of [32], the model B 3 is evaluated to be the most accurate, followed by GL 2000, and the ACI 209 is the least accurate.

Table 3.7: Coefficients of variation [-] of prediction errors of various creep models

Prediction Model	ACI 209 [6]	B 3 [24, 25, 26]	MC 90-99 [185]	GL 2000 [123]
GARDNER [122]				
only f_{cm}	0.30	0.29	0.37	0.26
all data	0.30	0.27	0.29	0.22
BAŽANT et al. [32]				
compliance	0.388	0.283	0.306	0.285
relative compliance	0.590	0.244	0.293	0.273

In the study of KEITEL [208], sensitivity and uncertainty analysis for both correlated and uncorrelated input parameters is studied. The predictions according to ACI 209 and GL 2000 are most sensitive to the modulus of elasticity. The models GL 2000 and B 3 are evaluated to be more accurate in comparison to the other models, which show a very high model uncertainty up to 0.33. In the case that specific experimental data is available for a certain concrete, an evaluation method based on *Bayes* updating is presented in [209]. This methodology extends the method by BAŽANT and CHERN [27] in order to take into account inaccurate measuring data. One major conclusion is that increasing the measurement error leads to an increasing uncertainty of the identified parameters and the model prognosis. Moreover, two different evaluation methods, the stochastic model selection and uncertainty quantification, are presented in order to compare different models in a quantitative procedure. The quantification of total uncertainty in the model predictions is found to be a more reliable assessment method, due to the insensitivity to the number of measuring points. Furthermore, the uncertainty quantification is suitable for the assessment of creep models even for durations exceeding the experimental duration.

An evaluation method, which is capable of quantifying the uncertainties of creep prediction from selection of a creep model, time-integration method, and from parameter uncertainty is presented in [207]. A numerical example for a commonly used concrete column cross section under varying stresses quantifies the uncertainty, caused mainly by the selection of creep models and to some extent from parameter uncertainty. The selection of time-integration is much less sensitive to the uncertainty in the prediction of creep. Increases in the reinforcement ratio and in load duration are more significant for the time-integration method, but it is still low in comparison to the two other sources of uncertainty.

3.3 Shrinkage of Concrete

3.3.1 Phenomenon and models

The shrinkage of concrete describes the phenomenon of volume change without any external load. This physical process can be separated into drying and chemical shrinkage. On one side, the drying shrinkage is induced due to the loss of volume caused by temperature reduction and moisture exchange of the concrete with the environment [335]. On the other side, the hydration of cement to cement paste, as well as carbonation, determines the chemical shrinkage process. For purposes of structural analysis, both processes can be combined to give the cumulative shrinkage [147].

The interactions between the pure shrinkage strain, elastic, and creep strains caused by concrete shrinkage result in a linear strain distribution over the cross-section depth. In the case of same environmental conditions at both surfaces, the shrinkage strain distribution is constant. Shrinkage cracks may occur at the surfaces of the cross-section due to the tensile stresses (local residual stresses), which are one major reason for cracks in concrete structures [147, 378].

Further stresses occur due to structural constraints or reinforcement bars in composite cross-sections. In the case of unrestrained conditions, no further forces are generated besides these local stresses. Especially in over-reinforced concrete cross-sections, the stiffness of the reinforcement bars induces an internal resistance against the shrinkage concrete strains. Therefore, a residual stress state exists which results in a negative pre-strain in the composite section [220]. In general, tensile stresses in the concrete and compressive stress in the reinforcing steel arise. A high shrinkage strain, reinforcement ratio, and a low concrete tensile strength can cause a predetermined crack pattern. Moreover, an asymmetrical reinforcement layout causes an additional curvature and, thus, vertical displacements of reinforced concrete beams.

Microcracking starts to occur inside the concrete when sufficient residual stresses are developed, which is approximately above 50% of the tensile strength [180]. As the residual stresses increase, these microcracks develop more extensively. Finally, microcracks begin to fuse and a single crack can be localised in the concrete element. This process is not exclusively dependent on the properties of the concrete mixture, because the degree of restraint is additionally a major influence factor [335]. The additional shrinkage term may be generally greater in comparison to strain induced by direct external loads. The computation of the mean reinforcing steel strains (tension stiffening, see Sec. 3.1.4) is not influenced by the concrete shrinkage strains [220].

Water content, water/cement ratio, aggregate type, humidity, and the shape and size of the concrete element are the main influence for the shrinkage strain. The shrinkage deformation occurs when hardened concrete is exposed to air with a relative humidity less than 100 %. A larger shrinkage strain occurs for either a higher water content or a lower environmental humidity. Moreover, a smaller volume-to-surface-ratio V/S results in greater shrinkage and a steeper evolution shrinkage curve [206]. With decreasing water/cement ratio and cement content, the shrinkage of concrete decreases [74]. Structures which are sensitive to such restrained drying shrinkage caused by a low volume to surface ratio are e.g. pavements, bridge decks, walls, and industrial floors [405, 407].

Several shrinkage models are proposed but still a huge difference is asssessed between model predictions and a large number of experiments studied in the RILEM data bank (426 shrinkage tests) [287]. Even more complex models such as those proposed by BAŽANT and BAJEWA [25], or models with a high number of required input parameters such as ACI 209 [6], show differences when compared to the experimental data. Similarly, simpler models or models with less input parameters such as Model Code 2010 [187] and Gardner and Lockman [123] show some discrepancy when compared to the experimental investigations. These models are based on exponential and power functions which are shown in in the following (t_d … age of concrete [d] at the beginning of shrinkage).

American Concrete Institute **ACI 209** [6]

$$\epsilon_{c,sh}\left(t,t_d\right)=\epsilon_{shu}\gamma_{sh}\frac{\left(t-t_d\right)}{f+\left(t-t_d\right)} \tag{3.83}$$

ϵ_{shu}	…	ultimate shrinkage
γ_{sh}	…	humidity, concrete composition, and geometry
f	…	time-ratio, 35 d/55 d

Bažant and Bajewa **B 3** [25]

$$\epsilon_{c,sh}\left(t,t_d\right)=-\epsilon_{sh\infty}k_h\tanh\left(\frac{\left(t-t_d\right)}{\tau_{sh}}\right)^{0.5} \tag{3.84}$$

$\epsilon_{sh\infty}$	…	ultimate shrinkage
k_h	…	humidity coefficient
$f\tau_{sh}$	…	shrinkage half-time

Model Code 90-99 **MC 90-99** [185], Model Code 2010 **MC 10** [187]

$$\epsilon_{c,sh}\left(t,t_d\right)=\epsilon_{ds0}\left(f_{cm}\right)\beta_{RH}\left(\frac{\left(t-t_d\right)}{0.035h^2+\left(t-t_d\right)}\right)^{0.5}+\epsilon_{as0}\left(f_{cm}\right)\left(1+\mathrm{e}^{-0.2\sqrt{t}}\right) \tag{3.85}$$

ϵ_{ds0}	…	ultimate drying shrinkage
ϵ_{as0}	…	ultimate chemical shrinkage
β_{RH}	…	humidity coefficient
h	…	cross-section geometry parameter

Gardner and Lockman **GL 2000** [123]

$$\epsilon_{c,sh}\left(t,t_d\right)=\epsilon_{shu}\left(f_{cm}\right)\beta_{RH}\left(\frac{\left(t-t_d\right)}{t-t_d+0.15\frac{V}{S}^2}\right)^{0.5} \tag{3.86}$$

ϵ_{shu}	…	ultimate shrinkage
β_{RH}	…	humidity coefficient
V/S	…	cross-section geometry parameter

3.3.2 Comparison and evaluation of shrinkage models

In the design guideline MC 10, the variation in the prediction of the shrinkage is estimated with $CV_{\mathrm{MC\,10}}=0.35$ [187]. Comparison of these shrinkage models to experimental data (RILEM data bank [287]) is investigated by Gardner [122]. If all available input information is used, GL 2000 and B 3 models are significantly more accurate predicting shrinkage based on the normalised root mean square (RMS, unbiased indicator) errors of $0.19 < CV_{\mathrm{RMS}} < 0.20$, see Tab. 3.8. In the case that only the concrete strength is used as input information, GL 2000 is better than the other methods with $CV_{\mathrm{RMS}} = 0.25$.

In the study by GOEL et al. [148], predicted values of shrinkage are compared with the experimental results of [358] and the RILEM data bank [287]. Conclusions from the comparison between the shrinkage prediction and the experimental measurements are: ACI 209 shows much scatter and illogical trends, due to the lack of size effect in the time term of the prognoses; MC 90-99 underestimates shrinkage; B 3 is in better agreement; and GL 2000 is almost as good as the B 3 model. In the statistical evaluation of shrinkage models by AL-MANASEER et al. [2], the B 3 and GL 2000 models are the best in comparison with the models presented above. In general, B 3 tends to underestimate the shrinkage strains while the GL 2000 model overestimate the experimental data from the RILEM data bank.

Table 3.8: Coefficients of variation [-] of prediction errors of various shrinkage prediction models

Prediction Model	ACI 209 [6]	B 3 [24, 25, 26]	MC 10 [185]	GL 2000 [123]
GARDNER [122]				
only f_{cm}	0.34	0.31	0.32	0.25
all data	0.41	0.20	0.25	0.19
BAŽANT et al. [32]				
shrinkage	0.444	0.374	0.481	0.433
relative shrinkage	0.518	0.418	0.479	0.483

In the unbiased statistical comparison of shrinkage prediction models by BAŽANT et al. [32], the variation of the prediction error is quantified in comparison with the experimental data which is listed in Tab. 3.8. Comments regarding the results of GARDNER are included in Sec. 3.2.2. The relative shrinkage is defined as [32]:

$$\bar{\epsilon}_c\left(t, t_0\right) = \epsilon_c\left(t, t_0\right) / \epsilon_0 \,, \tag{3.87}$$

in which ϵ_0 is the initial shrinkage strain for 28 days of drying. The uncertainties in the model predictions are assessed to be $CV_{\mathrm{ACI\,209}} = 0.444$, $CV_{\mathrm{B\,3}} = 0.374$, $CV_{\mathrm{MC\,10}} = 0.481$, and $CV_{\mathrm{GL\,2000}} = 0.433$. Relative to the lowest model uncertainty, found in the B 3 model, the partial model quality may be assessed as:

- ACI 209 $MQ_{\mathrm{PM}}^{\mathrm{ACI\,209}} = 0.374/0.444 = 0.84$
- B 3 $MQ_{\mathrm{PM}}^{\mathrm{B\,3}} = 0.374/0.374 = 1.00$
- MC 10 $MQ_{\mathrm{PM}}^{\mathrm{MC\,10}} = 0.374/0.481 = 0.78$
- GL 2000 $MQ_{\mathrm{PM}}^{\mathrm{GL\,2000}} = 0.374/0.433 = 0.86$

3.4 Thermal action on concrete structures

3.4.1 Prediction of temperature

In the design of structures, especially bridges, thermal effects are recognised as an important design factor n the case that the thermal movements are restrained [93, 120]. Bridges are generally more sensitive to thermal actions compared to buildings. The massive concrete volume and the exposed condition to solar radiation cause this higher significance of thermal actions [383]. For statically indeterminate structures, a combination of restraint forces and displacements arises due to the temperature distribution whereas in determinate structures only displacements occur.

In the past decades, many cracks in prestressed concrete bridges can be attributed to non-uniform temperature variations [93]. For example, LEONHARDT et al. [247] reported damage in a two span continuous box girder bridge within five years of completion. Large cracks were observed along one of the webs in the shorter span with crack widths greater than 5 mm (insufficient shear reinforcement enabled the cracks to extend horizontally). In general, such thermal cracks may occur in the deck slabs or in the webs of concrete box girder bridges, depending on the stiffness ratio between both components and on the solar radiation path [114]. Moreover, several cracks are found in many box-girder bridges in Sweden, with cracks being more frequent in the south side than the north. This indicates that concrete bridges may be sensitive to solar radiation which can cause large stresses [237]. Therefore, partial prestressing is recommended in the design for temperature sensitive structures in combination with sufficient reinforcing steel.

In particular, the adequate determination of the thermal response of modern long-span prestressed concrete bridges with limited numbers of expansion joints and bearings is significant for the structural design [20]. The thermal response of structures, especially bridges, is a complex transient phenomenon. Many parameters influence the temperature distribution in concrete cross-sections. A fundamental factor is the time-dependent solar radiation. In addition, the thermal response is affected by ambient temperature, wind speed, material properties, surface characteristics and section geometry [324, 385], see Fig. 3.29. Moreover, climatic influence factors such as daily and seasonal variations of the outside air temperature, rain, snow, and so on, cause changes in the temperature distribution of bridge structures [418].

A thermal interaction exists between the deck and its environment which is considered in a prediction model for the first time by EMERSON [96]. This in and out heat flow of the structure is affected by convection and radiation. The phenomenon of thermal action in concrete structures/bridges is commonly determined by the *Fourier* heat flow equation. In general, the *Fourier* conduction equation can be applied for the analysis of the thermal response of an isotropic solid with a boundary, in contact with air. Conductivity of the material is assumed to be independent of the temperature and axis orientation. Such thermal response is caused by variations in ambient temperature Θ_a and the rate of heat q transferred from the environment to the concrete surface. It is defined as [238, 324, 322, 359]:

$$\lambda\left[\frac{\partial^2\Theta}{\partial x^2}+\frac{\partial^2\Theta}{\partial y^2}+\frac{\partial^2\Theta}{\partial z^2}\right]+q_v-\rho C\frac{\partial\Theta}{\partial t}=0\,, \tag{3.88}$$

with the boundary condition (heat exchange between structural surface and surrounding environment):

$$\lambda\left(\frac{\partial\Theta}{\partial x}n_x+\frac{\partial\Theta}{\partial y}n_y+\frac{\partial\Theta}{\partial z}n_z\right)-q=0\,. \tag{3.89}$$

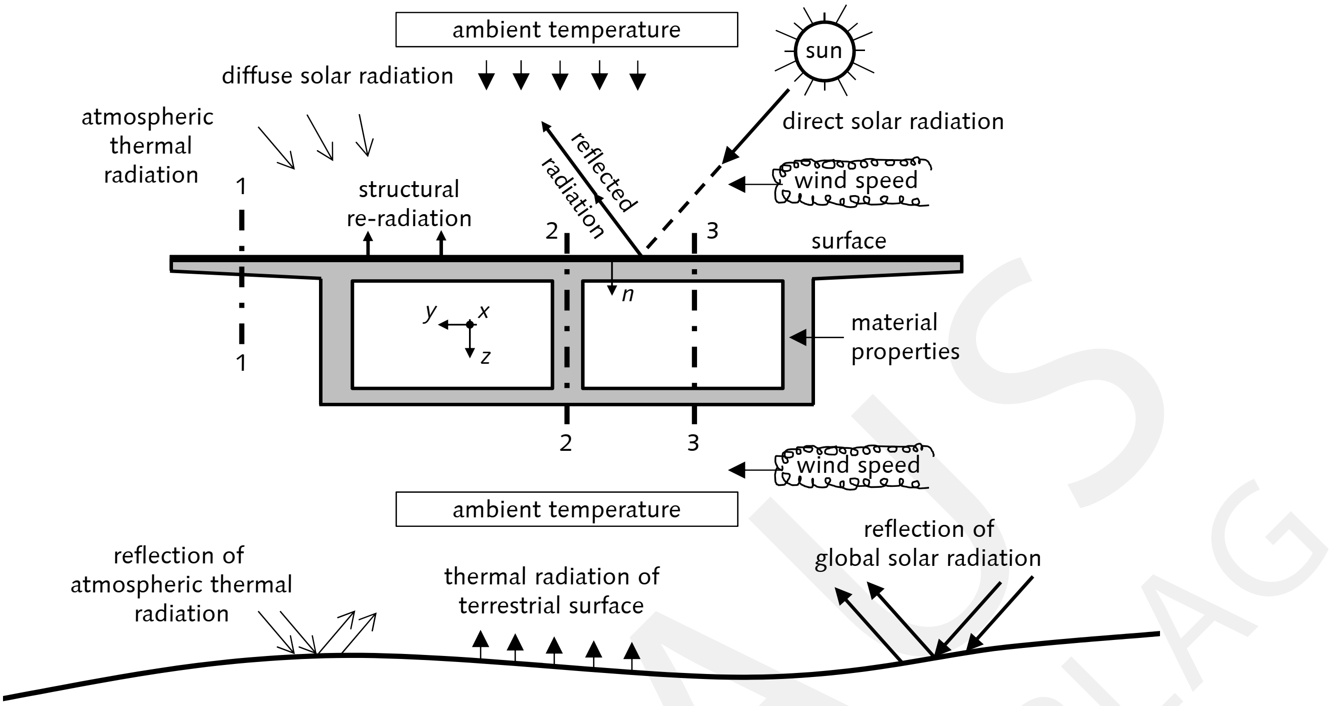
ambient temperature
sun
diffuse solar radiation
atmospheric thermal radiation
direct solar radiation
reflected radiation
wind speed
structural re-radiation
1
2
3
surface
n
y
x
z
material properties
1
2
3
wind speed
ambient temperature
reflection of global solar radiation
reflection of atmospheric thermal radiation
thermal radiation of terrestrial surface

Figure 3.29: Influence factors affecting thermal response, based on [324, 385], vertical lines 1-1, 2-2, 3-3 necessary for one-dimensional analysis

In Eq. 3.88 and Eq. 3.89, Θ is the temperature, q_v is time rate of heat generated per volume (e.g. heat of the hydration reaction of cement) caused by hydration of cement, λ is isotropic thermal conductivity, ρ is density, C is specific heat capacity of the solid, Θ_o is solid boundary temperature, h_c is boundary heat transfer coefficient (mainly dependent on the speed of air across the boundary), t is time, and n_x, n_y, n_z are the cosine directions of the outward unit vectors normal to the boundary surface.

In general, the challenging task for the prediction of temperature in a structure is the determination of the boundary conditions and the climatic exposure [236]. For simplicity, the heat exchange at the surface may be reduced to purely convective heat exchange q_c [120, 359], see Eq. 3.90b. Thermal power due to the direct and diffuse solar radiation q_s, thermal power produced by long-wave radiation q_r, and absorbed through the material surface, and emissivity of the surface can be additionally considered [359] in the boundary conditions:

$$q = q_s + q_c + q_r \tag{3.90a}$$

or simplified:

$$q = q_c = h_c\,(\Theta_o - \Theta_a) \tag{3.90b}$$

The thermal material properties are listed in Tab. 3.9, which are generally liable to many variances (parameter uncertainty). The determination of average values used in several research studies even varies significantly for the thermal properties conductivity λ and specific heat capacity C.

Sine the parameters q, Θ_a and h are general complex functions of time, direct analytical solution of the *Fourier* heat equation is a non-trivial procedure and impractical since the equation of heat conduction becomes non-linear [359]. Therefore, the application of three-dimensional FE simulations is generally more applicable and appropriate [324, 419].

Table 3.9: Thermal material properties

Material	Conductivity λ [W/(mK)]	Density ρ [kg/m^3]	Specific Heat Capacity C [J/(kgK)]	Reference
concrete	1.50	2400	1000	[50]
	1.50	2400	960	[89, 94]
	2.10	2400	1000	[115]
	1.50	2480	900	[120]
	1.40	2400	960	[159]
	2.50	2400	900	[236]
	1.50	2400	960	[248]
	1.38	2480	922	[321]
	1.81	2350	792	[359]
asphalt	0.80	2200	900	[50]
	0.93	2100	920	[89, 94]
	0.75	2240	1080	[115]
	0.70	2300	900	[120]
	1.10	2100	900	[159]
	0.70	2200	880	[239]
	1.00	2240	920	[248]
	0.74	2240	838	[321]
still air	0.0225	1.3	921	[120]
	0.0225	1.3	922	[321]

The three dimensional differential equation can be substantially simplified for ambient thermal loading of bridges. For example, the heat flow, even for sections of complex geometry (superstructure), caused by solar radiation and ambient temperature variations is mainly perpendicular to the deck surface [322]. The variation of temperature distributions in the direction of the longitudinal axis of the bridge is usually not significant. For example, the long-term monitoring program of a 220 m continuous concrete box girder bridge ("Casilina" bridge in Central Italy) by FROLI et al. [120] confirm this assumption, because two different monitored segments show nearly identical temperature distributions. For that reason, a two-dimensional finite element representation may be analysed in order to simulate the temperature distribution in the cross section and subsequently assigned for the entire structure [94]. The study by LANIGAN [235] adopted this approach with comparison of theoretical and experimental results of laboratory specimens subjected to input radiation on one surface. Moreover, it has been shown in [323] that for most bridge sections, transverse heat flow in bridge sections is insignificant. Heat flow through the depth may be considered one-dimensionally because of the large thermal inertia and relatively low diffusivity of concrete [383]. Hence, the three-dimensional case according to Eg. 3.88 can be further simplified to the one-dimensional form:

$$\lambda \frac{\partial^2 \Theta}{\partial z^2} + Q = \rho C \frac{\partial \Theta}{\partial t} \, , \tag{3.91}$$

which can be solved in conjunction with Eq. 3.89 by numerical solution techniques. For more complex cross-section such as a box-girder, it may be necessary to compute more than one vertical line and finally combine the results of various vertical lines, see vertical lines 1-1, 2-2, 3-3 in Fig. 3.29. Nevertheless, a two-dimensional simulation is more accurate for analysing more complex sections and is currently commonly applied [237, 238, 240]. In order to compute temperature distributions in box girder bridges, both two-dimensional temperature field and bi-directional heat flow should be considered in the analysis. Superstructure depth and the ratio between the deck's upper and bottom slab widths are the most influential geometric parameters for box girders [281]. Unicellular and multicellular concrete box girders have very similar thermal responses. Former observations by Capps [59] and Emerson [95] indicate that the temperature of the air trapped in the cells of cellular decks changes by only 1 or $2\,^{\circ}C$ throughout the day. Hence, it is reasonable to assume that this air temperature is constant for design purposes [159].

The response of structures subjected to external loads such as dead and live loads are comparatively insensitive to the material properties in comparison to thermally induced stresses caused from constraint deformations [322]. In contrast, the accuracy of the theory for structural and sectional analysis is more sensitive to external loads. On one side, the thermal response is mainly influenced by thermal conductivity, density, and specific heat. On the other side, modulus of elasticity and coefficient of thermal expansion α_T significantly influence the thermal response of structures.

Table 3.10: Coefficients of thermal expansion for water-cured concrete with several aggregate types [260, 322]

Aggregate Type	Coefficient of thermal expansion α_T [10^{-6}/K]	Aggregate Type	Coefficient of thermal expansion α_T [10^{-6}/K]
Limestone	6.0	Basalt	9.5
Andesite	6.5	Sandstone	10.0
Pumice	7.0	Greywacke	11.0
Foamed Slag	9.0	Quartzite	13.0
Granite	9.0		

The basis for thermal actions in structures is the thermal expansion capability of the materials which is physically determined by the coefficient of thermal expansion. For concrete, this coefficient is generally in the range of $5 \cdot 10^{-6}$/K and $15 \cdot 10^{-6}$/K and mainly depends on the aggregate type. Andesites and limestone result in lowest values and quartzites typically give highest values, see Tab. 3.10. For structures which may be sensitive to thermal actions caused by restraint effects, it is appropriate to investigate the thermal expansion for the actual concrete mixture by experimental tests [260]. The thermal expansion coefficient for structural steel is recommended in design guidelines to be $\alpha_T = 12 \cdot 10^{-6}$/K [129, 104]. In a structural analysis of composite materials like reinforced concrete, the coefficient can be assumed to be $\alpha_T = 10 \cdot 10^{-6}$/K for both materials within the temperature range of $-20\,^{\circ}$C and $+180\,^{\circ}$C [187, 104]. For prestressed steel, this material property can be taken as $10 \cdot 10^{-6}\,1$/K within the temperature range of $-40\,^{\circ}$C and $+180\,^{\circ}$C [187].

In the study by Fouad [115], a non-linear simulation of instationary temperature fields in structures subjected to thermal action are investigated and validated against monitoring data of structures. Based on Finite Element Method, the main matrix equation is determined by:

$$[\mathbf{K}]\,\{\Theta\} + [\mathbf{C}]\left\{\dot{\Theta}\right\} = \{Q\}\ , \tag{3.92}$$

in which [**K**] is the sum of thermal conductivity, convection, and radiation matrix, [**C**] is the specific heat capacity matrix, Θ is the nodal temperature vector, $\dot{\Theta}$ is the temperature flow vector, and Q is the element nodal heat flux vector considering heat flow due to internal heat generation, convection, radiation, and conduction [114]. This numerical model is validated according to a long-term monitoring program at box girder bridges in Germany ("Brohltal", "Ahrtal", measured by German "Federal Highway Research Institute" BASt). The maximum difference between predicted and measured temperature is assessed to be 2 K over the entire monitoring program, which illustrates a very good agreement, see Fig. 3.30 [385].

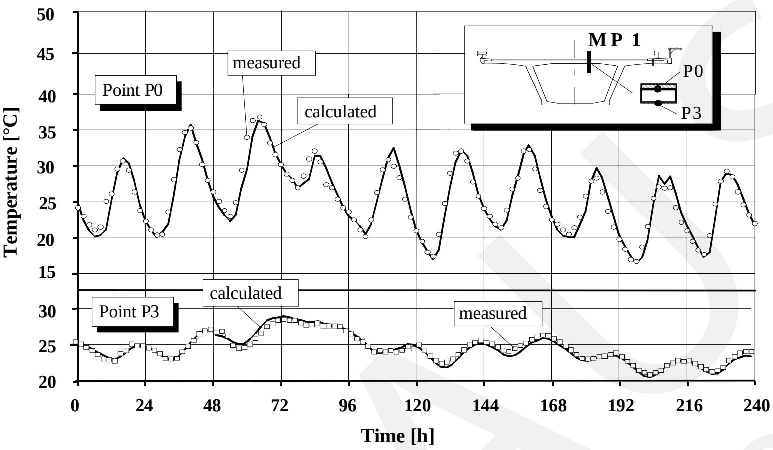

Figure 3.30: Validation of numerical model by Fouad for simulation of temperature distributions, [114]

In addition, a parametric study for box girder cross-sections of varying depth, web thickness, upper and lower deck thickness, web inclination angle, ratio between cantilever length and web depth, and surface thickness is performed in order to obtain the sensitive geometrical parameters and finally to determine critical thermal effects. The uniform temperature component is assessed to be independent of the bridge orientation. The vertical temperature gradient is similarly independent of the bridge orientation. For the transverse gradient, the bridge orientation is very sensitive with the greatest gradients for east-west orientation and lowest gradients for north-south. The simulation results and the experimental data both illustrate that temperature differences induce not only continuity but also large residual stresses in a concrete box girder. Maximum stresses are obtained mostly in summer time when solar radiation is at a maximum. Moreover, a significant geometric parameter applies to the overhanging slabs in the temperature distribution of box girders [114].

In the study by Lichte and Mangerig [248, 260], multi-year climate data set (1980-2000) with hourly measurement data of air temperature, wind speed and solar radiation are used in a numerical simulation. An improvement in the model is investigated according to the long-wave atmospheric radiation. In addition, the external thermal boundary conditions are enhanced by more adequate ansatz functions which increase the model accuracy. Separation of the temperature components into a time period and a random temperature component allows the determination of seasonal and stochastic properties of the thermal action. For double T-beams with given structural and environmental conditions, the range of these temperature parts under the given meteorological data is determined and the corresponding combination rules are analysed. One major conclusion is that the thermal actions in steel, composite and concrete decks cause different combination surfaces between the uniform and linearly varying temperature components, see Sec. 3.4.3. This is in accordance with the different thermal behaviour of these cross-section types. Moreover, the analysis evaluated that even short-term weather events, such as a thunderstorm, may adversely affect the temperature distribution in the investigated composite deck.

3.4.2 Prediction of stress levels

The temperature distribution of an arbitrary cross-section is computed relatively to some convenient datum $\Delta T\,(z)$. In the case of totally unrestrained expansion at all heights in a cross-section, the free strain profile is:

$$\epsilon_{c,t,\mathrm{free}}\,(z) = \alpha_t \cdot T\,(z) \tag{3.93}$$

where α_t is the linear coefficient of thermal expansion, see Fig. 3.31.

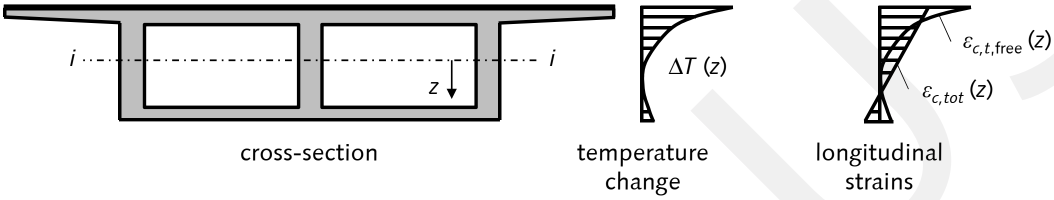

Figure 3.31: Vertical distribution of longitudinal thermal strain, based on [324]

Considering the *Bernoulli* hypothesis that cross-sections remain plane under deformation process leads to the total strain distribution $\epsilon_{c,tot}$. The difference between the free strain $\epsilon_{c,t,\mathrm{free}}$ and the resulting plane strain distribution $\epsilon_{c,tot}$ implies residual stresses $\sigma_{c,t,\mathrm{res}}$ with the magnitude:

$$\sigma_{c,t,\mathrm{res}}(z) = E_c \cdot (\epsilon_{c,tot}(z) - \epsilon_{c,t,\mathrm{free}}(z)) = E_c \cdot (\epsilon_{c,tot}(z) - \alpha_t T(z))\ . \tag{3.94}$$

In statically determinate structures, the residual stresses are self-equilibrating [93]. The maximum stresses calculated near top surfaces are primarily controlled by the high local temperatures and relatively little by the precise shape of the temperature distribution. Fairly crude approximations for the temperature distribution away from the surfaces can be made without seriously affecting accuracy [159]. In summer when the solar radiation is at a maximum and the length of shade of the overlapping part over the webs is large, a temperature distribution in the cross-section occurs with largest residual stresses [94]. Moreover, design for critical conditions may appear in the case of a large daily range of ambient temperature and a minimum wind speed. An asphalt deck accentuates the stresses caused by temperature. With a larger cross-section depth, the residual stresses increase and are not much different between a solid slab, cellular slab, and box girder. Integration of Eq. 3.94 over the section depth h results in the axial force:

$$F_{c,t,\mathrm{res}}(z) = E_c \cdot \left(\epsilon_{c,tot(z)} - \alpha_t T(z)\right) \cdot b(z)\,\mathrm{d}z\,, \tag{3.95}$$

where $b(z)$ is the net section width at height z. The internal moment about the neutral axis due to the temperature distribution $T(z)$ can be computed by:

$$M_{c,t,\mathrm{res}}(z) = E_c \cdot \left(\epsilon_{c,tot(z)} - \alpha_t T(z)\right) \cdot b(z) \cdot z\,\mathrm{d}z\,. \tag{3.96}$$

As a consequence of cracking, section properties, moments and forces vary along the span. The neutral axis changes as thermal expansion (or contraction) near the neutral axis closes (or extends) the cracks [159]. In comparison to uncracked sections, the thermal behaviour is more complicated for cracked cross-sections and structural members. The simulation method considered in this thesis are appropriate to consider the interaction between concrete cracking and thermal response. For a combination of external loading and temperature loading, the structural response based on non-linear simulations is analysed in Sec. 3.5.

3.4.3 Design recommendations

The temperature field simulations as studied by Fouad [115] and Lichte [248] may be characterised by a very highly complex time-dependent analysis of structures such as bridges. For engineering applications, it may not be of interest to establish a temperature field simulation and subsequently analyse the time-dependent temperature distribution. Hence, the application of such simulations in the design is impractical, inefficient, and may only be applied in exceptional cases. The design of bridges is more focused on the control of the representative temperature loads. On the basis of these transient heat flow analyses discussed in Sec. 3.4.1, it is possible to establish representative design temperature components, which generally represent maximum temperature states with a certain probability of occurrence.

For beams considering the *Bernoulli* hypothesis, the non-uniform temperature distributions can be described with idealised temperature components [260]. The method to access design values (representative temperature loads) can be separated into four major phases:

① measuring temperature in long-term monitoring program,
② establishing numerical model and validation according to measurements,
③ parametric study and determination of representative values, and
④ assessment of significance of representative values for serviceability and ultimate limit state.

Local ambient characteristics like variation of solar radiation, ambient temperature and wind speed are used for the prediction of the representative design gradients. These design gradients are subsequently used in the computation of stress levels. The critical design gradient, according to Priestly, shows that thermal gradient, likely to occur within the expected life of the bridge, which induces maximum soffit tension stresses [324]. The overall distribution can be represented in a temperature profile which subdivides the non-uniform temperature distribution into different components, see Fig. 3.32. These components are determined in such a way that they correspond to mechanical quantities (displacement, curvature) and internal forces (normal force, moment). The temperature profiles are commonly recommended in design codes such as EC 1-1-5 [104], which defines certain values for thermal actions and temperature profiles. These are the characteristic value (with return period of 50 years), infrequent value (with return period of 1 year), frequent value (with return period of 2 weeks), and the quasi-permanent value (with return period of 6 days) [383].

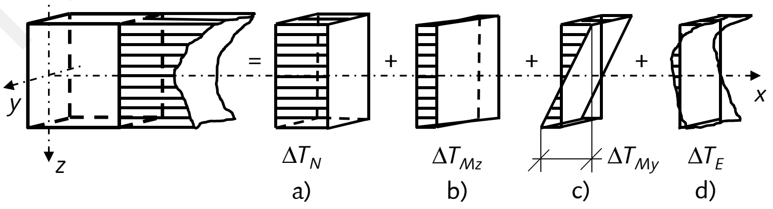

Figure 3.32: Temperature profile according to EC 1-1-5 [104]

In order to design structures using a practical and efficient approach, the temperature distribution in a cross-section according to Fig. 3.32 can be represented by the following temperature components:

- a) T_N uniform temperature component may cause normal force N,
- b) T_{Mz} linearly varying temperature difference component may cause bending moment M_z,
- c) T_{My} linearly varying temperature difference component may cause bending moment M_y, and
- d) T_E non-linear temperature difference component.

In the EC 1-1-5, these temperature components are separately assessed for different bridge types containing the following categories [104]:

Type 1	Steel deck:	steel box girder, steel truss or plate girder
Type 2	Composite deck	
Type 3	Concrete deck	concrete slab, concrete beam, concrete box girder

The characteristic values of minimum and maximum shade air temperatures for the construction site location may be obtained, e.g. from national maps of isotherms. These values represent shade air temperatures for mean sea level in open country with an annual probability of being exceeded by 0.02 [104]. The German National Annex for thermal action [139] defines the minimum $T_{\text{min}} = -24\,^{\circ}\text{C}$ and maximum characteristic shade air temperature $T_{\text{max}} = +37\,^{\circ}\text{C}$. Moreover, an additive term considering the characteristic of the different cross-section types $T_{\text{min/max,cs}}$ is recommended, see Tab. 3.11. For structural design, the characteristic value of the maximum negative change (contraction) of the uniform temperature component $\Delta T_{N,\text{con}}$ is recommended to be:

$$\Delta T_{N,\text{con}} = T_0 - T_{\text{e,min}}\,, \tag{3.97}$$

and the maximum positive change (expansion) of the uniform temperature component $\Delta T_{N,\text{exp}}$ is defined as:

$$\Delta T_{N,\text{exp}} = T_{\text{e,max}} - T_0\,, \tag{3.98}$$

where T_0 is the datum temperature in the design of the structure. The temperature at that time when the bride is restrained should be used for this temperature reference value [383]. In the case T_0 is unknown, EC 1-1-5 [104] recommends to use $T_0 = 10\,^{\circ}\text{C}$.

One one side (**approach 1**), the effect of vertical temperature differences can be considered by applying an equivalent linear temperature component $\Delta T_{M,\text{heat}}$ and/or $\Delta T_{M,\text{cool}}$. For the "heat" state, the upper cross-section surface is subjected to a higher temperature than the lower surface, and for "cool" it is the opposite. These temperature components should be applied between the top and the bottom of the bridge deck and are listed in Tab. 3.11 for an asphalt surface thickness of 5 cm. For other surface thicknesses, these values should be multiplied by the factor k_{sur}, which are also listed in Tab. 3.11.

On the other side (**approach 2**), the effect of the vertical temperature differences can be considered by the analysis of non-linear temperature components ΔT. In Fig. 3.33. The term 'heating" refers to a state in which solar radiation, among other factors, causes a gain in heat through the top surface of the bridge deck. In contrast, "cooling" indicates conditions such that heat is lost from the top surface of the bridge deck as a result of re-radiation, among other factors. This temperature difference ΔT incorporates ΔT_M and ΔT_E together with a small part of the component ΔT_N. This latter part is already included in the uniform bridge temperature component ΔT_N [104]. Hence, the integration of ΔT along the cross-section

Table 3.11: Characteristic values of temperature components according to DIN EN 1991-1-5/NA:2010-12 [139], linear gradients for asphalt surface thickness of 5 cm

Temperature Component	Unit/ Surface Thickness	Type 1 Steel Deck	Type 2 Composite Deck	Type 3 Concrete Deck Box Girder	Type 3 Concrete Deck Beam	Type 3 Concrete Deck Slab
$T_{\mathrm{min,cs}}$	°C	-3	$+4$	$+8$		
$T_{\mathrm{max,cs}}$	°C	$+16$	$+4$	$+2$		
$T_{\mathrm{e,min}}$	°C	-27	-20	-16		
$T_{\mathrm{e,max}}$	°C	$+53$	$+41$	$+39$		
$\Delta T_{M,\mathrm{heat}}$	[K]	18	15	10	15	15
$\Delta T_{M,\mathrm{cool}}$	[K]	13	18	5	8	8
$k_{\mathrm{sur,heat}}$	0 cm	0.7	0.9	0.8		
	10 cm	0.7	1.0	0.7		
	15 cm	0.7	1.0	0.5		
$k_{\mathrm{sur,cool}}$	0 cm	0.9	1.0	1.1		
	10 cm	1.2	1.0	1.0		
	15 cm	1.2	1.0	1.0		

depth leads to a certain uniform component, which should be considered by a reduction of the uniform bridge temperature components ΔT_N.

The non-linear temperature difference causes residual stresses in the cross-section due to the principle of plain strain distribution over the cross-section depth [269]. In common design practice, the uniform temperature component and the linearly varying temperature difference are the most important components [383]. For example, the German National Annex [139] recommends first approach considering the uniform temperature and the linearly varying temperature component ΔT_M. Nevertheless, the non-linear temperature component ΔT can generally be applied for design purposes as recommended by EC 1-1-5 [104] and EMERSON [95, 97, 98].

Based on EC 1-1-5 [104], a simultaneous consideration between uniform $\Delta T_{N\mathrm{exp}}$ (or $\Delta T_{N\mathrm{con}}$) and temperature component $\Delta T_{M,\mathrm{heat}}$ (or $\Delta T_{M,\mathrm{cool}}$). This combination of both components may be necessary for e.g. frame structures. The combination of both components can be determined by the following expressions which should be interpreted as load combinations:

$$\Delta T_{M,\mathrm{heat}}\ (\mathrm{or}\ \Delta T_{M,\mathrm{cool}}) \oplus \omega_N \Delta T_{N,\mathrm{exp}}\ (\mathrm{or}\ \Delta T_{N,\mathrm{con}})\ , \tag{3.99}$$

or

$$\omega_M \Delta T_{M,\mathrm{heat}}\ (\mathrm{or}\ \Delta T_{M,\mathrm{cool}}) \oplus \Delta T_{N,\mathrm{exp}}\ (\mathrm{or}\ \Delta T_{N,\mathrm{con}})\ , \tag{3.100}$$

where the most adverse effect should be chosen. Combination factors for the concurrent occurrence of both temperature parts ($\omega_N = 0.35$, $\omega_M = 0.75$) are included to account for their coincident probability [104, 139]. For the second approach with consideration of the non-linear temperature component ΔT, the term ΔT_M should be replaced in Eq. 3.99 and Eq. 3.100 by ΔT, because the non-linear component includes ΔT_M and ΔT_E. For hollow or solid concrete piers, a linear temperature difference between the opposite outer faces should be taken into account. The recommended value for the linear temperature difference is $\Delta T_{M,\mathrm{pier}} = \pm 5\,\mathrm{K}$ [104, 139].

As an example for the design load conditions in a frame bridge, Fig. 3.34 shows the load cases for a com-

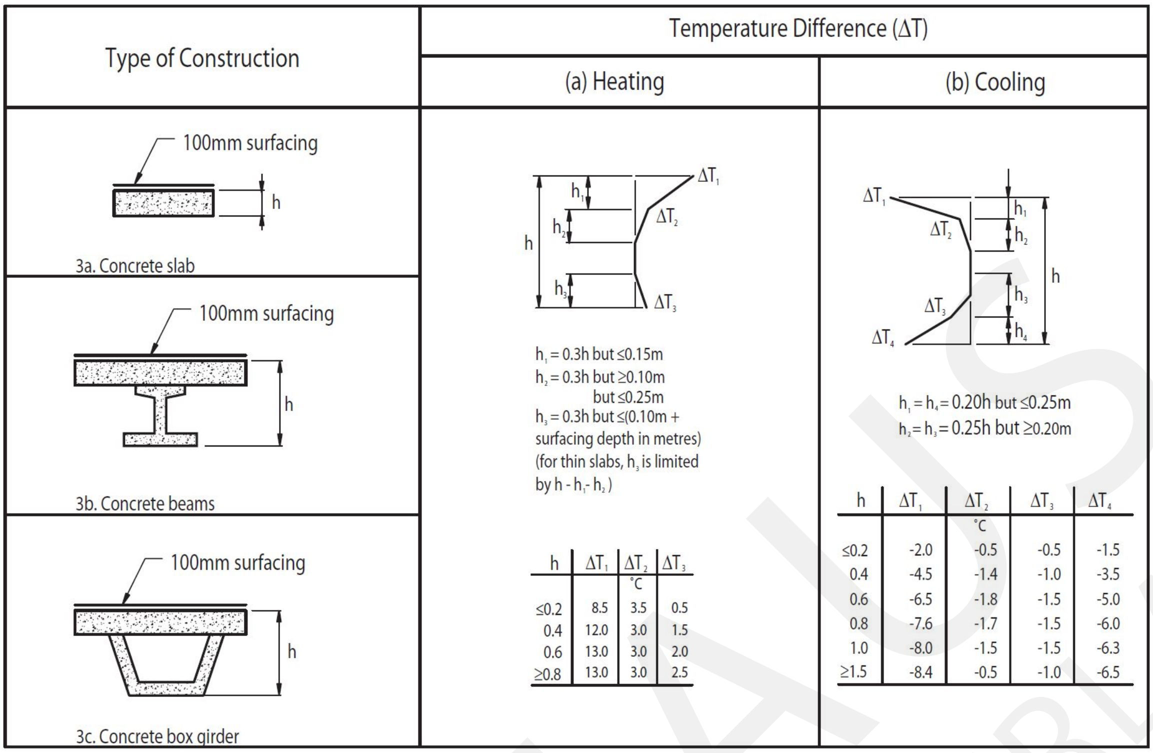

$h_1 = 0.3h$ but ≤ 0.15m
$h_2 = 0.3h$ but ≥ 0.10m
but ≤ 0.25m
$h_3 = 0.3h$ but $\leq (0.10$m + surfacing depth in metres)
(for thin slabs, h_3 is limited by $h - h_1 - h_2$)

h	ΔT_1	ΔT_2	ΔT_3
		°C	
≤0.2	8.5	3.5	0.5
0.4	12.0	3.0	1.5
0.6	13.0	3.0	2.0
≥0.8	13.0	3.0	2.5

$h_1 = h_4 = 0.20h$ but ≤ 0.25m
$h_2 = h_3 = 0.25h$ but ≥ 0.20m

h	ΔT_1	ΔT_2	ΔT_3	ΔT_4
		°C		
≤0.2	-2.0	-0.5	-0.5	-1.5
0.4	-4.5	-1.4	-1.0	-3.5
0.6	-6.5	-1.8	-1.5	-5.0
0.8	-7.6	-1.7	-1.5	-6.0
1.0	-8.0	-1.5	-1.5	-6.3
≥1.5	-8.4	-0.5	-1.0	-6.5

Figure 3.33: Temperature differences for concrete bridge decks according to EC 1-1-5 [104]

bined loading of external loads and temperature components. In this study [11], the section forces N_{Ed} and M_{Ed} are investigated in the ultimate limit state based on the linear-elastic stiffness of the frame bridge with the dimensions $L = 14.0$ m and $H = 5.5$ m. At the frame corner, the amount of necessary reinforcement increases by 17 % and by 25 % in the frame span when considering the thermal action. Therefore, in structures which are sensitive against thermal actions, the design might be crucially dependent on the temperature loading condition in addition to the external loads. Nevertheless, the analysis with the uncracked elastic stiffness is generally not appropriate for the computation of restraint effects, which is discussed in Sec. 3.5. Non-linear simulation determines the structural behaviour much more adequately by considering the material non-linearities and resulting in stiffness degradation. This allows for the consideration of restraint force degradation and finally leads to a much more reliable, safe, and improved economical design of the structure.

In the study by Lichte [248], the consideration of wind speed course in the temperature field simulation, instead of a seasonal wind speed average value, leads to higher variation in the daily extreme values of the temperature components. In addition, singular events such as thunderstorms or slow wind speeds on very warm days are considered in this study. Therefore, the extreme value's distribution and the corresponding extrapolation of the rare extreme events are influenced by these additionally considered meteorological information. A great difference is observed in the comparison between the results of this study and the design recommendations (characteristic values), see Tab. 3.12. Nevertheless, the design recommendations of EC 1 are evaluated for various cross-section types and geometrical parameter combinations, varying system parameters, environmental conditions and a subsequent statistical evaluation. Therefore, the direct comparison between both results should be carefully checked. The difference should only illustrate the high sensitivity of the temperature field conditions in the estimation of characteristic temperature values.

The combining factors between uniform components and linearly varying temperature components are

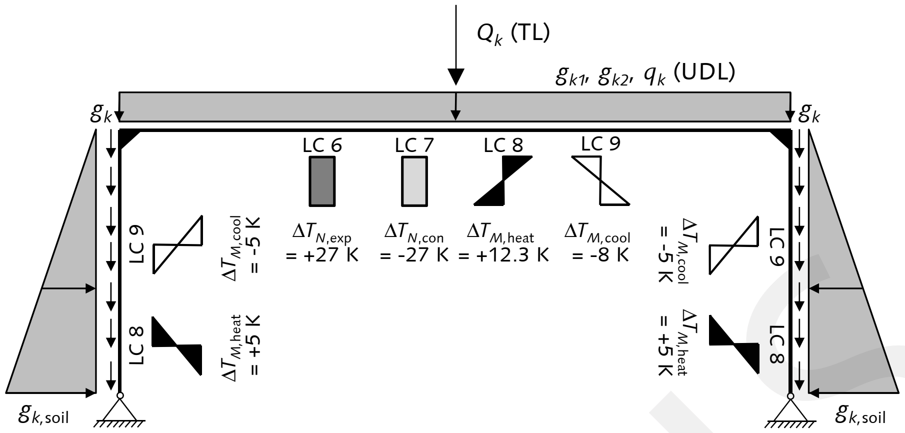
Q_k (TL)
g_{k1}, g_{k2}, q_k (UDL)
g_k
g_k
LC 6
LC 7
LC 8
LC 9
$\Delta T_{N,\text{exp}}$ = +27 K
$\Delta T_{N,\text{con}}$ = -27 K
$\Delta T_{M,\text{heat}}$ = +12.3 K
$\Delta T_{M,\text{cool}}$ = -8 K
LC 9
$\Delta T_{M,\text{cool}}$ = -5 K
LC 8
$\Delta T_{M,\text{heat}}$ = +5 K
LC 9
$\Delta T_{M,\text{cool}}$ = -5 K
LC 8
$\Delta T_{M,\text{heat}}$ = +5 K
$g_{k,\text{soil}}$
$g_{k,\text{soil}}$

Figure 3.34: Load cases for combined loading of external load and temperature in a frame bridge, based on [11]

assessed for the different types of cross sections, see Tab. 3.12. These results are only valid for the characteristic values assessed in this study [248]. The critical condition for the combination is found in midsummer with high levels of solar radiation which causes high $\Delta T_{N,\text{exp}}$ and $\Delta T_{M,\text{heat}}$. The bridge orientation is not sensitive to the combination between both temperature components. For the steel and concrete decks, the occurrence of a uniform temperature component lower than 0 °C with a simultaneous, linearly varying "heating" component is not analysed for the entire temperature field analysis. For concrete box girders, Lichte [248] expects combination factors much smaller than 0.9. Finally, the percentage of the combination between both components by applying combination factors is generally applicable. The general design recommendation mentioned above is independent of the type of structures and may therefore be extended to consider different cross sections and material characteristics.

Table 3.12: Characteristic values of temperature components and combination factors according to Lichte [248] (reference temperature $T_0 = 10\,°\text{C}$) in comparison to DIN EN 1991-1-5/NA:2010-12 [139], 100 % equal to DIN EN 1991-1-5, linear gradients for asphalt surface thickness of 5 cm

Temperature Component	Unit/ Surface Thickness	Type 1 Steel Deck		Type 2 Composite Deck Beam		Type 3 Concrete Deck	
$\Delta T_{N,\text{neg}}$	°C	−16	40 %	−10	38 %	−7	39 %
$\Delta T_{N,\text{pos}}$	°C	+51	86 %	+42	120 %	+35	113 %
$\Delta T_{M,\text{heat}}$	[K]	22	122 %	23	153 %	18	120 %
$\Delta T_{M,\text{cool}}$	[K]	9	69 %	24	133 %	6	75 %
ω_N	[-]	0.84	240 %	0.67	191 %	0.92	263 %
ω_M	[-]	0.69	92 %	0.54	72 %	0.89	119 %

Until the release of the design recommendation DIN FB 101 in 2009 [129], the partial safety factor for the thermal action was defined as $\gamma_{Q,T} = 1.5$, similar to a variable load. This factor considers uncertainties due to variation in the thermal expansion coefficient, approximation errors caused by the uniform temperature components, structural model, and high uncertainty in the actual temperature at that time when the structure is restrained. Based on the research studies [118, 248], Mangerig et al. [260] assessed the existing design recommendations for thermal actions in order to check the general validity for future design projects. The common approach of linear temperature components is still used in order to allow a practical design procedure. The design temperature value is defined as:

$$E_T = \gamma_{Q,T} \left[\alpha_T C_{\mathrm{sys}} \left(T_{t,k} - T_{0,k}\right)\right] , \tag{3.101}$$

and considering the separate uncertainty sources leads to:

$$E_T = \left(\gamma_{\alpha_T} \gamma_{C_{\mathrm{sys}}} \gamma_{T_{N,M}}\right) \left[\alpha_T C_{\mathrm{sys}} \left(T_k - \frac{T_0 \pm T_0^*}{\gamma_{T_{N,M}}}\right)\right] , \tag{3.102}$$

in which γ_{α_T} considers the variance in the thermal expansion coefficient, $\gamma_{C_{\mathrm{sys}}}$ considers modelling uncertainties, $\gamma_{T_{N,M}}$ takes into account the variance in the characteristic values, and T_0^* represents the uncertainty related to the temperature at the time when the structure is restrained. Due to the unavoidable variance in determination of α_T, it is common in bridge engineering to use a partial safety factor of $\gamma_{\alpha_T} = 1.05$ [260].
In the last decades, some extreme air temperature events have occurred, such as 40.3 °C in Perl-Nennig (2003-08-08), 40.2 °C in Karlsruhe (2003-08-09, 2003-08-13), and −42.0 °C in Albstadt (2001-12-24). These events initiated a discussion about the safety requirements for thermal action on bridges. Moreover, the daily extreme values reported over more than 100 years in Hamburg, Berlin, and Munich show a shade air temperature range between −31.7 °C and 37.7 °C. Nevertheless, MANGERIG et al. [260] concludes that the characteristic positive shade air temperature of 37 °C is reasonable, because the upper limit value for the determination of the safety factor for Germany is defined as 40.5 °C. In contrast, the obviously lower deviation of the negative shade air temperature might not be appropriate. Hence, the temperature range between −30 °C and 40 °C is used in this study [260] in order to analyse the required safety factor. In the assessment of the linearly varying temperature component, a small difference between the design guidelines and the determined results is obtained. Finally, the safety assessment of the temperature components defined in the design guideline EC 1-1-5 [139] leads to a proposed safety factor of $\gamma_{Q,T} = 1.35$ [260].
In conclusion, in this thesis the thermal action is represented as partial models in the model class temperature recommend by the temperature profiles defined in the design guideline Eurocode 1 [139]:

- vertical temperature gradient with uniform temperature component,
  $\omega_N \cdot \Delta T_N \oplus \Delta T_M \oplus \Delta T_{M,\mathrm{pier}}$
- uniform temperature component with vertical temperature gradient,
  $\Delta T_N \oplus \omega_M \cdot \Delta T_M \oplus \Delta T_{M,\mathrm{pier}}$,
- non-linear component with uniform temperature
  $\omega_N \cdot \Delta T_N \oplus \Delta T \oplus \Delta T_{M,\mathrm{pier}}$, and
- uniform temperature with non-linear component
  $\Delta T_N \oplus \omega_M \cdot \Delta T \oplus \Delta T_{M,\mathrm{pier}}$.

3.4.4 Monitoring temperature in concrete structures

In some applications, particularly for monitoring existing structures, it may be impractical to set up temperature sensors especially at depths inside the structural members. Measuring surface temperatures and applying the heat flow analysis may be adequate for predicting the internal temperatures in the cross sections [322].
Direct measurements of surface temperatures lead to typical relationships between temperature and time,

see Fig. 3.35. These temperature data indicate the daily distribution throughout a hot day for top and bottom surfaces of a bridge deck. The periodic nature of temperature distribution on a cool day is similar, but the temperature changes induce a smaller amplitude of variation and a cooler top than bottom.

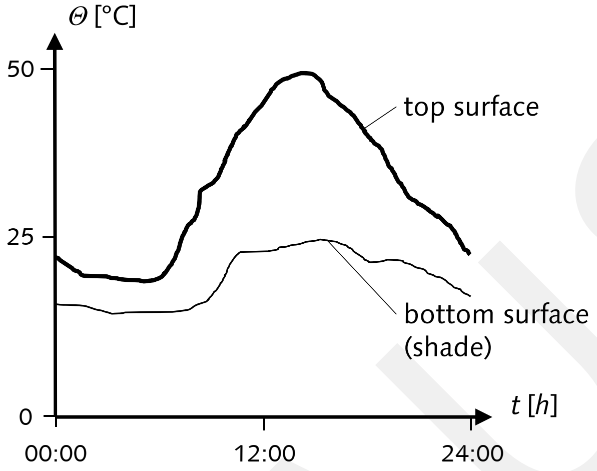

Figure 3.35: Temperature distribution of bridge deck during a hot summer day [159]

Based on measurement data ΔT_{meas}, the constant temperature component can be determined by [120, 238, 269, 385]:

$$\Delta T_N = \frac{1}{A} \int_A \Delta T_{\text{meas}}(y, z)\, \mathrm{d}A\,, \tag{3.103}$$

the temperature gradient may causing bending moment M_y to be:

$$\Delta T_{My} = \frac{h}{I_y} \int_A \Delta T_{\text{meas}}(y, z) \cdot z\, \mathrm{d}A\,, \text{and} \tag{3.104}$$

and the non-linear temperature component to be:

$$\Delta T_E(z) = \Delta T_{\text{meas}}(z) - [\Delta T_N + \Delta T_{My}(z)]\ . \tag{3.105}$$

For the development of the Eurocode recommendations, SOUKHOV [383] analysed both statistical data of temperature distributions and meteorological data, and performed numerical simulations for a parametric study, which is initially validated with the measurement data. These data are recorded between 1984-1985 at the "Lucka" bridge in Thuringia (Germany) and analysed in [117]. Moreover, climatic data for a time period of 10 years between 1981-1990 are used for the parametric study computed by numerical simulation with the meteorological data of Giessen in Hessen (Germany, representative for Central Europe). For the box girder, T-girder, and slab cross sections, the representative values are assessed and the characteristic values are listed in Tab. 3.13. The temperature distribution is a stochastic process and the representative values are computed based on an extreme value distribution type III (for maximum). Moreover, the combination factors ψ for the representative infrequent value 0.8, frequent 0.6, and quasi-permanent value 0.5 are proposed.

All these results are analysed for a surface with thickness of 5 cm. Differences in the surface thickness will only affect the linear temperature gradient [383]. Multiplying the characteristic values listed in Tab. 3.13 with the correction factor k_{sur} can account for this effect. It is proposed that for the surface thickness of 15 cm, $k_{\text{sur}} = 0.5$, for 10 cm, $k_{\text{sur}} = 0.7$, and without any surface, $k_{\text{sur}} = 1.5$.

Statistical analysis of the temperature distribution for the "Casilina" bridge in Central Italy (prestressed continuous concrete box girder bridge, mentioned in Sec. 3.4.1) is performed for a three-year monitoring

Table 3.13: Characteristic values of thermal action assessed by Soukhov [383] using measurement and meteorological data, $T_0 = 10\,°\mathrm{C}$

Cross-Section Type	Depth [m]	ΔT_N [K]	ΔT_{My} [K]
box girder	1.95	26.6	11.4
	2.00	27.9	11.5
	3.30	27.4	10.3
	4.70	26.9	9.6
T-girder	1.20	28.5	19.0
	1.80	27.8	16.0
	2.40	27.3	14.1
slab	0.60	27.6	18.0
	0.90	26.5	13.8
	1.20	25.9	10.8

program [20]. Based on the measurement data and the statistical assessment, the correlation between the uniform temperature component $T_{e,\max}$, $T_{e,\min}$ and the ambient air temperature $T_{\max}$, $T_{\min}$ are determined by the long-term monitoring program and subsequently compared to the empirical formulation of EC 1, which is originally studied from bridges in the United Kingdom reported in [98]. The linear relationship recommended in the EC 1 is contained within the dispersion band of the monitoring data. A good agreement is observed despite the latitude difference between the UK and Central Italy. Therefore, an acceptable degree of reliability for the recommendations of EC 1 is assessed for the correlation between ambient shade air temperature and the structural uniform temperature [20].

In a long-term monitoring progam by Maurer et al. [269], a concrete prestressed girder bridge (5 spans, $L_{\mathrm{tot}} = 171.0\,\mathrm{m}$, maximum slenderness ratio $\lambda_{\max} = 39/1.05 = 37$) designed with high performance concrete (HPC, C 70/85) was monitored with 28 measurement points over the time period between 05/2001 and 05/2004. The extreme values measured in this monitoring program are shown in Tab. 3.14, in which the measurements for the bridge without surface are measured during 2001/07/01 - 2002/06/30 and with surface during 2002/07/01 - 2004/05/21. In Fig. 3.36(a), a representative time interval is shown for the summer time. The daily variations are apparent and the maximum temperature gradient reaches the minimum value at 8 a.m. and the maximum value $T_{M,\mathrm{heat}} = 12.4\,\mathrm{K}$ at 6 p.m.. Moreover, Fig. 3.36(b) shows the computed temperature components which are based on the previously mentioned equations.

Therefore, the maximum uniform bridge temperature component is analysed to be $T_{e,\max} = +37°\mathrm{C}$ and the minimum component to be $T_{e,\min} = -17°\mathrm{C}$. The temperature gradient is determined without surface to $T_{M,\mathrm{heat}} = 1.5 \cdot 15 = 22.5\,\mathrm{K}$, $T_{M,\mathrm{cool}} = -8.0\,\mathrm{K}$, and with surface to be $T_{M,\mathrm{heat}} = 0.82 \cdot 15 = 12.3\,\mathrm{K}$, $T_{M,\mathrm{cool}} = -8.0\,\mathrm{K}$. Comparison with the temperature values defined in DIN FB 101 [129] shows that the $T_{M,\mathrm{heat}}$ value agrees very well, because the design recommendation is $T_{M,\mathrm{heat}} = 12.4\,\mathrm{K}$ instead of the computed $T_{M,\mathrm{heat}} = 12.3\,\mathrm{K}$. In contrast, the analysed value for the construction state (without surface) of $T_{M,\mathrm{heat}} = 22.5\,\mathrm{K}$ is very conservative in comparison to the design recommendation of $T_{M,\mathrm{heat}} = 12.8\,\mathrm{K}$. Nevertheless, Maurer et al. [269] and Arnold [11] conclude that the long-term measurements confirm the design recommendations.

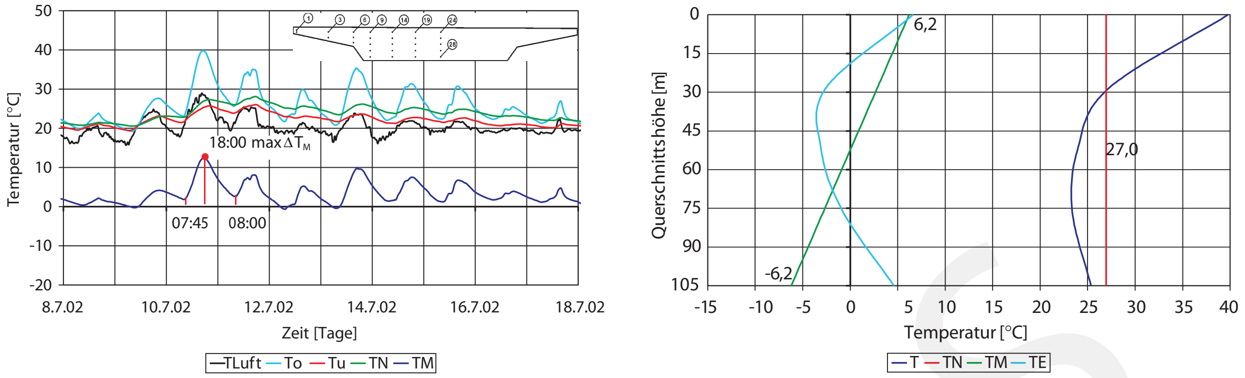

(a) 10 days in summer 2002 with $T_{M,\mathrm{heat}} = 12.4\,\mathrm{K}$, hor. axis: time, ver. axis: temperature

(b) temperature components due to time at $T_{M,\mathrm{heat}} = 12.4\,\mathrm{K}$, hor. axis: temperature, ver. axis: cross-section depth

Figure 3.36: Temperature measurements and computed gradients of long-term monitoring of prestressed concrete girder bridge assessed by MAURER et al. [269]

Table 3.14: Extreme temperature values of monitoring of HPC prestressed girder bridge in Germany between 05/2001-05/2004 [269]

Temperature Component	Symbol	Unit	without surface max	without surface min	with surface max	with surface min
air temperature	T_{air}	[°C]	33.5	-16.7	32.9	-11.8
average temp. in structure	T_N	[°C]	30.0	-6.4	31.1	-9.3
temperature gradient	ΔT_M	[K]	12.8	-3.2	12.4	-4.1
temperature at upper surface	T_{up}	[°C]	40.9	-7.6	39.8	-10.9
temperature at lower surface	T_{lo}	[°C]	27.5	-7.1	30.6	-9.3

3.5 Restraint effects

3.5.1 Theory and experimental studies

Loading conditions in structures can be generally distinguished between direct actions (such as dead, live, traffic, snow, wind load) and indirect actions which are caused by imposed deformations and their restraint/constraint in structures (such as temperature changes, creep, shrinkage, settlements), see Fig. 3.37. Different phenomena cause restraint effects in concrete structures, which can be subdivided into internal (e.g. changes in temperature, creep, shrinkage) and external (e.g. support settlements, imperfections) indirect loading conditions. In general, the magnitude of restraint effects is mainly influenced by the constraint conditions and absolute and relative stiffness distribution in the structure. Therefore, the adequate and reliable prognosis of restraint effects is only feasible for prediction models which are able to consider the stiffness degradation due to concrete cracking [92].

In design guidelines, either linear-elastic computation of the section forces with subsequent non-linear dimensioning of critical cross sections, or global non-linear structural simulations with the check of material limit stresses/strains can be generally used in the design of engineering structures. These design procedures strongly interact with the resulting magnitude of restraint effects which should be considered in the design. The linear-elastic analysis is adequate for the computation of section forces and moments as the basis for the design of structural components, such as statically determined flexural members. Internal forces due to

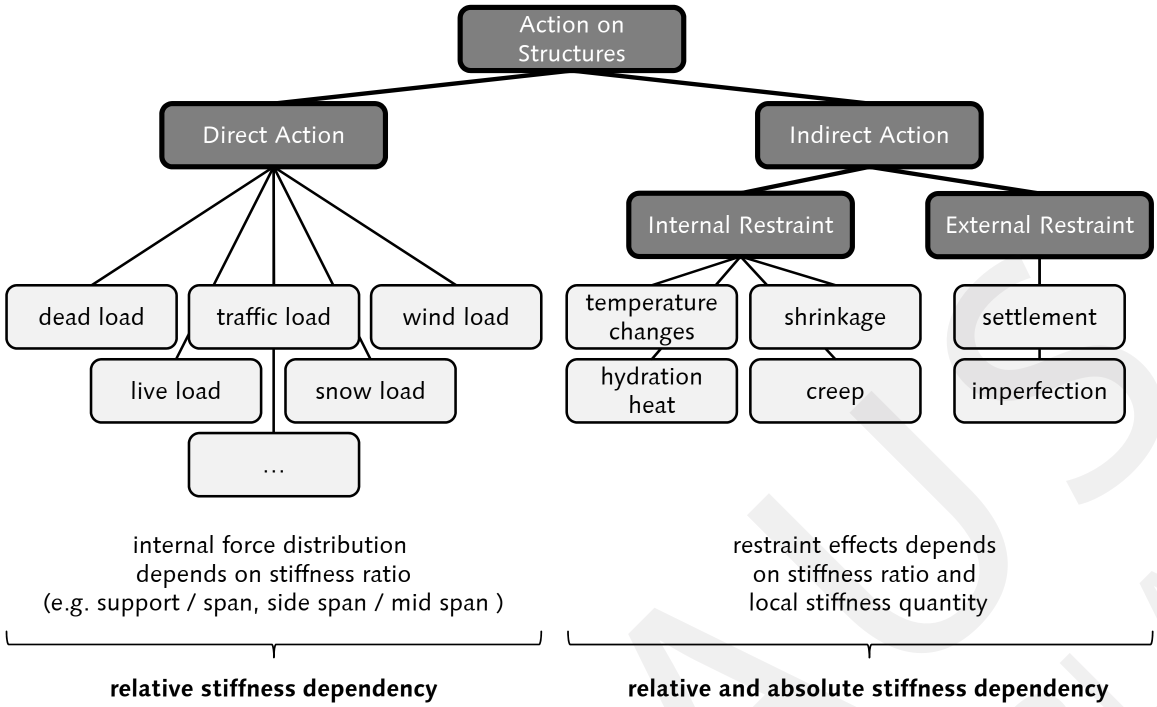
Action on Structures
Direct Action
Indirect Action
Internal Restraint
External Restraint
dead load
traffic load
wind load
live load
snow load
...
temperature changes
shrinkage
hydration heat
creep
settlement
imperfection
internal force distribution depends on stiffness ratio (e.g. support / span, side span / mid span)
restraint effects depends on stiffness ratio and local stiffness quantity
relative stiffness dependency
relative and absolute stiffness dependency

Figure 3.37: Distinction of action on structures into direct and indirect action

restraint require a more complex non-liner simulation [85]. Therefore, cracking and stiffness degradation for short-term, and additionally creep, and shrinkage in long-term analysis should be considered in the analysis of restraint effects. This ensures an economical and reliable design of the structure. In structures with confined boundary conditions, the influence of the restraint loading cannot be neglected in the serviceability assessment. In the ultimate limit state, the restraint effects may be significantly reduced and no longer affect certain structural response values, such as internal forces and stresses. Nevertheless, this should be assessed based on a non-linear simulation of the structure in order to determine an accurate estimation of the restraint effects in the serviceability as well as ultimate limit states.

Thermal action

Reinforced concrete bars are tested by Falkner [107] with a length of $l = 6\,\mathrm{m}$ and several reinforcement ratios. These elements (7 specimens) are loaded with constant temperature distribution over the cross section depth $\Delta T_N = -60\,\mathrm{K}$ and, thus, a centric restraint condition is investigated. The single crack formation stage is reached due to the contraction temperature condition, but the completed crack formation is not found in these experiments. The resulting restraint normal force measured in the experiment is about $\approx 12\,\%$ of the analytical computed value using the uncracked in-plane stiffness EA_i^I [85]. But, the measured restraint force is still much higher than the forces computed by the pure cracked stiffness EA_i^{II}.

In order to develop and validate an engineering model for predicting the influence of cracking on the thermal response of reinforced concrete bridges, Thurston et al. [392] performed experimental tests for simply supported and continuous T-beams (bridges in 1/5 scale models) subjected to thermal and gravity loads. The top surface of the cross sections are heated by infrared lamps up to a test temperature of $40\,^{\circ}\mathrm{C}$ to $60\,^{\circ}\mathrm{C}$. The primary thermal stresses induced in simply supported bridges are small and may be ignored. A discrepancy of $45\,\%$ between the measured temperature restraint moment and the computed moment based on linear-elastic stiffness is analysed for the continuous beams. The authors suggest the significance of concrete cracking, which causes stiffness degradation and, therefore, a reduced significance of thermal action, even for concrete bridges where cracking may occur.

Symmetrical reinforced concrete beams (15) under combined loading of external load and temperature gradient ΔT_M are studied by ALAVIZADEH-FARHANG [3, 4]. Two test series are performed based on simply supported beams and beams with partial fixity using prestressed steel tie rods. The prestressing force acts in such a way, that the support moment is smaller than in the span and, therefore, the redistribution is initiated in the span. The temperature gradient causes restraint moments without any restraint normal force. The nominal length l, height h and width b of the beam are 3.60, 0.25 and 0.15 m, respectively. One major finding for the statically determinate beams is that the temperature gradient does not significantly affect the ultimate moment of the doubly reinforced concrete beams subjected to combined short-term mechanical and restraint loads. For the statically indeterminate beams, a 5 % reduction in the ultimate load occurs due to the presence of the temperature gradients. In the ultimate capacity of concrete structures, such small differences in an experimental study can be caused by the variation in the material properties and is not caused by the physical interaction between temperature restraint and structural behaviour [11]. In contrast, the temperature influences the rotational capacity of the beams. Some amount of the available plastic strain is dissipated in the range of the yielding zones caused by the additional temperature strains. Thus, a certain rotational capacity is absorbed by the thermal loading.

Experiments on statically indeterminate beams subjected to combined loading of external load and temperature gradient (heating: $\Delta T_M = +80\,\mathrm{K}$, cooling: $\Delta T_M = -80\,\mathrm{K}$) are performed by JOKELA [194] in the serviceability as well as ultimate load level. The measurements show no significant influence of the thermal action on the ultimate capacity.

In the study by KÜHLEN [233], four-point supported beams exclusively loaded by a temperature gradient are investigated in experiments. The major conclusion is that the completed crack formation stage can not be reached or exceeded purely from the restraint loading condition.

Theoretical studies on the load-deformation behaviour of two-span reinforced concrete beams due to combined line loading and temperature gradient $\Delta T_M = 35\,\mathrm{K}$ are performed by HOLSCHEMACHER [174]. The load level of the external load is in the range of 70 % of the ultimate load and, hence, in the serviceability range. Stiffness degradation in the support (23 % of EI^I) and span (42 % of EI^I) cross sections occurs, but some sections still remain in the uncracked state. The remaining restraint bending moment due to the temperature gradient, based on the non-linear simulation, is only $\approx$ 25 % of the section forces based on the full liner-elastic stiffness.

Support settlement

Short- and long-term experiments on reinforced concrete beams subjected to combined loading of external point loads and support settlement are performed by KORDINA et al. [228]. The reinforcement layout are designed according to the external load except for one beam where the additional restraint loading condition is considered in the design with a simplified approach of $EI = 0.70EI^I$. All tested beams are at one side fixed and at the other side simply supported, where upward or downward support settlements are adjusted after reaching an external load condition similar to serviceability condition. In the experiments it is observed that the restrained forces continuously decrease with increasing external loading level. An exception is investigated for the beam with additional embedded reinforcement, in which the resulting restraint effect is even higher than computed by the ansatz $EI = 0.70 \cdot EI^I$. For most of the tested beams, the restraint forces degraded fully caused by concrete cracking and less beam stiffness.

Ultimate capacity tests on 6 reinforced, continuous T-beams ($b/H/l = 1.50/0.40/6\,[\mathrm{m}]$) are studied by

Woidelko et al. [409, 410] by combined loading of external load and support settlement. The restraint effects are measured to decrease significantly with increase in external load, which causes stiffness degradation. An influence of the support settlements on the ultimate capacity is not observed. The general approach of applying a crude general reduction of linear-elastic stiffness is not capable of predicting responses reliably, because the restraint forces are excessively overestimated in comparison to the measurements.
The interaction between design procedures (material modelling) and the restraint effects is studied by [389] for a statically indeterminate reinforced concrete beam forced by a direct loading p and an indirect support settlement s, see Fig. 3.38.

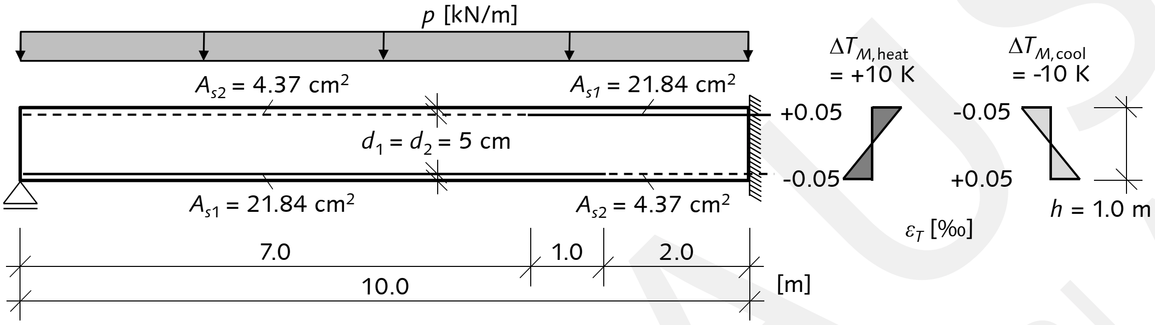

Figure 3.38: System for analysis of restraint effects based on several design procedures, based on [389]

The influence of the restraint effects on the load-bearing behaviour is analysed based on the following design procedures: linear-elastic, general stiffness degradation of linear-elastic stiffness, and non-linear analysis. The comparison of the results, presented in Tab. 3.15, shows that the influence of the restraint effects decreases with increasing external load p. In the case of an equal ultimate bending moment capacity M_u and ultimate support settlement s_u for all design procedures, the non-linear simulation enables a 68 % higher ultimate load p_u in comparison to the linear-elastic computation and a 25 % higher load compared to the general stiffness degradation ($EI \approx 60\,\%\,EI^I$). Therefore, the stiffness degradation in the highly loaded regions decreases the magnitude of the restraint moment $\Delta M_{\mathrm{restr},s_u}$ until the bearing capacity is reached, see Eq. 3.109a. For the non-linear simulation, the restraint moment caused in combination with the ultimate load contributes only 12 % to the bearing capacity moment, 25 % to the general stiffness degradation and 44 % to the linear-elastic simulation, respectively. Moreover, the maximum resisting support settlement $s_{\max}$ for a purely restraint loading condition $p = 0$ is 14.2 cm for the non-linear simulation, 6.5 cm for the general stiffness degradation, and 4.0 cm for the linear-elastic analysis.

Table 3.15: Influence of restraint effect caused by support settlement depending on design procedure, based on [389]

Response	Unit	Linear-Elastic EI^I	General Stiffness Degradation $60\,\%\,EI^I$	Non-Linear EI^{nonl}
p_u	[kN/m]	91	122	153
$\Delta M_{\mathrm{restr},s_u}/M_u$	[%]	44	25	12
$p = 0$, $s_{\max}$	[cm]	4.0	6.5	14.2

Remarks about restraint effects

The magnitude of restraint effects can be extremely reduced by stiffness degradation due to cracking and yielding, which tends to relieve these areas caused by disproportionately decreasing cross section stiffness.

The simulation of concrete structures considering material non-linearity allows the assessment of absolute stiffness degradation and redistribution of section forces caused by relative changes in stiffness between the structural components and sections, respectively. These non-linear effects are strongly dependent on the reinforcement ratio and level of pre-stress as well as on the load level. Furthermore, such redistributions require adequate rotational capacity of the cracked sections which can generally be provided by the material models considered in the non-linear simulation.

Restraint effects in statically indeterminate structures cause section forces that are directly dependent on the absolute and relative stiffness. Common restraint effects are caused by constrained thermal action, concrete shrinkage, hydration heat, and support settlements. A highly loaded structure that has undergone stiffness degradation, as described above, is subjected to a smaller amount of additional section forces due to restraint. The impact of restraint effects on the structural behaviour highly dependent on the load level. Therefore, an accurate representation of the structural behaviour, considering the non-linear behaviour, is necessary for determining the effects of indirect loading conditions in an adequate manner. Simplifications like assuming linear-elastic behaviour or crude approximations of stiffness degradation may lead directly to an unreliable, unsafe, or uneconomic design.

The restraint effects cause section forces in the range of the initial crack forces in most cases. The total cross section area and the tensile strength at that time when the restraint effects occur should be used in the analysis. In particular, residual stress states caused by shrinkage and hydration heat can significantly reduce the tensile strength [78, 268], which should be considered in the computation of restraint effects [325].

In the case of exclusively the restraint loading condition, the crack formation stage (see Sec. 3.1.4.1) determines the resulting restraint force. For every loading step where the normal force reaches the cracking normal force, see Fig. 3.16, the unloading branch is flatter when compared to the initial stiffness as a result of concrete cracking [295]. The exact determination of the discontinuous deformations in the crack formation stage is critically important for very short structural elements, such as the perimeter centrifugal concrete mast [296].

The following analysis of the restraint effects on cross sectional and structural levels is based on the study by Arnold et al. [11, 266], in which the numerical model is validated against the experiments for reinforced concrete beams [3, 107, 410] and prestressed concrete beams [91, 422]. Moreover, the results of the study by Djouahra et al. [85, 267] are used for the assessment of restraint effects in a concrete slab system. The results of Djouahra et al. are computed by non-linear Finite Element simulation considering the tension stiffening effect. The numerical model is validated against experiments presented in [3, 107, 190]. The results in the following Sec. 3.5.2 and Sec. 3.5.3 are computed either based on the "Energy Method with Integral Description of the Material Behaviour" (EIM, Sec. 4.1) or are analysed by the Finite Element Method (FEM, Sec. 4.2). A very good agreement between the simulation results and the results of Arnold et al. and Djouahra et al. is observed, because all physical phenomena, such as interaction between concrete cracking and combined loading conditions due to external loads and restraint effects, are reliably predicted. Therefore, the considered material models and both simulation methods are generally applicable for non-linear simulations and the assessment of restraint effects in concrete structures.

3.5.2 Cross sectional analysis

The results presented for the cross sectional analysis are predicted by the Energy Method (EIM). For the analysis of different cross sections, the following material grades are chosen: The concrete class is C 35/45 and the reinforcement class is B 500B with a high ductility capacity [134]. The non-linear stress strain relationship for the concrete under compression and the bi-linear relationship for the reinforcement are used according to [134]. Tension stiffening is considered after reaching the crack initiation strain ($\epsilon_c > \epsilon_{ct}$) in concrete according to the exponential function, see Sec. 3.1.4.4. The strength and strain values for all materials are listed in the appendix in Tab. A.1.

The influence of normal force N is neglected in the computation of load-deformation behaviour. The cross sections studied here are purely loaded by bending moment M_y. A similar study is performed by ARNOLD et al. [11, 266] and the obtained results based on the EIM, which are discussed in the following, show a very good agreement in comparison to ARNOLD et al. . Moment-curvature (M-κ) diagrams are an effective way to demonstrate effects like crack initiation, crack growth and plastic deformations. In order to analyse different deformation behaviours of variable crosssections, it is advisable to define relative (dimensionless) cross section properties. They depend on geometry dimensions and material properties. The relative bending moment μ and the normalized curvature $\overline{\kappa}$ can be calculated by:

$$\mu = \frac{M}{f_c b d^2}\,, \tag{3.106a}$$

$$\overline{\kappa} = d \cdot \kappa\,. \tag{3.106b}$$

The reinforcement ratio is defined as the mechanical reinforcement ratio ω_{s1} of the cross section and can be determined by:

$$\omega_{s1} = \frac{A_{s1}}{bd}\frac{f_y}{f_c}\,. \tag{3.107}$$

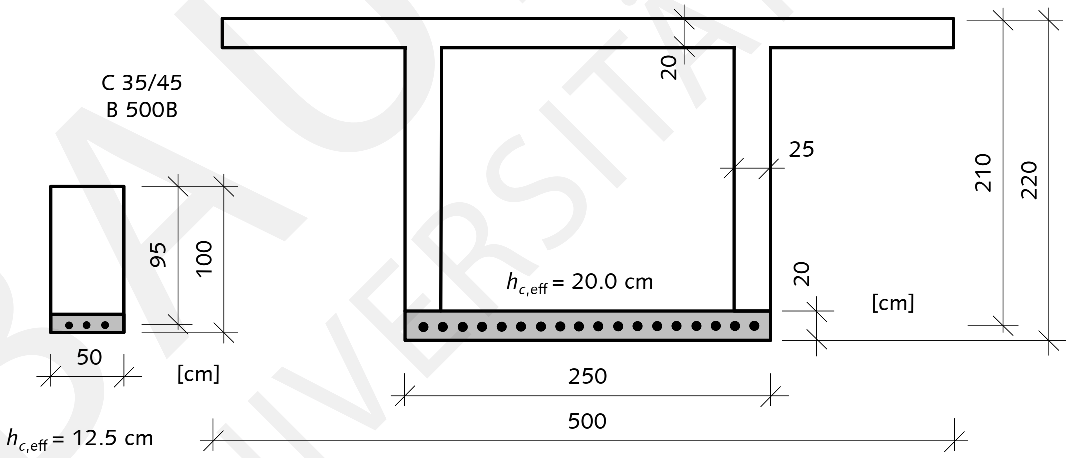
C 35/45
B 500B
95
100
50
[cm]
$h_{c,\mathrm{eff}}$ = 12.5 cm
20
25
210
220
$h_{c,\mathrm{eff}}$ = 20.0 cm
20
[cm]
250
500

Figure 3.39: Geometry of rectangular and box-girder cross section for cross sectional analysis

The amounts of reinforcement area are listed in the appendix in Tab. A.2. The influence of reinforcement ratio according to M-κ and EI-M ($EI = M/\kappa$) for a rectangular reinforced concrete cross section with dimensions 100/50/95 (height/width/effective depth in [cm], see Fig. 3.39) is shown in Fig. 3.40.

The minimum reinforcement ratio $\omega_{s1} = 0.029$ is defined according to the recommendation of EC 2 [101, 141]. The curvature is decisively affected by the reinforcement ratio. First, in an uncracked section, the tensile reinforcement does not affect the curvature (only slightly). When cracks occur, the bending stiffness is strongly affected by the ratio of longitudinal reinforcement. Typical cracking stages of reinforced

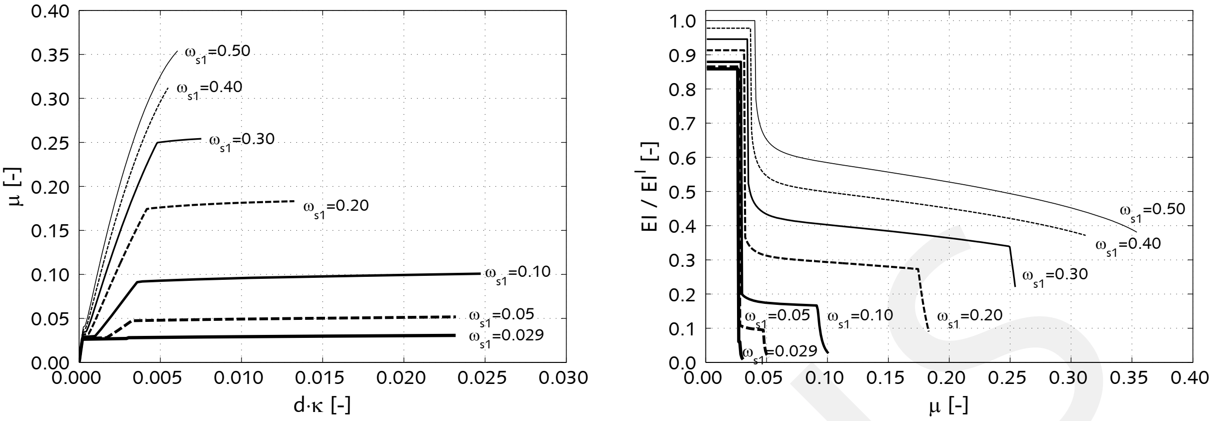

(a) relative moment - relative curvature

(b) relative bending stiffness - relative moment

Figure 3.40: Influence of reinforcement ratio on load-bearing behaviour of rectangular cross section with dimensions 100/50/95 in [cm]

concrete sections (crack formation stage, stabilised cracking stage, and steel yielding stage) are developed for a ratio lower than $\omega_{s1} = 0.30$. For reinforcement ratios of a higher degrees, the section fails due to brittle concrete compressive failure. Hence, the stiffness degradation is limited caused by a brittle failure mechanism. In the case that plastic strains occur, the reinforcement bars lead to a great increase in rotational capacity and high stiffness degradation appears for $\omega_{s1} < 0.30$.
In addition to the rectangular cross section, a typical cross section in bridge structures (box-girder) is investigated with the dimensions 220/500/210/250/20/25, see Fig. 3.39. The $M - \kappa$ relation of the box-girder with different reinforcement ratios is shown in Fig. 3.41. The possible maximum curvatures occur for reinforcement ratios of $\omega_{s1} \leq 0.05$ (box-girder). Reduced plastic deformations in the case of greater reinforcement ratios are related to a reduced depth of the compression zone. In the case of $\omega_{s1} \geq 0.20$, the section reinforcement does not cause plastic strains. In comparison to lower reinforcement ratios, the reduction of the bending stiffness after the crack moment is more influenced by the non-linear compressive range of the concrete for $\omega_{s1} \geq 0.20$. For all cross section types, the dependence on reinforcement ratios according to the load-deformation behaviour remains significant. Due to the fact that restraint effects are strongly dependent on the absolute and relative stiffness in the system, non-linear analysis should consider such adequate simulation of the load-deformation behaviour of cross sections in the structural models.

3.5.3 Structural analysis

In the study by Djouahra et al. [85, 267], a combined loading of external load and centric restraint is analysed for concrete slabs in office buildings. The centric restraint deformations are caused by concrete shrinkage ($\epsilon_{c,sh}$) and temperature variations (constant part ΔT_N). A parametric study on the load-bearing behaviour of two-sided, rigidly supported concrete slabs (system "fix") is performed to represent the central span of a continuous slab floor system. The cross section is a rectangular concrete slab with the dimensions $h/b/d = 100/20/17$ cm, see Fig. 3.42. In the system "fix", the computed restraint effects and resulting vertical displacement and crack width represent the upper limit values. The neighbouring and supporting structural elements in such office buildings may have some flexibility which results in less constrained sup-

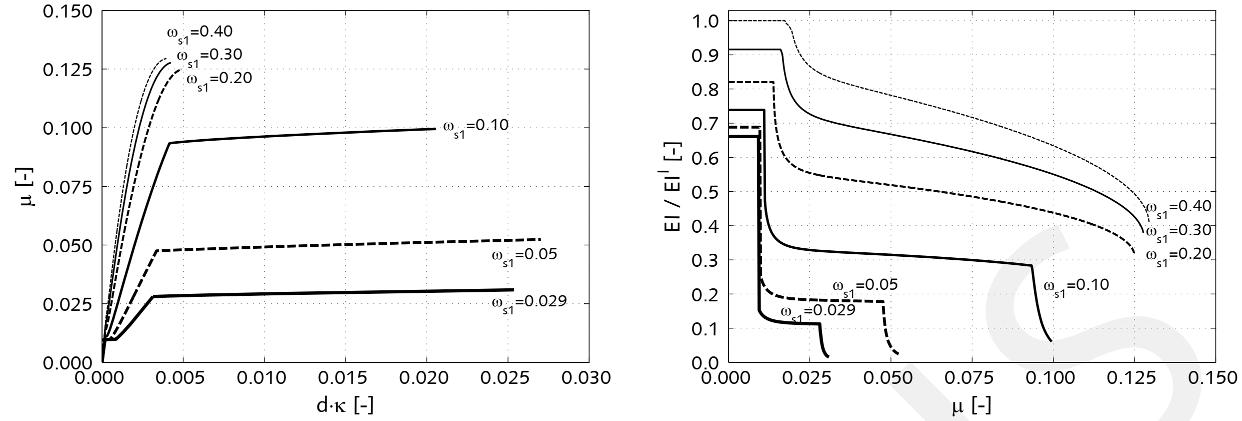

(a) relative moment - relative curvature

(b) relative bending stiffness - relative moment

Figure 3.41: Influence of reinforcement ratio on load-bearing behaviour of box girder with dimensions 220/500/210/250/20/25 in [cm]

port conditions. In addition to the rigid support condition, a horizontal unconstrained support at one side is adopted in the system "free" in order to analyse the lower limit values of the structural response.

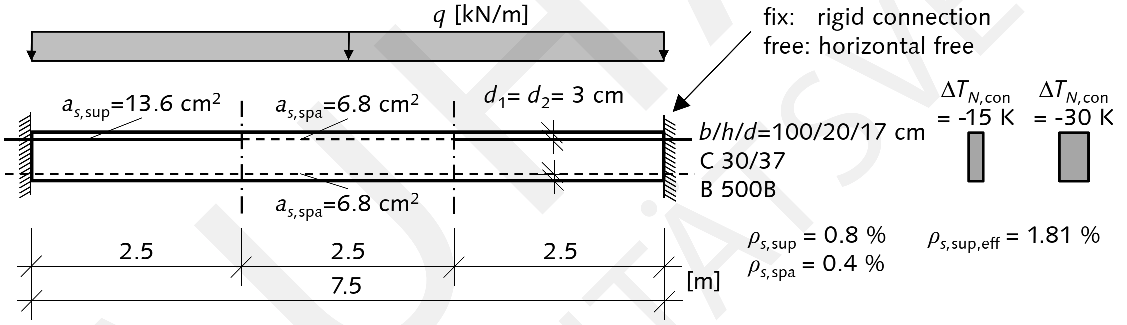

Figure 3.42: Concrete slab in office building due to external load and temperature restraint, based on [85, 267]

The load-deformation behaviour of the concrete slab is analysed by simulations based on Finite Element Method (Sec. 4.2) and the tension stiffening model "multi-lin" (Sec. 3.1.4.3) and the results are subsequently compared to the simulations of DJOUAHRA [85] which used a modification of the reinforcing steel stress-strain relationship. The characteristic loads are $g_k = 8.5\,\text{kN/m}$, $q_k = 5.0\,\text{kN/m}$ and the quasi-permanent load combination with the combination factor $\psi_2 = 0.5$ leads to $q_{\text{perm}} = 11\,\text{kN/m}$ in the serviceability limit state (SLS). For the ultimate limit state (ULS), $q_{Ed} = 19\,\text{kN/m}$ is defined according to EC 0 [100]. The non-linear response of the structure due to external load q is shown in Fig. 3.43. The structural system with a one-sided horizontal unconstrained support condition is labelled "free" and the two-sided is labelled "fix". High compressive strains occur in the case of the fixed support conditions. Hence, the load-deformation behaviour does not have a distinct yielding in the reinforcement. The structural system fails due to the exceedance of ultimate concrete compressive strain. In contrast, the "free" systems show a much more ductile behaviour and the support and span cross sections are already cracked in the SLS.

For the combined loading due to external load and temperature, a constant temperature contraction state

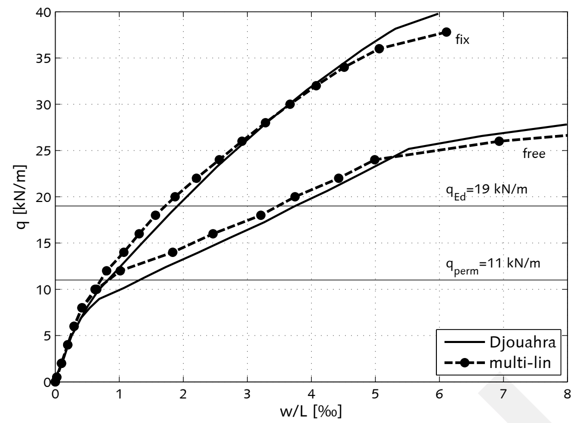

Figure 3.43: Load-deformation behaviour of concrete slab due to external load q, results: DJOUAHRA [85], compared to own simulations by multi-lin model according to Sec. 3.1.4.3

is used according to either an indoor ($\Delta T_{N,\text{cont}} = -15\,K$) or an outdoor ($\Delta T_{N,\text{cont}} = -30\,K$) construction element. Therefore, no curvatures are forced in the cross sections by assuming an equal thermal expansion coefficient α_T for concrete and reinforcing steel. In the system "free", no influence of the constant temperature contraction on the prediction of the section forces and displacements occurs. Therefore, the combined loading is analysed for the fixed support condition. Similar to shrinkage, the contracting loading state causes a tensile restraint normal force N_T which interacts with the compressive force due to external load p. The restraint force can computed indirectly by [85]:

$$N_T = N\left(q + \Delta T_N\right) - (q)\ . \tag{3.108}$$

In the case of a pure restraint loading condition ($q = 0$), cracking in the concrete slab occurs for both thermal contraction states. Increase in external load develops a compressive zone, which leads to an increased computational in-plane stiffness of the already cracked cross sections, see Fig. 3.44(a). Hence, the restraint normal force increases in some loading levels until cracking occurs in the adjacent cross sections. Moreover, the restraint effects significantly affect the vertical displacements of the concrete slab, see Fig. 3.44(b). For example, the displacement at a SLS loading level q_{perm} in the combined loading condition is more than two times greater than the purely external load condition. The reason for this is the stiffness degradation due to cracking under restraint forces which decreases the overall stiffness of the concrete slab. In summary, the additional centric restraint condition significantly influences vertical displacement and crack width. Displacements are most sensitive to the constraint support conditions and the slenderness ratio. Reinforcement ratio and restraint loading condition mainly affect the crack width [267].

In addition to the two-sided fixed concrete slab, a continuous beam structure is studied with the Energy Method (EIM). The reference system is a two-span beam with the same span length ($l_1 = l_2 = 10\,\text{m}$) and reinforcement layout in each span, see Fig. 3.45. It is used to analyse load and restraint effects and moment redistribution of concrete beams on a structural level. The cross sections have a tensile reinforcement ratio of $\omega_{s1} = 0.10$ ($A_{s1} = 21.84\,\text{cm}^2$) and compression reinforcement of ($A_{s1} = 1/5 \cdot A_{s1} = 4.37\,\text{cm}^2$). The concrete and reinforcement properties are listed in Tab. A.1. The restraint strains are induced by a temperature gradient between the top and bottom across the section depth. The differences are $\Delta T_{M,\text{heat}} = +10\,\text{K}$ and $\Delta T_{M,\text{cool}} = -10\,\text{K}$. Up to a loading level of $p = 20\,\text{kN/m}$, the concrete sections are uncracked in

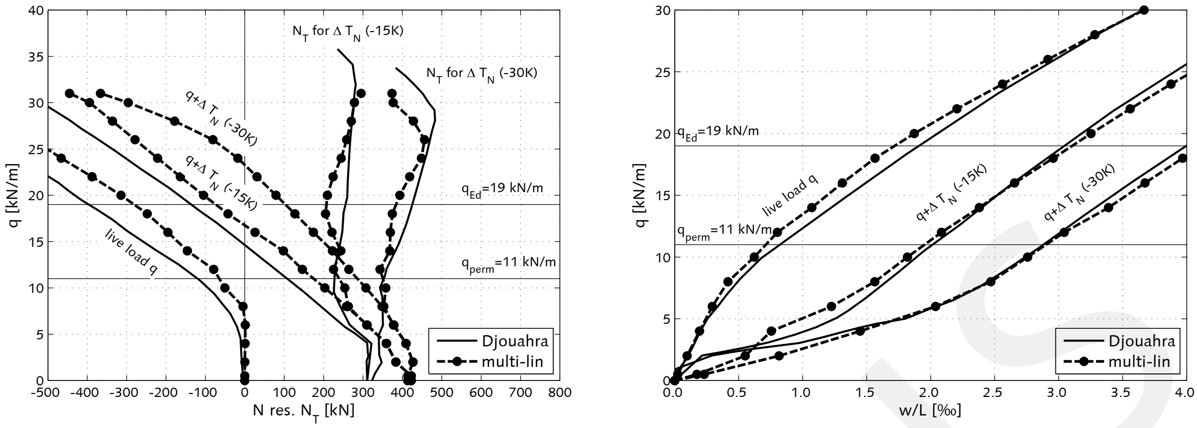

(a) normal force N and restraint normal force N_T

(b) relative displacement

Figure 3.44: Load-deformation behaviour of concrete slab for combined loading of external load q and temperature constant $\Delta T_{N,\text{cont}}$, results: DJOUAHRA [85], compared to own simulations by multi-lin model according to Sec. 3.1.4.3

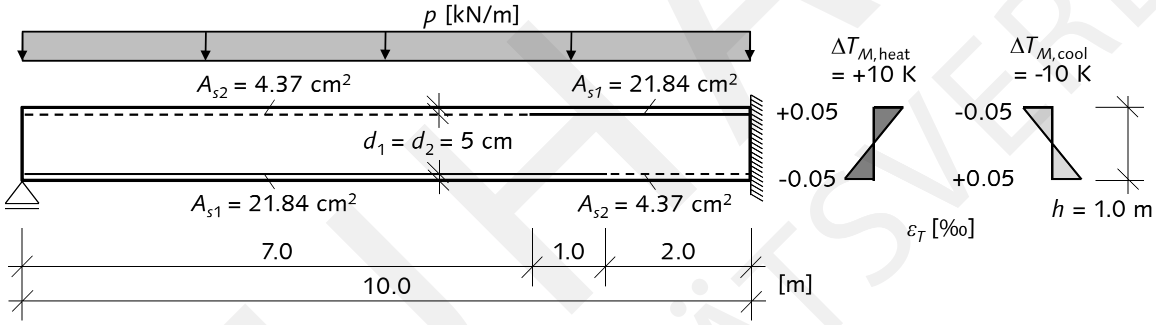

Figure 3.45: Geometry and loading conditions for continuous reinforced concrete beam subjected to combined mechanical and temperature gradient loading, $\omega_{s1} = 0.10$

the linear-elastic stage, see Fig 3.46(a). The bending stiffness of the support and span reduces after crack initiation and subsequently in the crack formation stage. Hence, the restraint section forces are reduced due to the stiffness degradation of the local cross sections. Depending on the stiffness ratio between both sections, proportional moment redistribution occurs (relative stiffness dependency). The concrete cracking decreases the restrained effect and increases the moment redistribution. The restraint section forces are degraded by exceeding a load level of $p = 50\,\text{kN/m}$. Due to the extensive cracking in the crack formation stage, the restraint moment distribution approaches the moment distribution caused by the direct loading condition. In the case of an ultimate limit load, the restraint forces are degraded completely. The temperature restraint does not affect the ultimate load of $p_{\text{ul}} = 133\,\text{kN/m}$.

The degradation of the restraint forces due to the concrete cracking can be characterised by the following sectional force ratio η:

$$\eta = \frac{\Delta M_{\text{restr}}}{M^{I}_{\text{restr}}}\,, \tag{3.109a}$$

where

$$\Delta M_{\text{restr}} = M\left(p + \Delta T\right) - M\left(p\right)\,, \tag{3.109b}$$

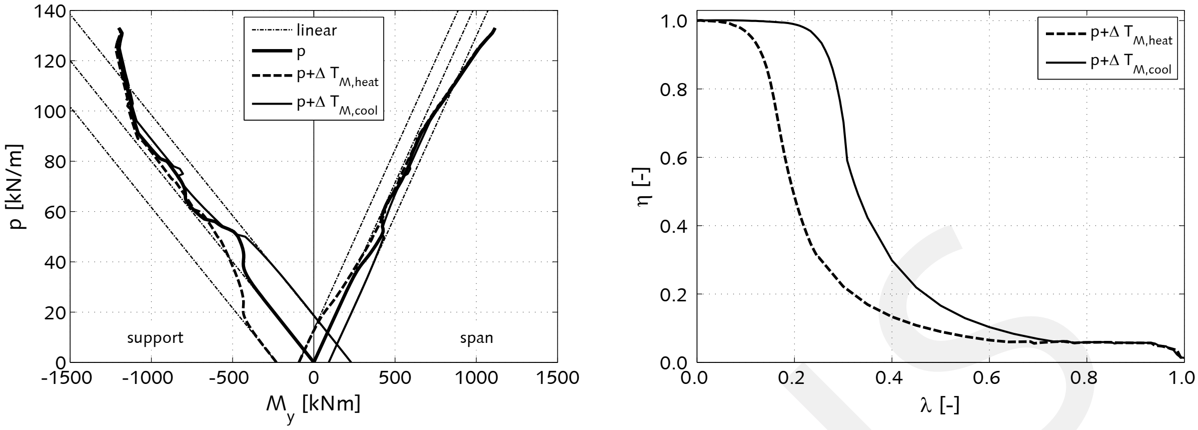

(a) moment redistribution

(b) restraint force degradation at support

Figure 3.46: Load-bearing behaviour of continuous reinforced concrete beam subjected to combined mechanical and temperature gradient loading, $\omega_{s1} = 0.10$

where M^{I}_{restr} is the bending moment due to temperature load in the uncracked stage. Moreover, the loading condition can be considered by the relative load level λ:

$$\lambda = \frac{p}{p_{\mathrm{ul}}} . \tag{3.109c}$$

With the aid of both dimensionless parameters, the results of the non-linear simulation are demonstratively compared with those of the linear one. The first crack initiation in the support section for the temperature load $T_{M,\mathrm{heat}}$ decisively reduces the restrained bending moment by a load ratio of $\lambda < 0.2$, see Fig. 3.46(b). This bending moment is reduced up to 60 % in comparison to the linear solution. For $T_{M,\mathrm{cool}}$, the crack initiation in the support section causes an equivalent behaviour. The main degradation of the restraint section forces caused by both temperature gradients appears in the range of 10 % to 30 % of the ultimate limit load (service load state).

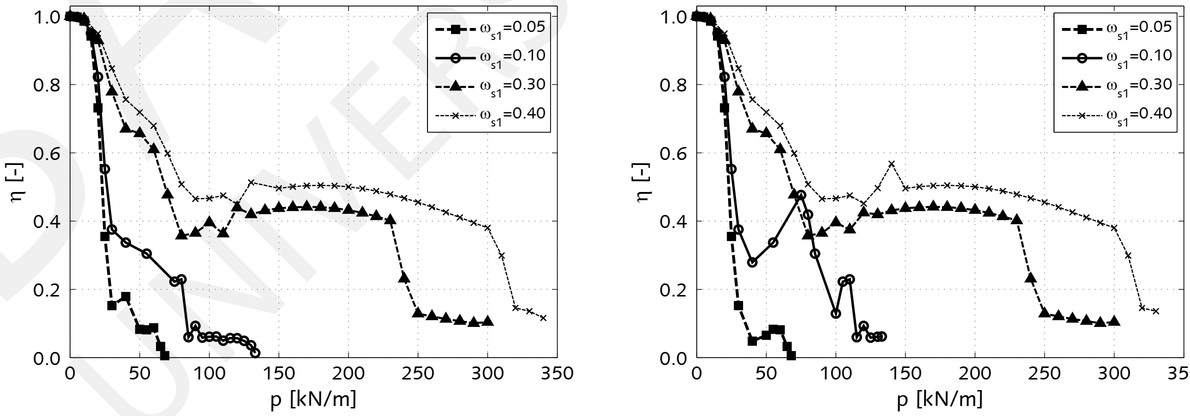

(a) support

(b) span

Figure 3.47: Influence of reinforcement ratio ω_{s1} on degradation of restraint forces caused by temperature gradient $T_{M,\mathrm{cool}} = -10\,\mathrm{K}$

The influence of the reinforcement ratio ω_{s1} on the degradation of the temperature restraint forces for

$T_{M,\text{cool}} = -10\,\text{K}$ is illustrated in Fig. 3.47. The discontinuous curve shape results from the influence of the start values in the numerical non-linear optimisation method. With the first initial crack formation, a significant reduction in the restraint forces is apparent. The reinforcement ratio influences the behaviour after the crack initiation. In the case of a low reinforcement ratio $\omega_{s1} = 0.05$, the restraint force is reduced up to 80 %. They still degrade with a reduction of up to 60 % for higher reinforcement ratios than $\omega_{s1} > 0.10$. In the ultimate limit state, the restraint force is completely degraded with $\omega_{s1} = 0.05$ and $\omega_{s1} = 0.10$. The range of completed crack formation is extended with higher reinforcement ratios. By reaching the ultimate concrete compressive strain in the support cross section, the plastic deformations of the reinforcement bars are limited. Therefore another reduction of restraint force is prevented due to the confined rotational capacity for the high reinforcement ratios of $\omega_{s1} = 0.30$ and $\omega_{s1} = 0.40$.

3.5.4 Restraint sensitive structures

3.5.4.1 Buildings

Structures may be sensitive to restrained drying shrinkage especially for components with a low volume to surface ratio. These structural components are exemplified by pavements, bridge decks, walls, and industrial floors [405, 407]. Temperature and shrinkage cause restraint effects which may cause large internal stresses in thick walls [352]. These stresses can cause very narrow cracks that start at the surface. In the case that the restraint effects continue to develop, incipient cracks between the separation cracks may occur. Moreover, massive concrete members, such as thick power plant slabs, or waterproof concrete walls, or wall/foundation slabs, may be highly sensitive to restraint caused by hydration induced stresses. Such stresses can result in visible crack patterns which reduces durability and concrete impermeability, see Fig. 3.48(a). An adequate consideration of the stiffness and strength hardening process of concrete, shrinkage of concrete, and the hydration heat is generally important in order to predict reliable results for these structural components.

Concrete slabs in buildings constrained to neighbouring components (such as stability cores, utility cores, walls) may be sensitive to restraint effects caused by shrinkage and temperature. Therefore, concrete slabs in buildings are subjected to indirect deformations in addition to the main external bending stress state, see Fig. 3.48(b). The two building cores induce constraint conditions in the concrete slabs and, consequently, restraint effects are caused by the indirect deformations. These additional load conditions lead to an increased crack formation and may cause positive effects, such as degradation of restraint effects and moment peaks. In contrast, wide cracks can occur and expose imperviousness, shear force capacity, and may subsequently force greater displacements of other structural components.

An extensive parametric study by Schnell et al. [371] for reinforced concrete slabs is performed by varying concrete strength and stiffness, uniform temperature component, slab depth, slab span, and considering/neglecting creep. Slender slabs or long span slabs tend to sustain excessive vertical displacements due to stiffness degradation caused by tensile restraint forces. Higher concrete grades lead to even softer structural behaviour, because the tensile restraint force is higher which causes the concrete to crack. Compact slabs, particularly with a small span, are sensitive to yielding strains in the reinforcement. Consequently, wide cracks may occur in these types of slabs.

Restrained bending moments caused by temperature gradients significantly influence the required amount of reinforcement in cooling tower shells [41]. The tensile forces at inner and outside shells caused by temperature bending moment can exceed the loading level due to external wind action. Based on physical and

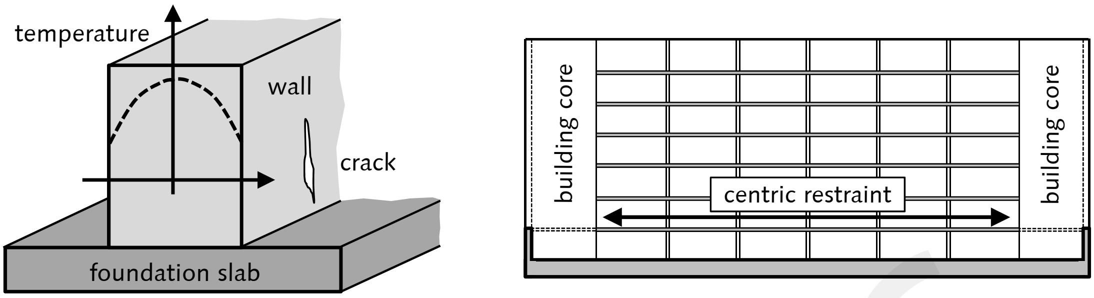

(a) wall/foundation system (b) structure for restraint sensitive concrete slabs based on [85]

Figure 3.48: Sensitive restraints on concrete wall/foundation and slab system

geometric non-linear analysis, the ultimate bearing capacity of the tower is not influenced by the restraint forces any longer. In contrast, restraint effects cause forces in the serviceability limit state which results in considerable stresses and should not be neglected in the design. Structural design with linear-elastic stiffness and a general assumed stiffness degradation is not adequate and may lead to a very conservative and uneconomical reinforcement layout.

3.5.4.2 Integral and semi-integral bridges

Integral bridges are gaining more and more interest lately because they are associated with significant cost savings in building maintenance. The waiving of the non-durable bearings and joints as a result of the bearingless and jointless connections of the structural components leads to significant cost saving in structural maintenance. However, the design of these bridges induces very high requirements on the planners, which have to take into account many complex phenomena for the simulation and the design of such structure. Integral bridges have superstructures that are monolithically coupled to supports and abutments at all bridge axes. Semi-integral bridges have bearings on one or both abutments and may additionally have bearings on the bridge piers. In the United States alone, more than 9, 000 integral and more than 4, 000 semi-integral bridges have been constructed. In Europe, the amount of integral bridges may be less, but a trend towards more integral-design projects is evident [67, 264]. Nevertheless, simplicity in the construction of integral bridges due to elimination of expansion joints and bearings is associated with more complexity in the structural design of the bridges. This relationship is addressed herein.

A lot of complex, partially difficult to captured and challenging to modelled phenomena have to be considered in the analysis of the entire structure [67, 214, 355, 425]. Therefore, the design of the integral bridge projects present demanding challenges for structural engineers. In particular, the assessment of the restraint effects caused by the creep, the shrinkage, the relaxation, the temperature, and their degradation forced by the cracking of the concrete and the flexibility of the soil and foundation poses high requirements on the modelling process. The stiffness of the soil, the foundation and the stiffness of the bridge interact together, especially in the case of the restraint sensitive integral bridges [82, 99, 108, 232].

High demand for the design of integral bridges may be attributed to the horizontal loads and deformations characteristic of railway bridges, in which these forces are generated from train braking and acceleration. For long railway bridges, such forces may achieve fourteen-time higher values in comparison to road bridges [264]. The design of the entire structure is significantly influenced by these loading conditions in combination with the high demand of deformation and vibration control of bridges. In the deformation process of integral and semi-integral bridges, the bridge's complete load-bearing behaviour is activated and contributes in load distribution and limitation of deformation and vibration. Therefore, the application of integral bridges includes remarkable advantages in comparison to bridges with superstructures supported on bearings (conventional bridges).

In integral bridges, temperature expansion or contraction is mainly covered by centric tensile or compressive forces in the superstructure. Internal forces caused by these thermal actions are independent of bridge length, because of the approximately complete deformation expansion/contraction under constraint conditions ($N = EA\alpha_T \Delta T$). A linear dependency is apparent between these forces and the in-plane stiffness of the superstructure. Abutments carry the main portion of tensile and compressive forces in the longitudinal direction. However, relatively little load is transferred into the bridge piers and, hence, a very high horizontal capacity should be achieved, especially in the abutments. Nevertheless, a certain flexibility in the abutments appears in the "real" structure which may significantly reduce the temperature forces, especially for very short integral bridges [264]. Moreover, the increase in bridge length reduces the significance of abutment stiffness and horizontal forces, due to reduced thermal action. The application of fully integral bridges may be primarily suitable for short and long bridges.

The load-deformation behaviour of semi-integral bridges is fundamentally different compared to that of integral bridges, particularly for loading conditions which cause stresses due to restraint effects. In semi-integral bridges, the bending-resistant bridge piers may generally have a large longitudinal deformation capability which allows the superstructure to horizontally deform without a significant constraint introduced by the piers. During interaction with pier bending stiffness and deformable length, significant restraint forces may occur. Hence, slender and flexible bridge piers are recommended for semi-integral bridges in order to limit restraint forces [264]. Several types of semi-integral bridges exist which differ primarily in their longitudinal deformation behaviour, and capacity, see Fig. 3.49.

For bridges with bearings at both abutments, the horizontal force is equally distributed to the piers. This type of semi-integral bridge is more applicable and suitable for motorway bridges. In contrast, the much greater amount of horizontal forces due to crossing trains cause an essentially fixed point with corresponding high stiffness and capacity. Either strut bracing at the centre of the bridge or a monolithic connection at one abutment are commonly used in semi-integral railway bridges. Nevertheless, restraint effects are still transmitted into the other bridge piers. Therefore, minimising restraint forces due to pre-stressing of concrete, creep, shrinkage, and temperature variations is of great importance for the design of the structure and the choice of construction technology.

semi-integral

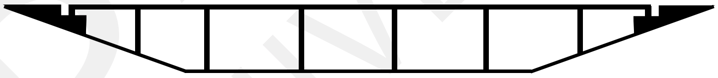

fixed point distributed on all bridge piers along superstructure length

semi-integral with fixed point by struts

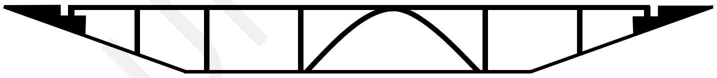

fixed point by strut bracings at centre of superstructure

semi-integral with fixed point at one abutment

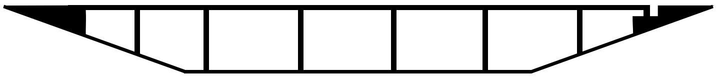

fixed point by monolithically connection at one abutment

Figure 3.49: Different types of semi-integral bridges, bearing at the abutments, except the semi-integral bridge with a fixed point at one abutment, based on [264]

Advantages of frame and integral bridges in comparison to conventional bridges with bearings can be summarised to (based on arguments as [263, 264, 425]):

- distribution of static and dynamic loads to all components
- increase in ductility, durability, robustness, and redundancy
- higher achievable slenderness
- increase in structural ultimate capacity despite slender elements
- reduced buckling length of piers
- favourable transmission of horizontal loads
- enhanced response behaviour during seismic or other extreme events
- more simplified construction without bearings
- high economic potential due to elimination of expansion joints and bearings

Nevertheless, such structures cannot be considered as a "maintenance-free" type of structure due to several predicted uncertainties involved in the design of the structure [425]. In principal, on-site temperature changes and mechanical properties of the soil are comparatively challenging for determining a highly accurate assessment in the preliminary design. Therefore, analysis of the interaction between superstructure and soil should be carefully considered in the corresponding time-dependent deformation process caused by seasonal temperature variations, shrinkage and creep [326]. These uncertainties may lead to a discrepancy between simulation results and the real structural behaviour. Therefore, parametric and sensitivity studies are commonly effective in assessing the expected structural response. For the analysis of structures which are sensitive to creep and shrinkage, BAŽANT [27] recommends performing short-term measurements for the actual concrete mixture. Afterwards, the long-term concrete behaviour can be extrapolated by combining the measured data with prior statistical information on creep and shrinkage of concrete in general. The *Bayes*'ian statistical approach may be used for this concern, see Sec. 2.5.2. In a similar way, BROKKS [54] endorses experimental tests for modulus of elasticity or short-term creep and shrinkage in order to obtain a more accurate estimate for the long-term concrete behaviour.

In order to limit and reduce restraint effects in integral bridges, a very efficient and effective design aspect is to reduce the in-plane stiffness of the superstructure by as much as possible. Reducing cross section surface or avoiding pre-stressing of concrete may be reasonable ways to permit reduced stiffness. The construction process influences the amount of restraint effects caused by concrete shrinkage significantly [263]. Therefore, an efficient construction process may effectively reduce forces due to indirect loading conditions. Reduction in rotational and lateral foundation stiffness of the bridge piers can decrease the restraint forces in the piers. Therefore, the application of one instead of two or more pile rows in the longitudinal bridge direction at each axis is a sufficient solution for the structural design, see Fig. 3.51. Moreover, concrete hinges may be applied, which are another design aspect to help limit the amount of restraint forces but still allow bearingless bridge construction [264].

The semi-integral solution of superstructure, piers, and piles according to Fig. 3.51(b), was applied in the railway valley bridge "*Viaduct Scherkondetal*". This bridge was completed in 2010 and has a total length of 576.5 m and a regular span length of 44.0 m, see Fig. 3.50. The cross section is a single box girder with a depth of 2.00 m at the span and 3.50 m at the supports resulting in a slenderness of $44/2 = 22$, which is generally very high for high-speed railway bridges [264]. Due to the high horizontal train loads, a fixed point solution is applied at one abutment and, wherever it is possible, moment-resisting connections between piers and superstructure are designed [366]. The final stage of bridge pier inclination due to the long-term behaviour of the superstructure (pre-stressing, shrinkage, creep) may be minimised by the construction process. Therefore, the piers can be reversely constructed compared to their final position. The subsequent connections between superstructure and piers and their corresponding long-term behaviour finally lead to the desired vertical alignment of the bridge piers.

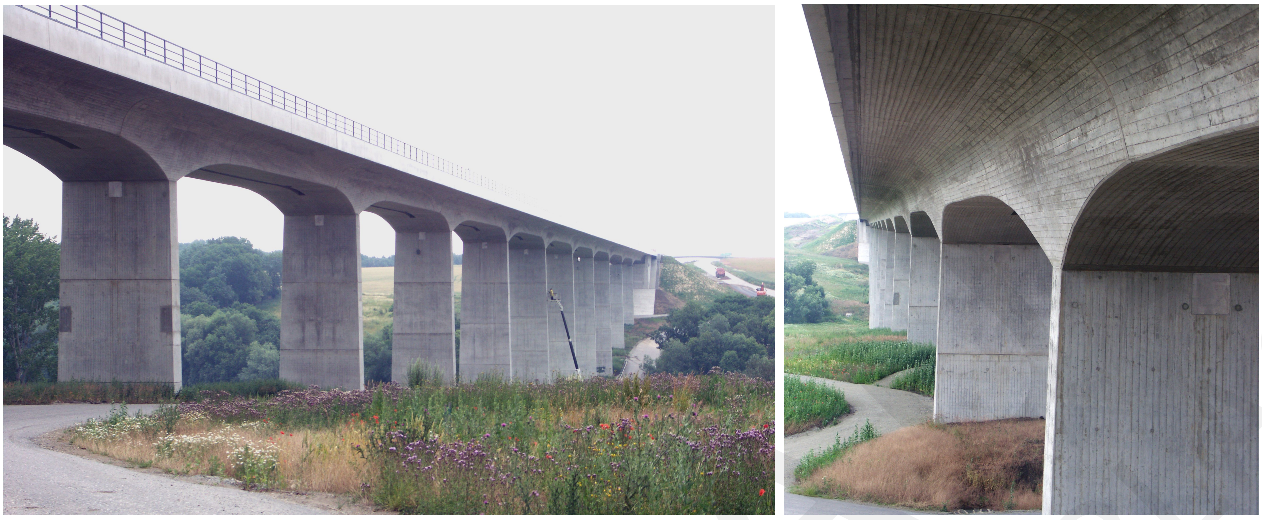

Figure 3.50: Semi-integral "*Viaduct Scherkondetal*"

In the following, semi-integral bridges are mentioned in addition to the "Viaduct Scherkondetal", which are newly built bridges for the high-speed line Erfurt to Leipzig/Halle (Germany) which are all a part of the trans-European train axes Berlin-Verona/Mailand-Bologna-Neapel-Messina-Palermo. These bridges are:

• "*Viaduct Unstruttal*",	semi-integral bridge, $L_{\text{tot}} = 2,668\,\text{m}$, 4 continuous joint- and bearingless 10 span girders with individual length of 580 m, regular span between two piers of 58 m, single box girder, arch-shaped strut bracing at centre of each continuous girder, 41 very slender piers with stiff transverse and flexible longitudinal stiffness, structural joints applied by separating piers	[264, 366]
• "*Viaduct Gänsebachtal*",	semi-integral bridge, $L_{\text{tot}} = 1,012\,\text{m}$, continuous superstructure segments of span 112 m, average span between two columns of 24.50 m, double-tracked and double-web pre-stressed T-beam with construction height of 2.08 m, circular concrete columns of diameter 1.00 ... 1.10 m, stiffened braking span at centre of each section	[264, 365]
• "*Viaduct Stöbnitztalbrücke*".	semi-integral bridge, $L_{\text{tot}} = 297\,\text{m}$, circular concrete columns, horizontal load distribution due to frame construction of superstructure, piers and pile cap with piles, separating columns, single pile rows under normal piers resulting in five-time less stiffness compared to pile cap solution of frame construction	[199]

These bridge examples show that semi-integral bridges can be designed even for highly loaded structures and long span bridges. In every one of these projects, the significance of restraint effects, their adequate modelling, and limitation of resulting forces in terms of the entire structure is mentioned to be absolutely essential for the design and construction of these bridges. The most influential restraint effects are caused by concrete creep, shrinkage and temperature variations (shortening of superstructure due to pre-stressing also affects this) resulting in deformation and section forces which are very critical aspects of the design. These horizontal deformations and bending moments in the pier-superstructure connection should be minimised in order to reduce the amount of reinforcement at these sections. The control and limitation of restraint effects based on reliable and accurate simulations and experimental studies are a key design aspect in integral and semi-integral bridges.

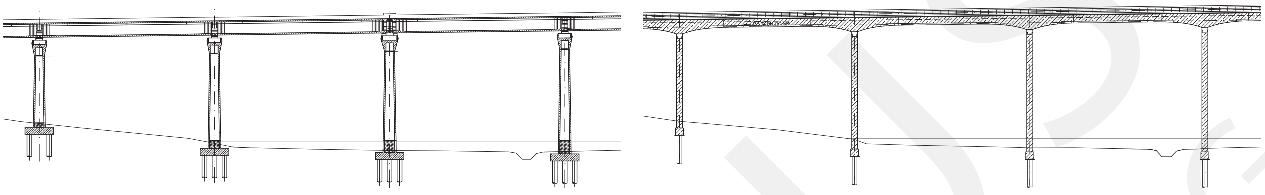
(a) conventional
(b) semi-integral

Figure 3.51: Comparison of longitudinal sections for conventional superstructure with bearings and semi-integral bridge, based on [264, 366]

Various studies about the behaviour of integral bridges are based on monitored structures and numerical simulations. The load-deformation behaviour is commonly evaluated for integral abutment bridges, where the superstructure is monolithically connected to the abutments and the superstructure to pier connections are either hinged (continuous superstructure over several span) or fixed (frame bridge). The analysis of soil–structure interaction behind the abutments and in the range of the foundation piles is a significant design aspect in estimating accurate simulation results for integral abutment bridges [82, 232, 425], see Fig. 3.52(a). Considering the influence of a backfill behind the abutments in the global simulation model is commonly assessed to result in greater superstructure support and abutment moments and smaller superstructure span and pier moments. The daily and annual expansion/contraction of the superstructure is mainly caused by temperature changes, see Fig. 3.52(b). Therefore, the soil behind the bridge abutments is subjected to cyclic loadings which leads to complex soil-structure interaction [86]. Such complexity may cause considerable uncertainties in the simulation and less reliability in the design of the structure [215].
Parametric and sensitivity studies based on variations in soil and concrete properties, temperature variations, and foundation stiffness may be necessary and very reasonable in order to analyse the structural behaviour. Assessment of a set of possible solutions instead of exclusively analysing a single parameter set can reach to a higher confidence in the simulation results and finally to ensure a reliable design.
In the study by Bloodworth et al. [45], the influence of thermal cyclic loadings on the prediction of earth pressure on integral bridge abutments is studied using laboratory cyclic stress-path measurements (triaxial apparatus) and validating a numerical model. Soil samples of stiff clay and sand are tested under stress paths, which may be typical behind integral bridge abutments. A distinct behaviour between the two tested soils are analysed in which a stiff clay shows relatively little buildup of lateral stress with cycles. In contrast, stresses in sand increase continuously, exceed at-rest pressure and finally approach the full passive earth pressure. Following this, a numerical model is investigated in order to analyse the soil-structure interaction by determining the horizontal stresses acting on the bridge abutment. In the assessment of these interactions, the wall friction is assessed to induce no significant influence on the predicted earth pressures. Between stiff and most flexible concrete piled abutment walls, a reduction of about 10 % in earth pressures

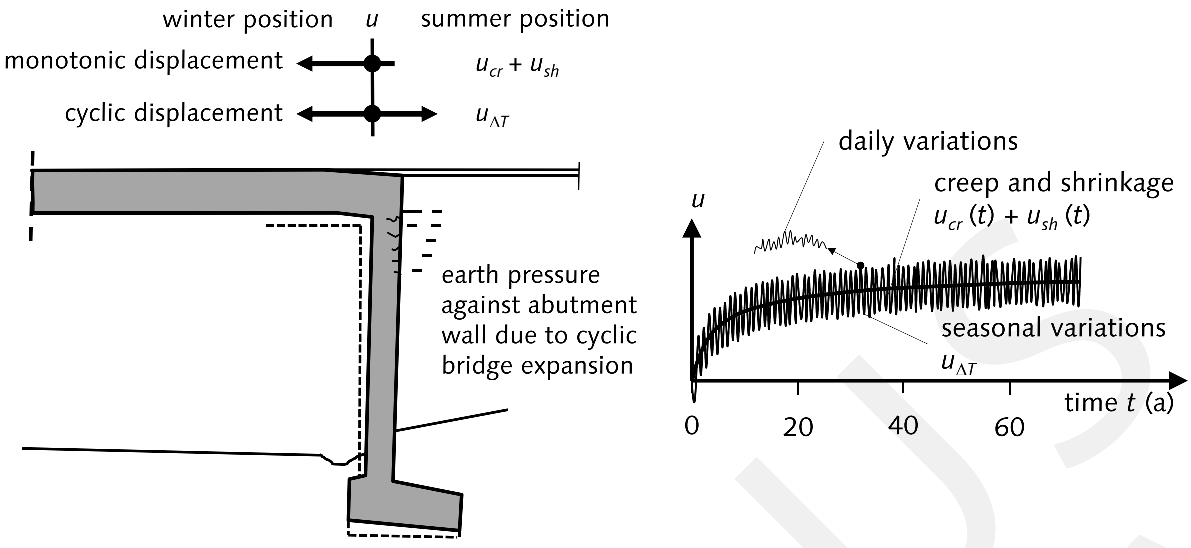

(a) interaction with abutment-backfill, based on [42]

(b) distribution of u, based on [86]

Figure 3.52: Time-dependent horizontal bridge deck displacement u due to creep, shrinkage, and thermal variations for integral bridges

is computed for practical ranges of wall stiffness.

Temperature changes are frequently assessed to be one of the critical aspects in determining the entire bridge design. An extensive study by ZORDAN et al. on one of the longest integral abutment bridges is performed based on parametric analysis and temperature pushover analysis [424, 425]. This structure is the "*Isola della Scala bridge*" bridge located in Verona (Italy). The bridge was completed in 2007 with a total length of about $L_{\text{tot}} \approx 400\,\text{m}$, consists of 13 continuous spans with an average span of 30 m, and cross sections built by V-shaped prestressed concrete segments with a depth of 1, 80 m subsequently assembled to a continuous superstructure. Nevertheless, the connections between superstructure and piers are achieved using bearings, see Fig. 3.53(b). Temperature parametric studies are performed for uniform temperature components between -20 to $+20\,\text{K}$ and vertical temperature gradients of $+10$ and $-5\,\text{K}$ which are combined by $\omega_M \Delta T_M + \Delta T_N$ with $\omega_M = 0.75$. Loose, medium, and dense sets of soil properties are additionally considered in the parametric study. These indirect loading conditions (positive or negative temperature variations) induce axial forces in the girders and abutments, which are key factors in evaluating the bridge's response. Variability in soil conditions significantly affects the bending moment near the abutments and the axial force in the superstructure. This effect is even more evident for negative temperature changes [425]. Different characteristics in the stiffness due to passive and active soil pressures determine the lower significance for positive temperature changes. Hence, negative temperature variations should be considered with extreme caution. However, the soil-structure interaction may also be important for thermal expansion of the superstructure in such conditions where the abutments are deformed into the backfill [232].

A study by HUANG et al. [182], analysed similar integral abutment bridges using a parametric analysis with uniform temperature changes. The corresponding numerical 3-D Finite Element model is shown in Fig. 3.53(a). One major finding is that for the same total bridge length, bridges with shallow superstructures and more spans performed better than bridges with deep girders and fewer spans. Moreover, size and orientation of the wingwalls are not considerably significant in terms of the structural load-deformation behaviour. Nevertheless, wingwalls which are perpendicular to the direction of traffic induce the greatest superstructure curvatures and stresses in compression at the bottom girder flange. This is assessed by their larger restraint of the abutment backfill soil pressure to the bridge expansion. Pile curvatures and substructure deformations are assessed to be negligible with the studied parameter range.

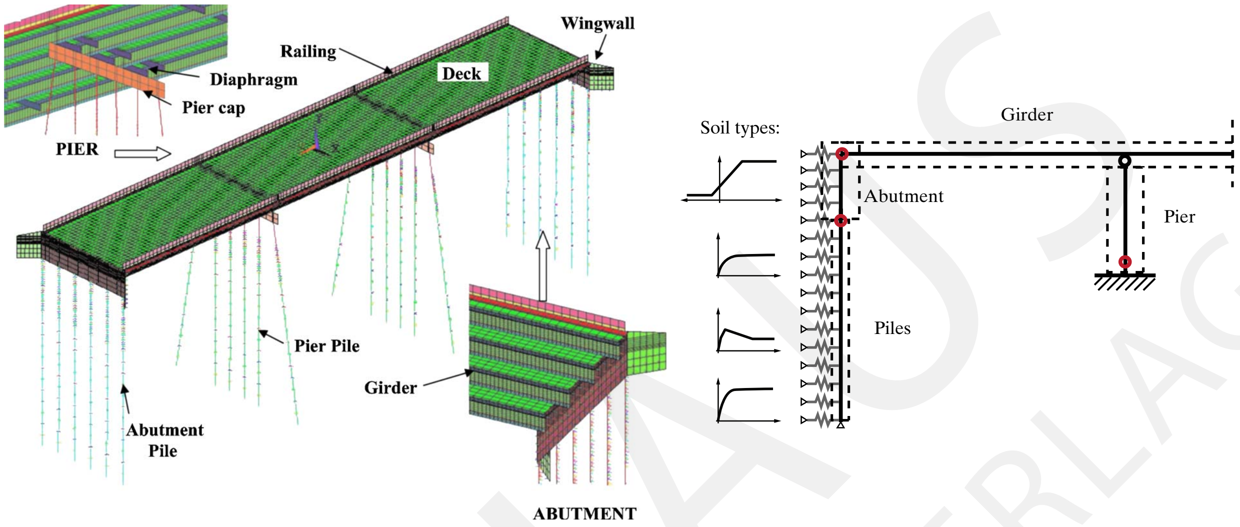

(a) 3-D Finite Element bridge model [182] (b) 2-D Finite Element bridge model [424]

Figure 3.53: Analysis of integral abutment bridges

In the study by Pugasep et al. [326], three integral abutment bridges are monitored since November 2002, November 2003, and September 2004. The assessment of the measured responses indicates that bridge deformations progress over time significantly affect the entire bridge response. Hence, long-term response analysis considering the time-dependent effects caused by concrete shrinkage, creep, prestressing, and strand relaxation are also significant factors in the design of integral abutment bridges. A similar conclusion is assessed in the study of Kim et al. [214, 215]. Structural response due to measured and numerical results indicates the significant influence of the time-dependent long-term effects of concrete components and soil-structure interaction. Moreover, less rotational stiffness and non-linear material behaviour of the abutment-to-backwall connections are assessed to influence the long-term structural behaviour. A parametric study is performed by varying thermal expansion coefficient, bridge length, backfill height, backfill stiffness, and pile soil stiffness with three magnitudes for each parameter considering a variation of practical bridge relevance. A direct correlation is found by increasing the total bridge length which leads directly to an increasing abutment displacement, girder bending moment, and girder axial force. The bending moments in the superstructure are mainly caused by thermal action and should be considered in the design. The thermal expansion coefficient is a highly sensitive parameter, which influences the superstructure axial force and moment, lateral force at the piles, pile moment and the displacement at the section between pile head and abutment, significantly. Height and stiffness of the backfill are evaluated to be relatively insignificant in terms of the bridge behaviour.

Ooi et al. [302, 304] monitored an integral abutment bridge over a period of 45 months. Additionally, the work mentioned other studies, in which integral bridges in the United States were field-instrumented and parametric studies were performed on integral abutment bridges. The measurements show the importance of deep seated soil movements, concrete creep and shrinkage, and thermal variations for the cumulative structural displacements.

A fully integral abutment bridge was designed for the "*Taxiway Bridge East 1*" at the Frankfurt Airport in Germany and was completed in the summer of 2011 [386]. In total, 5 integral taxiway bridges are designed in order to connect the new Northwest runway with the existing airport. The "east 1" bridge is the largest one with an overall deck area of about $20,000\,\mathrm{m}^2$, see Fig. 3.54(a). This frame bridge consists of three spans with the spans $32.8 - 29.7 - 26.0\,\mathrm{m}$ without any expansion joints or bearings. In order to reduce the earth pressure at the abutment walls, flexible abutments are adjusted on-site using polystyrene-layers in the backfill soil, see Fig. 3.54(b). Therefore, bridge contraction due to temperature, creep, and shrinkage causes no movement or gaps in the backfill.

The bridge is designed for a total load of 750 t, accounting for all current models for aircraft. Nevertheless, the modelling and limitation of restraint effects are very significant criteria for the design of this integral bridge. The foundations should be less stiff in comparison to conventional bridges and, therefore, only one pile row is designed to support the abutment walls. The restraint effects are initially analysed based on the linear-elastic stiffness, which results in enormous restraint forces and much higher tensile stresses in the concrete, exceeding its tensile strength. Therefore, stiffness degradation considering the tension-stiffening effect is considered in a non-linear structural analysis which approximately results in an cracked stiffness of about $0.8EI^I$ in the abutment walls and $0.6EI^I$ in the superstructure. The restraint condition for uniform temperature contraction of $\Delta T_N = -27\,\mathrm{K}$ mainly induces these high restraint forces and stiffness degradation, see Fig. 3.54(c). Based on the non-linear simulation, the amount of reinforcement in initial design of highly-reinforced sections based, on the linear-elastic stiffness could, therefore, be decreased in order to obtain a reliable and economical bridge project.

In conclusion, decoupling of the structural components is not an appropriate assumption in the numerical simulation of integral bridges. Numerous phenomena of the components (superstructure, piers, piles, abutment, backfill, soil) and their interactions lead to a load-deformation behaviour of the bridge, while performing as a single structural unit. The interplay among the stiffness of these structural components strongly influences the structural response and finally the entire design. Therefore, a global structural model should consider a direct coupling between these components for a simulation of the entire integral bridge. Iterative and non-linear analyses are commonly required in order to obtain results with high accuracy in comparison to measurements. Nevertheless, appropriate results may be analysed assuming linear abutment backfill and foundation soil behaviour in the structural model for short to medium span integral bridges [82]. In every one of the above mentioned integral bridges, the restraint effects are some of the most significant phenomena in the simulation and design of the bridges. Even the measuring data collected in long-term monitoring programs illustrate the crucial importance of restraint effects. The analysis of restraint effects should be performed using adequate models in order to achieve a reliable design of the entire integral structure. Semi-integral concrete bridges are studied in this thesis by the integrative sensitivity analysis in order to evaluate the structural load-deformation behaviour in a quantitative manner, see Sec. 6.3.

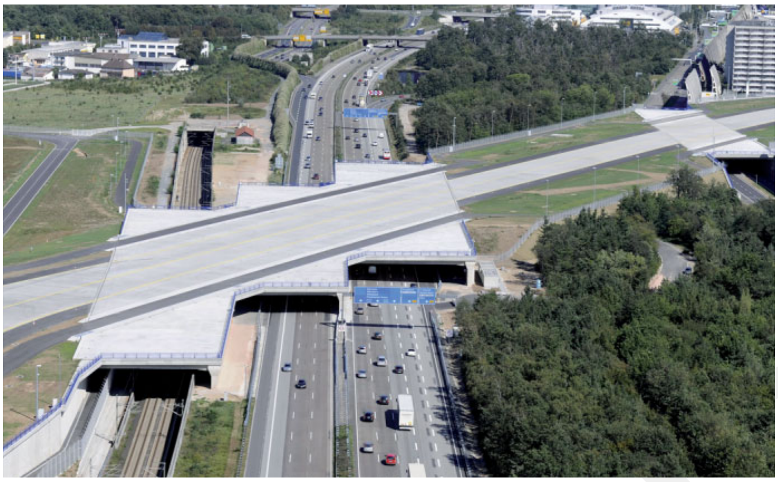

(a) completed bridge

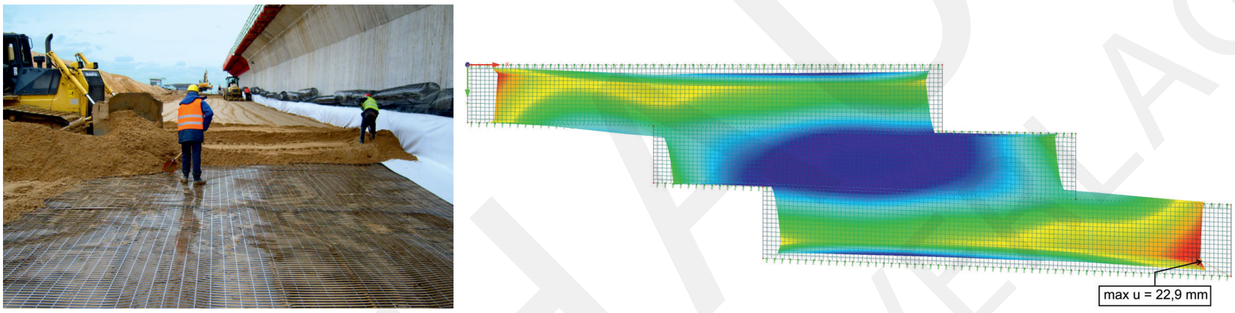

(b) flexible abutment (c) significant design restraint loading $\Delta T_N = -27\,\mathrm{K}$

Figure 3.54: Integral bridge "*Taxiway Bridge East 1*" at Frankfurt Airport [386]

3.6 Pile foundation

3.6.1 Vertically loaded piles

Vertical loading of pile groups can be analysed using analytical solutions and numerical techniques. The integral equation method (also known as Boundary Element Method, BEM) adopted by POULOS [316], POULOS and DAVIS [319], BUTTERFIELD and BANERJEE [56, 57], and BUTTERFIELD and DAVIES [18] is a commonly used numerical method based on the analytical solution of *Mindlin* [280]. The study by OTTAVIANI [305] is a fundamental approach of pile group settlement behaviour based on the Finite Element Method.

Furthermore, a number approximate analytical and semi-analytical solutions are investigated by COOKE [76], RANDOLPH and WROTH [332, 334], BAGUELIN and FRANK [14], SCOTT [375], NOGAMI and CHEN [297], CHOW [71], and FLEMING et al. [112, 113]. The maximum permissible foundation settlement is often a more stringent design criterion than the overall stability of the construction [332]. Therefore, single pile and pile group settlements need to be estimated with a reasonable accuracy.

A rather high number of different models for each methodology exists, which differs in their considered phenomena for the piles, their interaction in the group and the soil conditions. The research by RANDOLPH and WROTH about the behaviour of single piles [332] (see Fig. 3.55) and pile groups [334] is cited in almost every publication following and can be declared as a fundamental approach to determine the vertical stiffness of piles and piles groups.

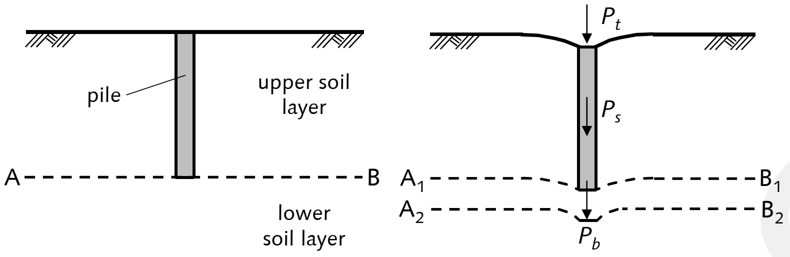

(a) upper and lower soil layers (b) separate deformation patterns

Figure 3.55: Decoupling between effects due to pile shaft and pile base, based on [332]

3.6.1.1 Single pile

Randolph and Wroth 1979 [332, 334]

The analysis is based on a linear-elastic soil description characterised by the shear modulus G_s, which may vary with depth, and *Poisson*'s ratio ν_s. The soil surrounding the pile is divided into two layers. The horizontal plane (AB) at the pile base level divides the soil into an upper and a lower layer, see Fig. 3.55(a). As an initial assumption, the upper soil layer is deformed exclusively by the load shed by the pile shaft P_s. The lower layer is deformed exclusively by the pile base load P_b. Consequently, separate deformation patterns are anticipated, see Fig. 3.55(b). The original plane (AB) is spread out to the planes (A_1B_1) and (A_2B_2). Both deformation patterns are not compatible, which lead to some interaction between both soil layers. These separate deformation patterns will be matched at the pile base and at large radii. The authors already indicate that these simplified assumptions cannot determine an exact solution, but a satisfactory solution for engineering purposes may be obtained [332]. Especially for piles with a slenderness ratio of $l_P/r_0 > 20$, the stress changes in the soil caused by load transfer at the pile base can be uncoupled from those caused by the load transfer down the pile shaft and the above mentioned assumption may be accurate enough.

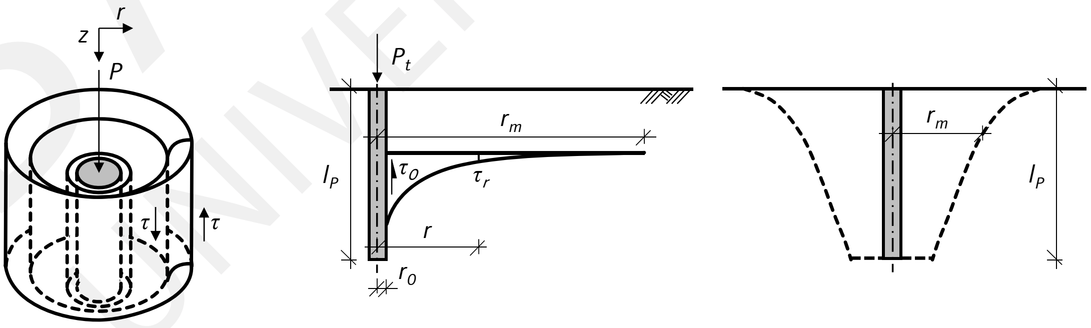

(a) Concentric cylinders describing the deformation process around pile shaft (b) Shear stress distribution with radial distance from pile shaft, based on [76] (c) Hypothetical variation of pile influence limit

Figure 3.56: Deformation mode and hypothetical pile influence variation, based on [332]

The soil deformation around the pile shaft may be idealized as shearing of concentric cylinders [332], see

Fig. 3.56(a). In the study by COOKE [76], the comparison between the resulting deformation patterns, based on this assumption and pile test measurements, shows a good agreement. Moreover, BAGUELIN [13] and FRANK [116] used Finite Element analysis to prove the validity of the assumption. The vertical equilibrium of a soil element is defined as:

$$\frac{\partial}{\partial r}(r\tau) + r\frac{\partial \sigma_z}{\partial z} = 0\,, \tag{3.110}$$

in which r is the radius, τ is the shear stress increment, and σ_z the vertical total stress increment (compressive stress is positive). The increase in shear stress is much greater in the pile shaft vicinity than the increase in vertical stress and thus Eq. 3.110 can be approximated by:

$$\frac{\partial}{\partial r}(r\tau) \cong 0\,. \tag{3.111}$$

The shear stress at the pile shaft for $r = r_0$ is defined as τ_0. The integration of Eq. 3.111 gives:

$$\tau = \frac{\tau_0 r_0}{r}\,. \tag{3.112}$$

The shear strain γ is:

$$\gamma = \frac{\tau}{G} = \frac{\partial u}{\partial z} + \frac{\partial w}{\partial r}\,, \tag{3.113}$$

in which u is the radial and w the vertical soil displacement. The primary displacement is vertical and thus ignoring $\partial u/\partial z$, integration leads to:

$$w_s \cong \frac{\tau_0 r_0}{G_s}\int_{r_0}^{\infty}\frac{\mathrm{d}r}{r} \tag{3.114}$$

in which w_s is the **pile shaft settlement**. An infinite pile settlement may occur based on this expression, which is generally not appropriate. Therefore, the basic assumption is that there is some “magical radius” r_m at which the shear stress becomes negligible [76, 116], see Fig. 3.56(b), and thus:

$$w_s(r) = \ln\left(\frac{r_{m,s}}{r}\right)\frac{\tau_0 r_0}{G_s} \qquad r_0 \le r \le r_m \tag{3.115a}$$

$$w_s(r) = 0 \qquad r > r_m \tag{3.115b}$$

and the deformation at the pile shaft is:

$$w_s(r_0) = \zeta\frac{\tau_0 r_0}{G_s} \tag{3.115c}$$

in which

$$\zeta = \ln\left(\frac{r_{m,s}}{r_0}\right)\,. \tag{3.115d}$$

The lower soil layer is deformed by the pile base acting as a rigid punch and at some large distance from the pile the base acts as a point load. Hence, the deformation of the plane (A_2B_2) decreases approximately inversely with radius r, see Fig. 3.55(b). Because this decrease is more rapid than the logarithmic variation defined by Eq. 3.114, the lower soil layer act as a restraint on the deformation of the upper layer. Hence, the vertical stress increments rise and nonzero terms in $\partial/\partial_r(r\tau)$ appear. For the shear stress τ acting as shown in Fig. 3.56(a), this latter inequality implies that the shear stress decreases more rapidly with r than determined by Eq. 3.112. With vertical distance above the plane (A_1B_1), see Fig. 3.55(b), the magnitude of the term $\partial/\partial_r(r\tau)$ increases. Therefore, the radius at which the shear stress becomes negligible r_m varies with depth and follows the shape as illustrated in Fig. 3.56(c). For a rigid pile, the pile shaft displacement w_s must be independent of depth and, thus, the shear stress τ_0 must also vary with depth in such a fashion that $(\tau_0 r_0/G_s)\ln(r_{m,s}/r_0)$ is constant. This variation of the shear stress at the interface between the pile and the soil is supported by the studies of Butterfield and Banerjee [56, 57], Frank [116], Ottaviani [305], and Poulos [316].

The displacements caused by loading a half space of a given shear modulus are proportional to $1-\nu_s$ [393]. Therefore, the stresses set up by the incompatibility of the displacement patterns along the planes (AB), see Fig. 3.55(b), vary in some fashion inversely with $1-\nu_s$. As a first approximation, the "magical" radius can be defined as proportional to $1-\nu_s$ [332]. In addition, the mean value of this radius is also proportional to the pile length l_P, thus $r_m \propto l_P(1-\nu_s)$. In a comparative study with the results obtained by integral equation analysis by Baguelin [13] and Frank [116], a suitable value for the average "magical" radius $r_{m,s}$ is determined by Randolph and Wroth [332]:

$$r_{m,s} = 2.5 \cdot l_P\,(1-\nu_s) \tag{3.116}$$

In general, the variation of the "magical" radius with depth is neglected and a single average value as defined by Eq. 3.116 is used in the study by Randolph and Wroth [332]. Moreover, the overall load deformation behaviour of the pile shaft is important and consequently it is sufficient to take $r_{m,s}$. Thus, for a rigid pile τ_0 is constant with depth. Hence, the determination of w_s according to Eq. 3.115 may be written as:

$$w_s = \zeta\frac{\tau_0 r_0}{G_s} = \frac{\zeta P_s}{2\pi l_P G_s}\,. \tag{3.117}$$

In general, the shear stress τ_0 is proportional to the shear modulus at a certain depth assuming a constant shear strain in the soil next to the pile shaft [116]. For soils where the shear modulus varies linearly with depth ("Gibson"-type soil [145, 146]), a factor for the degree of soil homogeneity ρ_{dsh} (see Fig. 3.61(b)) can be considered in the analysis by Randolph and Wroth [332, 334], which is defined as:

$$\rho_{\mathrm{dsh}} = \frac{G_{s,l_P/2}}{G_{s,l_P}}\,, \tag{3.118}$$

in which $G_{s,l_P/2}$ and G_{s,l_P} are the shear modulus at pile mid-depth and pile base, respectively. Consequently, the "magical" radius is defined as:

$$r_{m,s} = 2.5 \cdot \rho_{\mathrm{dsh}} \cdot l_P\,(1-\nu_s)\,, \tag{3.119}$$

and the pile shaft displacement is determined by:

$$w_s = \frac{\zeta P_s}{2\pi l_P \cdot \rho_{\mathrm{dsh}} \cdot G_{s,l_p}}\,. \tag{3.120}$$

The **pile base settlement** behaviour is similar to a rigid punch and can be described by the solution of TIMOSHENKO and GOODIER [393]:

$$w_b = \frac{P_b\,(1-\nu_s)}{4r_0\,G_s}\cdot\eta\,. \tag{3.121}$$

The factor η is defined in order to consider the depth of pile base below the surface, i.e. the interaction between the upper and lower soil layer. The original solution according to Eq. 3.121 (neglecting η) is determined for a punch at the surface of an elastic half space. Therefore, the factor η is established in order to take into account for the soil stiffening effect above the level of the loaded area. For a general case, a closed form solution is no longer possible and correction factors must be used. For a straight pile (i.e. not underreamed), $\eta > 0.85$ and is probably close to unity. For the overall analysis of pile behaviour, the correction factor η can be taken as unity $\eta = 1.0$ [332].

At some distance from the pile base, the loading will act as a point load. For a point load, the settlement decreases with the radius and is defined as:

$$w(r) = \frac{P\,(1-\nu_s)}{2\pi r G_s}\,. \tag{3.122}$$

The ratio between the point load settlement (Eq. 3.122) and the pile base settlement (Eq. 3.121) for a given load is:

$$\frac{w(r)}{w_b} = \frac{2}{\pi}\cdot\frac{r_0}{r}\,. \tag{3.123}$$

The settlement caused by the pile base at large radii should be equal to the settlement caused by a point load. Hence, the settlement profile at the top of the lower layer in Fig. 3.55(b) may be approximated by:

$$w(r) = w_b\cdot c\cdot\frac{r_0}{r}\,, \tag{3.124}$$

with $c = 2/\pi$ according to Eq. 3.123.

By combining w_s and w_b, a reasonable estimate for the deformation of a rigid pile in an homogeneous linear-elastic continuum can be determined, which is additionally checked against numerical simulations [332]. This determination provides a simple basis that may be modified to account for non-homogeneity of certain soil stratification.

In the case of a rigid pile, $w_t = w_s = w_b$ and $P_t = P_s + P_b$. The **overall pile behaviour** can be defined by combining Eq. 3.121 and Eq. 3.117:

$$\frac{P_t}{G_s r_0 w_t} = \frac{P_b}{G_s r_0 w_b} + \frac{P_s}{G_s r_0 w_s}\,, \tag{3.125a}$$

$$\frac{P_t}{G_s r_0 w_t} = \frac{4}{\eta\,(1-\nu_s)} + \frac{2\pi\rho_{\mathrm{dsh}}}{\zeta}\frac{l_P}{r_0}\,, \tag{3.125b}$$

$$K_{v,\mathrm{lin}} = \frac{P_t}{w_t}\,. \tag{3.125c}$$

Applying this determination for the pile stiffness prediction of a rigid pile in an homogeneous soil shows good agreement with the Boundary Element Method (BANERJEE [17]), see Fig. 3.57. The dimensionless load-settlement ratio $P_t/(G_s r_0 w_t)$ for several pile slenderness ratios l_P/r_0 and two different *Poisson*'s ratios, $\nu_s = 0.0$ and $\nu_s = 0.5$, is almost the same between both models.

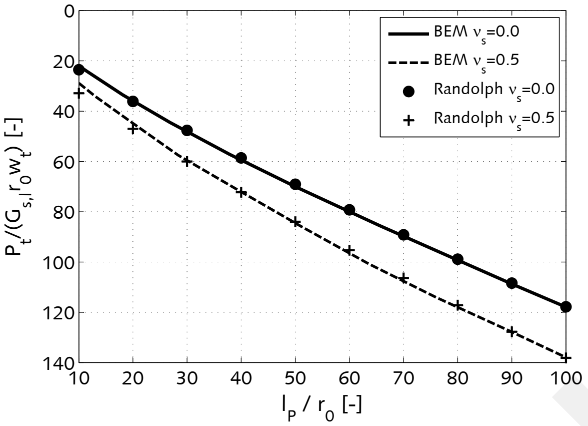

Figure 3.57: Load-settlement ratio for several pile slenderness ratios based on [332] in comparison with Boundary Element Method (BEM) [17]

This solution determined by Eq. 3.125a may be extended to the case of compressible piles [332], underreamed piles, and end-bearing piles. Only minor modifications are necessary, for example, the "magical" radius is reduced for the latter type of piles [333]. In this thesis, the pile compressibility and soil inhomogeneity in the radial pile direction are not considered in the previously introduced model.

Mylonakis and Gazetaz 1998 [291]

The aim of the study by MYLONAKIS and GAZETAS [291] is the development of a straightforward and effective methodology for pile group settlement analysis even for multi-layered soil stratification, see Fig. 3.58. The pile cap is assumed to be rigid and each soil layer is considered by a linear-elastic material with the soil modulus of elasticity E_i and the *Poisson*'s ratio $\nu_{s,i}$. Furthermore, no slippage is considered at the pile-soil interface. This method is generally applicable to groups containing different pile sizes and properties. However, the presented method is limited to identical, solid, cylindrical piles of pile length l_P, diameter d_P, cross-sectional area A_P, and modulus of elasticity E_P. The soil below the pile tip extends either to infinity (half-space, $h_b \to \infty$) or can be determined at the depth of bedrock, which is located at a depth h_b measured from the pile tip.

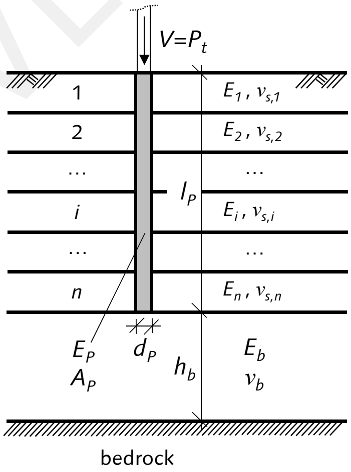

Figure 3.58: Sign convention for pile foundation with multi-layered soil stratification, based on [291]

The soil around a pile shaft can be represented by distributed springs (*Winkler* assumption) as determined by the model of RANDOLPH and WROTH [332], see Eq. 3.117. The stiffness per unit length of the pile can be written as:

$$k_z = \frac{P_s}{w_s} = \delta \cdot G_s\,, \tag{3.126a}$$

where

$$\delta = \frac{2\pi}{\ln\left(\dfrac{2r_m}{d_P}\right)}\,, \tag{3.126b}$$

with the dimensionless pile shaft load transfer parameter λ

$$\lambda = \sqrt{\frac{\delta G_s}{E_P A_P}}\,. \tag{3.126c}$$

In accordance with [332], the magical radius r_m is determined:

$$r_{m,\mathrm{s}} \approx \chi_1 \chi_2 \cdot l_P \left(1 - \nu_s\right)\,, \tag{3.127}$$

in which χ_1 and χ_2 are empirical factors to account for soil inhomogeneity [291]. In the study by RANDOLPH et al. [332], the recommended values are defined to be $\chi_1 = 2.5$ for piles in a half-space ($h_b \to \infty$) and $\chi_1 = 2.0$ for soil on rigid bedrock at a depth $2.5 l_P$. For a homogeneous half-space with the degree of homogeneity $\rho_{\mathrm{dsh}} = 1.0$ (see Fig. 3.61(b)), the empirical value of χ_2 is about 1.0. In contrast, χ_2 is about 0.5 for a soil with stiffness proportional to depth with $\rho_{\mathrm{dsh}} = 0.5$. For a multi-layered soil, it might be necessary to interpolate between the empirical values. However, the vertical pile stiffness is insensitive to the exact value of the "magical" radius r_m. For example, a large simulated difference in r_m of 50 %, results in a discrepancy between the interaction factors of less than 15 % [291], even for a pile group. This highest discrepancy is found for large pile space ratios in the range of $s/d_P = 10$. For piles more closely spaced, the average deviation is about 5 %. Therefore, engineering judgement in accordance with the recommendations of RANDOLPH et al. [332] is sufficient and MYLONAKIS et al. [291] recommend using the following values for analysing the settlement of single piles and pile groups:

- $\chi_1 \chi_2 = 2.5$ for homogeneous half-space soil condition,
- $\chi_1 \chi_2 = 1.0$ for "Gibson"-soil on bedrock condition.

The pile base behaviour is represented by a rigid circular disc on a surface of a homogeneous elastic stratum, which is sufficient, to adopt the arguments of [332, 375]. Hence, the corresponding pile base stiffness is defined as:

$$K_b = \frac{P_b}{w_b} \approx \underbrace{\frac{d_P E_b}{1 - {\nu_s}^2}}_{\text{RANDOLPH et al. [332], SCOTT [375]}} \cdot \underbrace{\left(1 + 0.65 \frac{d_P}{h_b}\right)}_{\text{GAZETAS [125], KAUSEL [202]}}\,, \tag{3.128a}$$

with the dimensionless pile base stiffness Ω [291]:

$$\Omega = \frac{K_b}{E_P A_P \lambda}\,. \tag{3.128b}$$

In order to take into account the presence of a rigid bedrock at depth equal to h_b below the pile tip, the factor in parentheses in Eq. 3.128a is additionally considered in comparison to the fundamental approach by RANDOLPH et al. [332]. In the case that no bedrock is present, $h_b \to \infty$ and the second term reduces to unity.

For a multi-layered soil stratification with n different soil layers, the settlement profile $W_{11}(z)$ (see Fig. 3.62) for each homogeneous layer can be determined by [291]:

$$W_{11}(z) = A_{11}\mathrm{e}^{(\lambda z)} + B_{11}\mathrm{e}^{(-\lambda z)} \,. \tag{3.129}$$

with the integration constants shown in the appendix, see Eq. A.2. Imposing the continuity of forces and displacements at each interface between the soil layers, a transfer matrix formulation can be established:

$$\begin{Bmatrix} W_{11}(h) \\ P_{11}(h) \end{Bmatrix}_{bb} = [\mathbf{F}] \begin{Bmatrix} W_{11}(0) \\ P_{11}(0) \end{Bmatrix}_{1} \,, \tag{3.130}$$

where

$$[\mathbf{F}] = [\mathbf{L}]_b \prod_{i=1}^{j} \left([\mathbf{L}]_i\right) \,. \tag{3.131}$$

The transfer matrix $[\mathbf{L}]_i$ is defined as:

$$[\mathbf{L}]_i = \begin{bmatrix} \cosh\left(\lambda_i h_i\right) & -\left(E_P A_P \lambda_i\right)^{-1} \sinh\left(\lambda_i h_i\right) \\ E_P A_P \lambda_i \sinh\left(\lambda_i h_i\right) & \cosh\left(\lambda_i h_i\right) \end{bmatrix} \tag{3.132}$$

and $[\mathbf{L}]_b$ is defined as:

$$[\mathbf{L}]_b = \begin{bmatrix} 1 & -K_b^{-1} \\ 0 & 1 \end{bmatrix} \,. \tag{3.133}$$

The stiffness of a single pile is obtained by enforcing the boundary conditions $W_{11}(h)_{bb} = 0$ and $W_{11}(0)_1 = 1$ from Eq. 3.130:

$$K_{v,\mathrm{lin}} = -\frac{F_{11}}{F_{12}} \,. \tag{3.134}$$

The vertical stiffness of a pile in a **homogeneous soil layer** can be computed by a closed-form expression considering the sign convention according to Fig. 3.63(a). The linear-elastic single pile stiffness, due to vertical loading, can be determined by:

$$K_{v,\mathrm{lin}} = E_P A_P \cdot \lambda \cdot \frac{\Omega + \tanh(h\lambda)}{1 + \Omega \tanh(h\lambda)} \,. \tag{3.135}$$

In the case of a pile embedded in a **two-layer soil** (sign convention see Fig. 3.63(b)), the vertical stiffness of a single pile subjected to axial force can be determined by another closed-form expression:

$$K_{v,\mathrm{lin}} = E_P A_P \lambda_1 \frac{\lambda_1 \tanh\left(h_1\lambda_1\right) + \lambda_1\Omega \tanh\left(h_1\lambda_1\right) \tanh\left(h_2\lambda_2\right) + \lambda_2\Omega + \lambda_2 \tanh\left(h_2\lambda_2\right)}{\lambda_1 + \lambda_1\Omega \tanh\left(h_2\lambda_2\right) + \lambda_2\Omega \tanh\left(h_1\lambda_1\right) + \lambda_2 \tanh\left(h_1\lambda_1\right) \tanh\left(h_2\lambda_2\right)} \,, \tag{3.136a}$$

with the corresponding dimensionless pile shaft load transfer parameters:

$$\lambda_1 = \sqrt{\frac{\delta G_{s,1}}{E_P A_P}} \quad \Rightarrow h_1 \,, \tag{3.136b}$$

$$\lambda_2 = \sqrt{\frac{\delta G_{s,2}}{E_P A_P}} \quad \Rightarrow h_2 \,. \tag{3.136c}$$

BAUHAUS
UNIVERSITÄTSVERLAG

It should be noted that by setting $h_1 = 0$, the stiffness determination according to Eq. 3.136 reduces to the stiffness for the homogeneous (single-layer) soil condition, see Eq. 3.135.
In order to illustrate the accuracy of the stiffness prediction and to justify the choice of the empirical values χ_1, χ_2, the model by MYLONAKIS et al. [291] is compared with the numerical solutions of POULOS and DAVIS [320], and the Finite Element results of VALLIAPPAN [400]. Therefore, the stiffness predictions are compared for an incompressible pile embedded in a two-layer soil deposit, see Fig. 3.59.

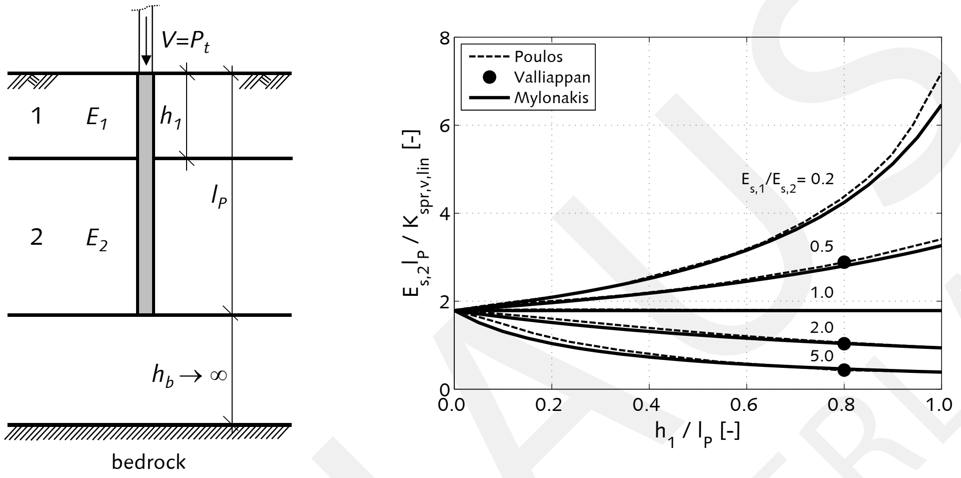

(a) geometry and soil condition (b) settlement factor $E_2 l_P / K_{v,\mathrm{lin}}$ - embedment ratio h_1/l_P

Figure 3.59: Comparison of settlement prediction for incompressible pile in two-layer soil, $\chi_1 = 2.5$, $\chi_2 = 1.0$, MYLONAKIS and GAZETAS [291], POULOS and DAVIS [320], and VALLIAPPAN et al. [400]

For the two-layer soil condition, the empirical values $\chi_1 = 2.5$, $\chi_2 = 1.0$ are still used for the determination of the "magical" radius. The bottom soil layer is related to the half-space condition and the corresponding ratio between the moduli of elasticity are investigated in the range from 0.2 to 5.0. Moreover, the embedment ratio h_1/l_P varies from 0 ($h_1 = 0$) to 1 ($h_1 = l_P$). The comparison shows a very good agreement between the stiffness prediction based on the previously discussed model and the numerical solutions of POULOS et al. [320] and VALLIAPPAN [400].

3.6.1.2 Pile group

Randolph and Wroth 1979 [334]

In the case of similarly loaded neighbouring piles, the overall pile settlement can be obtained by superimposing the individual displacements fields [76]. The settlement of two rigid piles is defined as the sum of the settlement caused by the piles' own loading w_1 and that due to the neighbouring piles' displacement field w_2. Therefore, the overall settlement may be described by:

$$w = w_1 + w_2 \,. \tag{3.137}$$

The displacement at the pile mid-depth is consequently defined as:

$$w_s = w_{s,1} + w_{s,2} = \frac{\tau_0 r_0}{G_{s,l_P}} \left[\ln\left(\frac{r_m}{r_0}\right) + \ln\left(\frac{r_m}{r_{ij}}\right) \right] , \tag{3.138}$$

in which r_{ij} is the pile spacing. This spacing is defined as the distance between the centre lines of the piles. The load-settlement ratio for each pile shaft is now:

$$\frac{P_s}{G_{s,l_P} r_0 w_s} = \frac{2\pi \rho_{\text{dsh}}}{\zeta + \ln\left(\frac{r_m}{r_{ij}}\right)} \frac{l_P}{r_0} \,. \tag{3.139}$$

For the pile base settlement, the overall displacement is similarly defined as:

$$w_b = w_{b,1} + w_{b,2} = \frac{P_b \left(1 - \nu_s\right)}{4 r_0 G_{s,l_P}} \left(1 + \frac{c r_0}{r_{ij}}\right) \,, \tag{3.140}$$

and the load-settlement ratio can be determined by:

$$\frac{P_b}{G_{s,l_P} r_0 w_b} = \frac{4}{1 - \nu_s} \frac{r_{ij}}{r_0 c + r_{ij}} \,. \tag{3.141}$$

Finally, the overall load-settlement ratio for two, three, and four **similarly loaded piles** is defined as:

$$\left(\frac{P_t}{G_{s,l_P} r_0 w_t}\right)_{\text{2 piles}} = \frac{4}{1 - \nu_s} \frac{s}{r_0 c + s} + \frac{2\pi \rho_{\text{dsh}}}{\zeta + \ln\left(\frac{r_m}{s}\right)} \frac{l_P}{r_0} \,, \tag{3.142}$$

$$\left(\frac{P_t}{G_{s,l_P} r_0 w_t}\right)_{\text{3 piles}} = \frac{4}{1 - \nu_s} \frac{s}{2 r_0 c + s} + \frac{2\pi \rho_{\text{dsh}}}{\zeta + 2\ln\left(\frac{r_m}{s}\right)} \frac{l_P}{r_0} \,, \tag{3.143}$$

$$\left(\frac{P_t}{G_{s,l_P} r_0 w_t}\right)_{\text{4 piles}} = \frac{4}{1 - \nu_s} \frac{s}{2.707 r_0 c + s} + \frac{2\pi \rho_{\text{dsh}}}{\zeta + \ln\left(\frac{{r_m}^3}{\sqrt{2} s^3}\right)} \frac{l_P}{r_0} \,. \tag{3.144}$$

The determination for piles in a group of three (Eq. 3.143) is only valid for an equilateral triangle of a side length equal to s, see Fig. 3.60. Moreover, the determination for piles in a group of four (Eq. 3.144) is applicable for a square group of a side length equal to s.

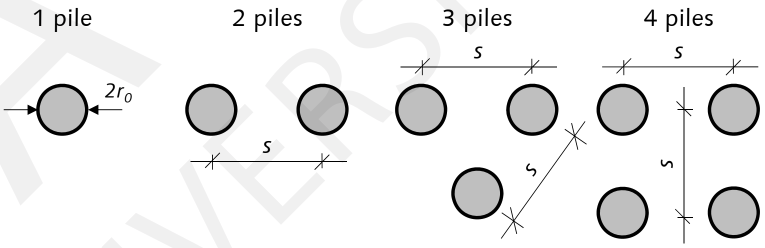

Figure 3.60: Spacing definition of similarly loaded piles, based on [334]

Based on these results, the interaction factor α_t can be defined as the inverse of the load-settlement ratio. For example, the decreased settlement of two similarly loaded piles (Eq. 3.142) in comparison to a single pile (Eq. 3.125) for a given load can be written as:

$$\left(\frac{G_{s,l_P} r_0 w_t}{P_t}\right)_{\text{2 piles}} = \left(1 + \alpha_t\right) \left(\frac{G_{s,l_P} r_0 w_t}{P_t}\right)_{\text{1 pile}} \,. \tag{3.145}$$

The concept of interaction factors is originally introduced by POULOS [316]. This study showed that the effects in pile groups can be assessed by superimposing the effects of only two piles at a time. In general, the interaction factors are useful for considering a part of the increasing settlement of one pile, due to a neighbouring pile, but they neglect the transfer of a higher proportion of load to the pile base that would occur for a single pile [144, 334]. This greater interaction is caused between the shaft and base displacement fields which finally lead to a higher load transfer to the pile base in pile groups compared to the deformation behaviour of a single pile. Therefore, the pile-to-pile interaction in a group of piles leads to a [291]:

- decrease in group stiffness,
- non-uniformly distributed cap load,
- additional shear stresses along pile shaft, and
- increased load transmitted to pile base.

Finally, each pile in a group of piles receives a different amount of the total load P_t, with the corner piles carrying more load than the central piles. Therefore, the analysis of similarly loaded pile groups, based on the interaction factor concept, is enhanced to the **analysis of rigid pile groups**, considering a generalised methodology for the settlement contributions. The model could be applied to any general geometry of pile groups. The only restriction being that all piles must be embedded to the same depth. For a pile group of n_P piles, the pile shaft settlement $[\mathbf{w}_s]_j$ of pile j is defined as:

$$[\mathbf{w}_s]_j = \sum_{i=1}^{n_P} [\mathbf{w}_s]_{ij} = \frac{1}{G_s} \sum_{i=1}^{n_P} [\tau_0]_i [\mathbf{r}_0]_i \ln\left(\frac{r_{m,\mathrm{g}}}{r_{ij}}\right) , \tag{3.146}$$

where $r_{ij} = r_0$ for $i = j$. The n_P different settlements can be related to the corresponding shear stresses τ_0, based on Eq. 3.146, to provide the following matrix equation [334]:

$$\mathbf{w}_s = [\mathbf{F}_s]\tau_0 , \tag{3.147a}$$

$$\tau_0 = [\mathbf{F}_s]^{-1}\mathbf{w}_s , \tag{3.147b}$$

$$\mathbf{P}_s = 2\pi r_0 l_P [\tau_0] . \tag{3.147c}$$

The base settlements can be determined by:

$$[\mathbf{w}_b]_j = \sum_{i=1}^{n_P} [\mathbf{w}_b]_{ij} = \frac{c\,(1-\nu_s)}{4G_{s,l_P}} \sum_{i=1}^{n_P} \frac{[\mathbf{P}_b]_i}{r_{ij}} , \tag{3.148}$$

in which $r_{ij} = c \cdot r_0$ for $i = j$. In a similar manner, the base settlements can be related to the pile base load defining another matrix equation:

$$\mathbf{w}_b = [\mathbf{F}_b]\mathbf{P}_b , \tag{3.149a}$$

$$\mathbf{P}_b = [\mathbf{F}_b]^{-1}\mathbf{w}_b . \tag{3.149b}$$

For a rigid pile cap, $[w_s]_i = [w_s]_j$, and for rigid or very stiff piles ($(EA)_P/(GL_P{}^2) \geq 10$), $w_s \cong w_b$. Therefore, the matrix Eq. 3.147a and Eq. 3.149a may be inverted to determine values of τ_0 and P_b for a given pile cap displacement, see Eq. 3.147b and Eq. 3.149b. Thus, the overall load-settlement ratio for the pile group can be computed by:

$$K_{v,\mathrm{lin}} = \sum_{i=1}^{n_P} \frac{\mathbf{P}_{t,i}}{\mathbf{w}_{t,i}} \tag{3.150}$$

The definition of the "magical" radius for single piles $r_{m,\mathrm{s}}$ and pile groups $r_{m,\mathrm{g}}$ may be different. A more extensive influence zone for a pile group is clearly expected compared to a single pile of the same pile length [334]. In general, the value of r_m is related to the amount of interaction between the upper and lower soil layers [332]. In the case that the pile group base is considered as a single, large, rigid punch, the deformation of the lower soil layer decreases more gradually with increasing radius. Thus, this reduces the amount of interaction which leads to larger values of $r_{m,\mathrm{g}}$ compared to $r_{m,\mathrm{s}}$. The increase in the "magical" radius for groups can be considered in the group influence factor r_g. Therefore, the estimation of the "magical" radius can be determined for piles embedded in an infinite layer according to:

$$r_{m,\mathrm{g}} = r_{m,\mathrm{s}} + r_g = 2.5 \cdot \rho_{\mathrm{dsh}} \cdot l_P \left(1 - \nu_s\right) + r_g \, . \tag{3.151}$$

The value of r_g is related to the dimension of the pile group. In the case of rectangular pile groups, the group influence factor may be taken as the radius of the circle of equivalent area to that covered by the pile group [334]. More generally, this radius beyond shear stresses becomes negligible and can be expressed as [157, 158]:

$$r_{m,\mathrm{g}} = A \frac{1 - \nu_s}{1 + \rho_{\mathrm{dsh}}} l_P + B r_0 + \alpha_{\mathrm{g}} r_{\mathrm{g}} \, . \tag{3.152}$$

The factors A and B are investigated in the study by Guo and Randolph [155, 157, 158] for several pile geometries, pile and soil stiffnesses, and various thicknesses of the finite soil layer, see appendix Eq. A.1. In the thesis by Lutz [251], it is proposed to adopt the determination of Randolph and Wroth [334] and extend it in order to take into account the total depth of the compressible soil stratum ($l_P + h_b \rightarrow$ see Fig. 3.63):

$$r_{m,\mathrm{g}} = \frac{1}{0.18182 + 0.43636 \dfrac{l_P}{l_P + h_b}} \cdot l_P \left(1 - \nu_s\right) \, . \tag{3.153}$$

These determinations are studied for the linear-elastic pile group behaviour. For the non-linear analysis of pile groups, Rudolf et al. [353, 354] found that the elastic definition of r_m overestimates the influence of the shear stress descending branch around the source pile which led to an underestimation of the pile group stiffness. Therefore, in the study by Rudolf the radius is defined as $r_{m,\mathrm{g}} = l_p$ [353]. Nevertheless, the "magical" radius only contributes to logarithmic terms; the overall load-deformation behaviour is not sensitive to the precise value of these terms in the response analysis [334]. A similar recommendation is made in the study by Mylonakis and Gazetas [291], discussed in previous section.

The load-settlement ratio for each individual pile of a 3x3 pile group, based on the model by Randolph and Wroth [334], is presented in Fig. 3.61. The pile spacing is $s_x = s_y = 5 r_0$ and the group influence factor is chosen to be $r_g = 6 r_0$. The comparison between the presented model and the Boundary Element Method of Banerjee [17] shows a sufficient agreement. On one side, the soil is assumed as incompressible

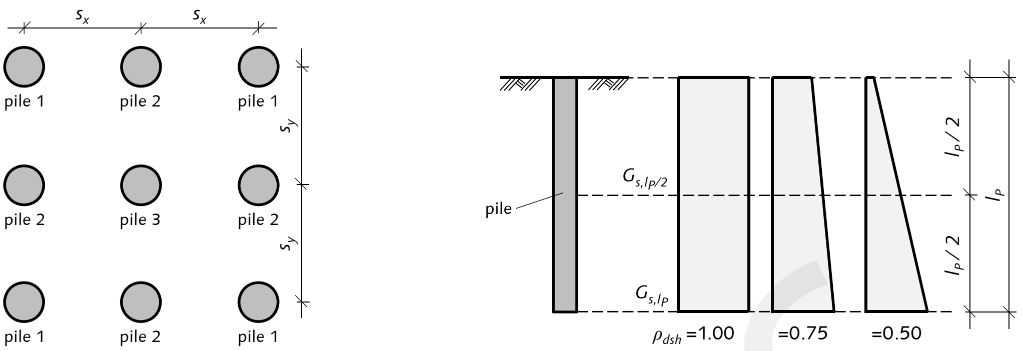

(a) pile spaces and types (b) definition soil stiffness

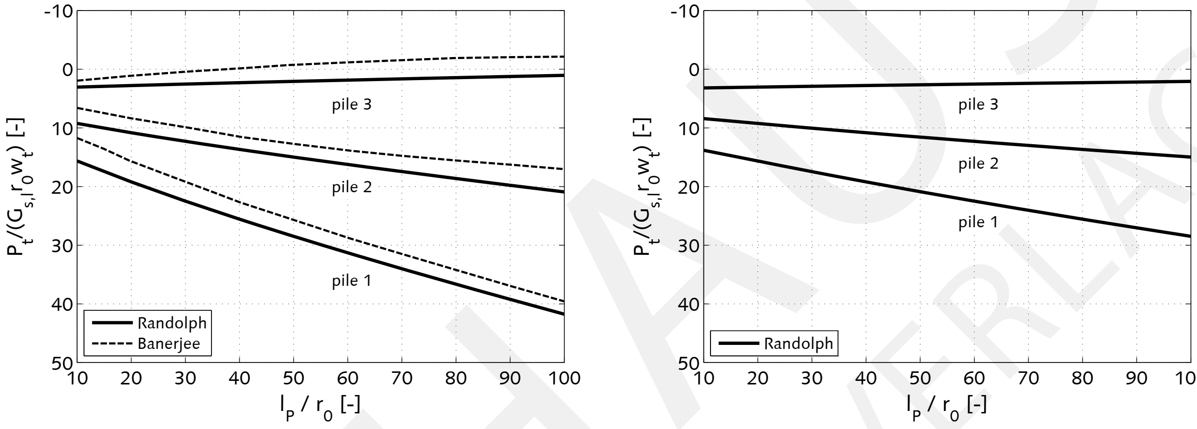

(c) homogeneous soil, $\rho_{\text{dsh}} = 1.0$, BANERJEE [17] (d) soil with stiffness proportional to depth, $\rho_{\text{dsh}} = 0.5$

Figure 3.61: Load-settlement ratio for piles in a 3x3 rigid group, incompressible soil $\nu_s = 0.5$, $s_x = s_y = 5r_0$, $r_g = 6r_0$, model RANDOLPH et al. [334]

and homogeneous, see Fig. 3.61(c). On the other side, the study of soil stiffness as a function of depth is illustrated in Fig. 3.61(d). For a given slenderness ratio l_P/r_0, the results show that the range of loads supported by the three different pile types is less in soil with stiffness proportional to depth than for pile groups in homogeneous soil. Finally, in this thesis, compressible pile group groups are not considered in the obtained results using the previously introduced model.

Mylonakis and Gazetaz 1998 [291]

The main difference between this model and that proposed by RANDOLPH et al. [334] is the determination of the pile-to-pile interaction. Individual piles in a pile group do not exactly follow the free-field displacement generated by their neighbours [291]. Axial pile rigidity and the soil reaction at the pile tip tends to reduce the settlement determined by the free-field displacement approach. Therefore, MYLONAKIS and GAZETAZ [291] propose an interaction method in order to account for these effects, which might be important, especially for piles in multi-layered soil.

The settlement profile of a single pile $W_{11}(z)$ can be determined according to Eq. 3.129. Within each distinct and homogeneous horizontal soil layer, the settlement attenuation with radial distance from the source pile follows almost the logarithmic variation of Eq. 3.159b, see Fig. 3.62. Hence, the attenuated soil settlement at the position of the unloaded receiver pile (if the pile is not present) is:

$$U_s\left(r_{ij}, z\right) = W_{11}(z)\psi_s\left(r_{ij}\right) . \tag{3.154}$$

In contrast, this displacement is reduced in most cases due to the existence of the receiver pile. The receiving pile's mechanical behaviour is in a sense the reverse of the loaded source pile. On one side, the loaded pile induces settlements in the soil and, on the other side, the soil induces the attenuated displacements on the receiver pile. The vertical equilibrium of an element of a receiver pile is defined as:

$$E_P A_P \frac{\mathrm{d}^2 W_{21}(z)}{\mathrm{d}z^2} - k_z \left[W_{21}(z) - U_s\left(r_{ij}, z\right) \right] = 0\,, \tag{3.155}$$

in which W_{21} is the settlement profile of the receiver pile, see Fig. 3.62. For each homogeneous soil layer, the solution of the differential equation is:

$$W_{21}(z) = \frac{\lambda}{2} \psi_s\left(r_{ij}\right) z \left[-A_{11} \mathrm{e}^{(\lambda z)} + B_{11} \mathrm{e}^{(-\lambda z)} \right] + A_{21} \mathrm{e}^{(\lambda z)} + B_{21} \mathrm{e}^{(-\lambda z)}\,, \tag{3.156}$$

with the integration constants shown in the appendix in Eq. A.2. In order to take into account a multi-layer soil stratification, Eq. 3.156 can be transferred into the following transfer matrix formulation:

$$\left\{ \begin{matrix} \left\{ \dfrac{W_{11}(h)}{P_{11}(h)} \right\} \\ \\ \left\{ \dfrac{W_{21}(h)}{P_{21}(h)} \right\} \end{matrix} \right\}_i = \begin{bmatrix} [\mathbf{L}] & [\mathbf{0}] \\ [\mathbf{LI}] & [\mathbf{L}] \end{bmatrix}_i \left\{ \begin{matrix} \left\{ \dfrac{W_{11}(0)}{P_{11}(0)} \right\} \\ \\ \left\{ \dfrac{W_{21}(0)}{P_{21}(0)} \right\} \end{matrix} \right\}\,, \tag{3.157}$$

in which [**L**] is the 2x2 transfer matrix accounting for the single pile response, and [**LI**] is the 2x2 transfer matrix accounting for the pile-to-pile interaction, which is shown in the appendix in Eq. A.3. Further detail about the matrix formulation can be found in the study by MYLONAKIS [290].

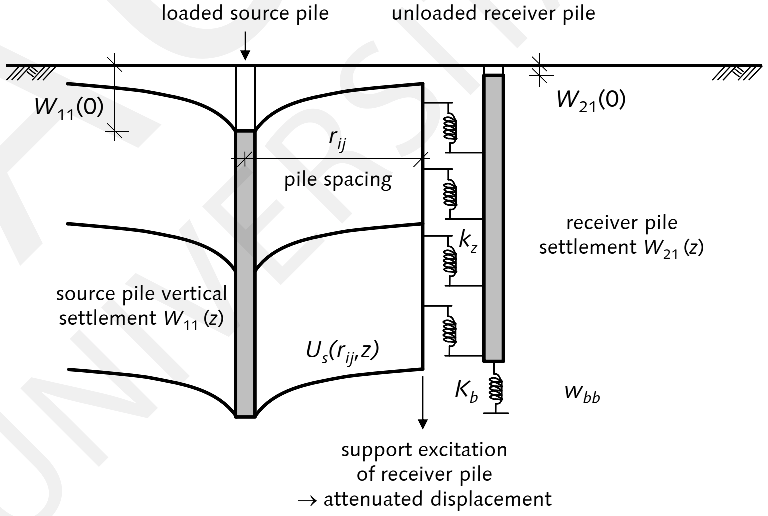
loaded source pile
unloaded receiver pile
$W_{11}(0)$
$W_{21}(0)$
r_{ij}
pile spacing
k_z
receiver pile settlement $W_{21}(z)$
source pile vertical settlement $W_{11}(z)$
$U_s(r_{ij},z)$
K_b
w_{bb}
support excitation of receiver pile → attenuated displacement

Figure 3.62: Schematic illustration for analysis of the influence of a head-loaded source pile on an adjacent (unloaded) receiver pile in a layered soil, based on [291]

For the pile group settlement analysis of n_P identical piles supported by a rigid pile cap, a general formulation for n soil layers involves the following matrix algebra:

$$P_t = \sum_{i=1}^{n_P} P_i = \left[\{1\}^T [\mathbf{A}]^{-1} \{1\}\right] \mathbf{w}_t = \mathbf{K}_{\mathrm{spr},v,\mathrm{lin}} \, \mathbf{w}_t \,, \tag{3.158}$$

where $[\mathbf{A}]$ is the $n_P \, x \, n_P$ interaction-factor matrix and $\{1\}$ is a $n_P \, x \, 1$ unit vector.
In the particular case of a **pile group in a homogeneous soil** (see Fig. 3.63(a)), an explicit expression for the shaft-to-shaft interaction factor α_s, based on Eq. 3.156, can be determined as a product of two functions:

$$\alpha_s = \psi_s(r_{ij}) \cdot \zeta_s \left(h\lambda, \Omega\right) \,, \tag{3.159a}$$

with the attenuation function $\psi_s(r_{ij})$ (free-field displacement):

$$\psi_s(r_{ij}) \equiv \frac{U_s\left(r_{ij}, z\right)}{U_s\left(d_P/2, z\right)} = \begin{cases} \dfrac{\ln\left(r_m\right) - \ln\left(r_{ij}\right)}{\ln\left(2 r_m\right) - \ln\left(d_P\right)} & \dfrac{d_P}{2} < r_{ij} < r_m \\ 0 & r_{ij} \geq r_m \\ 1 & r_{ij} = \dfrac{d_P}{2} \end{cases} \,, \tag{3.159b}$$

and the rigidity interaction function ζ_s:

$$\zeta_s = \frac{2h\lambda + \sinh\left(2h\lambda\right) + \Omega^2 \left[\sinh\left(2h\lambda\right) - 2h\lambda\right] + 2\Omega \left[\cosh\left(2h\lambda\right) - 1\right]}{2\sinh\left(2h\lambda\right) + 2\Omega^2 \sinh\left(2h\lambda\right) + 4\Omega \cosh\left(2h\lambda\right)} \,. \tag{3.159c}$$

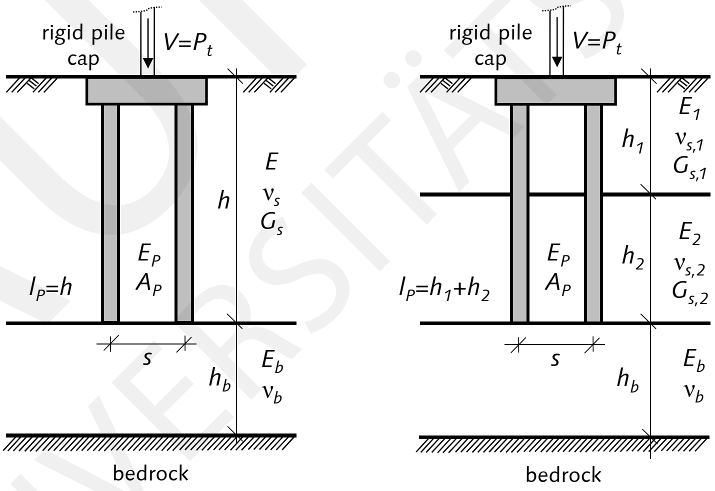

(a) homogeneous soil layer (b) two-layer soil

Figure 3.63: Sign convention for pile foundation model by Mylonakis and Gazetas [291] for vertically loaded pile groups

The attenuation function $\psi_s(r_{ij})$ describes the free-field displacement and the interaction function ζ_s represents the effect of the rigidity of the pile and the interaction between the pile and surrounding soil. In the model by Randolph and Wroth [334] it is assumed that the shaft of the receiving pile follows exactly the induced free-field soil settlement generated at mid-depth of the source pile. Hence, Randolph et al. [334] assumed that $\zeta_s = 1.0$ [291]. Therefore, the model by Randolph and Wroth [334] does not take into account the effect of the unloaded receiver pile on the settlement of the loaded source pile. Outside

r_m, no shaft-to-shaft interaction is considered, as also suggested by [242].

In addition to the pile shaft settlements, a displacement field below the pile bases is caused where some interaction between the pile bases may occur. Based on the expectation that the pile base behaves as a punch on the surface of a half-space, the attenuated settlement at a radial distance r_{ij} measured from the pile base can be determined by the approximation of RANDOLPH and WROTH [334]. The attenuated settlement field $\psi_b(r_{ij})\,W_b$ generated from the load P_b at the source pile base drags the base of the spring at the receiver pile tip downwards. Hence, a corresponding base interaction factor α_b, accounting for the base-to-base interaction, can be determined. For a homogeneous single-layer soil, the base interaction factor is explicitly defined as the product of the following functions:

$$\alpha_b = \psi_b(r_{ij}) \cdot \zeta_b\left(h\lambda, \Omega\right) \,, \tag{3.160a}$$

with the attenuation function for the soil settlement at the pile base $\psi_b(r_{ij})$:

$$\psi_b\left(r_{ij}\right) \equiv \frac{U_s\left(r_{ij}, l_P\right)}{U_s\left(d_P/2, l_P\right)} \approx \frac{d_P}{\pi r_{ij}} \,, \tag{3.160b}$$

and the pile base interaction factor ζ_b:

$$\zeta_b = \frac{2\Omega}{2\Omega\cosh\left(2h\lambda\right) + \sinh\left(2h\lambda\right)\left(\Omega^2+1\right)} \,. \tag{3.160c}$$

The overall interaction factor α_t is approximately equal to the sum of the shaft-to-shaft interaction α_s and base-to-base interaction α_b [291, 332]:

$$\alpha_t = \alpha_s + \alpha_b \,. \tag{3.161}$$

The attenuated settlement, due to the pile base, decreases inversely proportionate to the radial distance r_{ij}. In contrast, the vertical displacement, due to the pile shaft, decreases at a much slower rate. Hence, the shaft settlement affects a much bigger region than the pile base. In Fig. 3.64(a), the normalised base-to-base interaction factor $\zeta_b = \alpha_b/\psi_b\left(r_{ij}\right)$ is illustrated for various dimensionless base stiffness Ω and pile length $h\lambda$ values. It is obvious that the base-to-base interaction decreases very quickly with pile length and for most cases of practical interest $\zeta_b < 0.20$. Therefore, the base interaction factor α_b is a product of two small numbers and is much smaller than unity (order of 10^{-3}). Consequently, the pile base-to-base interaction is negligible and need not be considered in the interaction factor matrix [**A**] [291].

The more important shaft-to-shaft interaction is shown in Fig. 3.64(b). For short piles, the interaction increases rapidly with pile length for the dimensionless base stiffness Ω in the range between 0.05 and 0.20. A peak for the increasing portion is found at the value of $h\lambda \approx 0.5$. Hereafter, the shaft interaction turns to a decreasing function for longer piles approaching asymptotically the value of 0.50. With increasing base stiffness, this peak occurs at an increasing value of the pile length $h\lambda$. A good agreement with the study by POULOS et al. [320] and SHARNOUBY et al. [377] is found in a comparative parameter study [291].

In addition to the shaft-to-shaft interaction factor for a single-layer soil, a closed-form expression for a two-layer soil stratification, see Fig. 3.63(b), is defined as:

$$\alpha_s = \psi_s(r_{ij}) \cdot \zeta_s\left(h_1\lambda_1, h_2\lambda_2, \Omega, \Omega_1\right) \,, \tag{3.162a}$$

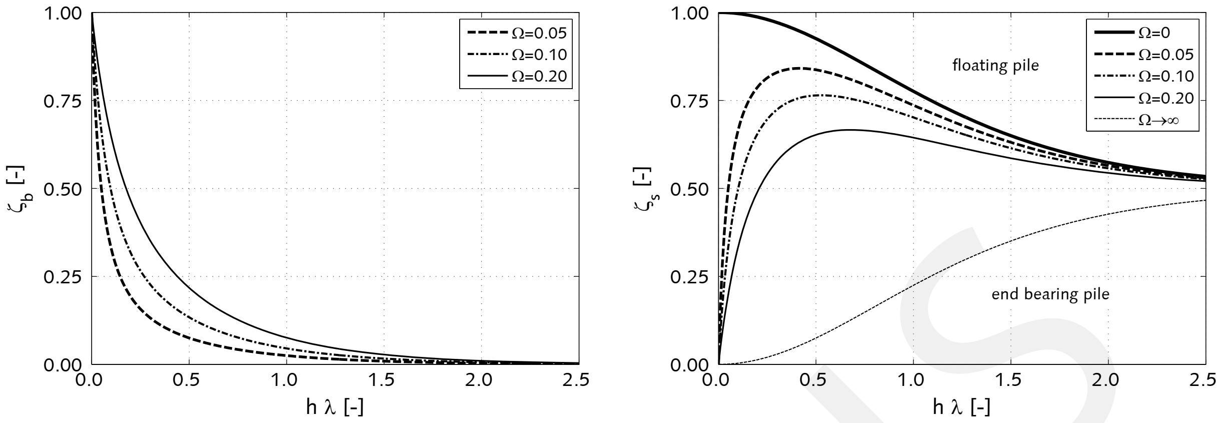

(a) normalised base-to-base interaction factor, $\zeta_b = \alpha_b / \psi_b\,(r_{ij})$

(b) normalised shaft-to-shaft interaction, $\zeta_s = \alpha_s / \psi_s\,(r_{ij})$

Figure 3.64: Interaction factors for piles embedded in single-layer soil for several dimensionless base stiffness Ω, based on [291]

in which the function $\zeta_s\,(h_1\lambda_1, h_2\lambda_2, \Omega, \Omega_1)$ is defined as:

$$\begin{aligned}\zeta_s = {} & \frac{2h_1\lambda_1 + \sinh(2h_1\lambda_1) + \Omega_1^2\left[\sinh(2h_1\lambda_1) - 2h_1\lambda_1\right] + 2\Omega_1\left[\cosh(2h_1\lambda_1) - 1\right]}{2\sinh(2h_1\lambda_1) + 2\Omega_1^2\sinh(2h_1\lambda_1) + 4\Omega_1\cosh(2h_1\lambda_1)} \quad \ldots \\ & + \frac{2\Omega_1}{2\Omega_1\cosh(2h_1\lambda_1) + \sinh(2h_1\lambda_1)\left(\Omega_1^2 + 1\right)} \quad \ldots \\ & \cdot \frac{2h_2\lambda_2 + \sinh(2h_2\lambda_2) + \Omega^2\left[\sinh(2h_2\lambda_2) - 2h_2\lambda_2\right] + 2\Omega\left[\cosh(2h_2\lambda_2) - 1\right]}{2\sinh(2h_2\lambda_2) + 2\Omega^2\sinh(2h_2\lambda_2) + 4\Omega\cosh(2h_2\lambda_2)}\,, \end{aligned} \tag{3.162b}$$

with

$$\Omega_1 = \frac{\lambda_2}{\lambda_1}\frac{\Omega + \tanh(h_2\lambda_2)}{1 + \Omega\tanh(h_2\lambda_2)}\,, \tag{3.162c}$$

and

$$\Omega = \frac{K_b}{E_P A_P \lambda_2}\,. \tag{3.162d}$$

In the case that $h_1 = 0$, the determination of the two-layer shaft-to-shaft interaction factor α_s according to Eq. 3.162 reduces to the single-layer closed-form solution represented by Eq. 3.159. For the pile slenderness ratios $l_P/d_P = 20$ and 40, and the soil embedment ratios $h_1/l_P = 1/3$ and 2/3, Fig. 3.65 illustrates α_s for various pile spacings r_{ij}/d_P. Less interaction between the shafts of neighbouring piles can be found with increase in the bottom layer's soil stiffness ($E_2 \rightarrow \lambda_2$). The effect of the embedment ratio is less important for the parameters studied in the comparison. Furthermore, for shorter distances between the piles $r_{ij}/d_P < 5$ an increase in the pile length from $l_P/d_P = 20$ to 40 leads to a relatively small decrease in the interaction factor. However, longer piles interact for greater pile spacing $r_{ij}/d_P > 10$ higher compared to the shorter ones. The comparison with the results based on the Boundary Element Method by KAYNIA [205] and VALLIAPPAN et al. [400] shows a satisfactory agreement between the methods, especially for the long piles [291].

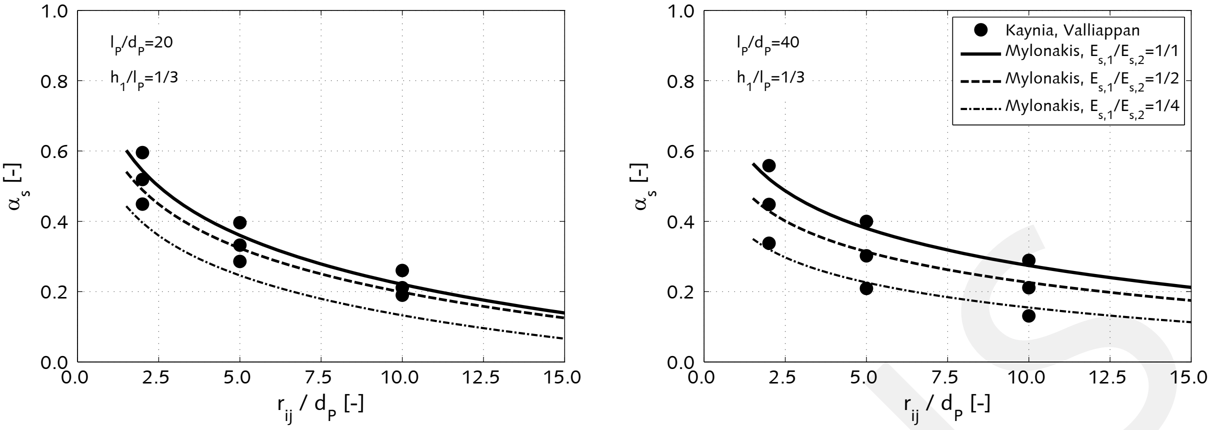

(a) $l_P/d_P = 20$, $h_1/l_P = 1/3$

(b) $l_P/d_P = 40$, $h_1/l_P = 1/3$

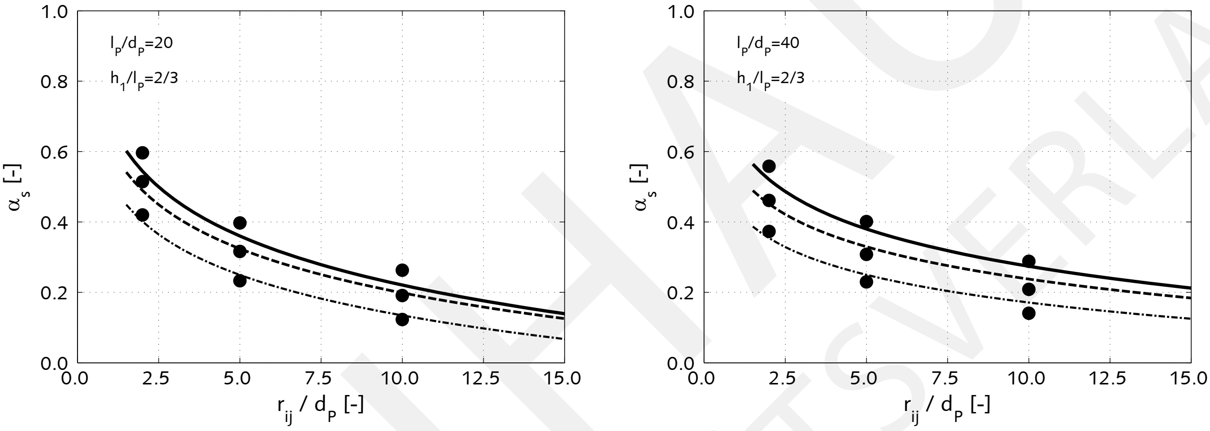

(c) $l_P/d_P = 20$, $h_1/l_P = 2/3$

(d) $l_P/d_P = 40$, $h_1/l_P = 2/3$

Figure 3.65: Interaction factors α_s for piles in two-layer soil according to MYLONAKIS et al. [291] for various soil stiffness ratios E_1/E_2 and pile embedment ratios h_1/l_P, compared with KAYNIA [205] and VALLIAPPAN et al. [400], $E_P/E_1 = 1000$, $\nu_s = 0.40$, $\chi_1 = 2.50$, $\chi_2 = 1.00$ for $E_1/E_2 = 1$ and $E_1/E_2 = 1/2$, $\chi_2 = 0.75$ for $E_1/E_2 = 1/4$

Rudolf 2005 [353]

In order to develop a practical design approach by determining nomograms, RUDOLF [353] investigates a numerical Finite Element model for pile groups, which take into account the soil non-linearity. The soil is modelled as a bi-linear material with the failure criteria according to *Mohr-Coulomb* [77, 282] in order to minimise the necessary parameters for the soil material modelling. In contrast, the reinforced concrete elements of the pile and pile cap are modelled as linear-elastic materials. In the bond zone between the pile and soil, no additional interface elements or contact areas are modelled, which lead to direct shear transfer at the pile shaft elements. This direct contact between the piles and the soil, and the influence on the overall pile group settlement behaviour is previously investigated in studies presented in [175, 353]. Finally, the direct contact description seems to be accurate enough, however, the element thickness at the pile shaft crucially influences the computational results [354]. Increase in the corresponding thickness raises the stiffness of the entire pile [272, 328]. Therefore, RUDOLF analysed in a comparative study the results between the direct coupling and the interface modelling using contact areas. An element thickness of about $0.15d_P$ around the pile shaft enables adequate results for the considered direct coupling modelling technique [354]. These nomograms published in [81, 353, 354] are developed based on extensive parameter studies, see Tab. 3.18, which are performed based on the previously described Finite Element analysis.

Table 3.18: Parameter study of RUDOLF [353, 354] for determining nomograms for settlement analysis of pile groups

Parameter	Symbol	Bandwidth of parameter	Unit
pile diameter	d_P	0.3, 0.4, 0.6, 0.9, 1.20, 1.5	[m]
pile length	l_P	9, 12, 18, 24	[m]
pile spaces	s	$3 \cdot d_P$, $6 \cdot d_P$, $9 \cdot d_P$	[-]
effective friction angle	$\varphi^{'}$	20 → 40	[°]
effective cohesion	$c^{'}$	0 → 40	[°]
soil modulus of elasticity	E	2.2 → 52	[MN/m^2]
specific gravity (earth-dry)	γ	17 → 21	[kN/m^3]

In addition to the Finite Element analysis, a mathematical model is developed, based on the linear-elastic pile group interaction approach by RANDOLPH and WROTH [332, 334]. Similar to the previously mentioned models by RANDOLPH et al. [334] and MYLONAKIS et al. [291], the pile cap behaviour is assumed to be rigid in the study by RUDOLF [353]. In addition, the pile itself is a rigid element in the mathematical model. As the major difference, the linear-elastic pile group stiffness prediction is enhanced to a physical non-linear pile group analysis. Due to the soil self-weight, the vertical σ_z and horizontal σ_x stresses are computed as the initial stress state, see Fig. 3.67. Shear stresses τ_{zx} do not occur in the initial stress state. These shear stresses increase in the incremental load-displacement analysis (see Fig. 3.66), and are thereby computed according to Eq. 3.117 ($\tau_{zx} = \tau_0$). The elements in the analysis at the pile shaft and pile base are described by a bi-linear material model. The failure criterion is determined by the *Mohr-Coulomb* condition [77, 282]:

$$\frac{\sigma_I^{'} - \sigma_{III}^{'}}{2} = \frac{\sigma_I^{'} + \sigma_{III}^{'}}{2} \sin\varphi^{'} + c^{'} \cos\varphi^{'} \,, \tag{3.163a}$$

$$F(\underline{\sigma}) = \frac{\sigma_I^{'}}{2}\left(1 - \sin\varphi^{'}\right) - \frac{\sigma_{III}^{'}}{2}\left(1 + \sin\varphi^{'}\right) - c^{'} \cos\varphi^{'} \,. \tag{3.163b}$$

In the case that the failure condition $F(\underline{\sigma}) \geq 0$, the cohesive strength τ_f determined by the *Mohr-Coulomb* shear criterion exceeds the maximum shear stress $\tau_{\max}$ caused by σ_z, σ_x, and τ_{zx}. In the non-linear analyses, the vertical and horizontal stresses at the pile shaft are assumed to be constant as computed in the initial stress state condition. Therefore, the average between the principal stresses $(\sigma_I^{'} + \sigma_{III}^{'}/2)$ remains constant, see Fig. 3.66. Comparison with the results obtained in the Finite Element analysis confirms this determination [353].

In the case that the **pile shaft** is considered a unique element, the load-deformation behaviour of the pile shaft resistance is linear up to a load level which causes failure criterion to be met. A more adequate consideration of the pile shaft resistance can be investigated by dividing the entire pile shaft into n_s elements. In addition, this segment analysis enables the consideration of vertical soil stratification. Hence, the failure criterion according to Eq. 3.163b is checked at each local element and a non-linear relationship

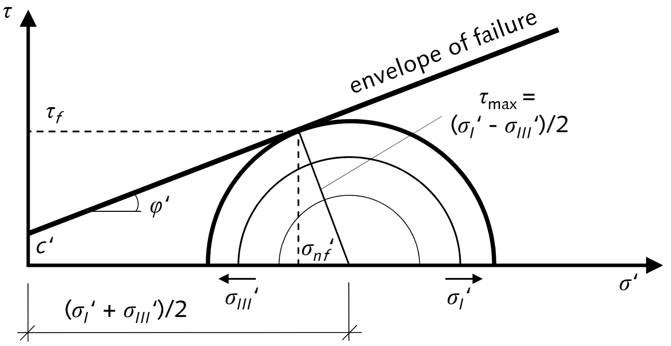

Figure 3.66: Increase in principal stresses $\sigma_I^{'}$, $\sigma_{III}^{'}$, due to incremental vertical loading up to *Mohr-Coulomb* failure criterion, based on [353]

can be considered in the pile shaft load-settlement behaviour. The shaft interaction factor f_{s,i,j,n_s} of the j pile on the i pile shaft settlement can be determined based on Randolph et al. [332], see Eq. 3.117:

$$f_{s,i,j,n_s} = \frac{w_s}{P_s} = \begin{cases} \dfrac{(1+\nu_s)}{E \cdot l_P \cdot \pi} \ln\left(\dfrac{r_{m,\mathrm{g}}}{r_{ij}}\right) & r_{ij} \leq r_{m,\mathrm{g}} \\ 0 & r_{ij} > r_{m,\mathrm{g}} \end{cases}, \tag{3.164}$$

in which $r_{ij} = r_0$ for $i = j$. The overall pile shaft stiffness can be computed by the sum of each pile shaft element, in which the *Mohr-Coulomb* failure criterion is directly checked at the pile shaft according to Eq. 3.163b. In the case that the failure criterion is exceeded, the interaction factor for the corresponding element at the pile shaft is set to zero ($f_{s,i,j,n_s} = 0$). An additional increase in the pile shaft load cannot be admitted in the corresponding pile shaft element for further load increments.

In accordance with Timoshenko and Goodier (Eq. 3.121), the **pile base** settlement can be described by the solution for a rigid punch. The corresponding settlement profile relative to the distance from the pile base is similarly determined in the model by Randolph and Wroth [334] (Eq. 3.124, Eq. 3.148) by the pile base interaction factor $f_{b,i,j}$:

$$f_{b,i,j} = \frac{w_b}{P_b} = \begin{cases} \dfrac{\left(1-\nu_s^2\right)}{E \cdot \pi \cdot r_{ij}} & i \neq j \\ \dfrac{\left(1-\nu_s^2\right)}{E \cdot d_P} & i = j \end{cases}, \tag{3.165}$$

Comparison to FEM simulation shows that this elastic determination overestimates the pile base stiffness even in the serviceability limit state. Therefore, Rudolf [353] proposed a method which considers the non-linear behaviour of the pile base stiffness. An imaginary plane under the pile base end is subdivided into several elements in order to meet the *Mohr-Coulomb* failure criterion, see Fig. 3.67.

Each element represents a subarea (A1 to A5) of the pile base. In the case that the failure criterion is exceeded, the corresponding subarea is not capable of resisting another load increment and, thus, the total area in the plane under the pile base is reduced. The elastic pile base stiffness according to Eq. 3.165 is enhanced to [353]:

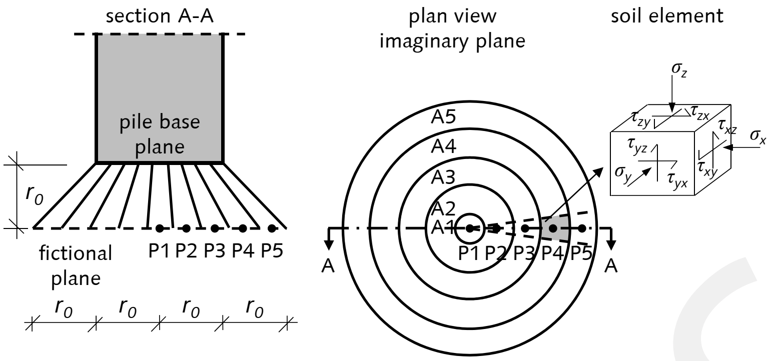

Figure 3.67: Imaginary plane below the pile base with corresponding subareas, based on [353]

$$f_{b,i,j} = \frac{w_b}{P_b} = \begin{cases} \dfrac{\left(1-\nu_s^2\right)}{E \cdot \pi \cdot r_{ij}} \cdot \dfrac{n_{\mathrm{el}}}{n_{\mathrm{el}} - n_{\mathrm{f}}} & i \neq j \\ \dfrac{\left(1-\nu_s^2\right)}{E \cdot d_P} \cdot \dfrac{n_{\mathrm{el}}}{n_{\mathrm{el}} - n_{\mathrm{f}}} & i = j \end{cases} . \tag{3.166}$$

n_{el} ... number of elements in imaginary plane
n_{f} ... number of failed elements in imaginary plane

The vertical and horizontal soil stresses are initially computed under the soil dead load condition in the plane stress state. In the incremental load-settlement analysis of the pile base, the increase in the stresses σ_z, σ_x, and τ_{zx} are analysed based on the solution by MINDLIN [280] for a vertical load at a certain depth inside an elastic half-space, as presented in [315], see in the appendix Fig. A.1 and Eq. A.4. The pile base loads are separately computed for each pile in the pile group analysis and therefore the interaction between the pile bases is already considered. Hence, no adjustment in the vertical force must be made at the imaginary plane. In order to check the *Mohr-Coulomb* failure condition, the pile bases are separately checked in each corresponding subarea. For the case that all subareas fail ($n_{\mathrm{f}} = n_{\mathrm{el}}$), no additional load can be carried by this pile base and therefore $f_{b,i,j} = 0$.

The load-settlement analysis of the pile group can be computed by the matrix notation $[\mathbf{A}]\{\mathbf{b}\} = \{\mathbf{c}\}$. Pile shaft-to-shaft ($f_{s,i,j,n_s}$) and base-to-base interaction factors ($f_{b,i,j}$) are stored in the matrix $[\mathbf{A}]$, the vector $\{\mathbf{b}\}$ contains the load, resistance and the vertical settlement, and the vector $\{\mathbf{c}\}$ consists of the unit load.

$$\begin{bmatrix} [f_{s,i,j,1}] & \dots & [0] & [0] & \{-1\} \\ \dots & \ddots & \dots & \dots & \dots \\ [0] & \dots & [f_{s,i,j,n_s}] & [0] & \{-1\} \\ [0] & \dots & [0] & [f_{b,i,j}] & \{-1\} \\ \{1\} & \dots & \{1\} & \{1\} & 0 \end{bmatrix} \cdot \begin{Bmatrix} \left\{R_{s,i,1}^{\bar{1}}\right\} \\ \dots \\ \left\{R_{s,i,n_s}^{\bar{1}}\right\} \\ \left\{R_{b,i}^{\bar{1}}\right\} \\ w_t^{\bar{1}} \end{Bmatrix} = \begin{Bmatrix} \{0\} \\ \dots \\ \{0\} \\ \{0\} \\ \bar{1} \end{Bmatrix} \tag{3.167}$$

Solving for the vector $\{\mathbf{b}\} = [\mathbf{A}]^{-1}\{\mathbf{c}\}$, the vertical settlement $w_t^{\bar{1}}$ can be computed as well as each specific resistance for the pile shaft $R_{s,i}^{\bar{1}}$ and pile base $R_{b,i}^{\bar{1}}$. The response of the pile group for a certain vertical load P_t is consequently determined:

$$w_t = w_t^{\bar{1}} \cdot P_t \, , \tag{3.168a}$$

$$R_{s,i} = R_{s,i}^{\bar{1}} \cdot P_t \, , \tag{3.168b}$$

$$R_{b,i} = R_{b,i}^{\bar{1}} \cdot P_t \, . \tag{3.168c}$$

This mathematical model for vertically loaded piles is initially checked for the load-settlement relationship of single piles in various soil conditions, see appendix Fig. A.2, with the corresponding soil properties listed in the appendix in Tab. A.3. On average, an adequate agreement between the mathematical and numerical models is found for various soil conditions [353]. The pile shaft resistance is slightly underestimated for all geometric and material variations. This systematic difference might occur due to the stress state assumptions mentioned previously. In the numerical analysis, a minor increase in the vertical and horizontal stresses close to the shear failure is observed. This phenomenon is not considered in the mathematical model, which leads to a difference as compared to the pile shaft resistance obtained from the Finite Element simulation. The pile base resistance is checked at the imaginary plane. This surface is under the pile shaft at a distance of r_0 with a diameter of $4r_0$, which considers a load distribution angle of 45°. The surface is subdivided into 5 subareas and the corresponding pile base resistance is checked according to the *Mohr-Coulomb* failure criterion. Comparison to the numerical model for all studied parameters illustrates a very good accuracy of the mathematical model when considering the imaginary plane [353].

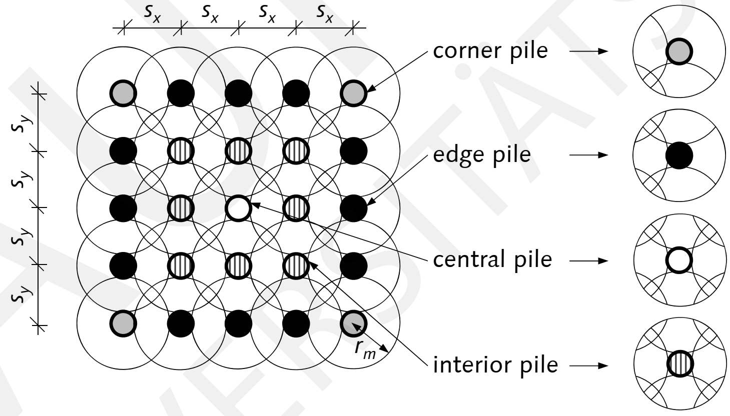

Figure 3.68: Pile layout for 5x5 group with corresponding effective influence areas determined by “magical” radius r_m for corner, edge, central, and interior pile

In order to prove the general applicability of the mathematical model, a quadratic pile group of 25 piles (5x5) under different conditions, such as soil properties and pile geometry, is studied based on Finite Element simulations and the mathematical model. The general pile layout is illustrated in Fig. 3.68. Because of the different interactions between each individual pile, the piles in the group are not similarly loaded and differences in the load-deformation behaviour and resistance-settlement relationship exist. Therefore, the piles in the entire group can be differentiated into several categories of corner pile, edge pile, central pile, and interior pile [218, 353].

The resistance-settlement behaviour of a 5x5 quadratic pile group with the pile spacing $s_x = s_y = 6d_P$, pile length $l_P = 9.0\,\text{m}$, and pile diameter $d_P = 0.9\,\text{m}$ embedded in a cohesive, normally-consolidated soil is

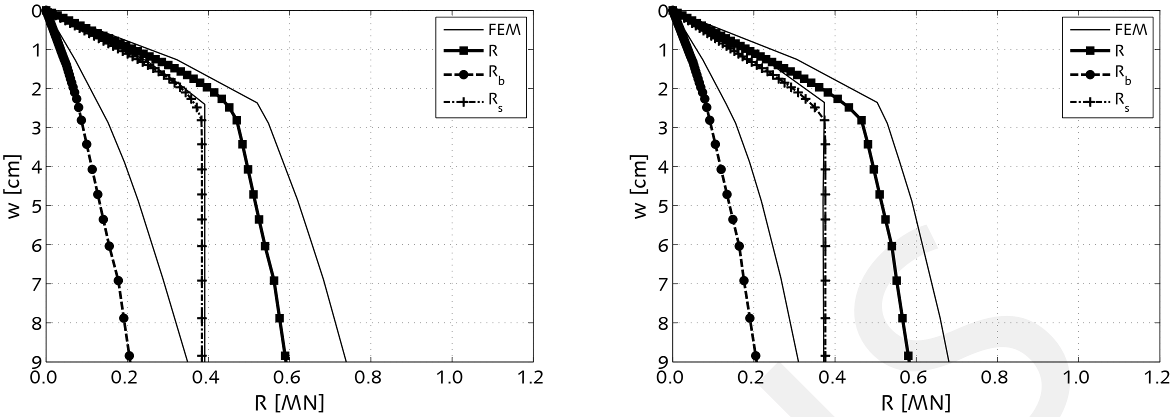

(a) central pile, $K_{v,\text{lin}} = 22\,\text{MN/m}$

(b) interior pile, $K_{v,\text{lin}} = 18\,\text{MN/m}$

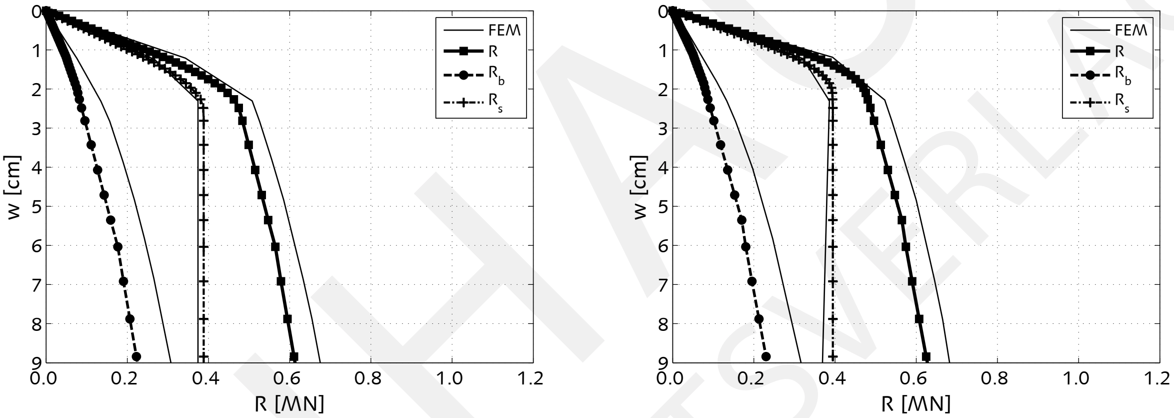

(c) edge pile, $K_{v,\text{lin}} = 24\,\text{MN/m}$

(d) corner pile, $K_{v,\text{lin}} = 30\,\text{MN/m}$

Figure 3.69: Comparison between mathematical model and numerical simulation based on RUDOLF [353] for 5x5 pile group, $r_{m,\text{g}} = l_p$, cohesive soil, normally-consolidated, $E = 6.5\,\text{MN/m}^2$, $l_P = 9.0\,\text{m}$, $d_P = 0.9\,\text{m}$, $s_x = s_y = 6d_P$, $K_{v,\text{lin}} = 594\,\text{MN/m}$

shown in Fig. 3.69. The corresponding soil properties are listed in the appendix in Tab. A.3 and the particular pile spacings r_{ij} are shown in the appendix in Tab. A.4. The comparison between the Finite Element simulations and the mathematical model assesses a satisfactory consistency for the overall load-deformation behaviour. The pile shaft stiffness prediction is very similar for both solution techniques. In contrast, the pile base behaviour is less stiff in the mathematical model compared to the numerical simulation. In addition, the resistance-settlement behaviour of a 5x5 quadratic pile group with the pile spacing $s_x = s_y = 6d_P$, pile length $l_P = 18.0\,\text{m}$, and pile diameter $d_P = 0.9\,\text{m}$ embedded in a cohesive, over-consolidated soil is shown in the appendix in Fig. A.3.

Comparison between model characteristics for axially loaded single piles and pile groups

Several model characteristics and corresponding input parameters for the considered vertical pile models are listed in Tab. 3.19. If the pile behaviour is assumed to be rigid, there is no need to define a modulus of elasticity for the pile. Therefore, this parameter is not considered in the model by RANDOLPH and WROTH [334] and by RUDOLF [353]. The soil parameters of friction angle and cohesion are needed for the description of the *Mohr-Coulomb* material model. They are exclusively included in the non-linear soil model by RUDOLF [353] and are not necessary for the other models, which assume a linear-elastic soil behaviour. Moreover, RUDOLF considers an initial stress state, due to the soil dead load, in order to accurately assess the failure criterion based on *Mohr-Coulomb*. A multi-layered soil condition can only be considered in the model by MYLONAKIS et al. and RUDOLF. In contrast, the model by RANDOLPH is restricted to homogeneous soil, as discussed in the previous sections.

The comparison of the model predictions is presented in the following paragraph according to full-scale tests of a 3x3 pile group investigated by KOIZUMI et al. [217]. Moreover, these models for vertically loaded pile groups are evaluated based on the uncertainty analysis considering model, parameter, and total uncertainty. Therefore, a study of two different pile groups is presented in Sec. 5.2.

Table 3.19: Pile model characteristics for vertical loading condition

criteria/ material property		RANDOLPH et al. [334]	MYLONAKIS et al. [291]	RUDOLF [353]
pile behaviour		rigid	compressible	rigid
soil behaviour		linear-elastic	linear-elastic	bi-linear *Mohr-Coulomb* failure criteria
soil stratification		homogeneous	multi-layered	multi-layered
pile modulus of elasticity	E_P	⊖	✓	⊖
soil modulus of elasticity	E	✓	✓	✓
soil shear modulus	G_s	✓	✓	✓
soil *Poisson*'s ratio	ν_s	✓	✓	✓
friction angle	φ	⊖	⊖	✓
cohesion	c	⊖	⊖	✓
earth pressure at rest coefficient	K_0	⊖	⊖	✓

Full-Scale load tests

A 3x3 steel pile group with the pile spacing of $s_x = s_y = 0.9\,\text{m}$ (three pile diameters) founded on a highly sensitive clay stratum resting on a sequence of sand and gravel layers at a depth of 14 m is tested by KOIZUMI et al. [217]. This full-scale load test is modelled by CAIRO et al. [58] and ZHANG et al. [416], among others, in a two-layer soil stratification with the upper layer extending to a depth of 1.70 m (sandy silt followed by silty clay). The external diameter of the steel piles is 300 mm and the thickness is 3.2 mm. The modulus of elasticity of the pile is measured to be $E_p = 200,000\,\text{MN/m}^2$) and the pile length is $l_P = 5.5\,\text{m}$. The pile cap is in contact with the soil. From laboratory and in situ tests, the shear strength τ_f is found to increase from approximately 25 at the pile head to $40\,\text{kN/m}^2$ at 3.50 m depth and decrease from $40 - 25\,\text{kN/m}^2$ at the pile tip. From inverse analysis of the single pile loading tests, CAIRO et al. [58] concluded that $\nu_s \approx 0.5$ and the values of the soil modulus of elasticity of the upper and lower soil layers are approximately 12.8 and $15.6\,\text{MN/m}^2$, respectively.

In the experimental study by O´NEILL [300], a group of nine piles is investigated. The steel piles are founded on soft to medium-stiff clay. The diameter is not constant over the pile length of $l_P = 18.45\,\text{m}$. The external diameter of these tapered steel piles is 419 mm and 203 mm at the head and tip of the pile, respectively. The steel thickness is 4.6 mm and the pile spacing is designed to be $s_x = s_y = 1.22\,\text{m}$. The pile cap is 1.22 m off the ground and therefore not in contact with the soil. The soil (saturated clay) can be described by a two-layer soil system with the average values of the undrained shear strength c_u for the upper (soil layer depth $h_1 = 12.2\,\mathrm{m}$) and lower layers 21.5 and $37.4\,\mathrm{kN/m^2}$, respectively.

Moreover, for a multi-layered soil condition (cohesive soils: stiff clay, stiff sandy clay, silt and sand layers) O´Neill et al. [301] tested closed-ended steel piles (external diameter of 273 mm, thickness of 9.3 mm) in a group of nine piles with the pile spacing $s_x = s_y = 3d_P$ and the pile length $l_P = 13.1\,\mathrm{m}$. The piles are capped with a rigid concrete cap suspended 0.9 m off the ground.

The interaction between two identical piles is investigated by Caputo et al. [60]. The load-deformation behaviour of the loaded pile is measured to be highly non-linear, whereas the adjacent load-free pile is linearly elastic. This behaviour is similarly investigated by Chow [70], which also assessed that non-linear response only develops near the loaded pile side, and the pile-to-pile interaction remains essentially elastic.

A group of five tubular steel piles is tested by Briaud et al. [52] with the pile length $l_P = 9.15\,\mathrm{m}$. These piles are connected by a rigid free-standing cap suspended 0.6 m off the ground. The bedrock is at a depth of 14.5 m

The behaviour of bored pile groups in medium dense and weakly cemented sands is studied by Ismael [189]. Axial load tests on single bored piles in tension and compression and compression tests on two pile groups each consisting of five piles with different pile spacing (two- and three-pile diameters) are performed.

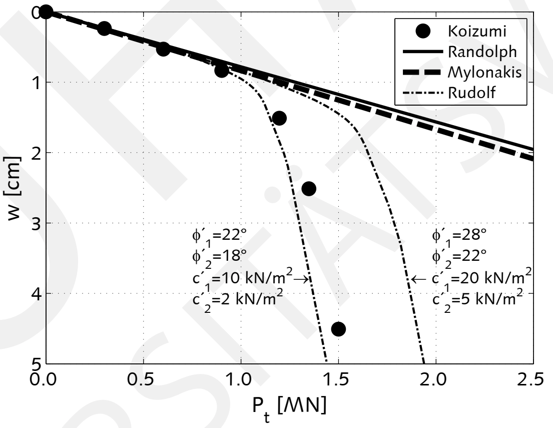

Figure 3.70: Comparison between prediction models and full-scale test of a 3x3 pile group investigated by Koizumi et al. [217], models: Randolph et al. [334], Mylonakis et al. [291], Rudolf [353]

The prediction of the pile models for axially loaded pile groups are compared to experimental full-scale test by Koizumi et al. [217], see Fig. 3.70. Based on the inverse analysis [58], the elastic moduli of the soil were are well investigated and, hence, the elastic response of the pile group is well-predicted by all models. Due to some lack of knowledge about the shear soil parameters on site, different friction angles and cohesion properties are chosen for the non-linear model by Rudolf [353]. Depending on these soil properties, the measured non-linear response of the experiment can be analysed with adequate accuracy. This comparison shows that all models used in the response analysis (either linear or non-linear) of vertically loaded pile groups are generally applicable.

3.6.2 Lateral loading

3.6.2.1 Deformation and failure mechanism

Pile foundations in bridge engineering are typically subjected to high vertical loads. Horizontal loads and displacements, due to braking forces, temperature contraction/extension, concrete shrinkage, and prestressed concrete, induce additional lateral loads on the pile foundations under the bridge piers. These external forces/displacements are applied to the pile with the soil resisting the load.

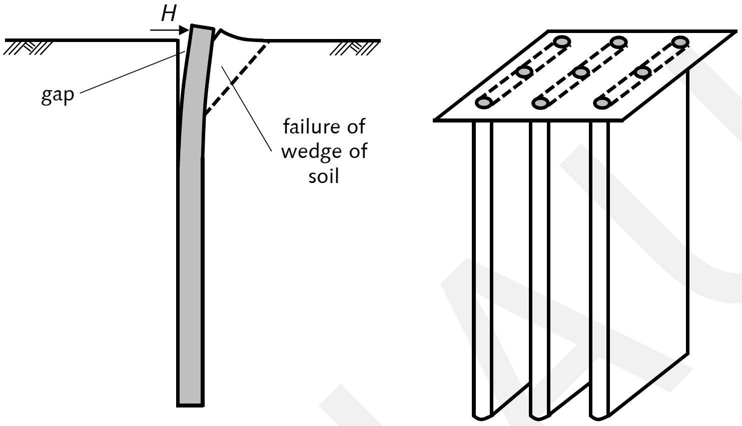

(a) single pile (b) pile row failure in pile group

Figure 3.71: Pile failure mechanism of single piles and pile groups under lateral load, based on [113]

Normal stresses increase in front of the pile and decrease behind the pile as a pile is loaded laterally. The soil displacements tend to radiate away from the pile in front of the pile and towards the pile behind the pile. A gap near the ground surface between the back of the pile and the soil might be opened at some loading level. Moreover, the soil in front of the pile may fail in a wedge type mechanism, see Fig. 3.71(a). The soil further down the pile shaft may fail by flowing around the pile with no gap present [113]. These different soil failure mechanisms must be taken into account in the analysis of the distribution of limiting pressure which may be mobilised by the pile. In general, pile collapse may occur in one of two modes. In one scenario, the pile can rotate essentially as a rigid body. This failure mode is mainly observable for short piles or piles with a large plastic moment. In another scenario, for longer piles, a plastic hinge can develop at some depth down the pile and only the upper part of the pile may undergo extensive displacements.

In a group of piles where the applied lateral load is parallel to the individual blocks, the relevant failure mechanism is the failure of the pile rows, see Fig. 3.71(b). This occurs in the case that the shearing resistance of the soil between the piles is less than the limiting resistance of an isolated pile. Moreover, rotation in the pile group, in addition to the lateral translation, can occur, see Fig. 3.72. Piles behind the axis of rotation may fail by uplift, whereas those in front may fail in compression [113].

The deformation behaviour of a pile under lateral loading is generally concentrated in the upper part of the pile. Below the ground surface at the depth of about ten-pile diameter, the deformation process is less significant [113, 331]. Hence, the pile length is rarely a relevant parameter when developing solutions for laterally loaded piles. The idealisation of piles subjected to lateral loads by an equivalent cantilever is a common (but imprecise) approach. The pile is modelled as a cantilever, fixed at some depth determined by empirical solutions, ignoring the soil support above that depth. The consideration of the soil influence on the deformation behaviour above that depth can increase the complexity and accuracy of the model

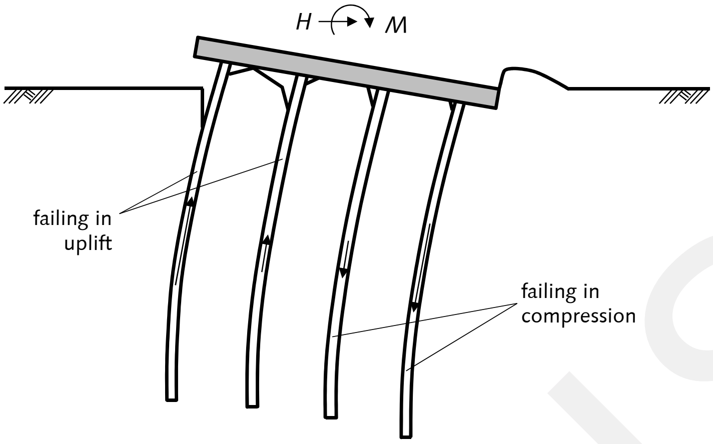

Figure 3.72: Pile failure mechanism of pile groups due to lateral translation and rotation, based on [113]

description. On one side, the soil can be represented by discrete springs down the length of the pile. On the other side, a more accurate consideration by a continuum soil model can be adopted.
The lateral load-deformation behaviour of pile groups is not only associated with the lateral deformation characteristics of the individual piles, but also the axial characteristics. Due to pile group rotation, piles at the group edges are loaded in tension and compression, providing considerable rotational stiffness to the group [113].

3.6.2.2 Models for pile groups under lateral loading

The response of piles subjected to lateral loads is initially analysed with the subgrade reaction approach in which the soil is modelled as a series of springs down the length of the pile (*Winkler* soil idealisation). Analytical solutions for a constant stiffness down the pile length are presented in [265]. For soil with stiffness that is proportional to depth, solutions can be found in [339]. A transfer matrix method for non-linear analysis of pile group responses is investigated by NOGAMI and PAULSON [298], which allows for pile-soil-pile interaction in the horizontal direction only. According to FLEMING et al. [113], the main limitation of these approaches lies in assessing an appropriate value of the subgrade reaction coefficient k for the soil. The correct choice depends not only on the soil properties, but also on the pile stiffness, and the form of loading. Moreover, there is no reasonable way in which interaction effects can be quantified when a group of piles is loaded laterally. Solutions based on the Finite Element and Boundary Element methods for pile and soil modelling, such as POULOS [317, 318] and RANDOLPH [330, 331], are studied to overcome these limitations. In the following paragraphs, a mathematical model investigated by Finite Element studies and a model based on a characteristic load method are presented, which are generally reasonable for linear and non-linear response analysis of laterally loaded pile groups. The pre-selection of these models was assisted in an cooperative study with STUTZ et al. and is presented in [197].

Randolph 1981

This model is investigated by Finite Element studies of an elastic soil continuum, which is originally described in the thesis of RANDOLPH [330]. A parametric study of piles in homogeneous soil described by a shear modulus, *Poisson* ratio, and in soil with stiffness proportional to depth, are performed. The rate of increase in shear modulus with depth can be described with the parameter m by [331]:

$$G = mz = mr_0 z/r_0 \, . \tag{3.169}$$

In the model by RANDOLPH [331], the interaction factors and the solution are presented based on normalisation of pile E_P and soil stiffness G_c determined by the corresponding stiffness ratio E_P/G_c. Therefore, any interaction factor is solely a function of the stiffness ratio and is independent of the pile length. The deformation analysis is generally insensitive to pile length. This is valid for all piles which are longer than the critical length l_c beyond which the pile length no longer affects the response under lateral loading (termed flexible piles). For piles with a length shorter than their critical length, the head deformation is larger than defined in the model by RANDOLPH. [331]. The increase in deflection is small until the pile length falls below about $0.8 l_c$ [113]. Solutions for such short piles are presented in [62, 320].

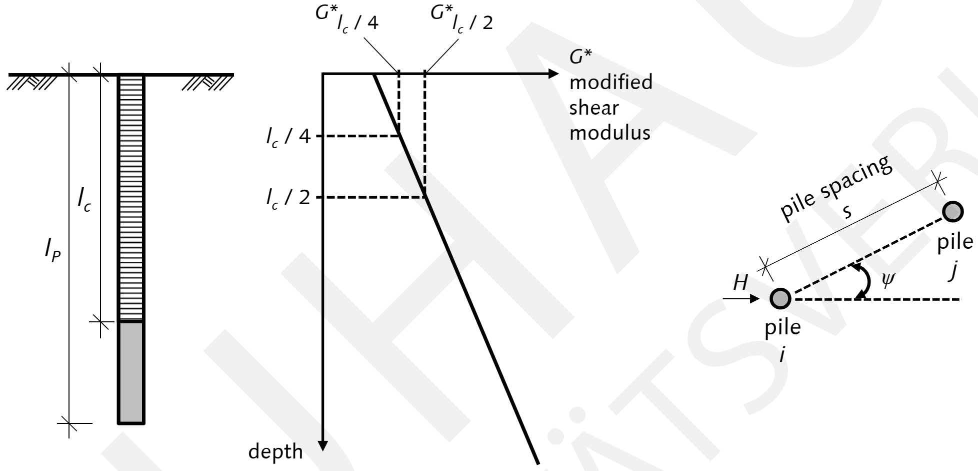

(a) ρ_{dsh}, G^*

(b) ψ

Figure 3.73: Definition of degree of homogeneity ρ_{dsh}, modified shear modulus G^*, and departure angle ψ, based on [331]

The effect of variations in *Poisson*'s ratio on the lateral deformation can be adequately represented by a modified shear modulus G^*. The modified shear modulus, the characteristic modulus G_c over the active length of pile, and the degree of homogeneity in the soil stiffness ρ_{dsh}, see Fig. 3.73(a), are defined as:

$$G^* = G\,(1 + 3\nu_s/4) \tag{3.170a}$$

$$m^* = m\,(1 + 3\nu_s/4) \tag{3.170b}$$

$$G_c = G^*_{l_c/2} \tag{3.170c}$$

$$\rho_{\text{dsh}} = G^*_{l_c/4}/G_c \tag{3.170d}$$

For piles without a solid circular cross-section, it is valuable to compute the pile behaviour based on an equivalent solid pile of diameter d_P. The effective modulus of elasticity of the pile can be computed by [331]:

$$E_P = \frac{(EI)_P}{\pi d_P^4/64} \, , \tag{3.171}$$

in which $(EI)_P$ is the bending stiffness of the actual pile cross-section. Therefore, general variations of soil stiffness with depth can be considered in the determination of the critical pile length l_c by:

$$l_c = d_P \left(\frac{E_P}{G_c}\right)^{2/7} . \tag{3.172}$$

Some iterations are necessary for general variations of shear modulus with depth (first guess for critical length may be $10d_P$). Based on the concept of the characteristic modulus G_c according to RANDOLPH [331], the computation of the horizontal displacement u and the rotation φ at the ground level due to the lateral loading (H, M) for a **single pile** can be computed by:

$$u = \frac{(E_P/G_c)^{1/7}}{\rho_{\mathrm{dsh}} G_c} \left[0.27\frac{H}{l_c/2} + 0.30\frac{M}{(l_c/2)^2}\right] \text{ and} \tag{3.173a}$$

$$\varphi = \frac{(E_P/G_c)^{1/7}}{\rho_{\mathrm{dsh}} G_c} \left[0.30\frac{H}{(l_c/2)^2} + 0.80\sqrt{\rho_{\mathrm{dsh}}}\frac{M}{(l_c/2)^3}\right] . \tag{3.173b}$$

These solutions are derived in the parametric study based on the Finite Element simulations with the soil modelled by as an elastic continuum. Moreover, the maximum moment of a pile under a lateral load H can be estimated by [331]:

$$M_{\max} = (0.1/\rho_{\mathrm{dsh}})\, H l_c . \tag{3.174}$$

The pile cap in a group of piles may prevent rotation of the head of the pile. For such fixed-headed piles, Eq. 3.173b can be used to find a moment M_f, with fixed the rotation $\varphi = 0$. This moment M_f is given by [331]:

$$M_f = -\left[0.1875/\left(\rho_{\mathrm{dsh}}\right)^{1/2}\right] H l_c , \tag{3.175}$$

leading to a deflection u which is approximately half that for a free-headed pile under the same lateral force.

In order to analyse **pile groups** with closely spaced piles under a lateral loading condition, the solution of a single pile can be extended to the pile group by applying the interaction factor concept. Basically, the interaction factor is defined as the fractional increase in deformation of a certain pile due to the presence of a similarly loaded neighbouring pile. The deformation of ith pile in a group of n_P piles can be computed by:

$$\delta_i = \frac{1}{K_{h,\mathrm{lin}}} \sum_{j=1}^{n_P} \alpha_{ij} P_j , \tag{3.176}$$

in which δ_i is the deformation of the ith pile, $K_{h,\mathrm{lin}}$ is the lateral stiffness, α_{ij} is the interaction factor between the ith and jth pile, and P_j is the load on the jth pile. For a pile group subjected to an external lateral load, different interaction factors, depend on the loading at the pile head and the deformation type, are proposed in the study by POULOS [318] as follows:

- α_{uH} ... deflection interaction of free-headed piles under lateral load,
- α_{uM} ... deflection interaction of free-headed piles under moment loading or for rotation of free-headed piles under lateral load,
- $\alpha_{\varphi H}$ ... rotation interaction of free-headed piles under lateral load, and
- $\alpha_{\varphi M}$ ... rotation interaction of free-headed piles under moment loading, and
- α_{uf} ... deflection interaction of fixed-headed piles (restrained against rotation).

Of most relevance in structural engineering is α_{uf}, since the rotational stiffness of pile groups is usually high, since the majority of pile groups are capped with a pile cap of sufficient stiffness to prevent significant rotation of the pile heads [113, 331]. Therefore, a single fixed-headed pile deflects only about one-fourth as much as a free-headed pile subjected to the same load. Hence, the rotational restraint due to the pile cap is a significant factor in the pile group behaviour analysis [303]. Nevertheless, the zero-rotation condition for fixed-headed piles is rarely achievable in the field even in a group that is constrained by a stiff concrete pile cap. A practical approach for determining the moment restraint that is provided by the pile cap as a support condition for investigating laterally loaded pile groups which are proposed by GUO [156], HOUSTON et al. [181], and MOKWA et al. [284].

Finite Element analysis of pile groups for fixed-headed piles [330] showed that the lateral movement patterns at the soil surface, around a laterally loaded pile, can be related directly to the interaction factor α_{uf} proposed in [318]. Based on the normalisation, the interaction factor for fixed-headed piles can be determined by:

$$\alpha_{uf} = 0.6\rho_{\mathrm{dsh}} \left(\frac{E_p}{G_c}\right)^{1/7} \frac{r_0}{s} \left(1 + \cos^2\psi\right) , \tag{3.177}$$

where s is the pile spacing and ψ is the angle of departure that the piles make with the direction of loading, see Fig. 3.73(b). The interaction for piles in the normal direction to the load direction ($\psi = 90°$) for a given spacing is half of that for piles along the line of loading ($\psi = 0°$). Moreover, the interaction for piles in a soil with stiffness proportional to depth ($\rho_{\mathrm{dsh}} = 0.5$) is half that for piles in homogeneous soil ($\rho_{\mathrm{dsh}} = 1$). Furthermore, the interaction factors are inversely proportional to the pile spacing [331]. For very closely spaced piles, the interaction factor based on Eq. 3.177 tends to overestimate the amount of interaction. Therefore, it is more adequate to replace this determination in the case that $\alpha_{uf} > 0.5$ with:

$$\alpha_{uf} = 1 - (4\alpha_{uf})^{-1} . \tag{3.178}$$

This modification of the interaction factor for very closely spaced piles additionally ensures that as the pile spacing tends to approach zero the computed interaction factor tends to approach unity. As proposed by POULOS [318], the interaction for fixed-headed piles is generally greater than for free-headed piles. Accurate results for α_{uH} can be obtained by replacing the multiplier 0.6 in Eq. 3.177 by 0.5 to get:

$$\alpha_{uH} = 0.5\rho_{\mathrm{dsh}} \left(\frac{E_p}{G_c}\right)^{1/7} \frac{r_0}{s} \left(1 + \cos^2\psi\right) , \tag{3.179}$$

and again, where this value of α_{uH} exceeds 0.5, a corrected determination by:

$$\alpha_{uH} = 1 - (4\alpha_{uH})^{-1} , \tag{3.180}$$

is reasonable to use [331]. The other interaction factors are smaller than α_{uH} at practical pile spacings. Accurate results can be obtained by the following determinations:

$$\alpha_{uM} = \alpha_{\varphi H} \approx \alpha_{uH}^2 , \tag{3.181}$$
$$\alpha_{\varphi M} \approx \alpha_{uH}^3 . \tag{3.182}$$

Duncan et al. 1996 [51, 87, 303]

This model is based on the characteristic load method (CLM), which is capable of providing a simple and accurate model to perform non-linear lateral pile analysis. The load-deformation analysis by DUNCAN et al. [87] is investigated by performing non-linear *p*-*y* (investigated by [271]) analyses for a wide range of free-headed and fixed-headed piles and drilled shafts in clay and sand. This method relates the reaction of the soil against the pile to the deflection of the pile by means of non-linear *p*-*y* curves which are established on the basis of numerical analyses.

The CLM is generally more simple than the *p*-*y* analyses, but it closely approximates *p*-*y* analyses results. Non-linear responses of piles subjected to lateral loads are caused by the non-linear soil behaviour around the pile. As the load transferred from the pile to the soil increases by a fraction of its value, the deflection increases by a greater fraction even if the pile itself remains linear [87]. In the case that the soil's strength becomes mobilised, additional loads must be transferred to greater depths, where the soil strength is not yet mobilised to the same degree. Therefore, the moment increases more rapidly down the pile than the load at the top of the pile.

Subsequently, the results are represented in the form of relationships among dimensionless variables to represent a wide range of practical conditions by means of a single relationship. In order to develop these dimensionless relationships, the actual loads H, M are divided by a characteristic load H_c and characteristic moment M_c, respectively. These parameters represent the properties of both piles (diameter, flexural stiffness) and soil (strength, stress-strain behaviour). Therefore, the characteristic load and moment determine the behaviour of the pile and the soil in response to lateral loads. A greater capacity of the pile and a smaller deflection under a given load is found for larger values of H_c (equivalent for a given moment and M_c). The characteristic load and moment are defined as [87]:

for clay:

$$H_c = 7.34 d_P^2 \cdot E_p \cdot \left(\frac{S_u}{E_P}\right)^{0.68} , \tag{3.183}$$

$$M_c = 3.86 d_P^3 \cdot E_p \cdot \left(\frac{S_u}{E_P}\right)^{0.46} , \tag{3.184}$$

for sand:

$$H_c = 1.57 d_P^2 \cdot E_p \cdot \left(\frac{\gamma' d_P \varphi' K_p}{E_P}\right)^{0.57} , \tag{3.185}$$

$$M_c = 1.33 d_P^3 \cdot E_p \cdot \left(\frac{\gamma' d_P \varphi' K_p}{E_P}\right)^{0.460} , \tag{3.186}$$

where E_p is the effective modulus of elasticity of the pile according to Eq. 3.171, S_u is the undrainded shear strength of clay, γ' is the effective unit weight of sand, φ' is the effective friction angle for sand (in degrees), and K_p is the *Rankine* coefficient of passive earth pressure ($K_p = \tan^2(45° + \varphi'/2)$). The most importance regarding the response of the pile to lateral load is the soil near the top of the pile. H_c and M_c should be averaged over a depth equal to $8d_P$ below the ground surface [87].

In order to determine an efficient and practical solution, equations that accurately represent the non-linear relationships between the variables are determined by Brettmann and Duncan [51]. An exponential equation in the form of $y = ax^b$ and in the inverted form $x = (y/a)^{1/b}$ is used for the non-dimensional relationships. An iterative, non-linear, least squares curve-fitting technique is used for determining the constants and exponents. The parameters are listed in Tab. 3.20 and the non-dimensional relationships are determined as:

$$(y_t/d_P) = a\,(H/H_c)^b \ , \tag{3.187}$$

$$(y_t/d_P) = a\,(M/M_c)^b \ , \tag{3.188}$$

in which y_t is the ground surface deflection, d_P is the pile diameter, H is the lateral load at top of pile, H_c is the characteristic load, M is the moment at top of pile, and M_c is the characteristic moment.

Table 3.20: Parameters for load-deflection and moment-deflection equations [51]

Parameter	Clay		Sand	
	free-headed	fixed-headed	free-headed	fixed-headed
load-deflection				
a	50.0	14.0	119.0	28.8
b	1.822	1.846	1.523	1.500
moment-deflection				
a	21.0		36.0	
b	1.412		1.308	

In a combined loading condition, both load and moment induce deflection, and, thus, both components must be considered. It is not sufficient to simply add the deflections caused by load and moment. The non-linear dependence can be taken into account by using a non-linear superposition procedure which is described in [87, 51].

This model for single piles can be extended to the deformation analysis of laterally loaded pile groups. The *p*-*y* for the characteristic load method may be applied according to Mokwa et al. [283] or Brettmann et al. [51]. Lateral pile models are not further discussed or evaluated in this thesis. The deterministic prediction of these models are used for the analysis of the semi-integral bridges presented in Sec. 6.3. An evaluation of these lateral pile models is presented in a cooperative study by the author and Stutz et al. in [197].

Load tests

Lateral load tests on model pile groups with aluminium piles ($E_P = 37,500\,\text{MN/m}^2$, external radius of 3.97 mm, wall thickness of 0.71 mm) embedded to a depth of 200 mm in dense, medium-grained to coarse-grained sand is studied by Williams [408]. These piles are loaded at a height of 125 mm above the sand surface.

Pile groups with fixed-headed piles are investigated by Kim and Brungraber [213] by measuring three series of lateral load tests on pile groups with contained piles are performed with spacing of either 1.22 m or 0.91 m. The top 0.305 m of the piles are embedded in a reinforced concrete cap in contact with the ground during testing. Each group contains six piles in a 3x2 arrangement with steel H-Piles ($E_P = 200,000\,\text{MN/m}^2$, external radius of 0.246 m, $I_P = 9.33\text{e}^{-5}\,\text{m}^4$). The soil profile is as following: 2.13 m thick layer of silty clay, 1.83 m of sandy clay loam, 3.35 m of clay loam, and about 4.88 m of limestone gravel.

Experimental studies on both single piles and circular groups of five and ten steel tubular piles ($E_P = 37,500\,\text{MN/m}^2$, external radius of 0.14 m, wall thickness of 8 mm) are performed in the study by NOGAMI et al. [298]. The soil is multi-layered with stiff clay, soft and very soft organic clay, very soft organic peat and humus, and very soft clay.

Full-scale cyclic load tests of pile groups in stiff clay are performed by ROLLINS et al. [350] in order to determine the interaction effects dependent on pile spacing. The piles are spaced in 3.3, 4.4, and 5.65 pile diameters in direction of loading with as many as five rows of piles. The first row of piles in the group receive the greatest load, while the second and third rows carry progressively smaller loads. In the case that fourth and fifth rows are present, such pile rows carry about the same load as the third row piles.

BAUHAUS
UNIVERSITÄTSVERLAG

4 Simulation methods

4.1 Energy Method with Integral Description of the Material Behaviour

Generally, numerical analyses, such as the Finite Element Method, see Sec. 4.2, solve a system of equations based on equilibrium conditions. Another method for the computation of numerical solutions is solving an optimisation problem based on extremum principles. An example of such a method is the Energy Method with Integral Description of the Material Behaviour (EIM) developed by RAUE [337, 338]. Further information and development of the method can be found in the thesis of SCHRÖTER [372].
According to the *Bernoulli* hypothesis, cross-sections normal to the axis of the element remain plane during the deformation process. Hence, the strain $\epsilon_x(y,z)$ at an arbitrary point in the cross-section with the coordinates y and z is defined by the linear function:

$$\epsilon_x(y,z) = \epsilon_0 + \kappa_y y + \kappa_z z\,. \tag{4.1}$$

The extremum formulation is based on the *Lagrange*'s principle of the minimum of total potential energy [338]. Using non-linear optimisation, the values ϵ_0, κ_y, and κ_z are found to minimise the following function:

$$\Pi^{\mathrm{C}}_{\mathrm{total}} = \Pi^{\mathrm{C}}_{\mathrm{i}}\left(\epsilon_0,\kappa_y,\kappa_z\right) + \Pi^{\mathrm{C}}_{\mathrm{e}}\left(\epsilon_0,\kappa_y,\kappa_z\right) \Rightarrow \mathrm{MIN} \tag{4.2}$$

The material models are described by an integral formulation of the stress-strain relationship depending on the strain $\epsilon(y,z)$. Therefore, the functions $W(\epsilon)$, $F(\epsilon)$ and $\Phi(\epsilon)$ are introduced, describing a unique and complete representation of the material behaviour (see Fig. 4.1), as in the stress-strain relationship $\sigma(\epsilon)$. They are defined as the following integrals:

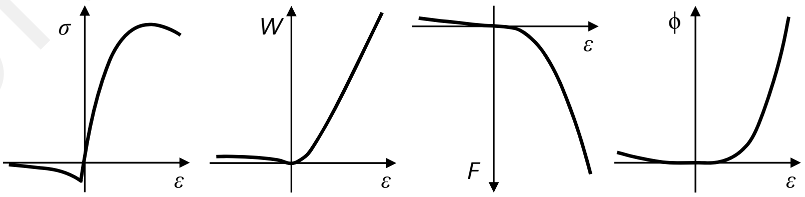

(a) $\sigma(\epsilon)$ (b) $W(\epsilon)$ (c) $F(\epsilon)$ (d) $\Phi(\epsilon)$

Figure 4.1: Integral formulation of stress-strain material models for Energy Method with Integral Description of the Material Behaviour (EIM), concrete material description as an example

$$W(\epsilon) = \int_0^{\epsilon} \sigma(\epsilon)\,\mathrm{d}\epsilon \tag{4.3a}$$

$$F(\epsilon) = \int_0^{\epsilon} W(\epsilon)\,\mathrm{d}\epsilon \tag{4.3b}$$

$$\Phi(\epsilon) = \int_0^{\epsilon} F(\epsilon)\,\mathrm{d}\epsilon \tag{4.3c}$$

With these integrals, the strain energy $\Pi_\mathrm{i}^\mathrm{C}$ of a cross-section with the region B is obtained by integration of the specific strain energy W.

$$\Pi_\mathrm{i}^\mathrm{C} = \iint_B W(y,z)\,\mathrm{d}y\mathrm{d}z = \iint_B W\left[\epsilon(y,z)\right]\,\mathrm{d}y\mathrm{d}z \tag{4.4}$$

The double integral is transformed into an integral along the contour by the *Gauss* theorem according to Eq. 4.5

$$\iint_B W(y,z)\,\mathrm{d}y\mathrm{d}z = \oint_L \left(-\frac{\kappa_z}{\kappa^2} F\,\mathrm{d}y + \frac{\kappa_y}{\kappa^2} F\mathrm{d}z\right)\,, \tag{4.5}$$

where the magnitude κ of the gradient is determined by:

$$\kappa = \sqrt{\kappa_y^2 + \kappa_z^2}\,. \tag{4.6}$$

The potential energy of the external forces of a cross-section loaded by a normal force N and the two bending moments M_y and M_z, is defined by the following equation:

$$\Pi_\mathrm{e}^\mathrm{C} = -\left(N \cdot \epsilon_0 + M_y \cdot \kappa_z + M_z \cdot \kappa_y\right)\,. \tag{4.7}$$

For the calculation on the structural level, the compatibility conditions are used between outside deformations and inner strains. The deformation parameters at the cross section depend on the displacements at the corresponding node of the element are determined by:

$$\epsilon_0 = u^{'}(x)\,, \tag{4.8a}$$

$$\kappa_y = -v^{''}(x)\,, \tag{4.8b}$$

$$\kappa_z = -w^{''}(x)\,. \tag{4.8c}$$

The strain energy of the element can be determined by integration of the strain energy of each cross-section $\Pi_\mathrm{i}^\mathrm{C}$ along the element length l:

$$\Pi_\mathrm{i}^\mathrm{E} = \int_0^l \Pi_\mathrm{i}^\mathrm{C}\mathrm{d}x\,. \tag{4.9}$$

The external energy can be obtained by the integral of the product of external loads and respective displacements over the length of the element:

$$\Pi_\mathrm{e}^\mathrm{E} = -\int_0^l \left[p_x(x)u(x) + p_y v(x) + p_z(x)w(x)\right]\mathrm{d}x\,. \tag{4.10}$$

The energy method (EIM) allows the consideration of the material non-linearities including cracking and tension stiffening. Therefore, the method is used for the simulation of the load-bearing behaviour of various cross-sections, see Sec. 5.1, and restraint effects studied in Sec. 3.5.

4.2 Finite Element Method

The Finite Element method model applied in this thesis was originally developed by KEITEL [206] and implemented in the software MATLAB. In this section, the basic characteristics of this simulation are described. The author recommends referring to the thesis by KEITEL [206] for further information. Geometric and physical non-linear simulations can be analysed for reinforced and prestressed concrete structures with consideration of the time-dependent concrete material behaviour.

Cracks in the concrete are modelled by a “smeared” stress-strain relationship as discussed in Sec. 3.1. *Bernoulli*'s beam theory is applied to the beam elements. Therefore, the strains along the cross section depth and width remain plane during the deformation process and shear deformations are excluded. Moreover, rigid bond, warping and torsional free cross sections, and the negligence of inertia forces are the basic assumptions in the simulation technique.

A beam with seven degrees of freedom according to [43] is presented. At the left and right sides of the beam element, a transverse and longitudinal displacement and a rotation, and additionally a horizontal displacement in the middle of the beam are the degrees of freedom. The displacement in the transverse direction is determined by the shape functions of HERMITE. The longitudinal displacement is computed by quadratic shape functions.

The axial and bending stiffnesses of the beam elements are computed by the integration over the area of the cross section, wherein the mathematical integrations are substituted by summations. Therefore, the cross section is discretised into layers (uniaxial bending) and fibers (biaxial bending) while the integral over the cross section width and depth is replaced by the sum over all layers or fibers. A constant stiffness and a linear distribution of stresses are assumed in each layer and fiber.

For the non-linear simulations caused by geometrical or physical non-linear response, the tangential stiffness matrix is updated in the Newton-Raphson Iteration after each iteration step and the new increment of deformation is determined for the residual forces.

BAUHAUS
UNIVERSITÄTSVERLAG

5 Partial model quality evaluation

5.1 Material modelling of reinforced concrete

Material modelling is a partial model with a potentially strong influence on the computational results and reliable prognosis models [79, 395, 412]. For instance, the analysis of internal forces for restraint sensitive structures, such as pavements, bridge decks, walls, industrial floors, constrained slabs, or integral and semi-integral bridges, is crucially dependent on the stiffness of the structural components and corresponding cross sections [195, 198], see Sec. 3.5. In numerical simulations, this stiffness is primarily determined by the description of the material model. For flexural members, the prognosis of bending stiffness EI is the most significant model output in order to describe the load-deformation behaviour. Moreover, the bending stiffness is one of the key parameters for components subjected to combined loading of restraint and external loads. The cross sectional and structural analysis discussed in Sec. 3.5 illustrates the interaction between stiffness and loading conditions, restraint forces respectively. Therefore, the material models are assessed according to the predicted bending stiffness. The corresponding results are presented in this section.

The uncertainty assessment on a structural level (continuous beams, frames, bridges) is not exclusively influenced by the material model's prognosis of a certain structural element or cross section. Due to the redistribution of internal forces, which is influenced by various conditions (e.g. absolute and relative stiffness ratio, layout of reinforcement bars), the uncertainty in the output from the structural simulation always includes a particular structural effect. This component is caused by force redistribution capacity, geometric conditions, loading distribution, or reinforcement and prestressing layout. These effects are evaluated by the global model evaluation discussed in theory in Sec. 2.5 and can be enhanced to the integrative sensitivity analysis explained in Chap. 6.

In order to independently evaluate the uncertainty in the material model prediction, the corresponding assessment is generally feasible for the load-deformation analysis of any type of cross section, for instance rectangular, circular, T-beams or box girders. This allows for the exclusive evaluation of the concrete material modelling phenomenon and partial model, respectively. In the following section, a common rectangular reinforced flexural cross section for a building is investigated. In general, this evaluation method is applicable to other concrete strength classes, different reinforcing grades, cross sectional types, and geometric conditions. The conditions in this section are specifically chosen in order to actualize the concept and results of the uncertainty analysis for a commonly designed cross section.

The aim of this assessment is to investigate the quantitative difference between the bending stiffness prediction of material models for reinforced concrete flexural members. Non-linear constitutive models for concrete in compression are frequently defined in design guidelines. Engineers would generally use either linear or non-linear compressive models specified in guidelines, such as those models were mentioned in Sec. 3.1.2. In the non-linear modelling of reinforced concrete in tension, various approaches are investigated and may be generally applicable for describing concrete's contribution between the cracks. The selection of a suitable model is usually based upon the engineer's judgement based on theoretical knowledge and

BAUHAUS
UNIVERSITÄTSVERLAG

experience (qualitative model selection).

For each application, it is not immediately apparent which model is the most appropriate to describe the phenomena with suitable accuracy. Therefore, model evaluation with the aid of uncertainty analysis is a useful methodology in order to compare various model predictions in a quantitative manner. More information about the theory of uncertainty analysis is previously discussed in Sec. 2.1. This probabilistic method is capable of assessing the prediction quality of several concrete material models in order to provide a quantitative model selection. In the design process of engineering structures, a lack of experimental data is often present, particularly in the preliminary design phase. Hence, the focus of this study is the assessment of material models without any specific measurement data in order to assist model selection in this project's phase. For that reason, the chosen uncertainty analysis does not use any specific data measurements for the quantification of the model and the parameter uncertainty.

The determination of the behaviour of cracked reinforced concrete is based on the characterisation of the tension stiffening, which describes average cracking along the transmission length, see Sec. 3.1.4. In the interest of the practical applicability of the material models, even for large structures, no discrete crack simulations are considered based on fracture mechanics. Either purely linear models, non-linear compressive models, or non-linear models with the tension stiffening effect are considered in the evaluation. In order to quantify the difference between several model predictions, uncertainty analysis is applied taken into account deterministic and probabilistic simulations. This assessment method investigates the model and parameter uncertainty of the model prediction. Finally, the total uncertainty is converted into a prognostic partial model quality.

5.1.1 Cross section and material models

The general application of uncertainty analysis investigates a commonly designed rectangular cross section with the dimensions $h/b/d/ = 60/25/54\,\text{cm}$, see Fig. 5.1. The amount of reinforcement is chosen to an area of 4∅20 with the following reinforcement ratio ω_{s1}:

$$\omega_{s1} = \frac{A_{s1}}{bd}\frac{f_y}{f_c} = \frac{4 \cdot 3.14}{25 \cdot 54}\frac{550}{21.68} = 0.236\,. \tag{5.1}$$

The distance from the bottom sectional edge to the centre of reinforcement is $d_1 = 6.0\,\text{cm}$. The height of the reinforced subsection (RCT) is defined to $h_{c,\text{eff}} = 2.5 \cdot d_1$ based on [141, 227], see Sec. 3.1.4.5. This value of the effective concrete area in tension is appropriate for cross sections subjected to bending loading condition for ratios $h/(h-d) \leq 10$. The load-deformation behaviour is analysed according to the prediction of bending stiffness $EI_y = M_y/\kappa_z$ where κ_z is the curvature of the strain distribution along the cross section's depth in z-direction. Curvature is a parameter representing the load-deformation behaviour comparable to the bending stiffness EI_y.

However, in the model uncertainty assessment, it is more adequate and accurate to use response quantities which are increasing or decreasing due to load increments even for linear-elastic models. Discussion of this statement is presented in Sec. 5.2.1.2. Therefore, the uncertainty in the prediction of curvature based on the considered models is assessed in order to quantify a partial model quality. The cross section is subjected due to an increasing bending moment M_y with a load increment of $\Delta M_y = 1\,\mathrm{kNm}$ until the cross section fails. Consequently, the dimensionless load increment $\Delta\mu$ is defined to:

$$\Delta\mu = \frac{\Delta M}{f_c b d^2} = \frac{100}{21.68 \cdot 0.25 \cdot 0.54^2} = 6.33\mathrm{e}^{-4}\,. \tag{5.2}$$

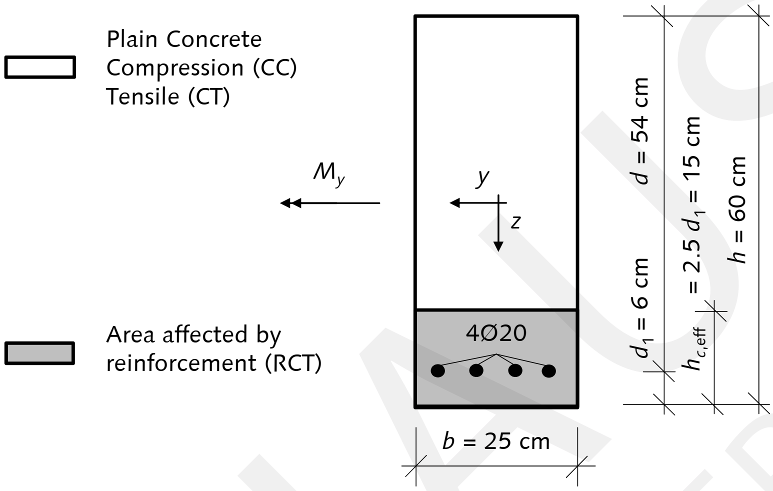

Figure 5.1: Rectangular cross section

This load-deformation simulation allows a quality assessment of material models for uncracked stage, crack formation stage, stabilised cracking stage and steel yielding stage. The material models are associated with the specific subsections of the cross section. For the plain concrete subsection, the concrete is modelled differently with respect to tensile or compressive strains. For the concrete under compression (concrete compression CC), the behaviour is simulated by the non-linear broken rational function of EC 2 [101] and Model Code 2010 [187], respectively.

For plain concrete in tension (concrete tension CT), the linear-elastic material description is applied until the tensile strength f_{ctm}. Different tension stiffening models are applied according to the modelling of the reinforced concrete subsection in tension (reinforced concrete tension RCT). The responses of the material models are quantitatively evaluated and the results are discussed in the following sections. The material models considered in this evaluation are listed in Tab. 5.1. These models consist of a purely linear-elastic model ("lin-el"), a non-linear compressive model ("br-func"), and several non-linear models that consider the tension stiffening effect ("e-func", "multi-lin", "mod-steel").

In the case of the fully linear-elastic material modelling, all special subsections are modelled assuming linear-elastic material behaviour. This material model does not allow any cracking of concrete due to tension and compression. Therefore, the bending stiffness degradation is excluded for all loading levels, which results in it being the simplest material model. This model is denoted as the partial model with the abbreviation "lin-el".

The material model with the abbreviation "br-func" takes the concrete crushing and resulting stiffness degradation in compression into account. The non-linear broken rational function of Eurocode 2 [101] and the Model Code 2010 [187], is applied in order to describe the non-linear material behaviour of concrete in the compressive zone. As a result, any type of cracking in tension is excluded in this material model.

Whereas, the non-linear material models ("e-func", "multi-in", "mod-steel") consider the stiffness degra-

Table 5.1: Material models considered for evaluation of prognosis model quality, abbreviations of the models are defined in first column

Partial Model		Concrete			Reinforcement
		CC	CT	RCT	
①	lin-el	linear-elastic	linear-elastic	linear-elastic	linear-elastic
②	br-func	broken rational function [101]	linear-elastic	linear-elastic	linear-elastic
③	e-func	broken rational function [101]	linear up to f_{ctm}	exponential-function [313]	bi-linear
④	multi-lin	broken rational function [101]	linear up to f_{ctm}	multi-linear stress-strain diagram [74, 187]	bi-linear
⑤	mod-steel	broken rational function [101]	-	-	modified steel strains [74, 126, 187]

dation due to tensile cracking as well as the tension stiffening effect in addition to the stiffness deg ration due to compression, see Tab. 5.1. These models based on the modification of concrete in tension in the subsection RCT consist of the same material descriptions in the plain concrete subsections (CC and CT). In contrast, no contribution of concrete in tension in the subsection CT is considered for the model "mod-steel", because the tensile forces are exclusively carried by the reinforcing steel. Furthermore, differences are visible in the consideration of the tension stiffening effect for these non-linear material models.

The comparison of the model characteristics, as discussed in the subsections of Sec. 3.1.4, leads to the statement, that the model with the modified steel strains ("mod-steel") and the model with the multi-linear definition of concrete in tension ("multi-lin") are the most complex models of the considered material models. A clear distinction between the cracking stages and the consideration of all geometry and material parameters allows more considerable physical phenomena in comparison to the other models ("lin-el", "br-func", "e-func"). In general, no difference in the considered phenomena between both models ("mod-steel","multi-lin") exists for the consideration of the characteristic cracking stages.

It should be noted that a unique numerical solution can be simulated applying the "mod-steel" model due to the continuously increasing potential for all loading levels. In contrast, in the "multi-lin" material model, the uniqueness of the solution which is close to the concrete tensile strength cannot be guaranteed in principle. Consequently, the "mod-steel" model with the adequate accuracy and numerical robustness is fixed as reference model for the other considered material models in the model uncertainty assessment. In order to clarify the choice of the benchmark model, the analysis by Quast [327] emphasises the model with the modified steel strains to be an adequate model in comparison with other tension stiffening models assessed in a validation study of experimental results. In particular, the "mod-steel" model is evaluated to be the most accurate for the flexural loading condition which is similarly considered in the following uncertainty assessment.

5.1.2 Deterministic load-deformation behaviour

The simulation with deterministic input parameters is computed by mean material properties specified afterwards. The results obtained by the different partial models are shown in Fig. 5.2 according to the moment-curvature and the bending stiffness-moment relationship. Dimensionless moment μ and curvature

$d \cdot \kappa$ are mentioned previously. The load-level dependent bending stiffness EI for each model is predicted by the numerical solution of the Energy Method (EIM). The optimized solution of EI is related to the analytical solution of the elastic bending stiffness EI^I:

$$EI^I = I_i \cdot E_c = 4.90197\mathrm{e}^{-3}\,\mathrm{m}^4 \cdot 29,307\,\mathrm{MN/m}^2 = 143.66\,\mathrm{MNm}^2\,. \tag{5.3}$$

In the case of the stiffness ratio $EI/EI^I = 1.0$, the predicted numerical stiffness and the analytical linear-elastic stiffness are equal. This ratio is visible in the range of small loading levels in which the numerical solution achieves the analytical initial bending stiffness. Linear-elastic, compressive and non-linear models considering tension-stiffening effect by modification of concrete stress-strain relationship are all capable to exactly predict the analytical linear-elastic bending stiffness. A discrepancy occurs for the model with modification of strain values of the bare reinforcing steel. All tensile forces in the cross section are exclusively represented by a concrete bar with depth $h_{c,\mathrm{eff}}$. This assumption neglects a certain amount of concrete contribution to the stiffness of the cross section. This is discussed in Sec. 3.1.4 and additionally mentioned by MAURER et al. [267]. In summation, the initial stiffness for the "mod-steel" model is less than the analytical stiffness.

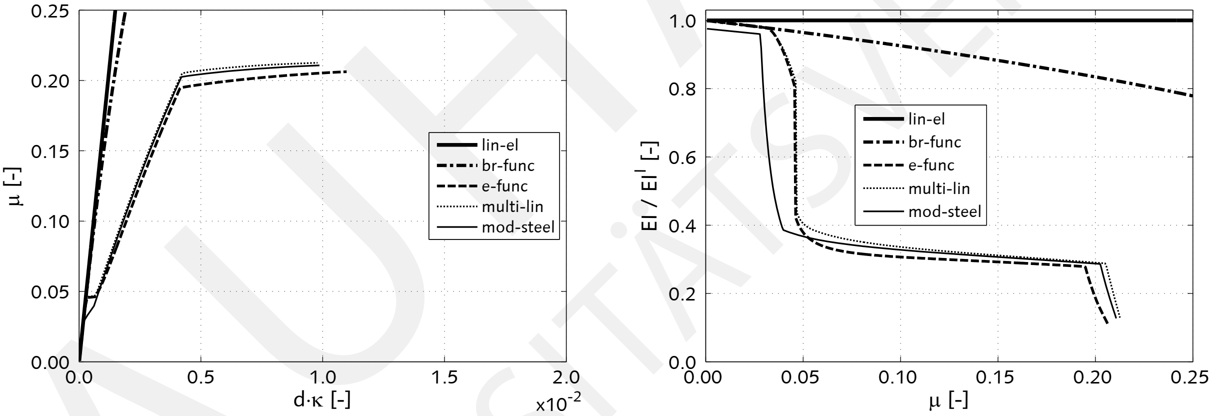

(a) dimensionless moment - dimensionless curvature (b) relative bending stiffness - dimensionless moment

Figure 5.2: Deterministic load-deformation behaviour of rectangular cross section

Increase in the external load causes concrete cracking and crushing and in response, the ratio EI/EI^I decreases. The mathematical computation of the crack moment M_{cr} is based on the linear-elastic bending stiffness for M_y causing the concrete stress f_{ctm}. This analysis results in $M_{cr} = 49\,\mathrm{kNm}$ with a dimensionless crack moment of $\mu_{cr} = 0.031$. Concrete crushing considered by the broken-rational function causes a stiffness degradation for loading levels smaller than this mathematical approximation. Nevertheless, this difference is negligible and the models "e-func" and "multi-lin" are able to still adequately predict the crack moment. The "mod-steel" model is not able to predict the initial load-deformation behaviour due to the fact it considers less initial bending stiffness. The main stiffness degradation occurs in the crack formations stage until the beginning of stabilised cracking stage. This degradation is in the range of $0.4\,EI^I$ for all non-linear models considering the tension stiffening effect.

The crack formation stage is similarly analysed by the exponential function and multi-linear determination, but in the stabilised cracking stage a higher concrete contribution between the cracks is determined in the model description for "multi-lin" in comparison to "e-func". Therefore, plastic strains in the reinforcing steel occur at smaller loading levels in the model with exponential function that describes the tension stiffening effect. Stabilised cracking stiffness ($\approx 0.4EI^I$), stiffness at yield moment ($\approx 0.3EI^I$) and stiffness at ultimate capacity ($< 0.2EI^I$) are closely analysed for "multi-lin" and "mod-steel". Due to the similarities in their model description the same simulation output is approximately analysed for both.

Comparison of the linear and compressive model illustrates that the non-linear models enable a much more accurate consideration of the stiffness degradation due to concrete cracking. When considering the concrete crushing in the compressive zone, this allows only a slight stiffness degradation of about $0.8EI^I$ even for higher loading levels than the ultimate capacity of the actual cross section. The fully linear-elastic model always predicts $1.0EI^I$ as a standard model property.

The different model predictions show that all model characteristics are considered in the optimised solutions based on the EIM. Therefore, the solutions are reliable and high level of accuracy is achieved. Differences between the models are previously discussed and the results of the model evaluation are subsequently presented.

5.1.3 Probabilistic load-deformation behaviour

5.1.3.1 Input parameters

The scatter in the model input parameters, such as a material strength, influences the uncertainty in the model prediction, which is quantified in the parameter uncertainty. For the study of the load-deformation behaviour of a reinforced concrete section, this uncertainty is considered on the resistance (material) side. The effect of action side is set to be deterministic without any variance.

The probabilistic input parameters for the assessment of parameter uncertainty are concrete compressive strength f_{cm}, concrete tensile strength f_{ctm}, concrete secant modulus of elasticity E_{cm}, reinforcing steel yielding strength f_y, reinforcing steel tensile strength f_t, and reinforcing steel modulus of elasticity E_s. The concrete grade C 30/37 is chosen as it is a commonly applied class for buildings. High ductility reinforcing steel B 500B is selected for the steel bars. The mean values of the material parameters for the

- concrete class C 30/37 according to EC 2 [101] are:
    - $f_{cm} = 38.0$ MN/m^2 ,
    - $f_{ctm} = 2.90$ MN/m^2 ,
    - $E_{cm} = 32,837$ MN/m^2 , and for the
- reinforcing steel B 500B the characteristic parameters are determined according to DIN 488 [135] :
    - $f_{yk} = 500$ MN/m^2 ,
    - $f_{tk} = 540$ MN/m^2 ,
    - $E_s = 200,000$ MN/m^2 .

The safety concept of EC 2 according to the German National Annex [141] defines the "calculation" material properties (expressed by index "R") for the physical non-linear simulations, see Sec. 2.6.4. Therefore, the mean material properties considering the safety concept for non-linear simulations are:

- concrete class C 30/37:
    - $f_{cR} = 21.68$ MN/m^2 ,
    - $E_{c0mR} = 29,307$ MN/m^2 , and for the
- reinforcing steel B 500B:
    - $f_{yR} = 550$ MN/m^2 ,
    - $f_{tR} = 594$ MN/m^2 .

The "calculation" material properties are used for the physical non-linear simulation of the load-deformation behaviour of the rectangular cross section. The sampling of the input parameters for the material models is performed using the Latin Hypercube Sampling Method [184, 254], see Sec. 2.1. Correlation between the input parameters significantly influences the results of the uncertainty analysis [208]. Consideration of parameter correlation in the sampling is more accurate in order to describe statistical characteristics of multi-dimensional sample sets. Therefore, correlation is taking into account in the sampling of the considered input parameters. Distribution type, mean value, standard deviation, coefficient of variation, and correlation of the material properties are listed in Tab. 5.2.

Table 5.2: Material input parameters for deterministic and probabilistic analysis, LN. . . log normal distribution, N. . . normal distribution

Mat. Prop.	$f_X(x)$	μ [MN/m^2]	σ [MN/m^2]	CV [-]		Correlation $\rho_{X_1X_2}$ [-]					
						f_{cR}	f_{ctm}	E_{c0mR}	f_{yR}	f_{tR}	E_s
							[149, 387, 388]			[105]	
f_{cR}	LN	21.68	4.12	0.19	[397]	1	0.82	0.80	0	0	0
f_{ctm}	LN	2.90	0.84	0.29	[105]	0.82	1	0.65	0	0	0
E_{c0mR}	LN	29,307	7,034	0.24	[401]	0.80	0.65	1	0	0	0
f_{yR}	N	550	27.50	0.05	[3, 370, 387]	0	0	0	1	0.85	0
f_{tR}	N	594	17.82	0.03	[3]	0	0	0	0.85	1	0
E_s	N	200,000	2,000	0.01	[63, 105, 387]	0	0	0	0	0	1

The results of Latin Hypercube sampling are illustrated for the correlated parameters in Fig. 5.3 and uncorrelated parameters in Fig. 5.4. The correlation is visible due to the linear dependency between concrete compressive strength and tensile strength, concrete compressive strength and modulus of elasticity, concrete tensile strength and modulus of elasticity, and steel yielding and tensile strength. The concrete properties are sampled according to the log normal distribution and the steel quantities based on the normal distribution. The long tail of the log normal distribution is obvious causing very high strength and stiffness parameters. Nevertheless, their influence is negligible for the uncertainty assessment but should be seriously proven for reliability analysis.

In contrast, no correlation is obvious for the relationship between steel yielding strength and modulus of elasticity, and steel tensile strength and modulus of elasticity. There is no linear dependence between these parameters predefined in the sampling process ($\rho_{X_1X_2} = 0$). The assessment of the stimulated samples illustrates this relation with a high level of accuracy. The low variance in E_s and the higher variance in f_{yR} in comparison to f_{tR} is also noticeable in the determined samples according to Fig. 5.4.

Comparison of the predefined statistical characteristics (distribution type, mean value, coefficient of varia-

BAUHAUS
UNIVERSITÄTSVERLAG

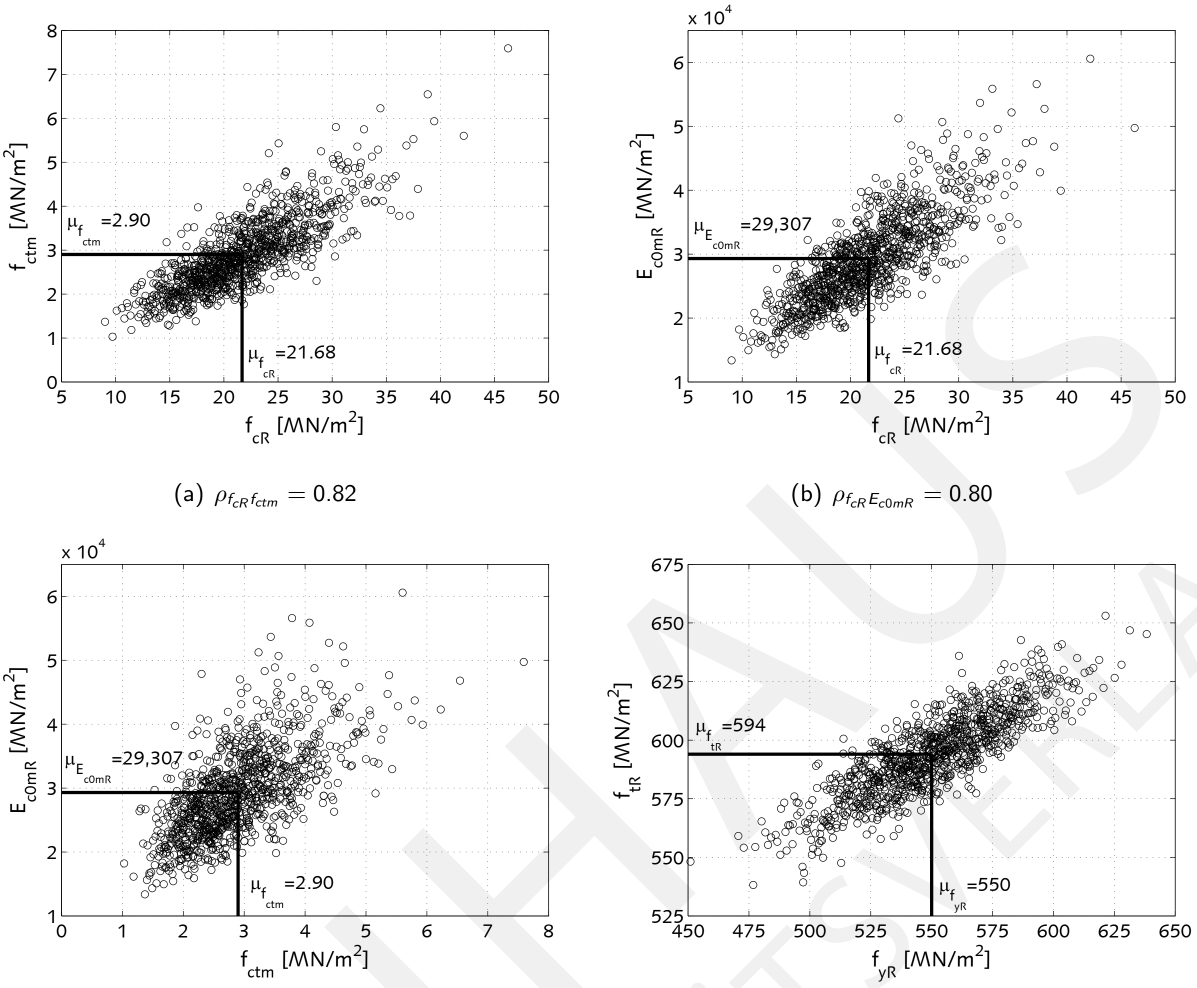

(a) $\rho_{f_{cR}f_{ctm}} = 0.82$

(b) $\rho_{f_{cR}E_{c0mR}} = 0.80$

(c) $\rho_{f_{ctm}E_{c0mR}} = 0.65$

(d) $\rho_{f_{yR}f_{tR}} = 0.85$

Figure 5.3: Joint probability distribution for correlated parameters of concrete and reinforcing steel for 1000 samples

tion, and correlation) and the computed properties of the samples exhibits a very good agreement. Hence, the computed samples are reliable enough to be considered in the desired statistical information.

5.1.3.2 Stress-strain relationship

The material behaviour of plain concrete under compression is modelled by the broken rational function recommended in EC 2 [101, 141]. Based on the probabilistic input parameters, several stress-strain relationships for 1000 samples are shown in Fig. 5.5(a). The mean compressive strength is $f_{cR} = -21.68\,\mathrm{MN/m^2}$ with the corresponding compressive strain of $\epsilon_{c1} = -2.16\,‰$ according to Eq. 3.16. The standard deviation of the strain is $\sigma_{\epsilon_{c1}} = -0.12\,‰$ and the coefficient of variation is consequently $CV_{\epsilon_{c1}} = 0.06$. Uncertain input parameters induce a standard deviation in the factor k (mean value $\mu_k = 2.92$) of the broken rational function of $\sigma_k = 0.40$ resulting in $CV_k = 0.14$. The ultimate strain is fixed to the recommended value of $\epsilon_{cu1} = -3.50\,‰$ according to EC 2. For plain concrete in tension, the probabilistic stress-strain relationships are shown in Fig. 5.5(b). For a loading level which causes a concrete stress equal to the tensile strength, no tensile force can be transmitted to the plain concrete past this loading level. The maximum admissible strain $\epsilon_{ct} = f_{ctm}/E_{c0mR}$ is on average $9.90\,\mathrm{e}^{-5}$. The corresponding standard deviation is $\sigma_{\epsilon_{ct}} = 2.12\,\mathrm{e}^{-5}$

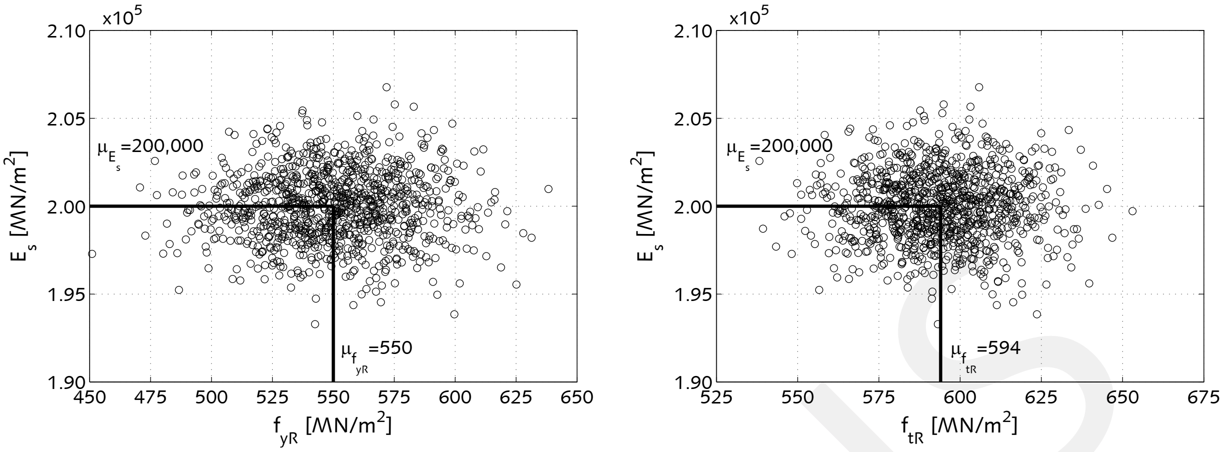

(a) $\rho_{f_{yR}E_s} = 0$ (b) $\rho_{f_{tR}E_s} = 0$

Figure 5.4: Joint probability distribution for uncorrelated parameters of reinforcing steel for 1000 samples

and the coefficient of variation is $CV_{\epsilon_{ct}} = 0.21$.

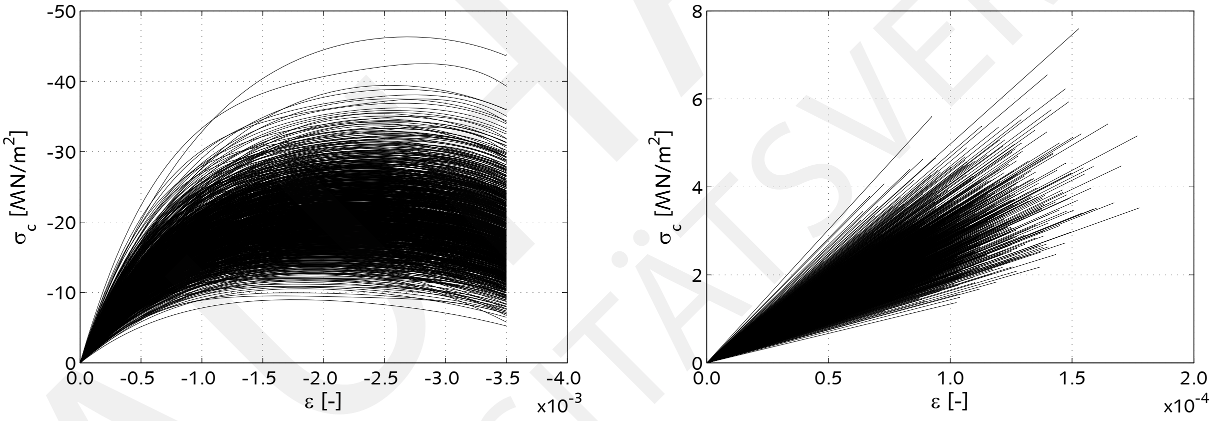

(a) broken rational function (b) linear-elastic up to f_{ctm}

Figure 5.5: Probabilistic σ-ϵ relationship for plain concrete under compression and tension

The probabilistic σ-ϵ relationships for the tension stiffening model with the exponential function is depicted in Fig. 5.6(a). This model describes the concrete contribution between the cracks for strains greater than $\epsilon_{ct} = f_{ctm}/E_{c0mR}$ by the exponential function in the crack formation and stabilised cracking stage. In the steel yielding stage, a liner relationship is considered determining the decreasing part of the concrete contribution between the cracks, which finally tends to zero. This concrete material model is additionally illustrated until the crack formation stage neglecting steel yielding stage in the appendix in Fig. B.3. The parameter α describing the tension stiffening effect in the crack formation and stabilised cracking stage is on average $\alpha = 3,027$. Probabilistic simulation lead to a coefficient of variation of $CV_\alpha = 0.29$. The coefficient of variation of the strain value ϵ_{c3} determining the intersection between stabilised cracking and steel yielding stage is $CV_{\epsilon_{c3}} = 0.06$. Uncertainty in the ultimate strain ϵ_{c4} is reduced to $CV_{\epsilon_{c4}} = 0.04$.
For the tension stiffening model with multi-linear material description, the probabilistic σ-ϵ relationships are shown in Fig. 5.6(b). In addition to the strain values describing the interaction between the cracking stages

as in the "e-func" model, this model considers the intersection between crack formation and stabilised cracking stage as a strain value ϵ_{c2}. The uncertainty in this strain value is $CV_{\epsilon_{c2}} = 0.25$. The variances in the strain values ϵ_{c3} and ϵ_{c4} are identical to the model "e-func". The "multi-lin" concrete material model is additionally illustrated until the crack formation stage neglecting steel yielding stage in the appendix in Fig. B.3.

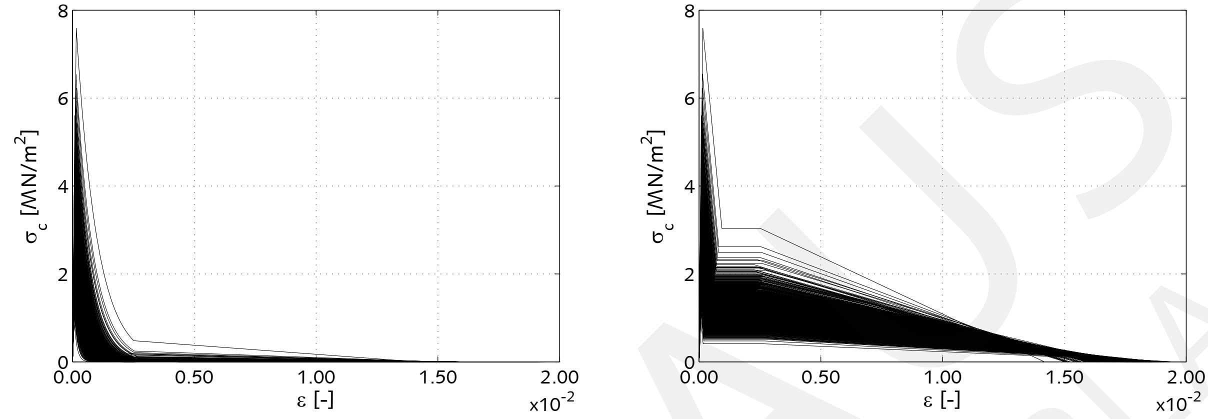

(a) exponential function

(b) multi-linear model

Figure 5.6: Probabilistic σ-ϵ relationship for reinforced concrete in tension, concrete models

The probabilistic σ-ϵ relationship for the tension stiffening model based on modified reinforcing steel strains is shown in Fig. 5.7. The variance of all strain values for the determination of the "mod-steel" model is reasonably as same as the concrete material models. Variance in the reinforcing steel stress determining the intersection between uncracked and crack formations stage σ_{s1} is computed to $CV_{\sigma_{s1}} = 0.26$ which is the same uncertainty as σ_{s2}. Uncertainty in σ_{s3} and σ_{s4} are justified as the predefined variance in f_{yR} and f_{tR}. The probabilistic stress-strain relationships for the bare reinforcing steel (bi-linear) are shown in the appendix in Fig. B.4 which are applied for the "e-func" and "multi-lin" models.

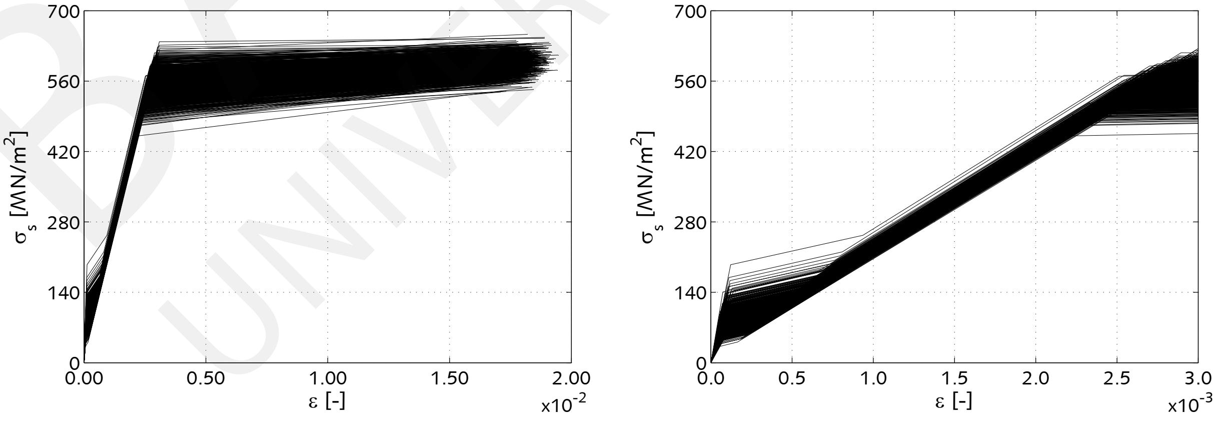

(a) all cracking stages

(b) until crack formation stage

Figure 5.7: Probabilistic σ-ϵ relationship for reinforced concrete in tension, modified steel strain model

5.1.3.3 Load-deformation behaviour

The probabilistic load-deformation behaviour of the rectangular cross section analysed with the linear-elastic material model ("lin-el") is shown in Fig. 5.8. Any crack formation, hence any stiffness degradation, is not considerable in this material model and are generally neglected for all loading increments. This means that the stiffness prediction is independent of the loading level. All the samples reach equilibrium for all of the external bending moments. Due to the log normal distribution of the concrete parameters, some samples lead to a high linear-elastic stiffness in the range $> 1.6EI^I$. The maximum uncracked bending stiffness is $1.97EI^I$ and the minimum one is $0.50EI^I$. This range of linear-elastic stiffness is the same for all of the material models because identical samples are used in the simulation of each material model.

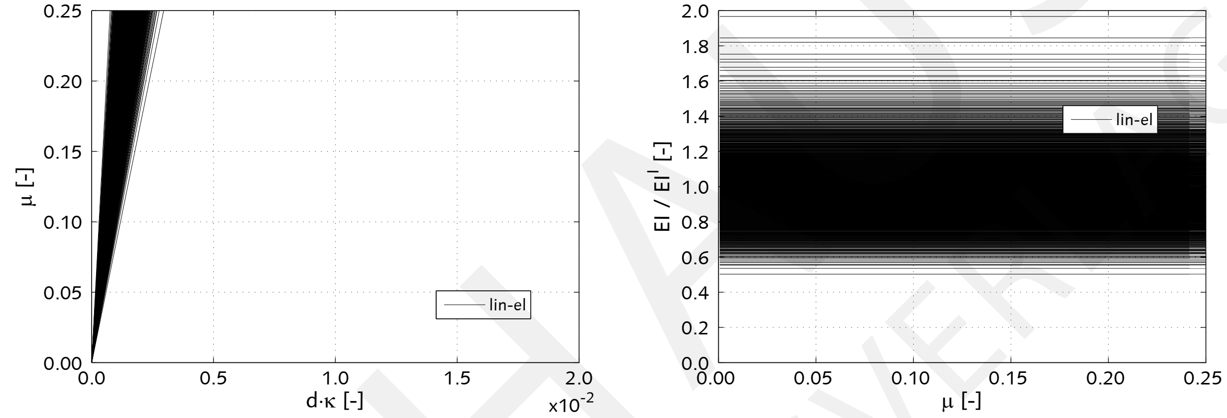

(a) dimensionless moment - dimensionless curvature (b) relative bending stiffness - dimensionless moment

Figure 5.8: Probabilistic load-deformation behaviour of rectangular cross section simulated by linear-elastic model "lin-el", 1000 samples

The first step in increasing the complexity in the model description is to consider the stiffness degradation of a reinforced concrete section by allowance of concrete compressive crushing. The model with broken rational function ("br-func") considers this phenomenon and the corresponding results are illustrated in Fig. 5.9. Stiffness degradation is even visible for small loading levels at the beginning of loading. Therefore, concrete crushing considered by the broken rational function results in a continuously decreasing bending stiffness over the entire loading level. Certain combinations of samples induce the failure condition in the cross section and therefore not all of the samples reach equilibrium condition for high bending moments of $\mu > 0.15$. Failure occur (in total 39 samples of 1000 samples) due to exceeding the maximum admissible compressive concrete strain $\epsilon_{c1u} = 3.5\,‰$ at the loading level $\mu = 0.253$ (equal to $M_y = 400\,\text{kNm}$).
Furthermore, the relationship between bending moment and simulated curvature considering the tension stiffening effect by the exponential function ("e-func") is illustrated in Fig. 5.10. The uncertainty of the material properties results in a large distribution of the loading levels in which the stabilised cracking stage is initiated. This range of the bending moment is between $0.018 < \mu < 0.114$ ($28 < M_y\,[\text{kNm}] < 180$) which is approximately 38 % of the entire loading range. In some samples, no plastic deformation occurs in the reinforcing steel which is associated with an high initial linear-elastic stiffness. Concrete modulus of elasticity and compressive strength mainly affect this stiffness. Low initial stiffness is caused by low quantities of these parameters and therefore the failure of the cross section is caused by exceeding the limit concrete compressive strain ϵ_{c1u}. A much more ductile behaviour is seen in samples for which this yielding

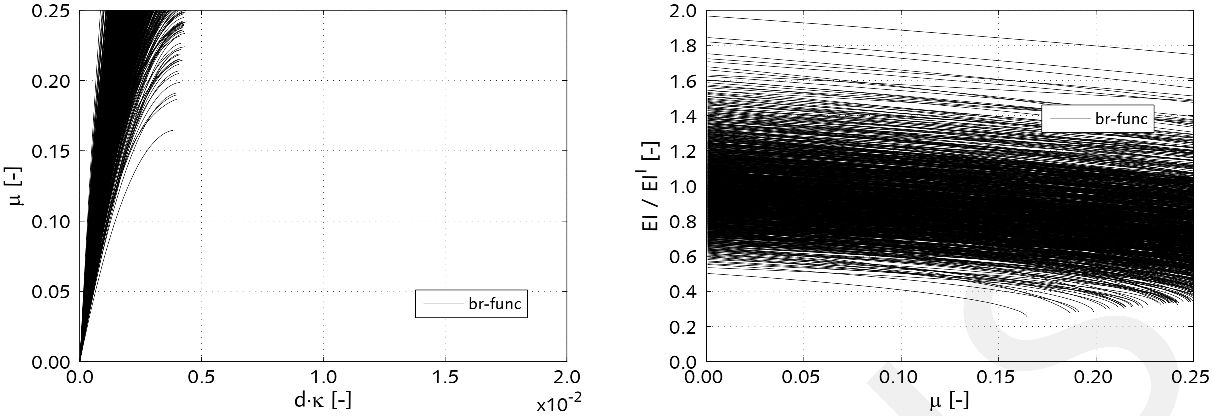

(a) dimensionless moment - dimensionless curvature (b) relative bending stiffness - dimensionless moment

Figure 5.9: Probabilistic load-deformation behaviour of rectangular cross section simulated by broken rational function model "br-func", 1000 samples

appears in the reinforcement. The range of the steel yielding stage is apparent for loading levels between $0.160 < \mu < 0.248$ ($253 < M_y$ [kNm] < 392), which is approximately 35 % of the entire loading range.

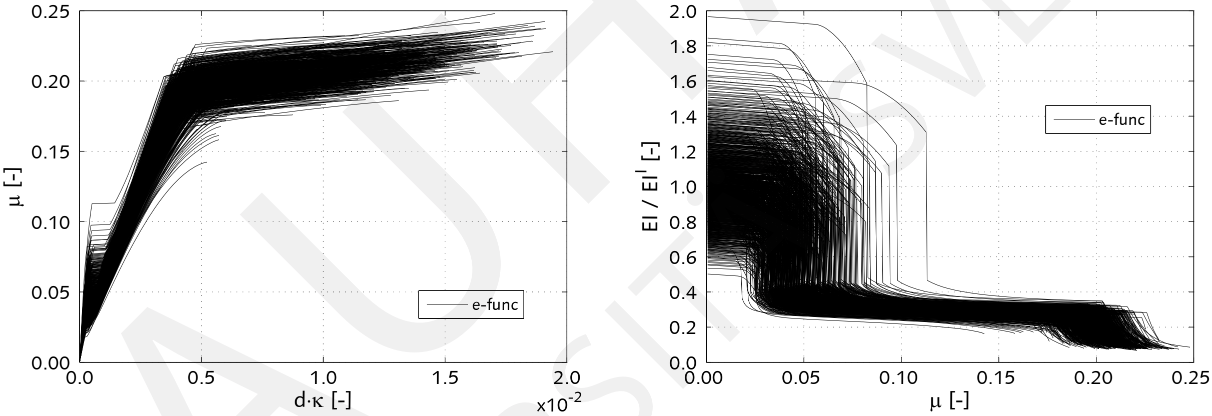

(a) dimensionless moment - dimensionless curvature (b) relative bending stiffness - dimensionless moment

Figure 5.10: Probabilistic load-deformation behaviour of rectangular cross section simulated by exponential function model "e-func", 1000 samples

Another model for determining the tension stiffening effect in the concrete material description is the multi-linear material model ("multi-lin"). The probabilistic load-deformation behaviour of the rectangular cross section computed by the multi-linear model description is shown in Fig. 5.11. The loading range for which the stabilized cracking stage is predicted is between $0.018 < \mu < 0.115$ ($28 < M_y$ [kNm] < 182). This is similar to 39 % of the entire loading range. Moreover, the loading spread for the steel yielding stage is $0.170 < \mu < 0.250$ ($269 < M_y$ [kNm] < 395) which is 32 % of the entire loading range. Both ranges are very similar to the "e-func" model. Only a slight difference is visible. The greater concrete contribution between the cracks in the stabilised cracking stage leads to an initiation of steel yielding for higher load levels compared to the model with the exponential function. In consequence, the ultimate capacity is also slightly increased. Crack initiation, crack formation stage until the beginning of stabilised cracking stage are comparable between the models "multi-lin" and "e-func".

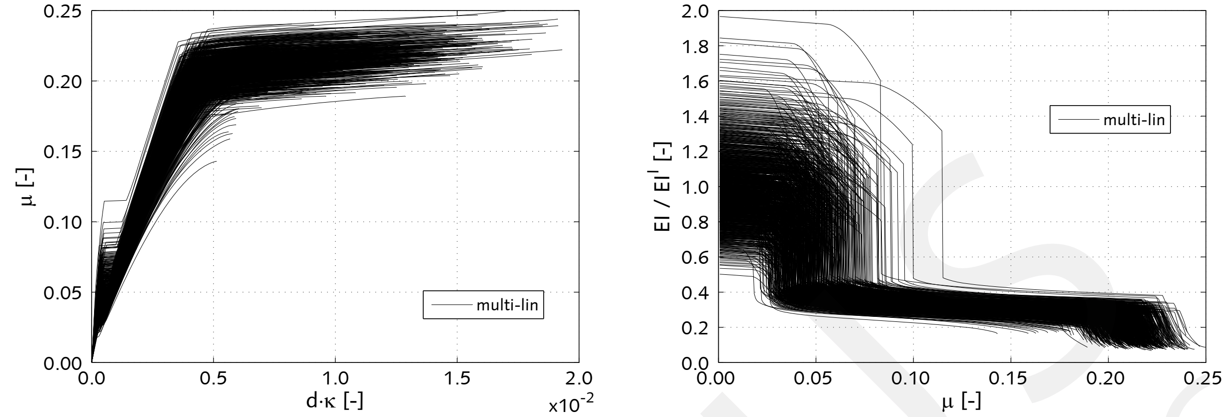

(a) dimensionless moment - dimensionless curvature (b) relative bending stiffness - dimensionless moment

Figure 5.11: Probabilistic load-deformation behaviour of rectangular cross section simulated by multi-linear model "multi-lin", 1000 samples

Moreover, the tension stiffening effect is further considerable in the stress-strain relationship for reinforcing steel. The relationship between the bending stiffness and corresponding curvature for the material model with the modified steel strains ("mod-steel") is shown in Fig. 5.12. The initial linear-elastic bending stiffness is underestimated by this model as discussed before. Therefore, the range of elastic stiffness at loading initiation is different in comparison to the models mentioned above. The maximum uncracked bending stiffness is $1.90EI^{I}$ and the minimum is $0.50EI^{I}$. The range in loading for initiation of stabilised crack stage is $0.015 < \mu < 0.098$ ($23 < M_y\,[\mathrm{kNm}] < 155$), which is 33 % of the entire loading range. Therefore, the stabilised cracking stage appears for smaller loading levels than in the models "e-func" and "multi-lin" models, due to the smaller inital bending stiffness preditiction. Furthermore, the loading spread for the steel yielding stage is $0.168 < \mu < 0.247$ ($265 < M_y\,[\mathrm{kNm}] < 395$) which is 33 % of the entire loading range.

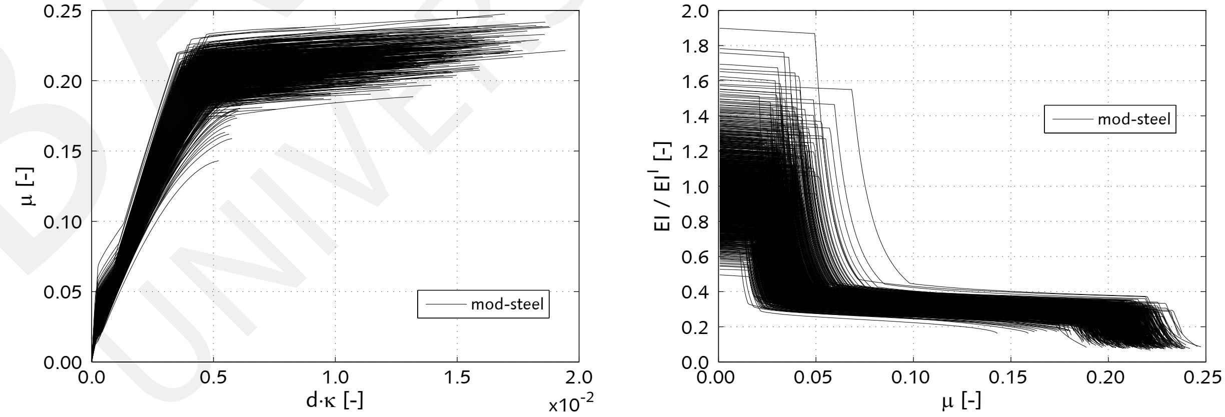

(a) dimensionless moment - dimensionless curvature (b) relative bending stiffness - dimensionless moment

Figure 5.12: Probabilistic load-deformation behaviour of rectangular cross section simulated by modified steel strain model "mod-steel", 1000 samples

5.1.4 Uncertainty analysis

5.1.4.1 Parameter uncertainty

The quantification of parameter uncertainty is simulated with 1000 samples of the probabilistic material properties for concrete and reinforcing steel according to Tab. 5.2. The analysis of the model output for 10, 100, 200, 500 and 1000 samples emphasises accurate results in the case of 1000 input samples, because the difference in the uncertainty for 500 and 1000 samples is negligible, see Fig. 5.13(b).

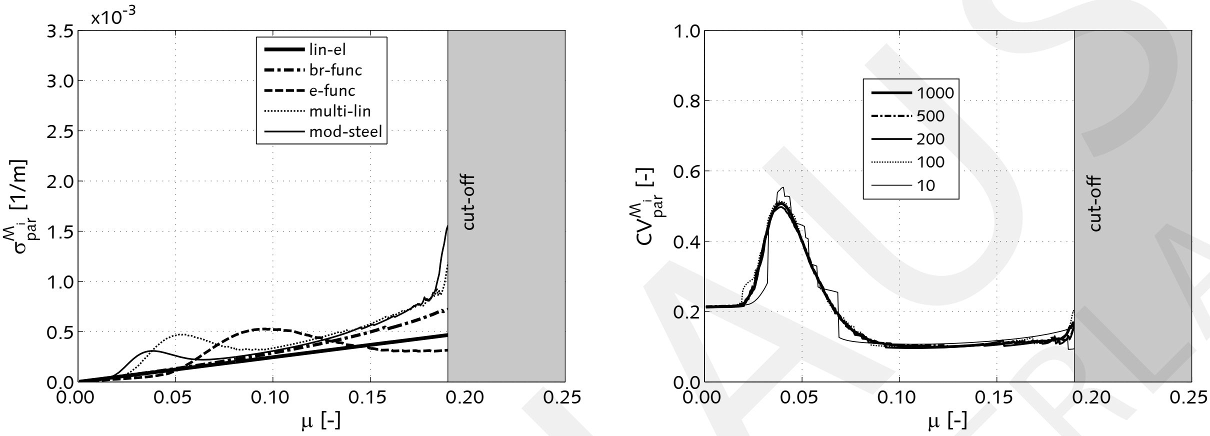

(a) standard deviation (b) sample size dependence

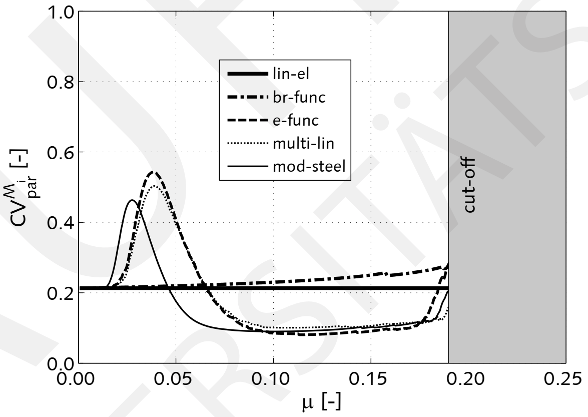

(c) coefficient of variation

Figure 5.13: Load level dependency of parameter uncertainty of material models

The influence that the probabilistic material properties have on the prediction of bending stiffness differs with respect to the loading level, see probabilistic simulations shown in Sec. 5.1.3. The effect of the uncertain model input parameters on the linear-elastic stage is significantly higher in comparison to the stabilised cracking stage. Therefore, the variance of the model response is higher in the uncracked stage, which is caused by the influence of all the uncertain input parameters in this stage, especially by variance in concrete modulus of elasticity and concrete compressive strength, refer to the following paragraph "Sensitivity analysis". However, for higher load levels some uncertain parameters are less influential on the bending stiffness prediction. Therefore, the variance of the model response decreases.

The relationship between variance in model prediction and probabilistic input parameters is quantified for

BAUHAUS
UNIVERSITÄTSVERLAG

all material models by parameter uncertainty evaluation, see Fig. 5.13. For high loading levels ($\mu > 0.150$, $M_y > 237$ kNm, see Sec. 5.1.3), it is obvious that not all of the 1000 samples reach equilibrium condition, because the failure of the cross section is predicted by the maximum material strains. The quantification of the model quality is limited to the loading level, where 90 % of all of the samples of all models reach a prediction without a bending failure due to exceedance of the material ultimate limit strains, see Fig. B.2 in the appendix. Hence, the results in the uncertainty graphs are limited to a loading level of $\mu \leq 0.190$ ($M_y \leq 300$ kNm), which is depicted by the "cut-off" in the graphs.

The linear-elastic material model ("lin-el") does not take any kind of stiffness degradation into account. Consequently the influence caused by the scatter of the input parameters is not dependent on the loading level. The parameter uncertainty for the linear-elastic material model remains constant with the magnitude of $CV_{\text{par}}^{\mathcal{M}_{\text{lin-el}}} = 0.21$. Whereas, the stiffness degradation due to the concrete being in compression in the material model "br-func" causes a slight increase in the parameter uncertainty for loading levels $\mu > 0.05$ ($M_y > 79$ kNm). The variance in the bending stiffness prediction of the samples increases for these loading ranges, which are caused by non-linear stress-strain relationship of the broken rational function in the range of $\sigma_c > 0.4 \cdot f_{cm}$. Therefore, a discrepancy occurs between the "lin-el" and "br-func" models.

In the case of the non linear material models that consider the tension stiffening effect, the parameter uncertainty is strongly affected by the loading level. For identical loading levels in the range of crack initiation moment, some samples remain in the uncracked stage while cracks already occur in other samples under tension. The bending stiffness for both stages varies significantly and hence the uncertainty increases in the prediction. A difference between the "mod-steel", "e-func" and "multi-lin" models is apparent in this stage, which results from the higher variance of the concrete material properties and the stronger influence of these properties on the bending stiffness as considered in the material "e-func" and "multi- lin" models. In the stabilised cracking stage, the parameter uncertainties of the tension stiffening models are similar and lower compared to the linear-elastic material modelling and the "br-func". The influence of the concrete tensile strength decreases in this stage and the stiffness is mainly defined by reinforcing steel modulus of elasticity. In the linear-elastic model "lin-el", all concrete material properties influence the prognosis of stiffness independence of the loading level. When close to the yielding bending moment, an analogous relationship to the crack initiation moment occurs. For an identical bending moment in this loading level, some samples remain in the stabilised crack stage while in others plastic stains appear in the reinforcing steel bars. The prediction of bending stiffness for both stages differs significantly, as a result the parameter uncertainty increases.

Sensitivity analysis

In order to quantify the influence of each random input parameter, the sensitivity analysis of Xu and Gertner [413] is appropriate to study models with correlated parameters. For this sensitivity study, a linear regression is used in order to quantify uncorrelated and correlated sensitivity of the input parameters. Therefore, the coefficient of determination R^2 identifies the capability of the regression curve to represent the simulation results. For the load-deformation analysis, the response of material models is extremely non-linear in the incremental load study. Therefore, various sample set sizes are analysed and the coefficient of determination for 1000, 10000, and 100000 is shown in Fig. 5.14(b).

The results of the "mod-steel" model show that sample size affects the accuracy of the regression for loading ranges in which the first samples have already failed due to exceeding material limit strains. Increase in sample size enables a more accurate computation of the regression analysis due to the fact that more data points are available for loading ranges although some samples are already failed. Comparison between the sensitivity indices for 1000, see Fig. 5.14(a), and 100000 samples, see Fig. 5.14(c) also shows this effect. The coefficient of determination in the elastic stage is 0.92 caused by the correlation between the random input parameters and their strong interaction in the prediction of bending stiffness.

For further load increments, the linear regression is comparatively inaccurate to represent the high non-linear behaviour between the intersection of elastic and crack formation stage. Therefore, R^2 decreases to 0.60 for $\mu = 0.023$. In the case that more or less samples are in the crack formation stage or even in the stabilised cracking stage, the regression is more accurate with R^2 similar to the elastic stage. A similar behaviour also occurs at the intersection between stabilised and steel yielding stage. In these loading stages, the difference in the response is extremely high and very non-linear. As a result, this behaviour cannot be accurately approximated by the linear regression. Therefore, the coefficient of determination decreases in the final loading levels.

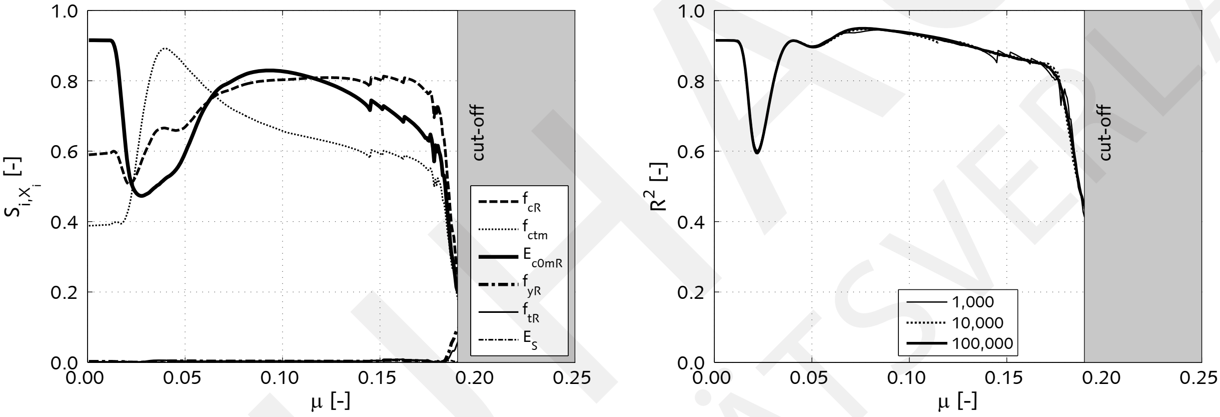

(a) first-order sensitivity index, 1000 samples

(b) coefficient of determination

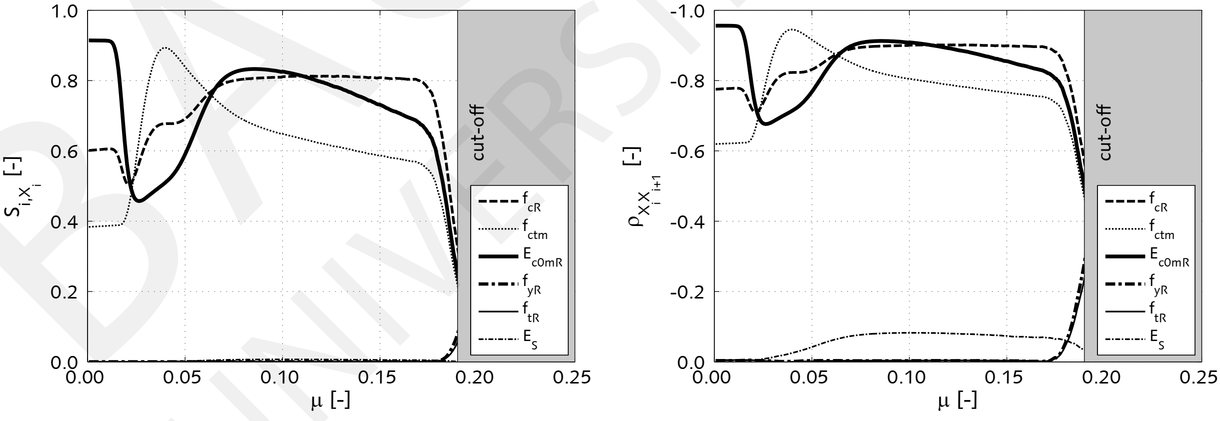

(c) first-order sensitivity index, 100000 samples

(d) linear correlation coefficient, 100000 samples

Figure 5.14: Load level dependency of random input parameter sensitivity on response of "mod-steel" material model

The comparison between the correlation coefficient $\rho_{X_iX_{i+1}}$ and the estimated sensitivity indices S_{i,X_i} shows a comparable relationship between the influences of the random parameters on the model prognosis. Therefore, the sensitivity values are still capable of giving general information about the influence of each parameter even for loading levels in which the linear regression is not adequate enough to represent the non-linearity of the simulation results. Nevertheless, the sensitivity values analysed in these loading ranges should not be seen as exact sensitivity indices for the non-linear model responses. Only the relationship between the parameters can be discussed as the comparison to the correlation coefficient shows.

The elastic bending stiffness is influenced by the concrete material properties. In decreasing order, the concrete modulus of elasticity, the compressive strength, and the tensile strength are the most influential sensitive parameters. However, in the loading range at which crack initiation occurs, the sensitivity of the concrete tensile strength increases and is in the end even more sensitive than the modulus of elasticity. The bending crack moment is influenced by the concrete tensile strength which essentially determines the loading condition in which stiffness degradation due to concrete cracking appears. Hence, the sensitivity of this material property is extremely high in comparison to the other random variables.

Further load increments lead to the stabilised cracking stage in which the bending stiffness is more influenced by concrete compressive strength and modulus of elasticity than sensitive to the value of tensile strength. The constant concrete contribution in the tension stiffening effect and the full cracked concrete parts of plain concrete in tension reduce the sensitivity of tensile strength. The bending stiffness is influenced more by the concrete compressive crushing. Hence, the sensitivity of compressive strength increases and is in the end the most influential material property in the stabilised cracking stage.

In the intersection between the stabilised cracking and the steel yielding stages, the sensitivity of the concrete properties significantly reduce and the sensitivity for the reinforcement properties increase. Many more samples samples fail for these loading conditions due to the smaller initial bending stiffness which is caused by the low values of concrete material properties. Therefore, the samples with failure condition that are more sensitive to the concrete properties are already excluded in the loading range of steel yielding stage. Finally, the remaining samples are more sensitive to variations in the steel yielding strength which reduces the influence of concrete properties and additionally increases the sensitivity of steel modulus of elasticity.

5.1.4.2 Model uncertainty

The load-deformation analysis predicts that the cross section resistance is being generally influenced by the selection of a certain models and the corresponding material characteristics. Material properties such as concrete compressive strength are defined in the design guidelines as in strength below 5 % of all test specimens may be expected to fail. In a similar way, the one-sided 95 % quantile (5 % quantile respectively) is used for the quantification of the model uncertainty and therefore $b = 0.608$ in order to represent the corresponding quantiles, see Sec. 2.1.3. Nevertheless, a comparative study between the assumptions of 90 % and 97.5 % quantile values evaluates a difference in model uncertainty smaller than $\Delta CV_{\text{mod}}^{\mathcal{M}_i} < 0.10$ for the comparison between 90 % and 97.5 % quantile values, see in the appendix in Fig. B.1.

The discussion of the model characteristics (see Sec. 5.1.1) leads to the conclusion that the model with modified steel strains is the most complex model that is considered. Therefore, this model is fixed as a reference model (benchmark) for all the others. The results of the model uncertainty are shown in Fig. 5.15. In the uncracked stage, the prediction of the bending stiffness is similar between the linear-elastic model and the non-linear models in comparison to the reference model. Hence, the model uncertainty is very low and considered negligible. This relationship in the model uncertainty changes in the cracked stages. The linear-elastic model ("lin-el") cannot consider any type of concrete cracking and crushing. Therefore, model uncertainty increases for further load increments, because stiffness degradation occurs in the non-linear

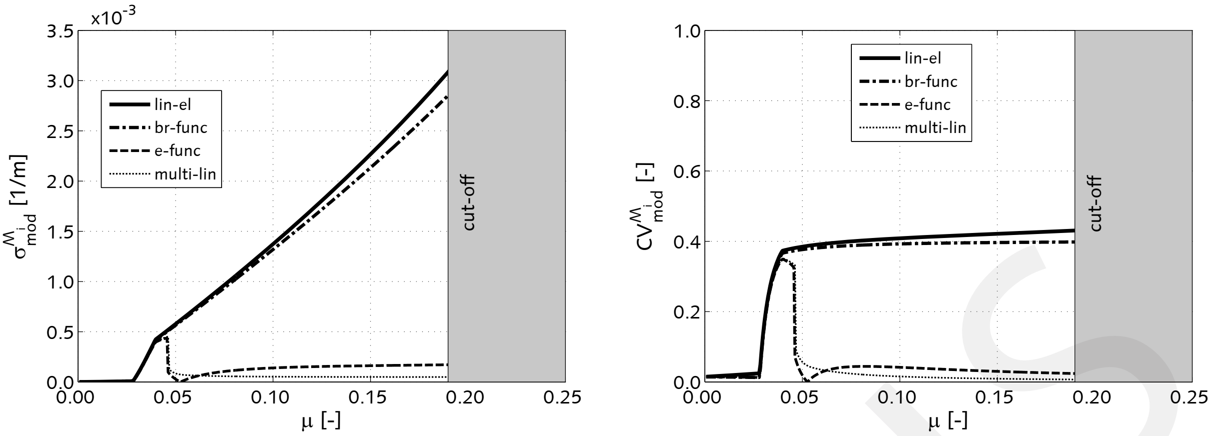

(a) standard deviation for 95 % quantile

(b) coefficient of variation for 95 % quantile

Figure 5.15: Load level dependency of model uncertainty of material models

models in the crack formation stage and stabilised cracking stage. In consequence, the model uncertainty of the "lin-el" model is increasing for the entire loading range starting at crack initiation. In the case of the "br-func" model, the bending stiffness degradation is exclusively caused by the loss of stiffness in the concrete compressive zone. Non-linear models with tension stiffening effect determine a more or less constant stiffness in the stabilised cracking stages in the load level range between $0.05 < \mu < 0.20$. The stiffness degradation in these loading levels is caused by concrete crushing that is described by the broken rational function, which is similarly taken into account in the "br-func" model. Therefore, the model uncertainty is constant for this model. In contrast, the uncertainty in the "lin-el" model increases due to the fact that concrete crushing is neglected.

The deterministic prediction of the bending stiffness of all tension stiffening models is comparable in the stabilised cracking stage (see Fig. 5.2). Differences appear for loading levels close to the crack initiation moment and the yielding moment. For those loading conditions, the tension stiffening "e-func" and "multi-lin" models predict a higher stiffness than compared to the reference model. Therefore, considerable model uncertainty is considered with respect to the "mod-steel" model prognosis.

5.1.4.3 Total uncertainty and model quality evaluation

The total uncertainty of the material models is shown in Fig. 5.16(a) for rectangular cross section subjected to bending moment incremental analysis. A direct determination of total uncertainty and model quality can be assessed according to Eq. 2.14 and the corresponding results are shown in Fig. 5.16(c). Based on this determination, the partial model quality is an identical expression of total uncertainty. In the case that the uncertainty of a model output is low, this means that there is a high reliability in the model prediction resulting in a high prognosis quality. When the model error (model uncertainty) and model output variance (parameter uncertainty) cause lower uncertainty in the model prediction, this model is more adequate compared to another model with high total uncertainty.

Furthermore, the partial model quality can be also determined based on the relative definition of Keitel [206], see Eq. 2.15 and the assigned results are shown in Fig. 5.16(b). Based on the relative definition between total uncertainty and partial model quality, it is easy apparent that this definition does not demonstrate a distinct expression of total uncertainty. In addition, the stiffness degradation induce extensive

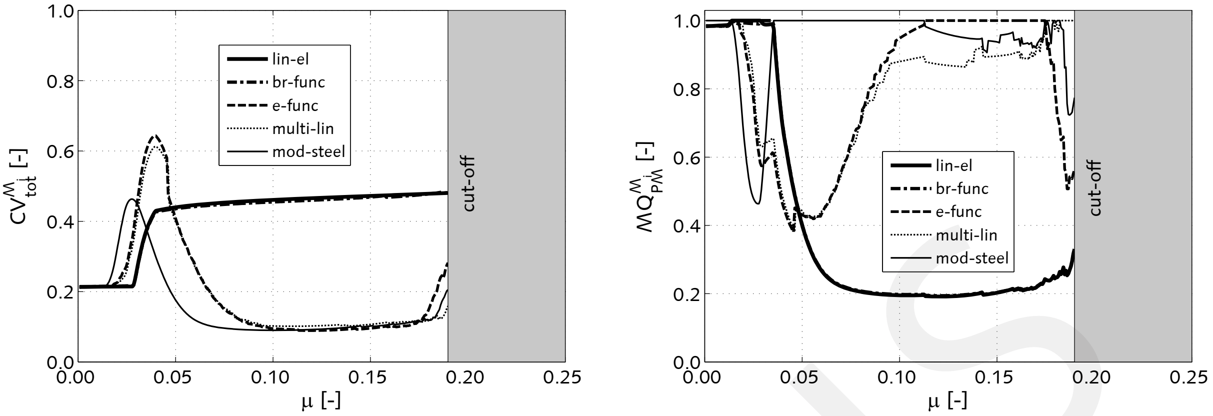

(a) total uncertainty

(b) relative determination of model quality

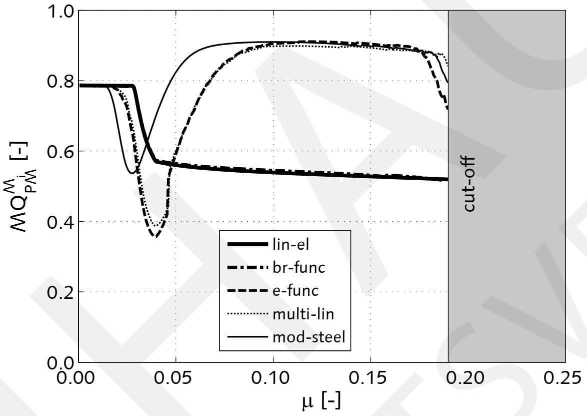

(c) direct determination of model quality

Figure 5.16: Load level dependency of total uncertainty and model quality of material models

non-linear model responses and the model differences between the reference model and the more simplified models vary in the entire load-deformation analysis. Hence, the model with lowest uncertainty and corresponding highest partial model quality changes several times depending on the loading level. Therefore, this determination is too sensitive to variations in the lowest total uncertainty and is consequently not adequate for the assessment of such models. The following results are based on the direct determination of model quality.

Between the uncracked stage and the crack formation stage as well as between the stabilised cracking stage and the steel yielding stage, a strongly varying scale in the model quality occurs. Some sample remain in the uncracked stage, while others have already reached tensile strains above the strains corresponding to the tensile strength, at identical loading levels. This behaviour results in a significant difference in the simulation output and therefore in a recognisable uncertainty. Furthermore, model uncertainties occur even for the non-linear "e-func" and "multi-lin" models, due to differences in the crack formation stage. A similar relationship between model characteristics and uncertainties occurs for loading levels in the stabilised cracking and the steel yielding stage.

The model quality tends to drop in the range of the cracking moment and the yielding moment. The consequence of selecting the simplified linear-elastic material model is a significant reduction in the prediction quality initiated by the first bending stiffness degradation causing a significant model uncertainty. The lower model uncertainty of the "br-func" model in the stabilised cracking stage compared to the "lin-el" model is overlapped with the higher parameter uncertainty. Therefore, the partial model quality of both models are similar $MQ_{PM}^{\mathcal{M}_{\text{lin-el}}} \approx MQ_{PM}^{\mathcal{M}_{\text{br-func}}}$ throughout the entire load-deformation analysis.

The highest qualities of the tension stiffening "e-func", "multi-lin" and "mod-steel" models are found in the stabilised cracking stage. The low parameter uncertainty and the comparableness in the prediction of the bending stiffness (model uncertainty) lead to a similar prediction quality. The quality of the complex model with the modified steel strains ("mod-steel") shows overall the best model prediction quality over the entire loading range due to less parameter and model uncertainty.

The uncertainty analysis of models for the load-deformation simulation of a reinforced cross section enables a clear and quantitative comparison between the different model predictions. Moreover, the entire analysis for all loading levels staring from the linear-elastic up to the steel yielding stage allow a clear insight in the model characteristics and corresponding model qualities. The results of this assessment emphasise that the quality of more complex or simplified material models can be quantitatively similar or diverse. In general, the model quality of the linear-elastic material model and the model considering the compressive stiffness degradation is opposite to the non-linear material models considering tension stiffening in loading levels in which stiffness degradation appears. The application of such simplified models for the simulation of the load-deformation behaviour of structures cause unreliable prognoses. For example, these models should not be used for the simulation of restraint sensitive structures due to high significance of stiffness degradation on the load-deformation behaviour [195, 198], see Sec. 3.5.

In addition, a more simplified non-linear tension stiffening material model is similarly adequate to a prognostic quality compared to a more complex one. A clear assignment between the complexity and quality of models does not exist in general, because of the crucial influence of the loading level on the load-deformation behaviour of a reinforced concrete cross section. Finally, material models with high quantitative model quality give reliable predictions and should be used in global structural models especially for structures which are sensitive to cracking and crushing. The question whether or not the material modelling itself is sensitive to the load-deformation behaviour of a entire structure can be quantified by the integrative sensitivity analysis which is discussed in Sec. 6.

5.1.4.4 Influence of reinforcement ratio

The amount of reinforcement influences the load-deformation behaviour of cross sections and structures, see Sec. 3.5.2 and Sec. 3.5.3 respectively. Therefore, the analysis of the cross section bending stiffness in all cracking stages is additionally simulated and assessed with varying reinforcement ratios in comparison to the previously presented results with the tensile reinforcement of 4∅20 ($\omega_{s1} = 0.236$, high reinforcement ratio). The influence of medium (3∅20, $\omega_{s1} = 0.177$) and low (2∅20, $\omega_{s1} = 0.118$) reinforcement ratio on the load-deformation behaviour is evaluated by the previously used material models and uncertainty analysis, see Fig. 5.17.

The reinforcement ratio is one of the many aspects that crucially affects the ultimate cross sectional capacity. Therefore, the maximum admissible bending moment (resisting moment) decreases as the reinforcement ratio decreases. The material models are assessed according to this load level at which 90 % of all samples do not fail, due to exceeding certain limit material strains. In the appendix in Fig. B.2, the number of samples in stable equlibrium for each load level is shown with repect to their dependence from all considered reinforcement ratios. Hence, the maxium load level for the assessesment of material models is decreasing

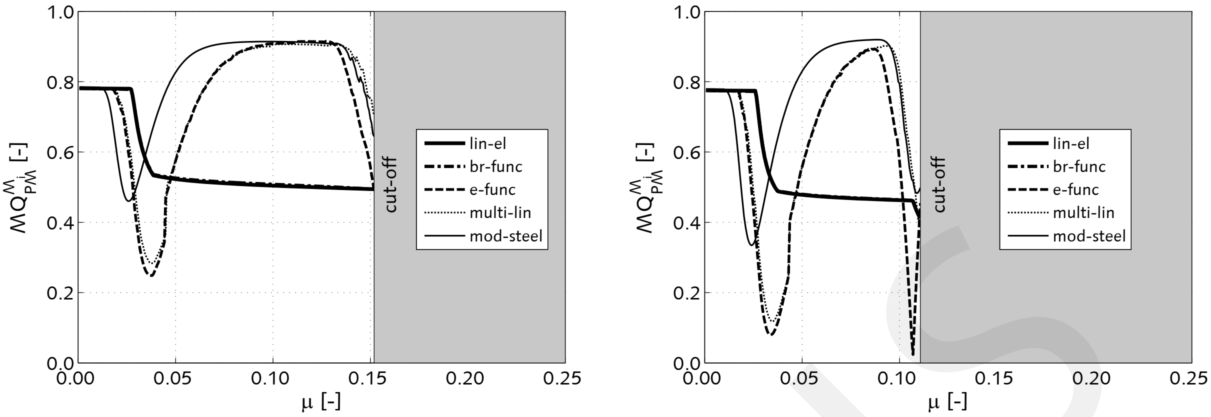

(a) medium reinforcement ratio, 3⌀20 (b) low reinforcement ratio, 2⌀20

Figure 5.17: Reinforcement ratio dependency of model quality for medium and low reinforcement ratio

similarly to the lower ultimate capacity from $\mu = 0.190$ (300 kNm) for the high reinforcement ratio to $\mu = 0.111$ (175 kNm) for the low reinforcement ratio, see Tab. 5.3.

For the medium reinforcement ratio (3⌀20, $\omega_{s1} = 0.177$), the deterministic load-deformation behaviour of the rectangular cross section simulated with the material models is shown in the appendix in Fig. B.5. The resisting moment is decreased from $\mu \approx 0.21$ for the high reinforcement ratio to $\mu \approx 0.16$ and therefore the maximum bending moment that is reasonable for the uncertainty analysis is similarly decreased. Correspondingly model and parameter uncertainty are depicted in the appendix in Fig. B.6 and total uncertainty in Fig. B.7. The prediction quality for the medium reinforcement ratio is shown in Fig. 5.17(a).

In the case of the low reinforcement ratio (2⌀20, $\omega_{s1} = 0.118$), the deterministic load-deformation behaviour is depicted in the appendix in Fig. B.8. Model and parameter uncertainties are shown in Fig. B.9, and total uncertainty in Fig. B.10. The resisting moment is decreased from $\mu \approx 0.16$ for the medium reinforcement ratio to $\mu \approx 0.11$ for the low reinforcement ratio and the prediction quality is shown in Fig. 5.17(b).

For the entire load incremental analysis, the minimum and maximum uncertainty values for each model are listed in Tab. 5.3. The lowest model uncertainty is not influenced by the reinforcement ratio. For all models, the minimum model uncertainty ranges between $0.00 < CV^{\mathcal{M}_i}_{\text{mod}} < 0.02$ and is independent of the reinforcement ratio throughout the entire load incremental analysis. With a smaller reinforcement ratio, there is a slight increase in maximum model uncertainty for all models in all flexural stages. For the medium reinforcement ratio, the increase in model uncertainty is about 110 % and is about 130 % for a lesser amount of steel bars than compared to the uncertainty of the high reinforcement ratio. This increase with lower amount of steel is caused in the crack formation stage in which a higher difference appears amongst the simplified model predictions in relation to the most complex "mod-steel" model. The high model uncertainty of the "e-func" with a value of $CV^{\mathcal{M}_{\text{e-func}}}_{\text{mod}} = 0.91$ exclusively occurs in one load increment in the intersection between the stabilised and the steel yielding stages. The less concrete contribution between the cracks in the "e-func" model causes plastic steel strains in lower loading level than compared to the "multi-lin" and "mod-steel" models. This divergence is more extensive with decreasing reinforcement ratio, which may cause such high model uncertainty. For loading levels in which yielding in the bars occurs for all non-linear models with tension stiffening, this high model uncertainty is reduced and is therefore not

Table 5.3: Influence of reinforcement ratio on concrete material models's evaluation, load level M_y (μ) for 90 % of samples without material failure, minimum and maximum coefficients of variation shown for entire load-deformation simulation analysis

	Unit / Model	high 4∅20 $\omega_{s1} = 0.236$	medium 3∅20 $\omega_{s1} = 0.177$	low 2∅20 $\omega_{s1} = 0.118$
EI^I	$\left[\mathrm{MNm}^2\right]$	143.66	140.82	137.91
M_y (90 % samples)	[kNm]	300	240	175
μ (90 % samples)	[-]	0.190	0.152	0.111
α (e-func)	[-]	3027	2270	1517
$CV_{\mathrm{mod}}^{\mathcal{M}_i}$	lin-el	0.01 − 0.43	0.02 − 0.46	0.02 − 0.54
	br-func	0.01 − 0.40	0.02 − 0.44	0.02 − 0.54
	e-func	0.00 − 0.35	0.00 − 0.39	0.00 − 0.45 (0.91)
	multi-lin	0.01 − 0.35	0.01 − 0.39	0.01 − 0.45
	mod-steel	-	-	-
$CV_{\mathrm{par}}^{\mathcal{M}_i}$	lin-el	0.21	0.22	0.22
	br-func	0.21 − 0.27	0.22 − 0.26	0.22 − 0.25
	e-func	0.08 − 0.54	0.07 − 0.65	0.09 − 0.83
	multi-lin	0.10 − 0.50	0.09 − 0.61	0.09 − 0.78
	mod-steel	0.09 − 0.46	0.09 − 0.54	0.08 − 0.67
$CV_{\mathrm{tot}}^{\mathcal{M}_i}$	lin-el	0.21 − 0.48	0.22 − 0.51	0.22 − 0.59
	br-func	0.21 − 0.48	0.22 − 0.51	0.22 − 0.59
	e-func	0.09 − 0.64	0.08 − 0.75	0.11 − 0.92 (0.98)
	multi-lin	0.10 − 0.61	0.09 − 0.72	0.09 − 0.88
	mod-steel	0.09 − 0.46	0.09 − 0.54	0.08 − 0.67

significant in the entire load-deformation behaviour.

The parameter uncertainty in the “lin-el” model is almost constant for all reinforcement ratios because of the small influence of the reinforcement ratio on the initial uncracked bending stiffness. In addition, the parameter uncertainty of the “br-func” model is similarly independent of the reinforcement ratio. The minimum parameter uncertainty for all loading levels is not considerably influenced by the reinforcement ratio, because this uncertainty occurs in the stabilised cracking stage in which the stiffness is constant for concrete in tension and no redistribution between steel and concrete occurs. In the case that these conditions appear in the majority of the samples, then the minimum uncertainty is similar for all reinforcement ratios. Nevertheless, the range of loading significantly decreases with respect to decreasing reinforcement ratio at which these conditions appear.

In contrast, a very high influence of the reinforcement ratio is visible to the maximum parameter uncertainty for the non-linear models considering tension stiffening in all loading stages. This maximum parameter uncertainty occurs in the intersection between the uncracked and the crack formation stages. An even higher parameter uncertainty occurs for the low reinforcement ratio in comparison to the high reinforcement ratio. For the medium reinforcement ratio the increase in parameter uncertainty is about 120 % and when considering a lesser amount of steel bars, it is about 152 % in comparison to the uncertainty of the high reinforcement ratio. For the “mod-steel” model, the increase in parameter uncertainty is slightly less compared to the “e-func” and “multi-lin” models. Due to a lesser amount of reinforcement, the change in reinforcement stress caused by concrete cracking is much higher for the low in comparison to the high reinforcement ratio. Therefore, a higher discrepancy in the simulation of the curvature occurs between the uncracked and the crack formation stages for a lower reinforcement ratio causing a significant incrase in parameter uncertainty.

In conclusion, the lowest total uncertainty (highest prediction quality) for all models throughout the entire load-deformation analysis is not influenced by the reinforcement ratio. For the "lin-el" and "br-func" models, this lowest value of uncertainty occurs in the initial uncracked stage, whereas in the "e-func", "multi-lin" and "mod-steel" models, this uncertainty appears in the stabilised cracking stage. In contrast, the maximum total uncertainty (lowest prediction quality) is significantly influenced by the reinforcement ratio and increases with a decreasing amount of reinforcing steel. The increase in the "lin-el" and "br-func" models is similar to 106 % for the medium and 123 % for the low reinforcement in comparison to the uncertainty of the high reinforcement ratio. For the "e-func", "multi-lin", and "mod-steel" models, the increase is about to 117 % for the medium and 144 % for the low reinforcement ratio. In conclusion, the "mod-steel" model is quantified to be the most adequate model for the analysis of load-deformation behaviour of reinforced concrete cross sections with various reinforcement ratios subjected to flexural loading condition.

5.1.5 Assessment of uncertainty hypothesis

In this section, the uncertainty hypothesis is investigated for the material models of reinforced concrete. This hypothesis claims that models with higher complexity reduce model uncertainty. In contrast, parameter uncertainty increases with higher complexity. Finally, the model with lowest total uncertainty is the most adequate model with best accuracy in order to describe the physical phenomenon.

The uncertainty of the models is quantified in the previous sections. The model complexity assessment is based on the study conducted by Snowling and Kramer [380], see Eq. 2.55. For concrete material model, the individual model complexity indices considering the state variables and processes in the model descriptions are listed in Tab. 5.4.

The processes n_j in the assessment of material models for reinforced concrete flexural members are the characteristic cracking stages, uncracked stage, crack formation stage, stabilised cracking stage, and steel yielding stage. Each model is evaluated separately in all bending stages, which are processes in the model complexity assessment. Corresponding state variables are analysed in the cross sectional subsections with X_i number of parameters and r_i number of mathematical operations determining the flexural stiffness in each subsection N_i.

In the case of the linear-elastic material "lin-el" model, the stiffness in the uncracked stage is determined exclusively and all other cracking stages are neglected. Therefore, the model complexity in theses stages is zero. In the uncracked stage, the modulus of elasticity is the parameter determining the material stresses and stiffness. The relationship between the parameters and the resulting stresses is computed by one mathematical operation, the multiplication of the modulus of elasticity and the material strains. Therefore, $X_i = 1$ and $r_i = 1$ for the subsections CC, CT, SC and ST. In the reinforced concrete subsection RCT, no additional description is considered in the material "lin-el" model. Finally, the model complexity of this linear-elastic material model is $I_{c,\text{lin-el}} = 4$.

Increase in model complexity should generally be possible by taking into account the stiffness degradation in the concrete compressive zone. The "br-func" model considers concrete crushing by a non-linear broken rational function. Therefore, the model complexity in this cross sectional subsection should increase in comparison to the linear-elastic material model. Four parameters and seven mathematical operations are necessary to describe the relationship between the concrete compressive strains and stresses. Hence, the model complexity is increased in the subsection CC from 1 ("lin-el") to 28 ("br-func") which confirms

Table 5.4: Complexity of material models for reinforced concrete, CC...concrete in compression, CT...concrete in tension, RCT...reinforced concrete in tension SC...steel in compression, ST...steel in tension

Process n_j,	State variable N_i										$\sum_{i=1}^{N} X_i \cdot r_i$
Model	CC		CT		RCT		SC		ST		
	X_i	r_i	X_i	r_i	X_i	r_i	X_i	r_i	X_i	r_i	
lin-el											$I_{c,\text{lin-el}} = \mathbf{4}$
uncracked stage	1	1	1	1	0	0	1	1	1	1	4
crack formation stage	0	0	0	0	0	0	0	0	0	0	0
stabilised cracking stage	0	0	0	0	0	0	0	0	0	0	0
steel yielding stage	0	0	0	0	0	0	0	0	0	0	0
br-func											$I_{c,\text{br-func}} = \mathbf{31}$
uncracked stage	4	7	1	1	0	0	1	1	1	1	31
crack formation stage	0	0	0	0	0	0	0	0	0	0	0
stabilised cracking stage	0	0	0	0	0	0	0	0	0	0	0
steel yielding stage	0	0	0	0	0	0	0	0	0	0	0
e-func											$I_{c,\text{e-func}} = \mathbf{96}$
uncracked stage	4	7	1	1	1	1	1	1	1	1	32
crack formation stage	0	0	0	0	4	4	0	0	0	0	16
stabilised cracking stage	0	0	0	0	0	0	0	0	0	0	0
steel yielding stage	0	0	0	0	4	4	4	4	4	4	48
multi-lin											$I_{c,\text{multi-lin}} = \mathbf{112}$
uncracked stage	4	7	1	1	1	1	1	1	1	1	32
crack formation stage	0	0	0	0	4	4	0	0	0	0	16
stabilised cracking stage	0	0	0	0	4	4	0	0	0	0	16
steel yielding stage	0	0	0	0	4	4	4	4	4	4	48
mod-steel											$I_{c,\text{mod-steel}} = \mathbf{114}$
uncracked stage	4	7	0	0	0	0	1	1	1	1	30
crack formation stage	0	0	0	0	0	0	0	0	4	4	16
stabilised cracking stage	0	0	0	0	0	0	0	0	6	4	24
steel yielding stage	0	0	0	0	0	0	4	4	7	4	44

the expected increase in model complexity. In the other subsections, no change in the model description is applied in the "br-func" model. Finally, the model complexity is $I_{c,\text{br-func}} = 31$.

The consideration of both stiffness degradation due to concrete cracking and steel yielding stage in the non-linear material "e-func" model should increase the model complexity compared to the "br-func" material model. Higher model complexity of the non-linear model is visible in the crack formation and steel yield stages. In contrast, no increase in model complexity appears in the stabilised cracking stage due to the fact that the exponential function is defined in the entire range between crack formation and stabilised cracking stages. No distinction is apparent between both cracking stages. Four parameters and four mathematical operations are necessary to describe the exponential function of the reinforced concrete subsection RCT. It is similar to the model complexity in the steel yield stage. Moreover, the bi-linear relationship of the reinforcing steel in compression and tension is described by four parameters and four mathematical operations. Therefore, the model complexity is increased throughout the entire model description, which confirms the expected increase compared to the "br-func" model. Finally, the model complexity is $I_{c,\text{e-func}} = 96$.

Another increase in model complexity in comparison to the model with exponential function should be appear in the case that the stabilised cracking stage is additionally considered in the model description.

The "multi-lin" model defines the intersection between crack formation and stabilised cracking stage at the strain value ϵ_{c2}. The concrete tensile behaviour in the stabilised cracking stage is also determined by four parameters and four mathematical operations. Therefore, the model complexity in the stabilised cracking stage increases in the subsection RCT from 0 ("e-func") to 16 ("multi-lin"), which confirms the expected increase. The model description in the steel yielding stage is the same as in the "e-func" model. Finally, the model complexity is $I_{c,\text{multi-lin}} = 112$.

The non-linear model that considers the tension stiffening effect by modifying the steel strain values does not determine concrete strain and stress values in the concrete tensile subsections. Hence, the model complexity in these areas is $I_c = 0$. In contrast, more parameters and mathematical operations are necessary to describe the behaviour of the reinforcing steel in the stabilised and the steel yielding stages. The model complexity increases consequently in the stabilised cracking stage to $I_c = 24$ compared to the tension stiffening "multi-lin" model. In the steel yielding stage, a decrease in model complexity is visible due to the fact that the material behaviour is determined in less subsections compared to the "multi-lin" model. Finally, the model complexity is $I_{c,\text{mod-steel}} = 114$ close to the complexity of the "multi-lin" material model, which reflects the similar model characteristics.

This quantification of model complexity in combination with the above analysed model uncertainties is used for the assessment of the uncertainty hypothesis, see Sec. 2.1. Therefore, the model complexity I_c is shown in the horizontal axis in Fig. 5.18. Model, parameter and total uncertainty are determined by the coefficient of variation CV and are represented in the vertical axis. The results are presented in the uncracked, crack formation, stabilised cracking, and steel yielding stages, see Fig. 5.18(a) to Fig. 5.18(d).

In the uncracked stage, a negligible model uncertainty appears for all of the material models, see Fig. 5.18(a). Therefore, the model's total uncertainty is approximately equal to the model's parameter uncertainty. There is no influence of model complexity on model uncertainties is visible to the prediction of linear-elastic bending stiffness.

In the intersection between crack formation and stabilised cracking stages, a strong effect of model complexity on the model uncertainties is visible, see Fig. 5.18(b). The bending stiffness is already degraded in the reference "mod-steel" model for this loading condition. In the other non-linear and linear models, the stiffness is close to the linear-elastic stiffness. Hence, the model uncertainty is constant and independent of model complexity except in the most complex reference model. In contrast, parameter uncertainty increases with increasing model complexity between the linear and non-linear models. The material "lin-el" and "br-func" models are even more adequate in the crack formation stage than the much more complex "e-func" and "multi-lin" models. Model and parameter uncertainty of the reference model "mod-steel" is smaller compared to other non-liner material models which significantly reduces the total uncertainty.

Another increase in external bending moment initiates to the stabilised cracking stage, see Fig. 5.18(c). In this stage, the stiffness is only about 30 % of the linear-elastic stiffness. The bending stiffness prediction is relatively the same between the non-linear models considering the tension stiffening effect. Therefore, model uncertainty decreases with increasing model complexity. In a similar manner, the parameter uncertainty decreases with increasing model complexity. This is in contradiction to the expected uncertainty hypothesis, which assumes that parameter uncertainty should be raised with increasing model complexity. All input parameters, especially the concrete material properties with high variance, affect the prediction in the simplified models. In contrast, the stiffness in the more complex models is less influenced by these parameters. Furthermore, the simulation of each sample set computes the same cracking stage in the cross section, which again reduces the parameter uncertainty of the more complex non-linear models.

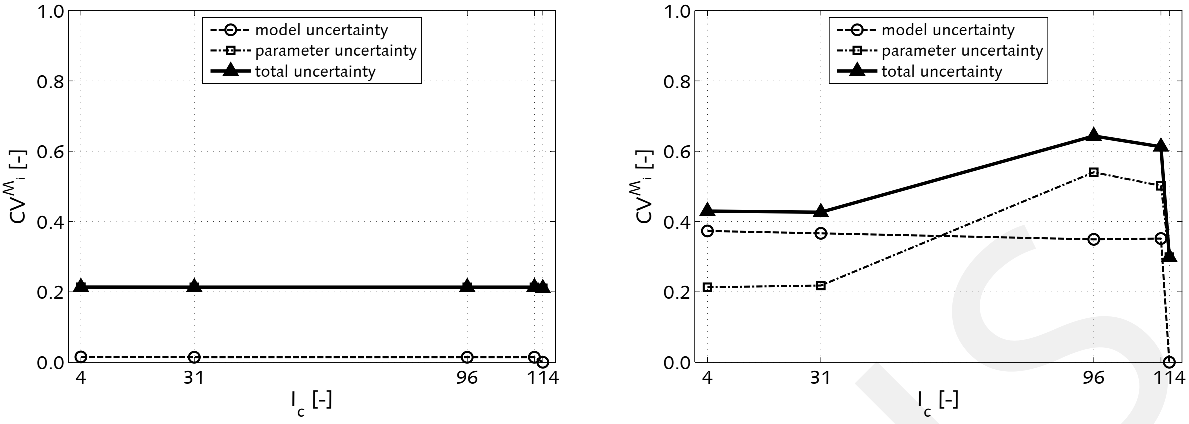

(a) uncracked stage, $\mu = 6.33e^{-4}$, $M_y = 1\,\text{kNm}$

(b) crack formation stage, $\mu = 0.04$, $M_y = 63\,\text{kNm}$

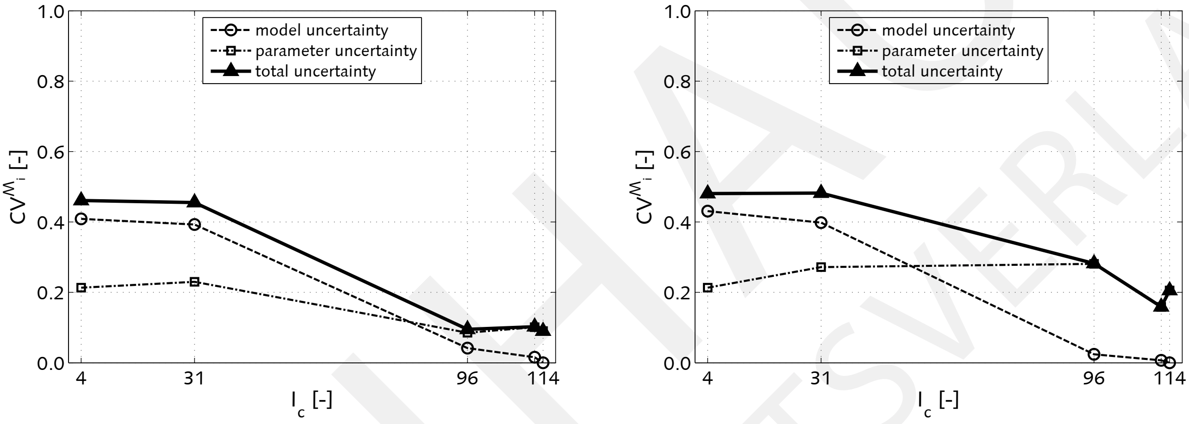

(c) stabilised cracking stage, $\mu = 0.10$, $M_y = 158\,\text{kNm}$

(d) steel yielding stage, $\mu = 0.19$, $M_y = 300\,\text{kNm}$

Figure 5.18: Assessment of uncertainty hypothesis for material models of reinforced concrete, hor. axis: complexity with $I_{c,\text{lin-el}} = 4$, $I_{c,\text{br-func}} = 31$, $I_{c,\text{e-func}} = 96$, $I_{c,\text{multi-lin}} = 112$, $I_{c,\text{mod-steel}} = 114$, ver. axis: uncertainty

In higher loading levels, some sample sets remain in the stabilised cracking stage while some samples lead to the steel yielding stage. Thus, the parameter uncertainty increases with increasing complexity between the simplified models and the non-linear “e-func” model, see Fig. 5.18(d). The greater amount of concrete contribution between the cracks in the “multi-lin” and “mod-steel” models induces smaller variance in the model output, because less samples are in between both cracking stages for these loading conditions. The relationship between model complexity and model uncertainty is also similar to the stabilised cracking stages.

The assessment of the relationship between model complexity and model, parameter, and total uncertainty is evaluated for all cracking stages in the prediction of bending stiffness. The statement that increasing the complexity reduces the model uncertainty is analysed to be an appropriate assumption in the assessment of the concrete material models. In contrast, the theorem that parameter uncertainty increases with increasing complexity cannot be generalised and does not represent the quantified results. Therefore, the relationship between total uncertainty and complexity is strongly dependent on the model characteristics and the loading condition.

The individual model characteristics and the influence of external loading condition on the model response significantly impacts the relationship between complexity and uncertainty. Therefore, a general determination of the dependence between complexity and uncertainty is not appropriate and should be carefully investigated in each application. The result of this assessment does not say that this hypothesis is inaccurate or wrong, it says that the hypothesis cannot be generalised as is shows in the presented results. Nevertheless, the quantification of uncertainty and complexity allows a clear and objective comparison between various models. Therefore, the choice of an adequate model for each application is assisted by quantitative information based on the uncertainty and not solely based on qualitative engineering judgement.

5.2 Pile foundation models

In Sec. 3.6, the behaviour of vertically and laterally loaded single piles and pile groups are discussed and corresponding prediction models are introduced. In this section, assessment of pile models is performed for the vertical stiffness prediction due to incremental load analysis of the vertical force N. In a cooperative study published in [197], an evaluation is similarly presented for laterally loaded pile groups with similar foundation and soil conditions as indicated in the following.
The models assessed in this study are presented in Sec. 3.6.1. These prediction models are generally applicable for computing the pile foundation stiffness for the purpose of structural analysis. Based on the uncertainty analysis that is similarly used in the assessment of concrete material models, the underlying uncertainty in the prediction of these models is evaluated in order to obtain a quantitative comparison. The evaluation is analysed for the prediction of pile group stiffness because this output quantity is the main input used for structural engineering problems such as load-deformation simulation of bridges.
Two different pile foundation arrangements are exemplary analysed in the evaluation of pile foundation models, see Fig. 5.19. On one hand, a pile group with one pile row in transverse direction to the bridge superstructure (I) and on the other side a square pile group (II) is investigated in the assessment. Both pile foundation constructions are used in the design for different types of bridge construction. Type (II) generates more lateral and rotational stiffness in comparison to the type (I). Therefore type (II) is applied for girder bridges (superstructure decoupled from substructure using bearings). In contrast, the type (I) is commonly used for semi-integral and integral bridges in order to reduce the lateral and rotational stiffness of the foundation. This increasing flexibility can reduce restraining forces in the entire structure, which are often a critical design criteria for integral bridges as previously discussed in Sec 3.5.4.2.

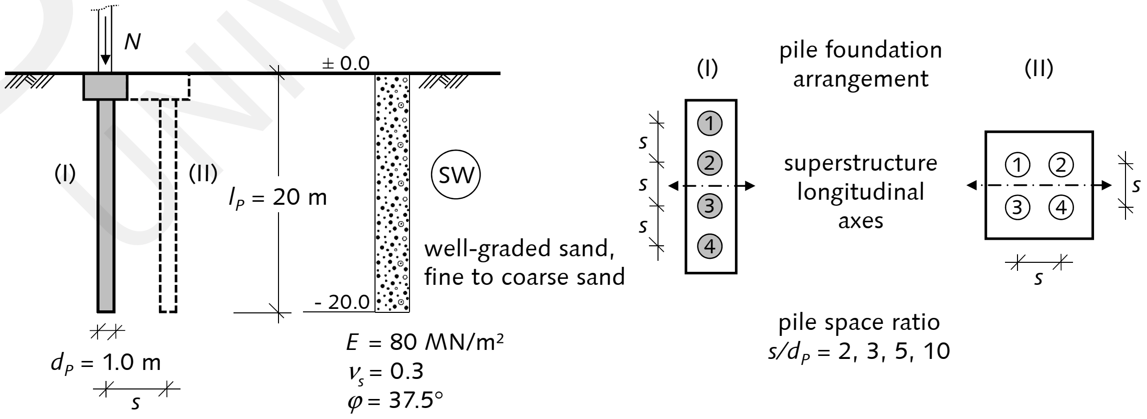

Figure 5.19: Geometry and soil conditions for pile group arrangements

Both pile foundations are embedded in a homogeneous non-cohesive soil (SW...well-graded sand, fine to coarse sand) as it is classified in the unified soil classification system [7, 140]. The interaction between piles is significantly influenced by the pile space ratio s/d_P. For a smaller ratio, the displacement fields of each pile in the group overlap much more than compared to groups with a greater pile space ratio. The question arises, if this ratio is also affecting the uncertainty in the prediction of vertical pile foundation stiffness? The uncertainty in model predictions has not yet been studied for vertical loaded pile groups. Therefore, the models are analysed in order to evaluate the underlying uncertainty in the prediction by considering several pile space ratios. These ratios are considered in the range of $2 \leq s/d_P \leq 10$ and the corresponding pile spaces measured between the centre of each pile are shown in the appendix in Tab. B.1 for type (I) and in Tab. B.2 for type (II) pile group arrangement.

The load-deformation behaviour of the pile groups can be generally analysed by the load dependent stiffness. In structural engineering problems such as bridge engineering, this stiffness is commonly considered in the simulation of the structure in order to account for foundation and soil flexibility, stiffness respectively. Therefore, the prediction of vertical pile group stiffness is the response value in the following uncertainty analysis and the models considered in this assessment are evaluated according to their prognosis of vertical stiffness.

5.2.1 Uncertainty analysis of pile foundation models

5.2.1.1 Stochastic input parameters

Information on parameter randomness is seldomly available for a soil characterised by soil classification systems. An extensive study for characterising soil variability is performed by Phoon et al. [310, 311, 312]. In general, the parameter uncertainty for sand is higher than for clay. The assessment of uncertainty in the friction angle φ for sand and clay is evaluated to be in the range of 5 to 20 % determined by the coefficient of variation. For the earth pressure at rest coefficient K_0, the range of 20 to 80 % for clay and 25 to 55 % for sand are evaluated. The highest uncertainty in soil properties is assessed in terms of the soil modulus of elasticity E. The range of the coefficient of variation is found to be 20 to 70 %. This assessment, among others [68, 183], show a very high variance in the soil properties. In most cases, a normal distribution or log normal distribution is assessed to be a reasonably applicable for describing randomness in soil properties.

For this assessment, the different input parameters and their distribution, mean, coefficient of variation and the correlation matrix are shown in Tab. 5.5. The stochastic input parameters are chosen as synthetic data according to several researches such as the study by Phoon. Therefore, the prediction of pile foundation stiffness is quantified for frequently-encountered soil conditions. Due to the high variation in soil properties, a log normal distribution is chosen in order to exclude meaningless negative strength and stiffness values.

Table 5.5: Stochastic input parameters of pile and soil properties, variation information based on [68, 183, 311, 312, 310]

Material Property		Distribution Type	Mean Value Range	CV [-]	Correlation Matrix $\rho_{X_iX_{i+1}}$ E_P	E	ν_s	φ
pile modulus of elasticity	E_P	log normal	30000 MN/m^2	0.15	1.0	0	0	0
soil modulus of elasticity	E	log normal	80 MN/m^2	0.20	0	1.0	0	0.4
soil *Poisson*'s ratio	ν_s	uniform	0.28. . . 0.32	-	0	0	1.0	0
friction angle	φ	log normal	37.5°	0.20	0	0.4	0	1.0

A comparison between defined stochastic properties and samples shows a very good agreement, see Fig. 5.20. Therefore, the samples are reliable and can be used in the uncertainty analysis. The earth pressure at rest coefficient is computed by:

$$K_0 \approx 1 - \sin\varphi\,, \tag{5.4}$$

which assumes a full dependency (correlation) between friction angle φ and earth pressure coefficient K_0.

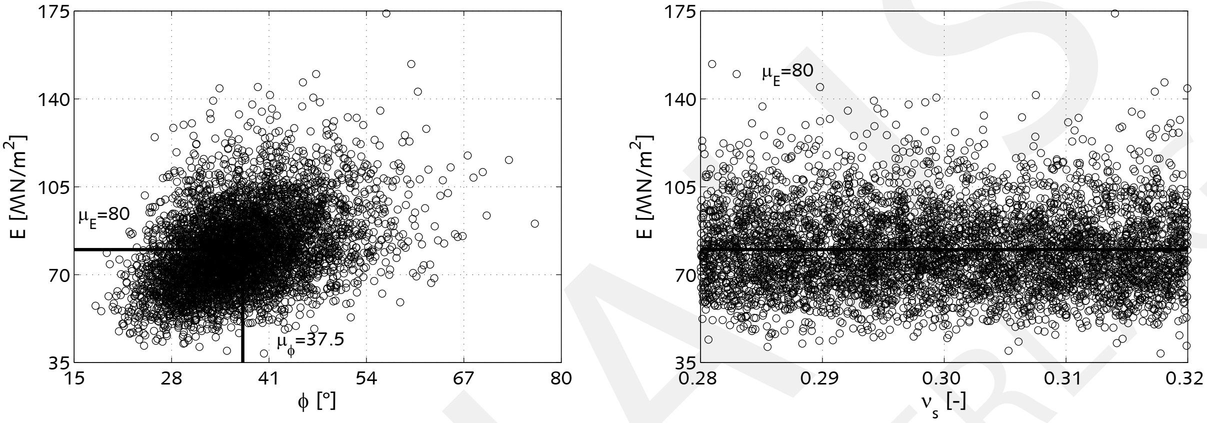

(a) $\rho_{\varphi E} = 0.4$ (b) $\rho_{\nu_s E} = 0$

Figure 5.20: Correlated samples between friction angle φ and soil modulus of elasticity E, and uncorrelated samples between soil *Poisson*'s ratio ν_s and soil modulus of elasticity E for pile foundation assessment, 10000 samples

The radius at which the shear stress becomes negligible $r_{m,\mathrm{g}}$ is determined by:

$$r_{m,\mathrm{g}} = 2.5 \cdot l_P \cdot (1 - \nu_s) = 2.5 \cdot 20 \cdot (1 - 0.3) = 35\,\mathrm{m}\,, \tag{5.5}$$

and is applied in each considered model in order to identically take into account the shear stress around the pile shaft. Furthermore, the discussion by the authors of these models according to this parameter similarly recommends the general applicability of the above expression. This parameter is fixed as a deterministic parameter in the model assessment.

5.2.1.2 Model uncertainty by deterministic simulation

The deterministic model predictions of the vertical pile group stiffness are listed in Tab. 5.6 for the linear-elastic response analysis of both pile group arrangements. Also, these initial elastic stiffness are shown in Fig. 5.21(a) for all considered models, pile space ratios, and both arrangements.

The models by RANDOLPH and RUDOLF uses the same stiffness determination for single piles and pile groups in the case of linear-elastic response in the pile group. Therefore, the deterministic stiffness between both models is identical for all of the investigated conditions. In the model by MYLONAKIS, the condition is chosen that no bedrock is present and therefore the height under the pile tip is $h_b \to \infty$ with the soil equal to the above considered homogeneous non-cohesive soil (SW). In consequence, the pile base stiffness is identically computed in all models. Due to the consideration of the pile modulus of elasticity $E_P = E_c$, the stiffness of a single pile is reduced to 77 % in the MYLONAKIS model in comparison to the other considered models.

Table 5.6: Deterministic elastic prediction of vertical pile foundation stiffness for pile groups 4x1, 2x2 with pile diameter $d_P = 1.0$ m, pile length $l_P = 20$ m, and various pile space/pile diameter ratios s/d_p in comparison to single pile stiffness

Pile Space	Linear-elastic Vertical Pile Stiffness					
Ratio	Randolph et al. [334]		Mylonakis et al. [291]		Rudolf [353]	
	$K_{v,\text{g}}$ [MN/m]	$K_{v,\text{g}}/K_{v,\text{s}}$ [%]	$K_{v,\text{g}}$ [MN/m]	$K_{v,\text{g}}/K_{v,\text{s}}$ [%]	$K_{v,\text{g}}$ [MN/m]	$K_{v,\text{g}}/K_{v,\text{s}}$ [%]
			single pile stiffness			
$K_{v,\text{s}}$	998 MN/m		773 MN/m		998 MN/m	
			4x1 pile group (I)			
$s/d_P = 2$	1619	162	1566	203	1619	162
$s/d_P = 3$	1800	180	1746	226	1800	180
$s/d_P = 5$	2083	209	2046	265	2083	209
$s/d_P = 10$	2648	265	2676	346	2648	265
			2x2 pile group (II)			
$s/d_P = 2$	1484	149	1429	185	1484	149
$s/d_P = 3$	1645	165	1583	205	1645	165
$s/d_P = 5$	1888	189	1832	237	1888	189
$s/d_P = 10$	2343	235	2329	302	2343	235

For both pile foundation arrangements (I) and (II), the interaction between the piles is different inside the groups due to the varying spaces between each pile. Therefore, the resulting vertical stiffness is not equal in both group arrangements. The interaction in the quadratic arrangement (II) is higher than if all of the piles are arranged in one row (I). In consequence, the stiffness of pile group (I) is higher than group (II).

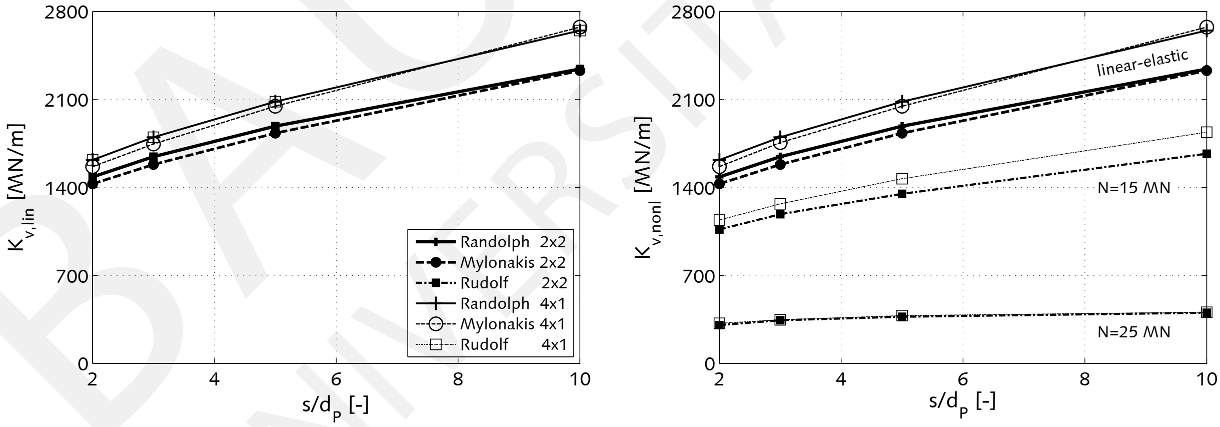

(a) linear-elastic response

(b) non-linear response

Figure 5.21: Pile foundation stiffness prediction for linear and non-linear loading condition, Randolph [334], Mylonakis [291], Rudolf [353]

A non-linear loading condition induces significant differences in the model predictions between the considered models in comparison to a loading condition which cause a linear-elastic group response, see Fig. 5.21(b). The models by Randolph and Worth [334], and Mylonakis and Gazetas [291] assume a linear-elastic soil behaviour. Therefore, the vertical stiffness prognosis is independent from the loading condition causing a recognisable difference compared to the non-linear by Rudolf [353]. The results according to the deterministic vertical stiffness for the non-linear loading depicted in Fig. 5.21(b) are the same compared to linear-elastic response analysis shown in Fig. 5.21(a).

The model by Rudolf [353] considers a bi-linear soil behaviour with the *Mohr-Coulomb* shear strength criteria. Therefore, the stiffness can be degraded in a large amount for loading conditions with a non-linear response in the pile group, soil respectively. In the results shown in Fig. 5.21(b), the axial loading for the pile foundation is causing either linear-elastic, or medium non-linear $N = 15\,\mathrm{MN/m}$, or even highly non-linear response $N = 25\,\mathrm{MN/m}$ in the pile foundation. Due to the bi-linear yielding surface of the *Mohr-Coulomb* shear strength criterion, the stiffness is not decreasing for further load-increments in the case that all pile elements are already in the yielding zone. For the highly non-linear loading condition, these elements along the pile depth are mainly in these conditions, which significantly reduce the effect of interaction between the piles on the pile group stiffness.

The interaction between piles remains substantially linear-elastic despite the non-linear deformation behaviour as it is investigated by several researchers and experiments [60, 70, 416], see Sec. 3.6.1. Therefore, the difference in stiffness between the pile group arrangements 4x1 and 2x2 decreases with increasing loading level caused by a more significant stiffness degradation in the soil itself along the pile shaft elements and at the pile base. Furthermore, the influence of the pile space ratio on the stiffness is similarly less for non-linear response compared to linear-elastic analysis. Therefore, the influence of soil behaviour determines the vertical stiffness more decisively in the non-linear response analysis than compared to the elastic pile-to-pile and base-to-base interaction.

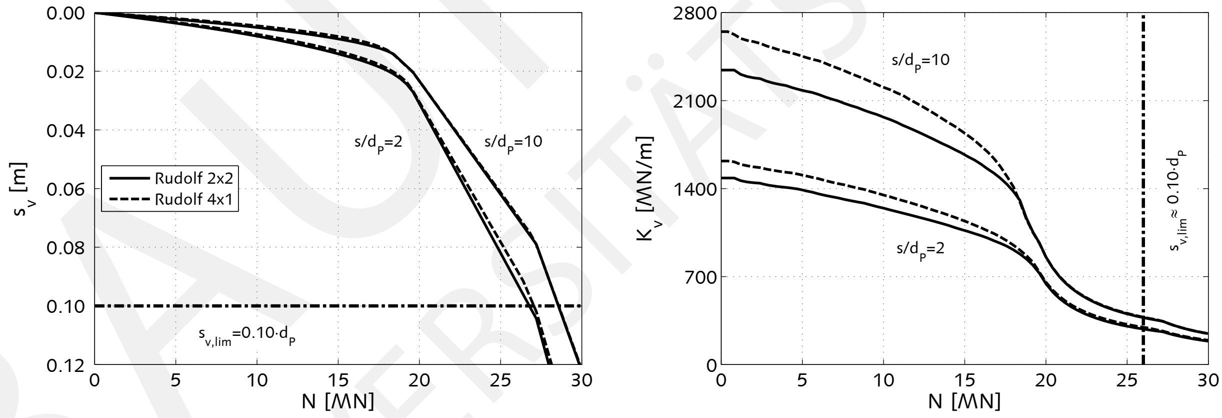

(a) axial force - vertical settlement

(b) axial force - pile foundation stiffness

Figure 5.22: Load-bearing behaviour of pile group for different pile arrangement (2x2, 4x1) and pile spacing ($s/d = 2$, $2/d = 10$), non-linear model Rudolf [353]

The discussion of the model characteristics is mentioned previously in Sec. 3.6.1.2. Based on the model attributes, the non-linear model by Rudolf [353] is chosen as the reference model, because it has the highest model complexity in comparison to the other pile models that are considered. The non-linear load-deformation analyses for a load increment of $\Delta N = 0.4\,\mathrm{MN}$ is shown in Fig. 5.22 for both pile group arrangements in combination with two different pile space ratios in each case. Smallest ratio of $s/d_P = 2$ and greatest ratio of $s/d_P = 10$ are exemplary chosen to illustrate the influence of pile spaces on the interaction in the pile group and corresponding uncertainty.

In general, the elastic stiffness is higher in the 4x1 than the 2x2 pile group arrangement. Furthermore, the increase caused by the greater pile space ratio is even more rapid for the 4x1 than the 2x2 pile group. For the 4x1 pile group, the increase in vertical stiffness is 164 % between $s/d_P = 2$ and $s/d_P = 10$ and 158 % for the 2x2 group which is similarly analysed in all considered models, see Tab. 5.6. The axial force can also be seen as the resistance of the pile group mobilised by a certain amount of vertical displacement that represents the commonly known resistance-settlement relationship. Based on the recommendation of the German Geotechnical Society [81], the settlement limit for the ultimate limit state is $s_{v,\text{lim}} = 0.10 d_P$ for vertically loaded piles determining the maximum admissible settlement in this assessment. Therefore, the non-linear model by RUDOLF is similarly simulated until this limit settlement. Hence, the results presented in the following assessment are limited up to the maximum axial force $N_{\text{max}} = 26$ MN which approximately corresponds to $s_{v,\text{lim}}$. A comparison to the probabilistic analysis, discussed in the next section, shows that more than 90 % of all samples reach this loading condition. Finally, this axial force as the maximum loading level is reasonable for the uncertainty analysis with respect to the design recommendations and the accuracy of the probabilistic simulations.

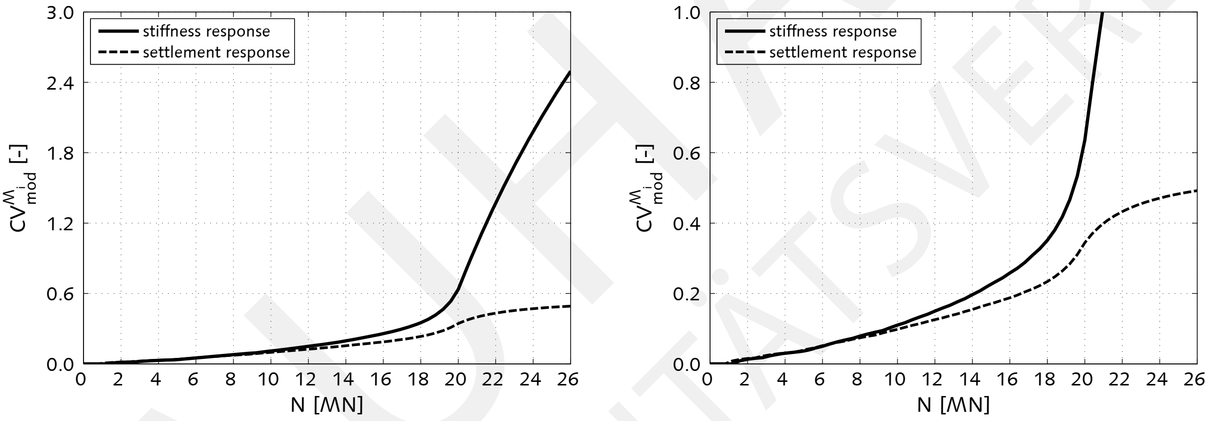

(a) full uncertainty

(b) $CV^{\mathcal{M}_i}_{\text{model}} \leq 1.0$

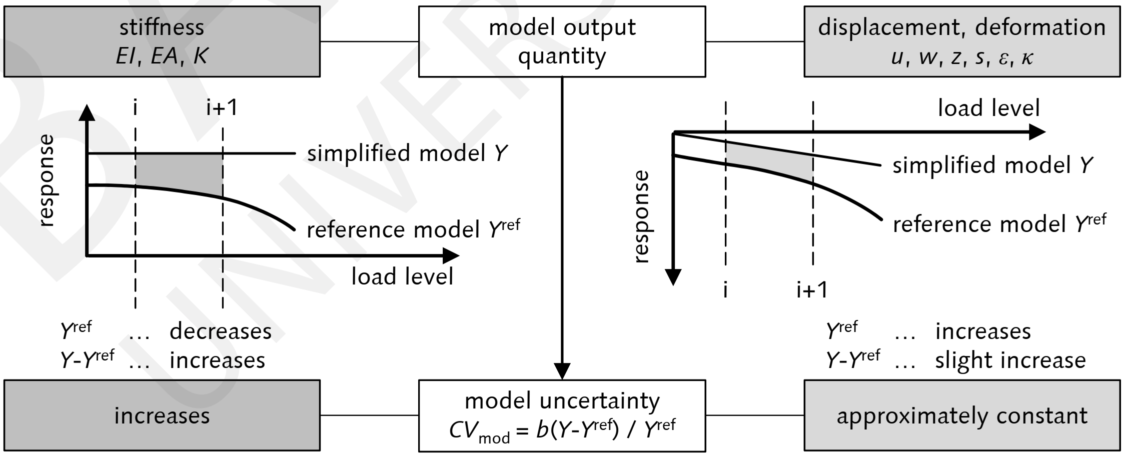
stiffness
EI, EA, K
model output
quantity
displacement, deformation
u, w, z, s, ε, κ
i
i+1
response
simplified model Y
reference model Y^{ref}
load level
Y^{ref} … decreases
Y-Y^{ref} … increases
load level
simplified model Y
reference model Y^{ref}
response
i
i+1
Y^{ref} … increases
Y-Y^{ref} … slight increase
increases
model uncertainty
$CV_{\text{mod}} = b(Y\text{-}Y^{\text{ref}}) / Y^{\text{ref}}$
approximately constant

(c) stiffness or settlement

Figure 5.23: Dependency of stiffness or settlement response quantity for model uncertainty assessment, example: RANDOLPH et al. [334] in relation to reference model RUDOLF [353], group 2x2 (II) with $s/d_P = 2$

The vertical stiffness should be used as the model output as it is the most influential quantity for purpose of structural analysis. The application of the stiffness as the response quantity in the uncertainty analysis is shown in Fig. 5.23. Moreover, the vertical settlement as another possible response quantity which is similarly capable to represent the pile foundation load-deformation behaviour and stiffness respectively. Due to the fact that the stiffness is constant for the elastic models (simplified models), the computation of model uncertainty, see Eq. 2.10b and Fig. 5.23(c), quantifies the difference in model predictions between a load-independent constant value and a load-dependent varying quantity in the reference model. In the case of selecting the stiffness response for the model output in the assessment, the reference value always decreases in the load-deformation analysis because no stiffening is possible in the considered models for an increase in external load. Therefore, standard deviation (difference between model predictions) increases and average value (model prediction of reference model) decreases between two neighbouring load steps.

When the relationship becomes more and more disproportional due to the high stiffness degradation in the non-linear reference model and the constant elastic stiffness in the simplified models, the model uncertainty is significantly overestimated and is not capable of representing the average load-deformation behaviour of the models that are discussed in the following paragraphs. This deterministic simulation is shown previously in Fig. 5.22 and it is easily apparent that a high non-linear stiffness degradation occurs in the loading range $6 < N\,[\mathrm{MN}] < 20$. Hence, the settlement increases disproportionally to the external load increment. Further load increments reduce the disproportional stiffness degradation resulting in an almost constant stiffness in the ultimate state. Therefore, the settlement increases proportionally to the external load increment. For the simplified elastic models, the increase in settlement is always proportional to the external load increment due to the same initial elastic pile foundation stiffness. Furthermore, the characteristic of the coefficient of variation CV is that a proportional change between standard deviation (numerator) and average value (denominator) lead to a constant CV between two neighbouring load steps.

All these aspects should be quantified and considered in the model uncertainty assessment. A comparison between the stiffness and settlement response applications for the uncertainty analysis shows that the settlement value is more adequate and accurate in the model uncertainty quantification, see Fig. 5.23. The uncertainty in the non-linear loading range is overestimated by the settlement criteria and the decrease in disproportional stiffness degradation for further load increments is not visible in the case that the stiffness response is applied in the model uncertainty assessment. In contrast, the settlement response determination is more reasonable and capable of representing the entire load-deformation behaviour of the pile foundation. Therefore, the settlement prediction is chosen as the model output in the uncertainty assessment being capable to investigate the entire load-deformation analysis. Similarities for the prediction of curvature and stiffness are visible in the evaluation of the material models for concrete as it is quantified in Sec. 5.1.

The results of the model uncertainty assessment are shown in Fig. 5.24 with respect to both pile group arrangements and pile space ratios $s/d_P = 2$ and $s/d_P = 10$. For the ratios $s/d_P = 3$ and $s/d_P = 5$, the results of the model uncertainty are presented in appendix in Fig. B.11. The difference in the model predictions between the models by RANDOLPH and MYLONAKIS is small and therefore model uncertainty is consequently comparable between both models. With increasing pile space ratio, the interaction is less between each pile in the groups and therefore the predictions are even more similar and finally the same in the case of great pile space ratios. In the loading range $N < 8\,\mathrm{MN}$, the model uncertainty in the elastic models are generally smaller than $CV_{\mathrm{model}}^{\mathcal{M}_i} < 0.08$ for the great pile space ratio and < 0.07 for the small pile space ratio. Therefore, all of the models considered predict a comparable stiffness in this loading range and hence the simplified elastic models are accurate for the prognosis of elastic stiffness. Hence, the

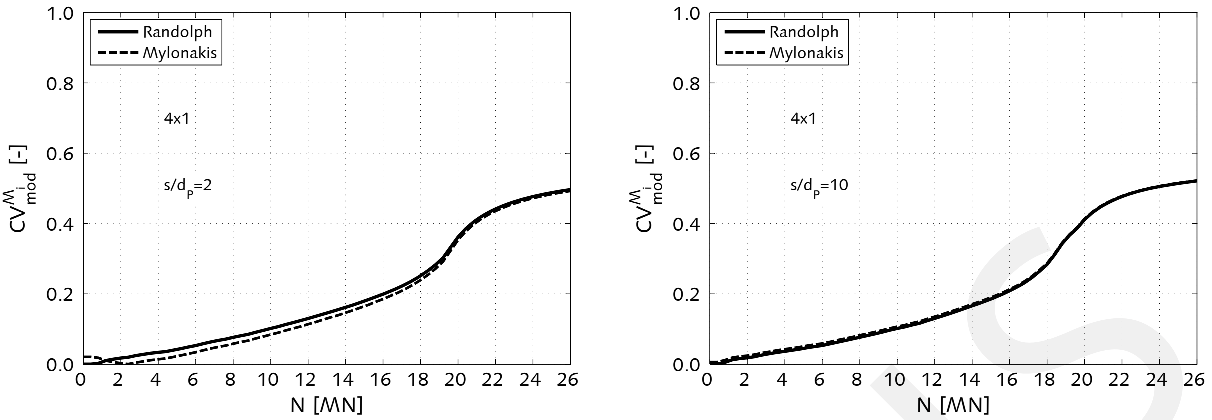

(a) group 4x1 (I) with $s/d_P = 2$

(b) group 4x1 (I) with $s/d_P = 10$

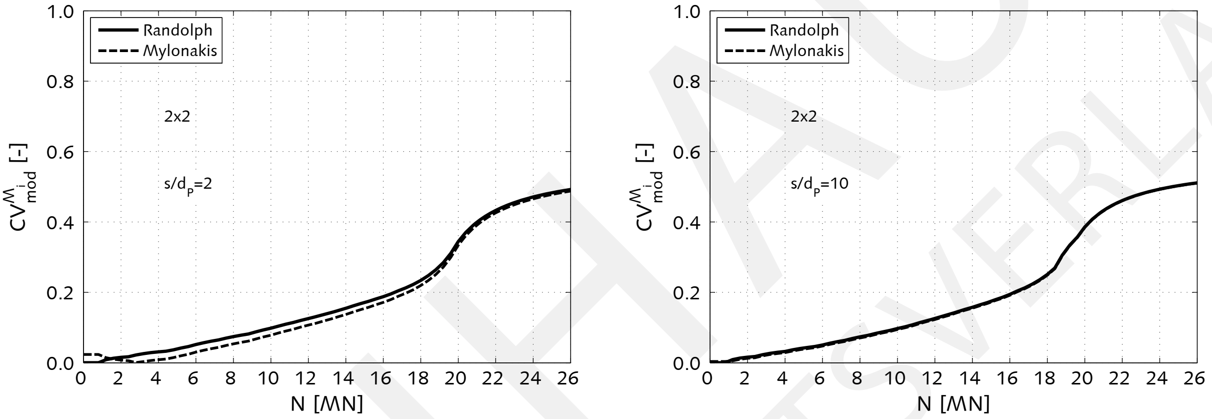

(c) group 2x2 (II) with $s/d_P = 2$

(d) group 2x2 (II) with $s/d_P = 10$

Figure 5.24: Model uncertainty $CV_{\text{mod}}^{\mathcal{M}_i}$ for pile foundation assembly 4x1 (I) and 2x2 (II), RANDOLPH et al. [334], MYLONAKIS et al. [291], reference model RUDOLF [353]

complexity in the model by RANDOLPH and WORTH [334], and the model by MYLONAKIS and GAZETAS [291] is adequate in order to determine the linear-elastic stiffness. In comparison to the complex model by RUDOLF, the highest model uncertainty is found at the final loading level in which the difference between linear-elastic and non-linear prognosis is the greatest. For the pile group 2x2 with $s/d_P = 2$, this uncertainty is 0.49 and 0.51 for $s/d_P = 10$. In a similar manner, the highest model uncertainty in the prediction of vertical pile group stiffness in pile group 4x1 with $s/d_P = 2$ is 0.49 and for $s/d_P = 10$ is 0.52.

Finally, a difference in model uncertainty is not quantified according to the different pile group arrangements. The scope of the load dependent uncertainty for the 4x1 and 2x2 groups is very similar and even the quantitative values are comparable as mentioned above. Furthermore, the influence of the pile space ratio is not distinctly obvious in the main part of loading. A slight increase in model uncertainty is visible for the great pile space ratio in the loading range between $18 < N < 24$ MN in comparison to the smaller pile space ratio. This effect is caused by a more extensive stiffness degradation for $s/d_P = 10$ in comparison to $s/d_P = 2$. For the 4x1 group and the small pile space ratio, the uncertainty for N=20 MN is 0.35 and 0.41 for the greater ratio. Similarly, for the group 2x2 and the small pile space ratio the model uncertainty is 0.33 and 0.38 for the greater pile space ratio .

5.2.1.3 Parameter uncertainty by probabilistic simulation

For the assessment of parameter uncertainty, probabilistic simulations are necessary in order to take into account the randomness in the model input parameters. The quantification of parameter uncertainty allows for the evaluation of the variance in each model depending on the load conditions. The results of the probabilistic simulation are shown in Fig. 5.25. On one side, the results according to the elastic model by Mylonakis et al. [291] and on the other side according to the non-linear pile foundation model by Rudolf [353] are illustrated for the pile group arrangement 4x1 (I) with the pile space ratio of $s/d_P = 2$. The prediction of the vertical stiffness K_v of each model is related to the deterministic (average) elastic model prognosis K_v^I which is $1,566\,\text{MN/m}$ for the model by Mylonakis and $1,619\,\text{MN/m}$ for the model by Rudolf.

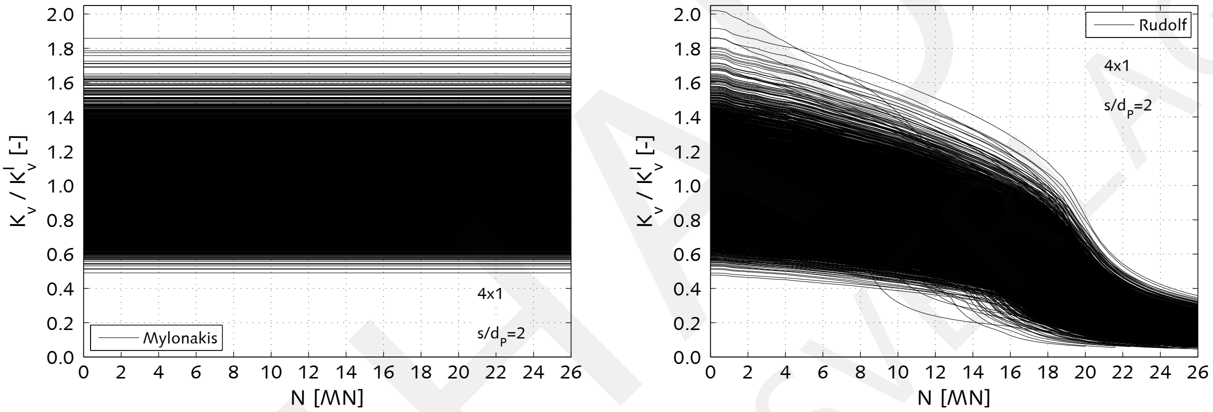

(a) Mylonakis et al. [291]

(b) Rudolf [353]

Figure 5.25: Probabilistic simulation of vertical pile foundation stiffness for either elastic or non-linear models, group 4x1 (I) with $s/d_P = 2$, 10000 samples

Based on these probabilistic simulations, a difference between the elastic and non-linear models is easily apparent for the entire loading range. No stiffness degradation is achievable in the elastic models and therefore the influence of the non-deterministic input parameters on the load-deformation behaviour is independent of the loading level. In contrast, the variance in the non-linear model is highly sensitive to the loading condition and the resulting soil response. The quantitative assessment of parameter uncertainty allows for the evaluation of the influence of the randomly varying input parameters on the model output and the results are discussed in the following paragraphs.

The parameter uncertainty for both pile group arrangements with corresponding pile space ratios $s/d_P = 2$ and $s/d_P = 10$ are shown in Fig. 5.26. For the pile space ratios $s/d_P = 3$ and $s/d_P = 5$, the results of parameter uncertainty are shown in the appendix in Fig. B.12. For the model by Mylonakis, the parameter uncertainty is $CV_{\text{par}}^{\mathcal{M}_{\text{MYL}}} = 0.19$ and is analysed to be independent of loading level, pile group arrangement, and pile space ratio. In a similar manner, a coefficient of variation is assessed to $CV_{\text{par}}^{\mathcal{M}_{\text{RAN}}} = 0.20$ for the Randolph pile foundation model also being independent of the previously mentioned conditions.

A load dependent parameter uncertainty is easily apparent in the non-linear model by Rudolf. For a sample set of model input parameter with corresponding higher initial stiffness in comparison to another sample set, the stiffness degradation occurs at higher loading levels. Therefore, for a sample set with lower initial stiffness subjected to a loading condition such as $N = 16\,\text{MN}$, some pile shaft or pile base elements

BAUHAUS
UNIVERSITÄTSVERLAG

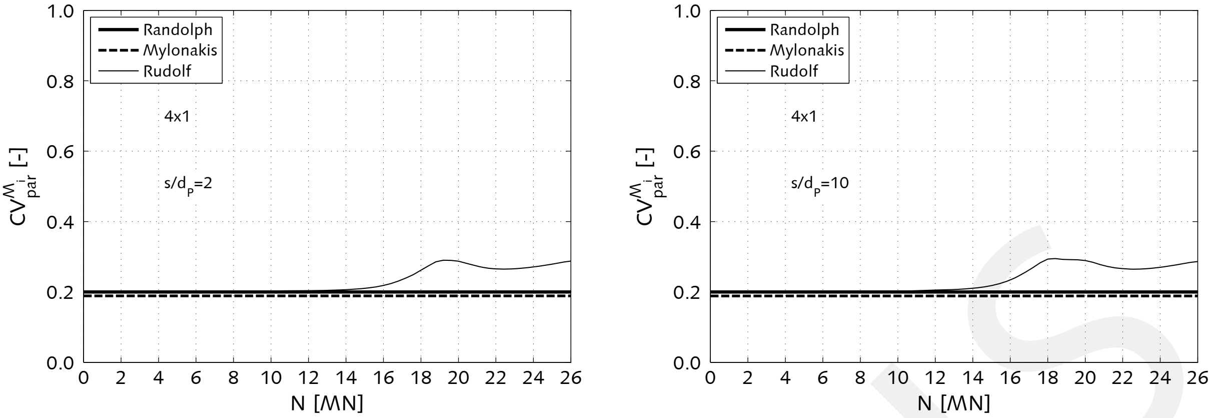

(a) group 4x1 (I) with $s/d_P = 2$

(b) group 4x1 (I) with $s/d_P = 10$

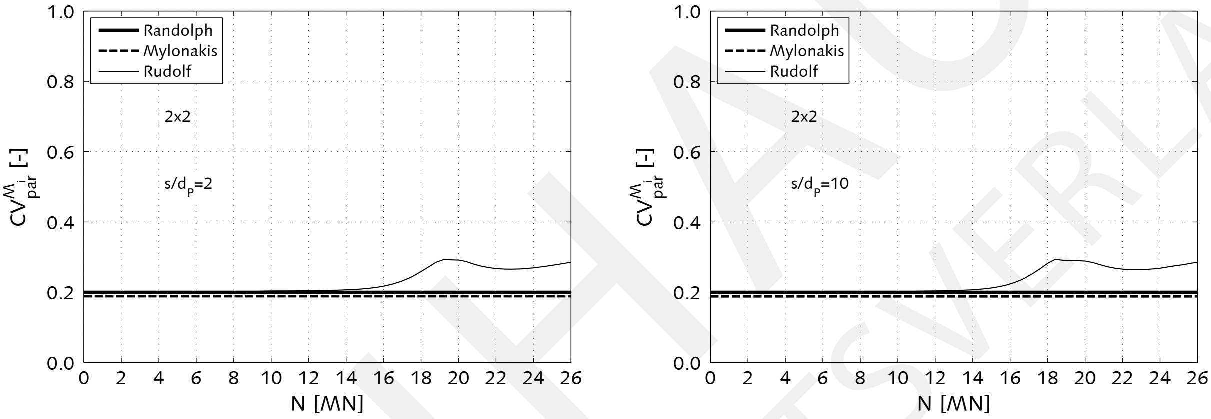

(c) group 2x2 (II) with $s/d_P = 2$

(d) group 2x2 (II) with $s/d_P = 10$

Figure 5.26: Parameter uncertainty $CV_{\text{par}}^{\mathcal{M}_i}$ for pile foundation arrangement 4x1 (I) and 2x2 (II), RANDOLPH et al. [334], MYLONAKIS et al. [291], RUDOLF [353]

are in the plastic zone according to the *Mohr-Coulomb* shear strength criterion. In contrast, these elements may be in the elastic stage for the same loading level for another sample set with corresponding higher initial stiffness. Settlement prediction is significantly different between both material stages and hence the parameter uncertainty increases in comparison to the elastic prediction models. In the initial elastic stage, the parameter uncertainty in the model by RUDOLF is comparable to the model by RANDOLPH, which is caused by the same description of pile-to-pile interaction. This parameter uncertainty is similarly independent of pile group arrangement and pile space ratio and is quantified to be 0.20.

Increase in the coefficient of variation is initiated at a loading level of about $N \approx 14\,\text{MN}$ for both pile foundation arrangements. For the greater pile space ratio, the increase is slightly more rapid and results for 2x2 group with $s/d_P = 10$ and $N = 18\,\text{MN}$ in a the parameter uncertainty of 0.28. In contrast, the coefficient of variation is 0.25 for $s/d_P = 2$. For the pile group 4x1, the corresponding uncertainties are 0.26 for the smaller pile space ratio and 0.30 for the greater. The maximum uncertainty of all loading conditions is 0.29 for both pile group arrangements and all pile space ratios, that occur in the loading range between $18 < N\,[\text{MN}] < 20$. For further load increments, this uncertainty is reduced because more and more samples are in the same plastic material condition and therefore the coefficient of variation in

BAUHAUS
UNIVERSITÄTSVERLAG

the stiffness prediction decreases in the load level range between $20 < N\,[\text{MN}] < 24$. Another stiffness degradation appears for further load-increments and hence an increase in parameter uncertainty occurs at the final ultimate loading stage.

The analysis of the influence of pile space ratio found that these geometric conditions does not affect the maximum and minimum parameter uncertainty values for the entire load-deformation analysis. These conditions in the pile group arrangement is slightly influential in the shape of the coefficient of variation along all loading levels. Nevertheless, the parameter uncertainty is in some cases independent of the pile group arrangement and pile space ratio.

5.2.1.4 Total uncertainty

Taking into account the model and parameter uncertainty leads to the total uncertainty for the considered vertical pile models in the entire load-deformation analysis. This uncertainty can be transferred to the model's prediction quality which allows a quantitative assessment of several models. Finally, for the analysis of engineering problems, the model with best prediction quality should be used in order to obtain reliable simulation results and to ensure a safe design of the structure.

The total uncertainty $CV_{\text{tot}}^{\mathcal{M}_i}$ in the prediction of vertical pile foundation stiffness is illustrated in Fig. 5.27 for both pile group arrangements and corresponding pile space ratios $s/d_P = 2$ and $s/d_P = 10$. Moreover, the quantification of total uncertainty is shown in the appendix in Fig. B.12 for the pile space ratios $s/d_P = 3$ and $s/d_P = 5$. The shape of the total uncertainty quantified by the coefficient of variation in the model prediction of vertical stiffness is not significantly influenced either by pile group arrangement or pile space ratio. The total uncertainty at the initial elastic loading stage is equal to the parameter uncertainty because the models predict on average a comparable vertical pile group stiffness that results in an negligible model uncertainty. Increase in external force N causes certain non-linear soil response and hence a discrepancy between the elastic and non-linear models. The model uncertainty of the elastic models by Randolph et al. [334] and Mylonakis et al. [291] increases for further load increments. However, the parameter uncertainty for the elastic models is constant over the entire loading range. Therefore, the basic contribution in the total uncertainty of these models is the parameter uncertainty of about 0.20. The additional magnitude is caused by the continuously increasing model uncertainty caused by the simplification in the underlying model descriptions.

Maximum total uncertainty appears for the elastic models at the final loading stage for $N = 26\,\text{MN}$ caused by the highest model uncertainty. This highest total uncertainty is assessed to be on average $CV_{\text{tot}}^{\mathcal{M}_{\text{RAN}}} = 0.55$ and $CV_{\text{tot}}^{\mathcal{M}_{\text{MYL}}} = 0.54$ for both pile group arrangements and pile space ratios. The non-linear model by Rudolf is chosen as the reference model and thus is not affected by model uncertainties. Therefore, the total uncertainty in this model is equal to the underlying parameter uncertainty as discussed in the previous section. The maximum total uncertainty for this non-linear model is equal to $CV_{\text{tot}}^{\mathcal{M}_{\text{RAN}}} = 0.30$ for both arrangements and pile space ratios. This uncertainty occurs at the intersection in the more rapid stiffness degradation at the loading range of $12 < N\,\text{MN} < 20$. For the initial loading range between $1 < N\,\text{MN} < 12$, the uncertainty in the complex non-linear models is identically to the uncertainty in the initial linear-elastic stage.

The total uncertainty can be transferred into the partial model quality $MQ_{\text{PM},Y}^{\mathcal{M}_i}$ of each pile foundation model. Either the total uncertainty of a certain model is related to the minimum uncertainty of all models as proposed by Keitel [206], see Eq. 2.15 and Fig. 5.28(a), or a direct representation of the total uncertainty according to Eq. 2.14 and Fig. 5.28(b). Both definitions are exemplary illustrated in Fig. 5.28 for the pile

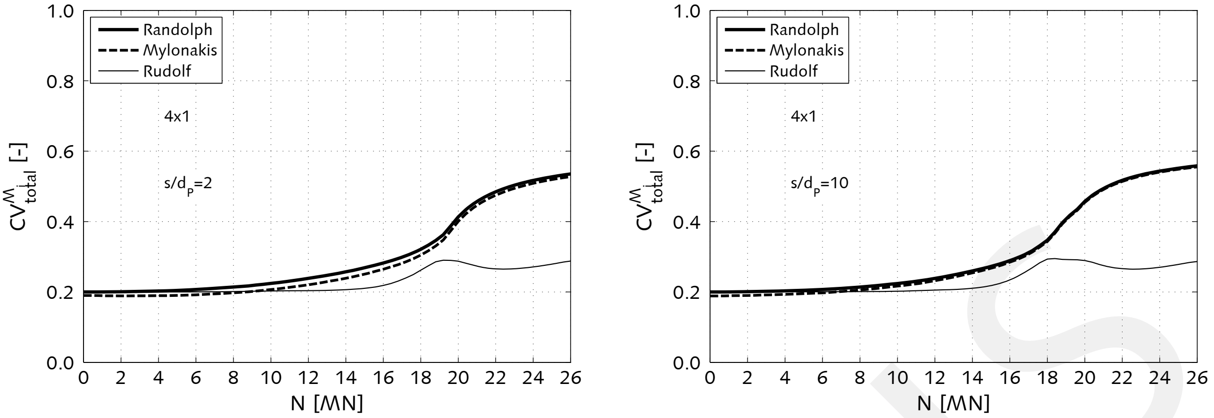

(a) group 4x1 (I) with $s/d_P = 2$ (b) group 4x1 (I) with $s/d_P = 10$

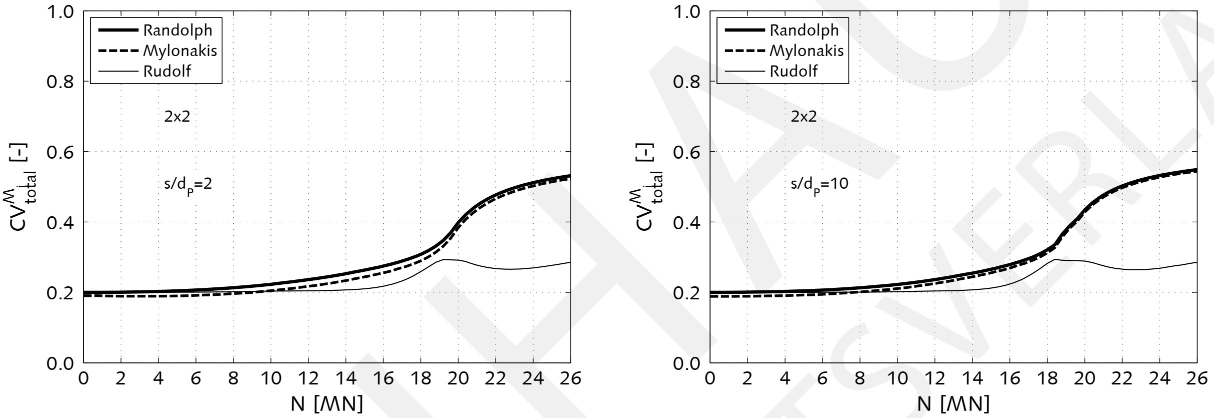

(c) group 2x2 (II) with $s/d_P = 2$ (d) group 2x2 (II) with $s/d_P = 10$

Figure 5.27: Total uncertainty $CV^{\mathcal{M}_i}_{\text{tot}}$ for pile foundation arrangement 4x1 (I) and 2x2 (II), RANDOLPH et al. [334], MYLONAKIS et al. [291], RUDOLF [353]

foundation arrangement 4x1 (I) with pile space ratio $s/d_P = 2$. The partial model quality for the other pile group conditions are not illustrated due to the fact that the shape and almost maximum and minimum values of total uncertainty are approximately independent of pile group arrangement and pile space ratio. Hence, corresponding partial model quality is very close to that shown in Fig. 5.28 for the other considered geometric conditions in the pile group arrangement.

The relative determination of partial model quality always associates from the model with lowest total uncertainty to the model with the best overall prediction quality resulting in $MQ^{\mathcal{M}_i}_{\text{PM},Y} = 1.0$. In the initial elastic pile group response up to $N = 8\,\text{MN}$, the model by MYLONAKIS et al. [291] is the model with best overall prediction quality and the other models are assessed to $MQ^{\mathcal{M}_i}_{\text{PM},Y} < 0.95$. Nevertheless, the total uncertainty is 0.19 for MYLONAKIS model and 0.20 for the other models. Therefore, the almost negligible difference in total uncertainty is transferred into a considerable difference in partial model quality which is generally too sensitive and finally overestimates the diversity in partial model quality for models with almost same total uncertainty.

For further load increments, the total uncertainty in the non-linear model is constant up to the loading level of $N = 14\,\text{MN}$. The increase in total uncertainty in the elastic models is more rapid than the

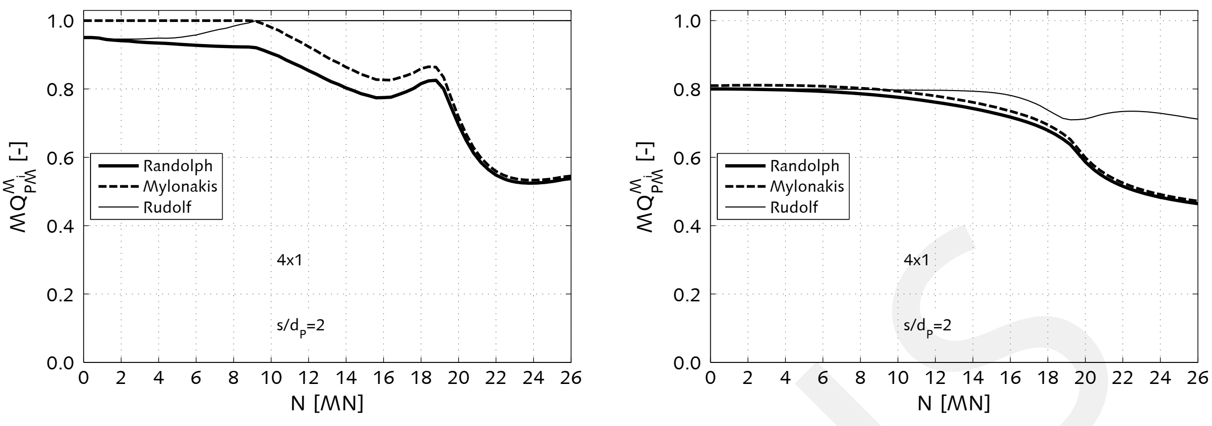

(a) $\frac{\text{MIN}\left[CV_{\text{tot},Y}^{\mathcal{M}}\right]}{CV_{\text{tot},Y}^{\mathcal{M}_i}}$ (b) $1 - CV_{\text{tot},Y}^{\mathcal{M}_i}$

Figure 5.28: Model quality $MQ_{\text{PM}}^{\mathcal{M}_i}$ for pile foundation arrangement 4x1 (I) with pile space ratio $s/d_P = 2$, Randolph et al. [334], Mylonakis et al. [291], Rudolf [353]

non-linear model. Therefore, the minimum total uncertainty appears in the model by Rudolf for all considered models. Hence, this non-linear model is the model with best partial model quality for loading conditions $N > 7\,\text{MN}$. Increase in total uncertainty in this model occurs at the loading range between $16 < N\,\text{MN} < 20$. The difference to the elastic models decreases for these loading conditions. Therefore, the partial model quality of the elastic models increases to a considerable amount. This is caused by the change in total uncertainty of another model and is not affected by the uncertainty in the prediction of the elastic models itself. Hence, this is similar to another adjustment of models with smaller accuracy and a model with greater complexity. This modification can be seen as modification representing one more model uncertainty assessment which is not adequate. The uncertainty and model quality should be as much as possible independent from other models in order to finally represent the model's characteristics and behaviour in the evaluation. In the model uncertainty, some relation to a reference (most complex model or experimental data) is necessary and unavoidable. Nevertheless, this relation does not cause this increase in partial model quality and is exclusively caused by an increase in total uncertainty in another model which finally does not anymore represent the model characteristics of each model itself.

The partial model quality should be quantified as a clear representation of the individual model characteristics. Therefore, a direct relation of prediction quality to total uncertainty is more appropriate than a relative determination that causes changes in the model characteristics of each model. Therefore, the determination of $MQ_{\text{PM},Y}^{\mathcal{M}_i} = 1 - CV_{\text{tot},Y}^{\mathcal{M}_i}$ identically represents the total uncertainty in the model prediction of each individual model. Constant total uncertainty over a certain loading range results in constant partial model quality of each individual model. Moreover, variations in model quality are exclusively caused by changes in total uncertainty of each individual model. Therefore, the characteristics of each model according to the load-deformation analysis are exactly and adequately represent by this determination. The consideration of further models then the considered ones and their assessment can be directly performed and added to models which are already assessed assuming that the reference in the model uncertainty evaluation is not influenced. This selection of the reference should be discussed and carefully checked in the case that additional models are considered in the uncertainty assessment. In conclusion, the direct relation of model quality and total uncertainty is more adequate compared to the relative determination and should be generally applied as the corresponding partial model quality in the assessment of global structural models.

6 Integrative assessment method

6.1 Integrative sensitivity analysis

This chapter presents an method for the assessment of partial models influence on the entire structural load-deformation behaviour. Hence, the assessment at local positions in the structure is enhanced to an overall evaluation method, which is applied to a simplified academic example and complex integral bridges. Integrative assessment method that includes integrative sensitivity analysis and integrative global model quality evaluation. The theory behind these assessment methods is discussed in this chapter and both methods are subsequently applied to simplified and complex engineering structures. The global model quality assessment at certain locations in the structure, see Sec. 2.5, is particularly valuable for the design of engineering structures with a linear-elastic computation of the section forces and the subsequent dimensioning of critical cross sections. Whereas, simulations of structures based on material non-linearities do not explicitly include the design of certain critical cross sections. Instead of the local safety check on cross sections, a global safety check for non-linear simulations should be performed on a structural level rather than on the local sections [5, 65, 66]. The design of the entire structure is always checked implicitly by the constitutive models at all positions with the corresponding conditions, such as the amount of reinforcement or the level of prestressing. Following the safety level concept for non-linear simulations, the model quality assessment cannot be exclusively referred to the partial model's sensitivity at local positions in the structure, particularly in the case of non-linear material simulations. Therefore, it is necessary to establish a sensitivity analysis, which is capable of evaluating the entire structure while taking into account all positions in the structure in an overall assessment method.

Furthermore, due to complicated and interactive conditions in the structure, it might be difficult to clearly identify the positions to assess the structural load-bearing evaluation. The false position identification will result in a model evaluation at positions in the structure with low significance for the design of the entire structure. For example, it may be difficult to identify the important positions for the assessment method in the case of the structural analysis of a high rise building (Which column, slab, or frame corner should be assessed?), or great shell structures (Which node should be assessed?), or dynamic analysis of structures (need to consider the entire structural system), or complex bridges (integral bridges, curved bridges).

Moreover, the sensitivity is strongly dependent on the position in the structure [196, 211]. Therefore, the quality of the prediction for the same partial model combination varies from position to position, due to either different sensitivity indices or partial model qualities. The quality assessment for each partial model combination should take into account the entire structure, especially for practical engineering problems. Thus, for each partial model combination, one global model quality should be assessed to quantify the overall load-deformation behaviour of the entire structure instead of evaluating each local position. Based on the proposed integrative assessment method, a global structural model with an adequate prediction quality can be selected in order to obtain reliable prognoses and a safe design of the entire structure.

The requirement of assessing the partial model's sensitivity on a structural level for non-linear simulations for overall assessment and the possible false position identification in the structure justifies the necessity to advance the existing sensitivity analysis and global model evaluation. The integrative sensitivity analysis extends the sensitivity analysis at local positions in the structure to an integrative assessment method of the entire structure. This enhancement considers the assessment of the partial model's importance in relation to the overall structural load-bearing behaviour. Furthermore, the integrative global model quality evaluation can consider a changing partial model quality along the positions in the structure. Therefore, the integrative assessment method is proposed in this section in order to assess the global model quality with respect to the entire structure. Hence, the decision making in selecting an adequate partial model combination for the entire structure can rely on the integrative assessment method.

The method considers the local response significance, the sensitivity information, and the partial model quality. If the local response significance is neglected, then the sensitivity analysis would assume an equal importance of each position in the structure based on the overall structural load-bearing behaviour. However, this is a very simplified assumption for engineering structures. Hence, the magnitude of a desired response quantity at each position is taken into account in the computation of the local response significance factors in order to strengthen the simplified assumption. Permissible material stresses defined in design codes can be applied as reference values, which render the local response significance similar to a utilization ratio. An alternative for the reference values is to use the absolute response maximum at all positions in the numerical structural model defining a relative determination of the local response significance factors.

The application of the integrative assessment method to the numerical simulations of semi-integral concrete bridges clarifies its general applicability for complex engineering structures, see Sec. 6.3. Therefore, the categorisation of the phenomena's importance in the numerical simulations of entire structural models can be assessed. The results illustrate where the accurate or simplified models can be used to represent various physical phenomena in the structural model. This quantitative model selection assists structural engineers in obtaining more reliable numerical simulation results and finally to ensure a safer design.

In principle, the integrative assessment method enables the categorisation of engineering structures according to the importance of various phenomena, which should be taken into account in the numerical simulation. Design recommendations in guidelines and codes can then be made in a quantitative manner by applying the integrative sensitivity analysis for various structures and corresponding conditions.

The total-effects sensitivity indices corresponding to model class S_{Ti}^{M} and model choice S_{Ti}^{MC} can be assessed at each nodal coordinate or in each element in the numerical model of the entire structure. The importance of the model class and the influence of the model choice on the focusing phenomenon are strongly dependent on the position and conditions within the structure [196]. These variance-based sensitivity values are independent of the structural response magnitude at each position. Hence, the significance of each position in the global numerical model of the structure is not considered in the variance-based sensitivity analysis.

In this context, the integrative sensitivity analysis enhances the existing sensitivity methods. This quantitative method describes the influence that model class or model choice has on the overall structural load-bearing behaviour. Consequently, the assessment of coupled numerical partial models does not anymore refer to a local response quantity at a particular position in the structure. The integrative sensitivity analysis assesses the model's importance in relation to the entire load-bearing behaviour of the structure.

The sensitivity indices at local positions in the structure are related to various response quantities Y, for example displacements, stresses, and section forces. The numerical integration of the sensitivity indices (S_{Ti}^{M}, S_{Ti}^{MC}) at each position over a chosen region l_j, e.g. the length of structural components (e.g. $l_{\text{superstructure}}$, $l_{\text{substructure}}$, $l_{\text{structure}}$) leads to an unweighted overall assessment of the sensitivity indices. The importance of the response values at each node is assumed to be equally essential for the evaluation of the structure represented by the coupled numerical partial models.

As an example, the prediction of the vertical displacement of a simply supported beam is much less important near the supports than near the centre of the span, see Fig. 6.1. The importance of each position can be considered by the local response response significance factor $\mathcal{S}$, which is zero at the supports and unity in the span for this academic example. Zero mean that this position is not influential according to the entire structural behaviour and unity expresses the most influential position in the entire structure. In contrast, the unweighted numerical integration assumes an equal importance of each position in the prediction of both displacements, which is not adequate for a quantitative assessment method in order to obtain a reliable global model quality. This academic example is further discussed in combination with the integrative global model quality evaluation in Sec. 6.2.

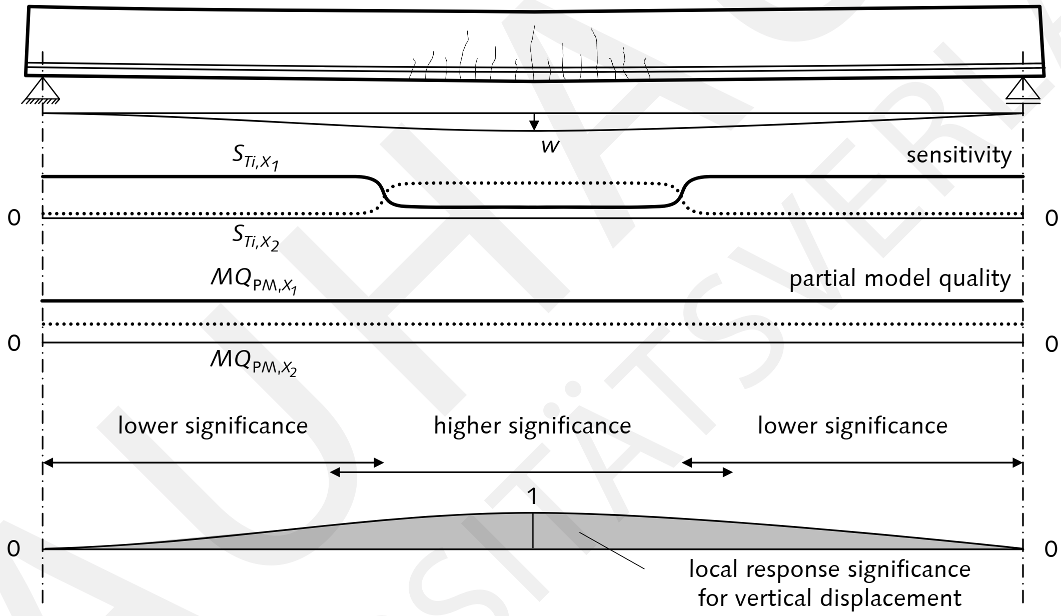

Figure 6.1: Sensitivity of partial models for simply supported beam in cracked stage with constant partial model quality and local response significance

In order to consider the significance of the position in the structure, the unweighted numerical integration of the sensitivity indices over a certain length is advanced with the help of the integrative sensitivity analysis. The integrative total-effects sensitivity index $\overline{S}_{Ti}^{\mathrm{M/MC}}$ can be assessed for specific structural components or the entire structure including all of its components and elements, which is considered in the length l_j. Therefore, the importance of the sensitivity indices at the various positions is expressed by the local response significance factor $\mathcal{S}_Y$. For the overall structural assessment, the integrative total-effects sensitivity index considers the required sensitivity and significance information and is defined as:

$$\overline{S}_{Ti,X_i}^{\mathrm{M/MC},Y} = \int\limits_{x=0}^{x=l_j} S_{Ti,X_i}^{\mathrm{M/MC},Y}(x)\cdot\mathcal{S}_Y(x)\,\mathrm{d}x\,. \tag{6.1}$$

The integrative sensitivity can be approximately determined assuming a piecewise linear distribution by:

$$\overline{S}_{Ti,X_i}^{\mathrm{M/MC},Y} \approx \sum_{n=1}^{N} \frac{S_{Ti,X_i}^{\mathrm{M/MC},Y}(n) \cdot \frac{1}{2} \cdot (x_{n+1} - x_{n-1}) \cdot \mathcal{S}_Y(n)}{\sum\limits_{n=1}^{N} \frac{1}{2} \cdot (x_{n+1} - x_{n-1}) \cdot \mathcal{S}_Y(n)} \tag{6.2}$$

with the initial summand $n = 1$ and the final summand $n = N$ of the midpoint rule as:

$$\begin{aligned} &\text{for: } n = 1 && (x_{n+1} - x_{n-1}) = (x_2 - x_1) \\ &\text{for: } n = N && (x_{n+1} - x_{n-1}) = (x_N - x_{N-1}) \end{aligned} \tag{6.3}$$

where $\mathcal{S}_Y(n)$ is the local response significance factor at the position n in the structure, N is the total number of all positions, and $S_{Ti,X_i}^{\mathrm{M/MC},Y}$ are the total-effects sensitivity indices for each partial model X_i with respect to the structural response quantity Y. The integrative sensitivity indices have to be separately quantified in the model class (M, first step) or model choice (MC, second step) assessment. The sensitivity analysis quantifies which model causes the variance in the structural model response. In addition, the local response significance factor $\mathcal{S}_Y$ considers the importance of the prediction at each node or element in relation to the overall structural behaviour. Thus, it is a parameter that requires a definition according to engineering considerations, which may change for different response quantities.

Two different definitions of $\mathcal{S}_Y$ are proposed. On one hand, the factor can be defined as the ratio between the maximum/minimum response value at a particular node (or element) $Y^{\mathrm{min/max}}(n)$ of the numerical model and the maximum/minimum response value of all nodes (or elements) over a chosen length of the structural components $Y_{l_j}^{\mathrm{min/max}}$, see Eq. 6.4a. On the other hand, the maximum or minimum response value at a particular node (or element) can also be related to a permissible value Y_{perm}, such as permissible material stresses defined in design codes or guidelines, rendering it similar to a utilization ratio, see Eq. 6.4b.

$$\mathcal{S}_{Y,\mathrm{rel}}(n) = \frac{Y^{\mathrm{min/max}}(n)}{Y_{l_j}^{\mathrm{min/max}}} \tag{6.4a}$$

$$\mathcal{S}_{Y,\mathrm{perm}}(n) = \frac{Y^{\mathrm{min/max}}(n)}{Y_{\mathrm{perm}}} \tag{6.4b}$$

The non-linear material response of structures and the probably complex conditions in structures cause the necessity for the quantification of the partial model's influence with respect to the entire structural behaviour. The integrative sensitivity analysis connects the sensitivity indices at each position in the structure with the response significance at the corresponding position. The numerical integrations of both quantitative information (sensitivity of the partial model and local response significance) over a chosen length, for example the length of the entire structure, enables the necessary overall assessment of the partial model's sensitivity. In addition to the varying sensitivity indices along the structural positions, the partial model quality may also be different from positions to positions. This even more complex problem can be considered in the integrative global model quality evaluation, which is discussed in the next section.

6.2 Integrative global model quality evaluation

In addition to variable sensitivity indices of the phenomena represented by partial models, the partial model quality itself can be different at each position in the structure. For example, the partial model quality of

BAUHAUS
UNIVERSITÄTSVERLAG

non-linear and linear material models for reinforced concrete are strongly dependent on the loading condition and cracking stage, see Sec. 5.1. Hence, the quality of the same partial model is different among positions in the structure in which concrete cracking occurs and positions with linear-elastic response.
Concrete cracking due to bending may occur in the span of the simply supported beam and linear-elastic material response may appear near the supports, see Fig. 6.2. Based on the results of the previously illustrated assessment of material models for reinforced concrete flexural members, the qualities of non-linear and linear models are similar in the uncracked stage, which occurs in structural positions near the support of the simply supported beam. In contrast, concrete cracking significantly decreases the bending stiffness of the cross sections in the span. The partial model quality of the linear models decreases in comparison to the non-linear models, due to the stiffness degradation. Finally, the partial model quality can also depend on the position in the structure, as does the sensitivity of the phenomenon, see Sec. 6.1.

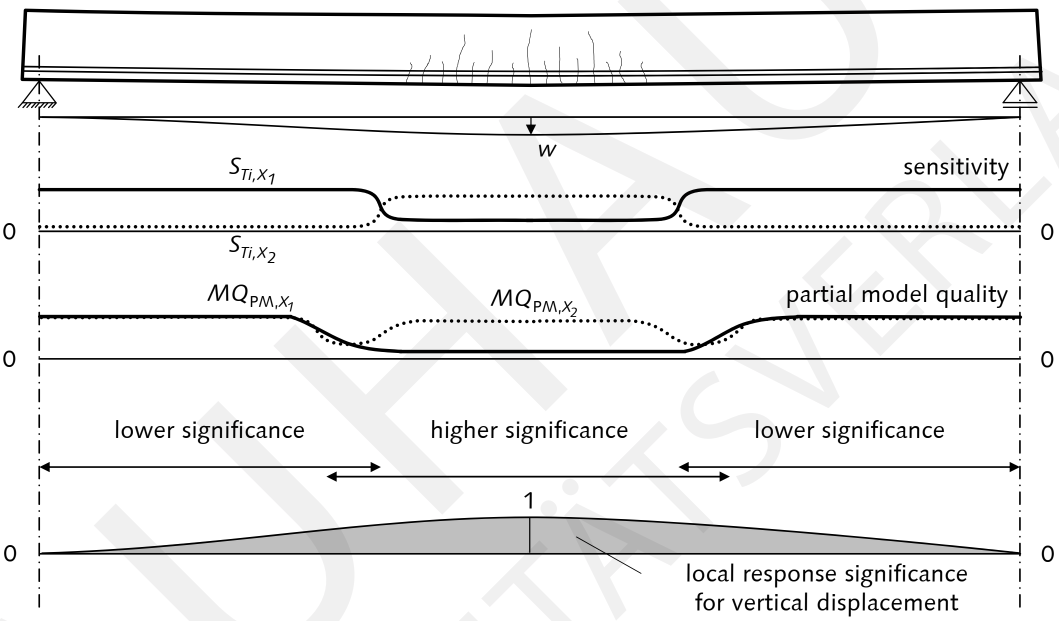

Figure 6.2: Variable partial model quality of simply supported beam in cracked stage with partial model's sensitivity and local response significance

The integrative assessment method is illustrated for the simple example of a simply supported beam in Tab. 6.1 for the position dependency of the sensitivity indices (Scenario ①) and the partial model quality (Scenario ②). The longitudinal coordinates of the beam are expressed by x in line 1 and the beam element length Δx is shown in line 2. The phenomenon may be X_1 for the linear-elastic material model and X_2 for the non-linear material model and the vertical displacement w of the simply supported beam is the response value of interest.
Due to the fact that concrete cracking only occurs in the span, the sensitivity of the linear-elastic model (line 3) is the opposite (to the sum equal to 1) of the non-linear model (line 4). The prediction of the vertical displacement near the supports is mainly influenced by the linear-elastic model and hence, the sensitivities of both partial models are assumed to be $S_{Ti,X_1} = 0.80$ and $S_{Ti,X_2} = 0.20$. In contrast, the vertical displacement at the span is significantly influenced by the non-linear model due to stiffness degradation, which is assumed by the sensitivity indices $S_{Ti,X_1} = 0.40$ and $S_{Ti,X_2} = 0.60$. More general description about the phenomena's sensitivity on the entire structural load-deformation behaviour is needed, especially for engineering design purposes, as discussed previously. Therefore, the importance of each position has to be

BAUHAUS
UNIVERSITÄTSVERLAG

determined in order to quantify its significance on the entire structure.

The local response significance factor $\mathcal{S}_Y$ is proposed, which enables the consideration of the importance of each position in the global model quality evaluation. Hence, a simplified numerical integration of the sensitivity values along the structure is enhanced to the integrative sensitivity analysis of the entire structure. For the example of the simply supported beam, the local response significance factor for the vertical displacements $\mathcal{S}_w$ are shown in line 5 of Tab. 6.1. At the support positions ($x = 0$ and $x = 1$), the vertical displacements are always zero and hence $\mathcal{S}_w(x = 0, x = 1) = 0$. The greatest vertical displacement appears at the mid span and consequently the local response significance factor is $\mathcal{S}_w(x = 0.5) = 1$. Between these positions, the shape of $\mathcal{S}_w$ is assumed to be a linear function, which is a more simplified determination compared to quadratic or cubic functions.

Based on these pieces of information, the sensitivity of each phenomenon $S_{Ti,i}$ and the local response significance factor for the structural response value $\mathcal{S}_Y$, the integrative sensitivity analysis can be computed in order to quantify the sensitivity of each phenomenon according to the entire structure and not exclusively analysed according to a certain position. The results of the integrative sensitivity analysis for the sensitivity indices according to Eq. 6.3 are shown in line 6 and 7 in comparison to the computation based on numerical integration by the midpoint rule. The integrative sensitivity indices for the partial models are $\overline{S}_{Ti,X_1} = 0.57$ and $\overline{S}_{Ti,X_2} = 0.43$. In comparison to the results of the numerical integration with the assumption of an equal importance of each position in the structure, according to the entire load-deformation analysis, a significant difference in the sensitivity indices appears. These results are $S_{Ti,X_1} = 0.66$ and $S_{Ti,X_2} = 0.34$ which lead to a difference of about 16 % and 21 %. Hence, the numerical integration underestimates the importance of the non-linear model X_2, because it assumes the same importance of the positions such as $x = 0.0$ (support) and $x = 0.5$ (span), which is a very simplified assumption and is not adequate to reasonably represent the load-deformation behaviour of the structure.

A first scenario for the global model quality evaluation is a constant partial model quality $MQ_{\mathrm{PM}}^{\mathcal{M}_i}$ at each position along the entire structure. Therefore, the influence of the cracking stage on the partial model quality is neglected for this scenario. The global model quality evaluation according to Keitel et al. [211], see Eq. 2.44, is enhanced to the integrative global model quality $\overline{MQ}_{\mathrm{GM},Y}$ considering the integrative sensitivity values $\overline{S}_{Ti,X_i}$:

$$\overline{MQ}_{\mathrm{GM},Y} = \sum_{i=1}^{n_{\mathrm{M,red}}} \frac{\overline{S}_{Ti,X_i}^{\mathrm{MC}} \cdot MQ_{\mathrm{PM},Y}^{\mathcal{M}_i}}{\sum\limits_{i=1}^{n_{\mathrm{M,red}}} \overline{S}_{Ti,X_i}^{\mathrm{MC}}} . \tag{6.5}$$

For the simply supported beam, a constant partial model quality is assumed to be $MQ_{\mathrm{PM}}^{\mathcal{M}_{X_1}} = 0.95$ and $MQ_{\mathrm{PM}}^{\mathcal{M}_{X_2}} = 0.40$, see line 8 in Tab. 6.1. The global model quality according to Eq. 2.44, considering the sensitivity values at each position is analysed in line 9. A range in the global model quality for all positions is computed to be between 0.62 (span) and 0.84 (supports). The non-linear model is more sensitive to the prediction of the vertical displacement in the span and the corresponding partial model quality is lower than the quality of the linear model. Hence, the global model quality at the supports is greater than in the span.

The numerical integration of these global model quality values at each position along the entire beam length leads to $MQ_{\mathrm{GM},w} = 0.76$, see line 10 in Tab. 6.1. The integrative global model quality $\overline{MQ}_{\mathrm{GM},w}$ is quantified to be 0.71, which leads to a considerable difference of 7 %.

Table 6.1: Influence of structural local position on sensitivity of partial models and global model quality analysed by integrative sensitivity analysis for a simply supported, cracked, concrete beam

	Parameter	PM	Position										
1	x		0.00	0.10	0.20	0.30	0.40	0.50	0.60	0.70	0.80	0.90	1.00
2	Δx		0.05	0.10	0.10	0.10	0.10	0.10	0.10	0.10	0.10	0.10	0.05
3	S_{Ti,X_i}	X_1	0.80	0.80	0.80	0.70	0.40	0.40	0.40	0.70	0.80	0.80	0.80
4		X_2	0.20	0.20	0.20	0.30	0.60	0.60	0.60	0.30	0.20	0.20	0.20
5	$\mathcal{S}_w$		0.00	0.20	0.40	0.60	0.80	1.00	0.80	0.60	0.40	0.20	0.00
6	$\overline{S}_{Ti,X_i}$	X_1	ISA: **0.57**		numerical integration:				0.66				
7		X_2	ISA: **0.43**						0.34				
Scenario ①: Sec. 6.1: constant partial model quality:													
8	$MQ_{\mathrm{PM}}^{\mathcal{M}_{X_1}} = 0.95$				$MQ_{\mathrm{PM}}^{\mathcal{M}_{X_2}} = 0.40$								
9	$MQ_{\mathrm{GM},w}$		0.84	0.84	0.84	0.79	0.62	0.62	0.62	0.79	0.84	0.84	0.84
10	$\overline{MQ}_{\mathrm{GM},w}$		ISA: **0.71**		numerical integration:				0.76				
Scenario ②: Sec. 6.2: variable partial model quality													
11	$MQ_{\mathrm{PM}}^{\mathcal{M}_{X_1}}$	X_1	0.95	0.95	0.80	0.60	0.30	0.30	0.30	0.60	0.80	0.95	0.95
12	$MQ_{\mathrm{PM}}^{\mathcal{M}_{X_2}}$	X_2	0.95	0.95	0.40	0.50	0.80	0.80	0.80	0.50	0.40	0.95	0.95
13	$MQ_{\mathrm{GM},w}$		0.95	0.95	0.72	0.57	0.60	0.60	0.60	0.57	0.72	0.95	0.95
14	$\overline{MQ}_{\mathrm{GM},w}$		ISA: **0.64**		numerical integration:				0.72				

The assumption that the partial model quality is independent of the cracking stage is a very simplified assumption, as it is analysed in Sec. 5.1. Hence, another enhancement of the global model quality evaluation method is necessary in order to consider variable partial model qualities at each position in the structure. For the example of the simply supported beam, the variable partial model qualities are shown in line 11 and 12 in Tab. 6.1 respresenting the scenario ②.

These quality values are adjusted to the quantified results of Sec. 5.1. Hence, the quality of linear and non-linear models in the linear-elastic stage are similar, which is considered in the example by $MQ_{\mathrm{PM}}^{\mathcal{M}_{X_1}}(x = 0.1) = MQ_{\mathrm{PM}}^{\mathcal{M}_{X_2}}(x = 0.1) = 0.95$. In contrast, due to concrete cracking and resulting stiffness degradation, the linear model is not adequate enough to represent the material behaviour. Hence, the quality of the linear model in the span is $MQ_{\mathrm{PM}}^{\mathcal{M}_{X_1}}(x = 0.5) = 0.30$. In contrast, the non-linear material model X_2 is much more accurate to compute the cracked element stiffness than the linear-elastic model X_1. The quality of the non-linear model is consequently better than the linear-elastic partial model quality and is assumed to be 0.80.

The global model quality may be computed according to the method of KEITEL, see Eq. 2.44 which leads to the range of global model quality $MQ_{\mathrm{GM},w}$ between 0.57 and 0.90 depending on the position in the structure, see line 13 in Tab. 6.1. What is the actual global model quality for selecting these two partial models? Is it the lowest or highest quality of all positions? Is it the average of both? Is it the numerical integration of all qualities at each position along the beam?

The integrative global model quality evaluation can consider a variable partial model quality along the entire structure. Therefore, the sensitivity $S_{Ti,X_i}^{\mathrm{MC}}(n)$, the partial model quality $MQ_{\mathrm{PM},Y}^{\mathcal{M}_i}(n)$, and the local response significance factor $\mathcal{S}_Y(n)$ should be taken into account in the assessment of global model quality which represents the entire load-deformation behaviour of the structure. The integrative global model quality is defined as:

$$\overline{MQ}_{\mathrm{GM},Y} = \int\limits_{x=0}^{x=l_j} S^{\mathrm{MC}}_{Ti,X_i}(x) \cdot MQ^{\mathcal{M}_i}_{\mathrm{PM},Y}(x) \cdot \mathcal{S}_Y(x)\,\mathrm{d}x\,. \tag{6.6}$$

The integrative global model quality can be approximately determined assuming a piecewise linear distribution by:

$$\overline{MQ}_{\mathrm{GM},Y} \approx \sum_{n=1}^{N} \sum_{i=1}^{n_{\mathrm{M,red}}} \frac{S^{\mathrm{MC}}_{Ti,X_i}(n) \cdot MQ^{\mathcal{M}_i}_{\mathrm{PM},Y}(n) \cdot \frac{1}{2} \cdot (x_{n+1} - x_{n-1}) \cdot \mathcal{S}_Y(n)}{\sum\limits_{n=1}^{N} \sum\limits_{i=1}^{n_{\mathrm{M,red}}} S^{\mathrm{MC}}_{Ti,X_i}(n) \cdot \frac{1}{2} \cdot (x_{n+1} - x_{n-1}) \cdot \mathcal{S}_Y(n)}\,, \tag{6.7}$$

with the initial summand $n = 1$ and the final summand $n = N$ of the midpoint rule as:

$$\begin{aligned} &\text{for: } n = 1 \qquad (x_{n+1} - x_{n-1}) = (x_2 - x_1) \\ &\text{for: } n = N \qquad (x_{n+1} - x_{n-1}) = (x_N - x_{N-1}) \end{aligned} \tag{6.8}$$

in which the determination of the integrative global model quality consists of the sum according to the positions in the structure N and the sum related to the important partial models assessed in the model choice assessment $n_{\mathrm{M,red}}$.

The integrative global model quality for the prediction of the vertical displacement is quantified for the simply supported beam to be $\overline{MQ}_{\mathrm{GM},w} = 0.64$, according to line 14 in Tab. 6.1. The numerical integration leads to 0.72 with a corresponding difference of 11 % in comparison to the integrative global model quality evalution.

In conclusion, the academic example of a simply supported beam with variable sensitivity values and its constant and variable partial model qualities shows the general methodology of the proposed integrative sensitivity analysis and integrative global model quality evaluation. The difference between the assessment of sensitivity and global model quality at each position and the entire quantification of the load-deformation behaviour of the structure is even obvious for this simple type of structure.

The integrative assessment method allows for the quantification of the sensitivity and global model quality with respect to the entire structure. Hence, it is possible to analyse and quantify the load-deformation behaviour of the structure by considering all positions with the proposed local response significance factor $\mathcal{S}_Y$. For each combination of partial models, overall quantitative information can be assessed, which allows for a more general and adequate insight into the structure in comparison to exclusively looking at a certain position in the structure.

The integrative sensitivity analysis and integrative global model quality evaluation are applied to a much more complex structure of semi-integral concrete bridges and the corresponding results are discussed in the following sections. In this extensive study, various pier heights, different limit states, and several structural response values are considered in the integrative assessment method. Furthermore, the consideration or negligence of the foundation flexibility is quantified and the load-deformation behaviour of a continuous girder bridge is compared to the coupled integral bridges. Integral bridges are chosen because a lot of partial models and a strong interaction between the several phenomena determine the entire load-deformation behaviour, see Sec. 3.5.4.2. Therefore, the method is applied to a complex engineering problem in order to illustrate its general applicability and adequateness for challenging structures.

6.3 Application to semi-integral concrete bridges

6.3.1 Geometry and Material Properties

In the present study, piers with varying cross section stiffness and heights are considered in order to analyse the interaction between the structural components for different geometric conditions. It should be noted that the load level condition also has a significant influence on the response of the structure and the partial model's sensitivity. Therefore, the serviceability limit state (SLS) as well as the ultimate limit state (ULS) are taken into account in the structural behaviour assessment using the integrative sensitivity analysis.

The bridge considered here consists of 3 spans with corresponding span lengths of $L_1 = L_3 = 40\,\mathrm{m}$ (side spans) and $L_2 = 48\,\mathrm{m}$ (mid span). The geometry of the prestressed concrete bridge and the tendon profile are illustrated in Fig. 6.3. Two different pier heights of $H^1 = 5\,\mathrm{m}$ and $H^2 = 10\,\mathrm{m}$ are considered in combination with unmodified geometrical conditions of the superstructure. For the pier foundations, single rows of piles in the transverse direction of the bridge are chosen according to the predimensioning. Each pile row consists of 4 piles with a length of $L_P = 25.0\,\mathrm{m}$, a diameter of $D_P = 1.0\,\mathrm{m}$, and a clear spacing of $s = 1.0\,\mathrm{m}$. This small clear spacing induces a high interaction between the piles in the group. The pile partial models representing the foundation flexibility consider these interactions.

The cross section of the superstructure is a prestressed single box girder with a width of 14.50 m and a depth of 2.35 m, see Fig. 6.3. The width is a standard cross section of a three-lane road with an additional lane for one direction (2+1 system). The slenderness ratios $\lambda = L/h$ of the prestressed concrete box girder at the side spans are $\lambda_1 = \lambda_3 = 14$ and respectively $\lambda_2 = 13$ at the mid span, which are both in the range of a medium slenderness.

The cross sectional geometry of the piers with the different pier heights is predesigned using the pier (respectively column) slenderness ratio $\lambda_{\mathrm{col}} = l_0/i$ with $l_0 = H_{\mathrm{pier}} \cdot \beta$ as the effective column length and $i = \sqrt{I/A}$ as the radius of gyration of the uncracked concrete cross section. In the range of $22 < \lambda_{\mathrm{col}} < 100$, the geometric second-order effect should be considered [402]. More details on slenderness limits for rectangular reinforced concrete columns can be found in [261]. For the bridge piers of the semi-integral concrete bridges, the slenderness of $\lambda_{\mathrm{col}} = 50$ is chosen. The geometric properties of the piers in relation to the varying pier heights are shown in Fig. 6.3. The material properties of the concrete, the reinforcing steel, and the prestressing steel for the single box girder and the rectangular piers are listed in Tab. 6.2.

The check of decompression in the serviceability limit state is used for the predesign of the prestressing tendons according to the provisions of the German national annex of Eurocode 2 [143]. Here, decompression is checked in the quasi-permanent load combination [100]. In order to fulfil the decompression requirement, the tensile stresses of the concrete are controlled to have a zero tensile stress at the extreme fibres of the cross sections. The result of the predesign is 11 prestressing tendons in the side spans ($A_{p1} = A_{p3} = 247.5\,\mathrm{cm}^2$) and 13 prestressing tendons at the mid span ($A_{p2} = 292.5\,\mathrm{cm}^2$).

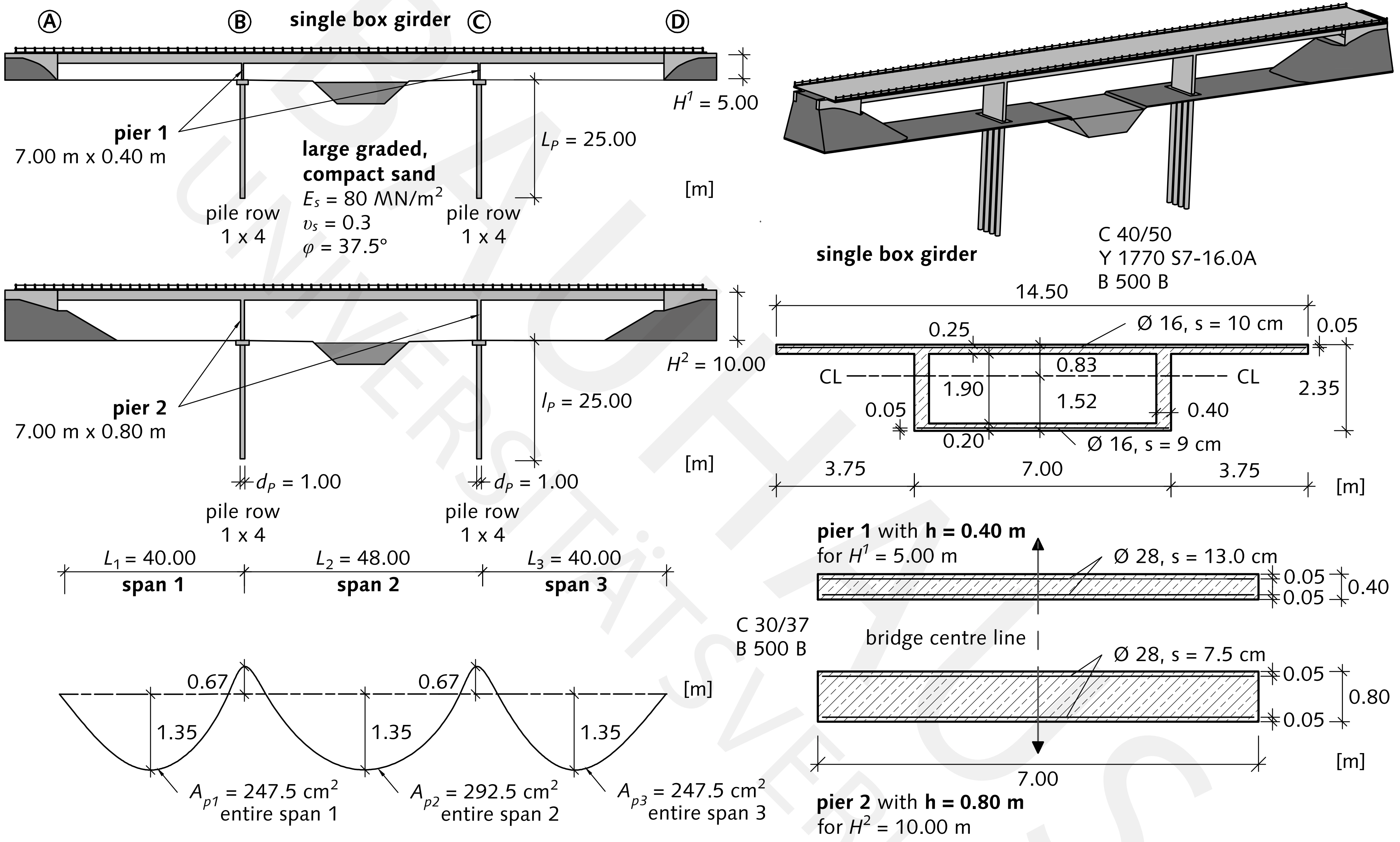
Ⓐ
Ⓑ
single box girder
Ⓒ
Ⓓ
$H^1 = 5.00$
pier 1
7.00 m x 0.40 m
large graded,
compact sand
$E_s = 80$ MN/m^2
$\upsilon_s = 0.3$
$\varphi = 37.5°$
$L_P = 25.00$
[m]
pile row
1 x 4
pile row
1 x 4
$H^2 = 10.00$
pier 2
7.00 m x 0.80 m
$l_P = 25.00$
[m]
$d_P = 1.00$
$d_P = 1.00$
pile row
1 x 4
pile row
1 x 4
$L_1 = 40.00$
span 1
$L_2 = 48.00$
span 2
$L_3 = 40.00$
span 3
0.67
0.67
1.35
1.35
1.35
[m]
$A_{p1} = 247.5$ cm^2
entire span 1
$A_{p2} = 292.5$ cm^2
entire span 2
$A_{p3} = 247.5$ cm^2
entire span 3
single box girder
C 40/50
Y 1770 S7-16.0A
B 500 B
14.50
0.25
Ø 16, s = 10 cm
0.05
0.83
CL
CL
1.90
1.52
2.35
0.05
0.40
0.20
Ø 16, s = 9 cm
3.75
7.00
3.75
[m]
pier 1 with h = 0.40 m
for $H^1 = 5.00$ m
Ø 28, s = 13.0 cm
0.05
0.40
0.05
C 30/37
B 500 B
bridge centre line
Ø 28, s = 7.5 cm
0.05
0.80
0.05
[m]
7.00
pier 2 with h = 0.80 m
for $H^2 = 10.00$ m

Figure 6.3: Longitudinal geometry of semi-integral concrete bridges and tendon eccentricity with respect to box girder centre line (left side); isometric view of semi-integral concrete bridge and cross section geometry of the box girder and the piers (right side)

BAUHAUS
UNIVERSITÄTSVERLAG

Table 6.2: Material properties of concrete, reinforcing steel, and prestressing steel for superstructure and piers of semi-integral concrete bridges

Material Property	Unit	Superstructure	Piers
Concrete		C 40/50	C 30/37
CEM		CEM II 52.5 N	CEM II 42.5
E_{cm}	[MN/m^2]	35,000	33,000
E_{c0}	[MN/m^2]	36,750	34,650
f_{cm}	[MN/m^2]	48.0	38.0
f_{cR}	[MN/m^2]	28.9	21.7
f_{ctm}	[MN/m^2]	3.5	2.9
Reinforcing Steel		B 500 B	
E_s	[MN/m^2]	200,000	
f_y	[MN/m^2]	500	
f_{yR}	[MN/m^2]	550	
f_{tR}	[MN/m^2]	594	
Prestressing Steel		Y 1170 S7 - 16.0A	
E_p	[MN/m^2]	195,000	
$f_{p0,1k}$	[MN/m^2]	1,520	
$f_{p0,1R}$	[MN/m^2]	1,672	
f_{pR}	[MN/m^2]	1,947	

6.3.2 Limit states and material modelling

The serviceability limit state (SLS) and the ultimate limit state (ULS) are considered in the quantification of the sensitivity indices in order to analyse the structural load-bearing behaviour for different loading conditions. The quasi-permanent load combination is applied according to the SLS and the permanent load combination is used for the ULS [100]. The timeline of the loading and the restraint conditions for the semi-integral bridges is shown in Fig. 6.4 and the characteristic loads are listed in Tab. 6.3.

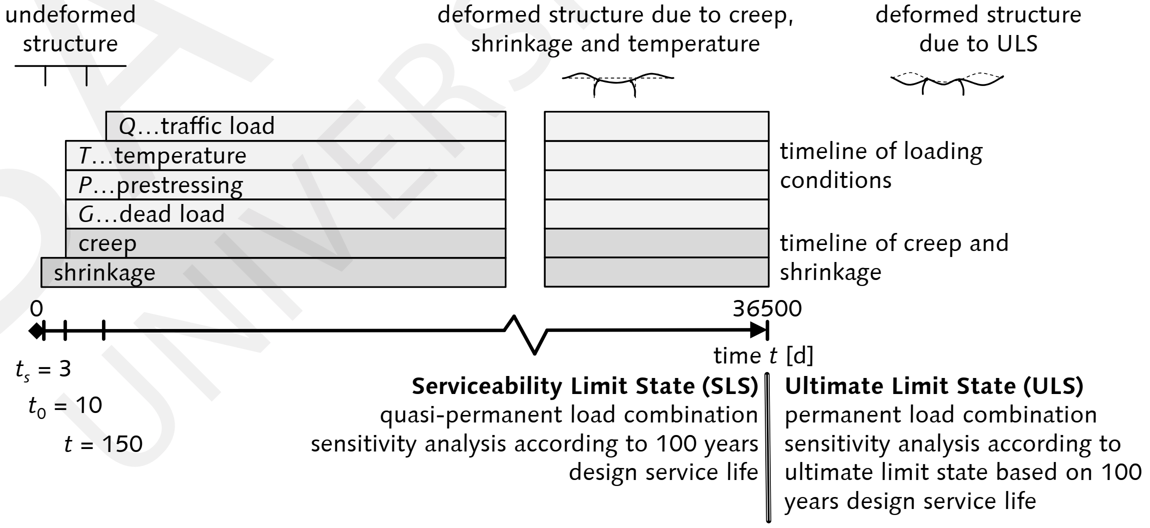
undeformed structure
deformed structure due to creep, shrinkage and temperature
deformed structure due to ULS
Q…traffic load
T…temperature
P…prestressing
G…dead load
creep
shrinkage
timeline of loading conditions
timeline of creep and shrinkage
0
36500
time t [d]
t_s = 3
t_0 = 10
t = 150
Serviceability Limit State (SLS)
quasi-permanent load combination
sensitivity analysis according to 100 years design service life
Ultimate Limit State (ULS)
permanent load combination
sensitivity analysis according to ultimate limit state based on 100 years design service life

Figure 6.4: Timeline of inner and outer loading conditions for the limit states

The compressive concrete stresses in SLS are controlled to be less than $\sigma_c \leq 0.40 \cdot f_{cm}$. A linear-elastic

Table 6.3: Loading conditions

Type of Load	Symbol	Characteristic Loads	
dead load	G_k	superstructure	$g_{k1} = 162.38\,\mathrm{kN/m}$
		pavement	$g_{k2} = 45.60\,\mathrm{kN/m}$
prestressing	P_k	superstructure	$\sigma_{pm0} = 1292\,\mathrm{MN/m^2}$
traffic load [142]	Q_k	uniformly distributed load	$q_{k1} = 57.00\,\mathrm{kN/m}$
		tandem load	$q_{k2} = 1200\,\mathrm{kN}$
temperature [104]	T_k	superstructure	$\Delta T_{N,\mathrm{con}} = -26\,\mathrm{K}$
			$\Delta T_{M,\mathrm{cool}} = -5\,\mathrm{K}$
		piers	$\Delta T_M = +5\,\mathrm{K}$

material behaviour of the concrete in this compressive stress ratio can be generally assumed. Therefore, the concrete is modelled as a linear-elastic material with the secant modulus of elasticity E_{cm} [187]. The cracking of the concrete on the tension side after reaching the average concrete tensile strength f_{ctm} is modelled using a smeared crack model. In the area affected by the reinforcement $h_{ct,\mathrm{eff}}$, the tensile stresses decrease to $\beta_t \cdot f_{ctm}$, thereby allowing for the tension stiffening effect. The depth of the area is defined as 2.5 times the distance from the reinforcing steel centroid to the surface of the cross section [16, 141]. This model [187] assumes a constant contribution of stress to the concrete after cracking, expressed by the integration factor for the steel strain along the mean transmission length β_t. In the other "unreinforced" concrete layers of the cross section, the tensile stress decreases immediately to zero for strains greater than $\epsilon_{ct} = f_{ctm}/E_{cm}$.

In the SLS, the reinforcing bars and the prestressing tendons are modelled as linear-elastic materials. The ULS defines significantly higher loading levels and therefore the response of the structure is influenced by the non-linear behaviour of the material. In the ULS, the assumption of the physical linearity of the material models is not appropriate. The model selection of adequate stress-strain relationships for the material description is fundamentally important for the non-linear simulations. The behaviour of the concrete under compression at ULS is modelled using the non-linear stress-strain relationship for the structural load-bearing analysis (broken-rational function) according to [101, 187].

The material behaviour of the concrete cracking under tension in the ultimate limit state is modelled similarly to the serviceability limit state, except for the integration factor β_t. The ultimate limit state is a short-term loading state. Hence, the completeness factor is time-independent and has a constant value of $\beta_t = 0.4$ [187]. The reinforcing and prestressing steel in the ULS are modelled as bi-linear materials with the "calculation values" according to [141], see Tab. 6.2.

6.3.3 Model classes and structural response values

The model classes: (1) cracking of the concrete under tension in the superstructure and (2) in the piers, (3) the creep and (4) the shrinkage of concrete, (5) the geometrically non-linear kinematics, (6) the thermal action, and the (7) foundation flexibility are taken into account for the simulation of the semi-integral concrete bridges. The model classes "cracking tension superstructure" (X_1) and "cracking tension piers" (X_2) describe the importance of the consideration of the concrete cracking under tension. If these model classes are activated, the cracking is considered according to the comments of Sec. 6.3.2. The deactivation of both model classes describes a purely linear-elastic stress-strain relationship of the concrete, even in tension. The compressive relationship is not influenced by these model classes.

BAUHAUS
UNIVERSITÄTSVERLAG

The model classes “creep” (X_3) and “shrinkage” (X_4) of the concrete are computed using the model published in the Model Code 90-99 [185]. If the model class is activated, then the creep strains $\epsilon_{c,cr}(t)$ are computed according to [185]. In contrast, if the creep phenomenon is deactivated, the creep strains are $\epsilon_{c,cr}(t) = 0$. The shrinkage phenomenon in the sensitivity analysis is considered equivalent to the creep model class. Either the shrinkage strains $\epsilon_{c,sh}(t)$ are calculated according to Model Code 90-99 [185], or $\epsilon_{c,sh}(t) = 0$ in the case of the deactivation of the “shrinkage” model class.

The non-linear kinematic relationship between the nodal displacements and the cross sectional strains in the Finite Element analysis is considered in the “geometric kinematic” model class. In the practical design of engineering structures, the second order theory is commonly used. The non-linear kinematics of the beam element (X_5) are considered in the simulation of the bridge load-bearing behaviour, which results in an increase in complexity and accuracy of the computational model in comparison to the simplified second order theory.

Thermal actions of the superstructure and the piers are applied according to the specifications of EC 1 [104] and are considered in the “thermal action” model class. The thermal loading condition considered for the superstructure is the contraction state with the constant part $\Delta T_{N,con} = -26\,\mathrm{K}$ and the linear temperature cooling gradient of the magnitude $\Delta T_{M,cool} = -5\,\mathrm{K}$. The piers of the concrete bridge are subjected to a linear temperature gradient of $\Delta T_M = +5\,\mathrm{K}$. In the case of the deactivated “thermal action” model class (X_6), the thermal strains are defined as $\epsilon_{c,t}(t) = 0$.

The stiffness prediction of the pile foundation is computed by different pile group models for the separate loading conditions. In the case of the vertical pile group stiffness, the model by Randolph and Wroth [334] is applied, see Sec. 3.6.1. For the calculation of the displacement due to the lateral loading of the pile group, the model according to Randolph [331] is used. Taking into account the multiplier coefficients of Poulos [318], the lateral and rotational spring stiffnesses for the pile group are computed at the pile top. Both models for vertical and lateral loading conditions consider the assumption of an elastic soil continuum. The horizontal, vertical, and rotational stiffnesses are implemented in the bridge Finite Element model by support springs. If the model class “foundation flexibility” (X_7) is deactivated, the support springs are substituted into fixed support conditions at the pier base ($u = w = \varphi = 0$) on both bridge axes.

The sensitivity analysis for the considered model classes is strongly dependent on the structural response values. The importance of the model classes may change with respect to the various response output values, which are typically the horizontal translations, the vertical displacements, the concrete stresses, the reinforcing steel stresses, and the prestressing steel stresses. For the assessment of the load-bearing behaviour of the semi-integral concrete bridges, the sensitivities of the model classes are hence quantified using the integrative sensitivity analysis for these various response values, see Fig. 6.5. The displacements u and w are evaluated at each node of the Finite Element model. The concrete stresses σ_{c1} and σ_{c2} are the stresses at the top and bottom level of the cross sections of the girder and the piers, respectively. The positions of the reinforcement stresses σ_{s1} and σ_{s2} in the cross sections are similarly defined for the top (index 1) and bottom (index 2) concrete stresses. The prestressing steel stresses σ_p are evaluated at each finite element of the superstructure, similar to the concrete and reinforcement stresses . The results of the integrative sensitivity analysis for the structural assessment of the semi-integral bridges in the serviceability limit state and ultimate limit state are presented in the following sections.

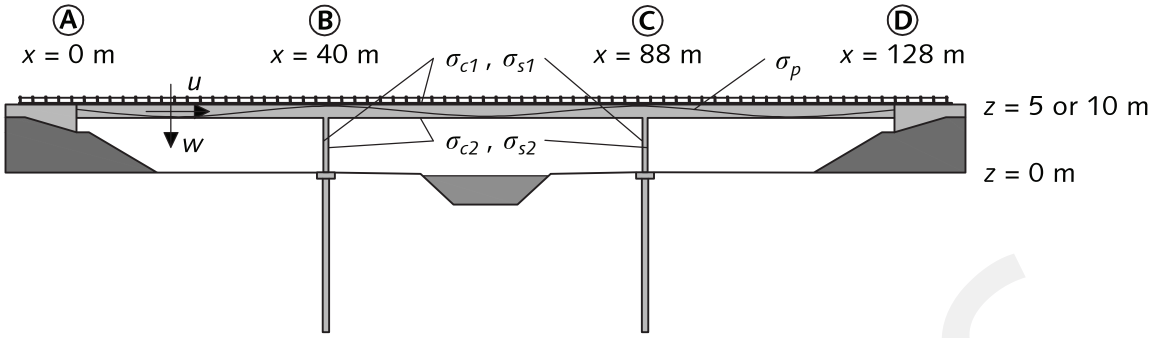

Figure 6.5: Response values of semi-integral concrete bridges for assessment of load-bearing behaviour based on integrative sensitivity analysis

6.3.4 Results of integrative assessment method

6.3.4.1 Sensitivity indices and local response significance factor

The integrative sensitivity analysis is applied to the above-mentioned semi-integral concrete bridges. In this study, the focus is the important evaluation of the physical phenomena represented by the partial models. Several model combinations between the partial models are necessary to compute the sensitivity of each phenomenon according to the structural response value. In the assessment of model choice, 128 model combinations ($n_{\text{comb}} = 2^7$, see Eq. 2.41) are analysed by numerical simulation of the semi-integral concrete bridges based on FEM. The sensitivity indices can subsequently be computed based on these predictions.

As an example of the several predictions, the vertical displacements w in the left side span at the point of the applied traffic load between bridge axis A and B, the settlement s_z at the pier base at bridge axis B, the horizontal displacement u at the abutment at bridge axis A, and the displacement at the pier base at bridge axis B are shown in Fig. 6.6 in a relative determination $Y_i/Y_{i,\max}$.

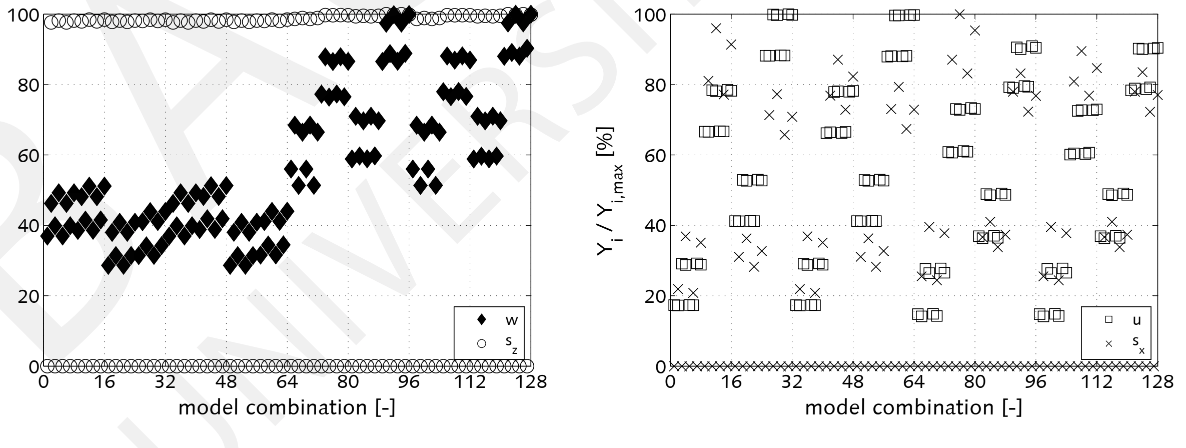

(a) vertical displacements w in side span, s_z at pier base (b) horizontal displacements u at abutment, s_x at pier base

Figure 6.6: Relative scatter of model predictions for each model combination, ultimate limit state, semi-integral concrete bridge with pier height $H^1 = 5\,\text{m}$

Each model prediction Y_i is related to the corresponding maximum response quantity $Y_{i,\max}$. The several relative model outputs for the vertical displacement w and the settlement s_z are shown in Fig. 6.6(a).

BAUHAUS
UNIVERSITÄTSVERLAG

For model combinations with fixed support conditions, the settlement is zero and hence $Y_{s_z}/Y_{s_z,\max} = 0$. In contrast, in the case that the pile foundation flexibility is considered, the relative model responses are similar and close to 1.0. Only very small interaction between the partial models appears in the prediction of this settlement, which is obvious in the relative determination of the model responses.

Very high interaction occurs in the model output of the vertical displacement w in the left side span at the point of applied vehicle loading. One major variance is predicted between model combinations considering either linear-elastic concrete tensile behaviour (model combination 1 up to 64) or the non-linear modelling considering the tension stiffening effect ((model combination 65 up to 128). Due to the fact that concrete cracking appears in the ultimate limit state, the stiffness of the beam elements in the superstructure decreases, which finally leads to greater vertical displacements in the side span. Hence, the consideration of the material non-linearity results in greater displacement prediction instead of the assumption of linear-elastic material behaviour.

In the prediction of the horizontal displacement s_x at the pier base, no displacements are allowed in the case that the partial model pile foundation flexibility is not considered in the global structural model, as similar for s_z. In contrast to the vertical settlement, some interaction appears in the prediction of the horizontal displacement. The greatest displacement appears for the case that the pile foundation flexibility, cracking in the superstructure, shrinkage, and thermal action are considered in the global structural model.

Strong interaction is also visible in the prognosis of horizontal displacement at the abutment. The maximum displacement occurs in the case that creep of concrete, shrinkage, and thermal action are all considered in the simulation. For such strong interactions between the partial models, it is not obvious which model influences the response of the structure. Therefore, the sensitivity analysis is necessary in order to quantify the importance of each partial model on the structural load-deformation behaviour.

Which phenomenon influences these response values is assessed in the following section. Moreover, the above presented results are only local information at a certain structural position. The following results show that these relationships and corresponding sensitivity indices differ with respect to the structural position and the load-deformation behaviour, respectively. In order to obtain a general quantitative value for the sensitivity of the partial models, the integrative sensitivity analysis is applied to complex semi-integral concrete bridges.

As a first result of the analysis, the assessment of the **partial model's sensitivity** is illustrated in Fig. 6.7 for the concrete stresses at the bottom level σ_{c2} in the serviceability limit state as well as the ultimate limit state of the prestressed single box girder with the pier height $H^1 = 5\,\mathrm{m}$. On the right side of Fig. 6.7, the computed sensitivity indices are shown along the pier height (inner side), in which $z = 0\,\mathrm{m}$ is the foundation ground level and $z = 5\,\mathrm{m}$ is the top of the bridge pier in the centre of the box girder.

The horizontal axis for the box girder expresses the position in the longitudinal direction of the superstructure. The vertical axis for the box girder in the graph shows the total-effects sensitivity index $S^{\mathrm{M},\sigma_{c2}}_{Ti,X_i}$, which takes into account all possible interactions among the partial models. For the bridge pier on the right side, the axes show just the opposite.

The strong dependency of the partial model's sensitivity on the position in the structure and the limit state is clearly evident. In general, a significant influence of the partial models of the concrete shrinkage and creep is visible in the ranges of the side spans and the mid span. These internal restraint effects caused by the statical indeterminacy result in a large influence of both partial models on the structural response prediction. At the monolithic connection between the superstructure and the piers, the thermal action and the foundation flexibility are also important phenomena.

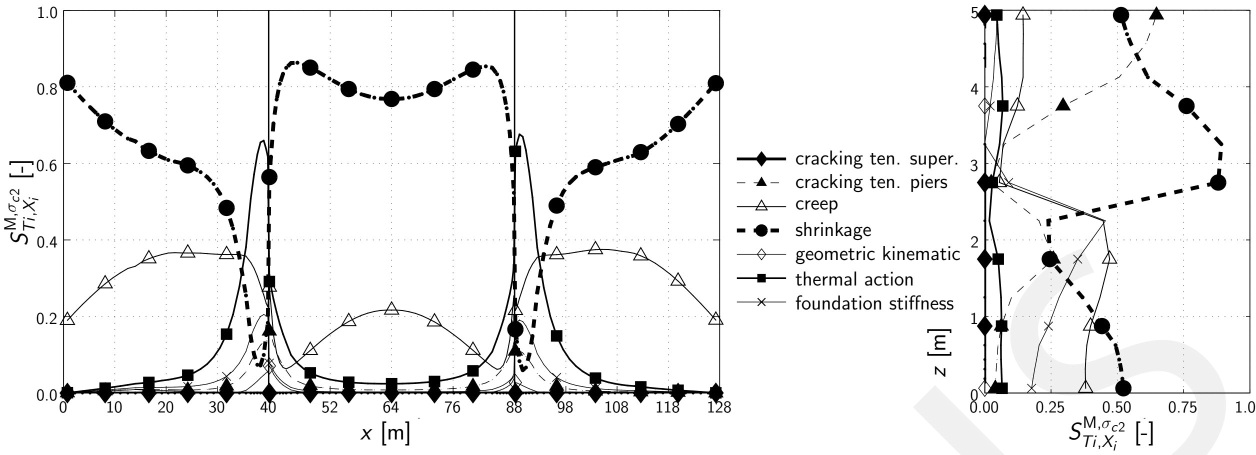

(a) serviceability limit state

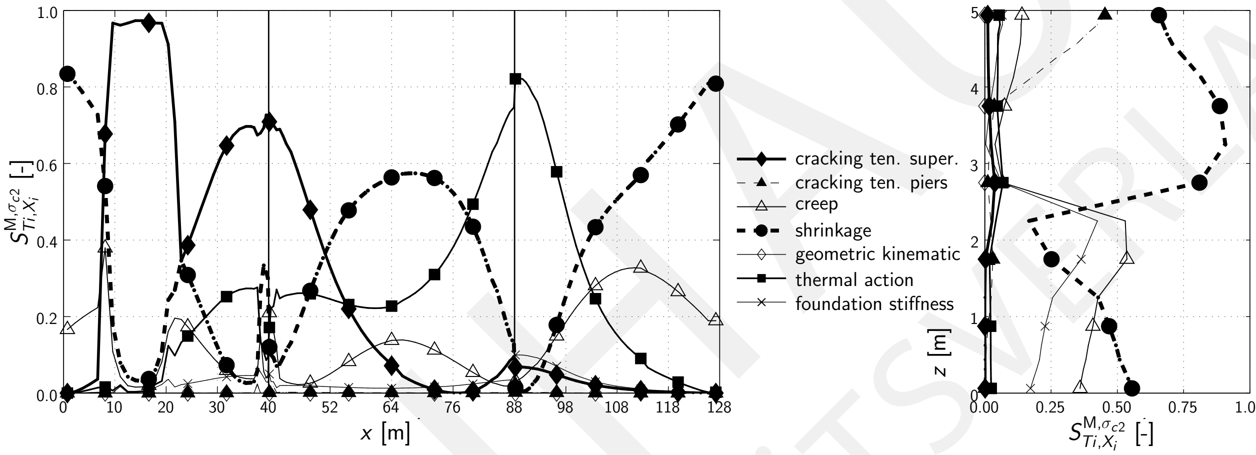

(b) ultimate limit state

Figure 6.7: Total-effects sensitivity index $S^{\mathrm{M},\sigma_{c2}}_{Ti,X_i}$ for concrete stresses σ_{c2} at box girder's bottom level with respect to position at superstructure (left side), and for piers's inner side at bridge axis B (right side); semi-integral concrete bridge with pier height $H^1 = 5\,\mathrm{m}$

In the ultimate limit state, the sensitivity of the partial models is changed compared to the serviceability limit state. The prediction of the concrete stress at the bottom level of the box girder is mainly influenced by the material modelling of the superstructure in the ultimate limit state. In the range of the right side span, the loading level is less compared to the left side span, because the position of the traffic tandem load is applied at the left side span (position: $x = 14.75\,\mathrm{m}$). Hence, the higher loading condition in the range of the left side span causes more non-linear material response compared to the right side span. Moreover, the consideration of the cracking of the superstructure is less important on the right side span compared to the left side span. This will reverse if the point of applied load for the tandem load is transferred to the right span. In addition, this bending stiffness degradation is also recognisable at the left frame corner connection point between the box girder and the bridge piers.

For the semi-integral concrete bridges, the visible importance of the restraint effects in the serviceability limit state is caused by the creep, shrinkage, and thermal action model classes. In the ultimate limit state, the reduction of the cross section stiffness, due to the tensile cracking at various positions in the bridge girder, results in the degradation of the restraint effects. This interaction between the material non-linear behaviour and the restraint effects is generally observable in statically indeterminate structures [195], see Sec. 3.5, which is similarly assessed by the sensitivity indices.

In addition to the concrete stress σ_{c2}, the total-effects sensitivity indices for the vertical displacements w at all points of the super- and substructure are shown in Fig. 6.8 for the semi-integral concrete bridge with the pier height of $H_1 = 5\,\mathrm{m}$.

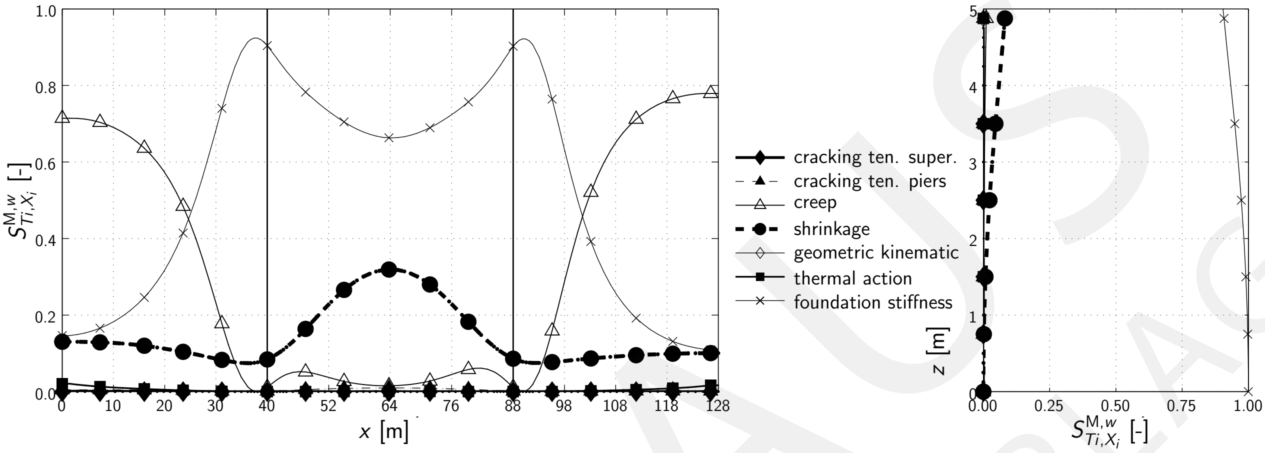

(a) serviceability limit state

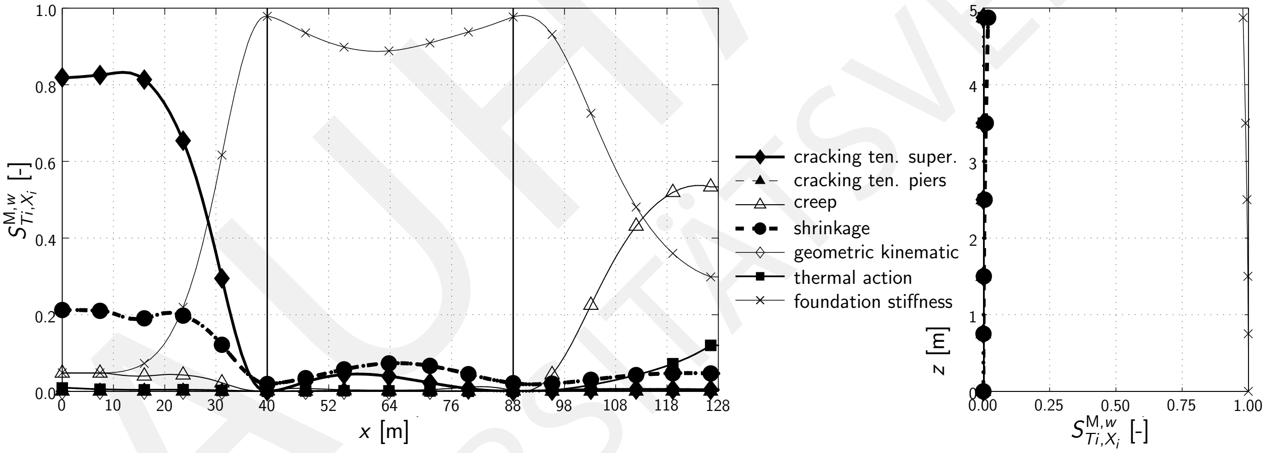

(b) ultimate limit state (tandem load in left span)

Figure 6.8: Total-effects sensitivity index $S^{\mathrm{M},w}_{Ti,X_i}$ for vertical displacements w with respect to position at superstructure (left side), and bridge axis B (right side); semi-integral concrete bridge with pier height $H^1 = 5\,\mathrm{m}$

In the serviceability limit state, the most important partial models are the foundation flexibility, creep, and shrinkage and almost negligible are the concrete cracking in superstructure and piers, geometric kinematic, and thermal action, see Fig. 6.8(a). The foundation is evaluated either by considering the pile group flexibility or introducing fixed support conditions at the pier base ($u = w = \varphi = 0$). Hence, a great difference in the prediction of vertical displacement occurs between both scenarios which finally results in the highest sensitivity of the foundation flexibility.

The sensitivity of the foundation flexibility is 0.92 and 0.66 between the superstructure-pier corners and the mid-span. Concrete creep is mainly important close to the supports at the side spans with the sensitivity between 0.78 and 0.60. In contrast, the sensitivity of concrete shrinkage is higher in the mid span with 0.32

and less at the side spans and abutments with 0.13. Moreover, the vertical displacements of the bridge piers are mainly influenced by the foundation flexibility and slightly by concrete shrinkage.
The sensitivity results according to the other structural response values and the bridge pier height of $H^2 = 10\,\mathrm{m}$ are illustrated in appendix C with the following figures:

- concrete stress σ_{c1} Fig. C.1,
- concrete stress σ_{c2} Fig. C.2,
- reinforcement stress σ_{s1} Fig. C.3,
- reinforcement stress σ_{s2} Fig. C.4,
- horizontal displacement u Fig. C.5, and
- vertical displacement w Fig. C.6.

The results of the sensitivity analysis presented in these figures show the crucial influence of the local position in the structure on the partial model's sensitivity which is very adequate and effective in order to quantify the load-deformation behaviour for any type of structure. Based on the discussion of the academic example of a simply supported beam, the global model quality is changed from position to position according to variable sensitivity indices, see Sec. 6.2, and/or variable partial model qualities, see Sec. 6.1.
In order to quantify the overall global model quality for the entire structure, the significance of each position with respect to the entire structure has to be quantified. Therefore, the integrative assessment is proposed considering both variable sensitivity values by the integrative sensitivity analysis and inconstant partial model qualities by the integrative global model quality evaluation.
The integrative sensitivity analysis computes the influence of the partial models by a weighted numerical integration of the total-effects sensitivity indices in order to assess an overall quantitative importance in relation to the entire load-bearing behaviour of the structure. Therefore, the **local response significance factor** $\mathcal{S}_Y$ can be applied for this purpose. The distribution of $\mathcal{S}_Y$ for the concrete stress at the top level of the box girder $\mathcal{S}_{\sigma_{c1}}$ and bottom level $\mathcal{S}_{\sigma_{c2}}$, the outside $\mathcal{S}_{\sigma_{c1}}$ and inner side of bridge piers at axis B $\mathcal{S}_{\sigma_{c2}}$, and the horizontal translations $\mathcal{S}_u$, and the vertical displacements $\mathcal{S}_w$ are shown in Fig. 6.9(b) for the serviceability limit state and the shorter piers.
Due to the fact that the superstructure and the piers are designed with different concrete strength classes, the local response significance factors $\mathcal{S}_{\sigma_{c1}}$, and $\mathcal{S}_{\sigma_{c2}}$ are assessed separately between the single box girder and the piers, because of the different concrete material strength classes with corresponding varying strength characteristics. On one hand, the order of magnitude of concrete compressive stress σ_c at each node (or element) can be related to the minimum value of all nodes (or elements) of the entire single box girder and bridge piers, respectively. This determination of the local response significance factor can be computed according to Eq. 6.9.

$$\mathcal{S}_{\sigma_c,\mathrm{rel}}(n) = \sigma_c^{\min}(n) \;/\; \sigma_{c,l_{\mathrm{superstructure}}}^{\min} \tag{6.9}$$

$$\mathcal{S}_{\sigma_c,\mathrm{perm}}(n) = \sigma_c^{\min}(n) \;/\; \sigma_{c,\mathrm{perm}} \tag{6.10}$$

$$\mathcal{S}_{u,\mathrm{rel}}(n) = u^{\max}(n) \;/\; u_{l_{\mathrm{structure}}}^{\max} \tag{6.11}$$

$$\mathcal{S}_{w,\mathrm{rel}}(n) = w^{\max}(n) \;/\; w_{l_{\mathrm{structure}}}^{\max} \tag{6.12}$$

On the other hand, the significance of the local response of the concrete compressive stress of a certain finite element/node can be related to a permissible concrete stress, see Eq. 6.10. In the case of the serviceability

BAUHAUS
UNIVERSITÄTSVERLAG

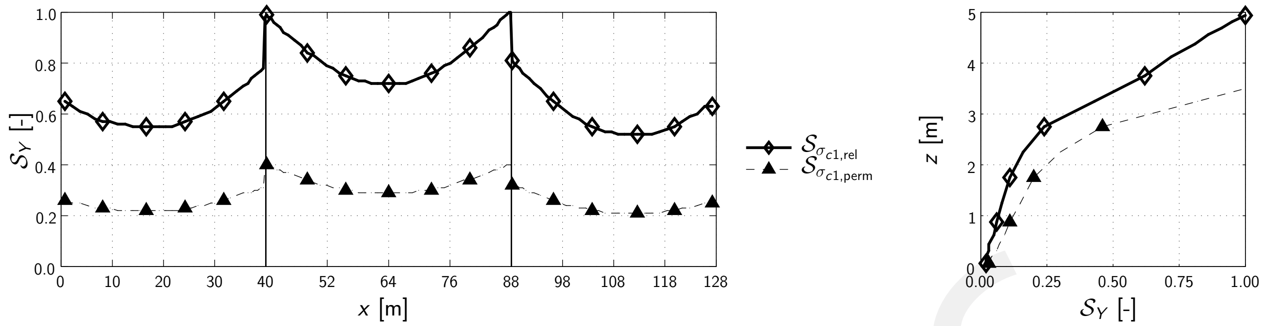

(a) σ_{c1}, top cross sectional level of box girder, outside of bridge pier at axis B

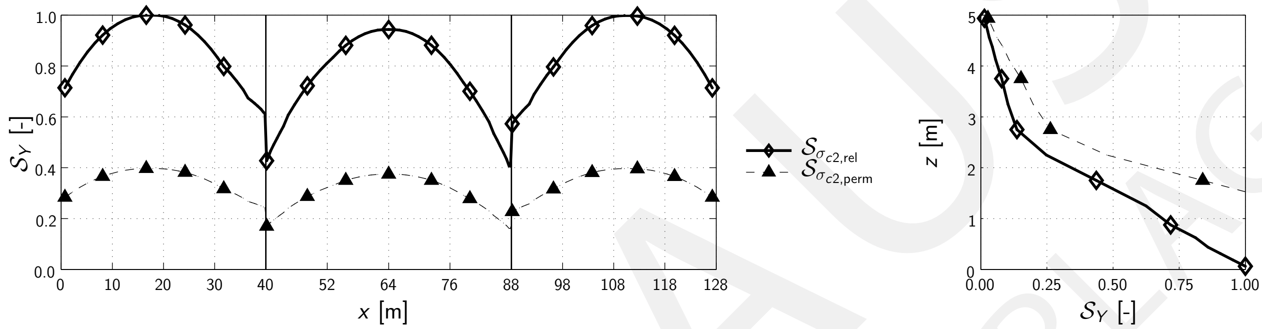

(b) σ_{c2}, bottom cross sectional level box girder, inner side of bridge pier at axis B

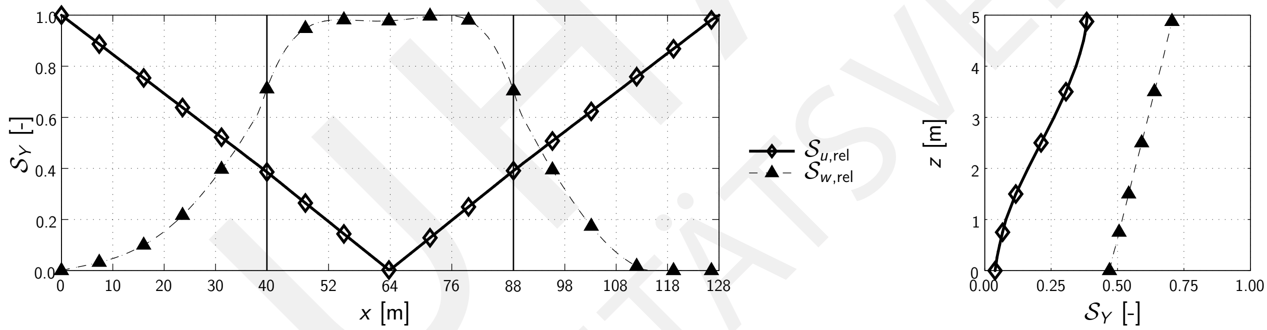

(c) u, w, displacements

Figure 6.9: Local response significance factors $\mathcal{S}_Y$ for serviceability limit state and pier height $H^1 = 5\,\mathrm{m}$; concrete stress at top and bottom level: relative definition $\mathcal{S}_{\sigma_{c1,2},\mathrm{rel}}$, permissible definition $\mathcal{S}_{\sigma_{c1,2},\mathrm{perm}}$, horizontal displacements $\mathcal{S}_{u,\mathrm{rel}}$, vertical displacements $\mathcal{S}_{w,\mathrm{rel}}$

limit state, the Eurocode 2 [141] permits $\sigma_{c,\mathrm{perm}} = 0.45 \cdot f_{ck}$ for the quasi-permanent load combination. The determination of the local response significance factor for both proposals ($\mathcal{S}_{\sigma_c,\mathrm{rel}}$, $\mathcal{S}_{\sigma_c,\mathrm{perm}}$, both sectional levels σ_{c1} and σ_{c2}) is shown in Fig. 6.9(b). The minimum concrete stress at the bottom level of the single box girder occurs at both side spans and has the magnitude of $\sigma_{c2}^{\min} = -7.1\,\mathrm{MN/m^2}$. The permissible stress is $\sigma_{c,\mathrm{perm}} = 0.45 \cdot -40 = -18.0\,\mathrm{MN/m^2}$. Therefore, the local response significance factor for all elements of the superstructure is $\mathcal{S}_{\sigma_{c2},\mathrm{perm}}(n) < 0.40$, see Fig. 6.9(b).

The local response significance factor for the concrete stress σ_{c1} is very close to the opposite of the stress σ_{c2}. The main compressive stresses appear at the connections between the superstructure and the piers. Hence, the local response significance factor is greater at these local positions than the positions at mid and side spans. The compressive concrete stress at the top level of the single box girder has the magnitude of $\sigma_{c1}^{\min} = -7.2\,\mathrm{MN/m^2}$ and is comparable to the minimum stress at the bottom level. Therefore, the local response significance factor for both sectional levels at the box girder for all elements is very similar, because $\mathcal{S}_{\sigma_{c1},\mathrm{perm}}(n) < 0.40$ is similarly quantified, see Fig. 6.9(a).

For the outer side and inner side of the bridge pier at axis B, compressive stresses are higher than the permissible stress level according to Eurocode 2. Hence, $\mathcal{S}_{\sigma_c,\mathrm{perm}}(n) > 1.00$ is quantified at the pier top for σ_{c1} and at the pier base for σ_{c2}. Such high stresses occur for the combination of activated concrete shrinkage and thermal action model class in the case of linear-elastic material modelling. All the other phenomena are deactivated in this model selection. The highest compressive stress at the outside cross sectional level is $\sigma_{c1}^{\min} = -25.7\,\mathrm{MN/m^2}$ and results in $\mathcal{S}_{\sigma_{c1},\mathrm{perm}}(n = 5\,\mathrm{m}) = 1.90$ at the pier top. At the inner side of the bridge pier, the values are $\sigma_{c2}^{\min} = -25.9\,\mathrm{MN/m^2}$ and $\mathcal{S}_{\sigma_{c2},\mathrm{perm}}(n = 0\,\mathrm{m}) = 1.92$ at the pier base.

Hence, such high local response significance factors introduce a significant importance to these locations in the assessment of numerical models compared to positions in which the response is under the permissible recommendation of guidelines and codes. This methodology scales the importance of each location in the structure according to engineering design criteria. The evaluation of global structural models can be related to any criteria, which may be different depending on the design purposes. Finally, the integrative assessment method for the entire structure can automatically consider any design requirements, such as stress limitations, displacement limits, reinforcement design and others in the evaluation method. Hence, the global model qualities quantified by this method allow for the selection of an adequate model, with respect to the design criteria, with high reliability.

In contrast, the relative determination scales the minimum stress at each element to the minimum stress of the entire box girder. Therefore, the local response significance factor is $\mathcal{S}_{\sigma_{c2},\mathrm{rel}}(n : 10 < x\,[\mathrm{m}] < 20) \approx 1.00$ in the left side span between the bridge axes A and B. In the span between the bridge axes C and D, the local response significance factor is similarly $\mathcal{S}_{\sigma_{c2},\mathrm{rel}}(n : 105 < x\,[\mathrm{m}] < 115) \approx 1.00$.

Furthermore, the distribution of the local response significance factors for the horizontal ($\mathcal{S}_{u,\mathrm{rel}}$, see Eq. 6.11) and vertical ($\mathcal{S}_{w,\mathrm{rel}}$, see Eq. 6.12) displacements is illustrated in Fig. 6.9(b). The maximum horizontal displacements occur in the sliding bearings at the transition between the box girder and the embankment. The horizontal translations in the centre of the mid span are almost zero for all model combinations. Therefore, the local response significance factor for the horizontal translations at the end of the side spans is $\mathcal{S}_{u,\mathrm{rel}}(n : x = 0\,\mathrm{m}) = \mathcal{S}_{u,\mathrm{rel}}(n : x = 128\,\mathrm{m}) = 1.00$ and in the centre of the mid span $\mathcal{S}_{u,\mathrm{rel}}(n : x = 64\,\mathrm{m}) = 0.00$. The maximum vertical displacement occurs at the centre of the mid span due to the pile foundation settlement, the creep and the shrinkage of the concrete. The vertical displacements at the bridge abutment axes are assumed to be fixed ($w = 0$). Thus, the local response significance factor for the vertical displacements in the range of the mid span is $\mathcal{S}_{w,\mathrm{rel}}(n : 50 < x\,[\mathrm{m}] < 78) \approx 1.00$ and in the abutment axes $\mathcal{S}_{w,\mathrm{rel}}(n : x = 0\,\mathrm{m}) = \mathcal{S}_{w,\mathrm{rel}}(n : x = 128\,\mathrm{m}) = 0.00$.

In the ultimate limit state, the permissible concrete compressive stress is different when compared to the previously mentioned criteria in the serviceability limit state. The peak compressive strength f_{cR}, according to the non-linear safety concept of Eurocode 2, see Sec. 2.6.4, is applied for the computation of permissible local response significance factor $\mathcal{S}_{\sigma_c,\mathrm{perm}}(n)$ in the ULS. Hence, the permissible concrete stress $\sigma_{c2,\mathrm{perm}}$ is f_{cR} in the ULS, see Eq. 6.10. The relative determination of the local response significance factor for the concrete, reinforcement, prestressing steel stresses and the vertical and horizontal displacements is similarly defined in the ULS compared to the SLS, see Eq. 6.9, 6.11, 6.12. The determination of the local response significance factors for the concrete stresses σ_{c1}, σ_{c2}, and vertical w, horizontal u displacements are shown in Fig. 6.10.

In the assessment of concrete stresses, the minimum stresses (compressive stresses) are analysed at the top and bottom levels of the cross sections. The prestressing of concrete induces, compressive stresses in the concrete in those areas in which tensile stresses may occur, due to external loadings, such as dead load or traffic loading. The external loading level in the ULS is much higher when compared to the SLS. Therefore, the compressive stresses due to prestressing are reduced and tensile stresses may also occur. Hence, the local response significance factors are very different for the concrete compressive stress between SLS and ULS.

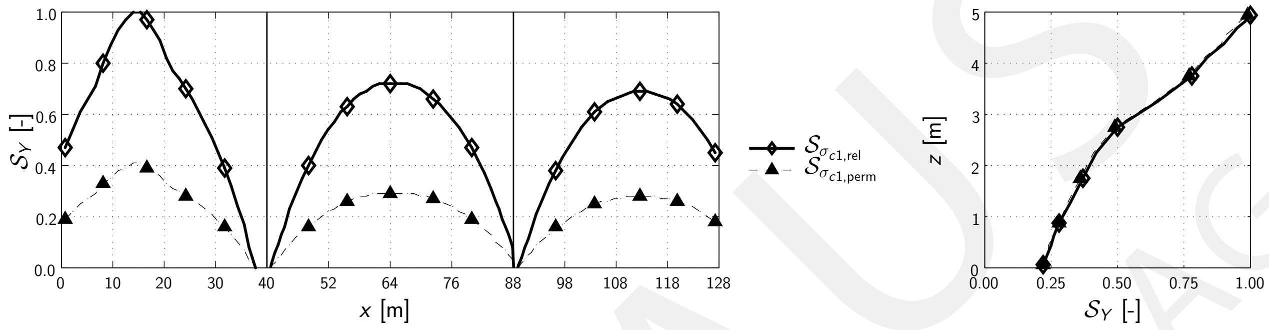

(a) σ_{c1}, top cross sectional level of box girder, outside of bridge pier at axis B

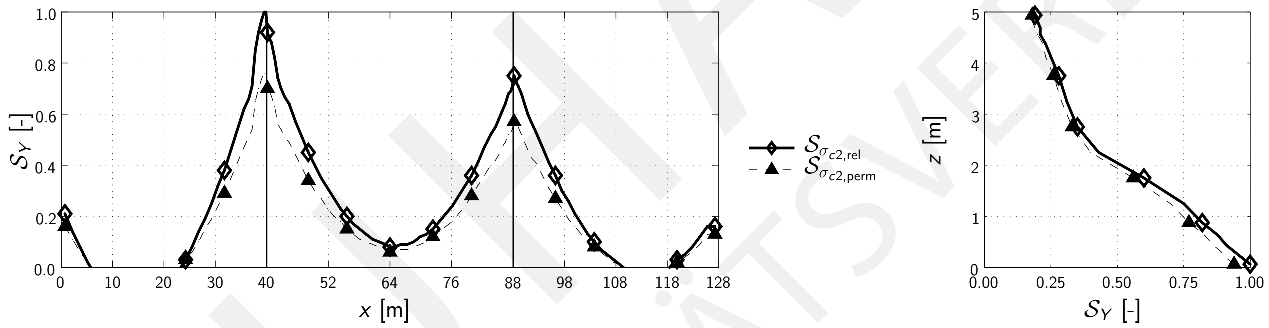

(b) σ_{c2}, bottom cross sectional level box girder, inner side of bridge pier at axis B

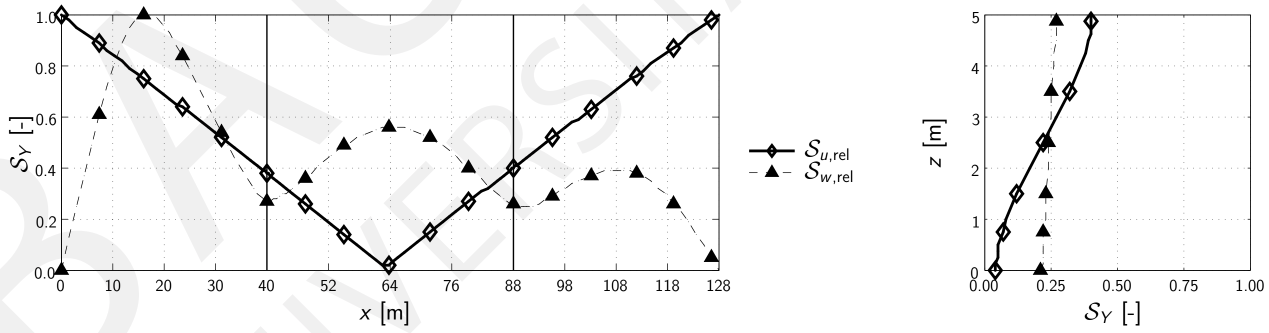

(c) u, w, displacements

Figure 6.10: Local response significance factors $\mathcal{S}_Y$ for the ultimate limit state and the pier height $H^1 = 5\,\mathrm{m}$; concrete stress at top and bottom level: relative definition $\mathcal{S}_{\sigma_{c1,2},\mathrm{rel}}$, permissible definition $\mathcal{S}_{\sigma_{c1,2},\mathrm{perm}}$, horizontal displacements $\mathcal{S}_{u,\mathrm{rel}}$, vertical displacements $\mathcal{S}_{w,\mathrm{rel}}$

The loading condition in the ULS induces tensile stresses at the superstructure‘s top level in the frame corners at bridge axes B ($x = 40\,\mathrm{m}$) and C ($x = 40\,\mathrm{m}$) for all model combinations. Therefore, no concrete compressive stresses occur in these structural positions and, consequently, the local response significance factor is $\mathcal{S}_{\sigma_{c1}} = 0$, at positions in which exclusively tensile stresses are predicted for all model combinations. In Fig. 6.10(a), it is evident that tensile stresses appear at the top level of the superstructure in the corner

BAUHAUS
UNIVERSITÄTSVERLAG

positions between superstructure and piers. Compressive stresses are predicted in the mid span and side spans. The tandem vehicle load is applied in the left side span between bridge axes A and B and hence the local response significance is $\mathcal{S}_{\sigma_{c1},\mathrm{rel}}(n : x = 14.75\,\mathrm{m}) = 1.00$ at the point of the applied load. The greatest compressive stress in the superstructure at the top level is $-11.7\,\mathrm{MN/m^2}$ and hence $\mathcal{S}_{\sigma_{c1},\mathrm{perm}} \leq 0.40$, because $\sigma_{c,\mathrm{perm}} = f_{cR} = 28.9\,\mathrm{MN/m^2}$.

At the outside cross sectional level of the bridge pier at axis B, the maximum concrete compressive stress is close to the permissible strength value. Hence, the permissible and relative determination of the local response significance factor is close to 1.00 at the top of the bridge pier. Furthermore, the trend and shape of both determinations are very similar, see right side of Fig. 6.10(a).

The results of the local response significance for the opposing cross sectional levels σ_{c2} are shown in Fig. 6.10(b) for the superstructure and piers. Tensile stresses are predicted at the bottom level of the box girder in the side spans for all model combinations, which similarly leads to $\mathcal{S}_{\sigma_{c2}} = 0$. Maximum compressive stress is predicted at the left corner of bridge axis B and at the bottom of bridge pier at axis B. Hence, the relative determination is 1.00 at these structural positions.

In the prediction of the horizontal displacements u at each node of the entire structure, the shape of the response along the entire structure is relatively similar between the ultimate and serviceability limit states. The absolute values are much higher in the ULS, but the general relative scope of minimum and maximum horizontal displacements are comparable between both limit states. Therefore, the local response significance factors for these displacements are similar for the SLS and ULS, see Fig. 6.9(c) and 6.10(c).

Major differences between both limit states appear in the significance of each position in the structure with respect to the prognosis of vertical displacements. The much greater loading level in the ultimate limit state increases the loading level, which causes concrete cracking, especially in the side span between axes A and B, in which the tandem vehicle load is applied at $x = 14.75\,\mathrm{m}$. Therefore, the stiffness of the superstructure decreases due to the non-linear material behaviour, which causes great vertical displacements in these positions. The local response significance factor is consequently 1.0 under the point of applied vehicle load.

For the application of the integrative assessment method, the local response significance factors are computed by the relative determination ($\mathcal{S}_{\mathrm{rel}}$) and the structural load-bearing behaviour is expressed by several response quantities. These are: the horizontal translations u, the vertical displacements w, the concrete stresses $\sigma_{c1,c2}$, the reinforcing steel stresses $\sigma_{s1,s2}$, and the prestressing steel stresses σ_p.

6.3.4.2 Integrative sensitivity analysis

Serviceability limit state

Based on the integrative sensitivity analysis, the results for the structural load-bearing assessment of the semi-integral concrete bridge with the shorter pier height $H^1 = 5\,\mathrm{m}$ in the serviceability limit state are shown in Fig. 6.11(a) and listed in the appendix in Tab. C.1. In the case of the longer pier height $H^2 = 10\,\mathrm{m}$, the quantification of the phenomena‘s influence is illustrated in Fig. 6.11(b) and listed in the appendix in Tab. C.2.

The creep, shrinkage, and thermal strains induce horizontal displacements. Therefore, the prediction of the horizontal translations u in the bridges is mainly sensitive to the phenomena of creep and shrinkage. In addition, a considerable influence of the thermal action is recognisable. The concrete shrinkage has an integrative sensitivity of 0.74 for the shorter bridge piers and an influence of 0.75 for the longer bridge

BAUHAUS
UNIVERSITÄTSVERLAG

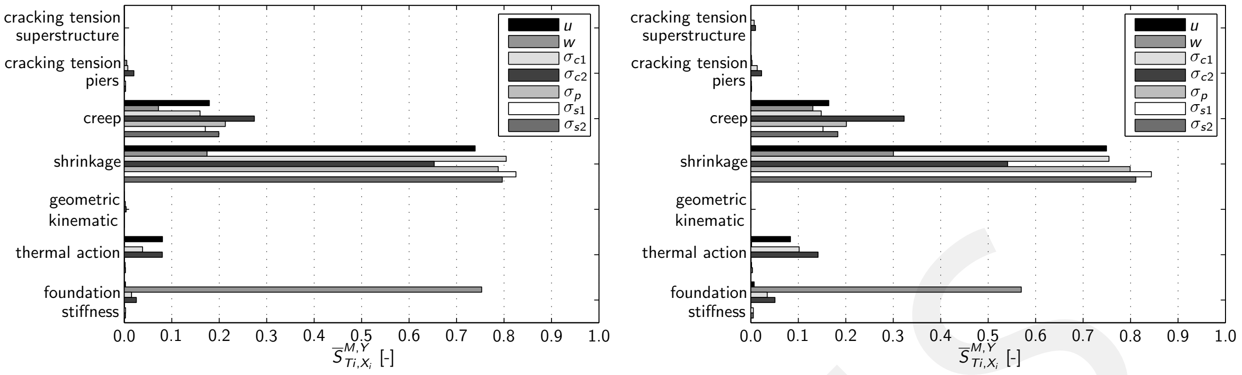

(a) $H^1 = 5\,\text{m}$

(b) $H^2 = 10\,\text{m}$

Figure 6.11: Integrative sensitivity indices $\overline{S}_{Ti,X_i}^{\text{M},Y}$ for semi-integral concrete bridges with different pier heights (H^1, H^2) in serviceability limit state (SLS), 7 model classes considered, foundation flexibility additionally modelled

piers. In contrast, the concrete creep has a sensitivity of 0.18 for the shorter pier height and 0.16 for the longer pier height. The sensitivity of the thermal action is 0.08 for both pier heights. In order to predict the horizontal translations in the semi-integral concrete bridges in SLS, the structural model mainly requires adequate shrinkage and creep models.

In the entire structural model, a high variation in the prediction of vertical displacement w is caused by considering or neglecting the pile foundation flexibility. This is mainly due to the fact that the deactivation (disregard) of the pile foundation flexibility is considered by fixed support conditions at both pier bases ($u = w = \varphi = 0$) and the activation (consideration) is considered by support springs ($u \neq 0$, $w \neq 0$, $\varphi \neq 0$). Hence, the high variation in the prediction of the vertical displacement is forced by the foundation, which leads to a corresponding high sensitivity. Furthermore, maximum vertical displacements occur at the bridge piers, the mid span, and at the range in the side span close to the bridge piers. This is considered in the response significance factor, see Fig. 6.9(b). Hence, the foundation flexibility has a high sensitivity at these positions where the maximum vertical displacements occur. Consequently, the vertical displacement prognoses are mainly influenced by the foundation flexibility. The pile foundation flexibility has an integrative sensitivity of 0.75 for the shorter pier height.

In general, the foundation flexibility determines the structural behaviour more decisively for shorter piers in comparison to longer piers. In this respect, the integrative sensitivity analysis computes a similar interaction between the pile foundation flexibility and the pier height. The integrative sensitivity is reduced to a magnitude of 0.57 for the longer bridge piers. In addition to the foundation flexibility, creep and shrinkage of concrete have a relevant importance for the vertical displacement predictions. Finally, the selection of the pile foundation model and the determination of the soil material properties at the construction site are fundamentally important for predicting the entire vertical displacements.

The overall load-bearing behaviour for both semi-integral concrete bridges in the serviceability limit state, see Fig. 6.11(a) and Fig. 6.11(b), is not significantly influenced by the concrete tensile cracking in the superstructure and piers. The concrete tensile cracking in the superstructure and in the piers have a very small overall influence (< 0.03) due to the SLS for all response quantities. Consequently, the concrete tensile cracking for both structural components can either be neglected or considered with simplified models in the SLS. For other structures with different prestressing layout, prestressing forces, cross section stiffness, or girder span - pier height ratio, the concrete tensile cracking can be more sensitive, even in the serviceability limit state.

Ultimate limit state

In addition to the SLS, the load-bearing behaviour of the semi-integral concrete bridges is similarly assessed in the ULS, based on the integrative sensitivity analyses for various response quantities. For the shorter pier height, Fig. 6.12(a) and Tab. C.1 in the appendix illustrate the importance of the various phenomena. Moreover, the results for the longer piers are illustrated in Fig. 6.12(b) and listed in Tab. C.2 in the appendix.

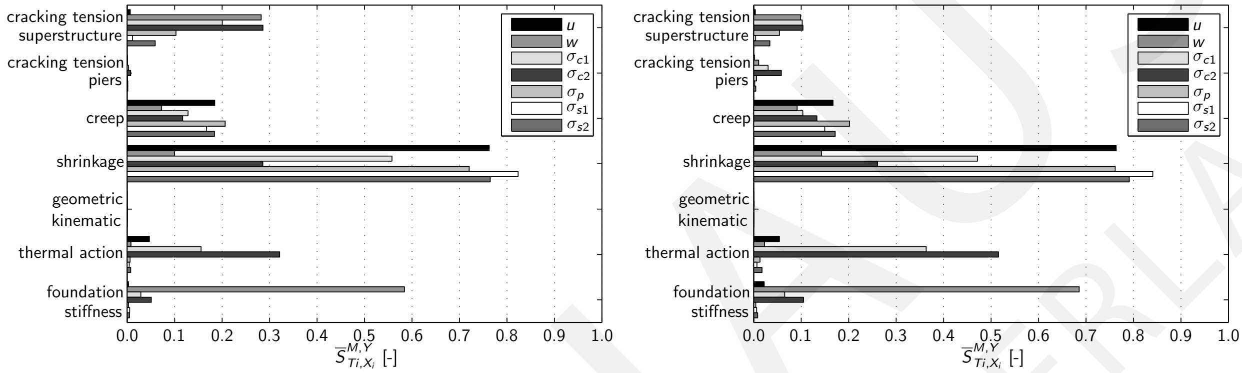

(a) $H^1 = 5\,\mathrm{m}$ (b) $H^2 = 10\,\mathrm{m}$

Figure 6.12: Integrative sensitivity indices $\overline{S}^{M,Y}_{Ti,X_i}$ for semi-integral concrete bridges with different pier heights (H^1, H^2) in ultimate limit state (ULS), 7 model classes considered, foundation flexibility additionally modelled

The concrete tensile cracking in the box-girder and bridge piers has no importance for all structural response values in the serviceability limit state. In contrast, in the ultimate limit state, the concrete tensile cracking in the entire structure has a high influence on the overall structural load-bearing behaviour.

The prediction of the concrete stress at the upper cross section level σ_{c1} is mainly influenced by concrete shrinkage and tensile cracking in the superstructure. In the case of the shorter piers, the shrinkage has an overall integrative sensitivity of 0.56 and the concrete tensile cracking has a sensitivity of 0.20. The concrete shrinkage influence is reduced to 0.47 for the longer bridge piers. Furthermore, the influence of the concrete tensile cracking is similarly reduced to 0.10 for the longer piers. An opposite effect in the stress prediction is visible in the sensitivity of the thermal action. The thermal action has an integrative sensitivity of 0.16 for the shorter piers and a sensitivity of 0.36 for the longer piers. Due to the higher horizontal and rotational rigidities of the shorter piers, the restraint loading conditions cause much higher section forces in comparison to the longer piers. The influence of the thermal action (especially constant temperature component) compared to the shrinkage of concrete is less, because the shrinkage strain of the box girder is high (higher than the temperature strain) and the corresponding safety factors and combination rules additionally affect the importance of both phenomena.

Therefore, the restraint section forces increase in the range of the mid span and the connection positions between the superstructure and the piers for the shorter pier height. These indirect loading conditions cause more non-linear material responses in the structure. Hence, the importance of the concrete cracking, due to tension, is higher for the shorter piers compared to the longer piers. These results represent a clear interaction between the magnitude of restraint effects and the material non-linear responses in the structure. The less cross section stiffness degradation for the longer piers and the consequently greater remaining restraint effects result in a higher sensitivity of the thermal induced strains in the ultimate limit state.

The thermal contraction loading state considered in this analysis has a much higher influence on the concrete stress at the bottom cross section level σ_{c2}. As a result, the integrative sensitivity of the thermal action is higher in comparison to the prediction at the upper cross section level. The thermally induced strains have a sensitivity of 0.34 for the shorter piers and 0.53 for the longer piers. This shows again the interaction between the restraint thermal effects and the concrete cracking on the prediction of the concrete stresses in the entire structure. The concrete tensile cracking in the superstructure, shrinkage, and creep additionally influence the prediction of the concrete stresses at the bottom layer of the cross sections.

The thermally induced strains are not completely degraded, due to the concrete tensile cracking, even in the ultimate limit state. Therefore, it is necessary to use non-linear material models in order to analyse the effect of the thermal action on the overall load-bearing behaviour in an accurate way. The linear-elastic material models are not capable of analysing the restraint effects in integral bridges and should not be used for structural designs in the SLS and ULS. Nevertheless, in the case that the prestressing cause compressive stresses in the cross sections at SLS load level, the linear-elastic material modelling can still be considered as adequate and accurate.

6.3.4.3 Integrative global model quality evaluation

In order to illustrate the significance of the integrative assessment method, the global model quality assessment is shown in Table 6.4 in the serviceability limit state for the shorter piers at several positions. The concrete stress at the bottom level of the cross sections σ_{c2} is chosen as an exemplary response value. The creep, shrinkage, thermal action and the foundation flexibility influence this concrete stress prediction, see Fig. 6.7 and Fig. 6.11(a).

Table 6.4: Global Model Quality Evaluation based on Partial Model Quality Scenario in the Serviceability Limit State

Position	X_3 creep $MQ_{\mathrm{PM},X_3} = 0.70$	X_4 shrinkage $MQ_{\mathrm{PM},X_4} = 0.90$	X_6 thermal action $MQ_{\mathrm{PM},X_6} = 0.50$	X_7 foundation stiffness $MQ_{\mathrm{PM},X_7} = 0.60$	$MQ^{\sigma_{c2}}_{\mathrm{GM}}$
local position sensitivity			$S^{M,\sigma_{c2}}_{Ti,X_i}$		
$x = 14.75\,\mathrm{m}$ (span 1)	0.34	0.64	0.03	0.01	0.82
$x = 39.68\,\mathrm{m}$ (axis B)	0.23	0.18	0.62	0.20	0.61
$x = 64.00\,\mathrm{m}$ (span 2)	0.22	0.77	0.02	0.00	0.85
integrative assessment method			$\overline{S}^{M,\sigma_{c2}}_{Ti,X_i}$		
entire structure	0.27	0.65	0.08	0.03	**0.81**

The partial model qualities are assumed by the following scenario $MQ_{\mathrm{PM},X_3} = 0.70$, $MQ_{\mathrm{PM},X_4} = 0.90$, $MQ_{\mathrm{PM},X_6} = 0.50$, and $MQ_{\mathrm{PM},X_7} = 0.60$. In addition, these qualities are chosen as constant values along each position in the structure. Hence, the integrative global model quality evaluation according to Sec. 6.2

with Eq. 6.5 is applied for the presented results.

The assessment at local positions shows the significant influence of each position on the sensitivity indices, see Table 6.4. Therefore, the global model quality for the same partial model combination is different at each position due to the changed sensitivity values. Moreover, it is also obvious that some phenomena have no influence at a certain position in the structure on the response quantity. In contrast, they can affect the structural load-bearing behaviour at other positions. Consequently, for three positions in the structure listed in Table 6.4, the quality assessment quantifies three different global model qualities for the same partial model combination.

In practical engineering problems, there is no requirement to establish various global models with the corresponding best (highest) prediction quality at a local position in the structure for design purposes. For example, it would not be feasible for practical engineering projects to choose a certain global model with high quality for predicting a response quantity at the side span and subsequently select a different global model with high quality for predicting the same response quantity at the mid span. The structural engineer needs to have a global model with an acceptable and adequate overall prediction quality.

But what are the partial model's influences with respect to the entire structure? What is the global structural prediction quality for the entire structure? These questions cannot be answered by the local position sensitivity assessment. Consequently, the integrative assessment method is established, which is capable of computing quantitative information to address these questions.

The enhancement to the integrative assessment method enables an overall evaluation of the entire structural load-bearing behaviour. Hence, the global model quality for the same partial model combination based on the integrative assessment method is not dependent on the local position, because all positions are taken into account by the local response significance factors. Finally, an overall sensitivity index for each partial model and, subsequently, entire structural prediction quality for each partial model combination can be assessed. Hence, for each partial model combination (here only one scenario is presented) a representative structural prediction quality $MQ^{\sigma_{c2}}_{\mathrm{GM,scenario}} = 0.81$ can be evaluated, see Table 6.4.

A quantitative comparison between several global structural models is then clearly feasible on the entire structural level. The integrative assessment method assists the structural engineers in the decision making process in various project design phases. The engineers can then choose a structural model with an adequate prediction quality for the entire structure in order to obtain more reliable simulation results and finally a safer and more economical design.

6.3.4.4 Design recommendations

The results of the integrative sensitivity analysis in the serviceability and the ultimate limit states present a clear quantification of the importance of certain phenomena on the overall structural load-bearing behaviour. The decomposition of integral bridges into superstructure and substructure is only valid on a geometric level. In the establishment of a numerical model for semi-integral bridges, the girder, pier, and foundation (soil) components have to be directly coupled in order to consider the high interaction between these structural parts. A decoupled design of the integral bridge structure separating the superstructure and substructure, is not appropriate and cannot provide reliable predictions.

The shrinkage and the creep of the concrete have a significant influence on the structural load-bearing behaviour for the SLS and ULS. These phenomena are mainly influenced, among others, by the modulus of elasticity and the concrete compressive strength, which both have generally a high variance (parameter uncertainty). The parameters defined in design codes and guidelines are only imprecise estimates. Therefore,

BAUHAUS
UNIVERSITÄTSVERLAG

it can be necessary and very useful to perform short-term (modulus of elasticity, compressive strength) and long-term (creep and shrinkage) experiments in order to measure more accurate data for a particular concrete mixture. This parameter estimation can significantly reduce the uncertainty in the model prediction. Finally, the design of the entire structure becomes safer and more reliable.

In addition, the foundation and soil stiffness is quantified to be very sensitive according to the vertical bridge displacements. Hence, the foundation flexibility should also be carefully checked on the construction site in the preliminary design. Material properties for the surrounding soil and the piles should not be exclusively related to experience and empirical values. Soil tests or even pile foundation tests should be performed on site, because such experiments already include the interaction between the soil and the pile and can additionally reduce the model prediction uncertainty.

For integral bridge structures with high rigidity of the structural components (e.g. shorter bridge piers), the restraint effects due to temperature, shrinkage and creep could lead to a material non-linear response in the structure. The higher rigidity of the shorter piers results in larger section forces due to the restraint effects, which cause the concrete cracking. In the application example, concrete cracking under tension is not sensitive to the structural behaviour for the SLS, but being a considerable sensitivity for the ULS. This relationship cannot be generalised, because a lot of factors, such as loading conditions, cross section stiffness/shape, material properties, prestressing forces, or the span - height ratio affect the magnitude of the restraint effects. In general, structural engineers should care about the non-linear material behaviour and cannot assume a simplified linear-elastic material description for integral bridges. The linear-elastic computation only will otherwise result in highly inaccurate sectional forces, due to the restraint effects, and thus the amount of reinforcement increases significantly. In contrast, concrete cracking and stiffness degradation reduce the section forces due to these indirect loading conditions. Therefore, a non-linear simulation leads to a more suitable design approach.

Due to the fact that integral bridges are very sensitive to the material and structural component stiffness, the structural engineers have to take care about the model selection and should assess the main influencing phenomena. This analysis will illustrate where the global structural model has to use more accurate partial models and where even simplified partial models can suffice. Therefore, the integrative assessment method is a powerful tool, which can significantly reduce the uncertainty in model predictions. The design of engineering structures in accordance with the recommendations of codes and guidelines should be performed based on the results of a global structural model with a high prediction quality in order to obtain a safer and more reliable design.

6.4 Semi-integral concrete bridges neglecting foundation flexibility

In the preliminary project phases of engineering structures, the first major design proofs are checked without exactly knowing some parameters, such as the detailed pile foundation layout. Hence, in most cases some basic support conditions are assumed at the foundation nodes in the global structural model. The vertical, lateral, and rotational stiffness/flexibilities are considered by either free or fixed support conditions in the corresponding displacement criteria. Such change in the global structural model may modify the importance of the phenomena due to a different load-deformation behaviour. Therefore, the integrative sensitivity analysis is similarly applied to the simulation of semi-integral concrete bridges with simplified support conditions at the pier base ($u = w = \varphi = 0$) in order to quantify the influence of neglecting a certain phenomenon such as the pile foundation flexibility.

The influence of the partial models on the prediction of vertical and horizontal displacements is shown in Fig. 6.13(a), quantified by the total-effects sensitivity indices $S^{\mathrm{M},Y}_{Ti,X_i}$. The results of the integrative sensitivity analysis are shown in Fig. 6.14 by the determination of the local response significance factors $\mathcal{S}_Y$ along the entire structure. Both results are presented for the short pier height $H^1 = 5\,\mathrm{m}$ and the serviceability limit state.

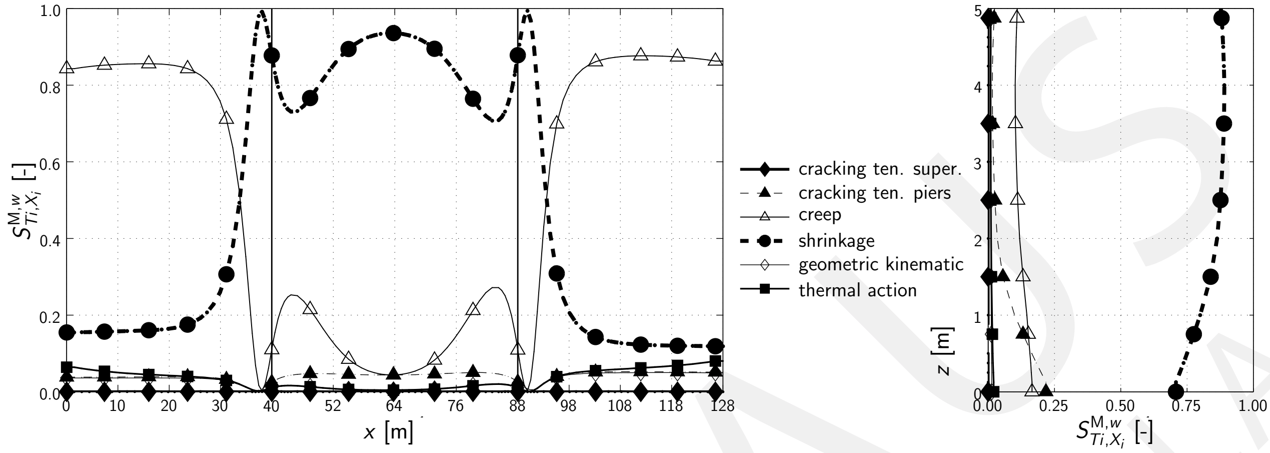

(a) sensitivity $S^{\mathrm{M},Y}_{Ti,X_i}$, serviceability limit state

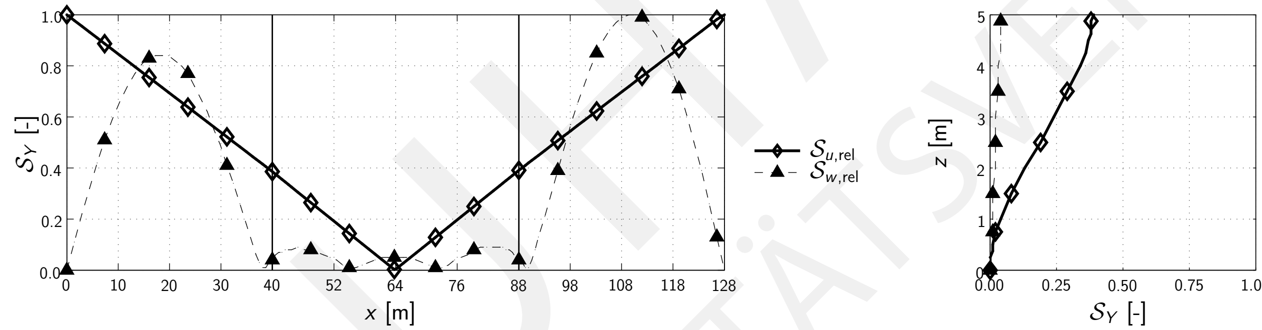

(b) local response significance factors $\mathcal{S}_Y$, serviceability limit state

Figure 6.13: Sensitivity indices and local response significance factors for vertical w and horizontal u displacements with respect to positions at superstructure (left side), and bridge axis B (right side); semi-integral concrete bridge with pier height $H^1 = 5\,\mathrm{m}$ and fixed support conditions in serviceability limit state

The vertical displacement of the bridge pier is mainly influenced by the shrinkage ($0.7 < S^{\mathrm{M},w}_{Ti,\mathrm{shrinkage}} < 0.9$) instead of the pile foundation flexibility as assessed in the previous section, see Fig. 6.8(a). In the mid span of the superstructure, shrinkage shows even a higher sensitivity than the creep. Nevertheless, concrete creep mainly affects the prediction of vertical displacements in the side spans resulting in $S^{\mathrm{M},w}_{Ti,\mathrm{creep}} \approx 0.86$. The numerical integration of these sensitivity indices along the superstructure and piers is computed to be $S^{\mathrm{M},w}_{Ti,\mathrm{creep}} = 0.48$ and $S^{\mathrm{M},w}_{Ti,\mathrm{shrinkage}} = 0.51$. These results indicate almost same importance of both phenomena with respect the vertical displacements.

However, an identical importance of each position in the structure is assumed in the numerical integration. The enhancement to the integrative sensitivity analysis additionally takes into account the local response significance of each node/beam in the entire structure. The relative determination $\mathcal{S}_{w,\mathrm{rel}}$ is shown in Fig. 6.13(b). Due to the fixed pier base ($w = 0$), the local response significance at these positions is 0.00 and is smaller than 0.04 for the entire bridge piers. Hence, the high sensitivity of the shrinkage on the vertical displacements of the bridge piers has a very small effect on the load-deformation behaviour of the entire structure. Moreover, the vertical displacements are very small in the mid span and hence the corresponding local response significance is similarly small.

The absolute maximum displacements occur in the side spans and are negative (upward) displacements, due to the combination of prestressing and external loading conditions. The tandem vehicle load is applied in the left side span and hence the upward is smaller compared to the right side span. Therefore, the local response significance is a bit higher in the right side span. The integrative sensitivity analysis computes an overall influence of both phenomena to be $\overline{S}^{\mathrm{M},w}_{Ti,\mathrm{creep}} = 0.79$ and $\overline{S}^{\mathrm{M},w}_{Ti,\mathrm{shrinkage}} = 0.21$, which is an increase of 0.31 (65 %) for the creep and a decrease of 0.30 (41 %) for the shrinkage, compared to the numerical integration. This example additionally illustrates the necessity of considering sensitivity indices and local response significance factors together in order to quantify the load-deformation behaviour of the entire structure.

The results of the integrative sensitivity analysis are shown in Fig 6.14 for both limit states and both pier heights. Moreover, the results according to the serviceability and ultimate limit states are listed in the appendix in Tab. C.3 for the pier height $H^1 = 5\,\mathrm{m}$ and in Tab. C.4 for $H^2 = 10\,\mathrm{m}$. The concrete cracking in the superstructure and piers does not influence the entire structural behaviour, which is as same as the one for the global model with consideration of the pile foundation flexibility, see Sec. 6.3.4.2.

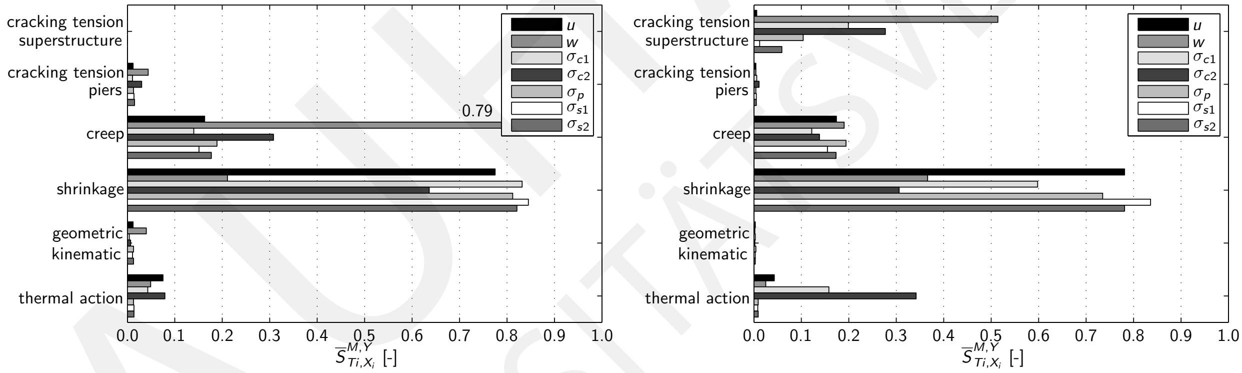

(a) SLS, $H^1 = 5\,\mathrm{m}$

(b) ULS, $H^1 = 5\,\mathrm{m}$

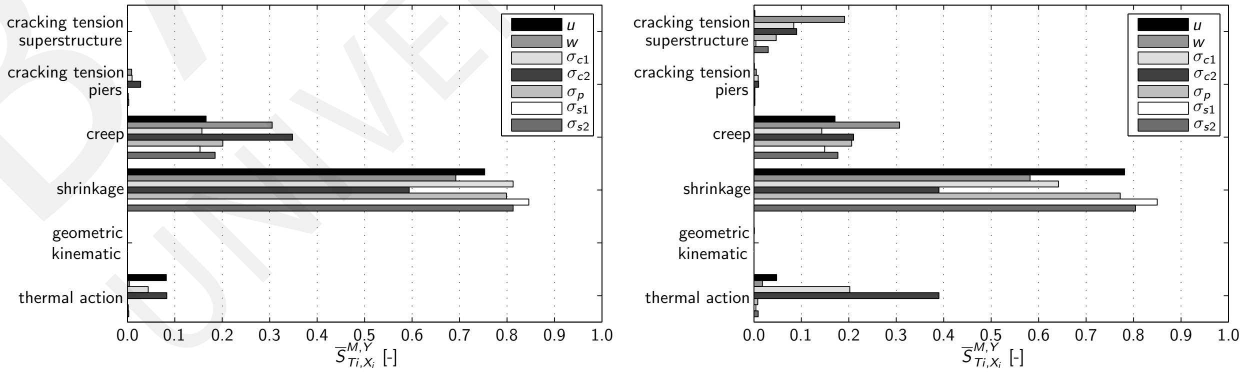

(c) SLS, $H^2 = 10\,\mathrm{m}$

(d) ULS, $H^2 = 10\,\mathrm{m}$

Figure 6.14: Integrative sensitivity indices $\overline{S}^{\mathrm{M},Y}_{Ti,X_i}$ for semi-integral concrete bridges with different pier heights (H^1, H^2) in serviceability limit state (SLS) and ultimate limit state (ULS), 6 model classes considered, foundation flexibility neglected

The main difference appears in the prediction of the vertical displacement, as previously discussed. For the pier height of $H^2 = 10\,\mathrm{m}$, greater vertical displacements are induced, due to concrete shrinkage, which leads to a local response significance along the pier axis of about $0.0 < \mathcal{S}_{w,\mathrm{rel}} < 0.3$. The maximum displacement occurs at the mid span where the shrinkage additionally mainly influenced the vertical displacement. Hence, the integrative sensitivity indices are $\overline{S}^{\mathrm{M},w}_{Ti,\mathrm{creep}} = 0.31$ (39 %) and $\overline{S}^{\mathrm{M},w}_{Ti,\mathrm{shrinkage}} = 0.69$ (329 %), which are much different when compared to the shorter pier height $H^1 = 5\,\mathrm{m}$.

In the ultimate limit state, the vertical displacement is mainly influenced by concrete cracking in the superstructure and also the shrinkage. The stiffness degradation is higher, due to the increasing stiffness of the entire structure, compared to the global model with consideration of the foundation flexibility. Hence, concrete cracking in the superstructure has an integrative sensitivity of 0.51 for the fixed support condition and only 0.28 for the consideration of pile group flexibility in the case of the short pier height $H^1 = 5\,\mathrm{m}$. For the longer piers, the sensitivity values are 0.19 and 0.10, respectively.

The presented results show that the consideration or disregard of a certain phenomenon can cause considerable changes in the integrative sensitivity values, due to the changing structural load-deformation behaviour. Therefore, the pre-selection of the phenomena and corresponding partial models by the engineers is very important and crucially influences the results of the quantification of partial model sensitivity and finally the global model quality.

6.5 Girder bridge on bearings

In addition to the semi-integral bridges, the load-deformation behaviour of a conventional girder bridge is quantified and the results are presented in the following section. All geometric, material, prestressing, and loading conditions are the same as studied for the semi-integral bridges except for the bridge piers and pile groups. Therefore, the “foundation flexibility” and “cracking tension piers” model classes are not considered in this assessment.

The girder is modelled as a continuous three-span beam with one vertical and horizontally fixed abutment, two vertically fixed pier axes and one vertically fixed abutment axis. The results of the integrative sensitivity analysis are shown in Fig. 6.15. In addition, the results are listed in the appendix, see Tab. C.5.

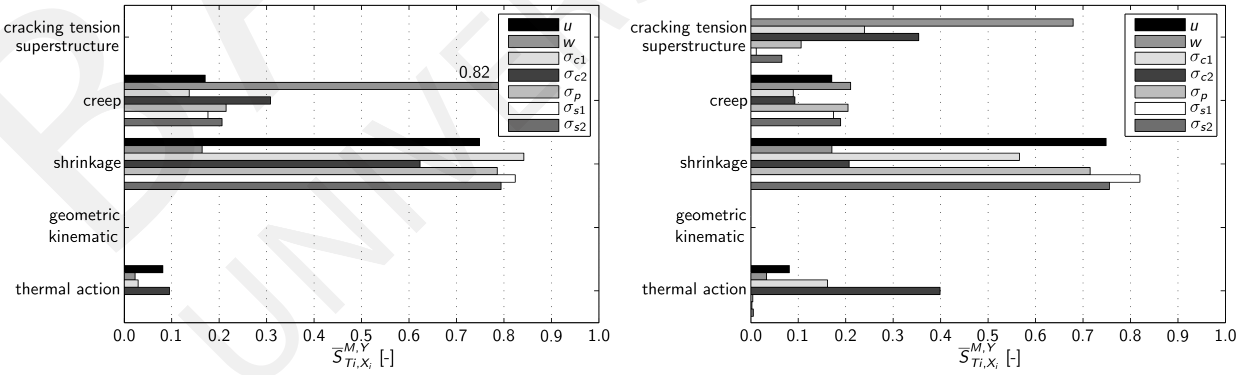

(a) SLS

(b) ULS

Figure 6.15: Integrative sensitivity indices $\overline{S}^{\mathrm{M},Y}_{Ti,X_i}$ for concrete girder bridge in serviceability limit state (SLS) and ultimate limit state (ULS), 5 model classes

In the serviceability limit state, the concrete cracking has no influence on the entire structural behaviour.

BAUHAUS
UNIVERSITÄTSVERLAG

The restraint effects, which cause additional section forces in the semi-integral bridges, are limited in the bridge girder. Therefore, no tensile stresses occur at the top and bottom surfaces of the box girder. Due to the one-dimensional beam structure in the longitudinal bridge direction, the geometric kinematic has no effect in the SLS and ULS.

The vertical displacement is mainly influenced in the serviceability limit state by creep of concrete and in the ultimate limit state by the concrete cracking in the box girder. The corresponding integrative sensitivity values are 0.82 for the creep in SLS and 0.68 for the concrete cracking in the ULS. No tensile stresses occur in the SLS because less section forces are predicted caused by the combination of direct and indirect loading conditions.

Therefore, concrete cracking does not occur in the SLS; hence, the non-linear material modelling can be neglected in the tensile zone of the cross section. In contrast, a great amount of stiffness degradation is predicted in the ULS, which causes great integrative sensitivity of the "cracking tension superstructure".

The thermal action mainly affects the concrete stress at the bottom level of the box girder σ_{c2}. In the SLS, the integrative sensitivity is 0.10 and in the ULS is 0.40. The higher importance of the temperature strains in the ULS is caused by the higher loading level (according to the combination rule of EC 0) of the induced bending moments by the temperature component ΔT_M.

BAUHAUS
UNIVERSITÄTSVERLAG

BAUHAUS
UNIVERSITÄTSVERLAG

7 Conclusions

The assessment of material models for reinforced concrete highlights that the quality of simplified or more complex material models can be quantitatively similar as well as diverse. A clear assignment between the complexity and quality of models does not exist in general. The statement of the uncertainty hypothesis that increasing the complexity can reduce the model uncertainty is analysed to be an appropriate assumption in the assessment of concrete material models. In contrast, the theorem that parameter uncertainty increases with increasing complexity cannot be generalised and does not represent the quantified results. The relationship between total uncertainty and complexity is strongly dependent on the model characteristics and the loading condition.

The individual model characteristics and the influence of external loading conditions on the model response significantly impact the relationship between complexity and uncertainty. Consequently, a general determination of the dependence between complexity and uncertainty is not appropriate and should be carefully investigated in each application. It is not the result of this assessment, that the hypothesis is inaccurate or even wrong, but it cannot be generalised as it is shown in the presented results. Nevertheless, the quantification of uncertainty and complexity allows a clear and objective comparison between various models. Therefore, the choice of an adequate model for each application is assisted by quantitative information which is based on the uncertainty and not solely on qualitative engineering judgement.

The assessment of pile foundation models shows the crucial influence of selecting a constant, such as initial linear-elastic stiffness or a variable reference value, such as the displacement in the model uncertainty assessment. In the case of the selection of a constant response value in the assessment, the standard deviation (difference between model predictions) increases and average value (model prediction of reference model) decreases between two successive load steps. If this relation becomes more and more disproportional due to the high stiffness degradation in the non-linear reference model and the constant elastic stiffness in the simplified models, the model uncertainty is significantly overestimated and is not capable of representing the average load-deformation behaviour of the models.

For simplified elastic models, the increase in displacement/deformation/settlement is always proportional to the external load increment due to the same initial elastic stiffness. Similarly, the coefficient of variation is characterised as a proportional change between standard deviation and average value leads to a constant coefficient of variation between two neighbouring load steps, which should be considered in the model uncertainty assessment. The evaluation of the stiffness and deformation response in the uncertainty analysis shows that the deformation response value is more adequate and accurate in the model uncertainty quantification, because by the selection of this model output enables the uncertainty analysis of investigating the entire load-deformation analysis.

On the structural level, the assessments at local positions show the significant influence of each position on the sensitivity indices of the phenomena. Therefore, the global model quality for the same partial model combination is different at each position due to the changed sensitivity values or partial model qualities. Moreover, it is also obvious that some phenomena have no influence at certain positions in the structure indicated by the response quantity. In contrast, they can affect the structural load-bearing behaviour at other positions. Consequently, the quality assessment at local structural positions quantifies different global model qualities for the same partial model combination.

In practical engineering problems, there is no requirement to establish various global models with the corresponding best prediction quality at a local position in the structure for the design purposes. Engineers need to have a global model with an acceptable and adequate overall prediction quality. Hence, the integrative assessment method is established, which is capable of computing quantitative information in order to assess global structural prediction qualities for each partial model combination in relation to the entire structural load-deformation behaviour.

Hence, the global model quality for the same partial model combination based on the integrative assessment method is not dependent on the local positions, because all positions are taken into account by the local response significance factors. Finally, an overall sensitivity index to each partial model and, subsequently the entire structural prediction quality for each partial model combination can be assessed.

A quantitative comparison between several global structural models is then clearly feasible on the entire structural level. The integrative assessment method assists the structural engineers in the decision making process in various project's design phases. The engineers can then choose a structural model with an adequate prediction quality for the entire structure in order to obtain more reliable simulation results and finally a more economical design. An adequate global model quality in the structural model allows the reduction of the corresponding safety factor of the model uncertainty.

Nevertheless, the presented results show that the consideration or disregard of a certain phenomenon can cause significant changes in the integrative sensitivity values due to the changes in the structural load-deformation behaviour. Therefore, the pre-selection of the phenomena and corresponding partial models by engineering judgement is still very important and crucially influences the results of the quantification of partial model sensitivity and finally the global model quality.

The applications of the integrative assessment method to the evaluation of the load-deformation behaviour of complex semi-integral concrete bridges show that shrinkage and creep of concrete have a significant influence on the structural load-bearing behaviour for the serviceability limit state and ultimate limit state. Therefore, it can be necessary and very useful to perform short-term (modulus of elasticity, compressive strength) and long-term (creep and shrinkage) experiments in order to measure more accurate data for a particular concrete mixture in comparison to the imprecise values of the existing design codes such as the Eurocode 2. This parameter estimation can significantly reduce the uncertainty in the model prediction. Finally, the design of the entire structure becomes more reliable.

In addition, the foundation and soil stiffness is quantified to be very sensitive with respect to the vertical bridge displacements. Soil tests or even pile foundation tests should be performed on site, because these studies can further reduce the model prediction uncertainty.

For integral bridge structures with high rigidity of the structural components, the restraint effects due to temperature, shrinkage and creep could lead to a non-linear material response of the structure material. In the application examples, concrete cracking under tension is not a sensitive phenomenon with respect to the structural behaviour for the serviceability limit state, but is a sensitive parameter for the ultimate limit state. This relationship cannot be generalised, because a lot of factors, such as loading conditions, cross section stiffness/shape, material properties, prestressing forces, or the span - height ratio affect the magnitude of the restraint effects.

In general, engineers should care about the non-linear material behaviour and cannot assume a simplified linear-elastic material description for integral bridges. Otherwise, the linear-elastic computation will only result in highly inaccurate sectional forces, due to the restraint effects, and thus the amount of reinforcement increases significantly. In contrast, concrete cracking and stiffness degradation reduce the section forces due to these indirect loading conditions. Therefore, a non-linear simulation leads to a more suitable design approach.

Due to the fact that integral bridges are very sensitive to material and structural component stiffness, structural engineer should take care of the model selection process and assess the main influencing phenomena. This analysis illustrates where more accurate partial models and where simplified partial models can suffice in the establishment of the global structural model. Therefore, the integrative assessment method is a powerful methodology, which can significantly reduce the uncertainty in model predictions. The design of engineering structures in accordance with the recommendations of codes and guidelines should be performed based on the results of a global structural model with a high prediction quality in order to obtain a more reliable design.

BAUHAUS
UNIVERSITÄTSVERLAG

BAUHAUS
UNIVERSITÄTSVERLAG

8 Outlook

In the assessment of partial models, the evaluation of model uncertainty and parameter uncertainty should be extended to the failure regions. In some engineering fields, such as reliability analysis, it is not necessary to know the exact distribution type in the range of the mean values. Knowledge about the tail of the distribution is much more important and influential for the simulated results. Therefore, research is needed to assess models in the failure region. How is it possible to quantify the difference of the failure of a certain structural element or the entire structure at a loading condition based on a specific model selection versus another model that may predict a stable equilibrium for the same loading level and structural elements?

Hence, it is necessary to combine the model quality assessment and the reliability analysis. Each model will compute a different probability of failure for the system of interest. But what is the actual failure probability? Therefore, the model uncertainty of the partial models may be scaled according to their effect on the structural level using the integrative assessment method. This should be analysed in further research studies in order to quantify the difference between the several predicted probabilities of failure for the same structure. Based on such results, it should be possible to assess the partial safety factors for the model uncertainty for each model. Hence, for the structural engineering design practice, some more accurate information about the safety factors can be given to the semi-probabilistic design concept.

The consequent application of the integrative assessment method according to the various types of engineering structures could make it possible to deduce design recommendations for the modelling and simulation process. Therefore, statements in guidelines and textbooks regarding the design of structures can then be given based on the quantitative evaluation of various phenomena and loading levels under different conditions. In the ensuing decades, it would be more appropriate to give recommendations regarding methods, such as the integrative assessment method, which are able to quantify the influence of the phenomena and can adequately assess the prediction quality rather than giving the design recommendations for a specific type of structure or structural element.

Engineers can then analyse the load-deformation behaviour for the structure of interest by the assessment method. Therefore, clear insight into the structural behaviour and the model evaluation can lead to the selection of an accurate model, which finally can reduce modelling errors and design mistakes. In design guidelines, a lot of the text is related to a specific type of structure for which the engineers should care about certain phenomena. Due to the fact that the importance of phenomena varies for different structural types and conditions in the design, a lot of recommendations are mentioned and extended to the length and detail of design codes and text books. Hence, it may be more efficient to recommend methods, such as the integrative assessment method, which are more accurate and efficient at quantifying and recognizing the sensitive phenomena that the engineers should give consideration to in the design process of specific structures.

Engineers and researchers should be motivated to objectively discuss their model selection and always should have in mind that numerical and mathematical simulation methods are approximations of the “reality”. More research about the evaluation methods for the assessment of partial and global structural models such as the proposed integrative assessment method, have to be studied in comparison to experimental models in order to evaluate the interaction between measurement data and simulation results.

9 Bibliography

[1] Akaike, H.: *A New Look at the Statistical Model Identification*. IEEE Transactions on Automatic Control, 19(6):716–723, 1974.

[2] Al-Manaseer, A. and Lam, J. P.: *Statistical Evaluation of Shrinkage and Creep Models*. ACI Materials Journal, 102(3):170–176, 2005.

[3] Alavizadeh-Farhang, A.: *Concrete structures subjected to combined mechanical and thermal loading*. PhD thesis, Royal Institute of Technology, Stockholm, 2000.

[4] Alavizadeh-Farhang, A. and Silfwerbrand, J.: *Responses of plain and steel fiber-reinforced concrete beams to temperature and mechanical loads: Experimental study*. Transportation Research Record, 1740:25–32, 2000.

[5] Allaix, D.L., Carbone, V.I., and Mancini, G.: *Global safety format for non-linear analysis of reinforced concrete structures*. Structural Concrete, 14(1):29–42, 2013.

[6] American Concrete Institute: *Prediction of Creep, Shrinkage, and Temperature Effects in Concrete Structures (ACI 209R-92)*, 1992.

[7] American Society for Testing and Materials: *Standard Practice for Classification of Soils for Engineering Purposes (Unified Soil Classification System, ASTM D2487-06)*, 2006.

[8] Anderson, T.L.: *Fracture mechanics: Fundamentals and applications*. CRC Taylor & Francis, Boca Raton, 3rd edition, 2005.

[9] Arioglu, N., Girgin, Z.C., and Arioglu, E.: *Evaluation of Ratio Between Splitting Tensile Strength and Compressive Strength for Concretes up to 120 MPa and its Application in Strength Criterion*. ACI Materials Journal, 103(1):18–24, 2006.

[10] Arioz, O., Ramyar, K., Tuncan, M., Tuncan, A., and Cil, I.: *Some Factors Influencing Effect of Core Diameter on Measured Concrete Compressive Strength*. ACI Materials Journal, 104(3):291–296, 2007.

[11] Arnold, A.: *Zum Einfluss der Zwangschnittgrößen aus Temperatur bei Tragwerken aus Konstruktionsbeton mit und ohne Vorspannung*. PhD thesis, Technische Universität Dortmund, Dortmund, 2008.

[12] Babuska, I. and Oden, J.T.: *Verification and validation in computational engineering and science: basic concepts*. Computer Methods in Applied Mechanics and Engineering, 193(36-38):4057–4066, 2004.

[13] Baguelin, F.: *La Capacité Portante des Pieux*. PhD thesis, Annoles de l'Institut Technique du Batiment et des Trovoux Publies, Paris, 1975.

[14] Baguelin, F. and Frank, R.: *Theoretical studies of piles using the finite element method*. Numerical Methods in Offshore Piling, pages 83–91, 1979.

[15] Baker, J.W and Cornell, C.A: *Uncertainty propagation in probabilistic seismic loss estimation*. Structural Safety, 30(3):236–252, 2008.

BAUHAUS
UNIVERSITÄTSVERLAG

[16] Balázs, G.L.: *Design for SLS according to fib Model Code 2010*. Structural Concrete, 14(2):99–123, 2013.

[17] Banerjee, P.K.: *A contribution to the study of axially loaded pile foundations*. PhD thesis, University of Southampton, 1970.

[18] Banerjee, P.K. and Davies, T.G.: *The behaviour of axially and laterally loaded single piles embedded in nonhomogeneous soils*. Géotechnique, 28(3):309–326, 1978.

[19] Barr, P.J. and Angomas, F.: *Differences between Calculated and Measured Long-Term Deflections in a Prestressed Concrete Girder Bridge*. Journal of Performance of Constructed Facilities), 24(6):603–609, 2010.

[20] Barsotti, R. and Froli, M.: *Statistical Analysis of Thermal Actions on a Concrete Segmental Box-Girder Bridge*. Structural Engineering International, 10(2):111–116, 2000.

[21] Bascoul, A., Duprat, M., and Pinglot, M.: *Load Deflection Diagram of Over-Reinforced Concrete Beams*. Proceedings FRAMCOS-3, pages 1211–1222, 1998.

[22] Bausch, S. and Twelmeier, H.: *Zum Grenzverformungsvermögen biegebeanspruchter Stahlbetonbalken*. Beton- und Stahlbetonbau, 81(12,1):313–317, 16–20, 1986, 1987.

[23] Bažant, Z.P.: *Bažant, Z.P.; Kim, J.-K. Prediction of Concrete Creep Effects Using Age-Adjusted Effective Modulus Method*. ACI Journal, 69(4):212–217, 1972.

[24] Bažant, Z.P. and Bajewa, S.: *Creep and shrinkage prediction model for analysis and design of concrete structures - model B3*. Materials and Structures, 28(6):357–365, 1995.

[25] Bažant, Z.P. and Bajewa, S.: *Justification and refinements of Model B3 for concrete creep and shrinkage: 1. Statistics and sensitivity*. Materials and Structures, 28:415–430, 1995.

[26] Bažant, Z.P. and Bajewa, S.: *Justification and refinements of model B3 for concrete creep and shrinkage: 2. Updating and theoretical basis*. Materials and Structures, 28:488–495, 1995.

[27] Bažant, Z.P. and Chern, J. C.: *Bayesian Statistical Prediction of Concrete Creep and Shrinkage*. ACI Journal, 81(4), 1984.

[28] Bažant, Z.P., Hubler, M.H., and Yu, Q.: *Excessive Creep Deflections: An Awakening*. Concrete International, 33(8), 2011.

[29] Bažant, Z.P., Hubler, M.H., and Yu, Q.: *Pervasiveness of Excessive Segmental Bridge Deflections: Wake-Up Call for Creep*. ACI Structural Journal, 108(6):766–774, 2011.

[30] Bažant, Z.P., Kazemi, M.T., Hasegawa, T., and Mazars, J.: *Size Effect in Brazilian Split-Cylinder Tests: Measurements and Fracture Analysis*. ACI Materials Journal, 88(3):325–332, 1991.

[31] Bažant, Z.P. and Kim, J. K.: *Improved prediction model for time-dependent deformations of concrete: Part 3-Creep at drying*. Materials and Structures, 25(1):21–28, 1992.

[32] Bažant, Z.P. and Li, G. H.: *Unbiased Statistical Comparison of Creep and Shrinkage Prediction Models*. ACI Materials Journal, 105(6):610–621, 2008.

[33] Bažant, Z.P. and Oh, B.H.: *Crack band theory for fracture of concrete*. Matériaux et Constructions, 16(3):155–177, 1983.

[34] Bažant, Z.P. and Planas, J.: *Fracture and size effect in concrete and other quasibrittle materials*. New directions in civil engineering. CRC Press, Boca Raton, 1998.

[35] Bažant, Z.P. and Prasannan, S.: *Solidification Theory for Concrete Creep. I: Formulation*. Journal of Engineering Mechanics, 115(8):1691–1703, 1989.

[36] Bažant, Z.P. and Prasannan, S.: *Solidification Theory for Concrete Creep. II: Verification and Application*. Journal of Engineering Mechanics, 115(8):1704–1725, 1989.

[37] Bažant, Z.P., Yu, Q., and Li, G. H.: *Excessive Long-Time Deflections of Prestressed Box Girders. I: Record-Span Bridge in Palau and Other Paradigms*. Journal of Structural Engineering, 138(6):676–686, 2012.

[38] Bažant, Z.P., Yu, Q., and Li, G. H.: *Excessive Long-Time Deflections of Prestressed Box Girders. II: Numerical Analysis and Lessons Learned*. Journal of Structural Engineering, 138(6):687–696, 2012.

[39] Beck, J.L. and Yuen, K. V.: *Model Selection Using Response Measurements: Bayesian Probabilistic Approach*. Journal of Engineering Mechanics, 130(2):192–203, 2004.

[40] Beeby, A.W.: *Ductility in reinforced concrete: why is it needed and how is it achieved?* The Structural Engineer, 75(18), 1997.

[41] Bender, M., Bockhold, J., Meyer, J., and Mark, P.: *Zum Einfluß der Temperatur auf die Bemessung von Kühlturmschalen aus Stahlbeton*. Bautechnik, 82(11):755–763, 2005.

[42] Berger, D., Graubner, C. A., Pelke, E., and Zink, M.: *Besonderheiten bei Entwurf und Bemessung integraler Betonbrücken*. Beton- und Stahlbetonbau, 99(4):295–303, 2004.

[43] Betten, J.: *Finite Elemente für Ingenieure 2: Variationsrechnung, Energiemethoden, Näherungsverfahren, Nichtlinearitäten, Numerische Integrationen*. Springer-Verlag Berlin Heidelberg New York, Berlin and Heidelberg, zweite, neu bearbeitete und erweiterte auflage edition, 2004. `http://dx.doi.org/10.1007/3-540-35030-6`.

[44] Bissonnette, B., Pigeon, M., and Vaysburd, A.M.: *Tensile Creep of Concrete: Study of Its Sensitivity to Basic Parameters*. ACI Materials Journal, 104(4):360–368, 2007.

[45] Bloodworth, A.G, Xu, M., Banks, J.R, and Clayton, C.R.I: *Predicting the Earth Pressure on Integral Bridge Abutments*. Journal of Bridge Engineering, 17(2):371–381, 2012.

[46] Bockhold, J.: *Modellbildung und numerische Analyse nichtlinearer Kriechprozesse in Stahlbetonkonstruktionen unter Schädigungsaspekten*. PhD thesis, Ruhr-Universität Bochum, Bochum, 2005.

[47] Böckmann, A.: *Zuverlässigkeitsanalyse von ebenen Tragwerken aus Stahlbeton in Wechselwirkung mit dem Baugrund*. PhD thesis, university press, Technische Universität München, 1997.

[48] Boltzmann, L.: *Zur Theorie der elastischen Nachwirkung*. Wiener Berichte, 70(3), 1876.

[49] Box, G., Bisgaard, S., and Fung, C.: *An explanation and critique of taguchi's contributions to quality engineering*. Quality and Reliability Engineering International, 4(2):123–131, 1988.

[50] Branco, Fernando A. and Mendes, Pedro A.: *Thermal Actions for Concrete Bridge Design*. Journal of Structural Engineering, 119(8):2313–2331, 1993.

[51] Brettmann, T. and Duncan, J.M.: *Computer Application of CLM Lateral Load Analysis to Piles and Drilled Shafts*. Journal of Geotechnical Engineering, 122(6):496–498, 1996.

[52] Briaud, J.L., Tucker, L.M., and Ng, E.: *Axially loaded 5 pile group and single pile in sand*. Proceedings of the 12th International Conference on Soil Mechanics and Foundation Engineering, pages 1121–1124, 1989.

[53] Bristish Building and Civil Engineering Sector Policy and Strategy Committee: *BS EN 1990:2002: Eurocode: Basis of structural design*, 2002.

[54] Brooks, J.J.: *30-year creep and shrinkage of concrete*. Magazine of Concrete Research, 57(9):545–556, 2005.

BAUHAUS
UNIVERSITÄTSVERLAG

[55] Bucher, C.: *Computational analysis of randomness in structural mechanics*, volume 3 of *Structures and infrastructures series*. CRC Press, Boca Raton [Fla.] and London, 2009.

[56] Butterfield, R. and Banerjee, P.K.: *The Elastic Analysis of Compressible Piles and Pile Groups*. Géotechnique, 21(1):43–60, 1971.

[57] Butterfield, R. and Bannerjee, P.K.: *A Note on the Problem of a Pile Reinforced Half Space*. Géotechnique, 20(1):100–103, 1970.

[58] Cairo, R. and Conte, E.: *Settlement analysis of pile groups in layered soils*. Canadian Geotechnical Journal, 43(8):788–801, 2006.

[59] Capps, M.W.R.: *Temperature movements in the Medway bridge*. PhD thesis, Road Research Laboratory, 1965.

[60] Caputo, R. and Viggiani, C.: *Pile foundation analysis: A simple approach to nonlinearity effects*. Rivista Italiana di Geotecnica, 18(1):32–51, 1984.

[61] Carreira, D.J. and Chu, K.H.: *Stress-strain relationship for plain concrete in compression*. ACI Journal, 83(6):797–804, 1985.

[62] Carter, J.P. and Kulhawy, F.H.: *Analysis and design of drilled shaft foundations socketed into rock*. PhD thesis, Report to Electric Power Research Institute (Project RP1493-4,Report EL-5918), California, 1988.

[63] Casas, J.R., Wisniewski, D.F., Cervenka, J., Bruwhiler, E., Holm, G., and Plos, M.: *Sustainable Bridges - Safety and Probabilistic Modelling*. PhD thesis, 2007.

[64] Caspeele, R., Sykora, M., and Taerwe, L.: *Influence of quality control of concrete on structural reliability: assessment using a Bayesian approach*. Materials and Structures, 47(1-2):105–116, 2014.

[65] Cervenka, V.: *Global Safety Format for Nonlinear Calculation of Reinforced Concrete*. Beton- und Stahlbetonbau, 103(S1):37–42, 2008.

[66] Cervenka, V.: *Reliability-based non-linear analysis according to fib Model Code 2010*. Structural Concrete, 14(1):19–28, 2013.

[67] Chacón, R., Mirambell, E., and Real, E.: *Strength and ductility of concrete-filled tubular piers of integral bridges*. Engineering Structures, 46:234–246, 2013.

[68] Chan, C.K. and Low, B.K.: *Practical second-order reliability analysis applied to foundation engineering*. International Journal for Numerical and Analytical Methods in Geomechanics, 36(11):1387–1409, 2012.

[69] Chartrand, G.: *Introductory graph theory*. Dover books explaining science. Dover Publ, New York and NY, 1977th edition, 1985.

[70] Chow, Y.K.: *Discrete element analysis of settlement of pile groups*. Computers & Structures, 24(1):157–166, 1986.

[71] Chow, Y.K.: *Axial and lateral response of pile groups embedded in nonhomogeneous soils*. International Journal for Numerical and Analytical Methods in Geomechanics, 11(6):621–638, 1987.

[72] CIB Commission W81: *Action on Structures - Self-Weight Loads*, volume 115 of *CIB Report*. International Council for Building Research, Studies, and Documentation, Rotterdam, 1989.

[73] Cizelj, L., Mavko, B., and Riesch-Oppermann, H.: *Application of first and second order reliability methods in the safety assessment of cracked stream generator tubing*. Nuclear Engineering and Design, 147:359–368, 1994.

[74] Comité Euro-International du Béton: *CEB-FIP model code 1990: Design code*, volume 213/214 of *Bulletin d'information / Comité Euro-International du Béton*. Telford, London, 1993.

[75] Comité Euro-International du Béton: *Ductility of reinforced concrete structures*, volume 242 of *Bulletin d'information / Comité Euro-International du Béton*. Comité Euro-International du Béton CEB, Lausanne, 1998.

[76] Cooke, R.W.: *The Settlement of Friction Pile Foundations*. Proceedings, Conference on Tall Buildings, Kuala Lumpur, 1974.

[77] Coulomb, C.A.: *Essai sur une Application des Régles des Maximis et Minimis á quelques Problémes de Statique Relatifs á l' Architecture, An attempt to apply the rules of maxima and minima to several problems of stability related to architecture: Me'm. Acad. Roy. des Sciences*. 7:343–382, 1776.

[78] DBV-Merkblatt: *Begrenzung der Rißbildung im Stahlbeton- und Spannbetonbau*. Deutscher Beton Verein, Wiesbaden, 1986.

[79] Dede, T. and Ayvaz, Y.: *Nonlinear analysis of reinforced concrete beam with/without tension stiffening effect*. Materials & Design, 30(9):3846–3851, 2009.

[80] Dempster, A.P: *A generalization of bayesian inference*. Journal of the Royal Statistical Society. Series B (Methodological), (30):205–247, 1968.

[81] Deutsche Geselltschaft für Geotechnik: *Empfehlungen des Arbeitskreises Pfähle: EA-Pfähle*. Wiley-VCH, Hoboken, 2007.

[82] Dicleli, M. and Erhan, S.: *Effect of soil–bridge interaction on the magnitude of internal forces in integral abutment bridge components due to live load effects*. Engineering Structures, 32(1):129–145, 2010.

[83] Diener, J.: *Beitrag zur physikalisch und geometrisch nichtlinearen Berechnung langzeitbelasteter Bauteile aus Stahlbeton und Spannbeton unter besonderer Berücksichtigung des nichtlinearen Kriechens und der Rißbildung*. PhD thesis, university press, Bauhaus-Universität Weimar, 1998.

[84] Diestel, R.: *Graph Theory*. Springer, 4th edition, 2010.

[85] Djouahra, G.: *Verhalten von Stahlbetonbauteilen unter einer kombinierten Beanspruchung aus Last und zentrischem Zwang*. PhD thesis, Technische Universität, Dortmund, 2009.

[86] Dreier, D., Burdet, O., and Muttoni, A.: *Transition Slabs of Integral Abutment Bridges*. Structural Engineering International, 21(2):144–150, 2011.

[87] Duncan, J.M., Evans, L.T., and Ooi, P.S.K.: *Lateral Load Analysis of Single Piles and Drilled Shafts*. Journal of Geotechnical Engineering, 120(6):1018–1033, 1994.

[88] Durga Rao, K., Kushwaha, H.S, Verma, A.K, and Srividya, A.: *Quantification of epistemic and aleatory uncertainties in level-1 probabilistic safety assessment studies*. Reliability Engineering & System Safety, 92(7):947–956, 2007.

[89] Dwivedi, A.K., Bhargarva, P., and Bhandari, N.M.: *Temperature effects in the design of concrete bridges*. Proceedings of National Conference on Advances in Bridge Engineering, pages 555–568, 2006.

[90] Edwards, A.W.F.: *Likelihood: Expanded edition*. The Johns Hopkins Univ. Press, Baltimore, 1992.

[91] Eibl, J., Mora, J., and Strauß, P.: *Momentenrotation und Schubtragfähigkeit im Spannbetonbau*. PhD thesis, Unversität Karlsruhe, Karlsruhe, 1983.

[92] Eibl, J. and Retzepis, I.: *Nichtlineare Berechnungen der Schnittkraftumlagerungen und Zwangbeanspruchungen von Stahlbetontragwerken*. Beton- und Stahlbetonbau, 90(1,2):1–5,33–37, 1995.

[93] Elbadry, M. and Ghali, A.: *Thermal Stresses and Cracking of Concrete Bridges*. American Concrete Institute, 83(6):1001–1009, 1986.

[94] Elbadry, M.M. and Ghali, A.: *Temperature Variations in Concrete Bridges*. Journal of structural engineering, 109(10):2355–2374, 1983.

[95] Emerson, M.: *Temperature movements in the Hammersmith flyover*. PhD thesis, Road Research Laboratory, 1966.

[96] Emerson, M.: *The Calculation of the Distribution of Temperature in Bridges*. Transport and Road Research Laboratory, Crowthorne and England, 1973.

[97] Emerson, M.: *The Calculation of the Distribution of Temperature in Bridges*. Transport and Road Research Laboratory, Crowthorne and England, 1973.

[98] Emerson, M.: *Bridge Temperatures Estimated from the Shade Temperature*. PhD thesis, Transport and Road Research Laboratory, Crowthorne and England, 1976.

[99] Erhan, S. and Dicleli, M.: *Live load distribution equations for integral bridge substructures*. Engineering Structures, 31(5):1250–1264, 2009.

[100] European Committee for Standardisation (CEN): *EN 1990:2010-12: Eurocode: Basis of structural design*, 2010.

[101] European Committee for Standardisation (CEN): *EN 1992-1-1:2011-01: Eurocode 2: Design of concrete structures – Part 1-1: General rules and rules for buildings*, 2011.

[102] European Committee for Standardisation (CEN): *EN 12390: Testing hardened concrete*, 2012.

[103] European Committee for Standardisation (CEN): *EN 206:2012-03: Concrete - Specification, performance, production and conformity*, 2012.

[104] European Committee for Standardization (CEN): *EN 1991-1-5:2010-12: Eurocode 1: Actions on structures – Part 1-5: General actions - Thermal actions*, 2010.

[105] Faber, M.H. and Vrouwenvelder, A.C.W.M.: *Probabilistic Model Code, 12th draft*. Joint Committee on Structural Safety, 2001.

[106] Faber, M.H. and Vrouwenvelder, A.C.W.M.: *Interpretation of Uncertainties and Probabilities in Civil Engineering Descision Anlaysis: Bachground Documents on Risk Assessment in Engineering*, 2008.

[107] Falkner, H.: *Zum Zug- und Schubtragverhalten von Bauteilen aus hochfestem Beton: Zur Frage der Rißbildung durch Eigen- und Zwängspannungen infolge Temperatur in Stahlbetonbauteilen*, volume 208 of *German Board for Reinforced Concrete (DAfStb)*. Berlin, 1969.

[108] Faraji, S., Ting, J.M, Crovo, D.S, and Ernst, H.: *Nonlinear Analysis of Integral Bridges: Finite-Element Model*. Journal of Geotechnical and Geoenvironmental Engineering, 127(5):454–461, 2001.

[109] Ferson, S., Joslyn, C.A, Helton, J.C, Oberkampf, W.L, and Sentz, K.: *Summary from the epistemic uncertainty workshop: consensus amid diversity*. Reliability Engineering & System Safety, 85(1-3):355–369, 2004.

[110] Fingerloos, F., Hegger, J., and Zilch, K.: *Eurocode 2 für Deutschland: DIN EN 1992-1-1 Bemessung und Konstruktion von Stahlbeton- und Spannbetonbauwerken - Teil 1-1: Allgemeine Bemessungsregeln und Regeln für den Hochbau mit nationalem Anhang ; kommentierte Fassung*. Bauwesen. Beuth and Ernst & Sohn, Berlin, 1st edition, 2012.

[111] Fischer, A.: *Modelluntersuchungen zur Ermittlung des Rißabstandes dicker Bauteile aus Stahlbeton*. PhD thesis, Techn. Hochsch, Düsseldorf, 1993.

BAUHAUS
UNIVERSITÄTSVERLAG

[112] Fleming, W.G.K., Weltman, A.J., Randolph, M.F., and Elson, W.K.: *Piling engineering*. Blackie, Glasgow, 2nd edition, 1992.

[113] Fleming, W.G.K., Weltman, A.J., Randolph, M.F., and Elson, W.K.: *Piling engineering*. Taylor & Francis, New York and NY, 3rd edition, 2009.

[114] Fouad, N.A.: *Temperature Loading of Concrete Box Girder Bridges due to Environmental Thermal Actions*. fib Symposium Prague, 1999.

[115] Fouad, N.A.: *Rechnerische Simulation der klimatisch bedingten Temperaturbeanspruchungen von Bauwerken*. PhD thesis, Techn. Univ, Stuttgart and Berlin, 1998.

[116] Frank, R.: *Etude théorique du comportement des pieux sous charge verticale : introduction de la dilatance*. PhD thesis, Laboratoire Central des Ponts et Chaussées, Paris, 1975.

[117] Frenzel, B.: *Beitrag zur Ermittlung der repäsentativen Werte des linearen Temperaturunterschiedes an Betonbrücken und Überprüfung ihrer Einpassung in die Kombinationsregeln des EC 2*. PhD thesis, Bauhaus-Univerisität Weimar, 1994.

[118] Frenzel, B. and Freund, U.: *Bestimmung von Kombinationsbeiwerten und -regeln für Einwirkungen auf Brücken*. PhD thesis, Bundesministerium für Verkehr Abteilung Straßenbau, 1996.

[119] Fröbel, Toni: *Data coupled civil engineering applications : modeling and quality assessment methods*. PhD thesis, Bauhaus-Univerisität Weimar, Weimar, 2013.

[120] Froli, M., Hariga, N., Nati, G., and Orlandini, M.: *Longitudinal Thermal Behaviour of a Concrete Box Girder Bridge*. Structural Engineering International, 6(4):237–242, 1996.

[121] Gaganis, P. and Smith, L.: *A Bayesian Approach to the quantification of the effect of model error on the predictions of groundwater models*. Water Resources Research, 37(9):2309, 2001.

[122] Gardner, N.J.: *Comparison of prediction provisions for drying shrinkage and creep of normal-strength concretes*. Canadian Journal of Civil Engineering, 31(5):767–775, 2004.

[123] Gardner, N.J. and Lockman, M.J.: *Design Provisions for Drying Shrinkage and Creep of Normal-Strength Concrete*. ACI Materials Journal, 98(2):159–167, 2001.

[124] Garwood, F. and Wright, P.J.F.: *The effect of the method of test on the flexural strength of concrete*. Magazine of Concrete Research, 4(11):67–76, 1952.

[125] Gazetas, G.: *Analysis of machine foundation vibrations: State of the art*. International Journal of Soil Dynamics and Earthquake Engineering, 2(1):2–42, 1983.

[126] German Board for Reinforced Concrete (DAfStb): *Comments according DIN 1045-1 - 2nd revised version, in german: Erläuterungen zu DIN 1045-1*, volume 525 of *German Board for Reinforced Concrete (DAfStb)*. Beuth, Berlin, 2nd edition, 2010.

[127] German Board for Reinforced Concrete (DAfStb): *Erläuterungen zu DIN EN 1992-1-1 und DIN EN 1992-1-1/NA (Eurocode 2)*, volume 600 of *German Board for Reinforced Concrete (DAfStb)*. Beuth, Berlin, 1st edition, 2012.

[128] German Institute for Standardisation: *Grundlagen zur Festlegung von Sicherheitsanforderungen für bauliche Anlagen*. Beuth, Berlin, 1st edition, 1981.

[129] German Institute for Standardisation: *DIN-Fachbericht 101 - Einwirkungen auf Brücken*. Beuth Verlag GmbH, 2009.

[130] German Institute for Standardisation (DIN): *DIN 1055-5:1975-06: Actions on structures - Part 5: Snowloads and ice loads (retracted)*, 1975.

[131] German Institute for Standardisation (DIN): *DIN 1045:1978-12: Concrete and Reinforced Concrete - Design and construction*, 1978.

[132] German Institute for Standardisation (DIN): *DIN 1052-1:1988-04: Structural use of timber - Design and construction*, 1988.

[133] German Institute for Standardisation (DIN): *DIN 1053-1:1996-11: Masonary - Design and construction*, 1996.

[134] German Institute for Standardisation (DIN): *DIN 1045-1 Tragwerke aus Beton, Stahlbeton und Spannbeton - Teil 1: Bemessung und Konstruktion*, 2008.

[135] German Institute for Standardisation (DIN): *DIN 488-1: Reinforcing steels – Part 1: Grades, properties, marking*, 2009.

[136] German Institute for Standardisation (DIN): *DIN EN 1990:2010-12: Eurocode: Basis of structural design*, 2010.

[137] German Institute for Standardisation (DIN): *DIN EN 1991-1-1:2010-12: Eurocode 1: Actions on structures – Part 1-1: General actions - Densities, self-weight, imposed loads for buildings*, 2010.

[138] German Institute for Standardisation (DIN): *DIN EN 1991-1-3:2010-12: Eurocode 1: Actions on structures – Part 1-3: General actions - Snow loads*, 2010.

[139] German Institute for Standardisation (DIN): *DIN EN 1991-1-5/NA:2010-12: Eurocode 1: Actions on structures – Part 1-5: General actions - Thermal actions*, 2010.

[140] German Institute for Standardisation (DIN): *DIN 18196:2011-05: Earthworks and foundations - Soil classification for civil engineering purposes*, 2011.

[141] German Institute for Standardisation (DIN): *DIN EN 1992-1-1/NA:2011-01: National Annex - Eurocode 2: Design of concrete structures – Part 1-1: General rules and rules for buildings*, 2011.

[142] German Institute for Standardisation (DIN): *DIN EN 1991-2/NA:2012-08: Eurocode 1: Actions on structures – Part 2: Traffic loads on bridges*, 2012.

[143] German Institute for Standardisation (DIN): *DIN EN 1992-2/NA:2012-04: National Annex - Eurocode 2: Design of concrete structures – Part 2: Concrete bridges - Design and detailing rules*, 2012.

[144] Ghosh, N.: *A model scale investigation of the working load stiffness of single piles and groups of piles in clay under centric and eccentric vertical loads.* PhD thesis, University of Southampton, 1975.

[145] Gibson, R. E., Brown, P. T., and Andrews, K. R. F.: *Some results concerning displacements in a non-homogeneous elastic layer.* Zeitschrift für angewandte Mathematik und Physik ZAMP, 22(5):855–864, 1971.

[146] Gibson, R.E.: *Some Results Concerning Displacements and Stresses in a Non-Homogeneous Elastic Half-space.* Géotechnique, 17(1):58–67, 1967.

[147] Gilbert, R.I.: *Time Effects in concrete structures*, volume 23 of *Developments in civil engineering.* Elsevier, Amsterdam, 1988.

[148] Goel, R., Kumar, R., and Paul, D.K.: *Comparative Study of Various Creep and Shrinkage Prediction Models for Concrete.* Journal of Materials in Civil Engineering, 19(3):249–260, 2007.

[149] Gomes, H.M. and Awruch, A.M.: *Reliability of reinforced concrete structures using stochastic finite elements.* Engineering Computations, 19(7):764–786, 2002.

[150] Grasser, E. and Kraemer, U.: *Kriechen von Beton unter hoher zentrischer und exzentrischer Druckbeanspruchung*, volume 358 of *Deutscher Ausschuß für Stahlbeton.* Ernst, Berlin, 1985.

[151] Gribniak, V., Kaklauskas, G., Hung Kwan, A.K, Bacinskas, D., and Ulbinas, D.: *Deriving stress–strain relationships for steel fibre concrete in tension from tests of beams with ordinary reinforcement*. Engineering Structures, 42:387–395, 2012.

[152] Grimm, R.: *Einfluss bruchmechanischer Kenngrößen auf das Biege- und Schubtragverhalten hochfester Betone*. PhD thesis, Technical University of Darmstadt, Darmstadt (Germany), 1996.

[153] Gull, S.F.: *Bayesian inductive inference and maximum entropy*. In Erickson, G.J. (editor): *Maximum entropy and Bayesian methods in science and engineering*, volume 31 of *Fundamental theories of physics*, pages 53–74. Kluwer, Dordrecht, 1988.

[154] Guo, T., Sause, R., Frangopol, D.M, and Li, A.: *Time-Dependent Reliability of PSC Box-Girder Bridge Considering Creep, Shrinkage, and Corrosion*. Journal of Bridge Engineering, 16(1):29–43, 2011.

[155] Guo, W.D.: *Analytical and numerical analyses of pile foundations*. PhD thesis, The University of Western Australia, 1997.

[156] Guo, W.D.: *Laterally loaded rigid piles with rotational constraints*. Computers and Geotechnics, 54:72–83, 2013.

[157] Guo, W.D. and Randolph, M.F.: *Vertically loaded piles in non-homogeneous media*. International Journal for Numerical and Analytical Methods in Geomechanics, 21(8):507–532, 1997.

[158] Guo, W.D. and Randolph, M.F.: *An efficient approach for settlement prediction of pile groups*. Géotechnique, 49(2):161–179, 1999.

[159] Hambly, E.C.: *Temperature Distributions and Stresses in Concrete Bridges*. The Structural Engineer, 56 A(5):143–148, 1978.

[160] Hampe, E.: *Von der unsicheren Sicherheit zur sicheren Unsicherheit - From unsafe safety to safe unsafety*. Bautechnik, 66(10):329–335, 1989.

[161] Hansen, E.A., Leive, M., Rodriguez, J., and Cather, R.: *Mechanical Properties of High Strength Concrete - Influence of test Conditions, Specimens and Constituents*. In Holand, I. and Sellevold, E.J. (editors): *Proceedings of Fourth International Symposium on the Utilization of High Strength / High Performance Concrete*, 1996.

[162] Hartl, G.: *Die Arbeitslinie eingebetteter Stähle unter Erst- und Kurzzeitbelastung*. Beton- und Stahlbetonbau, 78(8):221–224, 1983.

[163] Hashin, Z.: *Analysis of Composite Materials - A Survey*. Journal of Applied Mechanics, 50(3):481, 1983.

[164] Hasofer, A.M. and Lind, N.C.: *Exact and Invariant Second-Moment Code Format*. Journal of the Engineering Mechanics Division, 100(1):111–121, 1974.

[165] Heidolf, T.: *Zeit- und beanspruchungsabhängiges Tragverhalten von polymermodifiziertem Beton unter mehrfach wiederholter Beanspruchung*. PhD thesis, Bauhaus-Univerisität Weimar, Weimar and Weimar, 2007.

[166] Heilmann, H.G.: *Beziehungen zwischen Zug- und Druckfestigkeit des Betons*. Beton, 2:68–70, 1969.

[167] Heilmann, H.G., Hilsdorf, H., and Finsterwalder, K.: *Festigkeiten und Verformungen von Beton unter Zug*, volume 203 of *German Board for Reinforced Concrete (DAfStb)*. Beuth, Berlin, 1st edition, 1969.

[168] Hermans, E., Bossche, F. van den, and Wets, G.: *Uncertainty assessment of the road safety index*. Reliability Engineering & System Safety, 94(7):1220–1228, 2009.

[169] Hillerborg, A.: *The theoretical basis of a method to determine the fracture energy GF of concrete*. Materials and Structures, 18(4):291–296, 1985.

[170] Hillerborg, A., Modéer, M., and Petersson, P. E.: *Analysis of crack formation and crack growth in concrete by means of fracture mechanics and finite elements*. Cement and Concrete Research, 6(6):773–781, 1976.

[171] Hilsdorf, H.K.: *Concrete*. In Eibl, J. (editor): *Concrete structures*. Ernst & Sohn, Berlin, 1994.

[172] Hofstetter, G. (editor): *Numerical modeling of concrete cracking*, volume 532 of *CISM courses and lectures*. Springer, Wien, 2011.

[173] Hognestad, E.: *A study of combined bending and axial load in reinforced concrete members*. PhD thesis, University of Illinois, Urbana and USA, 1951.

[174] Holschemacher, K.: *Zur Berechnung von Rissbreiten und Zwangsschnittgrößen in Stahlbeton- und Spannbetonbauteilen*. PhD thesis, Technische Universität, Leipzig, 1992.

[175] Holzhäuser, Jörg: *Experimentelle und numerische Untersuchungen zum Tragverhalten von Pfahlgründungen im Fels*. PhD thesis, Technischen Universität Darmstadt, Darmstadt, 1998.

[176] Homma, T. and Saltelli, A.: *Importance measures in global sensitivity analysis of nonlinear models*. Reliability Engineering & System Safety, (52):1–17, 1996.

[177] Hoover, C.G., Bažant, Z., Vorel, J., Wendner, R., and Hubler, M.H.: *Comprehensive concrete fracture tests: Description and results*. Engineering Fracture Mechanics, 114:92–103, 2013.

[178] Hoover, C.G. and P. Bažant, Z.: *Comprehensive concrete fracture tests: Size effects of Types 1 & 2, crack length effect and postpeak*. Engineering Fracture Mechanics, 110:281–289, 2013.

[179] Hordijk, D.A.: *Tensile and tensile fatigue behaviour of concrete*. Heron, 37(1), 1992.

[180] Hossain, A.B. and Weiss, J.: *Assessing residual stress development and stress relaxation in restrained concrete ring specimens*. Cement and Concrete Composites, 26(5):531–540, 2004.

[181] Houston, W.N., Walsh, K.D., Harraz, A.M., and Houston, S.L.: *Moment/Rotation Effects on Laterally Loaded Drilled Shaft Group Response*. International Journal of Geomechanics, 5(4):304–310, 2005.

[182] Huang, J., Shield, C.K, and French, C.E.W: *Parametric Study of Concrete Integral Abutment Bridges*. Journal of Bridge Engineering, 13(5):511–526, 2008.

[183] Huh, J., Haldar, A., Kwak, K., and Park, J. H.: *Realistic risk assessment of axially loaded pile–soil system using a hybrid reliability method*. Georisk: Assessment and Management of Risk for Engineered Systems and Geohazards, 4(3):118–126, 2010.

[184] Iman, R.L and Conover, W.J.: *Small sample sensitivity analysis techniques for computer models with an application to risk assessment*. Communications in Statistics - Theory and Methods, 17(A9):1749–1842, 1980.

[185] International Federation for Structural Concrete: *Structural concrete, Textbook on behaviour, design and performance - updated knowledge of the CEB/FIB Model Code 1990*, volume 1,2,3 of *Bulletin / fib, International Federation for Structural Concrete Manual, textbook*. fib, Lausanne, 1999.

[186] International Federation for Structural Concrete: *Constitutive modelling of high strength/high performance concrete*, volume 42 of *Bulletin / International Federation for Structural Concrete State-of-art report*. fib, Lausanne, 2008.

[187] International Federation for Structural Concrete: *Model Code 2010 - Final draft*, volume 65 (Volume 1), 66 (Volume 2) of *Bulletin / International Federation for Structural Concrete Draft model code*. International Federation for Structural Concrete, Lausanne, 2012.

[188] International Organization for Standardisation: *ISO 1920-4:2005: Testing of concrete - Part 4: Strength of hardened concrete*, 2005.

[189] Ismael, N.F.: *Axial Load Tests on Bored Piles and Pile Groups in Cemented Sands*. Journal of Geotechnical and Geoenvironmental Engineering, 127(9):766–773, 2001.

[190] Jaccoud, J. P. and Favre, R.: *Flèche des Structures en Béton Armé – Vérification Experimentale d'une Méthode de Calcul*, 1982.

[191] Jackson, P.A.: *Safety format in non-linear analysis of concrete structures*. Proceedings of the ICE - Engineering and Computational Mechanics, 165(1):57–66, 2012.

[192] Jaeger, T. and Marti, P: *Reinforced Concrete Slab Shear Prediction Competition: Entries and Discussion*. ACI Structural Journal, 106(2009):309–318, 3.

[193] Jaeger, T. and Marti, P: *Reinforced Concrete Slab Shear Prediction Competition: Experiments*. ACI Structural Journal, 106(2009):300–307, 3.

[194] Jokela, J.: *Experimental Study Concerning Reinforced Concrete Beams under Thermal and Mechanical Load*. PhD thesis, Nordic Concrete Federation, Oslo.

[195] Jung, B., Morgenthal, G., Timmler, H. G, and Schröter, H. (editors): *Restraint Effects in Reinforced and Prestressed Concrete Structures*, 2011.

[196] Jung, B., Morgenthal, G., and Xu, D.: *Integral bridges: sensitivity of limit state modelling*. Bautechnik - Special Print "Modellqualitäten", 90:32–40, 2013.

[197] Jung, B., Stutz, H., Morgenthal, G., and Wuttke, F.: *Uncertainty Analysis of stiffness prediction for pile group models*. Proceedings of the 10th International Probabilistic Workshop, 2012.

[198] Jung, Bastian, Morgenthal, Guido, and Xu, Dong: *Integrative Sensitivity Analysis Applied to Semi-Integral Concrete Bridges*. Journal of Bridge Engineering, 19(6):04014014, 2014.

[199] Jung, R., Marx, S., Schenkel, M., and Stockmann, R.: *Entwurf und Ausführungsplanung der Stöbnitztalbrücke*. Beton- und Stahlbetonbau, 106(2):81–88, 2011.

[200] Kadleček, Vl. and Modrý, S.: *Size effect of test specimens on tensile splitting strength of concrete: general relation*. Materials and Structures, 35(1):28–34, 2002.

[201] Kang, H.D., Spacone, E., and Willam, K.J.: *A Study of Compressive Failure in Over-Reinforced Concrete Beams*. Proceedings FRAMCOS-3, pages 1195–1210, 1998.

[202] Kausel, E.: *Forced vibrations of circular foundations on layered media*. PhD thesis, Massachusetts Institute of Technology, 1974.

[203] Kaveh, A.: *Structural mechanics: Graph and matrix methods*, volume 1 of *Computational structures technology series*. Research Studies Press, Dover Publ, 3rd edition, 2004.

[204] Kaveh, A.: *Optimal structural analysis*. John Wiley and RSP Research Studies Pr, Chichester and Baldock and Herfordshire, 2nd edition, 2006. `http://www.loc.gov/catdir/enhancements/fy0827/2006014662-b.html`.

[205] Kaynia, A.M.: *Dynamic stiffness and seismic response of pile groups*. PhD thesis, Massachusetts Inst. of Technology, School of Engineering, Cambridge, 1982.

[206] Keitel, H.: *Evaluation Methods for Prediction Quality of Concrete Creep Models*. PhD thesis, university press, Bauhaus-Universität Weimar, 2012.

[207] Keitel, H.: *Quantifying Sources of Uncertainty for Creep Models under Varying Stresses*. Journal of Structural Engineering, 139(6):949–956, 2013.

[208] Keitel, H. and Dimmig-Osburg, A.: *Uncertainty and sensitivity analysis of creep models for uncorrelated and correlated input parameters*. Engineering Structures, 32(11):3758–3767, 2010.

[209] Keitel, H., Dimmig-Osburg, A., Vandewalle, L., and Schueremans, L.: *Selecting creep models using Bayesian methods*. Materials and Structures, 45(10):1513–1533, 2012.

[210] Keitel, H., Jung, B., Motra, H.B., and Stutz, H.: *Quality assessment of coupled partial models considering soil–structure coupling*. Engineering Structures, 59(2):565–573, 2014.

[211] Keitel, H., Karaki, G., Lahmer, T., Nikulla, S., and Zabel, V.: *Evaluation of coupled partial models in structural engineering using graph theory and sensitivity analysis*. Engineering Structures, 33(12):3726–3736, 2011.

[212] Keuser, M., Purainer, R., and Brunner, S.: *Bauteile aus Stahlbeton unter Zugbeanspruchung - RC-Members subjected to Tension State of Stress*. Beton- und Stahlbetonbau, 99(7):552–560, 2004.

[213] Kim, J.B. and Brungraber, R.J.: *Full-scale lateral load tests of pile groups*. Journal of the Geotechnical Engineering Division, 102(1):87–105, 1976.

[214] Kim, W.S. and Laman, J.A.: *Integral abutment bridge response under thermal loading*. Engineering Structures, 32(6):1495–1508, 2010.

[215] Kim, W.S. and Laman, J.A.: *Numerical analysis method for long-term behavior of integral abutment bridges*. Engineering Structures, 32(8):2247–2257, 2010.

[216] Kiureghian, A.D. and Ditlevsen, O.: *Aleatory or epistemic? Does it matter?* Structural Safety, 31(2):105–112, 2009.

[217] Koizumi, Y. and Ito, K.: *Field tests with regard to pile driving and bearing capacity of piled foundations*. Soils and Foundations, 7(3):30–53, 1967.

[218] Kong, G., Liu, H.L., Yang, Q., Liang, R., and Zhou, H.: *Mathematical Model and Analysis of Negative Skin Friction of Pile Group in Consolidating Soil*. Mathematical Problems in Engineering, 2013.

[219] König, G. and Fehling, E.: *Grundlagen zur Rißbreitenbeschränkung im Spannbetonbau*. Beton- und Stahlbetonbau, 83(12):317–323, 1988.

[220] König, G. and Fehling, E.: *Zur Rißbreitenbeschränkung im Stahlbetonbau: Limiting the crack width in reinforced concrete construction*. Beton- und Stahlbetonbau, 83(6,7):161–167,199–204, 1988.

[221] König, G. and Grimm, R.: *Hochleistungsbeton : Sonderdruck aus dem Betonkalender*. Ernst & Sohn, Berlin, 1996.

[222] König, G., Hosser, D., and Schobbe, W.: *Sicherheitsanforderungen für die Bemessung von baulichen Anlagen nach den Empfehlungen des NABau - eine Erläuterung*. Bauingenieur, 57:69–78, 1982.

[223] König, G., Meyer, J., and Sint, A.: *Round Robin analysis on modelling of over-reinforced concrete beams - Calculation of the load deformation behaviour of concrete beams with the BDZ model*. Proceedings FRAMCOS-3, pages 1241–1251, 1998.

[224] König, G., Pommerening, D., and Tue, N.V.: *Nichtlineares Last-Verformungs-Verhalten von Stahlbeton- und Spannbetonbauteilen, Verformungsvermögen und Schnittgrößenermittlung*, volume 492 of *German Board for Reinforced Concrete (DAfStb)*. Berlin : Beuth edition, 1999.

[225] König, G., Scheidler, D., and Fehling, E.: *Grundlagen zur Traglastermittlung unbewehrter Betonbauteile unter Zugbeanspruchung: Fundamentals to determine the load capacity of plain concrete structural members under tension*. Beton- und Stahlbetonbau, 81(11-12):292–296, 325–329, 1986.

[226] König, G., Soukhov, D., and Jungwirth, F.: *Sichere Betonproduktion für Stahlbetontragwerke*. Fraunhofer-IRB-Verlag, 1998.

[227] König, G. and Tue, N.V.: *Grundlagen und Bemessungshilfen für die Rißbreitenbeschränkung im Stahlbeton und Spannbeton sowie Kommentare, Hintergrundinformationen und Anwendungsbeispiele zu den Regelungen nach DIN 1045, EC2 und Model Code 90*, volume 466 of *German Board for Reinforced Concrete (DAfStb)*. Beuth, Berlin, 1996.

[228] Kordina, K., Rostásy, F.S., and Svensvik, B.: *Tragfähigkeit und Verformung von Stahlbetonbalken unter Biegung und gleichzeitigem Zwang infolge Auflagerverschiebung*, volume 336 of *German Board for Reinforced Concrete (DAfStb)*. Ernst, Berlin, 1982.

[229] Kordina, K., Schubert, L., and Troitzsch, U.: *Kriechen von Beton unter Zugbeanspruchung*, volume 498 of *German Board for Reinforced Concrete (DAfStb)*. Beuth, Berlin, 2000.

[230] Kotsovos, M.D.: *Effect of testing techniques on the post-ultimate behaviour of concrete in compression*. Matériaux et Constructions, 16(1):3–12, 1983.

[231] Kotsovos, M.D.: *Round Robin finite element analysis of over-reinforced concrete beams*. PhD thesis, Athens University, 1997.

[232] Krizek, J.: *Soil–Structure Interaction of Integral Bridges*. Structural Engineering International, 21(2):169–174, 2011.

[233] Kühlen, R.Th.: *Stahlbetonbiegebalken unter Zwangsbeanspruchung aus einseitiger Erwärmung*. PhD thesis, Technische Universität, Darmstadt, 1994.

[234] Lahmer, T., Knabe, T., Nikulla, S., and Reuter, M.: *Bewertungsmethoden für Modelle des konstruktiven Ingenieurbaus - Evaluation methods for models used in civil engineering*. Bautechnik - Sonderdruck "Modellqualitäten", 88:60–64, 2011.

[235] Lanigan, A.G.: *The Temperature Response of Concrete Box-Girder Bridges*. PhD thesis, university press, University of Auckland, 1973.

[236] Larsson, O.: *Modelling of temperature profiles in a concrete slab under climatic exposure*. Structural Concrete, 10(4):193–201, 2009.

[237] Larsson, O.: *Climatic Thermal Stresses in the Vätösund Box-Girder Concrete Bridge*. Structural Engineering International, 22(3):318–322, 2012.

[238] Larsson, O. and Karoumi, R.: *Modelling of Climatic Thermal Actions in Hollow Concrete Box Cross-Sections*. Structural Engineering International, 21(1):74–79, 2011.

[239] Larsson, O. and Thelandersson, S.: *Estimating extreme values of thermal gradients in concrete structures*. Materials and Structures, 44(8):1491–1500, 2011.

[240] Larsson, O. and Thelandersson, S.: *Transverse thermal stresses in concrete box cross-sections due to climatic exposure*. Structural Concrete, 13(4):227–235, 2012.

[241] Leamer, E.E: *Specification searches: Ad hoc inference with nonexperimental data*. Wiley series in probability and mathematical statistics. Wiley, New York and NY, 1978.

[242] Lee, K.M. and Xiao, Z.R.: *A simplified nonlinear approach for pile group settlement analysis in multilayered soils*. Canadian Geotechnical Journal, 38(5):1063–1080, 2001.

BAUHAUS
UNIVERSITÄTSVERLAG

[243] Legeron, F. and Mazars, J.: *Prediction of the Behavior of Over-Reinforced Concrete Beams with Two Levels of Simplified Approach*. Proceedings FRAMCOS-3, pages 1223–1232, 1998.

[244] Leonhardt, F.: *Rissebeschränkung*. Beton- und Stahlbetonbau, 71(1):14–20, 1976.

[245] Leonhardt, F.: *Zur Behandlung von Rissen im Beton in den deutschen Vorschriften*. Beton- und Stahlbetonbau, 80(7,8):179–184,209–215, 1985.

[246] Leonhardt, F.: *Cracks and Crack Control in Concrete Structures*. PCI Journal, 1988.

[247] Leonhardt, F., Kolbe, G., and Peter, J.: *Temperaturunterschiede gefähren Spannbetonbrücke*. Beton- und Stahlbetonbau, 60(7):157–163, 1965.

[248] Lichte, U.: *Klimatische Temperatureinwirkungen und Kombinationsregeln bei Brückenbauwerken*. PhD thesis, Universität der Bundeswehr, München, 2005.

[249] Lindner, C.P. and Sprague, J.C.: *Effect of depth of beam upon the modulus of rupture of plain concrete*. Proc. ASTM, 55, 1955.

[250] Lu, Z. H. and Zhao, Y. G.: *Empirical Stress-Strain Model for Unconfined High-Strength Concrete under Uniaxial Compression*. Journal of Materials in Civil Engineering, 22(11):1181–1186, 2010.

[251] Lutz, B.: *Beitrag zur Modellierung des Tragverhaltens kombinierter Pfahl-Plattengründungen (KPP) unter Verwendung geotechnischer Messungen*. PhD thesis, Institut und Versuchsanstalt für Geotechnik, Technische Universität Darmstadt, 2002.

[252] Macgregor, J.G and Bartlett, F.M: *Statistical Analysis of the Compressive Strength of Concrete in Structures*. ACI Materials Journal, 1996.

[253] MacKay, D.J.C.: *Bayesian Interpolation*. Neural Computation, 4(3):415–447, 1992.

[254] MacKay, M.D., Beckham, R.J., and Conover, W.J.: *A Comparison of three Methods for Selecting Values of Input Variables in the Analysis of Output from a Computer Code*. Technometrics, 21:239–245, 1979.

[255] Malárics, V.: *Ermittlung der Betonzugfestigkeit aus dem Spaltzugversuch an zylindrischen Betonproben*. PhD thesis, KIT, Karlsruhe and Hannover and Karlsruher Institut für Technologie, 2011.

[256] Malárics, V. and Müller, H.S.: *Experimental and numerical analysis of the fracture process in the splitting tension test of concrete*. Proceedings of Fracture Mechanics of Concrete and Concrete Structures (FraMCoS), 2007.

[257] Malárics, V. and Müller, H.S.: *Evaluation of the splitting tension test for concrete from a fracture mechanical point of view*. Proceedings of Fracture Mechanics of Concrete and Concrete Structures (FraMCoS), pages 709–716, 2010.

[258] Mancevski, D.: *Nichtlineare Analyse von Stahlbetonkonstruktionen mit konsistenten Simulationsalgorithmen*. PhD thesis, Ruhr-Universität Bochum, Bochum, 1998.

[259] Mang, H.A. and Hofstetter, G.: *Festigkeitslehre*. Springer Berlin Heidelberg, Berlin and Heidelberg and s.l, 4., aktualisierte aufl. 2013 edition, 2013. `http://dx.doi.org/10.1007/978-3-642-40752-9`.

[260] Mangerig, I., Lichte, U., and Beucher, S.: *Bewertung der Sicherheitsanforderungen von Temperatureinwirkungen auf Brücken*. Stahlbau, 79(3):167–180, 2010.

[261] Marí, Antonio R. and Hellesland, Jostein: *Lower Slenderness Limits for Rectangular Reinforced Concrete Columns*. Journal of Structural Engineering, 131(1):85–95, 2005.

[262] Mark, P. and Schnütgen, B.: *Grenzen elastischen Materialverhaltens von Beton*. Beton- und Stahlbetonbau, 96(5):373–378, 2001.

[263] Marx, S., Krontal, L., Bätz, S., and Vehlow, A.: *Die Scherkondetalbrücke, die erste semi-integrale Talbrücke der DB AG auf der Neubaustrecke Erfurt - Leipzig/Halle VDE 8.2*. Beton- und Stahlbetonbau, 105(3):134–141, 2010.

[264] Marx, S. and Seidl, G.: *Integral Railway Bridges in Germany*. Structural Engineering International, 21(3):332–340, 2011.

[265] Matlock, H. and Reese, L.C.: *Generalised solutions for laterally loaded piles*. Journal of the Soil Mechanics and Foundations Division, 86(5):63–94, 1960.

[266] Maurer, R. and Arnold, A.: *Bemessung von Tragwerken aus Stahlbeton und Spannbeton für eine kombinierte Beanspruchung aus Last und Biegezwang - Design of reinforced and prestressed concrete structures for combined effects due to loads and restrained deformations*. Bauingenieur, 84(10):427–437, 2009.

[267] Maurer, R. and Djouahra, G.: *Stahlbetonbauteile unter einer kombinierten Beanspruchung aus Last und zentrischem Zwang - Reinforced Concrete Elements subjected to a Combined Effect of Action due to Load and Centric Restraint*. Beton- und Stahlbetonbau, 105(10):640–652, 2010.

[268] Maurer, R., Tue, N.V., and Arnold, A.: *Mindestbewehrung zur Begrenzung der Rissbreiten bei dicken Wänden*. Bauingenieur, 80(10):479–485, 2005.

[269] Maurer, R., Weigel, F., and Arnold, A.: *Bauwerksmonitoring an einer Brücke aus Hochleistungsbeton*. Beton- und Stahlbetonbau, 100(3):195–206, 2005.

[270] Mazzotti, C. and Savoia, M.: *Nonlinear Creep Damage Model for Concrete under Uniaxial Compression*. Journal of Engineering Mechanics, 129(9):1065–1075, 2003.

[271] McClelland, B. and Focht, J.A.Jr.: *Soil modulus for laterally loaded piles*. Journal of the Soil Mechanics and Foundations Division, 123:1049–1063, 1958.

[272] Meissner, H.: *Tragverhalten axial und horizontal belasteter Bohrpfähle in körnigen Böden*. PhD thesis, Institut für Bodenmechanik und Felsmechanik der Univ. Fridericiana, Karlsruhe, 1983.

[273] Menegotto, M. and Pinto, PE.: *Method of analysis for cyclically loaded reinforced concrete plane frames including changes in geometry and nonelastic behaviour of elements under combined normal force and bending*. IABSE symposium of elements under combined normal force and bending, 1973.

[274] Meyer, B.L., Branson, D.E., Schumann, C.G., and Christiason, M.L.: *The Prediction of Creep and Shrinkage Properties of Concrete - Final Report No. 70-5*. PhD thesis, Iowa Highway Commission.

[275] Meyer, J.: *Ein Beitrag zur Untersuchung der Verformungsfähigkeit von Bauteilen aus Beton unter Biegedruckbeanspruchung*. PhD thesis, Universität Leipzig, Leipzig Germany, 1998.

[276] Mier, J.G. van: *Strain-Softening of Concrete under Multiaxial Loading Conditions*. Techn. Hogeschool, PhD thesis, Eindhoven, 1984.

[277] Mier, J.G. van: *Multiaxial strain-softening of concrete - Fracture and Load-Histories*. Materials and Structures, 19(3):179–200, 1986.

[278] Mier, J.G. van: *Mode II Fracture Localization in Concrete Loaded in Compression*. Journal of Engineering Mechanics, 135(1):1–8, 2009.

[279] Mier, J.G.M. and Ulfkjœr, J.P.: *Round-Robin analysis of over-reinforced concrete beams - Comparison of results*. Materials and Structures, 33(6):381–390, 2000.

[280] Mindlin, R.D.: *Force at a Point in the Interior of a Semi-Infinite Solid*. Journal of Apllied Physics, 7(5):195–202, 1936.

[281] Mirambell, E. and Aguado, A.: *Temperature and Stress Distributions in Concrete Box Girder Bridges*. Journal of Structural Engineering, 116(51):2388–2409, 1990.

[282] Mohr, O.C.: *Über die Darstellung des Spannungszustandes und des Deformationszustandes eines Körperelementes und über die Anwendung derselben in der Festigkeitslehre*. Civilingenieur, (28), 1882.

[283] Mokwa, R.L. and Duncan, J.M.: *Laterally Loaded Pile Group Effects and P-Y Multipliers*. ASCE Geotechnical Special Publication, 113:728–742, 2001.

[284] Mokwa, R.L. and Duncan, J.M.: *Rotational Restraint of Pile Caps during Lateral Loading*. Journal of Geotechnical and Geoenvironmental Engineering, 129(9):829–837, 2003.

[285] Montgomery, D.C. and Runger, G.C.: *Applied statistics and probability for engineers*. Wiley, Hoboken and NJ, 5th edition, 2011.

[286] Most, T.: *Assessment of structural simulation models by estimating uncertainties due to model selection and model simplification*. Computers & Structures, 89(17-18):1664–1672, 2011.

[287] Müller, H.S., Bažant, Z.P., and Kuttner, C.H.: *Database on Creep and Shrinkage Tests - RILEM Subcommittee 5 Report (RILEM TC 107-CSP)*, 1991.

[288] Müller, H.S. and Hilsdorf, H.K.: *Constitutive relations for structural concrete*. In *Selected justification notes*, volume 217 of *Bulletin d'information / Comité Euro-International du Béton, CEB*. Comité Euro-International du Béton CEB, Lausanne, 1993.

[289] Murzewski, J.: *Sicherheit der Baukonstruktionen*. VEB Verlag für Bauwesen, Berlin, 1974.

[290] Mylonakis, G.: *Contributions to static and seismic analysis of piles and pile-supported bridge piers*. PhD thesis, State University of New York at Buffalo, 1995.

[291] Mylonakis, G. and Gazetas, G.: *Settlement and additional internal forces of grouped piles in layered soil*. Géotechnique, 48(1):55–72, 1998.

[292] Neville, A.M: *Properties of concrete*. Pearson/Prentice-Hall, Harlow, 5th edition, 2011.

[293] Nilson, T. and Aven, T.: *Models and model uncertainty in the context of risk analysis*. Reliability Engineering & System Safety, 79:309–317, 2003.

[294] Noakowski, P.: *Verbundorientierte, kontinuierliche Theorie zur Ermittlung der Rißbreite. Wirklichkeitsnaher und einfacher Nachweis unter Berücksichtigung der Verbundgesetze und der Betonzugfestigkeit sowie unter Verknüpfung des Erstriß- und Endrißzustands*. Beton- und Stahlbetonbau, 80(7,8):185–190,215–221, 1985.

[295] Noakowski, P.: *Mitwirkungsgesetze zur Ermittlung der Verformungen und der Zwangbeanspruchung bei gleichzeitiger Lastbeanspruchung: Tension stiffening laws for the determination of deformations and constraint at loading*. Beton- und Stahlbetonbau, 81(12):318–325, 1986.

[296] Noakowski, P., Breddermann, M., Harling, A., and Schnetgöke, J.: *Rißbildung in turmartigen Tragwerken: Schleuderbetonmast versus Stahlbetonschornstein: Crack Formation in Tower like Structures - Mast of centrifugal concrete vs. chimney of normal concrete*. Beton- und Stahlbetonbau, 100(7):538–548, 2005.

[297] Nogami, T. and Chen, H.L.: *Simplified Approach for Axial Pile Group Response Analysis*. Journal of Geotechnical Engineering, 110(9):1239–1255, 1984.

[298] Nogami, T. and Paulson, S.K.: *Transfer matrix approach for nonlinear pile group response analysis*. International Journal for Numerical and Analytical Methods in Geomechanics, 9(4):299–316, 1985.

[299] Novák, B., Kuhlmann, U., and Euler, M.: *Einwirkung, Widerstand, Tragwerk*, volume 1 of *Werkstoffübergreifendes Entwerfen und Konstruieren*. Ernst & Sohn, Berlin, 2012.

[300] O'Neill, M.W: *Field study of pile group action, Interim report, Mathematical models and design of load tests*. Report FHWA/RD-81/001, US Federal Highway Administration, US Department of Transportation, 1981.

[301] O'Neill, M.W, Hawkins, R.A., and Mahar, L.J.: *Load Transfer Mechanisms in Piles and Pile Groups*. Journal of the Geotechnical Engineering Division, 108(12):1605–1623, 1982.

[302] Ooi, P.S K., Lin, X., and Hamada, H.S: *Numerical Study of an Integral Abutment Bridge Supported on Drilled Shafts*. Journal of Bridge Engineering, 15(1):19–31, 2010.

[303] Ooi, P.S.K. and Duncan, J.M.: *Lateral Load Analysis of Groups of Piles and Drilled Shafts*. Journal of Geotechnical Engineering, 120(6):1034–1050, 1994.

[304] Ooi, P.S.K., Lin, X., and Hamada, H.S.: *Field Behavior of an Integral Abutment Bridge Supported on Drilled Shafts*. Journal of Bridge Engineering, 15(1):4–18, 2010.

[305] Ottaviani, M.: *Three-dimensional finite element analysis of vertically loaded pile groups*. Géotechnique, 25(2):159–174, 1975.

[306] Ožbolt, J., Meštrović, D., Li, Y. J, and Eligehausen, R.: *Compression Failure of Beams Made of Different Concrete Types and Sizes*. Journal of Structural Engineering, 126(2):200–209, 2000.

[307] Pan, Z., Fu, C.C, and Jiang, Y.: *Uncertainty Analysis of Creep and Shrinkage Effects in Long-Span Continuous Rigid Frame of Sutong Bridge*. Journal of Bridge Engineering, 16(2):248–258, 2011.

[308] Pardey, A.: *Physikalisch nichtlineare Berechnung von Stahlbetonplatten im Vergleich zur Bruchlinientheorie*, volume 441 of *German Board for Reinforced Concrete (DAfStb)*. Beuth, Berlin, 1994.

[309] Park, I. and Grandhi, R.V: *Quantification of model-form and parametric uncertainty using evidence theory*. Structural Safety, 39:44–51, 2012.

[310] Phoon, K. K.: *Reliability-based design in geotechnical engineering: Computations and applications*. Taylor & Francis, New York and NY, 2008.

[311] Phoon, K. K. and Kulhawy, F.H.: *Characterization of geotechnical variability*. Canadian Geotechnical Journal, 36(4):612–624, 1999.

[312] Phoon, K. K. and Kulhawy, F.H.: *Evaluation of geotechnical property variability*. Canadian Geotechnical Journal, 36(4):625–639, 1999.

[313] Pölling, R.: *Eine praxisnahe, schädigungsorientierte Materialbeschreibung von Stahlbeton für Strukturanalysen*. PhD thesis, university press, Dülmen and Bochum, 2001.

[314] Popovics, S.: *A numerical approach to the complete stress-strain curve of concrete*. Cement and Concrete Research, 3(5):583–599, 1973.

[315] Poulos, H.: *Spannungen und Setzungen im Boden*. In Smoltczyk, Ulrich (editor): *Grundbau-Taschenbuch*. Ernst, Berlin, 2001.

[316] Poulos, H.G.: *Analysis of the settlement of pile groups*. Géotechnique, 18(3):449–471, 1968.

[317] Poulos, H.G.: *Behavior of laterally loaded piles: I Single Piles*. Journal of Soil Mechanics and Foundations Division, 97(5):711–731, 1971.

[318] Poulos, H.G.: *Behavior of laterally loaded piles: II Pile groups*. Journal of Soil Mechanics and Foundations Division, 97(5):733–751, 1971.

[319] Poulos, H.G. and Davis, E.H.: *The Settlement Behaviour of Single Axially Loaded Incompressible Piles and Piers*. Géotechnique, 18(3):351–371, 1968.

[320] Poulos, H.G. and Davis, E.H.: *Pile foundation analysis and design*. Seires in geotechnical engineering. Wiley, New York, 1980.

[321] Prakash Rao, D.S.: *Temperature Distributions and Stresses in Concrete Bridges*. American Concrete Institute, 83(4):588–596, 1986.

[322] Priestley, M.J.N.: *Long term observations of concrete structures analysis of temperature gradient effects*. Materials and Structures, 18(4):309–316, 1985.

[323] Priestly, M.J.N.: *Design Thermal Gradients for Concrete Bridges*. New Zealand Engineering, 31(9):213–219, 1976.

[324] Priestly, M.J.N.: *Design of Concrete Bridges for Temperature Gradients*. American Concrete Institute, 75(5):209–217, 1978.

[325] Puche, M.: *Self Equilibrating Stresses and Restraint in Concrete Structural Design*. Darmstadt Concrete, Annual Journal on Concrete and Concrete structures, (1), 1986.

[326] Pugasap, K., Kim, W., and Laman, J.A.: *Long-Term Response Prediction of Integral Abutment Bridges*. Journal of Bridge Engineering, 14(2):129–139, 2009.

[327] Quast, U.: *On the selection of an adequate method for considering the contribution of concrete in tension, in german: Zur Auswahl eines geeigneten Verfahrens für die Berücksichtigung der Mitwirkung des Betons auf Zug*. Bautechnik, 87(7):397–403, 2010.

[328] Rackwitz, F.: *Numerische Untersuchungen zum Tragverhalten von Zugpfählen und Zugpfahlgruppen in Sand auf der Grundlage von Probebelastungen*. PhD thesis, Gundbauinstitut, Technische Universität Berlin, 2003.

[329] Ralle, B.: *Höhere Mathematik: Formeln und Hinweise ; kleiner Wissensspeicher*. Dt. Verl. für Grundstoffindustrie, Leipzig, 12th edition, 1990.

[330] Randolph, M.F.: *A theoretical study of the performance of piles*. PhD thesis, University of Cambridge, Cambridge, 1977.

[331] Randolph, M.F.: *The response of flexible piles to lateral loading*. Géotechnique, 31(2):247–259, 1981.

[332] Randolph, M.F. and Wroth, C.P.: *Analysis of deformation of vertically loaded piles*. Journal of the Geotechnical Engineering Division, 104:1465–1488, 1978.

[333] Randolph, M.F. and Wroth, C.P.: *A simple approach to pile design and the analysis of pile tests*. Behavior of deep foundations : A Symposium, Boston, 1979.

[334] Randolph, M.F. and Wroth, C.P.: *An analysis of the vertical deformation of pile groups*. Géotechnique, 29(4):423–439, 1979.

[335] Raoufi, K., Pour-Ghaz, M., Poursaee, A., and Weiss, J.: *Restrained Shrinkage Cracking in Concrete Elements: Role of Substrate Bond on Crack Development*. Journal of Materials in Civil Engineering, 23(6):895–902, 2011.

[336] Raphael, J.M.: *Tensile strength of concrete*. ACI Journal, 81(2):158–165, 1984.

[337] Raue, E.: *Nichtlineare Querschnittsanalyse als Optimierungsproblem - Nonlinear analysis of cross-sections as an optimisation problem*. Bautechnik, 82(11):796–809, 2005.

[338] Raue, E. (editor): *Non-linear analysis of composite cross-sections by non-linear optimisation*, 2007.

[339] Reese, L.C. and Matlock, H.S.: *Non-dimensional solutions for laterally loaded piles with soil modulus proportional to depth*. Proc. 8th Texas Conf. on Soil Mech and Found. Eng., pages 1–41, 1956.

[340] Remmel, G.: *Zum Zug- und Schubtragverhalten von Bauteilen aus hochfestem Beton*, volume 444 of *German Board for Reinforced Concrete (DAfStb)*. Beuth, Berlin, 1994.

[341] Reuter, M.: *Multicriterial evaluation method for the prognosis quality of complex engineering models*. PhD thesis, Univ, Weimar and Weimar, 2012.

[342] Reuter, M. and Werner, F.: *Evaluation of complex engineering models using model quality analysis*. Engineering Structures, 42:410–419, 2012.

[343] RILEM TC 148-SSC: *Strain-softening of concrete in uniaxial compression*. Materials and Structures, 30(4):195–209, 1997.

[344] RILEM TC 148-SSC: *Test method for measurement of the strain-softening behaviour of concrete under uniaxial compression*. Materials and Structures, 33(6):347–351, 2000.

[345] Riley, M.E. and Grandhi, R.V.: *Quantification of model-form and predictive uncertainty for multi-physics simulation*. Computers & Structures, 89(11-12):1206–1213, 2011.

[346] Riley, M.E, Grandhi, R.V, and Kolonay, R.: *Quantification of modeling uncertainty in aeroelastic design: In: 51st AIAA/ASME/ASCE/AHS/ASC structures, structural dynamics and materials conference, Orlando, FL*, 2010.

[347] Rocco, C., Guinea, G.V., Planas, J., and Elices, M.: *Size effect and boundary conditions in the Brazilian test: Experimental verification*. Materials and Structures, 32(3):210–217, 1999.

[348] Rocco, C., Guinea, G.V., Planas, J., and Elices, M.: *Size effect and boundary conditions in the brazilian test: theoretical analysis*. Materials and Structures, 32(6):437–444, 1999.

[349] Roik, K.: *Vorlesungen über Stahlbau: Grundlagen*. Ernst & Sohn, Berlin, 2nd edition, 1983.

[350] Rollins, K.M., Olsen, R.J., Egbert, J.J., Jensen, D.H., Olsen, K.G., and Garrett, B.H.: *Pile Spacing Effects on Lateral Pile Group Behavior: Load Tests*. Journal of Geotechnical and Geoenvironmental Engineering, 132(10):1262–1271, 2006.

[351] Rossi, P., Wu, X., Maou, F., and Belloc, A.: *Scale effect on concrete in tension*. Materials and Structures, 27(8):437–444, 1994.

[352] Rostásy, F.S. and Henning, W.: *Zwang und Oberflächenbewehrung dicker Wände*. Beton- und Stahlbetonbau, 80(4,5):108–113,134–136, 1985.

[353] Rudolf, M.: *Beanspruchung und Verformung von Gründungskonstruktionen auf Pfahlrosten und Pfahlgruppen unter Berücksichtigung des Teilsicherheitskonzeptes*. PhD thesis, Universität Kassel, 2005.

[354] Rudolf, M. and Kempfert, H. G.: *Setzungen und Beanspruchungen bei Gründungen auf Pfahlgruppen - Settlements and pile resistance of foundations by pile groups*. Bautechnik, 83(9):618–625, 2006.

[355] Rui-Wamba, J., García-Acón, C., and Estrada, I.: *A Spanish Perspective on Integral High-Speed Railway Viaducts*. Structural Engineering International, 21(3):341–345, 2011.

[356] Rüsch, H.: *Researches Toward a General Flexural Theory for Structural Concrete*. ACI Journal, 57:1–28, 1960.

[357] Rüsch, H., Sell, R., and Rackwitz, R.: *Statistische Analyse der Betonfestigkeit*. Beuth Verlag GmbH, 1969.

[358] Russel, H.G. and Larson, S.C.: *Thirteen Years of Deformations in Water Tower Place*. ACI Structural Journal, 86(2):182–191, 1989.

[359] Saetta, A., Scotta, R., and Vitaliani, R.: *Stress Analysis of Concrete Structures Subjected to Variable Thermal Loads*. Journal of Structural Engineering, 121(3):446–457, 1995.

[360] Saltelli, A., Ratto, M., Andres, T., Campolongo, F., Cariboni, J., and Gatelli, D.: *Global Sensitivity Analysis: The Primer*. Wiley-Interscience, 1st edition, 2008.

[361] Saltelli, A., Tarantola, S., Campolongo, F., and Ratto, M.: *Sensitivity analysis in practice - A guide to assessing scientific models*. John Wiley & Sons Ltd, Chichester, 2004.

[362] Sanayei, M., Arya, B., Santini, E.M, and Wadia-Fascetti, S.: *Significance of Modeling Error in Structural Parameter Estimation*. Computer-Aided Civil and Infrastructure Engineering, 16(1):12–27, 2001.

[363] Sangha, C.M. and Dhir, R.K.: *Strength and complete stress-strain relationships for concrete tested in uniaxial compression under different test conditions*. Matériaux et Constructions, 5(6):361–370, 1972.

[364] Sargin, M.: *Stress - strain relationships for concrete and the analysis of structural concrete sections*. University of Waterloo, Waterloo and Ontario, 1971.

[365] Schenkel, M., Goldack, A., Schlaich, J., and Kraft, S.: *Die Gänsebachtalbrücke, eine integrale Talbrücke der DB AG auf der Neubaustrecke Erfurt-Leipzig/Halle*. Beton- und Stahlbetonbau, 105(9):590–598, 2010.

[366] Schenkel, M., Marx, S., and Krontal, L.: *Innovative Großbrücken im Eisenbahn-Hochgeschwindigkeitsverkehr am Beispiel der Neubaustrecke Erfurt-Leipzig/Halle*. Beton- und Stahlbetonbau, 104(11):782–789, 2009.

[367] Schießl, P.: *Mindestbewehrung zur Vermeidung klaffender Risse*. PhD thesis, München, 1985.

[368] Schlangen, E.: *Experimental and Numerical Analysis of Fracture Processes in Concrete*. PhD thesis, TU Delft, Delt, 1993.

[369] Schlune, H., Plos, M., and Gylltoft, K.: *Safety formats for nonlinear analysis tested on concrete beams subjected to shear forces and bending moments*. Engineering Structures, 33(8):2350–2356, 2011.

[370] Schlune, H., Plos, M., and Gylltoft, K.: *Safety formats for non-linear analysis of concrete structures*. Magazine of Concrete Research, 64(7):563–574, 2012.

[371] Schnell, J., Kautsch, R., Noakowski, P., and Breddermann, M.: *Verhalten von Hochbaudecken bei Zugkräften aus Zwang: Einfluß von Kriechen, Betonfestigkeit, Temperaturdifferenz, Plattendicke und Spannweite - Auswirkung auf Schnittgrößen, Stahlspannung, Rißbreite, Druckzonenhöhe und Durchbiegung*. Beton- und Stahlbetonbau, 100(5):406–415, 2005.

[372] Schröter, Hendrik: *Nichtlineare Analyse von Verbundelementen auf der Grundlage von Energieprinzipien unter Anwendung der mathematischen Optimierung*. PhD thesis, Univ, Kromsdorf and Weimar, 2014.

[373] Schuëller, G.I: *Einführung in die Sicherheit und Zuverlässigkeit von Tragwerken*. Ernst & Sohn, Berlin, 1981.

[374] Schwarz, G.: *Estimating the Dimension of a Model*. The Annals of Statistics, 6(2):461–464, 1978.

[375] Scott, R.F.: *Foundation analysis*. Prentice-Hall, 1981.

[376] Shafer, G.: *A mathematical theory of evidence*. Princeton Univ. Press, Princeton and N.J, 1976.

[377] Sharnouby, B. El. El and Novak, M.: *Stiffness constants and interaction factors for vertical response of pile groups*. Canadian Geotechnical Journal, 27(6):813–822, 1990.

[378] Shen, J. H.: *Lineare und nichtlineare Theorie des Kriechens und der Relaxation von Beton unter Druckbeanspruchung*, volume 432 of *Deutscher Ausschuss für Stahlbeton*. Beuth, Berlin, 1992.

[379] Sieber, E.: *Development of Deviation of Compressive Strength in Concrete*. Beton- und Stahlbetonbau, 102, Ed.7:450–455, 2007.

BAUHAUS
UNIVERSITÄTSVERLAG

[380] Snowling, S.D. and Kramer, J.R.: *Evaluating modelling uncertainty for model selection*. Ecological Modelling, 138(1-3):17–30, 2001.

[381] Sobol, I.M.: *Sensitivity Estimates for Nonlinear Mathematical Models*. Mathematical Modeling and Computational Experiment, 1:407–414, 1993.

[382] Somo, S. and Hong, H.P.: *Modeling error analysis of shear predicting models for RC beams*. Structural Safety, 28(3):217–230, 2006.

[383] Soukhov, D.: *Representative values of thermal actions for concrete bridges*. Progress in Structural Engineering and Materials, 2(4):495–501, 2000.

[384] Spaethe, G.: *Die Sicherheit tragender Baukonstruktionen*. Springer, Wien and New York, 2nd edition, 1992.

[385] Specht, M. and Fouad, N.A.: *Temperatureinwirkungen auf Beton-Kastenträgerbrücken durch Klimaeinflüsse*. Beton- und Stahlbetonbau, 93(10,11):281–285,319–323, 1998.

[386] Steiger, H., Zeißler, T., Bernhard, M., and Meyer, H.: *Integrale Großbrücken mit flexiblen Widerlagern*. Beton- und Stahlbetonbau, 107(3):175–182, 2012.

[387] Strauss, A., Bergmeister, K., and März, S.: *Reliability Assessment of Eccentric loaded Columns, in german: Zuverlässigkeitsbetrachtung exzentrisch belasteter Stahlbetonstützen*. Beton- und Stahlbetonbau, 102(4):223–230, 2007.

[388] Strauss, A., Bergmeister, K., Novák, D., and David, L.: *Probabilistic Response Identification and Monitoring of Concrete Structures*. Beton- und Stahlbetonbau, 99(12):967–974, 2004.

[389] Strauß, P.: *Untersuchungen zum Einfluss der Berechnungsmethode auf die Größe von Zwangschnittgrößen in Stahlbeton-Tragwerken*. Beton- und Stahlbetonbau, 105(10):653–659, 2010.

[390] Stroband, J.: *Experimental research into the bond behaviour of reinforcing bars in lightweight and normal weigth concrete*. PhD thesis, Delft University of Technology, Delft, 1991.

[391] Tasdemir, M.A., Maji, A.K., and Shah, S.P.: *Crack Propagation in Concrete under Compression*. Journal of Engineering Mechanics, 116(5):1058–1076, 1990.

[392] Thurston, S.J., Priestly, J.N., and Cooke, N.: *Influence of Cracking on Thermal Response of Reinforced Concrete Bridges*. Concrete International, 6(8):36–43, 1984.

[393] Timoshenko, S.P. and Goodier, J.N.: *Theory of elasticity*. Engineering societies monographs. McGraw-Hill, New York, 3rd edition, 1970.

[394] Trost, H.: *Auswirkungen des Superpositionsprinzips auf Kriech- und Relaxationsprobleme bei Beton und Spannbeton*. Beton- und Stahlbetonbau, 62:230–238, 1967.

[395] Tsang, S.W.F and Chu, L.Y.L: *An experimental study of the Tension Stiffening effect on the structural stiffness of Reinforced Concrete Cantilevered Balcony Structures using resonant frequency measurement approach*. Construction and Building Materials, 25(5):2690–2699, 2011.

[396] Tue, N.V.: *Zur Spannungsumlagerung im Spannbeton bei der Rißbildung unter statischer und wiederholter Belastung*, volume 435 of *German Board for Reinforced Concrete (DAfStb)*. Beuth, Berlin, 1993.

[397] Tue, N.V., Schenck, G., and Schwarz, J.: *Absicherung der statistisch erhobenen Festbetonkennwerte für die neue Normengeneration*, volume 3094 of *Bauforschung*. Fraunhofer-IRB-Verl, Stuttgart, 2005.

[398] Ulrik Nilsen, A. and Monteiro, P.: *Concrete: A three phase material*. Cement and Concrete Research, 23(1):147–151, 1993.

BAUHAUS
UNIVERSITÄTSVERLAG

[399] United States Enviromental Protection Agency: *Guidance on the Development, Evaluation, and Application of Environmental Models*, 2009.

[400] Valliappan, S., Lee, I.K., and Boonlualohr, P.: *Settlement analysis of piles in layered soil*. Australian Road Research Board (ARRB) Conference, 7th, 1974, Adelaide, 7(7):144–153, 1974.

[401] Vismann, U.: *Zuverlässigkeitstheoretische Verifikation von Bemessungskriterien im Stahlbetonbau*. PhD thesis, university press, Technische Universität München, 1995.

[402] Wang, J.: *Piers and Columns, in: Bridge Engineering - Handbook: Edited by Chen,W.-F. and Duan, L.* CRC Press, Boca Raton, 2000.

[403] Wang, P.T., Shah, S.P., and Naaman, A.E.: *Stress-strain curves of normal and lightweight concrete in compression*. ACI Journal, 75(11):603–611, 1978.

[404] Wee, T.H., Chin, M.S., and Mansur, M.A.: *Stress-Strain Relationship of High-Strength Concrete in Compression*. Journal of Materials in Civil Engineering, 8(2):70–76, 1996.

[405] Weiss, W.J., Yang, W., and Shah, S.P.: *Shrinkage Cracking of Restrained Concrete Slabs*. Journal of Engineering Mechanics, 124(7):765–774, 1998.

[406] Willems, P.: *Model uncertainty analysis by variance decomposition*. Physics and Chemistry of the Earth, Parts A/B/C, 42-44:21–30, 2012.

[407] William, G.W., Shoukry, S.N., and Riad, M.Y.: *Early age cracking of reinforced concrete bridge decks*. Bridge Structures, 1(4):379–396, 2005.

[408] Williams, D.J.: *The behaviour of model piles in dense sand*. PhD thesis, University of Cambridge, Cambridge, 1979.

[409] Woidelko, E. O.: *Zum Tragverhalten nach Traglastverfahren bemessener Stahlbetonplattenbalken*. PhD thesis, Universität, Stuttgart, 1983.

[410] Woidelko, E. O., Schäfer, K., and Schlaich, J.: *Nach Traglastverfahren bemessene Stahlbeton-Plattenbalken*. Beton- und Stahlbetonbau, 81(8,9):197–201,244–248, 1986.

[411] Woliński, S.: *Global safety factor for nonlinear design of concrete structures*. Archives of Civil Engineering, LVII(3), 2011.

[412] Wu, H.Q and Gilbert, R.I: *Modeling short-term tension stiffening in reinforced concrete prisms using a continuum-based finite element model*. Engineering Structures, 31(10):2380–2391, 2009.

[413] Xu, C. and Gertner, G.Z.: *Uncertainty and sensitivity analysis for models with correlated parameters*. Reliability Engineering & System Safety, 93(10):1563–1573, 2008.

[414] Yang, I.H.: *Uncertainty and sensitivity analysis of time-dependent effects in concrete structures*. Engineering Structures, 29(7):1366–1374, 2007.

[415] Zain, M.F.M., Mahmud, H.B., Ilham, A., and Faizal, M.: *Prediction of splitting tensile strength of high-performance concrete*. Cement and Concrete Research, 32(8):1251–1258, 2002.

[416] Zhang, Q. q. and Zhang, Z. m.: *Simplified Calculation Approach for Settlement of Single Pile and Pile Groups*. Journal of Computing in Civil Engineering, 26(6):750–758, 2012.

[417] Zheng, W., Kwan, A.K.H., and Lee, P.K.K.: *Direct tension test of concrete*. ACI Materials Journal, 98(1):63–71, 2001.

[418] Zichner, T.: *Temperaturunterschied infolge Witterungseinfluss und Beheizung von massiven Brücken*. PhD thesis, Technische Universität, Darmstadt, 1976.

[419] Zienkiewicz, O. C. and Parekh, C. J.: *Transient field problems: Two-dimensional and three-dimensional analysis by isoparametric finite elements*. International Journal for Numerical Methods in Engineering, 2(1):61–71, 1970.

[420] Zilch, K. and Zehetmaier, G.: *Bemessung im konstruktiven Betonbau: Nach DIN 1045-1 (Fassung 2008) und EN 1992-1-1 (Eurocode 2)*. Springer, Berlin, 2nd edition, 2010.

[421] Zimmermann, T., Strauss, A., and Haider, K.: *Determination of Material Parameters of Concrete for Non-Linear Modeling*. Advanced Materials Research, 651:321–324, 2013.

[422] Zink, M.: *Zum Biegeschubversagen schlanker Bauteile aus Hochleistungsbeton mit und ohne Vorspannung*. Forschung für die Praxis. Vieweg+Teubner Verlag, Wiesbaden, 2000. `http://dx.doi.org/10.1007/978-3-663-05914-1`.

[423] Zio, E. and Apostolakis, G.E: *Two methods for the structured assessment of model uncertainty by experts in performance assessments of radioactive waste repositories*. Reliability Engineering & System Safety, 54:225–241, 1996.

[424] Zordan, T., Briseghella, B., and Lan, C.: *Analytical Formulation for Limit Length of Integral Abutment Bridges*. Structural Engineering International, 21(3):304–310, 2011.

[425] Zordan, T., Briseghella, B., and Lan, C.: *Parametric and pushover analyses on integral abutment bridge*. Engineering Structures, 33(2):502–515, 2011.

BAUHAUS
UNIVERSITÄTSVERLAG

Solemn Declaration

I do solemnly declare that I have made this work without undue assistance from third parties and without the use of other than the referenced sources. From other sources directly or indirectly acquired data and concepts are identified by referencing the source.

Other people were not involved in the development of content and material of the present work. In particular, I have not used any paid help of mediation or counselling services (promotion consultants or other persons). No one has received directly or indirect monetary benefits from me for any work in connection with the content of the submitted dissertation.

The work has been neither submitted to any other Examining Authority in Germany nor abroad in the same or similar style. I certify on my honor that I have said the whole truth and that I concealed nothing.

Place, Date Signature

Ehrenwörtliche Erklärung

Ich erkläre hiermit ehrenwörtlich, dass ich die vorliegende Arbeit ohne unzulässige Hilfe Dritter und ohne Benutzung anderer als der angegebenen Hilfsmittel angefertigt habe. Die aus anderen Quellen direkt oder indirekt übernommenen Daten und Konzepte sind unter Angabe der Quelle gekennzeichnet.

Bei der Auswahl und Auswertung der Materialien für die vorliegende Disseration haben mir keine Personen geholfen. Insbesondere habe ich hierfür nicht die entgeltliche Hilfe von Vermittlungs- bzw. Beratungsdiensten (Promotionsberater oder anderer Personen) in Anspruch genommen. Niemand hat von mir unmittelbar oder mittelbar geldwerte Leistungen für Arbeiten erhalten, die im Zusammenhang mit dem Inhalt der vorgelegten Dissertation stehen.

Die Arbeit wurde bisher weder im In- noch im Ausland in gleicher oder ähnlicher Form einer anderen Prüfungsbehörde vorgelegt.

Ich versichere ehrenwörtlich, dass ich nach bestem Wissen die reine Wahrheit gesagt und nichts verschwiegen habe.

Ort, Datum Unterschrift

BAUHAUS
UNIVERSITÄTSVERLAG

Publications of the Author

International reviewed Journals:

- B. Jung, G. Morgenthal, D. Xu, H. Schröter
  Quality assessment of material models for reinforced concrete flexural members
  Structural Concrete (1) (2015) 125-136.

- B. Jung, G. Morgenthal, D. Xu
  Integrative sensitivity analysis applied to semi-integral concrete bridges
  Journal of Bridge Engineering 19(6) (2014) 04014014 1-13.

- H. Keitel, B. Jung, H.B. Motra, H. Stutz
  Quality assessment of coupled partial models considering soil-structure coupling
  Engineering Structures 59 (2014) 565-573.

- C. Liu, D. Xu, B. Jung, G. Morgenthal
  Reinforcement design for the anchorage of externally prestressed bridges with "tensile stress region"
  Computers and Concrete 11 (5) (2013) 383-397.

National Journals:

- B. Jung, G. Morgenthal, D. Xu
  Integral bridges: sensitivity of limit state modelling
  Bautechnik - Sonderdruck "Modellqualitäten" 90 (2013) 32-40.

- H. Keitel, H. Stutz, B. Jung, H.B. Motra
  Prognosequalität eines Gesamtmodells - Einfluss verschiedener Kopplungsszenarien auf die Interaktion Struktur - Boden
  Prediction quality of coupled partial models - Influence of different coupling scenarios on the soil-structure interaction
  Bautechnik - Sonderdruck "Modellqualitäten" 90 (2013) 19-25.

International Conference Papers:

- B. Jung, H. Stutz, G. Morgenthal, F. Wuttke
  Uncertainty Analysis of stiffness prediction for pile group models
  10th International Probabilistic Workshop
  Stuttgart, 15-16 November 2012.

- B. Jung, G. Morgenthal
  Assessment of Coupled Numerical Models applied to semi-integral bridge
  18th Congress of IABSE "Innovative Infrastructures - Toward Human Urbanism"
  Seoul, 19-21 September 2012.

- B. Jung, G. Morgenthal
  Global model quality evaluation of coupled partial models for restraint effects in reinforced and prestressed concrete structures
  The 9th fib International PhD Symposium in Civil Engineering
  Karlsruhe, Karlsruhe Institute of Technology (KIT), 22-25 July 2012.

- B. Jung, G. Morgenthal
  Assessment of integral bridges using quantitative model evaluation
  19th International Conference on the Application of Computer Science and Mathematics in Architecture and Civil Engineering
  Weimar, Bauhaus-Universität Weimar, 04-06 July 2012.

- B. Jung, G. Morgenthal
  Uncertainty analysis of tension stiffening approaches in reinforced concrete structures for the model quality evaluation
  fib Symposium Stockholm 2012 "Concrete Structures for Sustainable Community"
  Stockholm, KTH Royal Institute of Technology, 11-14 June 2012.

- B. Jung, H.-G. Timmler, G. Morgenthal, H. Schröter
  Restraint Effects in Reinforced and Prestressed Concrete Structures
  IABSE-IASS Symposium "Taller, Longer, Lighter - Meeting growing demand with limited resources"
  London, 20-23 September 2011.

Curriculum Vitae

Personal information:

Name: Bastian Jung
Date of birth: 6th of August 1985
Place of birth: Erfurt

Education:

1996 - 2004: Staatliches Gymnasium “Heinrich Hertz”, Erfurt

Academic studies:

2005 - 2008: Bachelor of Science in civil engineering, Bauhaus-Universität Weimar
2008 - 2010: Master of Science in civil engineering, Bauhaus-Universität Weimar

Professional experience:

2010 - 2013: Graduiertenkolleg 1462, Bauhaus-Universität Weimar, doctoral candidate
2012: Tongji University, Shanghai, People’s Republic of China
stay and research exchange within the framework of the promotion
since 2014: SGHG Ingenieurgesellschaft Bautechnik mbH, Erfurt,
structural engineer

BAUHAUS
UNIVERSITÄTSVERLAG

Lebenslauf

Persönliche Angaben:

Name:	Bastian Jung
Geburtsdatum:	06.08.1985
Geburtsort:	Erfurt

Schulbildung:

1996 - 2004:	Staatliches Gymnasium “Heinrich Hertz”, Erfurt

Studium:

2005 - 2008:	Bachelor of Science im Bauingenieurwesen, Bauhaus-Universität Weimar
2008 - 2010:	Master of Science im Bauingenieurwesen, Bauhaus-Universität Weimar

Berufstätigkeit:

2010 - 2013:	Graduiertenkolleg 1462, Bauhaus-Universität Weimar, Doktorant
2012:	Tongji University, Shanghai, Volksrepublik China Forschungsaufenthalt im Rahmen der Promotion
seit 2014:	SGHG Ingenieurgesellschaft Bautechnik mbH, Erfurt, Statiker

BAUHAUS
UNIVERSITÄTSVERLAG

A Appendix - modelling aspects

A.1 Restraint effects

Table A.1: Material properties for sectional analysis of restraint effects

Material	E $\left[\mathrm{MN/m^2}\right]$	f_R $\left[\mathrm{MN/m^2}\right]$	f_{uR} $\left[\mathrm{MN/m^2}\right]$	f_{ctm} $\left[\mathrm{MN/m^2}\right]$	ϵ_1 [‰]	ϵ_2 [‰]
concrete	33300	-25.29	-	3.2	-2.40	-3.50
reinforcing steel	200000	55.00	59.40	-	2.75	25.00

Table A.2: Reinforcement area for restraint effect analysis depending on reinforcement ratio

Cross-Section	Reinforcement Ratio ω_{s1} $[-]$	Tensile Reinforcement A_{s1} $\left[\mathrm{cm^2}\right]$	Compressive Reinforcement $A_{s2} = 1/5 \cdot A_{s1}$ $\left[\mathrm{cm^2}\right]$
rectangular	0.029	6.40	
	0.05	10.92	2.18
	0.10	21.84	4.37
	0.20	43.68	
	0.30	65.52	13.10
	0.40	87.36	17.47
	0.50	109.20	
box girder	0.029	128.00	
	0.05	218.39	
	0.10	436.79	
	0.20	873.57	
	0.30	1310.35	
	0.40	1747.13	

A.2 Pile foundation

The parameters for the estimation of the group "magical radius" based on the study of GUO and RANDOLPH according to Eq. 3.152 are defined to [157, 158]:

$$r_{m,\mathrm{g}} = A\frac{1-\nu_s}{1+\rho_{\mathrm{dsh}}} l_P + Br_0 + \alpha_{\mathrm{g}} r_{\mathrm{g}} \,, \tag{A.1a}$$

$$A = \frac{A_{\mathrm{h}}}{A_{\mathrm{oh}}}\left[\frac{1}{1+\rho_{\mathrm{dsh}}}\left(\frac{0.4-\nu_s}{\rho_{\mathrm{dsh}}+0.4} + \frac{2}{1-0.3\rho_{\mathrm{dsh}}}\right) + C_\lambda\left(\nu_s - 0.4\right)\right] \,, \tag{A.1b}$$

$$C_\lambda = \begin{cases} 0 & \lambda = 300 \\ 0.5 & \lambda = 1000 \\ 1.0 & \lambda = 10000 \end{cases} \,, \tag{A.1c}$$

$$\lambda = \frac{E_P}{G_{s,l_P}} \,, \tag{A.1d}$$

$$A_{\mathrm{h}} = 0.124\mathrm{e}^{2.23\rho_{\mathrm{g}}}\left(1-\mathrm{e}^{1-\frac{l_P+h_b}{l_P}}\right) + 1.01\mathrm{e}^{0.107\rho_{\mathrm{dsh}}} \,, \tag{A.1e}$$

$$\rho_{\mathrm{g}} = \frac{1}{1+\rho_{\mathrm{dsh}}} \,, \tag{A.1f}$$

$$B \approx \begin{cases} 1 & [157] \\ \dfrac{l_P}{r_0} < 20 & 5 \\ (l_P + h_B) \to \infty & 5 \end{cases} \,, \tag{A.1g}$$

$$\alpha_{\mathrm{g}} = 1 - \mathrm{e}^{1-\frac{l_P+h_b}{l_P}} \,, \tag{A.1h}$$

$$r_{\mathrm{g}} \approx \begin{cases} \dfrac{1}{3} \dots \dfrac{1}{2} \cdot s \\ (0.3 + 0.2\rho_{\mathrm{dsh}}) \cdot s \quad \text{with} \quad s \le A\frac{1-\nu_s}{1+\rho_{\mathrm{dsh}}} l_P + Br_0 \end{cases} \,. \tag{A.1i}$$

(A.1j)

The integration constants A_{11}, B_{11}, A_{21} and B_{21} for the pile settlement profiles based on the model by MOYLONAKIS and GAZETAS [291] are given by:

$$A_{11} = \frac{1}{2} - \frac{K}{2E_P A_P \lambda} \,, \tag{A.2a}$$

$$B_{11} = \frac{1}{2} + \frac{K}{2E_P A_P \lambda} \,, \tag{A.2b}$$

$$A_{21} = \frac{\psi(r_{ij})}{2}\left(\zeta - \frac{K}{2E_P A_P \lambda}\right) \,, \tag{A.2c}$$

$$B_{21} = \frac{\psi(r_{ij})}{2}\left(\zeta + \frac{K}{2E_P A_P \lambda}\right) \,. \tag{A.2d}$$

The 2 by 2 transfer matrix $[\mathbf{LI}]_i$ is defined to [291]:

$$[\mathbf{LI}]_i = \left(k_{z_i} + i\omega c_{z_i}\right) \frac{\psi\left(r_{ij}\right)}{2\lambda_i} \begin{bmatrix} -\dfrac{h_i}{E_p A_p} \sinh\left(h_i \lambda_i\right) & \dfrac{1}{\left(E_p A_p\right)^2 \lambda_i} \left[h_i \cosh\left(h_i \lambda_i\right) - \dfrac{\sinh\left(h_i \lambda_i\right)}{\lambda_i}\right] \\ h_i \lambda_i \cosh\left(h_i \lambda_i\right) + \sinh\left(h_i \lambda_i\right) & -\dfrac{h_i}{E_P A_P} \sinh\left(h_i \lambda_i\right) \end{bmatrix} \tag{A.3}$$

The stresses at a point in an elastic half-space due to a vertical load P_b at a certain depth (here pile length l_P, see Fig. A.1) can be computed according to the study of *Mindlin* [280, 315]:

$$\begin{aligned} \sigma_x = \frac{-P_b}{8\pi\left(1-\nu_s\right)} & \left[\frac{\left(1-2\nu_s\right)\left(z-l_P\right)}{R_1^3} - \frac{3x^2\left(z-l_P\right)}{R_1^5} + \frac{\left(1-2\nu_s\right)\left[3\left(z-l_P\right)-4\nu_s\left(z+l_P\right)\right]}{R_2^3}\right. \\ & - \frac{3\left(3-4\nu_s\right)x^2\left(z-l_P\right) - 6l_P\left(z+l_P\right)\left[\left(1-2\nu_s\right)z-2\nu_s\right]}{R_2^5} - \frac{30 l_P x^2 z\left(z+l_P\right)}{R_2^7} \\ & \left. - \frac{4\left(1-\nu_s\right)\left(1-2\nu_s\right)}{R_2\left(R_2+z+l_P\right)} \cdot \left(1 - \frac{x^2}{R_2\left(R_2+z+l_P\right)} - \frac{x^2}{R_2^2}\right)\right], \end{aligned} \tag{A.4a}$$

$$\begin{aligned} \sigma_z = \frac{-P_b}{8\pi\left(1-\nu_s\right)} & \left[-\frac{\left(1-2\nu_s\right)\left(z-l_P\right)}{R_1^3} + \frac{\left(1-2\nu_s\right)\left(z-l_P\right)}{R_2^3} - \frac{3\left(z-l_P\right)^3}{R_1^5}\right. \\ & \left. - \frac{3\left(3-4\nu_s\right)z\left(z+l_P\right)^2 - 3l_P\left(z+l_P\right)\left(5z-l_P\right)}{R_2^5} - \frac{30 l_P z\left(z+l_P\right)^3}{R_2^7}\right], \end{aligned} \tag{A.4b}$$

$$\begin{aligned} \tau_{zx} = \frac{-P_b \cdot x}{8\pi\left(1-\nu_s\right)} & \left[-\frac{\left(1-2\nu_s\right)}{R_1^3} + \frac{\left(1-2\nu_s\right)}{R_2^3} - \frac{3\left(z-l_P\right)^2}{R_1^5}\right. \\ & \left. - \frac{3\left(3-4\nu_s\right)z\left(z+l_P\right) - 3l_P\left(3z+l_P\right)}{R_2^5} - \frac{30 l_P z\left(z+l_P\right)^2}{R_2^7}\right]. \end{aligned} \tag{A.4c}$$

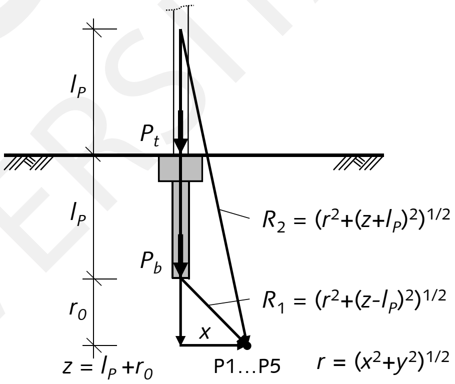

Figure A.1: *Mindlin* solution [280] for vertical load at a certain depth in elastic half-space, based on [315]

In comparison to Finite Element simulations, the mathematical model for vertical loaded single piles by Rudolf [353] is checked for the prediction of the resistance-settlement relation under various soil conditions, see Fig. A.2. The soil properties are listed in Tab. A.3. The soil layer below the surface is assumed to a soft soil layer with the depth of 3 m.

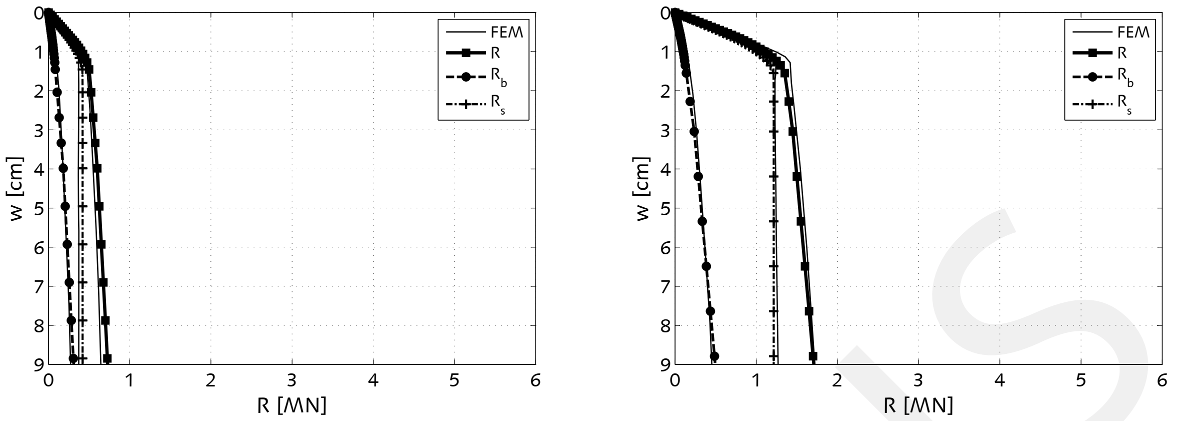

(a) $K_{v,\text{lin}} = 43\,\text{MN/m}$, $l_P = 9.0\,\text{m}$, $d_P = 0.9\,\text{m}$, cohesive soil, normal-consolidated, $E = 6.5\,\text{MN/m}^2$

(b) $K_{v,\text{lin}} = 122\,\text{MN/m}$, $l_P = 18.0\,\text{m}$, $d_P = 0.9\,\text{m}$, cohesive soil, over-consolidated, $E = 11.0\,\text{MN/m}^2$

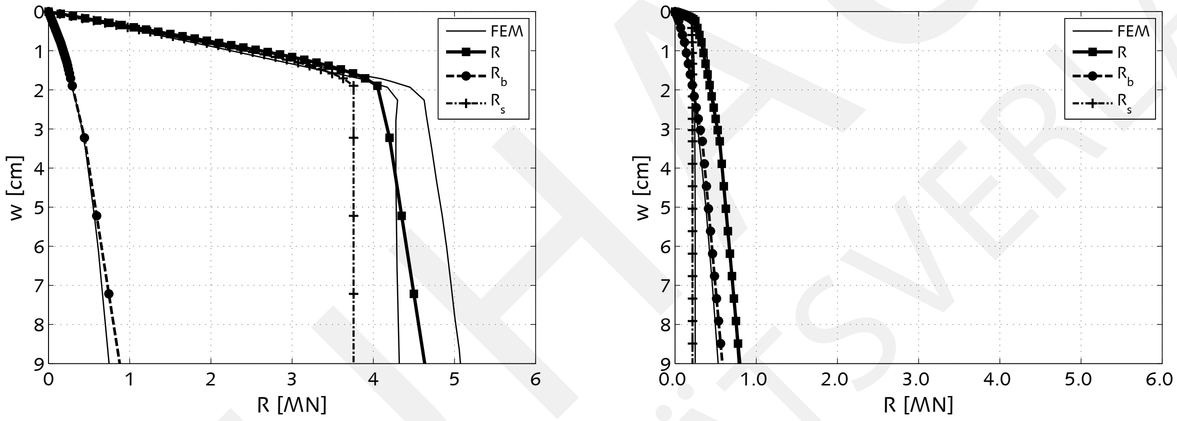

(c) $K_{v,\text{lin}} = 262\,\text{MN/m}$, $l_P = 24.0\,\text{m}$, $d_P = 0.9\,\text{m}$, cohesive soil, over-consolidated, $E = 19.0\,\text{MN/m}^2$

(d) $K_{v,\text{lin}} = 145\,\text{MN/m}$, $l_P = 9.0\,\text{m}$, $d_P = 0.9\,\text{m}$, non-cohesive soil, $\varphi' = 30°$, $\psi = 0$, $c' = 0$ $E = 22.0\,\text{MN/m}^2$

Figure A.2: Comparison between mathematical model and numerical simulation of resistance-settlement relation for single pile with various soil conditions, based on the study by RUDOLF [353, 353]

Table A.3: Soil properties considered in the study by RUDOLF [353], NC...normal-consolidated, OC...over-consolidated

Soil Property			Soft Layer	cohesive soil NC	cohesive soil OC		non-cohesive soil
friction angle	φ'	[°]	20.0	25.0	25.0	20.0	32.5
cohesion	c'	[kN/m^2]	0	10	10	40	0
unit weight (natural state)	γ	[kN/m^3]	14.0	19.5	17.5	19.5	17.0
unit weight under buoyancy	γ'	[kN/m^3]	4.0	9.5	7.5	9.5	9.5
soil oedometric modulus	E_s	[MN/m^2]	1.5	9.0	15.0	25.0	30.0
soil modulus of elasticity	E	[MN/m^2]	0.4	6.5	11.0	19.0	22.0
soil *Poisson*'s ratio	ν_s	[-]	0.45	0.30	0.30	0.30	0.30
earth pressure at rest coefficient	K_0	[-]	0.66	0.58	0.58	0.66	0.46

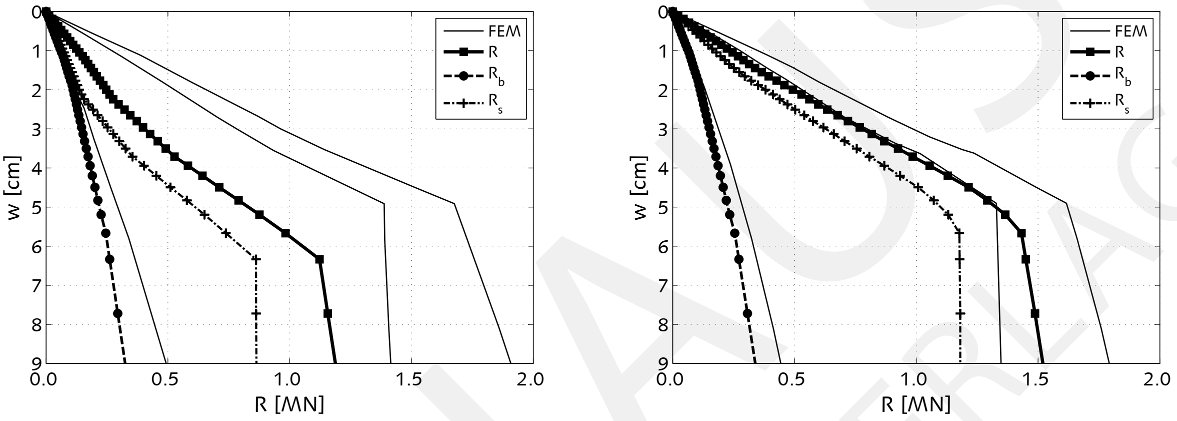

(a) central pile, $K_{v,\mathrm{lin}} = 13\,\mathrm{MN/m}$

(b) interior pile, $K_{v,\mathrm{lin}} = 23\,\mathrm{MN/m}$

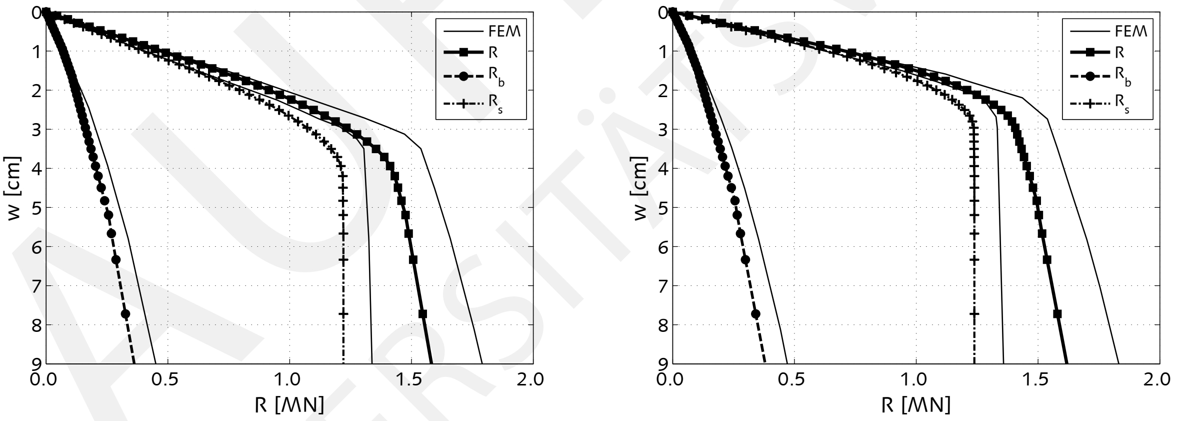

(c) edge pile, $K_{v,\mathrm{lin}} = 47\,\mathrm{MN/m}$

(d) corner pile, $K_{v,\mathrm{lin}} = 71\,\mathrm{MN/m}$

Figure A.3: Comparison between mathematical model and numerical simulation based on RUDOLF [353] for 5x5 pile group, $r_{m,\mathrm{g}} = l_p$, cohesive soil, over-consolidated, $E = 11.0\,\mathrm{MN/m^2}$, $l_P = 18.0\,\mathrm{m}$, $d_P = 0.9\,\mathrm{m}$, $s_x = s_y = 6d_P$, $K_{v,\mathrm{lin}} = 1017\,\mathrm{MN/m}$

Table A.4: Pile spaces r_{ij} in pile group 5x5 with pile diameter $d_P = 0.9\,\mathrm{m}$ for various pile space-pile diameter ratios $s/d_P = 6$

Pile	Pile Spaces r_{ij} [m]																								
Num.	1	2	3	4	5	6	7	8	9	10	11	12	13	14	15	16	17	18	19	20	21	22	23	24	25
1	0.45	5.40	10.80	16.20	21.60	5.40	7.64	12.08	17.08	22.27	10.80	12.08	15.27	19.47	24.15	16.20	17.08	19.47	22.91	27.00	21.60	22.27	24.15	27.00	30.55
2	5.40	0.45	5.40	10.80	16.20	7.64	5.40	7.64	12.08	17.08	12.08	10.80	12.08	15.27	19.47	17.08	16.20	17.08	19.47	22.91	22.27	21.60	22.27	24.15	27.00
3	10.80	5.40	0.45	5.40	10.80	12.08	7.64	5.40	7.64	12.08	15.27	12.08	10.80	12.08	15.27	19.47	17.08	16.20	17.08	19.47	24.15	22.27	21.60	22.27	24.15
4	16.20	10.80	5.40	0.45	5.40	17.08	12.08	7.64	5.40	7.64	19.47	15.27	12.08	10.80	12.08	22.91	19.47	17.08	16.20	17.08	27.00	24.15	22.27	21.60	22.27
5	21.60	16.20	10.80	5.40	0.45	22.27	17.08	12.08	7.64	5.40	24.15	19.47	15.27	12.08	10.80	27.00	22.91	19.47	17.08	16.20	30.55	27.00	24.15	22.27	21.60
6	5.40	7.64	12.08	17.08	22.27	0.45	5.40	10.80	16.20	21.60	5.40	7.64	12.08	17.08	22.27	10.80	12.08	15.27	19.47	24.15	16.20	17.08	19.47	22.91	27.00
7	7.64	5.40	7.64	12.08	17.08	5.40	0.45	5.40	10.80	16.20	7.64	5.40	7.64	12.08	17.08	12.08	10.80	12.08	15.27	19.47	17.08	16.20	17.08	19.47	22.91
8	12.08	7.64	5.40	7.64	12.08	10.80	5.40	0.45	5.40	10.80	12.08	7.64	5.40	7.64	12.08	15.27	12.08	10.80	12.08	15.27	19.47	17.08	16.20	17.08	19.47
9	17.08	12.08	7.64	5.40	7.64	16.20	10.80	5.40	0.45	5.40	17.08	12.08	7.64	5.40	7.64	19.47	15.27	12.08	10.80	12.08	22.91	19.47	17.08	16.20	17.08
10	22.27	17.08	12.08	7.64	5.40	21.60	16.20	10.80	5.40	0.45	22.27	17.08	12.08	7.64	5.40	24.15	19.47	15.27	12.08	10.80	27.00	22.91	19.47	17.08	16.20
11	10.80	12.08	15.27	19.47	24.15	5.40	7.64	12.08	17.08	22.27	0.45	5.40	10.80	16.20	21.60	5.40	7.64	12.08	17.08	22.27	10.80	12.08	15.27	19.47	24.15
12	12.08	10.80	12.08	15.27	19.47	7.64	5.40	7.64	12.08	17.08	5.40	0.45	5.40	10.80	16.20	7.64	5.40	7.64	12.08	17.08	12.08	10.80	12.08	15.27	19.47
13	15.27	12.08	10.80	12.08	15.27	12.08	7.64	5.40	7.64	12.08	10.80	5.40	0.45	5.40	10.80	12.08	7.64	5.40	7.64	12.08	15.27	12.08	10.80	12.08	15.27
14	19.47	15.27	12.08	10.80	12.08	17.08	12.08	7.64	5.40	7.64	16.20	10.80	5.40	0.45	5.40	17.08	12.08	7.64	5.40	7.64	19.47	15.27	12.08	10.80	12.08
15	24.15	19.47	15.27	12.08	10.80	22.27	17.08	12.08	7.64	5.40	21.60	16.20	10.80	5.40	0.45	22.27	17.08	12.08	7.64	5.40	24.15	19.47	15.27	12.08	10.80
16	16.20	17.08	19.47	22.91	27.00	10.80	12.08	15.27	19.47	24.15	5.40	7.64	12.08	17.08	22.27	0.45	5.40	10.80	16.20	21.60	5.40	7.64	12.08	17.08	22.27
17	17.08	16.20	17.08	19.47	22.91	12.08	10.80	12.08	15.27	19.47	7.64	5.40	7.64	12.08	17.08	5.40	0.45	5.40	10.80	16.20	7.64	5.40	7.64	12.08	17.08
18	19.47	17.08	16.20	17.08	19.47	15.27	12.08	10.80	12.08	15.27	12.08	7.64	5.40	7.64	12.08	10.80	5.40	0.45	5.40	10.80	12.08	7.64	5.40	7.64	12.08
19	22.91	19.47	17.08	16.20	17.08	19.47	15.27	12.08	10.80	12.08	17.08	12.08	7.64	5.40	7.64	16.20	10.80	5.40	0.45	5.40	17.08	12.08	7.64	5.40	7.64
20	27.00	22.91	19.47	17.08	16.20	24.15	19.47	15.27	12.08	10.80	22.27	17.08	12.08	7.64	5.40	21.60	16.20	10.80	5.40	0.45	22.27	17.08	12.08	7.64	5.40
21	21.60	22.27	24.15	27.00	30.55	16.20	17.08	19.47	22.91	27.00	10.80	12.08	15.27	19.47	24.15	5.40	7.64	12.08	17.08	22.27	0.45	5.40	10.80	16.20	21.60
22	22.27	21.60	22.27	24.15	27.00	17.08	16.20	17.08	19.47	22.91	12.08	10.80	12.08	15.27	19.47	7.64	5.40	7.64	12.08	17.08	5.40	0.45	5.40	10.80	16.20
23	24.15	22.27	21.60	22.27	24.15	19.47	17.08	16.20	17.08	19.47	15.27	12.08	10.80	12.08	15.27	12.08	7.64	5.40	7.64	12.08	10.80	5.40	0.45	5.40	10.80
24	27.00	24.15	22.27	21.60	22.27	22.91	19.47	17.08	16.20	17.08	19.47	15.27	12.08	10.80	12.08	17.08	12.08	7.64	5.40	7.64	16.20	10.80	5.40	0.45	5.40
25	30.55	27.00	24.15	22.27	21.60	27.00	22.91	19.47	17.08	16.20	24.15	19.47	15.27	12.08	10.80	22.27	17.08	12.08	7.64	5.40	21.60	16.20	10.80	5.40	0.45

B Appendix - partial model quality evaluation

B.1 Evaluation of concrete material models

B.1.1 Comparative study of model uncertainty

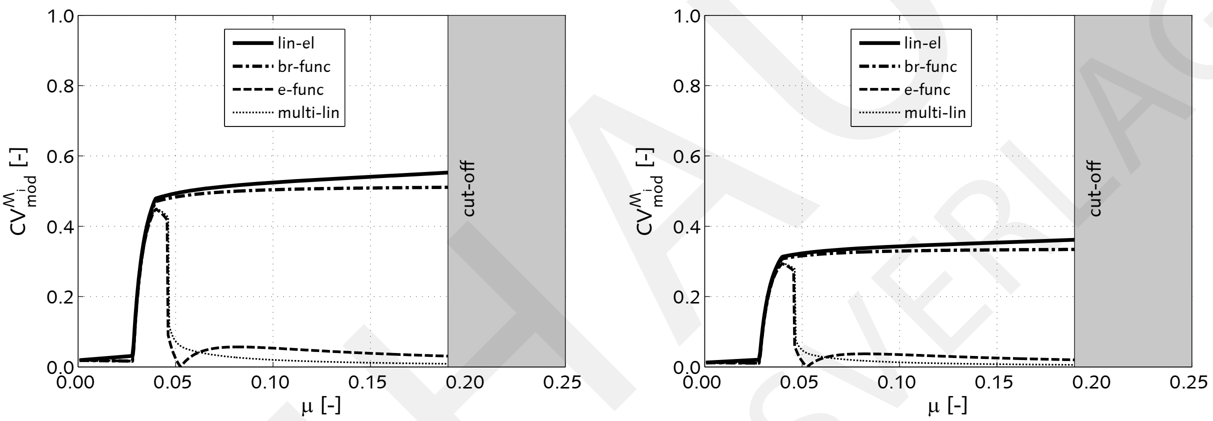

(a) coefficient of variation for 90 % quantile

(b) coefficient of variation for 97.5 % quantile

Figure B.1: Load level dependency of model uncertainty of material models

B.1.2 Samples in equilibrium condition for all loading levels

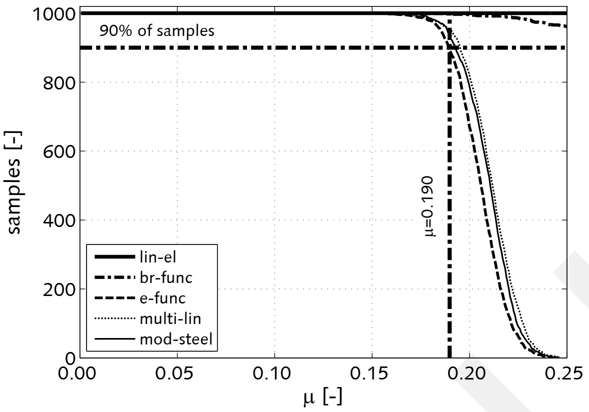

(a) high reinforcement ratio

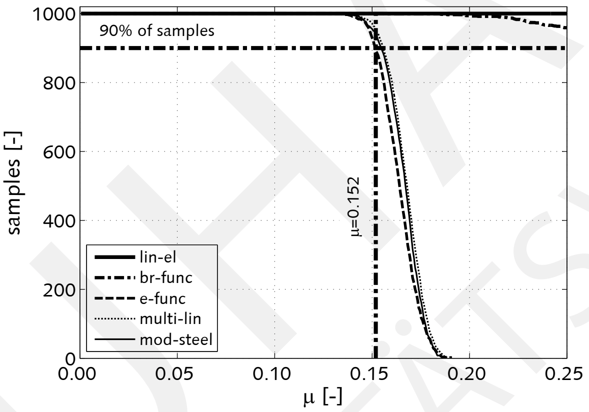

(b) medium reinforcement ratio

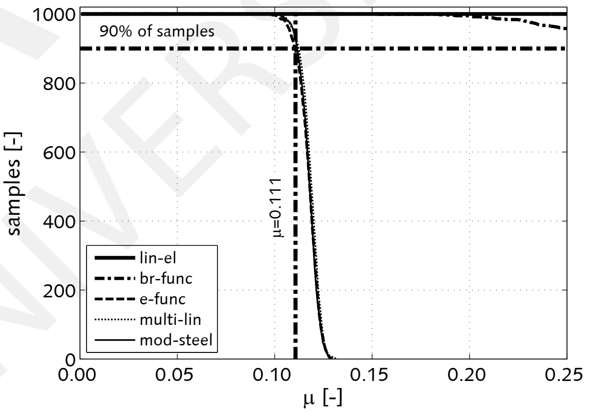

(c) low reinforcement ratio

Figure B.2: Number of samples without material failure

B.1.3 High reinforcement ratio

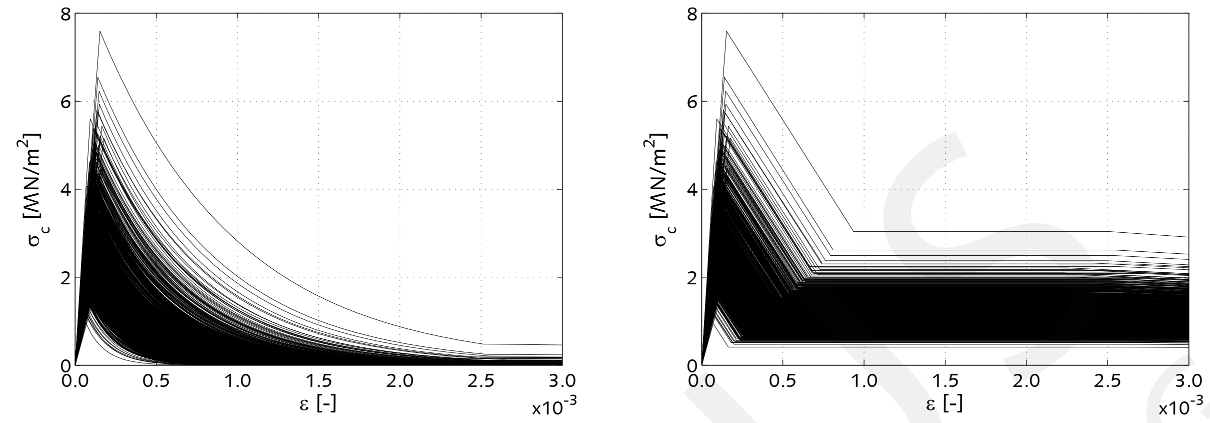

(a) exponential function model

(b) multi-linear model

Figure B.3: Probabilistic σ-ϵ relation for reinforced concrete in tension, concrete models until crack formation stage

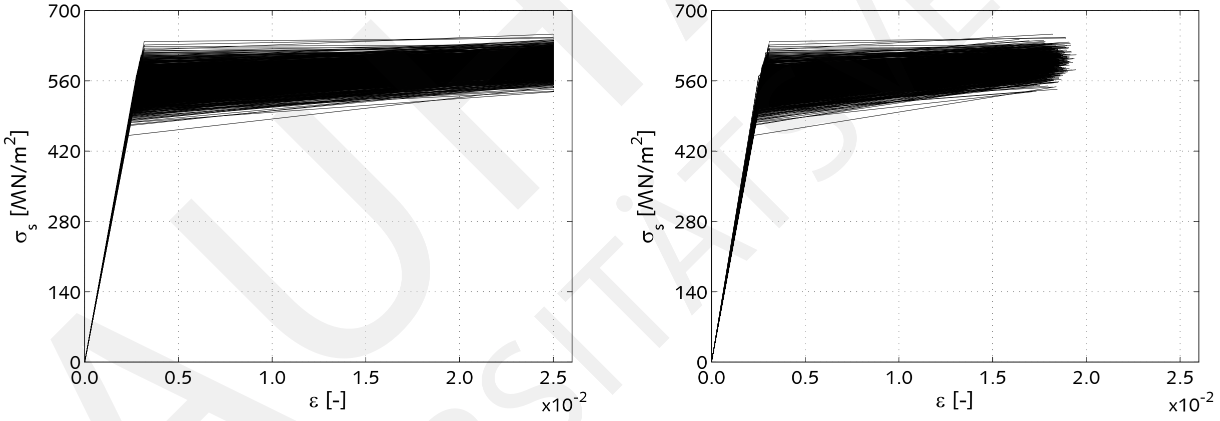

(a) bi-linear model for model "br-func"

(b) modified bi-linear model for model "e-func" and "multi-lin"

Figure B.4: Probabilistic σ-ϵ relation for bi-linear model of reinforcing steel

B.1.4 Medium reinforcement ratio

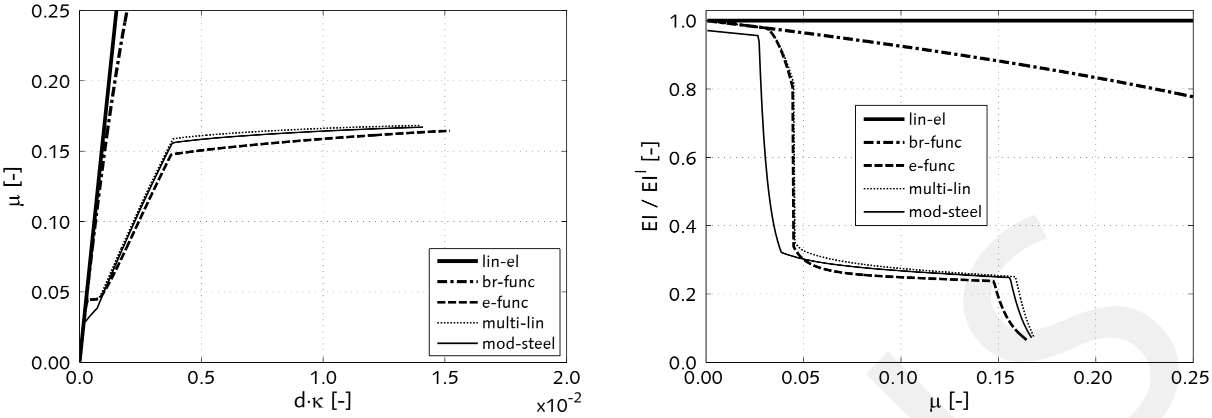

(a) dimensionless moment - dimensionless curvature (b) relative bending stiffness - dimensionless moment

Figure B.5: Deterministic load-bearing behaviour of rectangular cross-section for medium reinforcement ratio

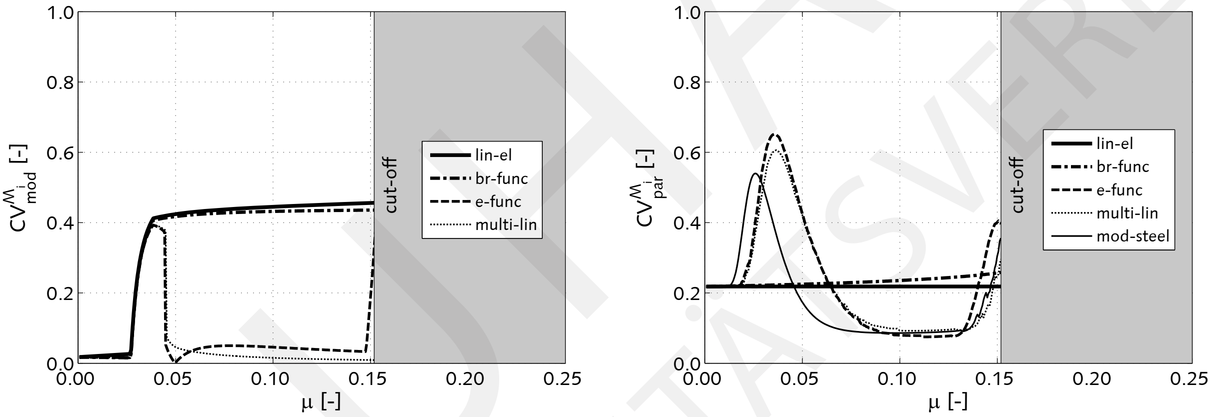

(a) model uncertainty (b) parameter uncertainty

Figure B.6: Load level dependency of model and parameter uncertainty of material models for medium reinforcement ratio

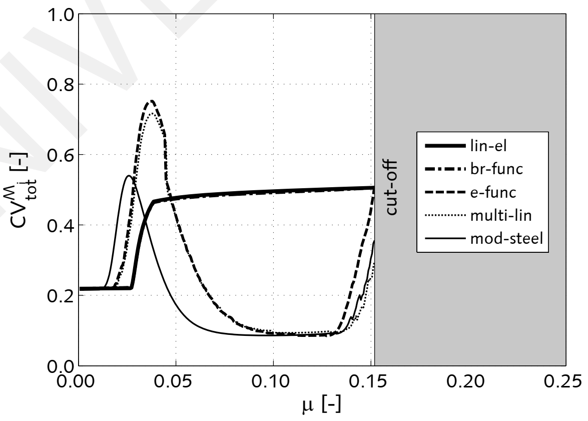

Figure B.7: Load level dependency of total uncertainty of material models for medium reinforcement ratio

B.1.5 Low reinforcement ratio

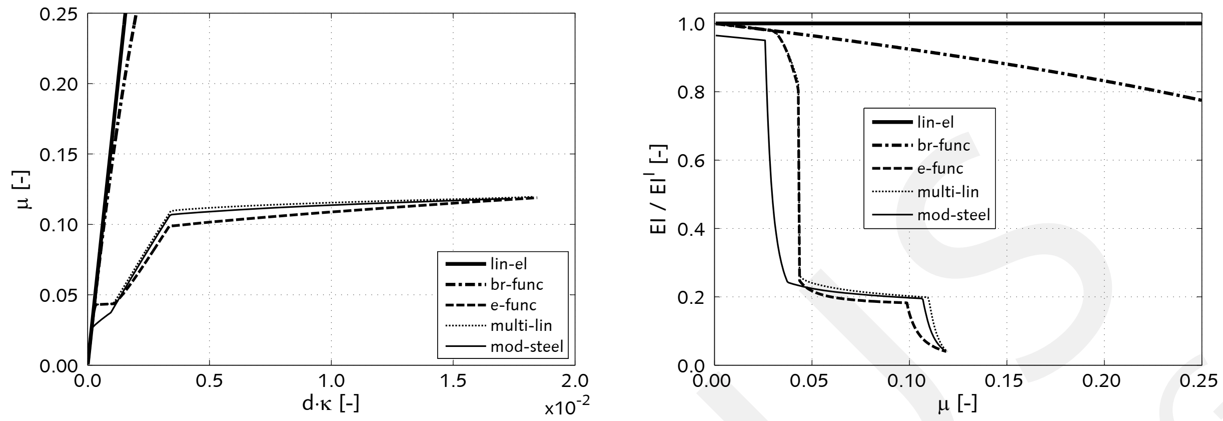

(a) dimensionless moment - dimensionless curvature (b) relative bending stiffness - dimensionless moment

Figure B.8: Deterministic load-bearing behaviour of rectangular cross-section for low reinforcement ratio

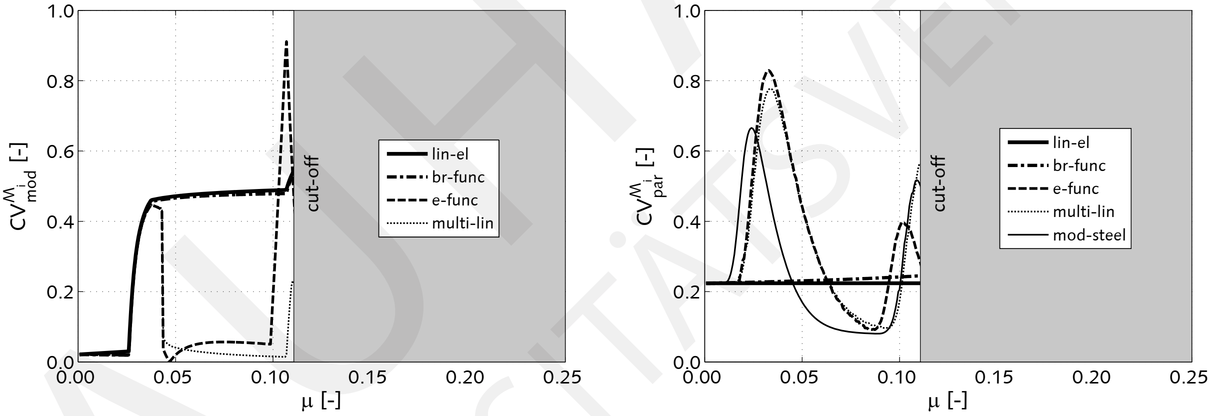

(a) model uncertainty (b) parameter uncertainty

Figure B.9: Load level dependency of model and parameter uncertainty of material models for low reinforcement ratio

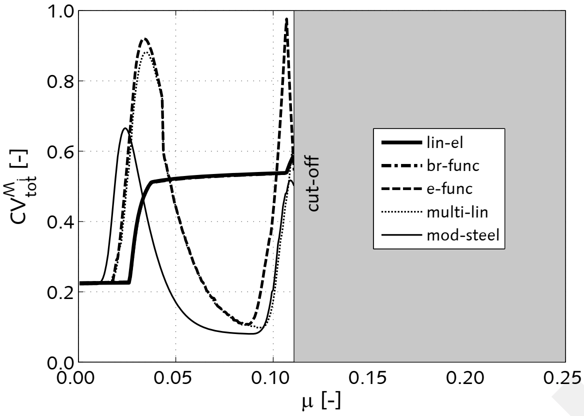

Figure B.10: Load level dependency of total uncertainty of material models for low reinforcement ratio

B.2 Pile foundation

Table B.1: Pile spaces r_{ij} in pile group 4x1 with pile diameter $d_P = 1.0\,\mathrm{m}$ for various pile space-pile diameter ratios s/d_P

Pile Space		Pile Spaces r_{ij} [m]			
Ratio	Pile Number	1	2	3	4
$s/d_P = 2$	1	0.5	2.0	4.0	6.0
	2	2.0	0.5	2.0	4.0
	3	4.0	2.0	0.5	2.0
	4	6.0	4.0	2.0	0.5
$s/d_P = 3$	1	0.5	3.0	6.0	9.0
	2	3.0	0.5	3.0	6.0
	3	6.0	3.0	0.5	3.0
	4	9.0	6.0	3.0	0.5
$s/d_P = 5$	1	0.5	5.0	10.0	15.0
	2	5.0	0.5	5.0	10.0
	3	10.0	5.0	0.5	5.0
	4	15.0	10.0	5.0	0.5
$s/d_P = 10$	1	0.5	10.0	20.0	30.0
	2	10.0	0.5	10.0	20.0
	3	20.0	10.0	0.5	10.0
	4	30.0	20.0	10.0	0.5

Table B.2: Pile spaces r_{ij} in pile group 2x2 with pile diameter $d_P = 1.0\,\text{m}$ for various pile space-pile diameter ratios s/d_P

Pile Space Ratio	Pile Number	Pile Spaces r_{ij} [m]			
		1	2	3	4
$s/d_P = 2$	1	0.500	2.000	2.000	2.828
	2	2.000	0.500	2.828	2.000
	3	2.000	2.828	0.500	2.000
	4	2.828	2.000	2.000	0.500
$s/d_P = 3$	1	0.500	3.000	3.000	4.243
	2	3.000	0.500	4.243	3.000
	3	3.000	4.243	0.500	3.000
	4	4.243	3.000	3.000	0.500
$s/d_P = 5$	1	0.500	5.000	5.000	7.071
	2	5.000	0.500	7.071	5.000
	3	5.000	7.071	0.500	5.000
	4	7.071	5.000	5.000	0.500
$s/d_P = 10$	1	0.500	10.000	10.000	14.142
	2	10.000	0.500	14.142	10.000
	3	10.000	14.142	0.500	10.000
	4	14.142	10.000	10.000	0.500

BAUHAUS
UNIVERSITÄTSVERLAG

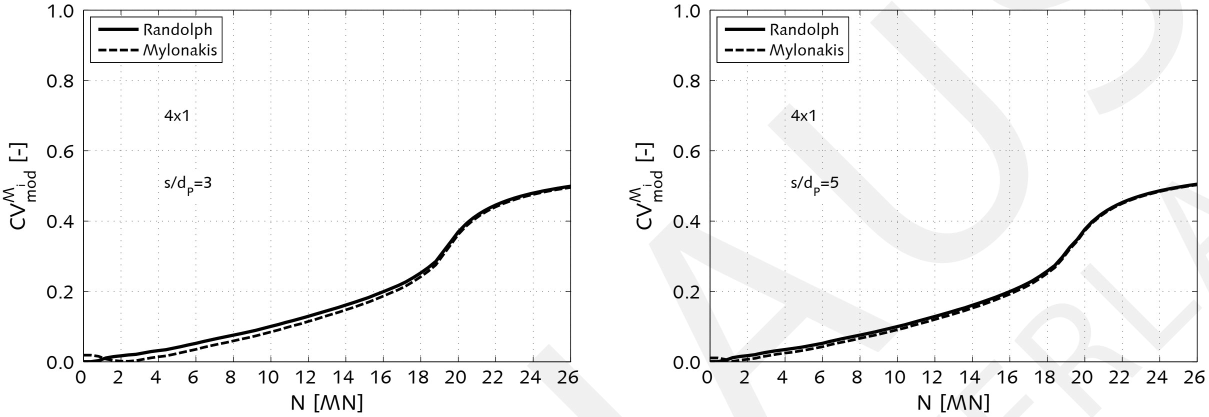

(a) group 4x1 (I) with $s/d_P = 3$

(b) group 4x1 (I) with $s/d_P = 5$

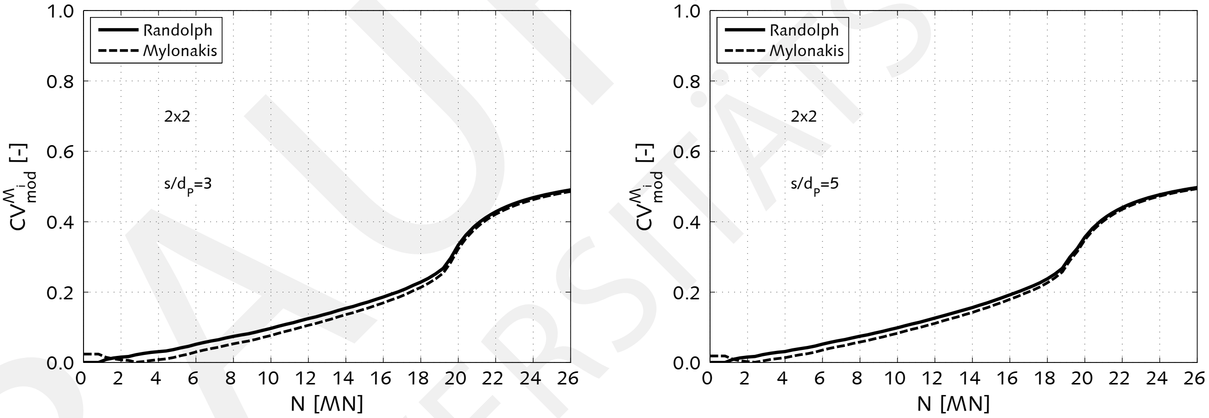

(c) group 2x2 (II) with $s/d_P = 3$

(d) group 2x2 (II) with $s/d_P = 5$

Figure B.11: Model uncertainty $CV_{\text{mod}}^{\mathcal{M}_i}$ for pile foundation assembly 4x1 (I) and 2x2 (II), RANDOLPH et al. [334], MYLONAKIS et al. [291], reference model RUDOLF [353]

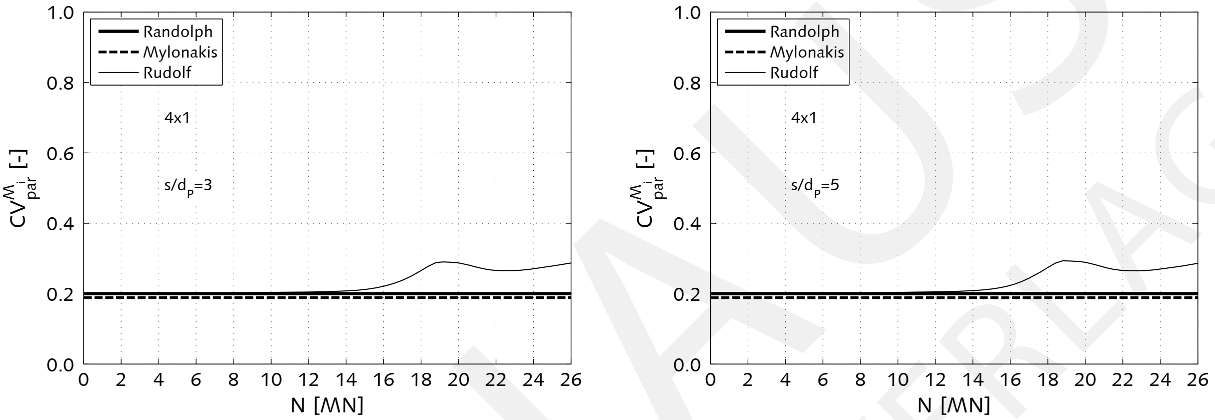

(a) group 4x1 (I) with $s/d_P = 3$

(b) group 4x1 (I) with $s/d_P = 5$

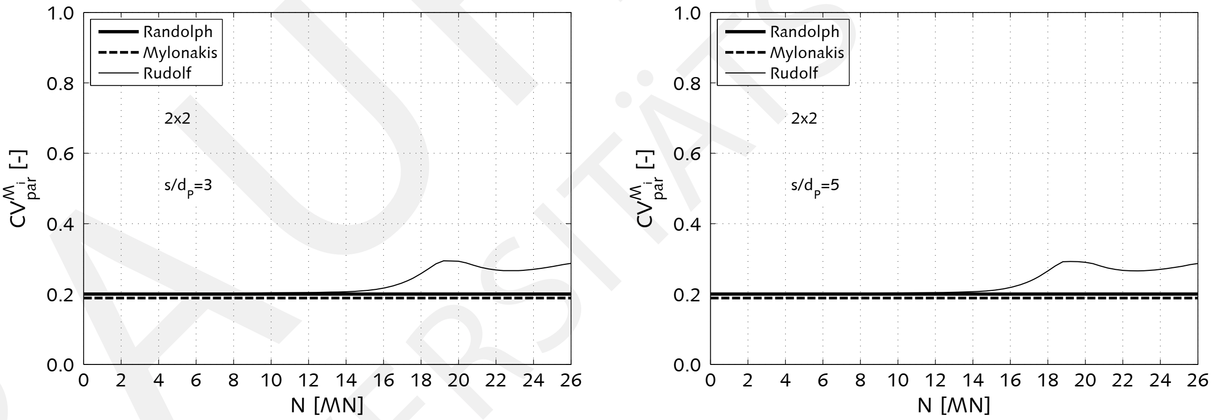

(c) group 2x2 (II) with $s/d_P = 3$

(d) group 2x2 (II) with $s/d_P = 5$

Figure B.12: Parameter uncertainty $CV_{\text{par}}^{\mathcal{M}_i}$ for pile foundation arrangement 4x1 (I) and 2x2 (II), RANDOLPH et al. [334], MYLONAKIS et al. [291], RUDOLF [353]

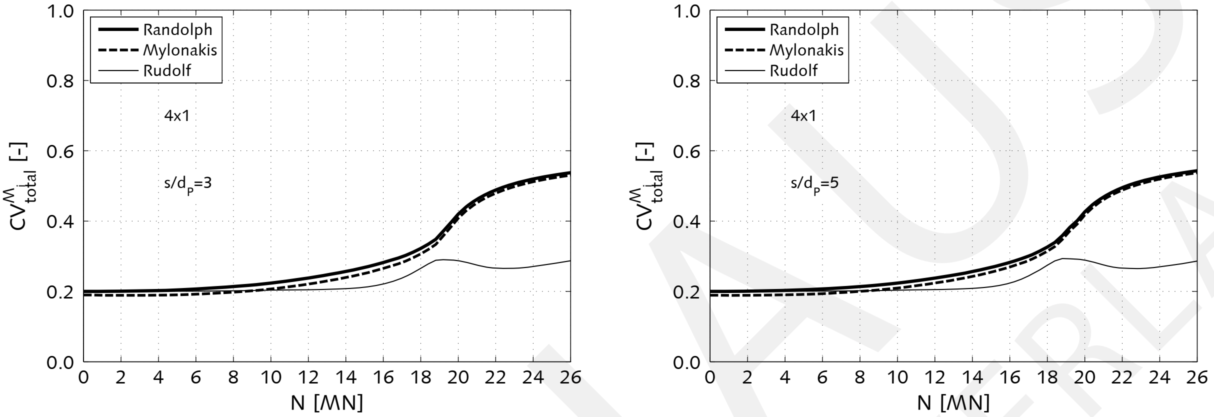

(a) group 4x1 (I) with $s/d_P = 3$

(b) group 4x1 (I) with $s/d_P = 5$

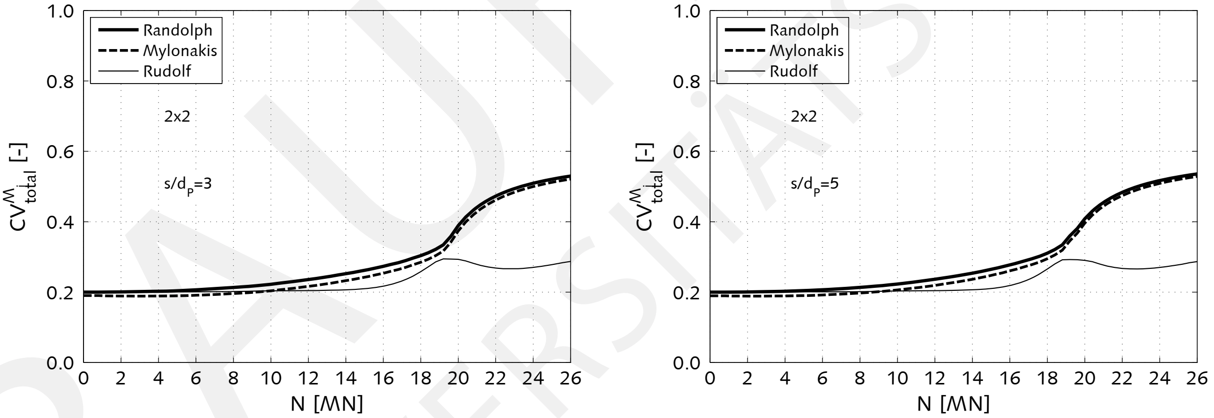

(c) group 2x2 (II) with $s/d_P = 3$

(d) group 2x2 (II) with $s/d_P = 5$

Figure B.13: Total uncertainty $CV_{\text{tot}}^{\mathcal{M}_i}$ for pile foundation arrangement 4x1 (I) and 2x2 (II), RANDOLPH et al. [334], MYLONAKIS et al. [291], RUDOLF [353]

C Appendix - integrative sensitivity analysis

C.1 Semi-integral concrete bridges

BAUHAUS
UNIVERSITÄTSVERLAG

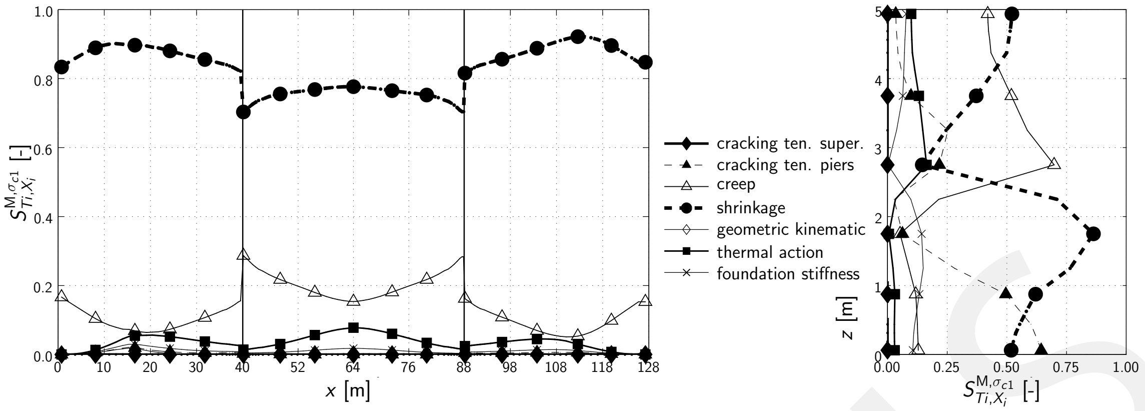

(a) serviceability limit state, $H^1 = 5\,\mathrm{m}$

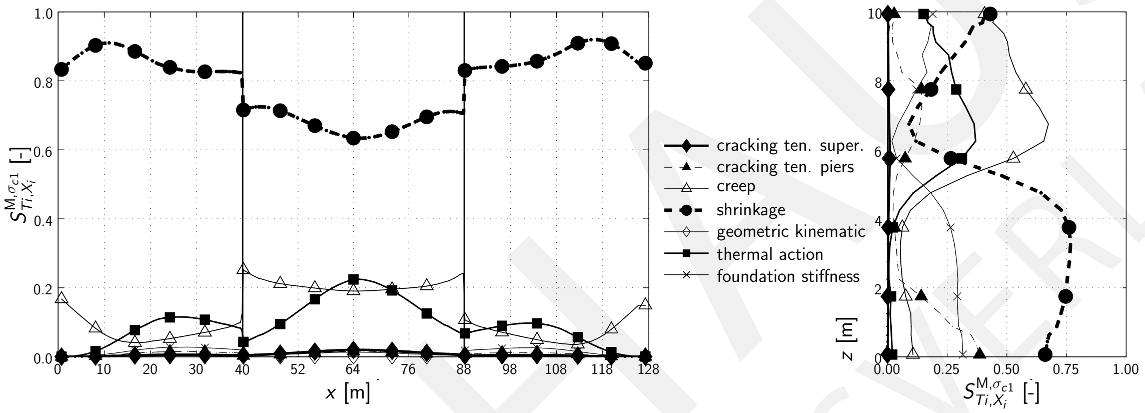

(b) serviceability limit state, $H^2 = 10\,\mathrm{m}$

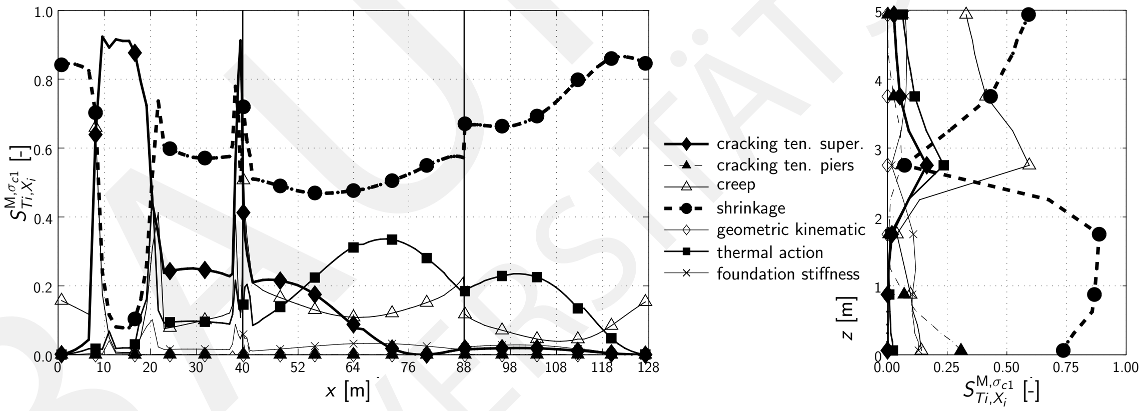

(c) ultimate limit state, $H^1 = 5\,\mathrm{m}$

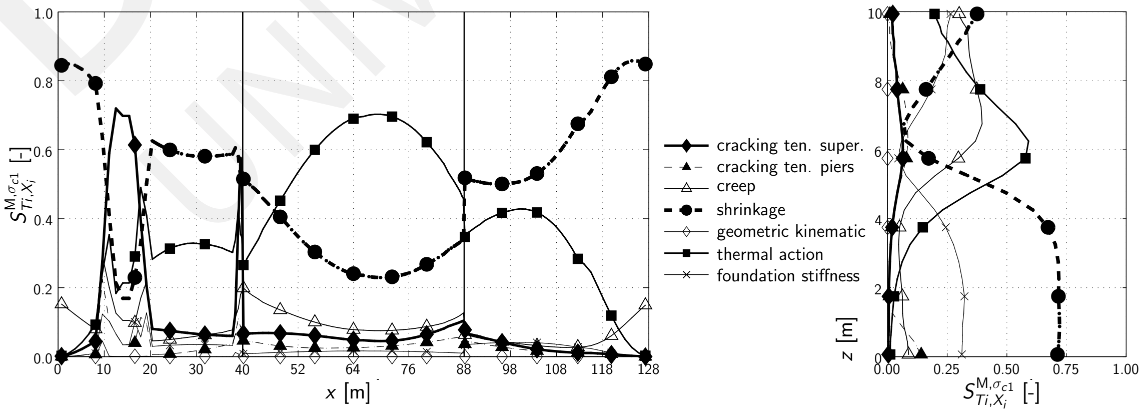

(d) ultimate limit state, $H^2 = 10\,\mathrm{m}$

Figure C.1: Total-effects sensitivity index $S^{M,\sigma_{c1}}_{Ti,X_i}$ for concrete stress at top level of the box girder σ_{c1} with respect to position x at superstructure (left side), and bridge pier outside at axis B (ride side)

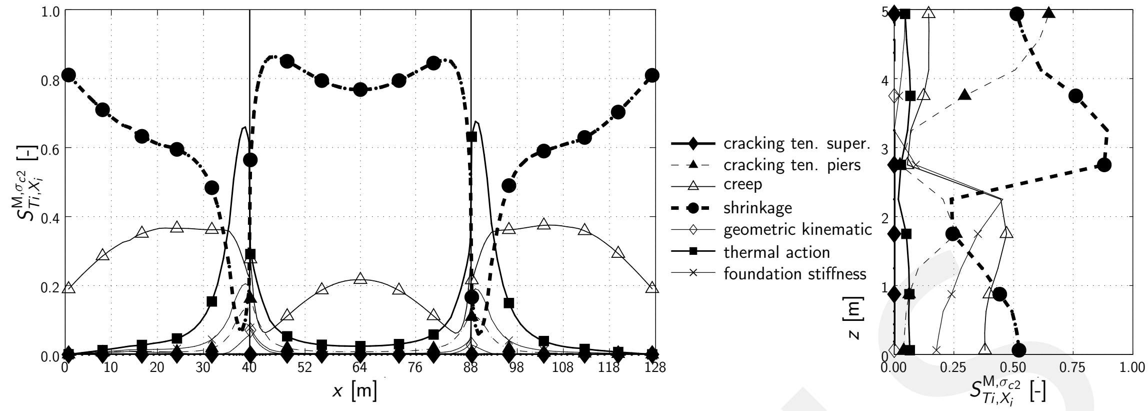

(a) serviceability limit state, $H^1 = 5\,\mathrm{m}$

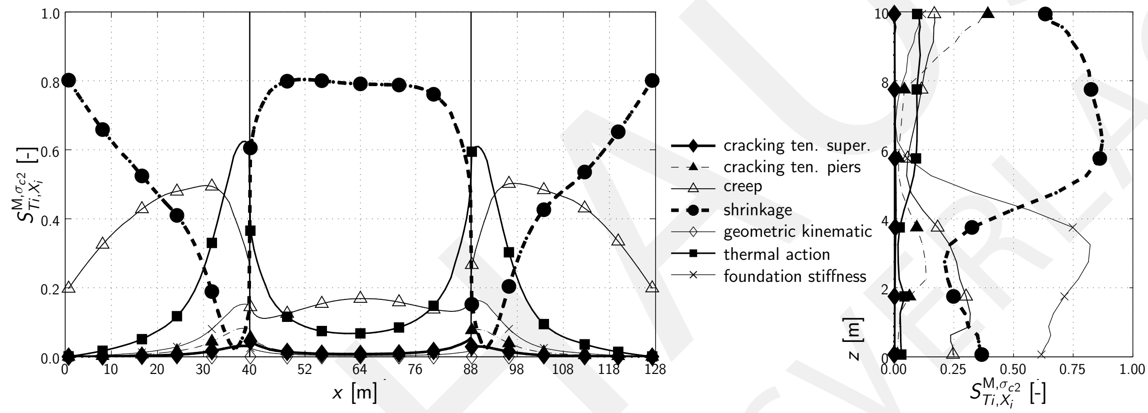

(b) serviceability limit state, $H^2 = 10\,\mathrm{m}$

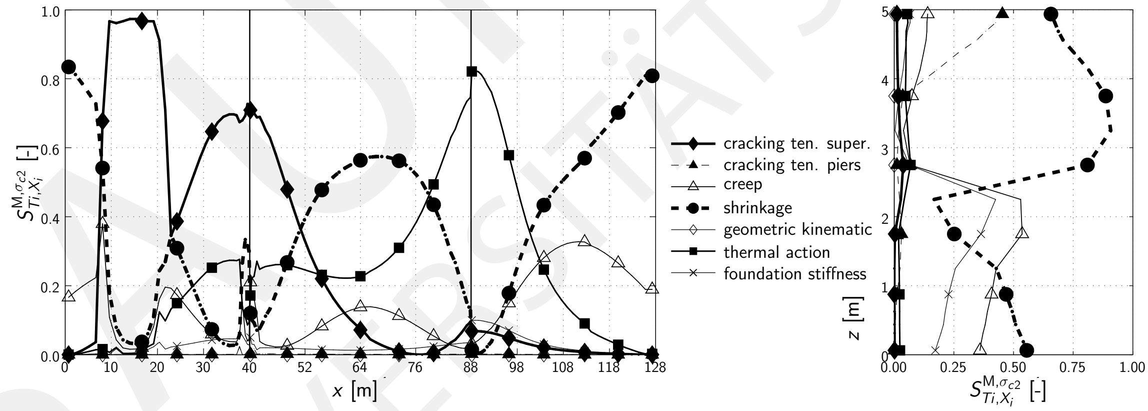

(c) ultimate limit state, $H^1 = 5\,\mathrm{m}$

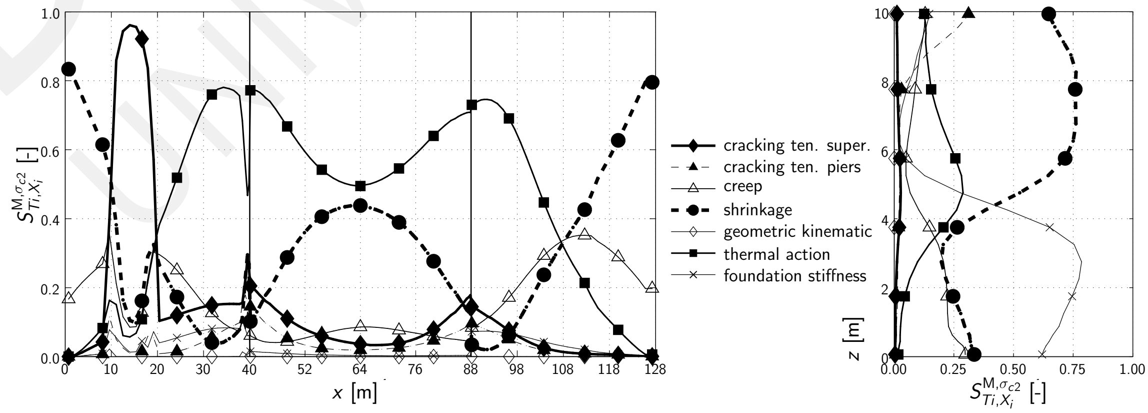

(d) ultimate limit state, $H^2 = 10\,\mathrm{m}$

Figure C.2: Total-effects sensitivity index $S^{\mathrm{M},\sigma_{c2}}_{Ti,X_i}$ for concrete stress at bottom level of the box girder σ_{c2} with respect to position x at superstructure (left side), and bridge pier inner side at axis B (ride side)

BAUHAUS
UNIVERSITÄTSVERLAG

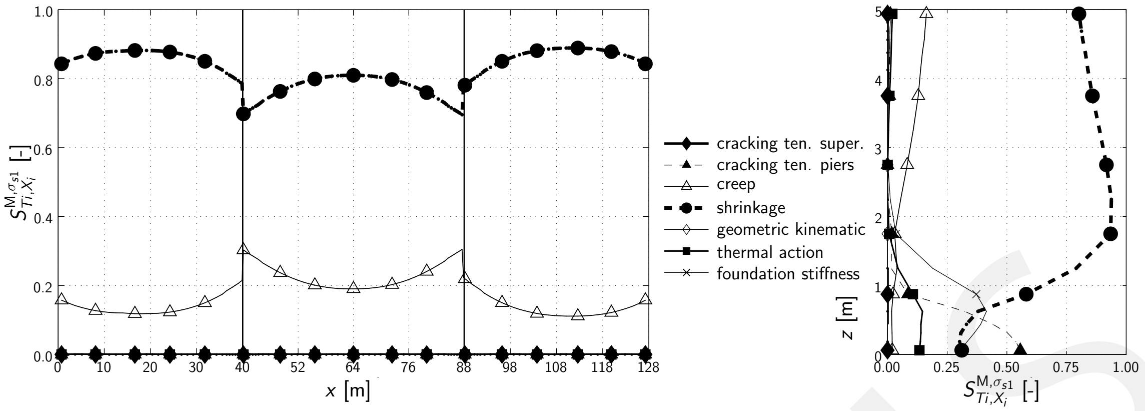

(a) serviceability limit state, $H^1 = 5\,\mathrm{m}$

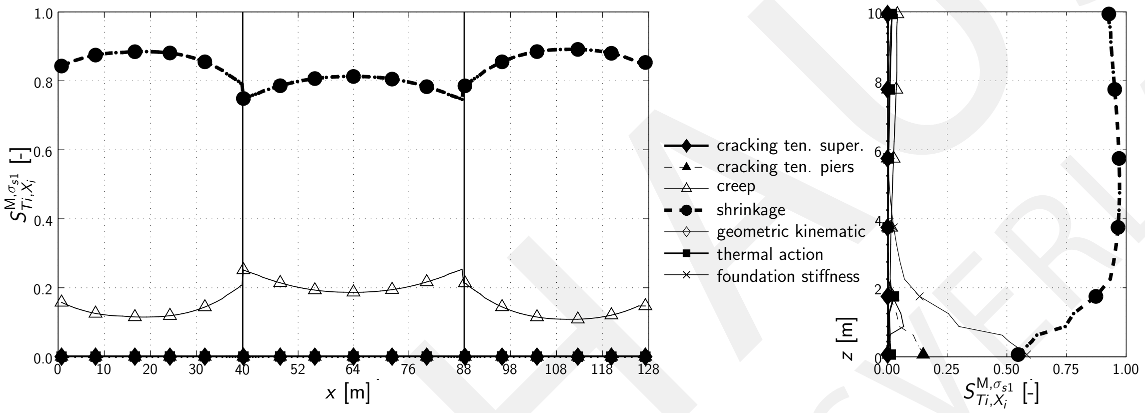

(b) serviceability limit state, $H^2 = 10\,\mathrm{m}$

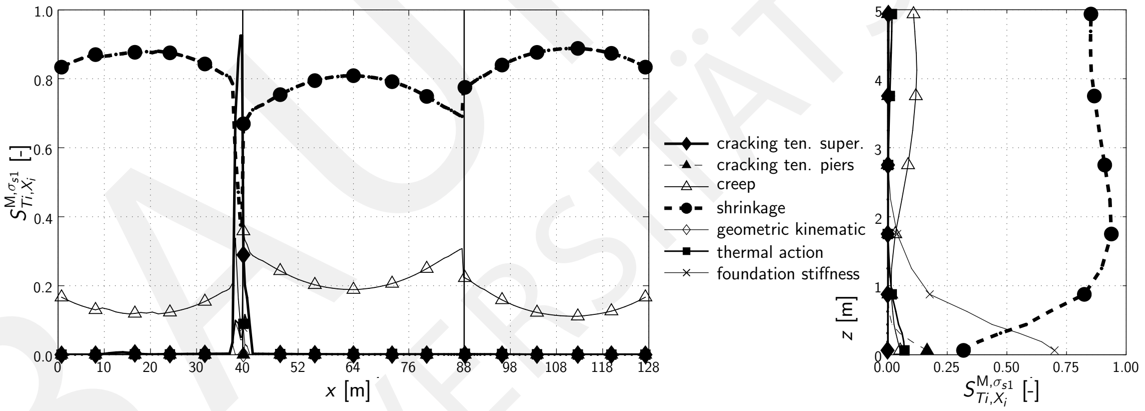

(c) ultimate limit state, $H^1 = 5\,\mathrm{m}$

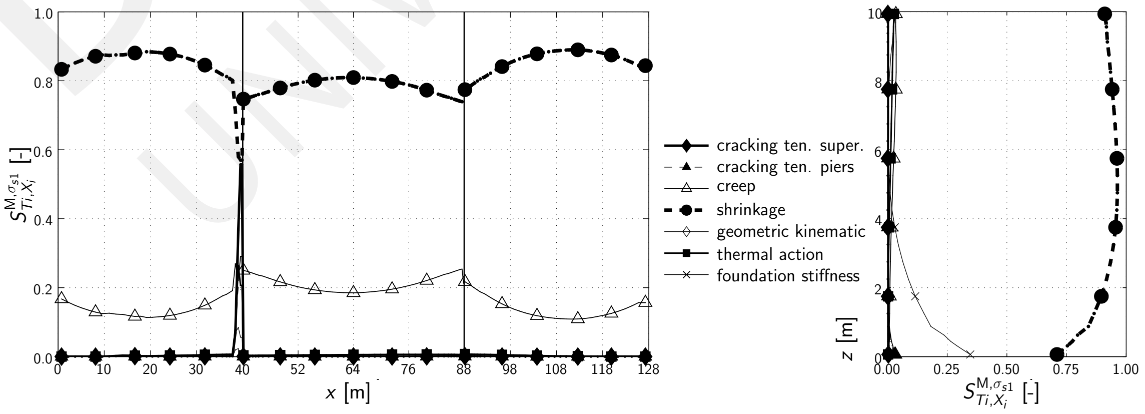

(d) ultimate limit state, $H^2 = 10\,\mathrm{m}$

Figure C.3: Total-effects sensitivity index $S_{Ti,X_i}^{M,\sigma_{s1}}$ for reinforcement stress at top level of the box girder σ_{s1} with respect to position x at superstructure (left side), and bridge pier outside at axis B (ride side)

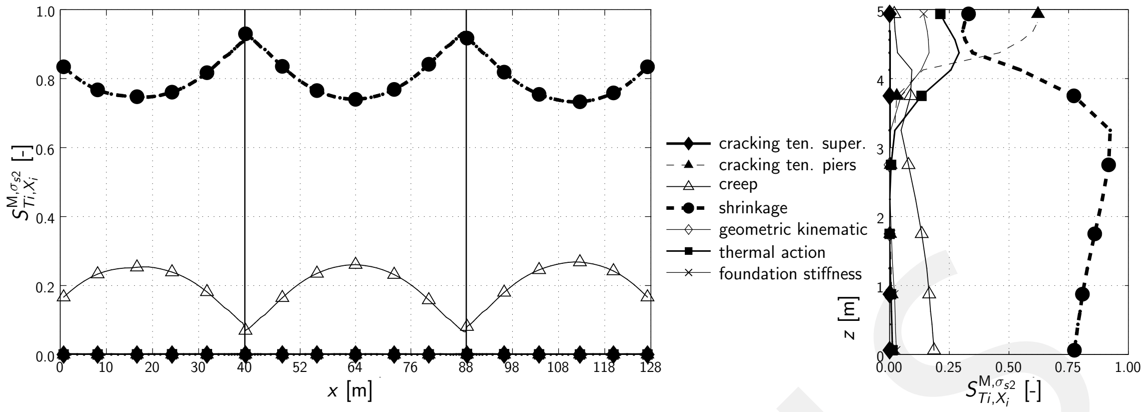

(a) serviceability limit state, $H^1 = 5\,\mathrm{m}$

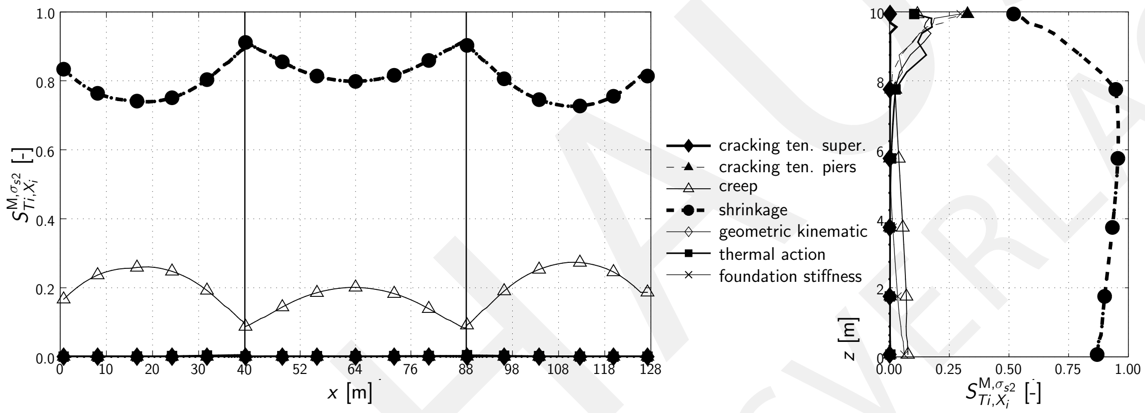

(b) serviceability limit state, $H^2 = 10\,\mathrm{m}$

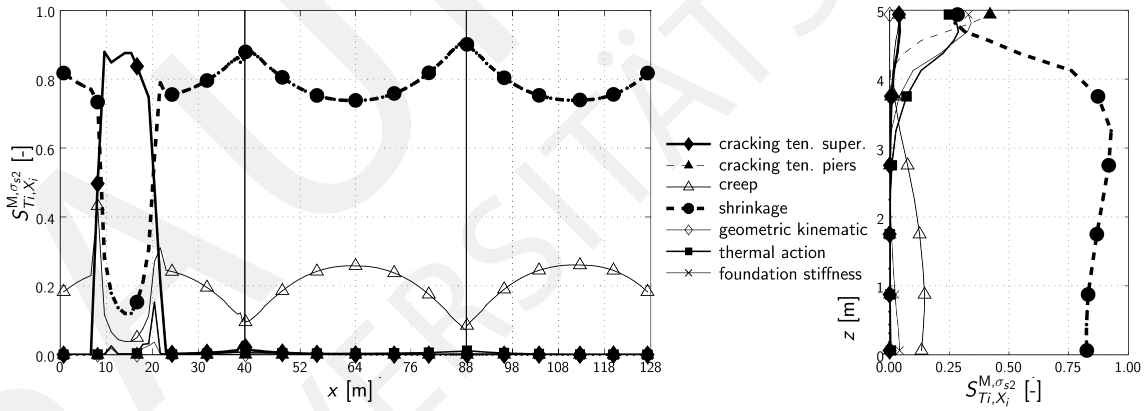

(c) ultimate limit state, $H^1 = 5\,\mathrm{m}$

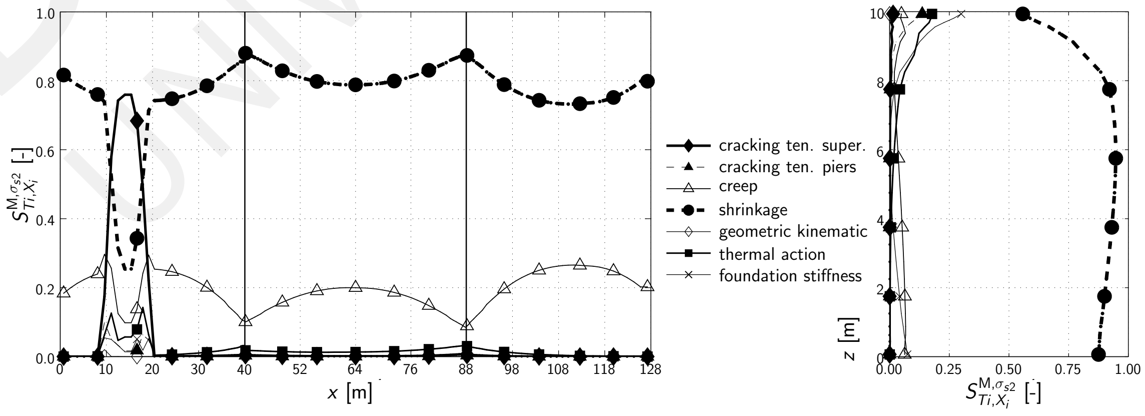

(d) ultimate limit state, $H^2 = 10\,\mathrm{m}$

Figure C.4: Total-effects sensitivity index $S^{M,\sigma_{s2}}_{Ti,X_i}$ for reinforcement stress at bottom level of the box girder σ_{s2} with respect to position x at superstructure (left side), and bridge pier inner side at axis B (ride side)

BAUHAUS
UNIVERSITÄTSVERLAG

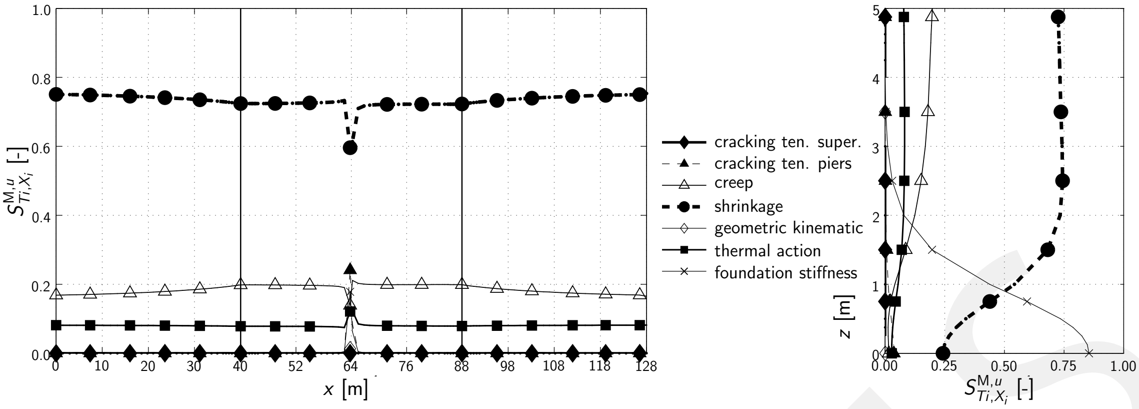

(a) serviceability limit state, $H^1 = 5\,\mathrm{m}$

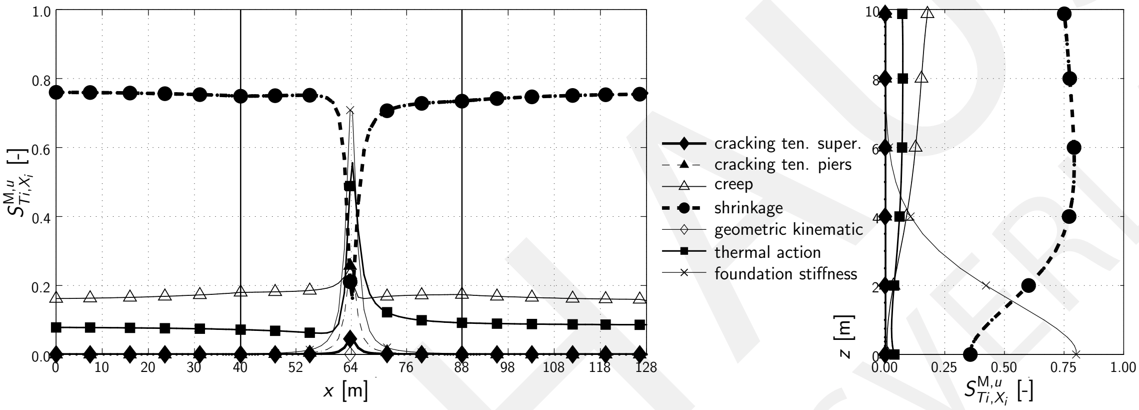

(b) serviceability limit state, $H^2 = 10\,\mathrm{m}$

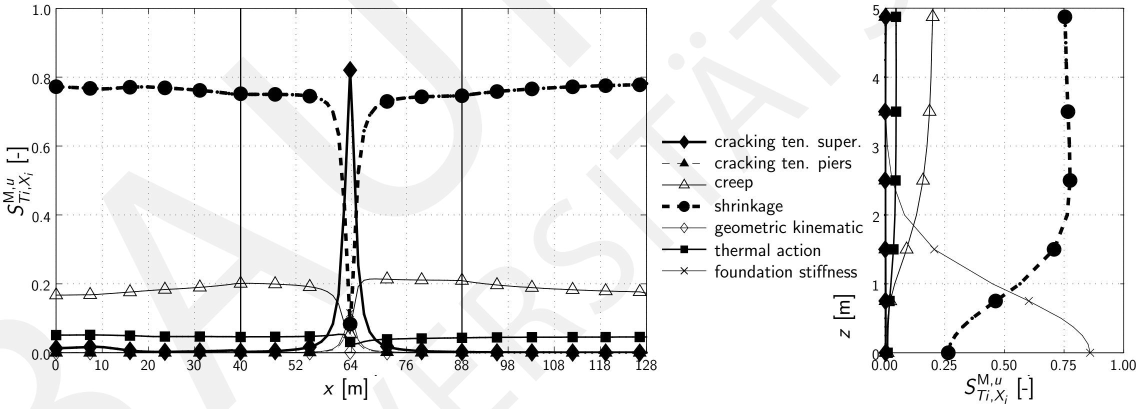

(c) ultimate limit state, $H^1 = 5\,\mathrm{m}$

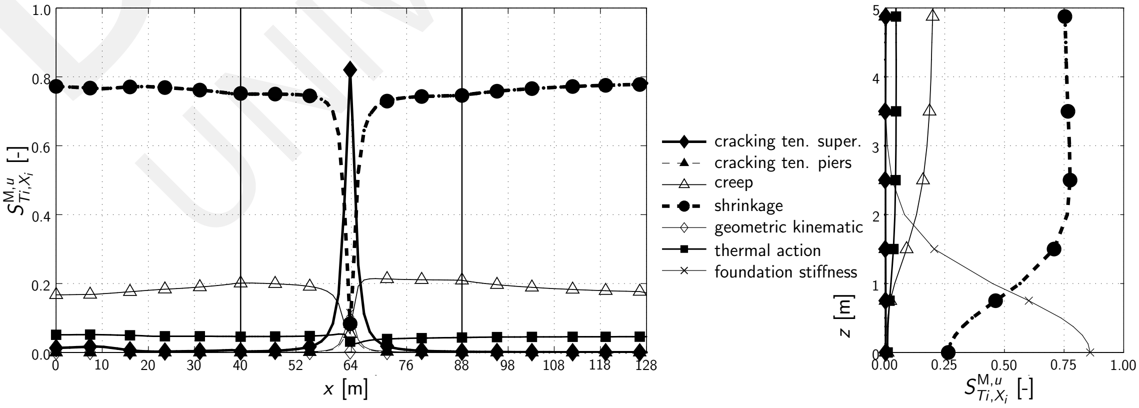

(d) ultimate limit state, $H^2 = 10\,\mathrm{m}$

Figure C.5: Total-effects sensitivity index $S^{\mathrm{M},u}_{Ti,X_i}$ for horizontal displacement u with respect to position x at superstructure (left side), and bridge pier at axis B (ride side)

BAUHAUS
UNIVERSITÄTSVERLAG

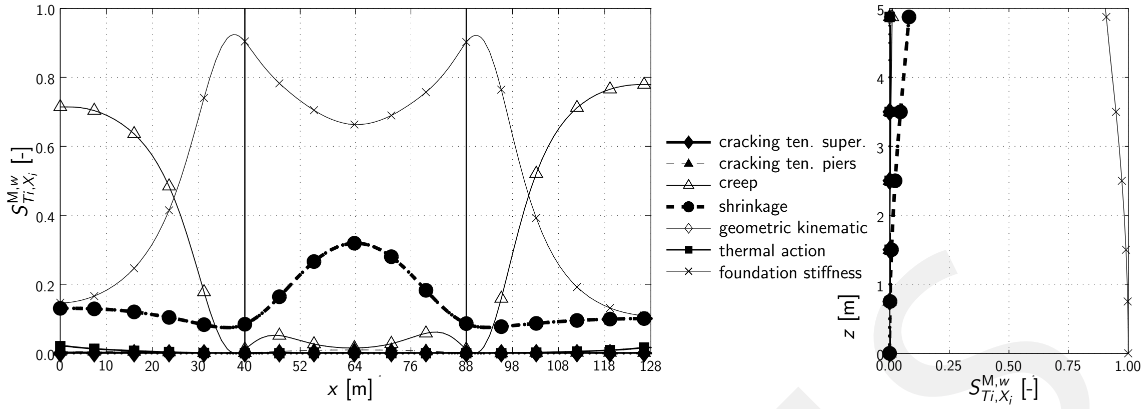

(a) serviceability limit state, $H^1 = 5\,\mathrm{m}$

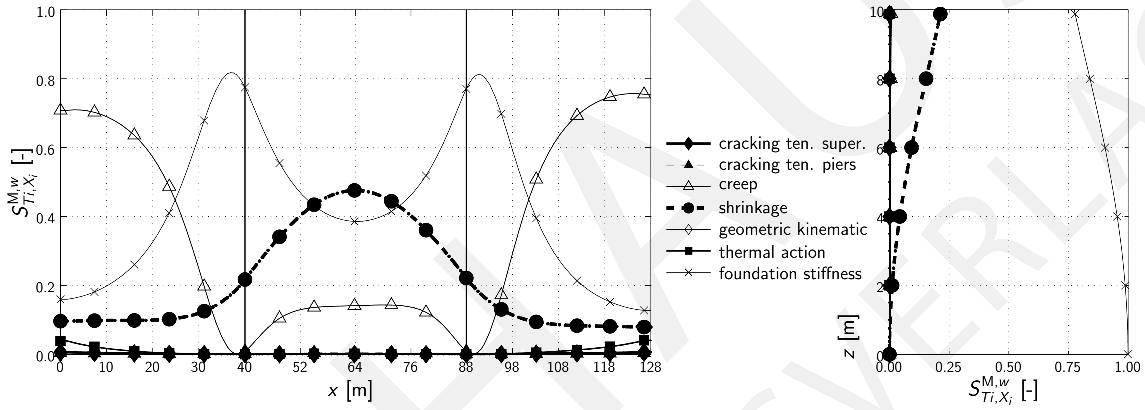

(b) serviceability limit state, $H^2 = 10\,\mathrm{m}$

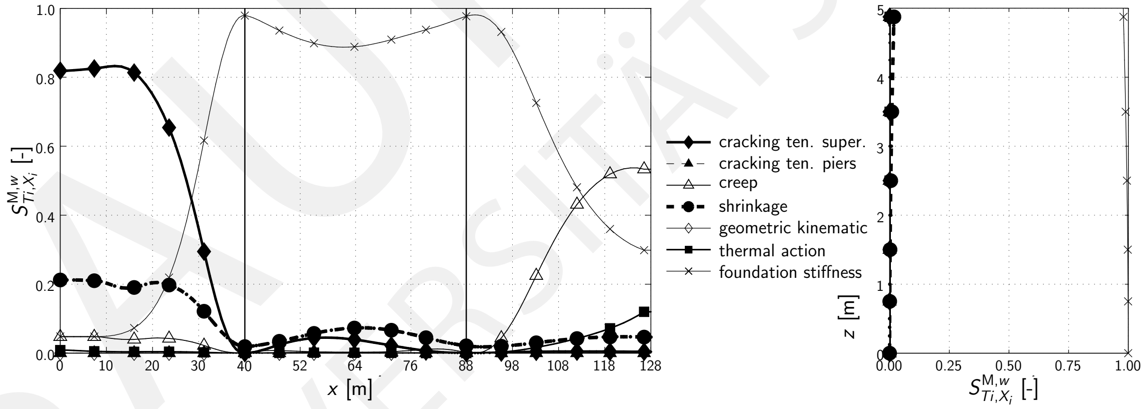

(c) ultimate limit state, $H^1 = 5\,\mathrm{m}$

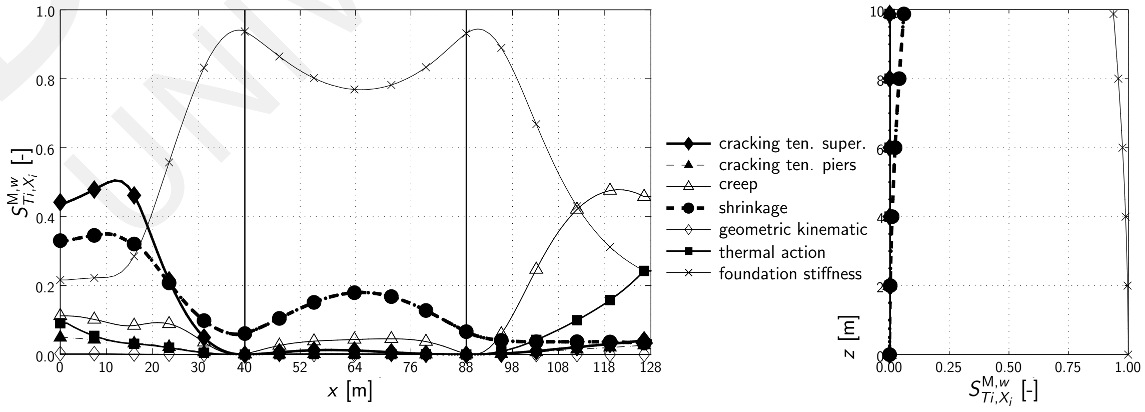

(d) ultimate limit state, $H^2 = 10\,\mathrm{m}$

Figure C.6: Total-effects sensitivity index $S^{M,w}_{Ti,X_i}$ for vertical displacement w with respect to position x at superstructure (left side), and bridge pier at axis B (ride side)

Table C.1: Integrative sensitivity indices $\overline{S}^{M,Y}_{Ti,X_i}$ for semi-integral concrete bridge with pier height $H_1 = 5\,\mathrm{m}$ in serviceability limit state (SLS) and ultimate limit state (ULS), 7 model classes considered, foundation stiffness additionally modelled

Limit state	Model Class	Integrative Sensitivity Index $\overline{S}^{M,Y}_{Ti,X_i}$ for several Structural Response Values Y						
		u	w	σ_{c1}	σ_{c2}	σ_p	σ_{s1}	σ_{s2}
SLS	cracking tension superstructure	0.00	0.00	0.00	0.00	0.00	0.00	0.00
	cracking tension piers	0.00	0.00	0.01	0.02	0.00	0.00	0.00
	creep	0.18	0.07	0.16	0.27	0.21	0.17	0.20
	shrinkage	0.74	0.17	0.80	0.65	0.79	0.83	0.80
	geometric kinematic	0.00	0.00	0.00	0.00	0.00	0.00	0.00
	thermal action	0.08	0.00	0.04	0.08	0.00	0.00	0.00
	foundation stiffness	0.00	0.75	0.02	0.03	0.00	0.00	0.00
ULS	cracking tension superstructure	0.01	0.28	0.20	0.29	0.10	0.01	0.06
	cracking tension piers	0.00	0.00	0.00	0.01	0.00	0.00	0.00
	creep	0.18	0.07	0.13	0.12	0.21	0.17	0.18
	shrinkage	0.76	0.10	0.56	0.29	0.72	0.82	0.76
	geometric kinematic	0.00	0.00	0.00	0.00	0.00	0.00	0.00
	thermal action	0.05	0.01	0.16	0.32	0.01	0.00	0.01
	foundation stiffness	0.00	0.58	0.03	0.05	0.00	0.01	0.00

BAUHAUS
UNIVERSITÄTSVERLAG

Table C.2: Integrative sensitivity indices $\overline{S}^{M,Y}_{Ti,X_i}$ for semi-integral concrete bridge with pier height $H_2 = 10\,\text{m}$ in serviceability limit state (SLS) and ultimate limit state (ULS), 7 model classes considered, foundation stiffness additionally modelled

Limit state	Model Class	Integrative Sensitivity Index $\overline{S}^{M,Y}_{Ti,X_i}$ for several Structural Response Values Y						
		u	w	σ_{c1}	σ_{c2}	σ_p	σ_{s1}	σ_{s2}
SLS	cracking tension superstructure	0.00	0.00	0.01	0.01	0.00	0.00	0.00
	cracking tension piers	0.00	0.00	0.01	0.02	0.00	0.00	0.00
	creep	0.16	0.13	0.15	0.32	0.20	0.15	0.18
	shrinkage	0.75	0.30	0.75	0.54	0.80	0.84	0.81
	geometric kinematic	0.00	0.00	0.00	0.00	0.00	0.00	0.00
	thermal action	0.08	0.00	0.10	0.14	0.00	0.00	0.00
	foundation stiffness	0.01	0.57	0.03	0.05	0.00	0.00	0.00
ULS	cracking tension superstructure	0.00	0.10	0.10	0.10	0.05	0.00	0.03
	cracking tension piers	0.00	0.01	0.03	0.06	0.01	0.00	0.00
	creep	0.17	0.09	0.10	0.13	0.20	0.15	0.17
	shrinkage	0.76	0.14	0.47	0.26	0.76	0.84	0.79
	geometric kinematic	0.00	0.00	0.00	0.00	0.00	0.00	0.00
	thermal action	0.05	0.02	0.36	0.52	0.01	0.01	0.02
	foundation stiffness	0.02	0.69	0.07	0.10	0.00	0.01	0.01

C.2 Semi-integral concrete bridges neglecting foundation stiffness

Table C.3: Integrative sensitivity indices $\overline{S}^{M,Y}_{Ti,X_i}$ for semi-integral concrete bridge with pier height $H_1 = 5\,\text{m}$ in serviceability limit state (SLS) and ultimate limit state (ULS), 6 model classes considered, foundation stiffness neglected

Limit state	Model Class	Integrative Sensitivity Index $\overline{S}^{M,Y}_{Ti,X_i}$ for several Structural Response Values Y						
		u	w	σ_{c1}	σ_{c2}	σ_p	σ_{s1}	σ_{s2}
SLS	cracking tension superstructure	0.00	0.00	0.00	0.00	0.00	0.00	0.00
	cracking tension piers	0.01	0.04	0.01	0.03	0.01	0.01	0.01
	creep	0.16	0.79	0.14	0.31	0.19	0.15	0.18
	shrinkage	0.77	0.21	0.83	0.64	0.81	0.85	0.82
	geometric kinematic	0.01	0.04	0.00	0.01	0.01	0.01	0.01
	thermal action	0.07	0.05	0.04	0.08	0.01	0.01	0.01
ULS	cracking tension superstructure	0.01	0.51	0.20	0.28	0.10	0.01	0.06
	cracking tension piers	0.00	0.00	0.01	0.01	0.00	0.00	0.00
	creep	0.17	0.19	0.12	0.14	0.19	0.16	0.17
	shrinkage	0.78	0.37	0.60	0.31	0.74	0.84	0.78
	geometric kinematic	0.00	0.00	0.00	0.00	0.00	0.00	0.00
	thermal action	0.04	0.02	0.16	0.34	0.01	0.01	0.01

Table C.4: Integrative sensitivity indices $\overline{S}^{M,Y}_{Ti,X_i}$ for semi-integral concrete bridge with pier height $H_2 = 10\,\text{m}$ in serviceability limit state (SLS) and ultimate limit state (ULS), 6 model classes considered, foundation stiffness neglected

Limit state	Model Class	Integrative Sensitivity Index $\overline{S}^{M,Y}_{Ti,X_i}$ for several Structural Response Values Y						
		u	w	σ_{c1}	σ_{c2}	σ_p	σ_{s1}	σ_{s2}
SLS	cracking tension superstructure	0.00	0.00	0.00	0.00	0.00	0.00	0.00
	cracking tension piers	0.00	0.01	0.01	0.03	0.00	0.00	0.00
	creep	0.17	0.31	0.16	0.35	0.20	0.15	0.19
	shrinkage	0.75	0.69	0.81	0.59	0.80	0.85	0.81
	geometric kinematic	0.00	0.00	0.00	0.00	0.00	0.00	0.00
	thermal action	0.08	0.00	0.04	0.08	0.00	0.00	0.00
ULS	cracking tension superstructure	0.00	0.19	0.08	0.09	0.05	0.00	0.03
	cracking tension piers	0.00	0.00	0.01	0.01	0.00	0.00	0.00
	creep	0.17	0.31	0.14	0.21	0.21	0.15	0.18
	shrinkage	0.78	0.58	0.64	0.39	0.77	0.85	0.80
	geometric kinematic	0.00	0.00	0.00	0.00	0.00	0.00	0.00
	thermal action	0.05	0.02	0.20	0.39	0.01	0.00	0.01

BAUHAUS
UNIVERSITÄTSVERLAG

C.3 Concrete girder bridge

Table C.5: Integrative sensitivity indices $\overline{S}_{Ti,X_i}^{M,Y}$ for concrete girder bridge in serviceability limit state (SLS) and ultimate limit state (ULS)

Limit state	Model Class	Integrative Sensitivity Index $\overline{S}_{Ti,X_i}^{M,Y}$ for several Structural Response Values Y						
		u	w	σ_{c1}	σ_{c2}	σ_p	σ_{s1}	σ_{s2}
SLS	cracking tension superstructure	0.00	0.00	0.00	0.00	0.00	0.00	0.00
	creep	0.17	0.82	0.14	0.31	0.21	0.18	0.21
	shrinkage	0.75	0.16	0.84	0.62	0.79	0.82	0.79
	geometric kinematic	0.00	0.00	0.00	0.00	0.00	0.00	0.00
	thermal action	0.08	0.02	0.03	0.10	0.00	0.00	0.00
ULS	cracking tension superstructure	0.00	0.68	0.24	0.35	0.11	0.01	0.07
	creep	0.17	0.21	0.09	0.09	0.20	0.17	0.19
	shrinkage	0.75	0.17	0.57	0.21	0.71	0.82	0.76
	geometric kinematic	0.00	0.00	0.00	0.00	0.00	0.00	0.00
	thermal action	0.08	0.03	0.16	0.40	0.00	0.00	0.01